Quantum Thermal Machines

PhD program

Nanoscience

Academic year

2019/2020

Scuola Normale Superiore

Candidate

Paolo Andrea Erdman

Supervisors

Dr. Fabio Taddei

Prof. Rosario Fazio

Except where acknowledged in the customary manner, the material presented in this thesis is, to the best of my knowledge, original and has not been submitted in whole or part for a degree in any university.

Paolo Andrea Erdman

Acknowledgements

First of all, I wish to thank my supervisors Dr. Fabio Taddei and Prof. Rosario Fazio which constantly guided me through my PhD and who gave me the possibility to work on interesting topics. Besides always finding the time - and patience - to discuss with me and help me out, I would like to thank Dr. Fabio Taddei for his friendliness and positiveness, and Prof. Rosario Fazio for his irony and for his abundance of ideas and connections no matter what is the subject. A special thanks goes to Prof. Vittorio Giovannetti, who taught me everything I know about quantum information, and with whom I had numerous great discussions. I am also very grateful to Prof. Jukka Pekola for welcoming and making me feel part of his research group at the Aalto University. I wish to thank him for teaching me so many things about experimental and theoretical aspects of his research, and for his cheerful and positive attitude. I also thank Prof. Marco Polini for his lessons and his fervor in science, and Prof. Stefano Roddaro, Dr. Francesco Rossella and Domenic for their passion for experimental physics and for teaching me a lot about their experiments. A special thanks goes to Dr.ssa Antonella De Pasquale for various scientific and personal discussions and for her altruistic kindness.

These years spent in Pisa would not have been the same without all of the other PhD students of the condensed matter theory group, which I wish to thank especially for their friendship and moments spent together, and for the various and useful scientific discussions. A special thanks goes to Marcello, for his great friendship, for his interesting opinions, and for his unsettling irony; to Bibek for being a great friend, collaborator and travel companion; to Vasco for his positiveness and friendliness, for the great collaborations, and for the numerous physical fights in front of the blackboard; to Salvatore for his strong dedication, his energy bursts and for being a worthy table soccer opponent; to Pietro for his apparent calmness, his deep reflection, and for being a worthy comrade at table soccer; to Gianmichele for his unconventional irony, and for putting up with the continuous invasions of his office; to Chessa for being a worthy table soccer opponent and for his time-independent mood and irony; to Farzad for his contagious positivity, and for never declining to go out; to Fanizza for his patience in listening, and for his mysterious happiness; to Luis for his energetic and enthusiastic approach to life and science; to Cusumano for being *the* comrade, to Yu for her kindness and cheerful mood; to Donato and Ashkan for the positive atmosphere we had within our shared office; to Belliardo for his unconventional thoughts; to Hari and Johannes for their positiveness; to Max for his carefully critic opinions.

I also wish to thank all the nice people I met during my stay in Helsinki, who taught me many things about experiments and theory, and who made me feel at home in a foreign country. A special thanks goes to Olivier, Jorden, Elsa, Bayan, Camilla, Paul, Elina, Joonas, Libin, Marco, Diego, Leila, Azat, Dima, Bivas, George, Rishabh and Florian.

I am also very grateful to the many other people I've met during these years at the Scuola Normale, to my flatmates, to my friends in my home-town, and to the "spezia gang". They have all contributed to supporting me during these four years.

Last but not least, I wish to say a very special thanks to Camilla, who has always encouraged me and with whom I visited so many interesting places, and to my parents and family, who have always unconditionally supported me in everything I did.

List of publications

- **P. A. Erdman**, F. Mazza, R. Bosisio, G. Benenti, R. Fazio, and F. Taddei
  Thermoelectric properties of an interacting quantum dot based heat engine
  Phys. Rev. B **95**, 245432 (2017).

- B. Bhandari, G. Chiriacò, **P. A. Erdman**, R. Fazio, and F. Taddei
  Thermal drag in electronic conductors
  Phys. Rev. B **98**, 035415 (2018).

- **P. A. Erdman**, B. Bhandari, R. Fazio, J. P. Pekola, and F. Taddei
  Absorption refrigerators based on Coulomb-coupled single-electron systems
  Phys. Rev. B **98**, 045433 (2018).

- B. Dutta, D. Majidi, A. G. Corral, **P. A. Erdman**, S. Florens, T. A. Costi, H. Courtois, and C. B. Winkelmann
  Direct probe of the Seebeck coefficient in a Kondo-correlated single-quantum-dot transistor
  Nano Lett. **19**, 506 (2018).

- D. Prete, **P. A. Erdman**, V. Demontis, V. Zannier, D. Ercolani, L. Sorba, F. Beltram, F. Rossella, F. Taddei, and S. Roddaro
  Thermoelectric Conversion at 30 K in InAs/InP Nanowire Quantum Dots
  Nano Lett. **19**, 3033 (2019).

- **P. A. Erdman**, J. T. Peltonen, B. Bhandari, B. Dutta, H. Courtois, R. Fazio, F. Taddei, and J. P. Pekola
  Nonlinear thermovoltage in a single-electron transistor
  Phys. Rev. B **99**, 165405 (2019).

- O. Maillet, **P. A. Erdman**, V. Cavina, B. Bhandari, E. T. Mannila, J. T. Peltonen, A. Mari, F. Taddei, C. Jarzynski, V. Giovannetti, and J. P. Pekola
  Optimal Probabilistic Work Extraction beyond the Free Energy Difference with a Single-Electron Device, Editors' Suggestion
  Phys. Rev. Lett. **122**, 150604 (2019).

- **P. A. Erdman**, V. Cavina, R. Fazio, F. Taddei, and V. Giovannetti
  Maximum power and corresponding efficiency for two-level heat engines and refrigerators: optimality of fast cycles
  New J. Phys. **21**, 103049 (2019).

- **P. A. Erdman**, F. Taddei, J. T. Peltonen, R. Fazio, and J. P. Pekola
  Fast and accurate Cooper pair pump, Editors' Suggestion
  Phys. Rev. B **100**, 235428 (2019).

- V. Cavina, **P. A. Erdman**, P. Abiuso, L. Tolomeo, and V. Giovannetti
  Maximum power heat engines and refrigerators in the fast-driving regime
  In preparation (2020).

- B. Bhandari, **P. A. Erdman**, R. Fazio, E. Paladino, and F. Taddei
  Heat rectification in low-dimensional quantum systems
  In preparation (2020).

Contents

Acknowledgements **v**

List of publications **vii**

1 Introduction **1**

2 Open quantum systems **5**
2.1 Weak-coupling regime 6
2.2 Beyond the weak-coupling regime 11

3 Quantum thermal machines **13**
3.1 Thermoelectric machines 13
3.2 Driven thermal machines 25

4 Thermoelectric properties of an interacting quantum dot-based heat engine **33**
4.1 Multi-level interacting QD 35
4.2 Linear response regime 41
4.3 Non-linear response 54
4.4 Summary 62

5 Thermoelectric conversion at 30 K in InAs/InP nanowire quantum dots **65**
5.1 Setup and measurements 66
5.2 Theoretical model and heat engine analysis 69
5.3 Summary 72

6 Non-linear thermovoltage in a single-electron transistor **73**
6.1 Experimental setup 74
6.2 Model 75
6.3 Results 76
6.4 Summary 79

7 Absorption refrigerators based on Coulomb-coupled single-electron systems **81**
7.1 Ideal setup 82
7.2 Optimal rates for cooling power and COP 83
7.3 Experimental proposals 86
7.4 Maxwell demon: mutual information flow 90
7.5 Summary 91

8 Heat rectification through a qubit **93**
8.1 Model . . . 95
8.2 Heat current and rectification . . . 97
8.3 Weak coupling regime . . . 98
8.4 Beyond weak coupling regime . . . 104
8.5 Summary . . . 111

9 Maximum power and corresponding efficiency for two-level heat engines and refrigerators: optimality of fast cycles **113**
9.1 Maximum power . . . 115
9.2 Heat engine mode [E] . . . 117
9.3 Refrigerator mode [R] . . . 119
9.4 Thermal accelerator [A] and heater [H] modes . . . 120
9.5 Finite-time corrections . . . 121
9.6 Summary . . . 121

10 Maximum power heat engines and refrigerators in the fast-driving regime **123**
10.1 The model . . . 125
10.2 Fast driving regime . . . 128
10.3 Simple relaxation case . . . 134
10.4 Case study: a qutrit heat engine . . . 139
10.5 Summary . . . 142

11 Conclusions **145**

A Appendix: thermoelectric properties of an interacting quantum dot-based heat engine **147**
A.1 The Pauli master equation always allows a non-trivial solution. . . . 147
A.2 The PDBEs are not consistent in general . . . 148
A.3 Conditions of validity of the linearized PDBEs . . . 149
A.4 Non-interacting QD: Non-linear effects . . . 155

B Appendix: Thermoelectric conversion at 30 K in InAs/InP nanowire quantum dots **161**
B.1 Materials and methods . . . 161
B.2 Measurement setup circuit . . . 162
B.3 Thermometer and heater calibration . . . 163
B.4 Quantum dot characterization . . . 164
B.5 Theoretical model . . . 166
B.6 Parameter estimation . . . 167

C Appendix: Non-linear thermovoltage in a single-electron transistor **169**
C.1 Computing charge and heat currents . . . 169

D Appendix: Absorption refrigerators based on Coulomb-coupled single-electron systems **175**
D.1 Pauli equation . . . 175
D.2 Optimal rates for cooling power and COP . . . 176
D.3 Derivation of the master equation for the system with three QDs . . . 176

D.4 Heat currents in the system with metallic islands 178

E Appendix: Heat rectification in low-dimensional quantum systems 179
E.1 Most Generic System-Bath Coupling 179
E.2 Rectification in the weak coupling regime 179
E.3 Tunneling Rates 180
E.4 Tunneling Rates in Specific Models 181
E.5 Thermal Averages 183
E.6 Lamb shift 184
E.7 Co-tunneling calculation 185
E.8 Non equilibrium Green's function calculation 187
E.9 Exact calculation 191

F Appendix: Maximum power and corresponding efficiency for two-level heat engines and refrigerators: optimality of fast cycles 195
F.1 Optimality of infinitesimal Otto cycles 195
F.2 Maximum power formula and finite-time corrections 197
F.3 Efficiency at maximum power 201
F.4 COP at maximum power 203

G Appendix: Maximum power heat engines and refrigerators in the fast-driving regime 207
G.1 Projected form of the ME 207
G.2 Asymptotic solutions of the fast periodically driven ME 212
G.3 Selection of the infinitesimal protocol 214
G.4 One control per temperature is sufficient for positive GAPs 217
G.5 Power of many interacting qubits 219
G.6 Qutrit model 221

References 223

1 Introduction

The search for ways to free humankind from manual work dates back to the 4^{th} millennium B.C., when mankind was using animals for traction and transport [1]. The first water wheels were developed around two thousand years ago, and the first windmills around one thousand years ago. Yet, it was not until the industrial revolution in the 18^{th} and 19^{th} century that mankind completely switched from relying on human workforce to mechanical work produced by heat engines powered by the combustion of wood and fossil fuels. By exploiting macroscopic objects with moving parts, such as turbines, we can now extract useful work from temperature differences. This revolution led to the birth of thermodynamics, which mainly deals with large macroscopic objects which are close to thermal equilibrium.

The massive increase of CO_2 emissions caused by the combustion of fossil fuels is destroying our ecosystems and posing a threat to our survival [2]. It is therefore ever more important to find alternative and efficient sources of energy. Among the many possibilities that are currently being explored, the interest of the scientific community in thermoelectricity has witnessed a large growth thanks to pioneering works that pointed to the possibility of developing small scale thermoelectric heat engines which are highly efficient and free from moving parts [3–5]. Thermoelectric devices could potentially be used to recover waste heat from all those activities which produce heat as a byproduct, ranging from most conventional engines (such as car engines), to industrial processes and to most kinds of power-plants. Thermoelectricity in low dimensional systems may also find applications in heat management at the nanoscale [6], which is becoming a problematic issue because of the ongoing miniaturization of electronic components (such as computing processors), and to perform on-chip active cooling [7].

The thermoelectric effect, which consists of the generation of a charge current or of a voltage bias across some material as a consequence of a temperature difference, was first observed by A. Volta [8], and the first actual experiment was conducted by T. J. Seebeck in 1822 [9]. Studies of the thermoelectric effect advanced in the 1950s thanks to Ioffe [10]: the role of doped semiconductors as good thermoelectric materials was understood and the Bi_2Te_3 compound was developed for commercialization. Nowadays, thermoelectric devices are commercially available, yet their efficiency is low compared to traditional heat engines relying on moving parts [11]. In the 90s, thanks to the pioneering works of Dresselhaus [3, 4]

and of Mahan and Sofo [5], it was realized that strongly confined low dimensional systems may yield highly efficient heat-to-work conversion. These systems, such as quantum dots, require a quantum description and are typically described by few degrees of freedom. These systems are profoundly different compared to the macroscopic objects that were considered when the field of thermodynamics was born. Indeed, thermodynamics was developed to deal with systems (such as gases and liquids) that are typically composed of an Avogadro number of particles (order 10^{23}); therefore, these systems are always near thermal equilibrium with negligible fluctuations, allowing us to describe such complicated many-body systems in terms of few macroscopic state variables, such as volume, pressure and temperature. This is a striking simplification compared to attempting to solve the classical dynamics of 10^{23} interacting particles.

Conversely, recent tremendous advances in nanofabrication techniques have enabled unprecedented control of quantum systems down to the single particle level. Now, experiments involving few quantum particles or degrees of freedom can be carried out in a variety of platforms, ranging from trapped ions [12, 13], to electron spins associated with nitrogen-vacancy centers [14], to circuit quantum electrodynamics [15], to single-electron transistors [16]. We are now at the point that it is possible to fabricate devices which behave as qubits, i.e. the smallest possible quantum system characterized only by two states, and couple them to thermal baths [17–19]. However, as opposed to macroscopic classical systems, these systems can be completely driven out-of-equilibrium, they can be strongly coupled to environments, and they are made up of few constituents.

These profound differences called for the extension of thermodynamics to account for finite-size effects, large fluctuations and strong system-bath coupling in a quantum setting. This gave birth to a currently active research field which is known as "quantum thermodynamics" [17, 20, 21]. Quantum thermodynamics deals with a variety of problems that arise when trying to apply thermodynamic concepts to small out-of-equilibrium quantum systems. Here are some of the questions that are being addressed: how can one define concepts such as heat, work and entropy in a meaningful way? How do non-equilibrium fluctuations extend to the quantum regime? Do quantum effects such as entanglement, coherence and non-commutativity, which lead to the so-called "quantum supremacy" idea in the field of computation, boost or decay the performance of nanoscopic thermal machines? What are the difficulties or opportunities entailed by a quantum evolution with respect to finite-time thermodynamics? How does equilibration emerge from a microscopic quantum description of many-body systems? What is the link between information and thermodynamics in the quantum regime?

The work presented in this thesis develops themes within the field of quantum thermodynamics. In particular, we focus on understanding how to use quantum mesoscopic devices, especially single-electron systems, which are experimentally accessible nowadays, to construct thermal machines such as heat engines and refrigerators. We study these systems both as steady-state thermoelectric thermal machines, and as driven quantum systems which perform cycles analogue to the classical Carnot and Otto cycles. On the one hand, we give an overview of the formalism necessary to describe these systems. On the other, we study how to optimize the performance of these devices, such as the extracted power of heat engines, the cooling power of refrigerators, the thermovoltage induced by a temperature difference, and the corresponding efficiencies. This allows us to simultaneously understand how to operate these devices, and to tackle fundamental questions such as finding ultimate limits to the extracted power and to the efficiency at maximum power, and understanding the impact of strong coupling to the environment. While this thesis is theoretical, we also present some

experimental measurements that we were able to describe.

The outline of the thesis is the following: in Chap. 2 we lay the theoretical foundations necessary to describe quantum systems coupled to thermal baths in the weak coupling regime and beyond. This formalism, based on a perturbative extension of the Markovian master equation, will be used throughout the entire thesis. In Chap. 3 we describe and characterize quantum thermal machines distinguishing between thermoelectric machines, and driven thermal machines. In particular, in Sec. 3.1 we describe the thermoelectric effect and we discuss the laws of thermodynamics in this context. We show how to exploit this effect to implement thermoelectric heat engines and refrigerators, and we characterize their performance. We then pedagogically apply the formalism presented in Chap. 2 to a simple yet paradigmatic system: a single-level quantum dot (QD) coupled to thermal baths. In Sec. 3.2 we show how to use the formalism presented in Chap. 2 to describe driven thermal machines, and we state the laws of thermodynamics in this context. We then show how to implement a driven heat engine and a refrigerator, and we pedagogically study the performance of a slowly-driven Otto cycle applied to the minimal quantum system, i.e. a qubit (a two level system).

The next chapters are devoted to presenting original studies. In Chap. 4 we study the thermoelectric properties of an interacting multi-level QD based heat engine. We investigate the performance of this system both in the linear (small temperature differences) and non-linear response regime, and we study the impact of multiple thermals baths, of the multi-level structure of the QD and of the Coulomb interaction on the power and efficiency of the system. In Chap. 5 we use the formalism developed in Chap. 4 to describe the thermoelectric performance of an actual experiment performed at the NEST laboratory, Pisa, Italy. The system is a multi-level interacting QD embedded in an InAs/InP nanowire. Thanks to our theoretical model, we are able to estimate the electronic efficiency of such device, which turns out to be close to its thermodynamic upper limit. In Chap. 6 we use the formalism developed in Chap. 2 to describe the thermovoltage of a single-electron transistor device which was measured in an experiment carried out at the Aalto University, Helsinki, Finland. We find that both a non-linear description and coherent quantum effects beyond the weak coupling regime are crucial to accurately describe the experimental data without any free fitting parameters. In Chap. 7 we study an absorption refrigerator, i.e. a system, coupled to three thermal baths, which is able to cool the coldest bath without requiring any external work. The absorption refrigerator is based on two Coulomb-coupled single electron systems, which are experimentally accessible devices [22]. The optimal working condition to maximize the cooling power is derived, and an interpretation of this effect based on information theory is given. In Chap. 8 we study thermal rectification across a qubit. We find strategies to maximize such effect and we find clear signatures of coherent quantum effects, beyond a weak-coupling description, in the thermal rectification. In Chap. 9 we study the maximum power of a driven two-level system in the weak-coupling regime. Without making any assumption on the particular cycle or driving strategy, and regardless of the microscopic details of the system (i.e. of the coupling between the two-level system and the baths), we find that the power is universally maximized by applying an Otto-cycle in the fast-driving regime, i.e. when the driving is faster than the typical thermalization rate of the two-level system. We also find that there is no general upper bound to the efficiency at maximum power other than Carnot's efficiency. In Chap. 10 we study an arbitrary quantum system, weakly coupled to multiple thermal baths, driven in the fast driving regime. We find that the power is universally maximized by "generalized Otto cycles", and we show that the complexity of these cycles depends on the size of the Hilbert space of the quantum system being driven. We then find classes of systems where the standard Otto cycle is optimal. Under this hypothesis, we

compare the efficiency of a collection of interacting and non-interacting qubits, finding that the there is a many-body enhancement of the power when the temperature difference between the baths is small. Finally, in Chap. 11 we draw the conclusions.

2

Open quantum systems

The aim of this thesis is to study the thermodynamic properties of quantum systems. In particular, we will focus on how quantum systems can be used to construct thermodynamic machines, such as heat engines and refrigerators. In this chapter, we lay the theoretical foundations necessary to treat these systems. In the following chapters we then use the formalism developed in this chapter to characterize and study various quantum thermal machines.

One of the main concepts in thermodynamics is the separation between the "local system", or "working fluid", upon which we can act and perform transformations, and the "heat baths", which are instead large macroscopic object with a well defined temperature. In order to study thermodynamics of quantum systems, we must be able to study the dynamics of a local system (typically a mesoscopic quantum system) coupled to heat baths, which play the role of the environment. The most generic evolution a system coupled to an environment can undergo is described by a completely positive trace preserving linear map (CPTL) [23]. However, deriving the explicit form of these maps is in general a formidable task. Furthermore, finding a meaningful definition of heat and work valid in a completely general quantum setting is still an open question. On the other hand, when the coupling between the system and the environment is weak, all thermodynamic quantities can be consistently defined, and it is possible to derive perturbative schemes to practically compute all quantities of interest.

In this thesis, we focus on perturbative schemes performed in the system-bath coupling strength. We first focus on a leading order expansion in the system-bath coupling, which we denote as "weak-coupling regime". Within this regime, the evolution of the local density matrix obeys a Lindblad master equation, which we derive and discuss in Sec. 2.1. As we will see, there are common regimes where this approach leads to rate equations for the probability of finding the system in a given instantaneous eigenstate, and the rates are determined by the Fermi golden rule. We then show in Sec. 2.2 how to perform calculations beyond the weak-coupling regime by perturbatively accounting for higher order processes. These calculations lead to effects such as "co-tunneling", where two electrons or excitations are coherently transported across the device.

2.1 Weak-coupling regime

In this section we lay the foundations for the description of the dynamics of a quantum system coupled to an arbitrary environment. For notation consistency with the following chapters, we denote with "heat bath" the environment, although the derivation in this section holds also when the environment is comprised of several heat baths, or even when it is not in a thermal state. The Hamiltonian of the total system, composed by the local system S and by the bath B, can be written as

$$H_{\text{tot}} = H_{\text{S}} + H_{\text{B}} + H_{\text{S,B}}, \tag{2.1}$$

where H_{S} is the Hamiltonian of our local system, H_{B} is the Hamiltonian describing the bath, and $H_{\text{S,B}}$ is the Hamiltonian describing the coupling between the system and the bath. The density matrix $\rho_{\text{tot}}(t)$ describing the state of the total system at time t evolves according to the von Neumann equation

$$\frac{d}{dt}\rho_{\text{tot}}(t) = -\frac{i}{\hbar}[H_{\text{tot}}, \rho_{\text{tot}}(t)], \tag{2.2}$$

where $\hbar$ is Planck's reduced constant and $[X, Y] = XY - YX$ denotes the commutator between two arbitrary operators X and Y.

Since the baths are assumed to be "macroscopic", they are comprised of many degrees of freedom which make it difficult to solve Eq. (2.2) exactly. Furthermore, since we are interested in thermodynamics, it is often unnecessary to have detailed information about the exact state of the heat bath. The goal of this section is therefore to derive a closed equation which governs the evolution of the *reduced* density matrix of the system

$$\rho(t) \equiv \text{Tr}_{\text{B}}[\rho_{\text{tot}}(t)], \tag{2.3}$$

which only embodies the degrees of freedom of our local system S. Notice that $\text{Tr}_{\text{B}}[X]$ denotes the partial trace of an arbitrary operator X over the degrees of freedom of the bath. To do so, we follow the standard derivation of the Lindblad master equation [24, 25] first put forward by Davies [26]. After a mathematical derivation, in Sec. 2.1.1 we discuss the physical assumptions underlying this method. In the following pedagogical derivation, which goes along the lines of Ref. [27], we will not delve too deep into formal aspects when the physical picture is clear.

We start by rewriting Eq. (2.2) in the interaction picture

$$\frac{d}{dt}\tilde{\rho}_{\text{tot}}(t) = -\frac{i}{\hbar}[\tilde{H}_{\text{S,B}}(t), \tilde{\rho}_{\text{tot}}(t)], \tag{2.4}$$

where the "tilde" denotes the interaction picture. For a time-independent Hamiltonian, interaction picture operators $\tilde{O}(t)$ are related to their Schrödinger representation $O(t)$ through the mapping

$$\tilde{O}(t) \equiv U_0^\dagger(t) O(t) U_0(t), \tag{2.5}$$

where

$$U_0(t) \equiv e^{-i(H_{\text{S}}+H_{\text{B}})t/\hbar} \tag{2.6}$$

is the time-evolution operator for the "free" part of the total Hamiltonian, and we assume $t = 0$ to be the initial time. The interaction picture state is instead defined as

$$\tilde{\rho}_{\text{tot}}(t) \equiv U_I(t)\rho_{\text{tot}}(0)U_I^\dagger(t), \tag{2.7}$$

where

$$U_{\mathrm{I}}(t) \equiv U_0^\dagger(t) e^{-iH_{\mathrm{tot}}\, t/\hbar}. \tag{2.8}$$

We now integrate each side of Eq. (2.4) between 0 and t, yielding

$$\tilde{\rho}_{\mathrm{tot}}(t) = \tilde{\rho}_{\mathrm{tot}}(0) - \frac{i}{\hbar}\int_0^t ds\, [\tilde{H}_{\mathrm{S,B}}(s), \tilde{\rho}_{\mathrm{tot}}(s)]. \tag{2.9}$$

Inserting Eq. (2.9) into the right-hand-side (r.h.s.) of Eq. (2.4), and taking the trace over the bath on both sides yields

$$\frac{d}{dt}\tilde{\rho}(t) = -\frac{1}{\hbar^2}\int_0^t ds\ \mathrm{Tr}_{\mathrm{B}}[\tilde{H}_{\mathrm{S,B}}(t), [\tilde{H}_{\mathrm{S,B}}(s), \tilde{\rho}_{\mathrm{tot}}(s)]], \tag{2.10}$$

where we have assumed that

$$\mathrm{Tr}_{\mathrm{B}}[\tilde{H}_{\mathrm{S,B}}(t), \tilde{\rho}_{\mathrm{tot}}(0)] = 0. \tag{2.11}$$

This last hypothesis, which will soon be written in a more explicit form, can always be enforced up to a redefinition of H_{S}, and it is automatically verified in all models considered in this thesis.

We are interested in obtaining a closed equation for $\tilde{\rho}(t)$, but Eq. (2.10) still contains $\tilde{\rho}_{\mathrm{tot}}(t)$. Since we want to find the dynamics of $\tilde{\rho}(t)$ in the weak coupling regime, we can replace $\tilde{\rho}_{\mathrm{tot}}(t)$ in the r.h.s. of Eq. (2.10) (which already contains second order terms in the coupling Hamiltonian) with an approximate expression valid for weak coupling. We therefore write

$$\tilde{\rho}_{\mathrm{tot}}(t) \approx \tilde{\rho}(t) \otimes \tilde{\rho}_{\mathrm{B}}. \tag{2.12}$$

Equation (2.12), known as the Born approximation, holds by further assuming that the bath is much larger than the system, so that its state will not change in time ($\tilde{\rho}_{\mathrm{B}}$ is assumed to be constant). Inserting Eq. (2.12) into Eq. (2.10) yields

$$\frac{d}{dt}\tilde{\rho}(t) = -\frac{1}{\hbar^2}\int_0^t ds\ \mathrm{Tr}_{\mathrm{B}}[\tilde{H}_{\mathrm{S,B}}(t), [\tilde{H}_{\mathrm{S,B}}(s), \tilde{\rho}(s) \otimes \tilde{\rho}_{\mathrm{B}}]], \tag{2.13}$$

which is a closed integro-differential equation for $\tilde{\rho}(t)$. We now perform the Markov approximation, which consists of replacing $\tilde{\rho}(s) \to \tilde{\rho}(t)$. Physically, we are assuming that the evolution of the state at a given time t only depends on the state at that given time t (Markovianity). As we argue in Sec. 2.1.1, this approximation is justified if we are only interested in solving the dynamics of the system on a coarse-grained time scale which is larger than τ_{B}, where τ_{B} is the typical decay timescale of the correlation function of the bath [see Eq. (2.24) for a mathematical definition]. Intuitively, τ_{B}^{-1} represents "the speed of the bath", which is assumed to be the fastest rate in the system. This yields

$$\frac{d}{dt}\tilde{\rho}(t) = -\frac{1}{\hbar^2}\int_0^t ds\ \mathrm{Tr}_{\mathrm{B}}[\tilde{H}_{\mathrm{S,B}}(t), [\tilde{H}_{\mathrm{S,B}}(s), \tilde{\rho}(t) \otimes \tilde{\rho}_{\mathrm{B}}]]. \tag{2.14}$$

At last we change the integration variable according to $s \to t - s$, and let the integration go to infinity. Again, this is a reasonable approximation if the timescale over which $\tilde{\rho}(t)$ varies is larger than τ_{B}. We therefore obtain

$$\frac{d}{dt}\tilde{\rho}(t) = -\frac{1}{\hbar^2}\int_0^\infty ds\ \mathrm{Tr}_{\mathrm{B}}[\tilde{H}_{\mathrm{S,B}}(t), [\tilde{H}_{\mathrm{S,B}}(t-s), \tilde{\rho}(t) \otimes \tilde{\rho}_{\mathrm{B}}]]. \tag{2.15}$$

This approximation is know as the Born-Markov approximation.

To further simplify Eq. (2.15), we expand $H_{\mathrm{S,B}}$ (in the Schrödinger picture) onto the product basis as follows

$$H_{\mathrm{S,B}} = \sum_{\alpha} S_\alpha \otimes B_\alpha, \tag{2.16}$$

where S_α and B_α are Hermitian operators acting respectively on the space of the system and of the bath. Next, we denote with E the (discrete) set of eigenvalues (energies) of H_{S}, and with $\Pi(E)$ the projector onto the eigenspace relative to the eigenvalue E. Using the completeness relation $\mathbb{1} = \sum_E \Pi(E)$, we can write

$$S_\alpha = \sum_{E',E} \Pi(E) S_\alpha \Pi(E') = \sum_{\Delta E} \sum_{E'-E=\Delta E} \Pi(E) S_\alpha \Pi(E') = \sum_{\Delta E} S_\alpha(\Delta E), \tag{2.17}$$

where $\sum_{\Delta E}$ denotes a sum over all energy differences, $\sum_{E'-E=\Delta E}$ denotes a sum over all energies E and E' such that the energy difference is ΔE, and

$$S_\alpha(\Delta E) \equiv \sum_{E'-E=\Delta E} \Pi(E) S_\alpha \Pi(E'). \tag{2.18}$$

We can therefore decompose S_α as a sum of $S_\alpha(\Delta E)$ operators. Using Eq. (2.18), it can be shown that the interaction picture of these operators simply becomes

$$\tilde{S}_\alpha(\Delta E) = e^{-i\Delta E\, t/\hbar}\, S_\alpha(\Delta E). \tag{2.19}$$

The interaction picture of the coupling Hamiltonian can thus be written as

$$\tilde{H}_{\mathrm{S,B}}(t) = \sum_{\alpha,\Delta E} e^{-i\Delta E\, t/\hbar}\, S_\alpha(\Delta E) \otimes \tilde{B}_\alpha(t), \tag{2.20}$$

where $\tilde{B}_\alpha(t)$ is the interaction picture representation of the B_α operators.

We notice that the hypothesis in Eq. (2.11) is enforced if

$$\mathrm{Tr}\Big[\tilde{B}_\alpha(t)\, \tilde{\rho}_{\mathrm{B}}\Big] = 0. \tag{2.21}$$

It can be shown that if the bath is described by free fermions or bosons, and if $\tilde{\rho}_{\mathrm{B}}$ is a thermal state, this condition is automatically verified whenever the coupling term destroys or creates excitations in the bath.

Inserting Eq. (2.20) into Eq. (2.15) yields, after some algebra,

$$\frac{d}{dt}\tilde{\rho}(t) = \sum_{\substack{\Delta E,\Delta E' \\ \alpha,\beta}} e^{i(\Delta E' - \Delta E)\, t/\hbar} G_{\alpha\beta}(\Delta E) \Big[S_\beta(\Delta E)\tilde{\rho}(t) S_\alpha^\dagger(\Delta E') - S_\alpha^\dagger(\Delta E') S_\beta(\Delta E)\tilde{\rho}(t) \Big] + h.c., \tag{2.22}$$

where $h.c.$ stands for Hermitian conjugate, and where we define

$$G_{\alpha\beta}(\Delta E) \equiv \frac{1}{\hbar^2} \int_0^\infty ds\, e^{i\Delta E\, s/\hbar} \left\langle \tilde{B}_\alpha^\dagger(t) \tilde{B}_\beta(t-s) \right\rangle. \tag{2.23}$$

Equation (2.23) is the one-sided Fourier transform of the bath correlation function

$$\left\langle \tilde{B}_\alpha^\dagger(t) \tilde{B}_\beta(t-s) \right\rangle = \mathrm{Tr}\Big[\tilde{B}_\alpha^\dagger(t) \tilde{B}_\beta(t-s)\, \tilde{\rho}_{\mathrm{B}} \Big]. \tag{2.24}$$

In the cases considered in this thesis, $\tilde{\rho}_{\mathrm{B}}$ is a thermal state, so it commutes with H_{B}. Under this hypothesis we have two simplifications: $\rho_{\mathrm{B}} = \tilde{\rho}_{\mathrm{B}}$, so we will drop the "tilde" from now on. Furthermore, the correlation function only depends on time differences, i.e. $\langle \tilde{B}^\dagger_\alpha(t)\tilde{B}_\beta(t-s)\rangle = \langle \tilde{B}^\dagger_\alpha(s)\tilde{B}_\beta(0)\rangle$, thus $G_{\alpha\beta}(\Delta E)$ does not depend on t.

We now perform the last approximation, known as the secular approximation. Equation (2.22) contains a sum over ΔE and $\Delta E'$. When $\Delta E \neq \Delta E'$, the exponential oscillates on a typical timescale $\tau_{\mathrm{S}} = \hbar/(E - E')$, where $E \neq E'$ are two energies of the system. If we assume that the smallest gap in the spectrum of H_{S} is large enough such that $\tau_{\mathrm{S}} \ll \tau_{\mathrm{T}}$, where τ_{T} is the typical thermalization timescale of the system (i.e. the timescale we are trying to resolve), then the exponential terms in Eq. (2.22) with $\Delta E \neq \Delta E'$ oscillate very quickly with zero mean, so we can neglect them. This leads to

$$\frac{d}{dt}\tilde{\rho}(t) = \sum_{\Delta E,\alpha,\beta} G_{\alpha\beta}(\Delta E)\left[S_\beta(\Delta E)\tilde{\rho}(t)S^\dagger_\alpha(\Delta E) - S^\dagger_\alpha(\Delta E)S_\beta(\Delta E)\tilde{\rho}(t)\right] + h.c. \tag{2.25}$$

We now decompose $G_{\alpha\beta}(\Delta E)$ as

$$G_{\alpha\beta}(\Delta E) = \frac{1}{2}\Gamma_{\alpha\beta}(\Delta E) + iM_{\alpha\beta}(\Delta E), \tag{2.26}$$

where

$$M_{\alpha\beta}(\Delta E) \equiv \frac{1}{2i}[G_{\alpha\beta}(\Delta E) - G^*_{\beta\alpha}(\Delta E)] \tag{2.27}$$

is a Hermitian matrix and

$$\Gamma_{\alpha\beta}(\Delta E) \equiv G_{\alpha\beta}(\Delta E) + G^*_{\beta\alpha}(\Delta E) = \int_{-\infty}^{+\infty} ds\, e^{i\Delta E\, s/\hbar}\, \langle \tilde{S}^\dagger_\alpha(s)\tilde{S}_\beta(0)\rangle \tag{2.28}$$

is a positive matrix which, as we will see, sets the typical timescale τ_{T} for the thermalization of S with its environment. Using these definitions, and switching back to the Schrödinger picture, we can rewrite Eq. (2.25) as

$$\frac{d}{dt}\rho(t) = -\frac{i}{\hbar}[H_{\mathrm{S}} + H_{\mathrm{LS}}, \rho(t)] + D[\rho(t)], \tag{2.29}$$

where

$$H_{\mathrm{LS}} = \sum_{\Delta E,\alpha,\beta} M_{\alpha\beta}(\Delta E)S^\dagger_\alpha(\Delta E)S_\beta(\Delta E) \tag{2.30}$$

is know as the Lamb shift Hamiltonian, and

$$D[\rho] = \sum_{\Delta E,\alpha,\beta} \Gamma_{\alpha\beta}(\Delta E)\left[S_\beta(\Delta E)\rho S^\dagger_\alpha(\Delta E) - \frac{1}{2}\left\{S^\dagger_\alpha(\Delta E)S_\beta(\Delta E), \rho\right\}\right] \tag{2.31}$$

is a linear superoperator (since it acts on the space of operators) known as the dissipator. $\{X, Y\} \equiv XY + YX$ denotes the anticommutator between two arbitrary operators X and Y. Equation (2.29) is the well know Lindblad master equation which describes the evolution of the local density matrix $\rho(t)$. It can be shown that it is indeed a CPTL map. The additional term H_{LS} can be shown to commute with H_{S}, so it simply renormalizes the energy scales of H_{S}. We therefore set $H_{\mathrm{LS}} = 0$ throughout this thesis unless explicitly stated. The dissipator instead describes the influence of the bath on the dynamics of the system.

If the environment is made up of a single thermal bath at temperature T, we have that

$$\rho_{\mathrm{B}} = \frac{e^{-H_{\mathrm{B}}/(k_B T)}}{Z}, \tag{2.32}$$

where $Z = \mathrm{Tr}\left[e^{-H_{\mathrm{B}}/(k_B T)}\right]$ is the partition function and k_B is Boltzmann's constant. Under this hypothesis, it can be shown that the rates $\Gamma_{\alpha\beta}(\Delta E)$ induced by the bath satisfy

$$\Gamma_{\alpha\beta}(\Delta E) = e^{-\Delta E/(k_B T)}\Gamma_{\beta\alpha}(-\Delta E). \tag{2.33}$$

Equation (2.33) guarantees that, under weak hypothesis, the local system evolves towards a steady state given by a thermal state for the local system [28, 29]:

$$\rho(t) \xrightarrow{t\to\infty} \frac{e^{-H_{\mathrm{S}}/(k_B T)}}{Z}. \tag{2.34}$$

We are now interested in finding a closed set of equations for the dynamics of the populations, i.e. of the probability $p_i(t)$ of finding the system at time t in the i^{th} eigenstate $|E_i\rangle$ of H_{S} with energy E_i:

$$p_i(t) \equiv \langle E_i|\rho(t)|E_i\rangle\,. \tag{2.35}$$

As we will see in the following chapters, in most cases the knowledge of the populations $p_i(t)$ is sufficient to compute the heat currents flowing through the system. Multiplying Eq. (2.29) by $\langle E_i|$ to the left, and $|E_i\rangle$ to the right, and assuming that the spectrum of H_{S} is non-degenerate, we find the *Pauli master equation*

$$\frac{d}{dt}p_i(t) = \sum_j \left[p_j(t)\Gamma_{j\to i} - p_i(t)\Gamma_{i\to j}\right], \tag{2.36}$$

where

$$\Gamma_{i\to j} \equiv \sum_{\alpha,\beta}\Gamma_{\alpha\beta}(E_i - E_j)\,\langle E_i|S_\alpha|E_j\rangle\,\langle E_j|S_\beta|E_i\rangle\,. \tag{2.37}$$

Equation (2.36) will be the starting point for many calculations performed in this thesis, and it has a very intuitive physical meaning. The probability of finding the system in state i will increase if we are in state j $[p_j(t)]$, and the bath induces a transition from j to i $(\Gamma_{j\to i})$, while it decreases if the system is already in state i $[p_i(t)]$, and the bath induces a transition to a different state j $(\Gamma_{i\to j})$. The rates $\Gamma_{i\to j}$ are exactly equivalent to the Fermi golden rule. This observation will allow us in the next section to extend this formalism to include higher order processes in the coupling strength. At last, we notice that Eq. (2.33) can be written for the rates $\Gamma_{i\to j}$ as

$$\Gamma_{i\to j} = e^{-(E_j - E_i)/(k_B T)}\Gamma_{j\to i}. \tag{2.38}$$

This relations is known as the *detailed balance equation*. Equation (2.38) tells us that the probability per unit time to absorbs energy ΔE is lower than the probability per unit time to release energy ΔE into the environment by a factor $e^{-\Delta E/(k_B T)}$.

As we will see in the following chapters, in the presence of multiple independent thermal baths the rates $\Gamma_{i\to j}$ decompose into the sum of rates relative to each bath. In this case, the rates relative to each bath individually satisfy Eq. (2.38) with the corresponding temperature.

2.1.1 Range of Validity

In this section we briefly discuss the various approximations and physical assumptions that allowed us to derive the master equation. First of all, we perform a perturbative expansion in $H_{\mathrm{S,B}}$, therefore the coupling must be weak. We then perform other approximations which rely on a precise timescale separation. There are three relevant timescales : (1) the system's typical timescale $\tau_{\mathrm{S}} = \hbar/\Delta E$, where ΔE is the smallest gap in the system, (2) the timescale of the bath τ_{B}, which is given by the typical decay time of the correlation function of the bath, and (3) the thermalization time τ_{T}, given by the inverse of the characteristic transition rate $\Gamma_{i\to j}$, which determines the timescale for the thermalization of the system with the bath. For the approximations to hold, τ_{B} must be smaller than all other timescales, i.e. the bath must be "large and fast". Furthermore, for the secular approximation to hold, i.e. for all terms with $\Delta E \neq \Delta E'$ to vanish in Eq. (2.22), we must have that $\tau_{\mathrm{S}} \ll \tau_{\mathrm{T}}$. The master equation approach is thus valid when we are in the regime

$$\tau_{\mathrm{B}} \ll \tau_{\mathrm{S}} \ll \tau_{\mathrm{T}}. \tag{2.39}$$

The last inequality, i.e. the fact that τ_{T} should be the largest timescale, is actually automatically satisfied if we are in the "weak coupling regime". Indeed, τ_{T} is inversely proportional to the coupling strength, while the other timescales do not depend on the coupling. So by decreasing the coupling strength, it is always possible to make τ_{T} the largest timescale.

2.2 Beyond the weak-coupling regime

In this section we discuss one possible way to perform calculations beyond the weak coupling regime which we have adopted in various scenarios. Our starting point is the Pauli master equation [Eq. (2.36)], and the fact that the rates $\Gamma_{i\to j}$ can be equivalently computed by using the Fermi golden rule. Let us denote with $|E_i\rangle$ the eigenstates of H_{S} with energy E_i, and with $|e_k\rangle$ the eigenstates of H_{B} with energy e_k. Since H_{S} and H_{B} describe independent degrees of freedom, the eigenstates of the total uncoupled system, $H_{\mathrm{S}} + H_{\mathrm{B}}$, are given by the product basis, i.e. by $|\psi_{ik}\rangle \equiv |E_i\rangle \otimes |e_k\rangle$, with corresponding energy $\varepsilon_{ik} \equiv E_i + e_k$, for all i and k.

The Fermi golden rule allows us to compute the transition rate between eigenstates of $H_{\mathrm{S}} + H_{\mathrm{B}}$ induced by the coupling term $H_{\mathrm{S,B}}$, which is treated perturbatively. Therefore, the transition rate from eigenstate $|E_i\rangle$ to eigenstate $|E_j\rangle$ in the local system S is given by a sum over all transitions from $|\psi_{ik}\rangle$ to $|\psi_{jk'}\rangle$, for all k and k', in the total system. We thus have that

$$\Gamma_{i\to j} = \sum_{k,k'} \frac{2\pi}{\hbar} W_{ik}(1 - W_{jk'}) \left| \langle \psi_{jk'} | \mathcal{T} | \psi_{ik} \rangle \right|^2 \delta(\varepsilon_{jk'} - \varepsilon_{ik}), \tag{2.40}$$

where W_{ik} and $W_{jk'}$ are the probabilities of finding the total system in state $|\psi_{ik}\rangle$ and $|\psi_{jk'}\rangle$ respectively, $\mathcal{T}$ denotes the $\mathcal{T}$-matrix [30–33] and $\delta(x)$ denotes the Dirac-delta. A perturbative representation of the $\mathcal{T}$-matrix is given by

$$\mathcal{T} = \mathcal{T}^{(1)} + \mathcal{T}^{(2)} + \dots \tag{2.41}$$

with

$$\mathcal{T}^{(1)} = H_{\mathrm{S,B}}, \qquad \mathcal{T}^{(2)} = H_{\mathrm{S,B}}\, G_0\, H_{\mathrm{S,B}}, \tag{2.42}$$

where $G_0 = 1/(\varepsilon_{ik} - H_{\mathrm{B}} - H_{\mathrm{S}} + i\eta)$ is the Green function of the uncoupled total system, and η is in infinitesimal positive quantity. The first order term, $\mathcal{T}^{(1)}$, yields the standard Fermi

golden rule rates, while the term $\mathcal{T}^{(2)}$ describes processes which involve interacting twice with $H_{\mathrm{S,B}}$.

A class of systems we will consider in many of the following sections are those where the bath is composed of a collection of free fermions, and where the local system can host electrons, for example a quantum dot or a metallic island. In these cases, the coupling Hamiltonian is chosen as to describe the tunneling of a single electron from one lead to the other. In this context, the first order term $\mathcal{T}^{(1)}$ allows us to compute *sequential tunneling rates*, i.e. the rate of single-electron tunneling between the bath and the system. The second order term $\mathcal{T}^{(2)}$, instead, allows us to compute the rate of coherent tunneling of two electron between the bath and the system, known as *cotunneling* [34].

We use the notation $\Gamma_{i\to j}$, without any superscript, to denote sequential tunneling only, i.e. Eq. (2.40) with $\mathcal{T} = \mathcal{T}^{(1)} = H_{\mathrm{S,B}}$. Instead, we denote with

$$\begin{aligned}\Gamma^{(\mathrm{cot})}_{i\to j} &\equiv \frac{2\pi}{\hbar}\sum_{k,k'} W_{ik}(1-W_{jk'})\left|\langle\psi_{jk'}|\mathcal{T}^{(2)}|\psi_{ik}\rangle\right|^2\delta(\varepsilon_{jk'}-\varepsilon_{ik}) \\ &= \frac{2\pi}{\hbar}\sum_{k,k'} W_{ik}(1-W_{jk'})\left|\sum_{l,k''}\frac{\langle\psi_{jk'}|H_{\mathrm{S,B}}|\psi_{lk''}\rangle\,\langle\psi_{lk''}|H_{\mathrm{S,B}}|\psi_{ik}\rangle}{\varepsilon_{ik}-\varepsilon_{lk''}+i\eta}\right|^2\delta(\varepsilon_{jk'}-\varepsilon_{ik}) \quad (2.43)\end{aligned}$$

the second order co-tunneling rates. In the second equality we inserted a sum over all eigenstates $|\psi_{lk''}\rangle$ of the uncoupled Hamiltonian $H_{\mathrm{S}}+H_{\mathrm{B}}$ with corresponding energy $\varepsilon_{lk''}$. By analyzing the structure of the last equality in Eq. (2.43), we can pictorially describe co-tunneling as a process where the interaction $H_{\mathrm{S,B}}$ evolves the intial state $|\psi_{ik}\rangle$ into an arbitrary *virtual* state $|\psi_{lk''}\rangle$, and then a second interaction $H_{\mathrm{S,B}}$ evolves the virtual state into the final state $|\psi_{jk'}\rangle$. Finally, all these virtual processes are summed up coherently (i.e. the sum over l, k'' inside the square modulus), and all initial and final states, compatible with the transition $i \to j$ in the local system, are summed up incoherently (the outer sum over k, k'). A detailed calculation of the co-tunneling rates in specific systems is described in App. C and E.

3 Quantum thermal machines

In this chapter we discuss how to implement, describe and characterize quantum thermal machines, and we discuss the laws of thermodynamics in this context. We mainly focus on two types of thermal machines: the heat engine, and the refrigerator. A heat engine is a device which converts part of the heat that would naturally flow from the hot bath to the cold one into useful work. The refrigerator instead is a device which requires work to extract heat from the cold bath.

There are two main classes of thermal machines: steady-state machines, which we denote as *thermoelectric machines*, and *driven thermal machines*. These machines are distinguished by different operational regime, and by different ways of exchanging work with the environment. Given these profound differences, we discuss thermoelectric machines in Sec. 3.1 and driven thermal machines in Sec. 3.2. We then present original work on thermoelectric machines in Chaps. 4, 5, 6, 7 and 8, and on driven thermal machines in Chaps. 9 and 10.

3.1 Thermoelectric machines

The thermoelectric effect, first observed by A. Volta [8] in 1794, consists of the generation of a steady-state charge current or of a voltage drop across some device (for example a metallic bar) by applying a temperature difference to it. The origin of this effect becomes quite clear once we realize that, in metallic objects, charge and heat are due to the same microscopic mechanisms, i.e. by the motion of electrons that carry charge and energy. Indeed, already in 1853 Gustav Wiedemann and Rudolph Franz observed empirically that in bulk metals the ratio of the thermal conductance K over the electrical conductance G was a constant at fixed temperature. Ludvig Lorenz then observed that the ratio K/G is to good approximation linear in T. These observations gave rise to the famous Wiedemann-Franz law [35]

$$\frac{K}{GT} = L, \tag{3.1}$$

where

$$L = \frac{\pi^2}{3}\left(\frac{k_B}{e}\right)^2 \tag{3.2}$$

is the Lorenz number, e being the modulus of the electron charge and k_B Boltzmann's constant.

As we will discuss in this section, the direct proportionality of the electrical and thermal conductance is a strong limiting factor to the efficiency of thermoelectric devices. Fortunately, this "coupling" between charge and heat breaks down in mesoscopic devices, where the transport mechanisms is not diffusive anymore. As we will show, this allows us to design mesoscopic devices where the Wiedemann-Franz law is strongly violated (an explicit example is given in Chap. 4), and conversely the efficiency as thermal engines is greatly enhanced.

This section is organized as follows: without relying on any specific formalism to compute the charge and heat currents, in Sec. 3.1.1 we define the prototypical setup we consider in this thesis, we show how the laws of thermodynamics are stated in this context, and we show how to construct and evaluate the performance of a heat engine and of a refrigerator. In Sec. 3.1.2 we focus on the linear response regime, i.e. on small temperature and voltage biases. In this context, we introduce the transport coefficients and the figure of merit ZT, which quantifies the efficiency of heat engines and of refrigerators. In Sec. 3.1.3 we discuss what properties a system must have in order to exhibit a large figure or merit, and we discuss why strongly confined systems, such as quantum dots, are expected to have high thermoelectric efficiency. In Sec. 3.1.4 we show how to explicitly compute the charge and heat currents flowing across our device building on the formalism introduced in Chap. 2. Finally in Sec. 3.1.5 we pedagogically apply the formalism developed in Chap. 2 and in Sec. 3.1.4 to compute the transport coefficients and to evaluate the performance of a single-level QD operated as a heat engine. We use this example to discuss various physical effects, such as the concept of energy filtering, which occur also in more complicated and realistic setups, and we discuss how they can enhance or limit the efficiency of thermoelectric devices.

3.1.1 Setup and characterization of thermal machines

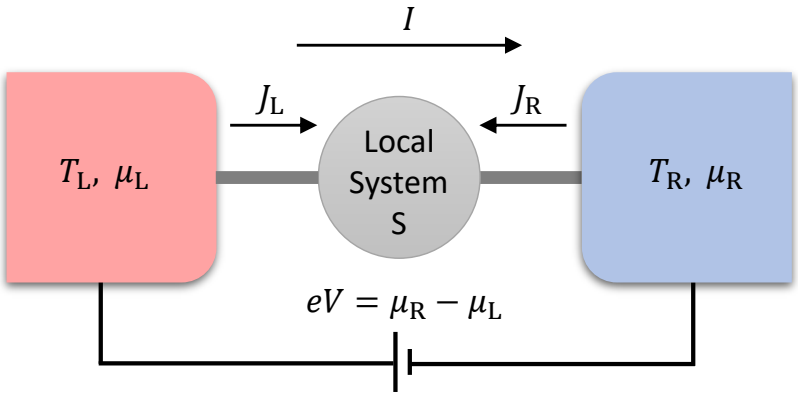

FIGURE 3.1: A quantum system S (gray circle) is coupled to two fermionic thermal baths characterized by temperatures T_{L} (left) and T_{R} (right), and by chemical potentials μ_{L} and μ_{R}. The difference in chemical potential is guaranteed by an applied voltage bias V. J_{L} and J_{R} denote the heat currents flowing out of the respective baths, while I denotes the charge current flowing from left to right.

Let us consider a generic local system S coupled to two fermionic heat baths characterized respectively by temperatures T_{L} (left) and T_{R} (right), and by chemical potentials μ_{L} and μ_{R}, as schematically shown in Fig. 3.1. Since the heat baths are assumed to be large "macroscopic"

objects, we assume that any interaction in the baths can be accounted for by a quasi-particle description emerging, for example, by applying a mean-field approximation. Therefore, the heat baths are described by a collection of free fermions. In this context, we write the environment Hamiltonian $H_{\rm B}$, defined in Eq. (2.1), as $H_{\rm B} = H_{\rm L} + H_{\rm R}$ where, for $\alpha = {\rm L}, {\rm R}$,

$$H_\alpha = \sum_k \epsilon_{\alpha k}\, c^\dagger_{\alpha k} c_{\alpha k}. \tag{3.3}$$

In Eq. (3.3), $c^\dagger_{\alpha k}$ ($c_{\alpha k}$) represents the fermionic creation (destruction) operator of an electron in bath α with single-particle energy $\epsilon_{\alpha k}$ and quantum number k which satisfy the usual anticommutation relation $\{c_{\alpha k}, c^\dagger_{\alpha' k'}\} = \delta_{\alpha,\alpha'}\delta_{k,k'}$ and $\{c_{\alpha k}, c_{\alpha' k'}\} = 0$, δ being the Kronecker delta. Since the baths are each in an thermal state with a well defined temperature and chemical potential, the state of the baths $\rho_{\rm B}$ is assumed to be prepared at some initial time as $\rho_{\rm B} = \rho_{\rm L} \otimes \rho_{\rm R}$, where

$$\rho_\alpha = \frac{e^{-(H_\alpha - \mu N_\alpha)/(k_B T_\alpha)}}{Z}. \tag{3.4}$$

$Z = {\rm Tr}\left[e^{-(H_\alpha - \mu N_\alpha)/(k_B T_\alpha)}\right]$ is the grand canonical partition function, and

$$N_\alpha \equiv \sum_k c^\dagger_{\alpha k} c_{\alpha k} \tag{3.5}$$

is the operator associated with the total number of electrons in bath α.

The temperature and chemical potential imbalance will drive S into an out-of-equilibrium steady-state which may admit steady-state currents. As schematically shown in Fig. 3.1, we denote with I the steady-state charge current flowing from left to right and with J_α the steady-state heat current flowing out of reservoir α. In general, these quantities are defined as

$$\begin{aligned} I &\equiv e\,\langle \dot{N}_{\rm L} \rangle\,, \\ J_\alpha &\equiv -\langle \dot{H}_\alpha - \mu_\alpha \dot{N}_\alpha \rangle\,, \end{aligned} \tag{3.6}$$

where, for an arbitrary operator O, the "dot" denotes the time derivative, which can be computed as $\dot{O} = (i/\hbar)[H_{\rm tot}, O]$, and where the expectation value is defined as $\langle O \rangle \equiv {\rm Tr}[\rho_{\rm tot}(t \to \infty) O]$. The definition of J_α provided in Eq. (3.6) can be derived from the first law of thermodynamics. Focusing on bath α, we define the internal energy U_α and the particle number n_α as

$$U_\alpha \equiv \langle H_\alpha \rangle\,, \qquad n_\alpha \equiv \langle N_\alpha \rangle\,. \tag{3.7}$$

The first law, for bath α, is given by

$$\dot{U}_\alpha = \mu_\alpha \dot{n}_\alpha - J_\alpha. \tag{3.8}$$

It is now easy to derive the definition of J_α, provided in Eq. (3.6), by combining Eqs. (3.7) and (3.8).

Since the dynamics of the total system is induced by a time-independent Hamiltonian $H_{\rm tot}$, the total energy is conserved. Assuming that in the steady state $\langle \dot{H}_{\rm S} \rangle = \langle \dot{H}_{\rm S,B} \rangle = 0$, energy conservation implies

$$\langle \dot{H}_{\rm L} \rangle + \langle \dot{H}_{\rm R} \rangle = 0. \tag{3.9}$$

Furthermore, if we assume that the system is also charge conserving, we have that

$$\langle \dot{N}_{\rm L} \rangle + \langle \dot{N}_{\rm R} \rangle = 0. \tag{3.10}$$

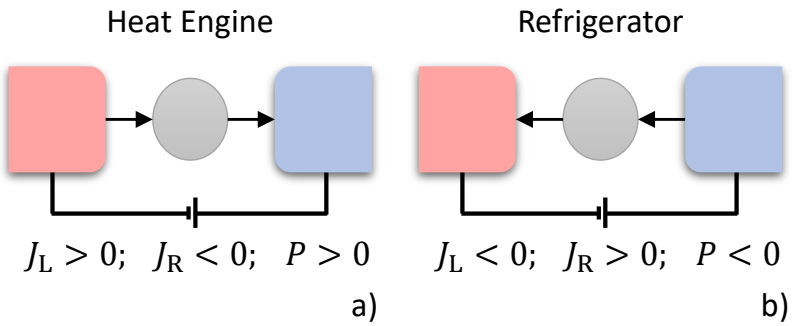

FIGURE 3.2: Schematic representation of a heat engine a), and of a refrigerator b). The corresponding sign of the heat currents and of the power is reported.

We now provide a definition of the power P extracted from our system. Formally, this can be done by stating the first law of thermodynamics for the local system S:

$$P = J_L + J_R. \tag{3.11}$$

Plugging Eqs. (3.6), (3.9) and (3.10) into Eq. (3.11), we find that

$$P = -VI, \tag{3.12}$$

where the voltage bias V is given by $eV = \mu_R - \mu_L$. Equation (3.12), which we derived from the first law, is very intuitive: work is extracted by driving a current against a chemical potential difference, which can be visualized as charging a macroscopic battery.

While the first law of thermodynamics is an energy conservation statement which treats heat and work on the same footing, the second law places a bound on the inter-conversion between these quantities. In steady state, the entropy of the local system S cannot change, so the second law simply reduces to

$$\frac{J_L}{T_L} + \frac{J_R}{T_R} \leq 0, \tag{3.13}$$

the equality sign being saturated when the transfer of heat occurs reversibly.

We now discuss how to construct a thermoelectric heat engine and refrigerator. Throughout this thesis, unless stated explicitly, we assume that $T_L > T_R$, and we define the temperature bias $\Delta T \equiv T_L - T_R \geq 0$ and the average temperature $T \equiv (T_L + T_R)/2$.

A heat engine, as schematically depicted in Fig. 3.2a, is a device which converts part of the heat naturally flowing from the hot lead to the cold lead into work. Therefore, $J_L \geq 0$, $J_R \leq 0$ and $P \geq 0$. We denote with $P_{[E]} \equiv P$ the power of a heat engine. Due to the second law, not all heat can be converted into work. Therefore the efficiency, defined as the ratio between the extracted work and the heat provided by the hot lead, is bound by the second law [Eq. (3.13)] to be smaller than Carnot's efficiency $\eta_c \equiv 1 - T_R/T_L$:

$$\eta \equiv \frac{P_{[E]}}{J_L} \leq \eta_c. \tag{3.14}$$

The charge and heat currents are a function of the temperature difference ΔT and of the voltage bias V. We can therefore define the maximum efficiency $\eta^{(max)}$ as the efficiency maximized over the voltage bias at fixed temperature difference, i.e.

$$\eta^{(max)} \equiv \max_V \eta. \tag{3.15}$$

In most scenarios, maximizing the efficiency yields a low extracted power. Intuitively, this is due to the fact that, in most systems, achieving Carnot's efficiency implies that the extracted power is zero. Therefore, maximizing the efficiency may not be the best choice in practical applications. It is thus important to introduce the concept of maximum power $P_{[\mathrm{E}]}^{(\max)}$, which we define as

$$P_{[\mathrm{E}]}^{(\max)} \equiv \max_{V} P_{[\mathrm{E}]}. \tag{3.16}$$

This definition prompts us to introduce also the concept of efficiency at maximum power $\eta(P_{[\mathrm{E}]}^{(\max)})$, which is the efficiency of the engine when it is operated at maximum power. Many attempts have been made in literature trying to place an upper bound to the efficiency at maximum power. For small temperature differences, as we show in Sec. 3.1.2, $\eta(P_{[\mathrm{E}]}^{(\max)}) \leq \eta_{\mathrm{c}}/2$ [11]. This bound was extended to finite temperature differences in Ref. [36] by concatenating many engines operating in the linear regime, finding that the efficiency at maximum power is bound by the Curzon-Ahlborn efficiency

$$\eta_{\mathrm{CA}} \equiv 1 - \sqrt{\frac{T_{\mathrm{R}}}{T_{\mathrm{L}}}}. \tag{3.17}$$

This bound was previously derived for an endoreversible model of a heat engine [37]. However, this is not a fundamental upper bound. Indeed, within the context of driven engines, it has been shown [38] that any system operating in the low dissipation regime, which means "slow enough", exhibits an efficiency at maximum power bound by the Schimdt-Seifert [39] efficiency

$$\eta_{\mathrm{SS}} \equiv \frac{\eta_{\mathrm{c}}}{2 - \eta_{\mathrm{c}}}, \tag{3.18}$$

which is larger than η_{CA}. Furthermore, in Chap. 4 we prove that the efficiency at maximum power of a thermoelectric heat engine based on an interacting multilevel quantum dot can exceed η_{CA} beyond the linear response regime, while in Chap. 9 we show that, by choosing a specific system-bath coupling, it is possible to construct a driven heat engine based on a qubit that exhibits an efficiency at maximum power arbitrarily close to η_{c}. While this implies that there is no fundamental upper bound to $\eta(P_{[\mathrm{E}]}^{(\max)})$ other than η_{c}, in most concrete setups strict upper bounds do emerge, and it is nonetheless an important thermodynamic quantity to study.

A refrigerator, as schematically depicted in Fig. 3.2b, is a device which requires work to extract heat from a cold bath, therefore $J_{\mathrm{L}} \leq 0$, $J_{\mathrm{R}} \geq 0$ and $P \leq 0$. The power (or cooling power) of a refrigerator is defined as $P_{[\mathrm{R}]} \equiv J_{\mathrm{R}}$. Also in this case, the second law places a bound on the inter-conversion between heat and work. The coefficient of performance (COP) C of a refrigerator, which plays the role of the efficiency for heat engines, is defined as the ratio between the cooling power and the power provided, and it is bound by $C_{\mathrm{c}} \equiv T_{\mathrm{L}}/\Delta T$:

$$C \equiv \frac{P_{[\mathrm{R}]}}{|P|} \leq C_{\mathrm{c}}. \tag{3.19}$$

We then define the maximum COP as

$$C^{(\max)} \equiv \max_{V} C. \tag{3.20}$$

As in the heat engine case, the cooling power $P_{[\mathrm{R}]}$ is typically small when the system is operated at maximum COP. We therefore define the maximum cooling power

$$P_{[\mathrm{R}]}^{(\max)} \equiv \max_{V} P_{[\mathrm{R}]}. \tag{3.21}$$

Also in this case, we define the COP at maximum power, denoted by $C(P_{[\mathrm{R}]}^{(\max)})$, as the COP when the system is operated at maximum power.

In the next section, we show how in the linear response regime $\eta^{(\max)}$, $\eta(P_{[\mathrm{E}]}^{(\max)})$, and $C^{(\max)}$ can all be expressed in terms of a single dimensionless quantity known as the figure of merit ZT.

3.1.2 Linear response regime

We talk about "linear response regime" when the charge and heat currents are linear in ΔT and V. Typically, this happens when $\Delta T/T \ll 1$ and $eV/(k_B T) \ll 1$. As we now show, the linear response regime allows us to characterize the performance of a heat engine and of a refrigerator in terms of a single dimensionless figure of merit ZT.

By definition, within the linear response regime we can write

$$\begin{pmatrix} I \\ J_{\mathrm{L}} \end{pmatrix} = \begin{pmatrix} L_{11} & L_{12} \\ L_{21} & L_{22} \end{pmatrix} \begin{pmatrix} V \\ \Delta T/T \end{pmatrix}, \tag{3.22}$$

or equivalently:

$$\vec{j} = L \cdot \vec{x}, \tag{3.23}$$

where $\vec{j} \equiv (I, J_{\mathrm{L}})$, $\vec{x} \equiv (V, \Delta T/T)$, and where the matrix L, with coefficients L_{ij}, is known as the Onsager matrix [11]. Notice that the heat current J_{R} is a function of I and J_{L} through the first law, i.e. Eqs. (3.11) and (3.12). The Onsager matrix L, which depends on the details of the system, satisfies the property $L_{12} = L_{21}$ in time-reversal symmetric systems. We will work under this assumption throughout the whole thesis. Furthermore, in order to guarantee positive entropy production, L must be positive semi-definite. This can be shown by plugging the expansion in Eq. (3.23) into Eq. (3.13), i.e. the second law, under the assumption $\Delta T/T \ll 1$, and requiring that the inequality is satisfied for all choices of ΔT and V.

In order to characterize the transport properties in terms of physically meaningful quantities, we introduce the following transport coefficient: the electric conductance G, the Seebeck coefficient S and the thermal conductance K. As we now show, these three quantities are in a one-to-one relation with L. The electric conductance, defined as

$$G \equiv \left.\frac{I}{V}\right|_{\Delta T=0} = L_{11}, \tag{3.24}$$

describes the electrical response of the system to a voltage bias while the temperature difference is zero. Since L is positive semi-definite, we have that $G \geq 0$. The Seebeck coefficient S, defined as

$$S \equiv -\left.\frac{V}{\Delta T}\right|_{I=0} = \frac{1}{T}\frac{L_{12}}{L_{11}}, \tag{3.25}$$

describes the voltage that the system develops, as a response to a temperature difference, in open circuit condition. This voltage, know as the thermovoltage, is responsible for enforcing $I = 0$ in the presence of a temperature difference. A high values of S means that a large voltage is necessary to balance the current that is induced by a temperature difference. At last, the thermal conductance, defined as

$$K \equiv \left.\frac{J_{\mathrm{L}}}{\Delta T}\right|_{I=0} = \frac{1}{T}\frac{\det(L)}{L_{11}}, \tag{3.26}$$

describes the thermal response of the system to a temperature difference in open circuit conditions. Under this hypothesis the power is zero so, thanks to the first principle, we have that $J_{\rm L} = J_{\rm R}$. Since L is positive semi-definite, both $L_{11} \geq 0$ and $\det(L) \geq 0$, so $K \geq 0$.

We now express the properties of a heat engine, namely $P_{[\rm E]}^{(\max)}$, $\eta^{(\max)}$ and $\eta(P_{[\rm E]}^{(\max)})$ in terms of the transport coefficients. To this end, we define the dimensionless figure of merit

$$ZT \equiv \frac{GS^2T}{K} \tag{3.27}$$

which, thanks to the positivity of the Onsager matrix, is a non-negative quantity. It is easy to show that the following relations hold

$$P_{[\rm E]}^{(\max)} = \frac{1}{4} GS^2\,\Delta T^2, \tag{3.28}$$

and

$$\eta^{(\max)} = \eta_{\rm c}\frac{\sqrt{ZT+1}-1}{\sqrt{ZT+1}+1}, \qquad \eta(P_{[\rm E]}^{(\max)}) = \frac{\eta_{\rm c}}{2}\frac{ZT}{2+ZT}, \tag{3.29}$$

where, within the linear response, $\eta_{\rm c} = \Delta T/T$. Because of Eq. (3.28), the combination GS^2 is known as "power factor". Interestingly, both the maximum efficiency and the efficiency at maximum power are growing functions of ZT. Therefore, finding an optimal device from a thermoelectric point of view is equivalent to finding devices with a large ZT. In Sec. 3.1.3 we discuss which characteristics a system must have to yield a large value of ZT. We notice that, as $ZT \to \infty$, $\eta^{(\max)}$ approaches $\eta_{\rm c}$, while $\eta(P_{[\rm E]}^{(\max)})$ approaches $\eta_{\rm c}/2$, as anticipated in Sec. 3.1.1. Therefore, within the linear response regime, for time-reversal symmetric systems, the efficiency at maximum power is exactly upper bounded by $\eta_{\rm c}/2$. Indeed, both upper bounds $\eta_{\rm CA}$ and $\eta_{\rm SS}$, introduced respectively in Eqs. (3.17) and (3.18), yield $\eta_{\rm c}/2$ when expanded to first order in $\Delta T/T$.

In the refrigerator case, the maximization of the cooling power $P_{[\rm R]}^{(\max)}$, within the linear response regime, yields the unphysical result $|V| \to \infty$. We therefore only consider the maximization of the COP. A simple optimization of C yields

$$C^{(\max)} = C_{\rm c}\frac{\sqrt{ZT+1}-1}{\sqrt{ZT+1}+1}, \tag{3.30}$$

where $C_c = T/\Delta T$ within the linear response regime. Interestingly, also $C^{(\max)}$ is a growing function of ZT with the same functional dependence on ZT as $\eta^{(\max)}$, see Eq. (3.29).

3.1.3 The best thermoelectrics

In the previous section, we expressed the thermodynamic properties of thermoelectric heat engines and refrigerators in terms of the transport coefficients. Thanks to Eqs. (3.28), (3.29) and (3.30), it is clear that a good thermoelectric device must have a large value of ZT, while retaining also a large power factor GS^2. We are therefore interested in finding devices with large values of G and S, which increases both the power factor and the figure of merit, and small values of K.

Unfortunately, most bulk materials have $ZT < 1$, while a value of at least $ZT \approx 3$ is required to make thermoelectric devices competitive with traditional heat engines based on moving parts [11]. The optimization of ZT is a very difficult task, since G, S and K cannot be varied independently. As anticipated earlier, one limiting factor is the Wiedemann-Franz

law [see Eq. (3.1)] which fixes the ratio GT/K in many bulk materials, preventing us from varying G and K independently. Furthermore, Ref. [11] argues that any good thermoelectric material is likely to strongly violate the Wiedemann-Franz law.

In a seminal work by Mahan and Sofo [5], it was shown that devices that act as "energy filters" yield a divergent value of ZT. In other words, we are interested in devices where only electrons with a given fixed energy contribute to transport. This can be achieved by considering, for example, low dimensional systems which exhibit peaked density of states, or considering the extreme case of a single-level quantum dot (QD), which is a fermionic system with a single energy level. As we show in Sec. 3.1.5, when a single-level QD is weakly coupled to the leads, only electrons which have the exact energy of the QD's energy level are allowed to tunnel between the baths and the QD, realizing an energy filter as prescribed by Mahan and Sofo. As we show, this system yields a divergent value of ZT by producing a divergent value of GT/K, which is a stark violation of the Wiedemann-Franz law. Physically, QDs exhibit a discrete spectrum, with an energy spacing even larger than the thermal energy (at cryogenic temperatures), thanks to extreme spatial confinement of the electrons. For example, in Chap. 5 we study the thermoelectric properties af a QD embedded in an InAs/InP nanowire, where the size of the QD is of the order of tens of nanometers, producing a level spacing of the order of 5 meV.

3.1.4 Computing charge and heat currents

In this section we discuss how to compute the charge and heat currents flowing across our device building on the framework described in Chap. 2. We assume that the out-of-equilibrium state of the system, described by the probabilities p_i solutions to Eq. (2.36) in the steady-state, are known. While the expressions we now derive can be obtained using a more formal approach, we present an intuitive derivation which sheds light on the microscopic mechanism responsible for charge and heat transport in the weak coupling regime. This approach also allows us to develop useful physical intuition necessary to compute charge and heat currents also beyond the weak coupling regime.

For concreteness, let us assume that we have two thermal baths, so $H_{\mathrm{B}} = H_{\mathrm{L}} + H_{\mathrm{R}}$. If the baths are independent (as we assume through the entire thesis), we can decompose the rates

$$\Gamma_{i\to j} = \Gamma^{(\mathrm{L})}_{i\to j} + \Gamma^{(\mathrm{R})}_{i\to j}, \tag{3.31}$$

where $\Gamma^{(\alpha)}_{i\to j}$, formally defined by Eq. (2.40) with $\mathcal{T} = H_{\mathrm{S},\alpha}$, is the transition rate induced by bath α. Furthermore, let us focus on I (which is the charge current flowing from left to right) and on J_{L} defined in Eq. (3.6). We recall that J_{L} is defined as the variation of the expectation values of

$$H_\alpha - \mu_\alpha N_\alpha. \tag{3.32}$$

Therefore, we can interpret I as $-e$ times the variation in electron number of the left bath, and J_{L} as the variation of energy of the left bath, minus μ_α times the variation in electron number of the left bath.

In this thesis, we study steady-state devices which are fermionic, and such that the eigenstates of H_{S} have a well define number of electrons (i.e. H_{S} commutes with the operator associated with the total fermionic number in S). This is equivalent to requiring that S, alone, does not create nor destroy electrons. Of course, this assumption encompasses also classes of interacting systems, such as electronic devices with Coulomb repulsion (examples are studied in Chaps. 4, 5, 6, 7 and 8). We therefore denote with N_i and E_i respectively the number of

electrons and the energy of eigestante $|E_i\rangle$ of H_S. From the derivation of the Pauli master equation, valid in the weak-coupling regime, we can draw the following physical picture: our system S undergoes transitions between eigenstates by interacting with the baths. We can associate a transition rate $\Gamma_{i\to j}$ to each transition from some state $|E_i\rangle$ to some state $|E_j\rangle$ of S. In most cases considered in this thesis, these transitions are due to electrons tunneling between the baths and the system. A transition between $|E_i\rangle$ and $|E_j\rangle$ changes the number of charges in S from N_i to N_j, and its energy from E_i to E_j. Since these transitions conserve the total number of electrons (by hypothesis of $H_{S,\alpha}$) and energy (at leading order in the coupling strength, the rates are computed with the Fermi golden rule, which imposes energy conservation), the number of electrons and the energy of the baths change respectively by $(N_i - N_j)$ and $(E_i - E_j)$ upon the transition. We can therefore compute I and J_L accounting for the transported quantity upon all possible transitions. This yields

$$\begin{aligned} I &= \sum_{i,j} p_i \, \Gamma^{(L)}_{i\to j} (-e)(N_j - N_i), \\ J_L &= \sum_{i,j} p_i \, \Gamma^{(L)}_{i\to j} \left[(E_j - E_i) - \mu_L (N_j - N_i) \right]. \end{aligned} \tag{3.33}$$

The sum over i is a sum over all possible states of S, while the sum over j describes all possible transition from state i to state j (notice that the terms within the sum vanish for $i = j$). The transition rate $\Gamma^{(L)}_{i\to j}$ is then multiplied by the corresponding transported quantity, i.e. the charge $-e(N_j - N_i)$ or the heat $(E_j - E_i) - \mu_L(N_j - N_i)$.

With a similar argument, we can also include the effect of co-tunneling in the charge and heat currents. A detailed derivation is provided in Chap. 6 and in App. C. All thermodynamics quantities, such as the power, efficiency and COP, can now be computed from Eq. (3.33).

3.1.5 Single-level quantum dot-based heat engine: an energy filter

In this section we use the formalism developed in Chap. 2 and in Sec. 3.1.4 to study the performance of a single-level QD-based heat engine. This example allows us to introduce some concepts and methods which are relevant also for more complicated systems, and we illustrate the idea of an "energy filter". While an exact solution, valid for arbitrary coupling strength, which allows us to compute the charge and heat currents through such a simple system is known [40, 41], we use the perturbative approach of Chap. 2 as a way to illustrate the formalism which can then be applied also to complicated interacting systems where exact solutions are hard, if not impossible, to find.

The Hamiltonian of the single-level QD is given by

$$H_S = E \, d^\dagger d, \tag{3.34}$$

where $d^\dagger$ (d) is the creation (destruction) fermionic operator of the electron in the QD, and the Hamiltonian of the baths is the one described in Eq. (3.3). Since we are considering two thermal baths, the coupling Hamiltonian will be given by $H_{S,B} = H_{S,L} + H_{S,R}$, where $H_{S,\alpha}$ describe the coupling between the QD and bath α. We assume that the QD is tunnel-coupled to bath α, i.e.

$$H_{S,\alpha} = \sum_k V_{\alpha k} \, d^\dagger c_{\alpha k} + h.c., \tag{3.35}$$

where $V_{\alpha k}$ are complex coefficients describing the system-bath coupling.

The starting point of our calculation is the Pauli master equation, see Eq. (2.36). The two states of our system are the empty state $|E_0\rangle \equiv |0\rangle$, where $|0\rangle$ is the fermionic vacuum state, and the occupied state, $|E_1\rangle \equiv d^\dagger |0\rangle$. State $|E_0\rangle$ is characterized by 0 energy and 0 electrons in the QD, while state $|E_1\rangle$ is characterized by energy E and 1 electron. Denoting with p_0 and p_1 the corresponding probabilities, the steady-state solution can be found setting $dp_1/dt = 0$ and recalling the normalization condition for probabilities, i.e.

$$\begin{aligned} p_0\Gamma_{0\to1} - p_1\Gamma_{1\to0} &= 0, \\ p_0 + p_1 &= 1, \end{aligned} \tag{3.36}$$

where $\Gamma_{i\to j}$ are the sequential tunneling rates describing a transition in the local system from state $|E_i\rangle$ to $|E_j\rangle$. We compute these rates using the Fermi golden rule Eq. (2.40) as discussed in Sec. 2.2.

Let us start from $\Gamma_{0\to1}$. We need to consider all eigenstates of the total uncoupled system which describe an electron tunneling from the baths to the empty QD. Therefore, the initial and final states are[1]

$$|\psi_{0\alpha k}\rangle = c^\dagger_{\alpha k}|0\rangle\,, \qquad\qquad |\psi_1\rangle = d^\dagger|0\rangle\,, \tag{3.37}$$

for all values of $\alpha = \mathrm{L},\mathrm{R}$ and k. Notice that while there are many initial states $|\psi_{0\alpha k}\rangle$, indexed by α and k, describing this transition, there is only one final state $|\psi_1\rangle$. The energy of $|\psi_{0\alpha k}\rangle$ is $\varepsilon_{0\alpha k} = \epsilon_{\alpha k}$, and the energy of $|\psi_1\rangle$ is $\varepsilon_1 = E$. Plugging this into the leading order Fermi golden rule Eq. (2.40) yields

$$\Gamma_{0\to1} = \frac{2\pi}{\hbar}\sum_{\alpha k} W_{0\alpha k}(1-W_1)|\,\langle 0|d\,H_{\mathrm{S},\alpha}c^\dagger_{\alpha k}|0\rangle\,|^2\delta(\epsilon_{\alpha k}-E). \tag{3.38}$$

Since the equilibrium thermal probability of finding a fermion with energy $\epsilon_{\alpha k}$ in bath α is given by the Fermi distribution $f_\alpha(\epsilon_{\alpha k}-\mu_\alpha) \equiv (1+e^{(\epsilon_{\alpha k}-\mu_\alpha)/(k_B T_\alpha)})^{-1}$, $W_{0\alpha k} = f_\alpha(\epsilon_{\alpha k}-\mu_\alpha)$, while $W_1 = 0$ since this process requires the QD to be initially empty ($\Gamma_{0\to1}$ is the conditional probability per unit time of having a transition from $|E_0\rangle$ to $|E_1\rangle$, provided that the QD is empty). Using these relations, plugging Eq. (3.35) into Eq. (3.38) and using the anticommutation relations, we find

$$\Gamma_{0\to1} = \sum_\alpha \Gamma^{(\alpha)}_{0\to1} \equiv \sum_\alpha \frac{2\pi}{\hbar}\sum_k f_\alpha(\epsilon_{\alpha k}-\mu_\alpha)|V_{\alpha k}|^2\delta(\epsilon_{\alpha k}-E), \tag{3.39}$$

where we split the sum over α in order to separate the contribution of the two baths. Notice that the energy conserving delta-function in Eq. (3.39) imposes that only electrons with energy $\epsilon_{\alpha k} = E$ can tunnel from the baths into the QD: this is precisely the mechanism producing the energy filter we mentioned earlier. Since the thermal baths are assumed to be large objects, the level spacing is assumed to be infinitesimal. This allows us to perform the following formal substitution

$$\sum_k g(\epsilon_k) \to \int_{-\infty}^{+\infty} d\epsilon\, D_\alpha(\epsilon) g(\epsilon), \tag{3.40}$$

[1] More precisely, one should consider all eigenstates of the baths, therefore also multi-electron states. One then associates to each configuration a probability given by the grand-canonical distribution. For simplicity, since the baths are non-interacting, we here adopt a single-particle picture such that we only consider single-particle states, and we associate to each state a probability given by the Fermi distribution. The two approaches yield identical results.

where $D_\alpha(\epsilon) \equiv \sum_k \delta(\epsilon - \epsilon_k)$ is the density of states of bath α, and $g(\epsilon)$ is an arbitrary function (sufficiently smooth on the energy spacing scale of bath α). This yields

$$\Gamma^{(\alpha)}_{0\to 1} = \gamma_\alpha f_\alpha(E - \mu_\alpha), \tag{3.41}$$

where

$$\gamma_\alpha \equiv \frac{2\pi D(E)|V_\alpha(E)|^2}{\hbar} \tag{3.42}$$

fixes the typical rate. In Eq. (3.42) we define $V_\alpha(\epsilon_k) \equiv V_{\alpha k}$. In most realistic cases, the density of states and the coupling constants are approximately constant on the energy scale where transport occurs (which is order of the largest between eV and $k_B T_\alpha$); therefore it is common to assume that γ_α does not depend on energy. Equations (3.41) and (3.42) describe a lot of physics: we see that the probability per unit time for an electron to tunnel from the lead to the QD is proportional to the occupation of the electrons in the lead, described by the Fermi distribution. Indeed, if the chemical potential of lead α is smaller than E, and the distance is much larger than $k_B T_\alpha$, then the rate becomes vanishingly small since there are no electrons which have a high enough energy to tunnel into the QD. If instead the chemical potential is larger than E, and the distance is much larger than $k_B T_\alpha$, than $\Gamma^{(\alpha)}_{0\to 1} \approx \gamma_\alpha$ reaches its maximum value, which depends on the square of the coupling terms $V_{\alpha k}$, and on the density of states of the bath. If instead $|E - \mu_\alpha|/(k_B T_\alpha) \lesssim 1$, then $\Gamma^{(\alpha)}_{0\to 1}$ will be a finite fraction of γ_α.

We now move to $\Gamma_{1\to 0}$, which also in this case will be given by the sum of the contributions of the two leads, i.e. $\Gamma_{1\to 0} = \sum_\alpha \Gamma^{(\alpha)}_{1\to 0}$. We could repeat the previous reasoning to the inverse process, however a faster way to compute this rate is to invoke the detailed balance equation. Indeed, the rate associated to a process is directly related to the rate associated with the inverse process through Eq. (2.38). Using the algebraic relation $f_\alpha(\epsilon)/[1 - f_\alpha(\epsilon)] = e^{-\epsilon/(k_B T_\alpha)}$, it is easy to show that

$$\Gamma^{(\alpha)}_{1\to 0} = \gamma_\alpha[1 - f_\alpha(E - \mu_\alpha)]. \tag{3.43}$$

The $1 - f_\alpha(E - \mu_\alpha)$ factor in Eq. (3.43) represents the fact that, because of the Pauli exclusion principle, the state in the baths at energy E must be unoccupied for the electron to tunnel from the QD to the bath.

The out-of-equilibrium state of the QD can be computed by plugging Eqs. (3.43) and (3.41) into (3.36), yielding

$$p_0 = \frac{\gamma_{\rm L}(1 - f_{\rm L}) + \gamma_{\rm R}(1 - f_{\rm R})}{\gamma_{\rm L} + \gamma_{\rm R}}, \qquad p_1 = \frac{\gamma_{\rm L} f_{\rm L} + \gamma_{\rm R} f_{\rm R}}{\gamma_{\rm L} + \gamma_{\rm R}}, \tag{3.44}$$

where, for ease of notation, we defined $f_\alpha \equiv f_\alpha(E - \mu_\alpha)$.

We can now compute the charge and heat currents. Equation (3.33) reduces to

$$\begin{aligned} I &= (-e)\, p_0 \Gamma^{(\rm L)}_{0\to 1} - (-e)\, p_1 \Gamma^{(\rm L)}_{1\to 0}, \\ J_{\rm L} &= (E - \mu_{\rm L})\, p_0 \Gamma^{(\rm L)}_{0\to 1} - (E - \mu_{\rm L})\, p_1 \Gamma^{(\rm L)}_{1\to 0}. \end{aligned} \tag{3.45}$$

Plugging Eqs. (3.41), (3.43) and (3.44) into Eq. (3.45) yields

$$\begin{aligned} I &= -e \frac{\gamma_{\rm L}\gamma_{\rm R}}{\gamma_{\rm L} + \gamma_{\rm R}}(f_{\rm L} - f_{\rm R}), \\ J_{\rm L} &= \frac{E - \mu_{\rm L}}{-e} I. \end{aligned} \tag{3.46}$$

It is now straightforward to compute the transport coefficients using their definition. Since the energies μ_α and E are defined up to an additive constant, without loss of generality we set $E = 0$. Furthermore, defining μ such that $\mu_{\mathrm{R}} = \mu + eV/2$ and $\mu_{\mathrm{L}} = \mu - eV/2$, it is easy to find

$$\begin{aligned} G &= \frac{e^2}{4k_BT}\,\frac{\gamma_{\mathrm{L}}\gamma_{\mathrm{R}}}{\gamma_{\mathrm{L}}+\gamma_{\mathrm{R}}}\,\frac{1}{\coth^2\left(\frac{\mu}{2k_BT}\right)}, \\ S &= \frac{\mu}{eT}, \\ K &= 0. \end{aligned} \tag{3.47}$$

As a function of the average chemical potential μ, the electrical conductance is bell-shaped, with the maximum at $\mu = 0$, i.e. at resonance, and with a characteristic width determined by the thermal energy k_BT. The electrical conductance then decays exponentially as μ increases. The Seebeck coefficient, instead, is a linear function of μ and it vanishes at resonance. Indeed, the Seebeck coefficient is zero when the system is particle-hole symmetric, and this occurs in our system when $\mu = 0$.

Strikingly, $K = 0$, which implies

$$ZT \to \infty. \tag{3.48}$$

Indeed, our system acts as a perfect energy filter thus, as predicted by Mahan and Sofo, its figure of merit diverges. The high efficiency and efficiency at maximum power of a single-level QD in the weak coupling regime is therefore due to the fact that it exhibits a finite power factor GS^2, while $K = 0$, resulting in $ZT \to \infty$. This surprising behavior of K is a direct consequence of the proportionality between I and J_{L} [see Eq. (3.46)]. Indeed, K is defined as the ratio between J_{L} and ΔT when the voltage bias is chosen as to guarantee $I = 0$. Crucially, if I and J_{L} are directly proportional, as in our case, $I = 0$ implies $J_{\mathrm{L}} = 0$, and therefore $K = 0$. It is thus the proportionality between J_{L} and I which maximizes the figure of merit, and this happens only if all electrons tunneling through the device have the same exact energy (in our case, they all carry energy E).

In reality, it is not possible to realize a device which has both finite power, and an exactly divergent ZT. There are (at least) two effects that break the proportionality between I and J_{L} by allowing electrons to tunnel through the device with different energies. The first is the presence of other energy levels in the QD. While all electrons obviously carry a charge $-e$, the presence of other energy levels allows electrons to tunnel through the device carrying different energies, and thus breaking the proportionality $I \propto J_{\mathrm{L}}$. An example of an experiment where this effect is dominant is described in Chap. 5. Another mechanisms is the so-called "level broadening", which arises by considering processes beyond leading order in the coupling strength. Indeed, processes such as co-tunneling allow electrons to tunnel *directly* from one lead to the other passing through a virtual state in the QD. This process is such that tunneling electrons are allowed to have an energy inside an energy windows centered around E with a characteristic width set by $\hbar\gamma_\alpha$. Therefore, it is as if we had a "leak" in our energy filter. One would be tempted to decrease the coupling γ_α as to make the filter more and more ideal. However, doing so reduces the power (which scales as $\hbar\gamma_\alpha$): this is one of the many cases where we witness a trade-off between efficiency and power. An example of an experiment where this effect is dominant is described in Ref. [42].

At last, another physical mechanism which reduces the efficiency of actual devices is the presence of phonons. They do not carry charge, so they do not contribute to G and S, but they carry energy, so they contribute to K by increasing the thermal conductance. While their impact becomes negligible at sufficiently low temperatures (for example at cryogenic

temperatures), they are definitely relevant at room temperature, and they only have a detrimental effect on the performance of thermoelectric device. Throughout this thesis, we only focus on the electronic degrees of freedom, therefore neglecting the impact of phonons.

Despite these limitations, the idea of implementing energy filters is a fundamental concept when building efficient thermoelectric devices. This idea resulted in numerous theoretical and experimental works (see Chap. 4 for an overview of the literature). For example, using QD-based devices, it was experimentally shown in Ref. [42] that an electronic efficiency at maximum power close to the Curzon-Ahlborn efficiency can be achieved at temperatures around $T = 1\,\mathrm{K}$, while in Chap. 5 we describe an experiment where an electronic figure of merit $ZT \approx 35$ can be achieved at temperatures around $T = 30\,\mathrm{K}$. In the former example, the efficiency is limited by the level-bradening effect, while in the latter by the multilevel structure of the QD.

3.2 Driven thermal machines

In this section we discuss how to implement a *driven thermal machine* and how to describe its performance. While the systems studied in Sec. 3.1 operate in the steady-state, and they perform work again a chemical potential difference, the systems we consider in this section are instead driven in time, i.e. the Hamiltonian of the local system $H_{\mathrm{S}}(\vec{u}(t))$ is explicitly *time-dependent* through a set of *control parameters* $\vec{u}(t)$. These control parameters could be for example gate voltages, electromagnetic fields, etc. In this scenario, work is performed by the external fields, for example by a gate voltage source. In this thesis, we only consider driven systems in the weak-coupling regime.

The operating principle of these machines is very similar to a classical thermodynamic heat engine. Let us consider the standard example of an ideal gas, which plays the role of our system S, inside a chamber with a movable piston. Assuming that the system remains close to equilibrium, we can describe the state of the system by specifying its pressure, volume and temperature. The evolution of the state of the system is described by the state equation, and it is influenced by two effects: we can couple the system to a heat bath, allowing heat to flow between the bath and the system, or we can act on the system with some time-dependent control which compresses or expands the gas. The state of the system will therefore change both because we can couple it to a heat bath, and because we can act on it with some time-dependent control. At last, we can extract work from the system by allowing the piston to expand in time. In this setup, work is performed against the external time-dependent force that is compressing or expanding the gas.

In the quantum case the state of the system can be driven completely out-of-equilibrium, so we cannot use an effective description in terms of a handful of macroscopic variables. Instead, the state of the system is described by the reduced density matrix $\rho(t)$. The state, which evolves according to the Lindblad master equation [see Eq. (2.29)], can change because we couple the system to a heat bath, or because we act on the system with some time-dependent control. Also in this case, work is performed against the time-dependent controls $\vec{u}(t)$.

In Sec. 3.2.1 we describe in detail how to compute the heat currents and the work in driven systems, and we present the laws of thermodynamics in this context. We then discuss how to implement a heat engine or a refrigerator, and we give some general properties of the efficiency at maximum power. In sec. 3.2.2 we pedagogically apply the formalism described in Sec. 3.2.1 to study a heat engine based on a driven qubit (two level system) in the infinitely

slow regime. Finite-time effects, studied using the formalism described in Chap. 2 and in Sec. 3.2.1 are studied in Chaps. 9 and 10.

3.2.1 Setup and characterization of thermal machines

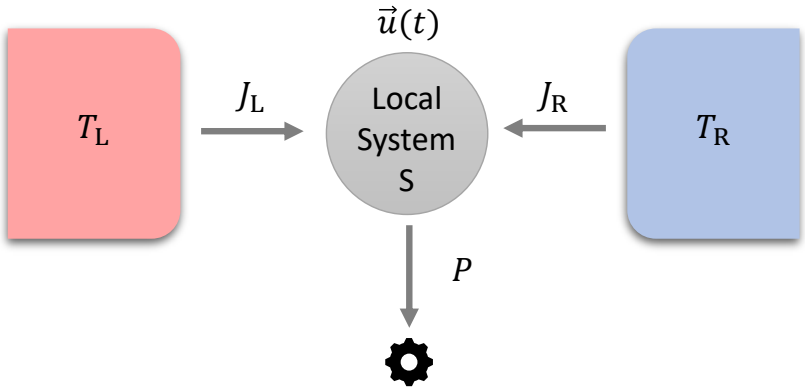

FIGURE 3.3: A quantum system S (gray circle), which is controlled through a set of control parameters $\vec{u}(t)$, can be coupled to a thermal bath at temperature T_L (left red box) or to a thermal bath at temperature T_R (right blue box). J_L and J_R denote the heat fluxes flowing out of the respective thermal baths, whereas P denotes the extracted power.

Let us consider a generic system S that can be coupled to two arbitrary heat baths characterized respectively by temperatures T_L (left) and T_R (right), as schematically shown in Fig. 3.3. We can control the system in time through a set of controls parameters $\vec{u}(t)$ which enter the Hamiltonian of the system so that $H_S(\vec{u}(t))$. Furthermore, we assume that we can arbitrarily couple and decouple the thermal baths to the system. As in the previous section, we consider two thermal baths, so we have that $H_B = H_L + H_R$, where H_α is the Hamiltonian of bath α with $\alpha = L, R$. We assume that the reduced density matrix $\rho(t)$ of the local system evolves according to the Lindblad master equation (2.29). Since we have two thermal baths, the dissipator decomposes naturally as $D_{\vec{u}(t)}[\rho] = D_{L,\vec{u}(t)}[\rho] + D_{R,\vec{u}(t)}[\rho]$. Neglecting the Lamb-shift Hamiltonian, the Lindbald master equation therefore reads

$$\frac{d}{dt}\rho(t) = -\frac{i}{\hbar}[H_S(\vec{u}(t)), \rho(t)] + \sum_\alpha \lambda_\alpha(t) D_{\alpha,\vec{u}(t)}[\rho(t)], \tag{3.49}$$

where $\lambda_\alpha(t) = 0, 1$ is an additional control parameter that allows us to switch on or off the coupling to bath α by setting to 0 the contribution of bath α. Since the control $\vec{u}(t)$ can change the spectrum of $H_S(\vec{u}(t))$, we use the notation $D_{\alpha,\vec{u}(t)}[\rho(t)]$ to emphasize the dependence of the dissipators on the controls. While the Lindblad equation was derived in Chap. 2 assuming that H_S did not depend on time, it can be shown that it holds as in Eq. (3.49), with dissipators computed using the *instantaneous* spectrum of $H_S(\vec{u}(t))$, if $H_S(\vec{u}(t))$ commutes with itself at all times, or if the driving speed of $\vec{u}(t)$ is slow enough as to guarantee the validity of the quantum adiabatic theorem for a closed system evolving only according to $H_S(\vec{u}(t))$ [43–45].

We now derive an expression to compute the extracted power and the heat currents flowing out of the baths. We start from the definition of work. Let us assume, for the moment, that $\rho(t)$ evolves only under the influence of $H_S(\vec{u}(t))$, i.e. we set $\lambda_\alpha(t) = 0$. In such case, there

are no heat baths, so the first law of thermodynamics for the system is given by

$$\dot{U}(t) = -P(t), \tag{3.50}$$

where $P(t)$ is the extracted power, and $U(t)$ is the internal energy defined as

$$U(t) = \mathrm{Tr}[\rho(t) H_{\mathrm{S}}(\vec{u}(t))]. \tag{3.51}$$

Taking the time derivative yields

$$\dot{U}(t) = \mathrm{Tr}[\dot{\rho}(t) H_{\mathrm{S}}(\vec{u}(t))] + \mathrm{Tr}\Big[\rho(t) \dot{H}_{\mathrm{S}}(\vec{u}(t))\Big], \tag{3.52}$$

where, with a slight abuse of notation, we denote $\dot{H}_{\mathrm{S}}(\vec{u}(t)) = d/(dt) H_{\mathrm{S}}(\vec{u}(t))$. Using Eq. (3.49) and the cyclic property of the trace, it is easy to see that the term proportional to $\dot{\rho}(t)$ vanishes if the evolution of $\rho(t)$ is unitary. Therefore the extracted power, for a closed system, is given by

$$P(t) = -\mathrm{Tr}\Big[\rho(t) \dot{H}_{\mathrm{S}}(\vec{u}(t))\Big]. \tag{3.53}$$

We now move to the case where also the baths are coupled, i.e. $\lambda_\alpha(t) \neq 0$. Denoting with J_α the heat flowing out of lead α, the first law of thermodynamics is given by

$$\dot{U}(t) = -P(t) + \sum_\alpha J_\alpha. \tag{3.54}$$

Differentiating $\dot{U}(t)$ as in Eq. (3.52) and using Eq. (3.49) yields

$$\dot{U}(t) = \mathrm{Tr}\Big[\rho(t) \dot{H}_{\mathrm{S}}[\vec{u}(t)]\Big] + \sum_\alpha \lambda_\alpha(t) \,\mathrm{Tr}\Big[D_{\alpha,\vec{u}(t)}[\rho(t)] H_{\mathrm{S}}(\vec{u}(t))\Big]. \tag{3.55}$$

We therefore identify the power as in Eq. (3.53), and the heat currents with [46]

$$J_\alpha = \lambda_\alpha(t) \,\mathrm{Tr}\Big[D_{\alpha,\vec{u}(t)}[\rho(t)] H_{\mathrm{S}}(\vec{u}(t))\Big]. \tag{3.56}$$

We are now able to compute the heat currents and the power extracted from our machine, but we still need to understand how to construct thermodynamic cycles. As in classical thermal machines, we wish to operate our system cyclically, such that the variation of internal energy is zero after each cycle. Thanks to the first law of thermodynamics, this implies that all the extracted work only comes from energy exchanged with the baths in the form of heat, and not from a particular preparation of the system's state. We therefore consider a periodic control with period T, such that $\vec{u}(t+T) = \vec{u}(t)$, and $\lambda(t+T) = \lambda(t)$. We may refer to this periodic control with the term "protocol". From Eq. (3.51) we see that the internal energy difference is zero after each cycle only if both the control and the state $\rho(t)$ are periodic. However, the state $\rho(t)$ is not in general periodic.

We can recover the standard concept of a cycle by exploiting an interesting property of the Lindblad master equation: the real part of the eigenvalues of the Lindbladian generator $\mathcal{L}_{\vec{u}(t),\lambda_\alpha(t)}$, defined as the linear operator such that Eq. (3.49) is written as $\dot{\rho}(t) = \mathcal{L}_{\vec{u}(t),\lambda_\alpha(t)}[\rho(t)]$, are all non-positive [27]. It can be shown that, under weak assumptions, this property implies that $\rho(t)$ admits a so-called "limiting cycle" [29]. This means that, if we apply a T periodic protocol $\vec{u}(t)$ and $\lambda(t)$, after a sufficiently long time the state $\rho(t)$ will also become a periodic function with the same period T. This asymptotic solution, known as the limiting cycle, does not depend on the initial condition for $\rho(t)$. Throughout

this thesis, we therefore focus on the regime where both the protocol and the state are periodic functions with the same period. In this regime, the internal energy difference is zero after each cycle.

Defining $\langle P \rangle$ as the average work and $\langle J_\alpha \rangle$ as the average heat exchanged during one cycle, i.e.

$$\langle P \rangle \equiv \frac{1}{T}\int_0^T P(t)\,dt, \qquad \langle J_\alpha \rangle \equiv \frac{1}{T}\int_0^T J_\alpha(t)\,dt, \tag{3.57}$$

the first law reduces to

$$\langle P \rangle = \langle J_{\rm L} \rangle + \langle J_{\rm R} \rangle\,, \tag{3.58}$$

and the second law, for the time averaged quantities, reduces to

$$\frac{\langle J_{\rm L} \rangle}{T_{\rm L}} + \frac{\langle J_{\rm R} \rangle}{T_{\rm R}} \leq 0. \tag{3.59}$$

We can now define a heat engine and a refrigerator as in Sec. 3.1.1 using the average power and heat currents instead of their steady-state counterpart. Let us assume that $T_{\rm L} \geq T_{\rm R}$. A heat engine is a system that converts part of the heat flowing from the hot lead ($\langle J_{\rm L} \rangle \geq 0$) to the cold lead ($\langle J_{\rm R} \rangle \leq 0$) into work ($\langle P \rangle > 0$). The power of a heat engine is therefore identified with $P_{\rm [E]} \equiv P$, and $\langle P_{\rm [E]} \rangle$ denotes its time average over a cycle. The efficiency is then defined as

$$\eta \equiv \frac{\langle P_{\rm [E]} \rangle}{\langle J_{\rm L} \rangle}. \tag{3.60}$$

The maximization of the efficiency is something that has been understood since Carnot, i.e. we must perform *reversible* transformations. This universal strategy typically requires infinitely slow transformations, which means that a finite amount of work is extracted over an infinite amount if time. Therefore, while it is possible to reach Carnot efficiency, this usually comes to the price that $\langle P_{\rm [E]} \rangle = 0$. It is therefore interesting to try to understand how to maximize the power.

The maximization of the extracted power, i.e. the maximization over all possible cycles described by all possible periodic functions $\vec{u}(t)$ and $\lambda_\alpha(t)$, is in general a formidable task. Indeed the power, which involves finite-time thermodynamics, strongly depends on the underlying dynamics of the system, and as such it is deemed as a model specific task, lacking universal traits. There have been many attempts in literature to design cycles yielding high power. These strategies range from the use of shortcuts to adiabaticity to speed up Carnot cycles [47–50], to optimal control techniques [51–56], to slow driving expansions [38, 57–60] (see Chap. 9 for an overview of the literature). In Chaps. 9 and 10 we show that, for small quantum systems obeying Lindblad dynamics, there may be universal features in the optimal protocols that deliver maximum power.

A concept closely related to the maximum power, which has received a lot of attention in literature, is that of the efficiency at maximum power $\eta(P_{\rm [E]}^{(\max)})$, defined as the efficiency of the heat engine while it is operating at maximum power. As in the steady-state case, many bounds have been derived in literature either for certain classes of systems, or in certain operational regimes. For example, the Curzon-Ahlborn efficiency [see Eq. (3.17)] emerges in various specific models [37, 61, 62], and it has been derived by general arguments from linear irreversible thermodynamics [36]. Notably, it has been shown in Ref. [38] that low dissipation heat engines, i.e. systems operated slow enough such that only leading order corrections in $1/T$ are accounted for respect to the infinitely slow regime, exhibit an efficiency

at maximum power that is exactly upper bounded by the $\eta_{\rm SS}$ efficiency [defined in Eq. (3.18)], valid for any temperature difference. However, in Sec. 9 we show that, for a simple two-level system, the maximum power is reached in the opposite regime, i.e. when the driving is faster than the typical thermalization rates induces by the bath, such that the state of the system is completely out-of-equilibrium. In this regime, we show that the only upper bound to efficiency at maximum power is given by the Carnot efficiency.

Analogously, we can construct a refrigerator, a machine that requires work ($\langle P\rangle \leq 0$) to move heat from the cold bath ($\langle J_{\rm R}\rangle \geq 0$) to the hot bath ($\langle J_{\rm L}\rangle \leq 0$). The power we are interested in is related to the heat extracted from the cold bath. We therefore define $P_{[\rm R]} \equiv J_{\rm R}$, and $\langle P_{[\rm R]}\rangle$ its average over a cycle. The COP is defined as

$$C \equiv \frac{\langle P_{[\rm R]}\rangle}{|\langle P\rangle|}. \tag{3.61}$$

As in the heat engine case, C can be maximized by performing reversible transformations, which allow us to reach the Carnot upper bound $C_{\rm c}$, at the price of vanishing power. We are therefore interested in studying the maximum power $P_{[\rm R]}^{(\max)}$, i.e. the average power maximized over all possible protocols. We can then study also the COP at maximum power $C(P_{[\rm R]}^{(\max)})$, defined as the COP when the system is delivering maximum power.

3.2.2 Slowly driven qubit-based Otto cycle

In this section we go through a simple example, namely a system comprised of a qubit coupled to two thermal baths. We study how the system performs by applying an infinitely slow Otto cycle. This allows us to understand how different Otto cycles can lead the system to operate as a heat engine or as a refrigerator. We then compute the efficiency and the COP. The maximization of the power of a qubit-based heat engine or refrigerator, accounting for finite-time effects, is performed in Chap. 9.

Assuming as usual that $T_{\rm L} \geq T_{\rm R}$, a quantum Otto cycle is made up of four strokes.

1. Hot isothermal stroke: S is placed in contact with the hot bath at temperature $T_{\rm L}$ for some time $\tau_{\rm L}$ while the controls are not varied. As a consequence, only heat is exchanged between the bath and S.

2. Adiabatic stroke: S is disconnected from the baths, and the controls are varied in time according to some protocol. The evolution during this stroke is unitary, thus only work is extracted/performed on the system.

3. Cold isothermal stroke: S is placed in contact with the cold bath at temperature $T_{\rm R}$ for some time $\tau_{\rm R}$ while the controls are not varied. Only heat is exchanged between the bath and S.

4. Adiabatic stroke: S is disconnected from the baths, and the controls are again varied in time according to some protocol. The evolution during this stroke is unitary, thus only work is extracted/performed on the system.

This protocol is then repeated periodically. As we see, heat and work are never exchanged simultaneously in an Otto cycle, thus the analysis is simpler. Furthermore, in this section, we study an "ideal" Otto cycle, where $\tau_\alpha \to \infty$. This implies that the system reaches full thermalization during the isothermal strokes. This huge simplification allows us to study the

system without taking into account finite-time effects, i.e. without even solving the Lindblad equation.

We study a working fluid comprised of a two-level system

$$H_{\rm S}(\epsilon(t)) = \frac{\epsilon(t)}{2}\sigma_z, \tag{3.62}$$

where $\epsilon(t)$ is our only control parameter [previously denoted with $\vec{u}(t)$] and σ_z is a Pauli matrix. Let us denote with $|E_0\rangle$ the instantaneous ground state with energy $-\epsilon(t)/2$ and with $|E_1\rangle$ the instantaneous excited state with energy $\epsilon(t)/2$, and let us define the corresponding probabilities $p_j(t) = \mathrm{Tr}[|E_j\rangle\langle E_j|\,\rho(t)]$, for $j = 0, 1$, such that $p_0 + p_1 = 1$. Physically p_0 is the probability of finding the system in the ground state, and p_1 of finding the system in the excited state. Notice that while the eigenvalues of $H_{\rm S}(\epsilon(t))$ depend on $\epsilon(t)$, the eigenstates do not: this is due to the fact that $H_{\rm S}(\epsilon(t))$ commutes with itself at all times.

Invoking the first principle, we can compute the total heat exchanged Q during the isothermal strokes as the difference between the final internal energy of the system and the initial one. Denoting with ρ_i (ρ_f) the initial (final) state of S during the isothermal stroke, with corresponding probabilities $p_j^{(i)}$ ($p_j^{(f)}$), and denoting with ϵ the fixed control parameter, we have

$$Q = \mathrm{Tr}[\rho_f\, H_{\rm S}(\epsilon)] - \mathrm{Tr}[\rho_i\, H_{\rm S}(\epsilon)] = \frac{\epsilon}{2}\left[(p_1^{(\rm f)} - p_1^{(\rm i)}) - (p_0^{(\rm f)} - p_0^{(\rm i)})\right]. \tag{3.63}$$

Invoking the first principle, we can also compute the work W extracted during the adiabatic strokes as the difference between the initial and final internal energy. We denote with ϵ_i (ϵ_f) the value of the control and with ρ_i (ρ_f) the state of S at the beginning (end) of the stroke. Since the evolution is unitary, and since $H_{\rm S}(\epsilon(t))$ commutes with itself at all times, the probabilities associated with ρ_i and ρ_f do not change. Denoting them with p_0 and p_1, we find

$$W = \mathrm{Tr}[\rho_i H_{\rm S}(\epsilon_i)] - \mathrm{Tr}[\rho_f H_{\rm S}(\epsilon_f)] = \frac{1}{2}(\epsilon_f - \epsilon_i)(p_0 - p_1). \tag{3.64}$$

Notice that the work only depends on the initial and final control parameters, while it does not depend on the specific path in control space, nor on the speed of the transformation. Again, this is a consequence of the fact that $H_{\rm S}(\epsilon(t))$ commutes with itself at all times, so Landau-Zener transitions, i.e. non-adiabatic transitions between the eigenstates of $H_{\rm S}(\epsilon(t))$ due to finite driving speed, cannot occur.

Let us denote with $\epsilon_{\rm L}$ ($\epsilon_{\rm R}$) the value of the control $\epsilon(t)$ during the hot (cold) isothermal stroke. Furthermore, since only the probabilities p_j are needed to compute the exchanged heat and work, let us denote with $p_j^{(\rm L)}$ the state at the end of the hot isothermal stroke, and with $p_j^{(\rm R)}$ the state at the end of the cold isothermal stroke. Since we assume that $\tau_\alpha \to \infty$, the local system S will thermalize with the bath, so these states will be thermal states, see Eq. (2.32). Therefore

$$p_0^{(\alpha)} = 1 - f_\alpha, \qquad\qquad p_1^{(\alpha)} = f_\alpha, \tag{3.65}$$

where we define

$$f_\alpha \equiv (1 + e^{\epsilon_\alpha/(k_B T_\alpha)})^{-1}. \tag{3.66}$$

We now go through each stroke of the Otto cycle and compute the heat and work during each of the four strokes of the Otto cycle using Eqs. (3.63) and (3.64). During the hot

isothermal stroke, the control is given by ϵ_{L}, and the state evolves from $p_j^{(\mathrm{R})}$ to $p_j^{(\mathrm{L})}$. Therefore the total heat Q_{L} extracted from the left bath during this stroke is given by

$$Q_{\mathrm{L}} = \epsilon_{\mathrm{L}} \left(f_{\mathrm{L}} - f_{\mathrm{R}}\right). \tag{3.67}$$

During the first adiabatic stroke, the state remains constant, described by $p_j^{(\mathrm{L})}$, and the control varies from ϵ_{L} to ϵ_{R}. Thus the work W_1 extracted during this stroke is given by

$$W_1 = -\frac{\epsilon_{\mathrm{L}} - \epsilon_{\mathrm{R}}}{2} \tanh\left(\frac{\epsilon_{\mathrm{L}}}{2k_B T_{\mathrm{L}}}\right). \tag{3.68}$$

During the cold isothermal stroke, the control is given by ϵ_{R}, and the state evolves from $p_j^{(\mathrm{L})}$ to $p_j^{(\mathrm{R})}$. Therefore the total heat Q_{R} extracted from the right bath during this stroke is given by

$$Q_{\mathrm{R}} = -\epsilon_{\mathrm{R}} \left(f_{\mathrm{L}} - f_{\mathrm{R}}\right). \tag{3.69}$$

At last, during the second adiabatic stroke, the state remain constant, described by $p_j^{(\mathrm{R})}$, and the control varies from ϵ_{R} to ϵ_{L}. Thus the work W_2 extracted during this stroke is given by

$$W_2 = \frac{\epsilon_{\mathrm{L}} - \epsilon_{\mathrm{R}}}{2} \tanh\left(\frac{\epsilon_{\mathrm{R}}}{2k_B T_{\mathrm{R}}}\right). \tag{3.70}$$

We can compute the total work extracted from the system as

$$W = W_1 + W_2 = \frac{\epsilon_{\mathrm{R}} - \epsilon_{\mathrm{L}}}{2} \left[\tanh\left(\frac{\epsilon_{\mathrm{L}}}{2k_B T_{\mathrm{L}}}\right) - \tanh\left(\frac{\epsilon_{\mathrm{R}}}{2k_B T_{\mathrm{R}}}\right)\right]. \tag{3.71}$$

We now analyze how to design an Otto cycle that operates as a heat engine. First, we notice that the heat and work remain unaltered if $\epsilon_\alpha \to -\epsilon_\alpha$, for both $\alpha = \mathrm{L}, \mathrm{R}$. Therefore, without loss of generality, we can set $\epsilon_{\mathrm{L}} \geq 0$. A heat engine is characterized by $Q_{\mathrm{L}} \geq 0$, $Q_{\mathrm{R}} \leq 0$ and $W \geq 0$. Using Eqs. (3.67), (3.69) and (3.71), it can be seen that these conditions are met if and only if

$$1 \leq \frac{\epsilon_{\mathrm{L}}}{\epsilon_{\mathrm{R}}} \leq \frac{T_{\mathrm{L}}}{T_{\mathrm{R}}}. \tag{3.72}$$

Notice that also $\epsilon_{\mathrm{R}} \geq 0$. Equation (3.72) tells us within which range of parameters we must choose $\epsilon_{\mathrm{L}}/\epsilon_{\mathrm{R}}$ in order for the system to behave as a heat engine. The range becomes smaller and smaller as the temperature difference becomes smaller: intuitively, this is due to the fact that it is "harder" to construct a heat engine between baths with very similar temperatures. Notably, plugging Eqs. (3.67) and (3.71) into the definition of η [see Eq. (3.60)], it can be seen that the efficiency of an Otto cycle is given by

$$\eta = \frac{Q_{\mathrm{L}}}{W} = 1 - \frac{\epsilon_{\mathrm{R}}}{\epsilon_{\mathrm{L}}}. \tag{3.73}$$

By plugging Eq. (3.72) into Eq. (3.73) we see that, for all values of ϵ_{L} and ϵ_{R} compatible with a heat engine,

$$\eta \leq \eta_{\mathrm{c}}, \tag{3.74}$$

where $\eta_{\mathrm{c}} = 1 - T_{\mathrm{R}}/T_{\mathrm{L}}$ is Carnot's efficiency. The equality is achieved when $\epsilon_{\mathrm{L}}/T_{\mathrm{L}} = \epsilon_{\mathrm{R}}/T_{\mathrm{R}}$. As we could expect, plugging this condition into Eq. (3.71) shows that the work, at Carnot efficiency, is zero.

We can also investigate when the system behaves as a refrigerator, which is characterized by $Q_{\mathrm{L}} \leq 0$, $Q_{\mathrm{R}} \geq 0$ and $W \leq 0$. As argued earlier we assume, without loss of generality, that $\epsilon_{\mathrm{L}} \geq 0$. It can be seen that the system operates as a refrigerator if and only if

$$\frac{T_{\mathrm{L}}}{T_{\mathrm{R}}} \leq \frac{\epsilon_{\mathrm{L}}}{\epsilon_{\mathrm{R}}}. \tag{3.75}$$

Also in this case, $\epsilon_{\mathrm{R}} \geq 0$. The coefficient of performance of an Otto cycle can be computed by plugging Eqs. (3.69) and Eq. (3.71) into the definition of the COP [see Eq. (3.61)]. This yields

$$C = \frac{Q_{\mathrm{R}}}{|W|} = \frac{\epsilon_{\mathrm{R}}}{\epsilon_{\mathrm{L}} - \epsilon_{\mathrm{R}}}. \tag{3.76}$$

Plugging Eq. (3.75) into Eq. (3.76) shows that, for all values of ϵ_{L} and ϵ_{R} compatible with the refrigerator,

$$C \leq C_{\mathrm{c}}, \tag{3.77}$$

where $C_{\mathrm{c}} = T_{\mathrm{R}}/(T_{\mathrm{L}} - T_{\mathrm{R}})$ is Carnot's COP. Also in this case, it is easy to see that Carnot's COP is reached when $\epsilon_{\mathrm{L}}/T_{\mathrm{L}} = \epsilon_{\mathrm{R}}/T_{\mathrm{R}}$, which implies $Q_{\mathrm{R}} = 0$.

4

Thermoelectric properties of an interacting quantum dot-based heat engine

As discussed in Sec. 3.1, heat-to-work conversion based on thermoelectricity promises an enhanced efficiency thanks to the "energy filtering" effect that can result from confinement and quantum effects [3–5]. The study of thermoelectric effects in nanostructures [11, 63–66] is thus attracting increasing interest.

A heat engine composed of a quantum dot (QD) is a paradigmatic example, since it is characterized by a spectrum of discrete levels which maximizes energy filtering. The thermoelectric properties of QD systems [67–90] and the performance of QD-based heat engines [91–122] has been studied theoretically by a number of authors (see Ref. [123] for a review). The vast majority of the papers dealing with QD-based heat engines consider a single degenerate energy level or two non-degenerate levels [91–95, 97–119]. The case of QDs with many levels has been addressed only in few papers [96, 120–122]. Moreover, the performance of QD-based heat engines has been mostly studied within the linear response regime [91, 92, 94, 95, 97, 98, 101–111, 121, 122], where the thermoelectric performance of the system is entirely characterized by ZT. The case of an interacting multi-level QD beyond the linear response has not been addressed so far. On the one hand, the presence of many levels is expected to yield important consequences. Indeed, already in the linear-response regime they have an impact on the thermopower, the thermal conductance and ZT [67, 68, 70, 122, 124]. On the other, non-linear effects, relevant when larger temperature and voltage biases are applied, are important as far as power and efficiency are concerned. We emphasize that a number of experiments assessing the thermoelectric properties of QDs have been reported in Refs. [42, 124–145].

In this chapter, we fill this gap by studying the thermoelectric properties and heat-to-work conversion performance of a multi-level QD in a multi-terminal configuration within the Coulomb blockade regime. We consider the limit of small tunnelling rates, i.e. the weak coupling regime described in Sec. 2.1, which in this context is known as sequential tunneling regime, and we study both the linear and non-linear response regimes. Coulomb interaction among electrons is accounted for by a finite and small capacitance C whose associated energy scale is its charging energy $(Ne)^2/(2C)$, where N is the number of electrons

in the QD and e is the modulus of the electron charge. Moreover, we consider a generic multi-terminal structure, whereby the QD is connected to many (two or more) reservoirs (electronic thermal baths). We will concentrate only on the optimization of the thermoelectric properties of the electronic system, neglecting the parasitic phononic contribution to heat transport. Our results therefore set an upper bound to the thermoelectric efficiency of the QD, approachable only in the limit in which suitable strategies to strongly reduce phonon transport are implemented.

Generalizing Refs. [69] and [70] to the multi-terminal case, by solving the Pauli master equation [see Eq. (2.36)] one can determine the probability of occupation of the energy levels of the QD in a multi-terminal setup, thus allowing to calculate the charge and heat currents for given values of the electrochemical potentials and temperatures of the reservoirs.

In the linear response regime, where voltage and temperature biases are small, we derive closed-form expressions for the charge and heat currents and specify their limits of validity. We define local and non-local transport coefficients and express them in terms of a generating function under the assumption that the tunneling rates are energy-independent. We then derive, in the low temperature limit, analytical expressions for all transport coefficients as a function of the average electrochemical potential μ. Along with the main features of the transport coefficients (located around values of μ equal to the dominant transition energies required to add or remove an electron from the QD), such expressions also describe a fine structure arising from the interplay between interaction and level quantization (controlled by the two energy scales: charging energy and level spacing). Furthermore, for the calculation of the thermal conductance we find that it is crucial to consider the presence of many levels. Within the linear response, we consider both the two-terminal and the three-terminal system aiming at addressing the performance of heat-to-work conversion. In the former case we obtain analytical expressions for the power factor Q and the figure of merit ZT finding, remarkably, that those quantities are simultaneously maximized for values of the electrochemical potential which differ by about $2.40k_BT$ with respect to the dominant transition energies. In addition, ZT shows a fine structure of secondary peaks whose height is independent of the system's parameters and can take values as large as $ZT = 9$. We compare the figure of merit with a non-interacting system, finding that Coulomb interactions dramatically increase ZT by strongly suppressing the thermal conductance. For the case of three terminals with energy-independent tunneling rates, we derive analytic expressions for the maximum power and corresponding efficiency, finding that the addition of a third terminal at an intermediate temperature decreases the efficiency at maximum power, but can increase the power. We also find particular intermediate temperatures where the third terminal increases the maximum power and achieves the same efficiency of a two terminal system.

We analyze the regime beyond the linear response by numerically solving the Pauli master equation, focusing on the two-terminal setup. Going beyond the linear response, i.e. considering large temperature and voltage biases, ΔT and V, is interesting for various reasons. On one hand, it allows to increase the Carnot efficiency η_c and the power generated by a heat engine (in our case the peak power scales approximately as $(\Delta T)^2$ also beyond the linear response regime). On the other hand, the efficiency at maximum power is not bounded by $\eta_c/2$, as in the linear response, and can even go above the Curzon-Alhborn efficiency [36, 37, 61, 62, 146]. In literature, the scattering theory of nonlinear thermoelectric transport in quantum conductors has been developed only recently [147–149]. The regime beyond linear response for QD-based heat engines has been theoretically addressed in Refs. [93, 96, 99, 100, 112–120], but limited to single or double level quantum dots.

In discussing the results, we first focus on the behavior of the non-linear Seebeck and

Peltier coefficients aiming at assessing the interplay between charging energy and level spacing on these two quantities and how the Onsager reciprocity relation that connects them is violated beyond linear response. Second, we study the efficiency and output power of a heat engine. In particular, we calculate the maximum efficiency and maximum power by maximizing such quantities with respect to the applied bias voltage, for fixed values of temperature bias and electrochemical potential. The maximum efficiency shows only quantitative changes, with respect to the linear response, by increasing the temperature bias. The efficiency at maximum power instead develops peaks which go beyond the $\eta_c/2$ linear-response limit and approach η_c for large temperature differences. Remarkably, the maximum power, normalized to its peak value, only slightly depends on the temperature bias and can be well approximated by the analytic expression obtained for the linear response regime. Moreover, we find that efficiency at maximum power and maximum power take approximately their peak values simultaneously, under the same conditions found for the linear response. Finally, we assess the impact of interactions by comparing the efficiency at maximum power in two situations, namely the case of a doubly degenerate level with interaction and the case of two non-degenerate levels without interaction. We find that, especially when charging energy and level spacing are of the order of the thermal energy, the efficiency at maximum power is much higher in the interacting case and goes above the Curzon-Alhborn efficiency. We also find that in the doubly degenerate interacting case the maximum power is enhanced by almost a factor 2 with respect to the non-degenerate case.

The chapter is organized as follows: in Sec. 4.1 we describe the system under investigation and we detail the theoretical model. In Sec. 4.2 the model is specified to the linear response regime. Here we report analytic expressions obtained in the quantum limit, Sec. 4.2.1, and calculate power and efficiency in the cases of a two-terminal system, Sec. 4.2.2 (with the efficiencies of interacting and non-interacting QDs compared in Sec. 4.2.3), and of a three-terminal system, Sec. 4.2.4. Sec. 4.3 is devoted to the discussion of the regime beyond the linear response in a two-terminal system: in Sec. 4.3.1 we study the non-linear Seebeck and Peltier coefficients and in Sec. 4.3.2 we discuss efficiency and output power of a heat engine. Finally, in Sec. 4.4 we provide a summary and discuss future developments. In addition, App. A presents the details of some calculations and the analytic non linear study of a single energy level QD system.

4.1 Multi-level interacting QD

In this section we briefly outline the formalism used to describe the thermoelectric properties of a *multilevel interacting QD*. We will only consider electron transport, neglecting any contribution due to phonons. As shown in Fig. 4.1 (left), the QD is tunnel-coupled to $\mathcal{N}$ electron reservoirs, each characterized by a given temperature T_α and electrochemical potential μ_α, so that the occupation of the electrons within reservoir α follows the Fermi distribution

$$f_\alpha(E) = \left[1 + \exp\left(\frac{E-\mu_\alpha}{k_B T_\alpha}\right)\right]^{-1}, \tag{4.1}$$

where k_B is Boltzmann's constant. In Fig. 4.1 (right), E_p (with $p = 1, 2, \ldots$ labeled in ascending order) are the QD single-electron energy levels (in the absence of interaction). These levels can be shifted by means of an applied gate voltage.

The QD is weakly coupled to the reservoirs through large tunneling barriers. More precisely, we assume that thermal energy $k_B T$, level spacing and charging energy are much

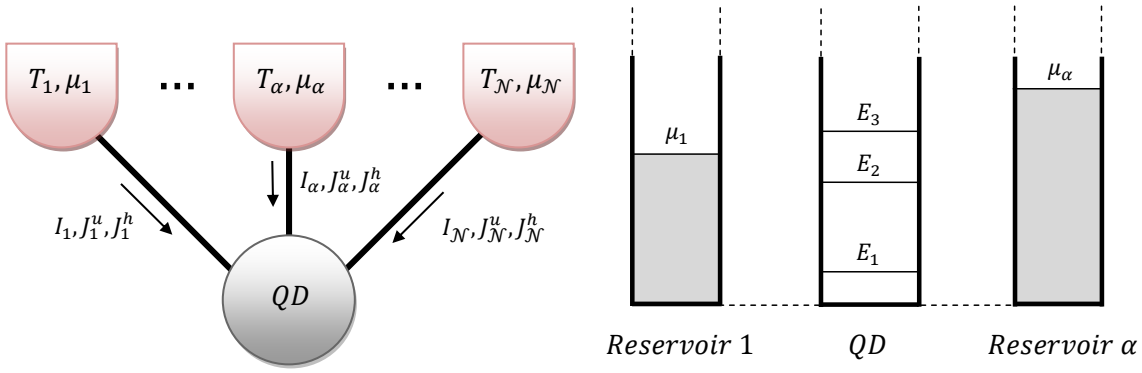

FIGURE 4.1: Left: A quantum dot (QD) is *tunnel-coupled to* $\mathcal{N}$ *reservoirs*, each kept at a temperature T_α and at an electrochemical potential μ_α, with $\alpha = 1, ..., \mathcal{N}$. Arrows represent charge, energy and heat currents (I, J^u_α, and J^h_α, respectively) flowing from the reservoirs α to the QD. Right: Schematic energy representation of a multilevel QD. E_1, E_2, etc. are the single-electron energy levels of the QD, while μ_1 and μ_α are the electrochemical potentials relative to reservoir 1 and α, respectively.

larger than the coupling energy between reservoirs and QD [$\hbar \sum_\alpha \Gamma_\alpha(p)$, where $\Gamma_\alpha(p)$ is the tunneling rate from level p to reservoir α, which we assume independent of the number N of electrons inside the dot]. As a consequence, the charge on the QD is quantized, i.e. each energy level E_p can have either zero or one electron, $n_p = 0$ or $n_p = 1$ (any degeneracy, like electron spin, can be taken into account counting each level multiple times), and transport occurs due to single-electron tunneling processes (*sequential tunneling regime*). The electrostatic energy associated with the electrons within the QD is given by $U(N) = E_C N^2$, where $E_C = e^2/2C$, $N = \sum_i n_i$ is the total number of electrons within the QD, and C is the capacitance of the QD. The QD is described by states characterized by a set of occupation numbers $\{n_i\}$ relative to the energy levels. The QD changes state whenever a single-electron tunneling process takes place. The non-equilibrium probability for a given state $\{n_i\}$ to occur, $p(\{n_i\})$, can be computed [34, 69] by writing a straightforward set of balance equations for $p(\{n_i\})$, which are equivalent to the Pauli master equation presented in Sec. 2.1. In this chapter, we present the Pauli master equation using intuitive arguments rather than a formal derivation. Our aim is to compute in stationary conditions the charge, energy and heat currents out of the electron reservoirs [denoted in Fig. 4.1 (left) by I, J^u_α and J^h_α, respectively], induced by the temperature and electrochemical potential differences.

4.1.1 Pauli master equation

In what follows we describe a generalization of the method put forward by Beenakker in Refs. [69] and [70]. The notation will slightly differ from the previous chapters. The single-electron tunneling processes that contribute to changing over time the probability $p(\{n_i\})$ are due to electrons that tunnel from the QD to the reservoirs and vice-versa. For an electron exiting the QD, initially with N electrons, from energy level E_p and going into reservoir α at energy E^{fin}, energy conservation imposes that

$$E_p + U(N) = E^{\text{fin}}(N) + U(N-1). \tag{4.2}$$

On the contrary, for an electron that tunnels from an initial state in reservoir α at energy E^{in} to the level E_p in the QD that initially had N electrons, energy conservation imposes that

$$E^{\text{in}}(N) + U(N) = E_p + U(N+1). \tag{4.3}$$

$p(\{n_i\})$ can then be determined by the following Pauli master equation, which is a set of equations, one for each configuration $\{n_i\}$:

$$\begin{aligned}\frac{\partial}{\partial t}p\left(\{n_i\}\right) = &-\sum_{p\alpha}\delta_{n_p,0}p\left(\{n_i\}\right)\Gamma_\alpha(p)f_\alpha\left(E^{\text{in}}(N)\right)\\ &-\sum_{p\alpha}\delta_{n_p,1}p\left(\{n_i\}\right)\Gamma_\alpha(p)\left[1-f_\alpha\left(E^{\text{fin}}(N)\right)\right]\\ &+\sum_{p\alpha}\delta_{n_p,0}p\left(\{n_i\},n_p=1\right)\Gamma_\alpha(p)\left[1-f_\alpha\left(E^{\text{fin}}(N+1)\right)\right]\\ &+\sum_{p\alpha}\delta_{n_p,1}p\left(\{n_i\},n_p=0\right)\Gamma_\alpha(p)f_\alpha\left(E^{\text{in}}(N-1)\right),\end{aligned} \tag{4.4}$$

where we have introduced the notation

$$p\left(\{n_i\},n_p=1\right) = p\left(\{n_1,\ldots,n_{p-1},1,n_{p+1},\ldots\}\right) \tag{4.5}$$

and

$$p\left(\{n_i\},n_p=0\right) = p\left(\{n_1,\ldots,n_{p-1},0,n_{p+1},\ldots\}\right) \tag{4.6}$$

for the QD states. The first term in Eq. (4.4) accounts for the decrease of the probability $p(\{n_i\})$, with the QD initially in the state $\{n_i\}$, due to an electron coming from a reservoir and occupying an empty level in the QD. The rate of electrons coming from reservoir α will be given by a sum over all empty levels p (such that $n_p = 0$) of the tunnel rate $\Gamma_\alpha(p)$, multiplied by the probability of finding the QD in this state, $p\left(\{n_i\}\right)$, and multiplied by the reservoir's occupation $f_\alpha\left(E^{\text{in}}(N)\right)$ at the correct energy $E^{\text{in}}(N)$ to tunnel to level p. The second term accounts for the decrease of the probability $p(\{n_i\})$, with the QD initially in the state $\{n_i\}$, due an electron leaving the QD from an occupied level to tunnel into a reservoir. The third term accounts for the increase of the probability $p(\{n_i\})$ if the QD is in a state with an extra electron in level p with respect to $\{n_i\}$, and if this electron leaves the QD, tunneling to the reservoirs. The forth term accounts for the increase of the probability $p(\{n_i\})$ if the QD is in a state with a missing electron in level p with respect to $\{n_i\}$, and if this electron enters the QD in level p, tunneling from the reservoirs. The *stationary solution* of the master equation, obtained imposing $\partial p/\partial t = 0$, together with the normalization request

$$\sum\nolimits_{\{n_i\}} p\left(\{n_i\}\right) = 1 \tag{4.7}$$

provides a complete set of equations that uniquely defines $p\left(\{n_i\}\right)$. The sum over $\{n_i\}$ means the sum over $n_i = 0, 1$, with $i = 1, 2, \ldots$.

4.1.2 Charge, energy, and heat currents

As described in Sec. 3.1.4, Charge I_α and energy J^u_α currents flowing from reservoir α to the QD can be calculated as the sum of all possible tunneling processes, since the QD can be in

any state $\{n_i\}$ with probability $p(\{n_i\})$ and an electron can tunnel into or out of any energy level E_p. More precisely, for the charge current we have

$$I_\alpha = -e\sum_{p=1}^{\infty}\sum_{\{n_i\}} p(\{n_i\})\Gamma_\alpha(p)\Big\{\delta_{n_p,0}f_\alpha(E^{\rm in}(N)) - \delta_{n_p,1}[1-f_\alpha(E^{\rm fin}(N))]\Big\}, \tag{4.8}$$

e being the modulus of the electronic charge, while for the energy current we have

$$J^u_\alpha = \sum_{p=1}^{\infty}\sum_{\{n_i\}} p(\{n_i\})\Gamma_\alpha(p)\Big\{\delta_{n_p,0}f_\alpha(E^{\rm in}(N))E^{\rm in}(N) - \delta_{n_p,1}[1-f_\alpha(E^{\rm fin}(N))]E^{\rm fin}(N)\Big\}, \tag{4.9}$$

$E^{\rm in}(N)$ $[E^{\rm fin}(N)]$ being the energy carried by an electron entering (exiting) the QD. The heat currents exiting the reservoirs can be calculated as $J^h_\alpha = J^u_\alpha + \frac{\mu_\alpha}{e}I_\alpha$. Using Eqs. (4.8) and (4.9), we find that

$$\begin{aligned} J^h_\alpha = &\sum_{p=1}^{\infty}\sum_{\{n_i\}} p(\{n_i\})\Gamma_\alpha(p) \\ &\times\Big\{\delta_{n_p,0}f_\alpha(E^{\rm in}(N))\Big[E^{\rm in}(N)-\mu_\alpha\Big] - \delta_{n_p,1}[1-f_\alpha(E^{\rm fin}(N))]\Big[E^{\rm fin}(N)-\mu_\alpha\Big]\Big\}. \end{aligned} \tag{4.10}$$

In order to numerically determine the stationary probability distribution $p(\{n_i\})$ from the master equation, we will consider a finite number L of energy levels. [1]. By organizing the values of $p(\{n_i\})$ into a 2^L-components vector $\vec{p}$ (two choices $n_i = 0, 1$ for each level), the master equation (4.4) for the stationary probability distribution, $\frac{\partial\vec{p}}{\partial t} = \vec{0}$, can be represented as the homogeneous linear system $M\vec{p} = \vec{0}$, where M is a $2^L \times 2^L$ matrix. M must have a null space of at least dimension 1, otherwise the only possible solution would be the trivial one ($\vec{p} \equiv 0$). This is demonstrated in App. A.1 by showing that summing together all the equations in the master equation yields zero. We can thus find the probabilities by including the normalization condition, Eq. (4.7).

By defining $\widetilde{N} = \sum_{i\neq p} n_i$ it is possible to show that the master equation for the stationary probability distribution can be written as

$$\sum_p(\delta_{n_p,1}-\delta_{n_p,0})\Big[p\left(\{n_i\},n_p=0\right)A_{\widetilde{N},p} - p\left(\{n_i\},n_p=1\right)B_{\widetilde{N},p}\Big] = 0, \tag{4.11}$$

where

$$A_{\widetilde{N},p} = \sum_\alpha \Gamma_\alpha(p) f_\alpha\left(E^{\rm in}(\widetilde{N})\right) \tag{4.12}$$

and

$$B_{\widetilde{N},p} = \sum_\alpha \Gamma_\alpha(p)\left[1-f_\alpha\left(E^{\rm in}(\widetilde{N})\right)\right] = \sum_\alpha \Gamma_\alpha(p) - A_{\widetilde{N},p}. \tag{4.13}$$

To derive Eq. (4.11) we have used the fact that $\widetilde{N} = N$, for the terms in the master equation proportional to $\delta_{n_p,0}$, and $\widetilde{N} = N-1$, for the terms in the master equation proportional to $\delta_{n_p,1}$, and the identity

$$E^{\rm fin}(N+1) = E^{\rm in}(N), \tag{4.14}$$

stemming from Eqs. (4.2) and (4.3). It is worth mentioning that using the master equation in the form of Eq. (4.11), it is possible to prove that the master equation always allows a non-trivial solution (see App. A.1).

[1] The results can be interpreted as the exact solution of a system with L energy levels or as an approximate solution of a system with infinite levels. In the latter case, one needs to check that the result are stable with increasing number of energy levels.

4.1.3 Probability detailed balance equations

It is clear that the master equation (4.11) is automatically satisfied when the following set of equations

$$p\left(\{n_i\}, n_p = 0\right) A_{\widetilde{N},p} - p\left(\{n_i\}, n_p = 1\right) B_{\widetilde{N},p} = 0 \tag{4.15}$$

are fulfilled for a given value of p and a given set of occupation numbers $\{n_i\}$. Equation (4.15), introduced in Ref. [69] with the name "detailed balance equations", are hereafter referred to as "probability detailed balance equations" (PDBEs) to avoid confusion with the detailed balance equation (2.38). Eqs. (4.15) represent a set of $L \cdot 2^{L-1}$ equations, since p can take L values and, at a given p, all other occupation numbers $(n_1, \ldots, n_{p-1}, n_{p+1}, \ldots, n_L)$ can be chosen in 2^{L-1} different ways. Of course, if a solution to the PDBEs exists, than it is also a solution of the master equation. We can show, however, that the PDBEs are not in general consistent, i.e. no set of $p(\{n_i\})$ exists that can simultaneously satisfy all the PDBEs (see App. A.2). This is also true in the linear response regime. In this case, however, we could prove (see App. A.3) that the PDBEs are consistent if $E_C = 0$, or if $\Delta T_\alpha = 0$ for all α, or when the tunneling rates are proportional to each other, namely when $\Gamma_\alpha(p) = k_\alpha \Gamma_1(p)$, for $\alpha > 1$, k_α being constants. Note that this condition is trivially satisfied when the rates Γ_α do not depend on p. As a result, the PDBEs do not allow in general a solution, but when they do they are useful in computing analytically the energy and heat currents in the linear response regime (see Sec. 4.2).

4.1.4 Level balance equations

We will now derive a set of equations that is always consistent and that can be used in the general case to obtain a closed-form expression of the charge current in the linear response regime (see Sec. 4.2). We impose that, in stationary conditions, the rate of electrons entering any given QD energy level p must equal the rate of electrons leaving that energy level. For electrons tunneling into the QD, initially with N electrons, from any reservoir, one has to require that level p is empty and must consider all possible states $(\{n_i\}, n_p = 0)$, where $\widetilde{N} = N$. The total rate of electrons entering energy level E_p is given by

$$\sum_{\alpha, \{n_i\}_{i \neq p}} p(\{n_i\}, n_p = 0) \Gamma_\alpha(p) f_\alpha\left(E^{\text{in}}(N)\right). \tag{4.16}$$

For electrons tunneling out of the QD, initially with N electrons, to any reservoir one has to require that level p is occupied and must consider states with $(\{n_i\}, n_p = 1)$, where $\widetilde{N} = N-1$. The total rate of electrons leaving level E_p is given by

$$\sum_{\alpha, \{n_i\}_{i \neq p}} p(\{n_i\}, n_p = 1) \Gamma_\alpha(p) \left[1 - f_\alpha\left(E^{\text{fin}}(N)\right)\right]. \tag{4.17}$$

If we equate the rates of electron entering and leaving level p, and use the notation introduced in Eqs. (4.12) and (4.13), we obtain

$$\sum_{\{n_i\}_{i \neq p}} \left[p(\{n_i\}, n_p = 0) A_{\widetilde{N},p} - p(\{n_i\}, n_p = 1) B_{\widetilde{N},p}\right] = 0. \tag{4.18}$$

We will refer to this set of L equations (one for each energy level p) as the *level balance equations* (LBEs) [2]. Note that, using an argument similar to that put forward in App. A.1,

[2] Note that the PDBEs (4.15) could be obtained using the same arguments, but assuming that the QD is in a specific configuration $(\{n_i\})_{i \neq p}$, instead of summing over all possible such configurations. To obtain the LBEs, the probability that level p is occupied is given by the marginal probability $\sum_{\{n_i\}_{i \neq p}} p\left(\{n_i\}, n_p = 1\right)$.

it is possible to prove that Eqs. (4.18) can be obtained from the master equation, thus the LBEs are always consistent with the master equation. However, the number of LBEs (equal to L) is smaller than the equations in the master equation (equal to 2^L) and they might not be sufficient to determine the probabilities $p(\{n_i\})$. Note that one can prove that Eqs. (4.18) yield charge current conservation: $\sum_\alpha I_\alpha = 0$.

4.1.5 Output power and efficiency

Under steady-state conditions, the output power P of a multi-terminal system is given by the sum of all the heat currents

$$P = \sum_{\alpha=1}^{\mathcal{N}} J_\alpha^h. \tag{4.19}$$

If $P > 0$, the system behaves as a heat engine, i.e. converting heat into work. In this situation the efficiency η is defined as the ratio between the output power and the total heat current absorbed by the system

$$\eta = \frac{P}{\sum\limits_{\alpha'} J_{\alpha'}^h}, \tag{4.20}$$

where the sum over α' runs over all positive heat currents. For a two-terminal system the efficiency cannot exceed the Carnot efficiency defined as $\eta_c = 1 - T_1/T_2$, with $T_2 > T_1$. In addition, for a multi-terminal system η cannot go beyond the two-terminal Carnot efficiency [101] calculated using the hottest and coldest temperatures among $T_1, T_2, ..., T_{\mathcal{N}}$.

We define the temperature and electrochemical potential differences as $T_\alpha = T + \Delta T_\alpha$ and $\mu_\alpha = \mu + \Delta\mu_\alpha$, with $\alpha = 1, ..., \mathcal{N}$, and choosing reservoir 1 as the reference value, i.e. $\Delta T_1 = \Delta\mu_1 = 0$. In what follows we fix the values of ΔT_α and calculate the maximum output power, $P^{(\max)}$, and maximum efficiency, $\eta^{(\max)}$, by varying $\Delta\mu_\alpha$. We also consider the efficiency at maximum power, $\eta(P^{(\max)})$, which is the efficiency when the values of $\Delta\mu_\alpha$ are chosen to maximize the power. These quantities are straightforward generalizations of the ones introduced in Sec. 3.1.1 to the multiterminal case.

As shown in Sec. 3.1.2, for a two-terminal system within the linear response regime, i.e. when the charge and heat currents depend linearly on the temperature and electrochemical potential differences, both the output power and efficiency can be written in terms of the transport coefficients, namely the electrical conductance G, the thermopower S and the thermal conductance K. Defining $\Delta T \equiv \Delta T_2 > 0$, the transport coefficients G, S and K are respectively defined as in Eqs. (3.24), (3.25) and (3.26). The efficiency at maximum power and the maximum efficiency can then be expressed in terms of ZT, defined in Eq. (3.27), through the relations in Eq. (3.29). By defining the power factor $Q = GS^2$, the expression of the maximum power given in Eq. (3.28) can be written as

$$P^{(\max)} = \frac{1}{4} Q \Delta T^2. \tag{4.21}$$

We recall that both $\eta(P^{(\max)})$ and $\eta^{(\max)}$ are monotonous growing functions of ZT; the only restriction imposed by thermodynamics is $ZT \geq 0$. When $ZT = 0$ both $\eta^{(\max)}$ and $\eta(P^{(\max)})$ vanish, while for $ZT \to \infty$, $\eta^{(\max)} \to \eta_c$, and $\eta(P^{(\max)}) \to \eta_{CA}$, where $\eta_{CA} = \eta_c/2$ is the so-called Curzon-Ahlborn efficiency [36, 37, 61, 62, 146] in linear response.

4.2 Linear response regime

As already mentioned above, in the linear response regime the applied temperature and electrochemical potential biases are small enough so that the currents depend linearly on them. Assuming that $|\Delta T_\alpha| \ll T$ and $|\Delta\mu_\alpha| \ll k_B T$, we follow Refs. [69] and [70] and suppose the probability $p(\{n_i\})$ to differ from its equilibrium distribution $p_{\rm eq}(\{n_i\})$ in the following way:

$$p(\{n_i\}) = p_{\rm eq}(\{n_i\})\,[1 + \psi(\{n_i\})]\,, \tag{4.22}$$

where ψ is a "small" function. In Eq. (4.22)

$$p_{\rm eq}(\{n_i\}) = \frac{1}{Z}\exp\left[-\frac{1}{k_B T}\left(\sum_{p=1}^{\infty} E_p n_p + U(N) - \mu N\right)\right] \tag{4.23}$$

is the Gibbs distribution in the grand canonical ensemble, when all reservoirs have the same temperature and electrochemical potential, with grand partition function given by

$$Z = \sum_{\{n_i\}} \exp\left[-\frac{1}{k_B T}\left(\sum_{p=1}^{\infty} E_p n_p + U(N) - \mu N\right)\right]. \tag{4.24}$$

In our expressions we will consider terms up to first order in ψ, $\Delta T_\alpha/T$, and $\Delta\mu_\alpha/k_B T$. By linearizing the LBEs with respect to the above small quantities, Eq. (4.18), one finds the relation

$$\begin{aligned}\sum_{\{n_i\}_{i\neq p}} p_{\rm eq}(\{n_i\}, n_p = 0) f\left(E_p + (2\widetilde{N}+1)E_C\right) \sum_\alpha \Gamma_\alpha(p)\Big\{\psi(\{n_i\}, n_p = 0) \\ - \psi(\{n_i\}, n_p = 1) + \frac{1}{k_B T}\left[\left(E_p + (2\widetilde{N}+1)E_C - \mu\right)\frac{\Delta T_\alpha}{T} + \Delta\mu_\alpha\right]\Big\} = 0,\end{aligned} \tag{4.25}$$

where $f(E)$ stands for the Fermi distribution at temperature T and electrochemical potential μ. By expressing $p(\{n_i\})$ in terms of $\psi(\{n_i\})$ and linearizing Eq. (4.8), we can use Eq. (4.25) to remove $\psi(\{n_i\})$ from the charge current, and we find the following closed-form expression:

$$\begin{aligned}I_\alpha = -\frac{e}{k_B T}\sum_{p=1}^{\infty}\sum_{N=1}^{\infty} p_{\rm eq}(N) F_{\rm eq}(E_p|N)\,[1 - f(\epsilon(N,p))] \sum_\beta \frac{\Gamma_\alpha(p)\Gamma_\beta(p)}{\Gamma_{\rm tot}(p)} \\ \times\left[(\epsilon(N,p) - \mu)\frac{\Delta T_\alpha - \Delta T_\beta}{T} + (\Delta\mu_\alpha - \Delta\mu_\beta)\right],\end{aligned} \tag{4.26}$$

where $\Gamma_{\rm tot}(p) = \sum_\alpha \Gamma_\alpha(p)$, and

$$\epsilon(N,p) = E_p + U(N) - U(N-1) = E_p + (2N-1)E_C \tag{4.27}$$

is the energy needed to add to the QD, initially occupied by $N-1$ electrons, the N-th electron to level p (and equivalently for the inverse process). In Eq. (4.26) the quantity

$$p_{\rm eq}(N) \equiv \sum_{\{n_i\}} p_{\rm eq}(\{n_i\})\delta_{\sum n_i, N} \tag{4.28}$$

is the equilibrium probability of finding N electrons in the QD, and

$$F(E_p|N) \equiv \frac{p_{\rm eq}(E_p \cap N)}{p_{\rm eq}(N)} = \frac{\sum\limits_{\{n_i\}} p_{\rm eq}(\{n_i\})\delta_{n_p,1}\delta_{\sum n_i, N}}{p_{\rm eq}(N)} \tag{4.29}$$

is the equilibrium conditional probability of finding level p occupied, when N electrons are in the QD. Note that expression (4.26) coincides with the one that can be derived using the PDBEs. However, the above derivation which uses the LBEs shows that Eq. (4.26) is always valid within the linear response regime.

Unfortunately, we were able to derive a closed-form expression for the energy current using Eq. (4.25) only in the absence of interaction ($E_C = 0$). For $E_C \neq 0$, the energy current J^u_α can be derived using the relation

$$\sum_\alpha \Gamma_\alpha(p)\Big\{\psi(\{n_i\}, n_p = 0) - \psi(\{n_i\}, n_p = 1) + \frac{1}{k_B T}\left[\left(E_p + (2\widetilde{N}+1)E_C - \mu\right)\frac{\Delta T_\alpha}{T} + \Delta\mu_\alpha\right]\Big\} = 0, \quad (4.30)$$

obtained by linearizing the PDBEs, Eq. (4.15) (which is equivalent to removing the sum over $\{n_i\}$ from Eq. (4.25)). Thus, in the domain of validity of the PDBEs, the heat current can be written as

$$J^h_\alpha = \frac{1}{k_B T}\sum_{p=1}^{\infty}\sum_{N=1}^{\infty} p_{\rm eq}(N)F_{\rm eq}(E_p|N)\left[1 - f(\epsilon(N,p))\right]\left[\epsilon(N,p) - \mu\right] \times \sum_\beta \frac{\Gamma_\alpha(p)\Gamma_\beta(p)}{\Gamma_{\rm tot}(p)}\left[(\epsilon(N,p) - \mu)\frac{\Delta T_\alpha - \Delta T_\beta}{T} + (\Delta\mu_\alpha - \Delta\mu_\beta)\right]. \quad (4.31)$$

We now define the transport coefficients, namely the electrical conductance $G_{\alpha\beta}$, the thermopower $S_{\alpha\beta}$ and the thermal conductance $K_{\alpha\beta}$, for the multi-terminal case, as [101]

$$G_{\alpha\beta} = \left(\frac{eI_\alpha}{\Delta\mu_\beta}\right)_{\substack{\Delta T_\gamma = 0\ \forall\gamma,\\ \Delta\mu_\gamma = 0\ \forall\gamma\neq\beta}}, \quad (4.32)$$

$$S_{\alpha\beta} = \left(\frac{\Delta\mu_\alpha}{e\Delta T_\beta}\right)_{\substack{I_\gamma = 0\ \forall\gamma,\\ \Delta T_\gamma = 0\ \forall\gamma\neq\beta}}, \quad (4.33)$$

and

$$K_{\alpha\beta} = \left(\frac{J^h_\alpha}{\Delta T_\beta}\right)_{\substack{I_\gamma = 0\ \forall\gamma,\\ \Delta T_\gamma = 0\ \forall\gamma\neq\beta}}. \quad (4.34)$$

Note that index β takes values in the range $2, ..., \mathcal{N}$, since reservoir 1 is chosen as the reference. Local and non-local transport coefficients are distinguished depending on whether the two indices are, respectively, equal or different.

The expressions for the currents [(4.26) and (4.31)] have an intuitive interpretation. Indeed, the currents depend on the probability that a given energy level of the QD is occupied $[p_{\rm eq}(N)F_{\rm eq}(E_p|N)]$ times the probability that there is an empty state with the correct energy in the reservoir $[1 - f(\epsilon(N,p))]$. The sum over all energy levels p and over the total number of electrons N in the QD accounts for all the various tunneling processes that can occur. Moreover, as far as the energy current is concerned, $\epsilon(N,p)$ is the energy carried by an electron that leaves the QD from level p when N electrons are present before the tunneling process, or equivalently, $\epsilon(N,p)$ is the energy carried by an electron that enters the QD into level p increasing the number of total electrons to N. We recall that Eq. (4.26) for the charge current is always valid, while Eq. (4.31) holds only when the PDBEs are valid (see App. A.3). The expressions for the charge and heat currents, in the case of two terminals, coincide with the ones obtained in Refs. [67, 69, 70].

If we assume that the tunneling rates do not depend on p, i.e. $\Gamma_\alpha(p) = \Gamma_\alpha$, we can rewrite the charge and heat currents in Eqs. (4.26) and (4.31) as follows:

$$I_\alpha = -\frac{e}{k_B T}\sum_\beta \frac{\Gamma_\alpha \Gamma_\beta}{\Gamma_{\text{tot}}}\mathcal{P}\left[(\epsilon-\mu)\frac{\Delta T_\alpha - \Delta T_\beta}{T} + \Delta\mu_\alpha - \Delta\mu_\beta\right], \tag{4.35}$$

and

$$J^h_\alpha = \frac{1}{k_B T}\sum_\beta \frac{\Gamma_\alpha \Gamma_\beta}{\Gamma_{\text{tot}}}\mathcal{P}\left[(\epsilon-\mu)\left((\epsilon-\mu)\frac{\Delta T_\alpha - \Delta T_\beta}{T} + \Delta\mu_\alpha - \Delta\mu_\beta\right)\right], \tag{4.36}$$

where $\mathcal{P}$ is the linear functional

$$\mathcal{P}[x] \equiv \sum_{p=1}^{\infty}\sum_{N=1}^{\infty} p_{\text{tot}}(N,p)x(N,p), \tag{4.37}$$

with

$$p_{\text{tot}}(N,p) = p_{\text{eq}}(N)F_{\text{eq}}(E_p|N)\left[1 - f(\epsilon(N,p))\right]. \tag{4.38}$$

For a two terminal system it is possible to define analogous equations that do not require the tunneling rates to be energy-independent [150], but we will not consider this case. We can thus use the definitions of the transport coefficients given in Eqs. (4.32), (4.33) and (4.34) to write them in terms of the functional $\mathcal{P}$ as

$$\begin{aligned} G_{\alpha\beta} &= \frac{e^2}{k_B T}\left(\delta_{\alpha\beta}\Gamma_\alpha - \frac{\Gamma_\alpha\Gamma_\beta}{\Gamma_{\text{tot}}}\right)\mathcal{P}\left[1\right], \\ S_{\alpha\beta} &= -\frac{1}{eT}\delta_{\alpha\beta}\frac{\mathcal{P}[\epsilon-\mu]}{\mathcal{P}\left[1\right]}, \\ K_{\alpha\beta} &= \frac{1}{k_B T^2}\left(\delta_{\alpha\beta}\Gamma_\alpha - \frac{\Gamma_\alpha\Gamma_\beta}{\Gamma_{\text{tot}}}\right)\left(\mathcal{P}[(\epsilon-\mu)^2] - \frac{\mathcal{P}^2[\epsilon-\mu]}{\mathcal{P}\left[1\right]}\right). \end{aligned} \tag{4.39}$$

These expressions only require the calculation of $\mathcal{P}[(\epsilon-\mu)^k]$, with $k = 0, 1, 2$, and make manifest various properties of the transport coefficients. Namely, i) all three transport coefficients are symmetric matrices (as required by the Onsager relations in the presence of time-reversal symmetry); ii) $G_{\alpha\beta}$ and $K_{\alpha\beta}$ have non-local terms, while the thermopower is only local (non-zero non-local $S_{\alpha\beta}$ occur when relaxing the assumption for which the tunneling rates do not depend on the energy levels [101]); iii) $\sum_\alpha G_{\alpha\beta} = \sum_\alpha K_{\alpha\beta} = 0$, stemming from charge and energy conservation.

By defining the generating function

$$\Omega[\lambda] \equiv \ln \mathcal{P}\left[e^{\lambda(\epsilon-\mu)}\right], \tag{4.40}$$

we can write the transport coefficients as follows:

$$\begin{aligned} G_{\alpha\beta} &= \frac{e^2}{k_B T}\left(\delta_{\alpha\beta}\Gamma_\alpha - \frac{\Gamma_\alpha\Gamma_\beta}{\Gamma_{\text{tot}}}\right)e^{\Omega[0]}, \\ S_{\alpha\beta} &= \frac{1}{eT}\delta_{\alpha\beta}\left.\frac{\partial\Omega}{\partial\lambda}\right|_{\lambda=0}, \\ K_{\alpha\beta} &= \frac{1}{k_B T^2}\left(\delta_{\alpha\beta}\Gamma_\alpha - \frac{\Gamma_\alpha\Gamma_\beta}{\Gamma_{\text{tot}}}\right)e^{\Omega[0]}\left.\frac{\partial^2\Omega}{\partial\lambda^2}\right|_{\lambda=0}. \end{aligned} \tag{4.41}$$

In the next Subsection, we will compute an analytic expression for $\Omega[\lambda]$ in the quantum limit.

4.2.1 Quantum limit

The quantum limit is characterized by having the energy spacing between levels of the QD and the charging energy much bigger than k_BT [while $k_BT \gg \hbar\Gamma_\alpha(p)$]. We start by observing that the sum over p and N in Eq. (4.37) accounts for the fact that electrons can enter or leave the QD with energy $\epsilon(N,p)$ through, in principle, any energy level E_p with the QD being occupied by any number of electrons N. The transition energies $\epsilon(N,p)$ are schematically shown in Fig. 4.2. At low temperatures we expect the lowest energy levels of the QD to

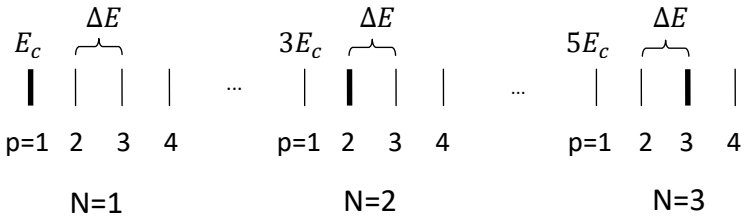

FIGURE 4.2: Schematic representation of the transition energies $\epsilon(N,p)$ as N and p vary. In this figure we are assuming $E_C \gg \Delta E$ and equidistant energy levels, $E_p - E_{p-1} = \Delta E$. The bold lines represent the dominant transition energies $\tilde{\epsilon}(N) = \epsilon(N, p = N)$.

be occupied, so that, if there are initially $N-1$ electrons in the QD, electrons can flow mainly through level $p = N$. Such process gives the dominant contribution to transport and is represented by the dominant transition energy $\tilde{\epsilon}(N) \equiv \epsilon(N, p = N)$ (depicted in bold in Fig. 4.2). Therefore, in the quantum limit one expects to get the sum over N and p appearing in $\mathcal{P}$ [Eq. (4.37)] reduced to few dominant terms [the three equilibrium probabilities $p_{\rm eq}(N)$, $F_{\rm eq}(E_p|N)$ and $f(\epsilon(N,p))$ becoming very sharp functions].

Following Ref. [70], one finds (see Ref. [150] for details) that the dominant contribution to $P_{\rm tot}$ in Eq. (4.37) occurs when $N = N_{\rm min}$ is the integer that minimizes the quantity

$$|\tilde{\epsilon}(N) - \mu|, \tag{4.42}$$

and for values of p such that $\epsilon(N_{\rm min}, p)$ is between the electrochemical potential μ and the dominant transition energy, i.e. such that $\tilde{\epsilon}(N_{\rm min}) \leq \epsilon(N_{\rm min}, p) < \mu$ or $\mu < \epsilon(N_{\rm min}, p) \leq \tilde{\epsilon}(N_{\rm min})$. In the former case, $p = N_{\rm min}, N_{\rm min}+1, N_{\rm min}+2, ..., \bar{p}$, where $\bar{p}$ is the largest integer such that $\epsilon(N_{\rm min}, p) < \mu$. In the latter case, $p = N_{\rm min}, N_{\rm min}-1, N_{\rm min}-2, ..., \bar{p}$ where $\bar{p}$ is the smallest integer such that $\epsilon(N_{\rm min}, p) > \mu$. We then find that Eq. (4.37) becomes

$$\mathcal{P}[x] = \frac{1}{4\cosh^2\left(\dfrac{\Delta_{\rm min}}{2k_BT}\right)} \sum_{p=N_{\rm min}}^{\bar{p}} x(N_{\rm min}, p), \tag{4.43}$$

where we have defined $\Delta_{\rm min} \equiv \tilde{\epsilon}(N_{\rm min}) - \mu$. Eq. (4.43) only keeps the dominant terms in the low-temperature limit.

This approximation must be improved when $\bar{p} = N_{\rm min}$, that is, the sum in $\mathcal{P}$ in Eq. (4.43) reduces to the single term $p = N_{\rm min}$ and transport is provided by the dominant transition energy $\tilde{\epsilon}(N_{\rm min})$ only. If in this case one imposes that $I_\alpha = 0$, then one obtains $J^h_\alpha = 0$, since $J^h_\alpha \propto I_\alpha$. As a consequence one gets $K_{\alpha\beta} = 0$ [3]. Thus, when $\bar{p} = N_{\rm min}$, we improve our

[3] This approximation for two terminals leads to zero thermal conductance and to the Carnot efficiency, as discussed for single-level quantum dots [5, 151, 152].

approximation of $\mathcal{P}$ by extending the sum over p to the two nearest integers, $p = N_{\min} \pm 1$. We have numerically verified that this approximation is valid when $2E_C > \Delta E$.

In order to obtain analytical expressions for the transport coefficients, hereafter we focus on the case of equidistant levels, $E_p - E_{p-1} = \Delta E$. After introducing the parameter

$$\xi \equiv \frac{4\cosh^2\left(\Delta_{\min}/2k_BT\right)}{e^{\Delta E/k_BT}} \tag{4.44}$$

and defining the integer $N_J \equiv \bar{p} - N_{\min}$, we obtain

$$\begin{aligned}\Omega[\lambda] = &-\ln\left[4\cosh^2\left(\frac{\Delta_{\min}}{2k_BT}\right)\right] + \lambda\Delta_{\min} \\ &+ \ln\left[\frac{e^{\lambda\Delta E(|N_J|+1)\mathrm{sign}(N_J)} - 1}{e^{\mathrm{sign}(N_J)\lambda\Delta E} - 1} + \xi\delta_{N_J,0}\left(\cosh\left(\lambda\Delta E\right) - \tanh\left(\frac{\Delta_{\min}}{2k_BT}\right)\sinh\left(\lambda\Delta E\right)\right)\right].\end{aligned} \tag{4.45}$$

Using Eqs. (4.41) and (4.45), we finally obtain the multiterminal transport coefficients

$$\begin{aligned}G_{\alpha\beta} &= \left(\delta_{\alpha\beta}\Gamma_\alpha - \frac{\Gamma_\alpha\Gamma_\beta}{\Gamma_{\mathrm{tot}}}\right)\frac{e^2}{4k_BT\cosh^2(\frac{\Delta_{\min}}{2k_BT})}\left(1 + |N_J|\right), \\ S_{\alpha\beta} &= -\delta_{\alpha\beta}\frac{1}{eT}\left(\Delta_{\min} + \frac{\Delta E}{2}N_J\right), \\ K_{\alpha\beta} &= \left(\delta_{\alpha\beta}\Gamma_\alpha - \frac{\Gamma_\alpha\Gamma_\beta}{\Gamma_{\mathrm{tot}}}\right)k_B\left(\frac{\Delta E}{k_BT}\right)^2 \\ &\qquad \times \begin{cases} \frac{1}{12}e^{-|\Delta_{\min}|/k_BT}|N_J|\left(|N_J|+1\right)\left(|N_J|+2\right) & \text{if } N_J \neq 0, \\ \dfrac{1}{e^{\Delta E/k_BT} + 4\cosh^2(\Delta_{\min}/2k_BT)} & \text{if } N_J = 0. \end{cases}\end{aligned} \tag{4.46}$$

We have computed $G_{\alpha\beta}$ and $S_{\alpha\beta}$ setting $\xi = 0$, since the term proportional to ξ in Eq. (4.45) only yields minor corrections that make these quantities more "smooth" as a function of μ; the calculation of $K_{\alpha\beta}$ instead requires a non null value of ξ. Eqs. (4.46) exhibit a number of interesting features. First of all, $G_{\alpha\beta}$ shows peaks as a function of the electrochemical potential μ every time $\Delta_{\min} = 0$, namely when $\mu = \tilde{\epsilon}(N)$. For example, the N-th peak corresponds to μ equal to the N-th dominant transition energy,

$$\mu = \mu_N \equiv (N-1)\Delta E + (2N-1)E_C. \tag{4.47}$$

We set $E_p = (p-1)\Delta E$, for $p = 1, 2, \ldots$, and therefore the separation between two nearby peaks is given by $\Delta E + 2E_C$. Due to the factor $\cosh^{-2}(\frac{\Delta_{\min}}{2k_BT})$ in $G_{\alpha\beta}$, these peaks have a bell shape with amplitude of the order of k_BT. On the other hand, the thermal conductance $K_{\alpha\beta}$ has plateaus of width $2\Delta E$ around μ_N [67], corresponding to the second line of the expression of $K_{\alpha\beta}$ for $N_J = 0$. For $N_J \neq 0$, the thermal conductance $K_{\alpha\beta}$ is then exponentially suppressed due to the term $e^{-|\Delta_{\min}|/k_BT}$. The local thermopower $S_{\alpha\alpha}$ vanishes at the values μ_N where the electrical and thermal conductances $G_{\alpha\alpha}$ and $K_{\alpha\alpha}$ exhibit a maximum. $S_{\alpha\alpha}$ has a linear dependence on μ with slope $dS_{\alpha\alpha}/d\mu = 1/eT$, with jumps when either $N_{\min}$ or N_J change by one. Therefore we have, for $E_C \gg \Delta E$, main oscillations of period $\Delta E + 2E_C$, and a fine structure with spacing ΔE [70]. We note that the fine structure is present also for $G_{\alpha\beta}$ and $K_{\alpha\beta}$, but in these cases the amplitude of the fine structure oscillations is exponentially small.

4.2.2 Two-terminal system

In the two-terminal case, the matrices $G_{\alpha\beta}$, $S_{\alpha\beta}$, and $K_{\alpha\beta}$ reduce to the familiar transport coefficients, namely the electrical conductance $G = G_{22}$, the thermopower $S = S_{22}$, and the thermal conductance $K = K_{22}$. From Eqs. (4.46) we recover the formulas for G and S well-known in literature [70], while our expression for K coincides for $N_J = 0$ with the result of Ref. [67], but also provides the fine structure oscillations for $N_J \neq 0$. Although such oscillations are not appreciable in K as a function of μ, we will see below that they give rise to a visible fine structure in ZT.

As we have discussed in Sec. 4.1.5, within the linear response regime the relevant quantities to characterize the performance of a thermoelectric device are the power factor Q and the figure of merit ZT. From the expressions of the transport coefficients in Eqs. (4.46), specified for the two-terminal case, one can compute Q and ZT analytically within the quantum limit. The obtained expressions are given below, and compared with a numerical calculation performed using the master equation.

Power factor

Let us start by studying the power factor Q. Within the quantum limit, we find that

$$Q = \frac{\gamma\,(1+|N_J|)}{4k_BT^3\cosh^2\left(\Delta_{\min}/(2k_BT)\right)}\left(\Delta_{\min}+\frac{N_J}{2}\Delta E\right)^2, \tag{4.48}$$

where we have defined $\gamma \equiv \Gamma_1\Gamma_2/(\Gamma_1+\Gamma_2)$. As for G, the power factor Q is dominated by a fast decrease, given by the term $\cosh^{-2}(\Delta_{\min}/2k_BT)$, thus becoming vanishingly small within a few k_BT around $\mu = \mu_N$ [see Fig. 4.3(a)]. In fact the fine structure, given by the terms with N_J, is not visible in Fig. 4.3(a) due to the rapid suppression given by the $\cosh^{-2}(\Delta_{\min}/2k_BT)$ term in Eq. (4.48). Differently from G, the power factor vanishes at $\mu = \mu_N$, due to the fact that in this point the thermopower $S = 0$. So as μ moves away from μ_N, Q increases quadratically due to the linear growth of the thermopower with μ, and then it rapidly decreases within a few k_BT due to the $\cosh^{-2}(\Delta_{\min}/2k_BT)$ term. Hence there are two symmetric peaks around $\mu = \mu_N$, within a few k_BT. These double peaks are the dominant feature of Fig. 4.3(a) and identify the optimal values of $\Delta_{\min}$ (and consequently of μ) to obtain the absolute maximum power $P_{\text{peak}}^{(\max)}$, namely when the power factor Q is maximum, $Q = Q^*$. From Eq. (4.48), we obtain that Q is maximum for values $\Delta_{\min}^*$ of $\Delta_{\min}$ such that

$$\frac{\Delta_{\min}^*}{2k_BT} = \coth\left(\frac{\Delta_{\min}^*}{2k_BT}\right). \tag{4.49}$$

The numerical solution is $\Delta_{\min}^* \simeq \pm 2.40 k_BT$, which corresponds to $\mu = \mu_N \pm 2.40 k_BT$. This result does not depend on any energy scale of the system except for k_BT, and coincides with the non-interacting single-level case (see App. A.4). The value Q^* of Q in these points is

$$Q^* \simeq 0.44\frac{\gamma k_B}{T}, \tag{4.50}$$

so that the peaks of the power factor only depend on γ and on the reference temperature. In conclusion, if we want to extract maximum power from this system, we must choose $\mu = \mu_N \pm 2.40 k_BT$. We will now show that also ZT reaches a local maximum at these same values of the electrochemical potential confirming that these are the optimal values for heat to work conversion in the quantum limit linear response regime.

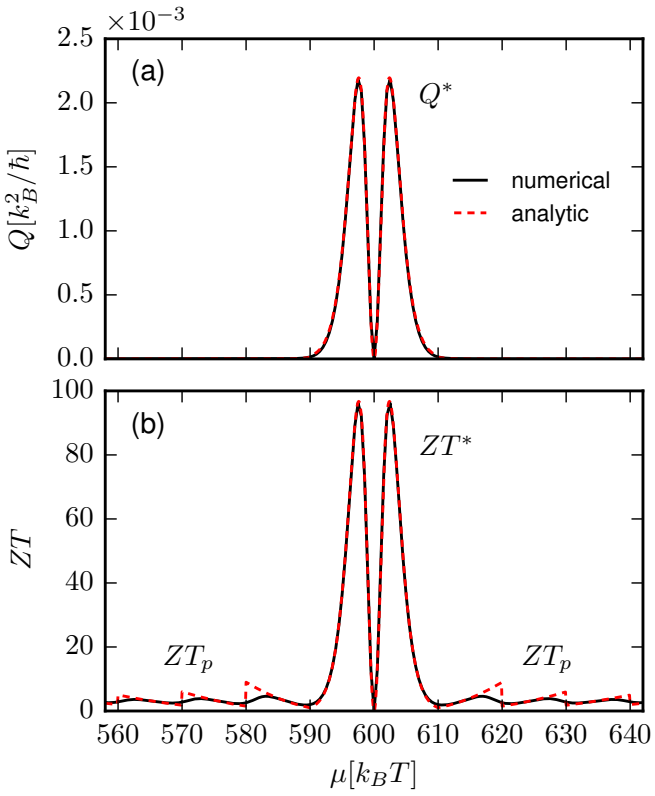

Figure 4.3: (Color online) Power factor Q (a) and figure of merit ZT (b) are plotted as a function of the electrochemical potential μ. For both quantities the analytical quantum limit [given by Eqs. (4.48) and (4.51)] is plotted as a red dashed curve, while the numerically calculated result is plotted as a black solid curve. All curves are calculated at $E_C = 50\,k_BT$, $\Delta E = 10\,k_BT$, and $\hbar\Gamma_1(p) = \hbar\Gamma_2(p) = (1/100)\,k_BT$.

Figure of merit

Let us now study the figure of merit ZT in the quantum limit. To obtain a more manageable analytical expression, we compute K from the function $\Omega[\lambda]$ expanded to the first order in ξ [this corresponds to approximating K with a constant plateau when $N_J = 0$, namely $4\cosh^2(\Delta_{\min}/2k_BT)$ is neglected with respect to $e^{\Delta E/k_BT}$ in the last line of Eqs. (4.46)]. We then obtain

$$ZT = \begin{cases} \frac{1}{4}\left(\frac{\Delta_{\min}}{\Delta E}\right)^2 \frac{e^{\Delta E/k_BT}}{\cosh^2\left(\frac{\Delta_{\min}}{2k_BT}\right)} & \text{if } N_J = 0, \\ \frac{3|N_J|}{2+|N_J|}\left(1 - 2\frac{|\Delta_{\min}|}{\Delta E|N_J|}\right)^2 & \text{if } N_J \neq 0, \end{cases} \tag{4.51}$$

which implies that the behavior of ZT is different for the two cases $|\mu - \mu_N| < \Delta E$ ($N_J = 0$) and $|\mu - \mu_N| > \Delta E$ ($N_J \neq 0$). In the former case K exhibits a plateau, so that ZT is directly proportional to Q and therefore it has the same double peak structure at $\mu = \mu_N \pm 2.40 k_BT$. This is clearly shown in Fig. 4.3(b) where ZT is plotted as a function of μ.

The value of ZT in these points is

$$ZT^* \approx 0.44 \frac{e^{\Delta E/k_BT}}{(\Delta E/k_BT)^2}. \tag{4.52}$$

This results has been obtained also in Ref. [153]. Eq. (4.52) shows that in the limit $\Delta E/k_BT \to \infty$, we have that $ZT \to \infty$. For example, for $\Delta E = 6k_BT$, we reach $ZT^* \approx 5$; for $\Delta E = 10k_BT$, we reach $ZT^* \approx 97$, and so on. This is consistent with Mahan and Sofo's observation [5] that a narrow transmission function yields $ZT \to \infty$. Furthermore, these peaks in ZT correspond to peaks in Q, so in these points we can maximize $P^{(\max)}$ and $\eta(P^{(\max)})$ simultaneously. Instead, when $N_J \neq 0$, ZT has a discontinuity every time $\mu = \epsilon(N,p)$ with $p \neq N$, which means with a ΔE spacing. This fine structure is the origin of the saw-tooth oscillations of Fig. 4.3(b). The value of ZT in each $\mu = \epsilon(N,p)$ is given by

$$ZT_p = \begin{cases} 3\frac{|N-p|+1}{|N-p|-1} & \text{if } |N-p| \geq 2, \\ 1 & \text{if } |N-p| = 1. \end{cases} \tag{4.53}$$

The height of these peaks, as opposed to ZT^*, has no dependance on the parameters of the system. The highest peak is obtained for $|N-p| = 2$, where $ZT_{p=N\pm2} = 9$. For values of p distant from N, the height of the peak decreases to an asymptotic value of $ZT_\infty = 3$.

4.2.3 Comparison with a non-interacting QD

Here we compare the efficiency of an interacting QD (with $2E_C > \Delta E$) with the efficiency of a non-interacting QD ($E_C = 0$) that has the same energy spacing ΔE; the comparison is performed within the linear response quantum limit for a two-terminal setup. The generating function in Eq. (4.45) cannot be used in the case $E_C = 0$ since it requires $2E_C > \Delta E \gg k_BT$. The generating function for $E_C = 0$ will be denoted as $\Omega_{\rm NI}[\lambda]$ (where NI stands for "non interacting") and calculated as follows. As we can see from Eq. (4.40), we must compute $\mathcal{P}[\exp\{\{\lambda(\epsilon(N,p)-\mu)\}\}]$ using the definition of $\mathcal{P}$ given in Eq. (4.37). When $E_C = 0$, $\epsilon(N,p) = E_p$, so the transition energies correspond to the energy levels of the QD, and they do not depend on the number of electrons in the QD. As a consequence, there is no dependance on N in the argument of $\mathcal{P}$, so we can explicitly perform the sum over N in Eq. (4.37) yielding the following expression:

$$\mathcal{P}_{\rm NI}[x(p)] \equiv \sum_{p=1}^{\infty} \frac{1}{4\cosh^2\left[(E_p-\mu)/2k_BT\right]} x(p). \tag{4.54}$$

Each term in the series in Eq. (4.54), as a function of μ, is a bell-shaped function centered around E_p of width set by k_BT. Therefore, within the quantum limit we can restrict the sum over p to the three bell-shaped functions closest to μ, namely $p = N_{\rm min}, N_{\rm min} \pm 1$ ($N_{\rm min}$, defined as in Eq. (4.42), is such that $E_{N_{\rm min}}$ is the closest energy level to μ). This approximation allows us to find

$$\Omega_{\rm NI}[\lambda] = -\ln\left[4\cosh^2\left(\frac{\Delta_{\rm min}}{2k_BT}\right)\right] + \lambda\Delta_{\rm min} + \ln\left[1 + 2\xi\cosh\left(\lambda\Delta E - \frac{\Delta_{\rm min}}{k_BT}\right)\right], \tag{4.55}$$

where $\Delta_{\rm min}$ in the non-interacting case reduces to the distance between μ and the nearest energy level: $\Delta_{\rm min} = E_{N_{\rm min}} - \mu$.

Let us now compare Eq. (4.55) with its interacting counterpart, Eq. (4.45), setting $N_J = 0$, thus neglecting the fine structure. We notice that the two expressions are identical when $\xi = 0$; this implies that $G_{\alpha\beta}$ and $S_{\alpha\beta}$ are equal in the interacting and non-interacting case [in Eqs. (4.46) $G_{\alpha\beta}$ and $S_{\alpha\beta}$ are calculated at $\xi = 0$], while $K_{\alpha\beta}$ is different in the two cases, since it is determined by the term proportional to ξ in Eqs. (4.45) and (4.55). We find that

$$K_{\alpha\beta}^{(\rm NI)} = 2k_B\left(\delta_{\alpha\beta}\Gamma_\alpha - \frac{\Gamma_\alpha\Gamma_\beta}{\Gamma_{\rm tot}}\right)\left(\frac{\Delta E}{k_BT}\right)^2 e^{-\Delta E/k_BT}\frac{2\xi + \cosh\left(\Delta_{\rm min}/k_BT\right)}{1 + 2\xi\cosh\left(\Delta_{\rm min}/k_BT\right)}. \tag{4.56}$$

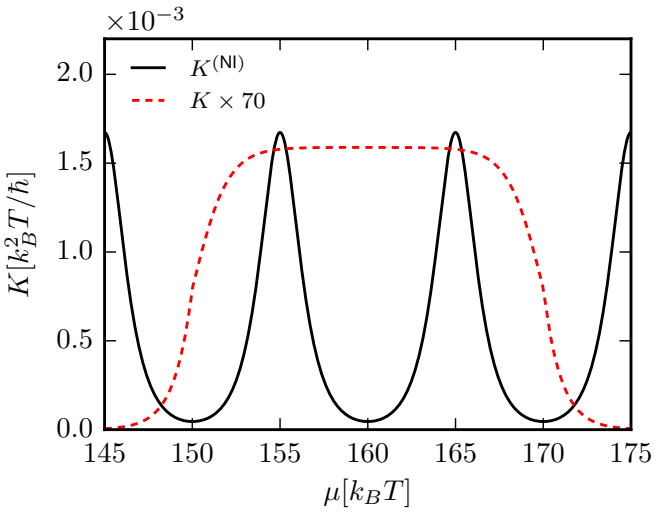

Figure 4.4: (Color online) Comparison between $K^{(\mathrm{NI})} = K_{22}^{(\mathrm{NI})}$ and $K = K_{22}$, given respectively by Eqs. (4.56) and (4.46), plotted as a function of μ. Both cases have been computed with the parameters used in Fig. 4.3, except for setting $E_C = 0$ in the non-interacting case. The interacting thermal conductance has been multiplied by a factor 70. In particular, its maximum value is half the minimum of $K^{(\mathrm{NI})}$.

A comparison between the interacting and non-interacting thermal conductances is plotted for a two-terminal system in Fig. 4.4, using Eqs. (4.46) and (4.56) at equal $\Delta E = 10 k_B T$. In this figure the dominant transition energy of the interacting system is located, see Eq. (4.47), at $\mu = \mu_{N=2} = 160\, k_B T$, while the energy levels of the non-interacting system are chosen as $E_p = (p-1)10 k_B T$ so that in both cases G has a peak in $\mu = 160\, k_B T$. We have verified that a numerical calculation is in very good agreement with Eq. (4.56) using the parameters of Fig. 4.4. As we can see from Fig. 4.4, $K^{(\mathrm{NI})} = K_{22}^{(\mathrm{NI})}$ and $K = K_{22}$ are very different. While K has a plateau of width $2\Delta E$ centered in $\mu_{N=2}$, $K^{(\mathrm{NI})}$ has a minimum in $\mu_{N=2}$, and reaches a maximum value for μ between two energy levels. Furthermore, by comparing Eq. (4.56) with the last line of Eqs. (4.46), we see that $K^{(\mathrm{NI})} \approx 2\cosh(\Delta_{\min}/k_B T) K$, so the minimum of $K^{(\mathrm{NI})}$, occurring at $\Delta_{\min} = 0$, is twice the maximum of K, and $K^{(\mathrm{NI})}$ increases exponentially respect to K as $\Delta_{\min}$ increases.

Intuitively, the striking difference between the two models can be explained as follows. As discussed in App. A.4, if we consider a single energy level QD the thermal conductance vanishes ($K = 0$) since K is computed at zero charge current and charge and heat currents are proportional in this case. However, K can be finite when at least two energy levels are available, and gets bigger by increasing the flux of electrons tunneling at different energies. Now, Coulomb interaction produces a correlation between electrons tunneling at different energies. Namely, if one electron enters the QD the electrostatic energy increases by $2E_C$, preventing other electrons from entering the QD at any other energy level. Therefore, until that electron tunnels out of the QD, all other processes are blocked: this is a manifestation of Coulomb blockade. On the contrary, in the non-interacting case all tunneling events are independent. This correlation is thus responsible for suppressing simultaneous tunneling through different energy levels in the interacting case, which results in a suppression of K.

So in general K is much smaller than $K^{(\mathrm{NI})}$. As a consequence of these observations, we

expect ZT to be suppressed in the non-interacting case.

By setting $\xi = 0$ in Eq. (4.56), we find

$$ZT_{\rm NI} = \frac{1}{8}\left(\frac{\Delta_{\rm min}}{\Delta E}\right)^2 \frac{e^{\Delta E/k_BT}}{\cosh^2\left(\frac{\Delta_{\rm min}}{2k_BT}\right)\cosh\left(\frac{\Delta_{\rm min}}{k_BT}\right)}. \tag{4.57}$$

Comparing Eq. (4.57) with Eq. (4.51), we see that, for $N_J = 0$, $ZT = 2\cosh\left(\Delta_{\rm min}/(k_BT)\right)ZT_{\rm NI}$, so $ZT_{\rm NI}$ is exponentially suppressed as $\Delta_{\rm min}$ increases. Given this suppression, the maximum of $ZT_{\rm NI}$ occurs at $\Delta^*_{\rm min} \approx \pm 1.36 k_BT$, corresponding to

$$ZT^*_{\rm NI} \approx \frac{1}{13.8}\frac{e^{\Delta E/k_BT}}{(\Delta E/k_BT)^2}.$$

This value is approximately 6 times smaller than ZT^* for the interacting case, see Eq. (4.52).

Furthermore, since K is "flat" around the dominant transition energies in the interacting case, the peak power $P^{(\rm max)}_{\rm peak}$ and the figure of merit ZT^* are reached at the same electrochemical potential, $\Delta^*_{\rm min} \approx \pm 2.40 k_BT$, so $ZT(P^{(\rm max)}_{\rm peak}) = ZT^*$. Instead in the non-interacting case these two quantities are not simultaneously maximized, due to the strong dependance of $K^{(\rm NI)}$ on μ, so we have that

$$ZT_{\rm NI}(P^{(\rm max)}_{\rm peak}) \approx \frac{1}{25.3}\frac{e^{\Delta E/k_BT}}{(\Delta E/k_BT)^2},$$

which is approximately 11 times smaller than $ZT(P^{(\rm max)}_{\rm peak})$, see Eq. (4.52).

In conclusion, within the linear response quantum limit, an interacting QD (with $2E_C > \Delta E$) has a considerably higher ZT with respect to a non-interacting QD both at peak efficiency, and at peak power, while having the same power factor (G and S being equal).

At last we will study how these two models violate the Wiedemann-Franz law, which states that for macroscopic ordinary metals the Lorenz ratio $L = K/GT$ is a constant equal to the Lorenz number $L_0 = (k_B/e)^2(\pi^2/3)$. Using Eqs. (4.46) and (4.56), we find that

$$L = \frac{L_0}{\pi^2}\left(\frac{\Delta E}{k_BT}\right)^2 \begin{cases} |N_J|(|N_J|+2) & \text{if } N_J \neq 0, \\ 12e^{-\frac{\Delta E}{k_BT}}\cosh^2\frac{\Delta_{\rm min}}{2k_BT} & \text{if } N_J = 0, \end{cases} \tag{4.58}$$

and

$$L_{\rm NI} = L_0\left(\frac{\Delta E}{k_BT}\right)^2 \frac{24}{\pi^2}e^{-\frac{\Delta E}{k_BT}}\cosh^2\frac{\Delta_{\rm min}}{2k_BT}\cosh\frac{\Delta_{\rm min}}{k_BT}, \tag{4.59}$$

where L refers to the interacting case, and the expression of K, for simplicity, has been computed at $\xi = 0$. In both cases the Wiedemann-Franz law is strongly violated: at $\Delta_{\rm min} = 0$, the Lorenz ratio is exponentially smaller than L_0 thanks to $(\Delta E/k_BT)^2\exp\{(-\Delta E/k_BT)\}$ (this has been noticed in Ref. [153] for the interacting model). In both cases the Lorenz ratio exponentially increases with $\Delta_{\rm min}$. In the non-interacting model the exponent is $2\Delta_{\rm min}/(k_BT)$ (twice the interacting case), and the maximum value, achieved at $\Delta_{\rm min} = \Delta E/2$, is of the order of $L_{\rm NI} \approx (\Delta E/k_BT)^2 L_0$. Interestingly, in the interacting case [Eq. (4.58)], when $|\Delta_{\rm min}| > \Delta E$, i.e. $N_J \neq 0$, we find plateaus whose height increases with N_J.

4.2.4 Three-terminal system

In this Section we consider the case of a three-terminal system, which allows to study the non-local transport coefficients and the influence of an additional terminal on the thermoelectric performance of the system. We focus on the simplest case when the couplings to the reservoirs are energy independent, that is, the rates Γ_α do not depend on p, and we will consider an equidistant QD spectrum. Analytical expressions in the quantum limit for the power and the efficiency at maximum power can be obtained also in this case on the basis of the expressions written in Ref. [101] and of Eqs. (4.46) for the transport coefficients. All considerations made in this Section are valid for both interacting and non-interacting systems.

In a three-terminal setup with time reversal symmetry we have nine independent coefficients: three electrical conductances G_{22}, G_{33}, and G_{23}, three thermopowers S_{22}, S_{33}, and S_{23}, and three thermal conductances K_{22}, K_{33}, and K_{23}. According to the expressions in Eqs. (4.46), valid in the quantum limit when the couplings to the leads are independent of energy, one finds that the local and non-local electrical (thermal) conductances are characterized by peaks (plateaus) located in the same positions as for the two-terminal case. The two local electrical (thermal) conductances G_{22}, G_{33}, (K_{22}, K_{33}), can have different heights if the coupling to reservoirs 2 and 3 are different ($\Gamma_2 \neq \Gamma_3$), while the non-local conductances, G_{23} and K_{23}, are negative. On the other hand, the local thermopowers S_{22} and S_{33} are equal and exhibit the same fine structure as in the two-terminal case. Moreover, the non-local thermopower S_{23} vanishes, as a consequence of energy independent tunneling rates.

The power and efficiency of a three-terminal system are defined in Eqs. (4.19) and (4.20). For definiteness, let's consider $T_3 \geq T_2 \geq T_1$, so $\Delta T_3 \geq \Delta T_2 \geq 0$. In general, Carnot's efficiency cannot be written only in terms of the temperatures T_1, T_2, and T_3, but it depends on the details of the system [101]. Nonetheless, if we fix the temperature of the hottest and coldest reservoir, that is, T_3 and T_1, it can be shown that $\eta_c \leq \eta_c^{(2)}$, where $\eta_c^{(2)} = 1 - T_1/T_3$ is the Carnot efficiency of the two-terminal system; the equal sign can be achieved when two reservoirs have the same temperatures. So adding a third terminal at an intermediate temperature cannot increase the maximum efficiency beyond the two terminal Carnot's efficiency.

Also in the three terminal case the efficiency at maximum power cannot go beyond the linear response Curzon-Ahlborn efficiency $\eta_{CA} = \eta_c^{(2)}/2$. Our aim is to maximize the power P with respect to $\Delta\mu_2$ and $\Delta\mu_3$, at given temperature differences. Then we will consider a fixed value of ΔT_3, and we will study the maximum power $P^{(\max)}$ and the efficiency at maximum power $\eta(P^{(\max)})$ varying T_2 between the fixed T_1 and T_3. These calculations can be performed by writing the currents in terms of the temperature and electrochemical potential differences through the Onsager matrix L_{ij} [101]; in turn, L_{ij} can be related to the transport coefficients. By rewriting Eqs. (4.41) as

$$\begin{aligned} G_{\alpha\beta} &= M_{\alpha\beta}\mathcal{G}, \\ S_{\alpha\beta} &= \delta_{\alpha\beta}\mathcal{S}, \\ K_{\alpha\beta} &= M_{\alpha\beta}\mathcal{K}, \end{aligned} \tag{4.60}$$

where

$$M_{\alpha\beta} = \delta_{\alpha\beta}\Gamma_\alpha - \frac{\Gamma_\alpha\Gamma_\beta}{\Gamma_{\text{tot}}}, \tag{4.61}$$

and by defining

$$\mathcal{Z}T = \frac{\mathcal{G}\mathcal{S}^2 T}{\mathcal{K}}, \qquad \Gamma_{ij} = \Gamma_i + \Gamma_j, \tag{4.62}$$

we can write the currents as

$$\begin{pmatrix} I_2/\Gamma_2 \\ I_3/\Gamma_3 \end{pmatrix} = \frac{\mathcal{G}}{e\Gamma_{\rm tot}} \begin{pmatrix} -\Gamma_{13} & \Gamma_{13} & \Gamma_3 & -\Gamma_3 \\ \Gamma_2 & -\Gamma_2 & -\Gamma_{12} & \Gamma_{12} \end{pmatrix} \begin{pmatrix} \Delta\mu_2 \\ e\mathcal{S}\Delta T_2 \\ \Delta\mu_3 \\ e\mathcal{S}\Delta T_3 \end{pmatrix}, \tag{4.63}$$

$$\begin{pmatrix} J_2^h/\Gamma_2 \\ J_3^h/\Gamma_3 \end{pmatrix} = \frac{\mathcal{K}}{\Gamma_{\rm tot}} \begin{pmatrix} \Gamma_{13} & \Gamma_{13} & -\Gamma_3 & -\Gamma_3 \\ -\Gamma_2 & -\Gamma_2 & \Gamma_{12} & \Gamma_{12} \end{pmatrix} \begin{pmatrix} 0 \\ \Delta T_2 \\ 0 \\ \Delta T_3 \end{pmatrix} + \mathcal{S}T \begin{pmatrix} I_2/\Gamma_2 \\ I_3/\Gamma_3 \end{pmatrix}. \tag{4.64}$$

Note that the quantities $\mathcal{G}$, $\mathcal{S}$, $\mathcal{K}$ and $\mathcal{Z}T$ only depend on the properties of the QD, which can be interacting or non-interacting, and on the reference electrochemical potential μ; they do not depend on the number of reservoirs nor on the tunneling rates.

The electrochemical potential differences that maximize P at given reservoir temperatures can be written as

$$\Delta\mu_\alpha = \frac{1}{2} e\mathcal{S}\Delta T_\alpha. \tag{4.65}$$

Inserting these expressions into P yields

$$P^{(\max)} = \frac{1}{4}\frac{\mathcal{Q}}{\Gamma_{\rm tot}} \left[\Gamma_1\Gamma_2\Delta T_2^2 + \Gamma_1\Gamma_3\Delta T_3^2 + \Gamma_2\Gamma_3\left(\Delta T_3 - \Delta T_2\right)^2\right], \tag{4.66}$$

where $\mathcal{Q} = \mathcal{G}\mathcal{S}^2$. The maximum power is thus an always positive quantity and, in the same manner as in the two-terminal case, see Eq. (4.21), it is proportional to $\mathcal{Q}$ and quadratic in the temperature differences. Furthermore, the properties of the QD and the chosen μ are all contained in the $\mathcal{Q}$ term, while the coupling to the reservoirs and the temperature differences are separately accounted for in the term between square parentheses in Eq. (4.66). The efficiency at maximum power instead is given by

$$\begin{aligned} \eta\left(P^{(\max)}\right) = \frac{\eta_{\rm c}^{(2)}}{2}\frac{\mathcal{Z}T}{\mathcal{Z}T+2} &\left[\Gamma_1\Gamma_2\Delta T_2^2 + \Gamma_1\Gamma_3\Delta T_3^2 + \Gamma_2\Gamma_3\left(\Delta T_3 - \Delta T_2\right)^2\right] \\ &\times \begin{cases} \frac{1}{\Gamma_1\Delta T_3(\Gamma_2\Delta T_2+\Gamma_3\Delta T_3)} & \text{if } \frac{\Gamma_3}{\Gamma_1+\Gamma_3}\Delta T_3 \le \Delta T_2 \le \Delta T_3, \\ \frac{1}{\Gamma_3\Delta T_3[\Gamma_1\Delta T_3+\Gamma_2(\Delta T_3-\Delta T_2)]} & \text{if } 0 \le \Delta T_2 \le \frac{\Gamma_3}{\Gamma_1+\Gamma_3}\Delta T_3. \end{cases} \end{aligned} \tag{4.67}$$

It is interesting to notice that in this equation the term before square parenthesis, which does not depend on Γ_α, is exactly equal to the two terminal efficiency at maximum power, see Eq. (3.29), since $\mathcal{Z}T = ZT$ for a two terminal system. The remaining part of Eq. (4.67) takes into account the particular temperatures and couplings to the three terminals. Furthermore the efficiency at maximum power, also in this 3 terminal system, only depends on $\mathcal{Z}T$. There are three limiting cases we will first study: $\Delta T_2 = 0$, $\Delta T_2 = \Delta T_3$ and $\Delta T_2 = \Delta T_3\Gamma_3/(\Gamma_1+\Gamma_3)$.

If $\Delta T_2 = 0$, $T_1 = T_2$, so we have one hot reservoir at temperature T_3 and two cold ones at the same temperature. In this case we obtain

$$P^{(\max)} = \frac{1}{4}\mathcal{Q}\Delta T_3^2 \frac{(\Gamma_1+\Gamma_2)\,\Gamma_3}{(\Gamma_1+\Gamma_2)+\Gamma_3}, \tag{4.68}$$

$$\eta\left(P^{(\max)}\right) = \frac{\eta_{\rm c}}{2}\frac{\mathcal{Z}\mathcal{T}}{\mathcal{Z}\mathcal{T}+2}. \tag{4.69}$$

Note that for a two-terminal system the maximum power, obtained by inserting Eq. (4.60) into Eq. (4.21), is given by

$$P_2^{(\max)} = \frac{1}{4}\mathcal{Q}\Delta T_2^2 \frac{\Gamma_1\Gamma_2}{\Gamma_1+\Gamma_2}. \tag{4.70}$$

Comparing Eq. (4.70) with Eq. (4.68), and Eq. (3.29) with Eq. (4.69), we notice that the 3 terminal system is formally equivalent to a 2-terminal system with temperature difference ΔT_3, with tunneling rate $\Gamma_1+\Gamma_2$ instead of Γ_1, and Γ_3 instead of Γ_2.

If $\Delta T_2 = \Delta T_3$, $T_2 = T_3$, so we have two hot reservoir at temperature T_3 and one cold reservoir at temperature T_1. In this case we obtain

$$P^{(\max)} = \frac{1}{4}\mathcal{Q}\Delta T_3^2 \frac{\Gamma_1\left(\Gamma_2+\Gamma_3\right)}{\Gamma_1+\left(\Gamma_2+\Gamma_3\right)}, \tag{4.71}$$

$$\eta\left(P^{(\max)}\right) = \frac{\eta_c}{2}\frac{\mathcal{Z}T}{\mathcal{Z}T+2}. \tag{4.72}$$

As in the previous limiting case, this system behaves like a 2-terminal with temperature difference ΔT_3 and with tunneling rate $\Gamma_2+\Gamma_3$ instead of Γ_2.

If $\Delta T_2 = \Delta T_3\Gamma_3/(\Gamma_1+\Gamma_3)$, reservoir 2 has an intermediate temperature such that $J_2^h = 0$. In fact this specific value of ΔT_2 distinguishes the two regimes where $J_2^h > 0$ and $J_2^h < 0$. In this case we obtain

$$P^{(\max)} = \frac{1}{4}\mathcal{Q}\Delta T_3^2 \frac{\Gamma_1\Gamma_3}{\Gamma_1+\Gamma_3}, \tag{4.73}$$

$$\eta\left(P^{(\max)}\right) = \frac{\eta_c}{2}\frac{\mathcal{Z}T}{\mathcal{Z}T+2}. \tag{4.74}$$

As in the other two limiting cases, this system behaves like a 2-terminal system, where reservoir 2 has been removed; this is to be expected because at this particular temperature, no heat flows through the second reservoir.

According to Eq. (4.67), all values of ΔT_2 other than the three cases discussed above decrease the efficiency at maximum power with respect to the two-terminal case. The maximum power instead, at given tunneling rates, is increased with respect to the two-terminal case. In fact the maximum power is formally equal to that of a two-terminal system, coupled to the same QD, with increased tunneling rates. So if we have fixed values of Γ_1, Γ_2 and Γ_3, we achieve the largest maximum power by choosing $\Delta T_2 = 0$ if $\Gamma_1 < \Gamma_3$ and $\Delta T_2 = \Delta T_3$ if $\Gamma_1 > \Gamma_3$. In Fig. 4.5, $P^{(\max)}$ and $\eta\left(P^{(\max)}\right)$ from Eqs. (4.66) and (4.67) are plotted as a function of $\Delta T_2/\Delta T_3$, choosing $\hbar\Gamma_1 = 0.02k_BT$ and $\hbar\Gamma_2 = \hbar\Gamma_3 = 0.01k_BT$. As we can see in panel (a), the power is maximum when $\Delta T_2 = \Delta T_3$ (this result is expected since $\Gamma_1 > \Gamma_3$). Furthermore the three maxima in panel (b) correspond to the three limiting cases previously studied, where $\eta\left(P^{(\max)}\right)$ reaches the two-terminal performance.

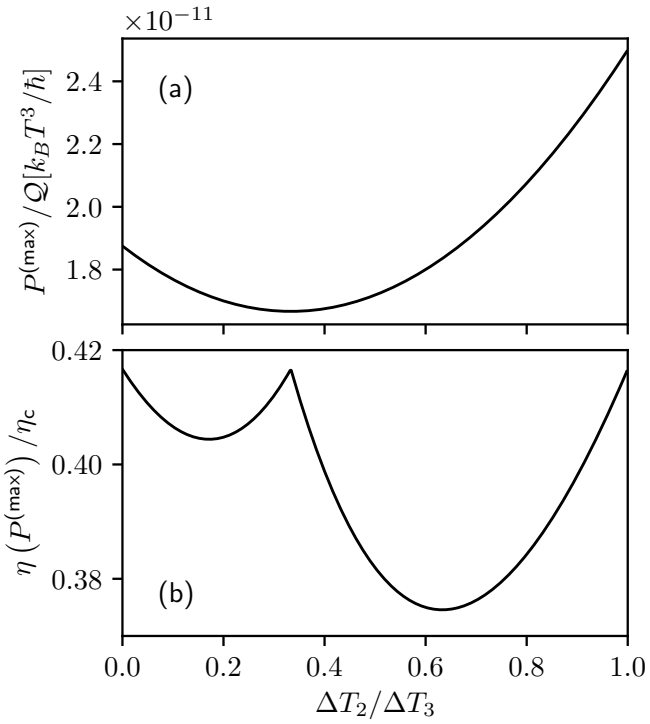

FIGURE 4.5: (a) Maximum power, Eq. (4.66), normalized to $\mathcal{Q}$ and (b) efficiency at maximum power, Eq. (4.67), normalized to Carnot's efficiency, plotted as a function of $\Delta T_2/\Delta T_3$. Curves computed with $\mathcal{Z}T = 10$, $\Delta T_3/T = 10^{-4}$, $\hbar\Gamma_1 = 0.02 k_B T$, $\hbar\Gamma_2 = \hbar\Gamma_3 = 0.01 k_B T$.

4.3 Non-linear response

The linear response theory describes correctly the thermoelectric properties of bulk materials in most experimental conditions. However, as discussed for instance in Ref. [154], non-linear effects are important in nanoscopic setups, since the temperature difference is applied across very small elements of the order of tens or hundreds of nanometers. As far as heat-to-work conversion is concerned, there is a practical reason to consider the non-linear response, namely efficiency and power output may increase with increasing temperature difference. Furthermore, for systems with time-reversal symmetry the efficiency at maximum power can overcome the limit of $\eta_c/2$ only beyond the linear response [4].

In this section we will consider a two-terminal QD system and discuss the numerical results obtained solving the master equation (4.4) as discussed in Sec. 4.1. We will focus our discussion on the thermoelectric properties, and on the efficiency and power produced by a QD-based heat engine. Let us define the charge current $I \equiv I_2 = -I_1$, thanks to charge current conservation, and the average reservoir temperature $\bar{T} = (T_1 + T_2)/2$, which determines the typical thermal energy scale of the system beyond linear response (all energies will be given in units of $k_B\bar{T}$). Furthermore, $\Delta\mu \equiv \Delta\mu_2 = -eV$, with V applied voltage, $\Delta T \equiv \Delta T_2$, and assume equidistant energy levels with spacing given by ΔE. In order to describe the potential drop between the QD and the two reservoirs, we will assume that the

[4] Note, however, that the Curzon-Ahlborn limit can be overcome also within linear response when time-reversal symmetry is broken, see Refs. [155–159].

set of energy levels is shifted as $E_p(V) = E_p - (1-\theta_0)eV$, where $0 \leq \theta_0 \leq 1$ is the fraction of potential V that drops over the tunnel barrier which couples reservoir 2 to the QD.

Regarding charge transport, we recall that in the linear response, within the quantum limit, the conductance exhibits peaks occurring at the dominant transition energies, i.e. when $\mu = \mu_N$, of width given by $k_B\bar{T}$. By applying a finite voltage bias V, in the absence of a temperature difference ($\Delta T = 0$), the differential conductance, defined as

$$G = \left(\frac{\partial I}{\partial V}\right), \tag{4.75}$$

exhibits the typical Coulomb diamond structure, with visible excited states, as a function of V and μ, see for instance Ref. [160].

4.3.1 Non-linear Seebeck and Peltier coefficients

In the non-linear regime the thermopower (Seebeck coefficient) can be defined as follows

$$S = -\left.\frac{V}{\Delta T}\right|_{I=0}, \tag{4.76}$$

i.e. as the ratio between the *thermovoltage* V that develops as a result of a finite ΔT applied, at open circuit ($I = 0$). In Fig. 4.6, S is plotted as a function of μ for various values of $\Delta T/\bar{T}$.

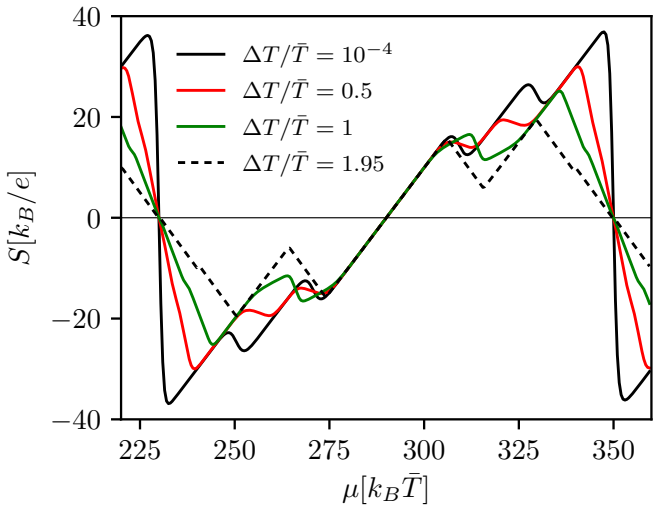

Figure 4.6: (Color online) Non-linear thermopower S plotted as a function of μ for various values of $\Delta T/\bar{T}$, and $\Delta E = 20k_B\bar{T}, E_C = 50k_B\bar{T}, \hbar\Gamma_L(p) = \hbar\Gamma_R(p) = 0.01k_B\bar{T}, \theta_0 = 1/2$.

The black solid curve (calculated for $\Delta T/\bar{T} = 10^{-4}$) is the linear-response reference that is well approximated by the expression given in Eqs. (4.46). As discussed in Sec. 4.2.1, the black solid curve presents main oscillations of period $\Delta E + 2E_C$, and a fine structure with a ΔE spacing [70]. Since we have chosen an equidistant energy spectrum, all curves share a number of features with the linear-response reference. Namely, i) S crosses zero with positive slope at the main transition energies μ_N and is periodic with periodicity $\Delta E + 2E_C$ (in Fig. 4.6 $\mu = 290\ k_B\bar{T}$ corresponds [see Eq. (4.47))] to $\mu_{N=3}$); ii) in the range of μ considered, S is

antisymmetric with respect to $\mu = 290\ k_B\bar{T}$; iii) S vanishes for values of μ in the middle points between two dominant transitions μ_N and μ_{N+1} (in Fig. 4.6 such points are located at $\mu = 230\ k_B\bar{T}$ and $\mu = 350\ k_B\bar{T}$). Moreover, since we set $\theta_0 = 1/2$, the linear increase of S for $\mu \simeq \mu_N$ does not depend on the ratio $\Delta T/\bar{T}$, i.e. it is well described by the linear-response proportionality coefficient $1/(e\bar{T})$. Interestingly, such features (except for the fine structure oscillations) can be understood in terms of a non-interacting model (see App. A.4), which also explains the reduction of the negative slope of S at the middle points as the ratio $\Delta T/\bar{T}$ increases.

Let us now discuss the behavior of S when departing from the linear response regime. Fig. 4.6 shows that for all values of ΔT the thermopower deviates from the linear-response curve only for μ above $310\ k_B\bar{T}$ (or below $270\ k_B\bar{T}$). A sharp departure already occurs at $\Delta T/\bar{T} = 0.5$ (red curve). This can be understood from the fact that, for $\mu > 310\ k_B\bar{T}$, S is of the order of $15\ k_B/e$ which corresponds to a value of the thermovoltage ($V = -7.5\ k_B\bar{T}/e$) such that $|eV| \gg k_BT$ [5]. Note that $\mu = 310\ k_B\bar{T}$ roughly corresponds to the first step of the fine structure in linear response. In particular, while the first step hardly moves by increasing ΔT from its position in linear response, the second step, occurring at $\mu = 330\ k_B\bar{T}$ in the linear response, shifts to a smaller value for increasing $\Delta T/\bar{T}$, eventually disappearing or merging with the first step. This behavior may be attributed to the combination of the following two effects. On one hand, the thermovoltage V, which determines the transport energy window, depends on μ and increases with ΔT according to the definition (4.76). On the other hand, an increase of $\Delta T/\bar{T}$ moves the lowest temperature (T_1) towards absolute zero, thus sharpening the Fermi distribution function $f_1(E)$. This last effect is also responsible for the sharpening of $S(\mu)$ as $\Delta T/\bar{T}$ increases. Note furthermore that the extremal values of S decrease as $\Delta T/\bar{T}$ increases.

Let us now consider the non-linear Peltier coefficient defined, for a given voltage V, as

$$\Pi = \left.\frac{J_2^h}{I}\right|_{\Delta T=0}. \tag{4.77}$$

Our aim is to assess the failure of the Onsager reciprocity relation $\Pi = TS$, which holds in the linear response regime. Beyond linear response, for a single-level non-interacting QD, one finds a "corrected" reciprocity relation, namely $\Pi + V/2 = \bar{T}S$ in the case where $\theta_0 = 1/2$ (see App. A.4). To single out the effect of interactions in a multi-level QD, in Fig. 4.7 we plot the ratio $r = (\Pi + V/2)/(\bar{T}S)$ as a function of μ for various values of $\Delta T/\bar{T}$ and $eV/(k_B\bar{T})$ ($\Delta T/\bar{T}$ is used to compute S, while eV/k_BT to compute Π). Fig. 4.7 shows that the ratio r departs significantly from 1, the linear response result (blue thin line), only far enough from the dominant transition energy $\mu_{N=3} = 290\ k_B\bar{T}$. In particular, when Π is in the linear response regime and S is not (black solid curve) the strong deviations occurring for μ around the middle points between dominant transition energies, namely $\mu = 230\ k_B\bar{T}$ and $\mu = 350\ k_B\bar{T}$, can be explained by a two-level non-interacting model (see App. A.4). However, the deviations occurring in the range of values of μ between $250\ k_B\bar{T}$ and $330\ k_B\bar{T}$ can be imputed to interaction effects. In the opposite case, where S is in the linear response and Π is not (red curve), the deviations of r from 1 are entirely due to interaction effects and r takes values between 0 and 1 in the entire range of values of μ. When both S and Π are beyond linear response the two behaviors discussed above coexist giving rise to the black dashed curve [6].

[5] We have also checked that we are well beyond the linear response for the electric conductance.

[6] The black dashed curve is actually equal to the product of the solid black and the red curve. Indeed, due

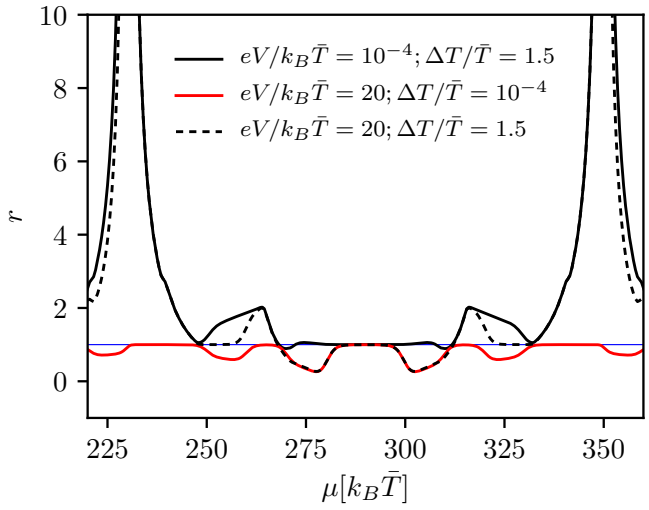

Figure 4.7: (Color online) Ratio $r = (\Pi + V/2)/(\bar{T}S)$ plotted as a function of μ for various values of eV/k_BT (for the Peltier coefficient) and of $\Delta T/\bar{T}$ (for the thermopower), for the same parameter values as in Fig. 4.6. The blue thin line is the reference $r = 1$.

4.3.2 Efficiency and output power

In this Section we consider the efficiency for heat-to-work conversion and output power in a two terminal system. Specifying Eq. (4.20) to a two terminal system where $\Delta T > 0$, we have that

$$\eta = \frac{P}{J_2^h}, \tag{4.78}$$

where $P > 0$ is the output power, defined in Eq. (4.19), and $J_2^h > 0$ is the heat current absorbed by the system. Apart from the system's parameters, η depends on V and ΔT.

Let us first consider the maximum efficiency $\eta^{(\max)}$, obtained by maximizing the efficiency η with respect to the applied voltage V, at given ΔT. $\eta^{(\max)}$ is plotted, normalized to η_c, in Fig. 4.8(a) as a function of μ for different values of $\Delta T/\bar{T}$. All plots show pairs of peaks close to μ_N, whose maximum is very close to η_c, and secondary peaks of smaller height. The solid black curve, relative to the linear response regime ($\Delta T/\bar{T} = 10^{-4}$), is related through Eq. (3.29) to the plot of ZT [Fig. 4.3(b)][7] discussed in Sec. 4.2.2. For the black curve a pair of maxima approaching η_c occur at $\mu = \mu_N \pm 2.40 k_B\bar{T}$, while $\eta^{(\max)}$ vanishes at the dominant transition energies (and at the middle points between two dominant transition energies). Moreover, a fine structure of secondary peaks, with spacing ΔE, appears for intermediate values of μ. Moving away from the linear response, the main observation is that an increase of $\Delta T/\bar{T} > 0.1$ produces only quantitative changes to the curves. As shown in Fig. 4.8(a), the main peaks of $\eta^{(\max)}$ are still approximately located at $\mu = \mu_N \pm 2.40 k_B\bar{T}$ and approaching the Carnot efficiency, while the peaks' width reduces slightly with increasing ΔT, and the fine structure of the secondary peaks gets simply distorted.

to the Onsager reciprocal relations in this product the linear response Peltier Π (which appears in the ratio r for the solid black curve) simplifies with the linear response $\bar{T}S$ (which appears in the ratio r for the red curve).

[7] Notice that in Fig 4.8 $\Delta E = 20\, k_BT$, while in Fig. 4.3 $\Delta E = 10\, k_BT$.

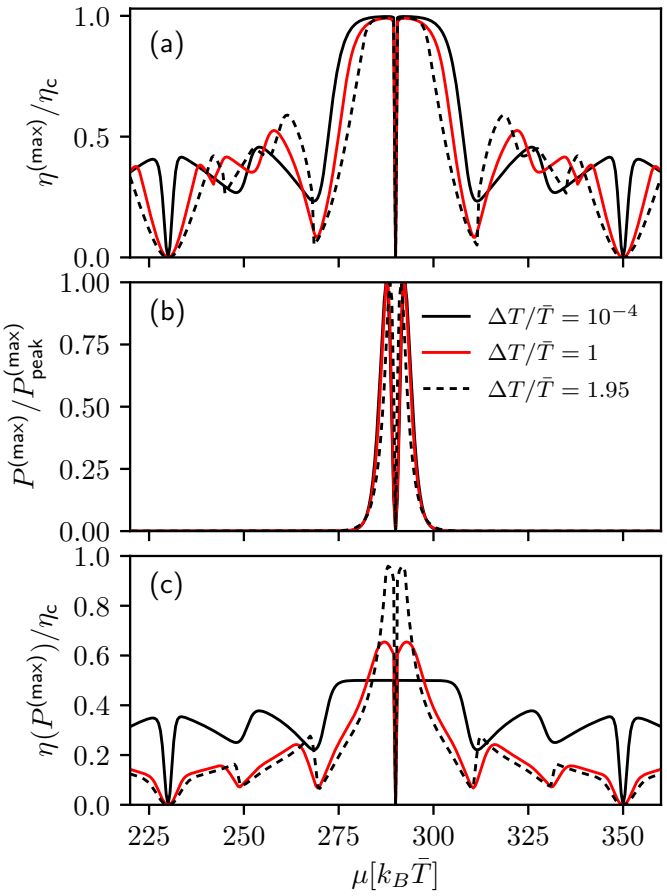

FIGURE 4.8: (Color online) (a) Maximum efficiency, normalized to Carnot's efficiency, (b) maximum output power $P^{(\max)}$, normalized to its peak value $P^{(\max)}_{\text{peak}}$, and (c) efficiency at maximum power $\eta(P^{(\max)})$, normalized to η_c, plotted as a function of μ for various values of $\Delta T/\bar{T}$, for the same parameter values as in Fig. 4.6.

Another important quantity in heat-to-work conversion is the maximum output power generated $P^{(\max)}$, which is obtained by maximizing the output power with respect to the applied voltage V. It turns out that $P^{(\max)}$ exhibits pairs of peaks approximately located at $\mu = \mu_N \pm 2.40 k_B\bar{T}$ whose height increases approximately quadratically with ΔT, as long as $\Delta T/\bar{T}$ is not to close to 2. Interestingly, Fig. 4.8(b) shows that the maximum output power $P^{(\max)}$, when normalized to its peak value $P^{(\max)}_{\text{peak}}$, only very weakly depends on the ratio $\Delta T/\bar{T}$. In particular, $P^{(\max)}/P^{(\max)}_{\text{peak}}$ is well approximated by the linear-response result, whose analytical expression is obtained by substituting Eq. (4.48) into Eq. (4.21).

The efficiency at maximum power $\eta(P^{(\max)})$ can now be calculated by taking, for each value of μ, the value of V which maximizes the power. $\eta(P^{(\max)})$ is plotted, as a function of μ, in Fig. 4.8(c) for various values of the ratio $\Delta T/\bar{T}$. By increasing such ratio starting from the linear response [solid black curve, related to the plot of ZT in Fig. 4.3(b) through Eq. (3.29)] one finds that the peak values, again occurring approximately at $\mu = \mu_N \pm 2.40 k_B\bar{T}$, increase well above $\eta_c/2$ (the upper limit for the linear response). On the contrary, the efficiency at maximum power for values of μ away from μ_N, relative to the fine structure, decreases

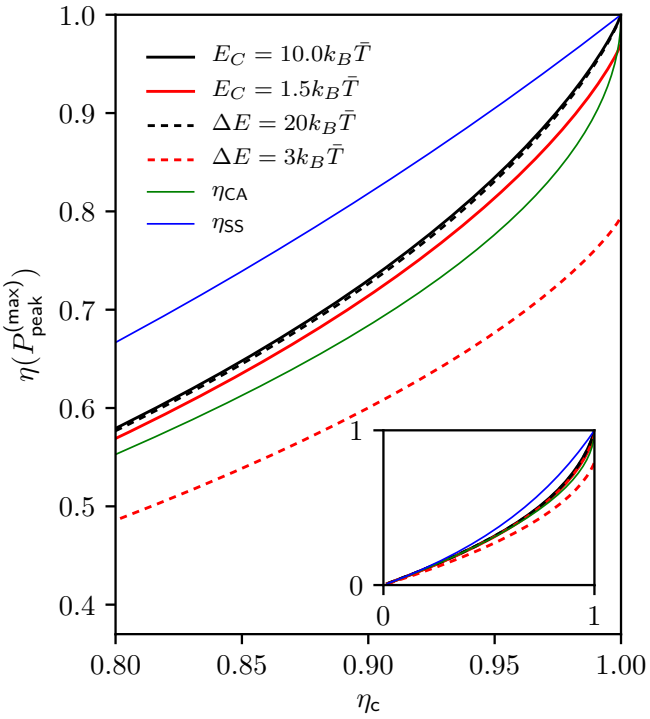

Figure 4.9: (Color online) Efficiency at maximum power $\eta(P^{(\max)}_{\text{peak}})$ plotted as a function of η_c for various values of E_C, with $\Delta E = 0$ (solid curves) and for various values of ΔE, with $E_C = 0$ (dashed curves). Thin solid curves represent the CA and SS efficiencies, see text. Tunneling rates are $\hbar\Gamma_1(p) = \hbar\Gamma_2(p) = 0.01 k_B\bar{T}$. The inset shows the same curves on the entire range $\eta_c \in [0, 1]$.

with increasing $\Delta T/\bar{T}$ beyond the linear response, but is only slightly different moving from $\Delta T/\bar{T} = 1$ (red curve) to $\Delta T/\bar{T} = 1.95$ (black dashed curve).

It is now interesting to compare the peak values of the efficiency at maximum power with various reference values, such as the Curzon-Alhborn (CA) efficiency [37] $\eta_{\text{CA}} = 1 - \sqrt{1-\eta_c}$ and the Schmiedl-Seifert (SS) efficiency [39] $\eta_{\text{SS}} = \eta_c/(2-\eta_c)$ [8] discussed in Sec. 3.1.1. To do so we calculate the peak power, i.e. maximizing the power with respect to V and μ, and plot the corresponding efficiency as a function of η_c (determined by the temperature difference) in various situations, see Fig. 4.9. In particular, we consider the case of a QD with one doubly degenerate level with a finite charging energy (solid thick curves) and the case of a QD with two non-degenerate levels and zero charging energy (dashed curves). The parameters are chosen such that the two situations can be compared, namely $\Delta E = 2E_C$, i.e. the differential conductance consists of two peaks separated by the same electrochemical potential. Figure 4.9 (inset) shows the following general feature for small η_c, i.e. in the linear response regime: $\eta(P^{(\max)}_{\text{peak}})$ increases linearly with η_c with slope determined by the value of ZT [see Eq. (3.29)]. In particular, the two black curves (relative to $E_C = 10\ k_B\bar{T}$ and to $\Delta E = 20\ k_B\bar{T}$) virtually coincide, and are equal to the one for a single non-interacting level QD [see App. A.4 and the first line of Eqs. (A.44)], since the parameters are such that $k_B\bar{T} \ll E_C, \Delta E$, where the transport is mostly accounted for by a single energy level. On the

[8] This is actually the upper bound of the Schmiedl-Seifert efficiency, see Refs. [38, 39].

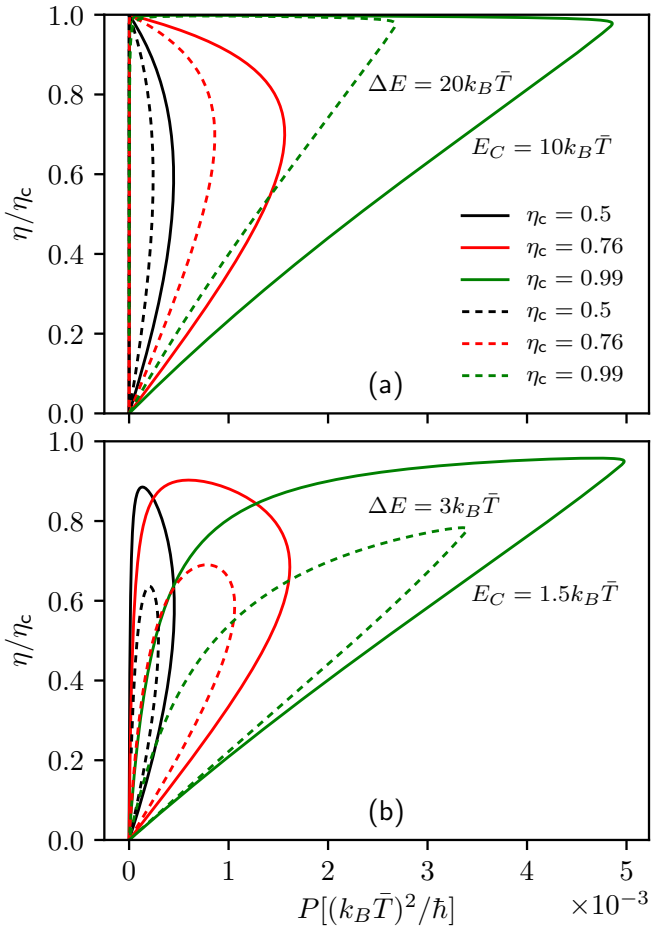

FIGURE 4.10: (Color online) Correlation between efficiency and output power calculated for a few points of the plots in Fig. 4.9, both for doubly degenerate interacting case (solid curves), and non-degenerate non-interacting case (dashed curves). Curves obtained by increasing the value of V from zero to the thermovoltage value, corresponding to the open-circuit situation, for various values of η_c. Panel (a) refers to $\Delta E = 20\ k_B\bar{T}$ (with $E_C = 0$, dashed curves) and to $E_C = 10\ k_B\bar{T}$ (with $\Delta E = 0$, solid curves), while panel (b) refers to $\Delta E = 3\ k_B\bar{T}$ (with $E_C = 0$, dashed curves) and to $E_C = 1.5\ k_B\bar{T}$ (with $\Delta E = 0$, solid curves).

contrary, the two red curves (relative to $E_C = 1.5\ k_B\bar{T}$ and to $\Delta E = 3\ k_B\bar{T}$) differ by a large extent, with the interacting case (solid red curve) exhibiting larger efficiency at maximum power with respect to the associated non-interacting case (dashed red curve). Note that the efficiency at maximum power relative to the interacting case goes beyond the CA efficiency, when η_c is larger than about 0.5, for all values of E_C between 1.5 $k_B\bar{T}$ and 10 $k_B\bar{T}$. Finally, we find that the SS efficiency is never overcome.

To complete the analysis, we show the correlation between efficiency and power corresponding to a few points (i.e. a few values of η_c) in the curve of Fig. 4.9. More precisely, Fig. 4.10 shows how the value of the power P and the efficiency η evolve by increasing the applied voltage V from zero (where both P and η vanish) to the thermovoltage (where P

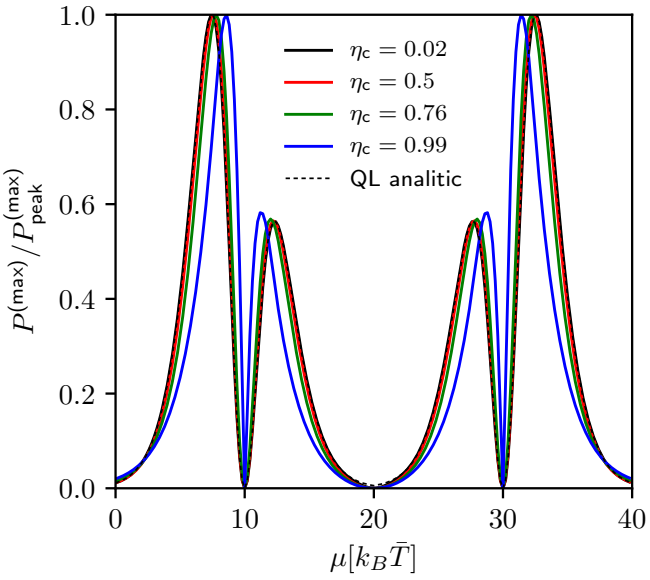

Figure 4.11: (Color online) Maximum power, normalized to the peak value, plotted as a function of μ for different values of η_c with $E_C = 10\ k_B\bar{T}$, $\Delta E = 0$ and considering a single doubly degenerate energy level. Surprisingly, not only the linear-response curve (black) is very well approximated by the analytic expression in Eq. (4.79) (black dashed curve) valid in the quantum limit. Tunneling rates are $\hbar\Gamma_1(p) = \hbar\Gamma_2(p) = 0.01 k_B\bar{T}$.

vanishes as a consequence of the fact that the charge current vanishes) [9]. In particular, panel (a) refers to the case $\Delta E = 20\ k_B\bar{T}$ (dashed curves) and $E_C = 10\ k_B\bar{T}$ (solid curves), while panel (b) refers to the case $\Delta E = 3\ k_B\bar{T}$ (dashed curves) and $E_C = 1.5\ k_B\bar{T}$ (solid curves). We checked that in the linear response (when $\eta_c \ll 1$) the power reaches its maximum when the efficiency is nearly equal to $\eta_c/2$. By increasing η_c, for all the curves in the figure, both maximum power and efficiency at maximum power increase. For large values of η_c (green curves), the efficiency remains close to the Carnot efficiency when V is increased beyond the point of maximum power. The general feature is that in the interacting case (solid curves) the power is much larger than in the associated non-interacting situation (dashed curves). When ΔE and E_C are of the same order as $k_B\bar{T}$ [Fig. 4.10(b)], both the maximum power and the efficiency at maximum power are increased in the interacting case as compared with the non-interacting case. A remarkable property of both regimes discussed in panels (a) and (b) is that in the strongly nonlinear regime, the maximum power is obtained for values where the efficiency is high and close to the maximum efficiency.

We finally discuss a peculiarity of the maximum power output considering a doubly degenerate energy level in the interacting case [10] (as we will point out, some considerations are also valid in the non degenerate case). Fig. 4.11 shows the maximum power, normalized with respect to the peak value, as a function of μ for different values of η_c including the linear-response case (parameter values are the same as for Fig. 4.9, with $E_C = 10\ k_B\bar{T}$).

[9] For a given value of η_c, we first find the values $\mu = \bar{\mu}$ and $V = \bar{V}$ leading to the peak value $P^{(max)}_{peak}$ for power. We then set $\mu = \bar{\mu}$ and vary the voltage V from zero to the thermovoltage.

[10] The effect of degenerate energy levels on the electron and thermal conductance and on thermopower of a QD was considered in Ref. [68].

The first remarkable feature is that the two peaks around a dominant transition energy have different heights (here $\mu_{N=1} = 10\ k_B\bar{T}$ and $\mu_{N=2} = 30\ k_B\bar{T}$); in the absence of degeneracy, within the quantum limit all the peaks have the same height (see Fig. 4.3). More precisely, see Eq. (4.79), the external peaks, displaced of $2.53k_B\bar{T}$ from μ_N are higher with respect to the internal peaks, displaced of $2.32k_B\bar{T}$ from μ_N, whose height is almost equal to the non-degenerate (interacting) case. The second feature is that all curves, apart from the case of very large η_c (blue curve), are well approximated by the linear-response quantum limit expression (black dashed curve in Fig. 4.11)

$$P^{(\max)} = \frac{\sqrt{2}\gamma}{16k_B\bar{T}}\left(\frac{\Delta T}{\bar{T}}\right)^2 \frac{\Delta_{\min}^2}{\cosh\left(\frac{\Delta_{\min}}{2k_B\bar{T}} \pm \frac{\log 2}{2}\right)\cosh\left(\frac{\Delta_{\min}}{2k_B\bar{T}}\right)}. \tag{4.79}$$

The plus (minus) sign in Eq. (4.79) is to be taken when $N_{\min}$ is even (odd). Eq. (4.79) allows us to find that level degeneracy gives rise to an enhancement of output power of about 1.77 times respect to the non-degenerate case, independently of the parameter values (see also Ref. [102]). Eq. (4.79) also makes clear that the origin of the asymmetry for $\Delta_{\min} \to -\Delta_{\min}$ and of the difference in peaks' height is the term $\pm\log 2/2$ occurring in the presence of degeneracy. The case of $E_C = 1.5\ k_B\bar{T}$ (not shown), which is not within the quantum limit, produces a much more asymmetric behavior. We have verified that also in the non degenerate case the analytic formula derived in the linear response regime [see Eq. (4.48)] well describes the maximum power also beyond the linear response regime.

4.4 Summary

In this chapter, we studied the thermoelectric properties of a multi-level interacting QD in the sequential tunneling regime, in a multi-terminal setup, both in the linear response regime and beyond. In particular, we have

- generalized the sequential tunneling method put forward by Beenakker in Refs. [69] and [70] to a multi-terminal configuration and set the range of validity of the expressions for the charge and heat currents in the linear response regime;
- found simple analytic formulas for the multi-terminal transport coefficients in the low temperature limit;
- found simple analytic formulas for the power factor Q and the figure of merit ZT in the low temperature limit for a two-terminal setup;
- found that Q and ZT can be simultaneously maximized for suitable values of the electrochemical potential;
- found that Coulomb interactions can dramatically enhance ZT by suppressing the thermal conductance;
- found that both the interacting an non-interacting models strongly violate the Wiedemann-Franz law;
- found analytic expressions for the maximum power and for the efficiency at maximum power in a three terminal setup;

- investigated the nonlinear Seebeck and Peltier coefficients in a two-terminal setup, identifying features of the breakdown on the Onsager reciprocity relation;
- computed numerically the maximum efficiency, the maximum power, and the efficiency at maximum power in the non-linear regime, finding optimal system parameters for heat-to-work conversion such that the efficiency at maximum power can go beyond Curzon-Alhborn's efficiency;
- compared the case of a doubly degenerate level with interaction and the case of two non-degenerate levels without interaction finding that the interacting case enhances the power output and, especially when charging energy and level spacing are of the order of the thermal energy, it increases the efficiency at maximum power that can go beyond Curzon-Alhborn's efficiency;
- found that the non-linear maximum power is well approximated by the analytic linear response expression;
- found that QDs with degenerate energy levels and Coulomb interactions achieve higher efficiency and output power than non-degenerate QDs; in particular the maximum power is enhanced almost of a factor 2;
- calculated the transport coefficients for a non-linear, non-interacting QD with 1 and 2 energy levels (App. A.4);
- found approximate analytic expressions for the maximum power and efficiency at maximum power for a non-linear, non-interacting QD with 1 energy level (App. A.4).

The multi-terminal formalism developed in this chapter and the expressions we have obtained for charge and heat currents, transport coefficients, power and efficiency could be used to design and analyze experimental data. Extensions of the studies presented in this chapter could include level spacings different from the equidistant and regimes beyond the quantum limit. Finally, a comprehensive description of the thermoelectric properties and performance of a QD should assess the role of quantum coherence going beyond the sequential tunneling limit and the relevance of phonon contribution to heat transport.

5

Thermoelectric conversion at 30 K in InAs/InP nanowire quantum dots

The progress in the fabrication and control of nanostructured systems has opened new prospects for thermoelectric (TE) research [5, 161] and has provided new ways to create improved TE devices [11, 63, 64, 123, 162]. As discussed in Sec. 3.1.3 and Chap. 4, quantum dots (QDs) were soon identified as ideal systems for the implementation of efficient heat engines [5] and for the creation of nanoscale thermometers [163]. The key property is their discrete density of states that yields a strong energy selectivity in their transmission profile thus opening the way to the realization of TE systems with an optimized performance [5]. As a consequence, TE effects in QDs have been extensively investigated both theoretically [67, 68, 70–74, 76–90, 118, 130, 131] and experimentally [42, 127, 132, 135, 138, 141, 164–168]. The TE behavior of electronic devices is characterized by the figure of merit ZT, see Eq. (3.27), that is larger in more efficient devices. Indeed, within linear-response regime, both the maximum efficiency and the efficiency at maximum power are solely determied by the figure of merit, and they are growing functions of ZT, see Eq. (3.29). In bulk materials the maximization of ZT has been proved to be highly nontrivial since G, S and K are intrinsically related. On the contrary, heat and charge transport in QD-based TE devices can be disentangled and larger values of ZT can be achieved. The performance of thermal machines based on QDs has been theoretically studied by many authors [86, 108, 109, 116, 118, 121, 169], while only one experimental investigation is available up to now [42]. We also note that QDs can provide a key building block for the fundamental investigation of quantum and stochastic thermodynamic effects, as shown for small-sized systems, where thermal fluctuations are of much relevance [17, 170, 171]. The investigation of TE effects in single-electron systems is usually performed in temperature regimes for which the thermal energy $k_{\mathrm{B}}T$ is smaller than the Coulomb gap. In addition, it is often desirable to implement devices where the individual energy levels are well-resolved with respect to the thermal energy so that only few levels contribute to the heat transport.

In this chapter we report of an experimental study, conducted at the NEST Laborary, Pisa, in which the strong confinement of QDs realized in InAs/InP heterostructured nanowires (NWs) [172–174] is exploited to demonstrate field-effect control on the thermopower S up to

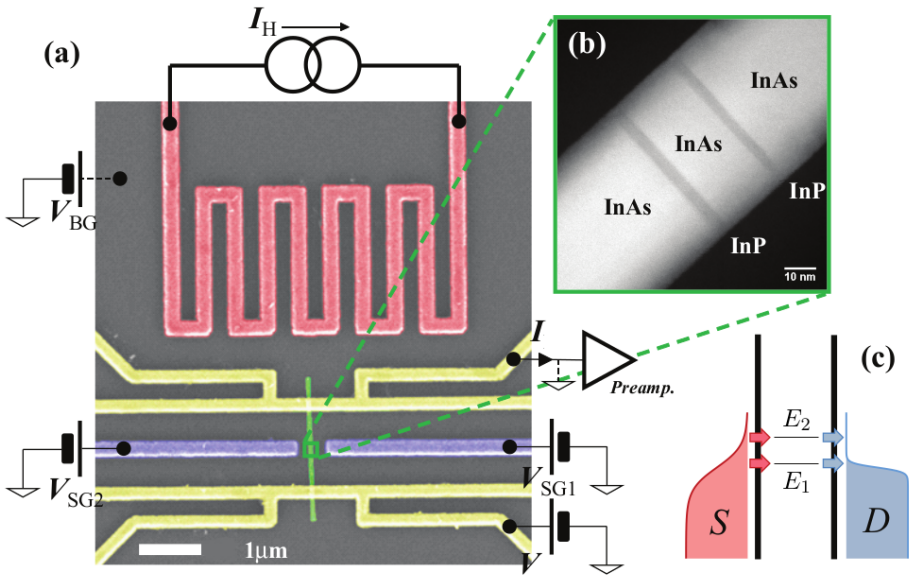

FIGURE 5.1: (a) Scanning electron micrograph of a typical device. A local heater (red) is used to establish a temperature difference ΔT between the two ends of the NW (green) embedding an InAs/InP heterostructured QD. The device is fabricated on top of a degenerately-doped SiO_2/Si p++ substrate (gray) and a set of Ti/Au electrodes (yellow) can be used both as electrical contacts to the NW and as local resistive thermometers. The QD electronic configuration can be controlled with a pair of side gates (SG, purple) or using the conductive substrate as a backgate electrode (BG). (b) Transmission electron micrograph of the heterostructured QDs. (c) Sketch of the energetics scheme: the QD implements a multi-level system that can mediate heat and charge transport between the a source (S) and a drain (D) electrodes, in the presence of thermal and electric biases. Two spin-degenerate levels E_1 and E_2 ($\Delta E = E_2 - E_1$) play a relevant role in the regime studied in the experiment.

temperatures of the order of 30 K. The high temperature regime has been little explored in similar systems [141], usually operated at much lower temperatures [42, 132]. Our devices allow for the application of a temperature gradient along the NW, the measurement of charge current and the Seebeck coefficient, as well as the direct measurement of local temperatures. The strong confinement of the electrons in our QDs allows us to obtain charging energies E_C exceeding 5 meV, with inter-level spacings ΔE of the order of 5 meV and thus to operate our devices at relatively high temperatures and close to the QD depletion. Employing the theoretical model developed in Chap. 4, and accounting for sequential tunneling mediated by two spin-degenerate levels [68, 69, 169], we can accurately reproduce the experimental conductance and thermopower. This allows us to estimate the electronic thermal conductance K, the power factor GS^2 and the electronic figure of merit ZT.

5.1 Setup and measurements

Figure 5.1(a) shows a scanning electron micrograph of one of the investigated devices, where different colors correspond to different elements (see App. B.1 for fabrication details). The device core is constituted by an InAs/InP heterostructured NW with a diameter of 52 ± 1 nm. As visible in the Fig. 5.1(b), the nanostructure embeds a 20 ± 1 nm InAs island separated

from the rest of the NW by two ≈ 4 nm-wide InP barriers. The NWs used for this study were grown by Au-seeded chemical beam epitaxy [175] and have a wurtzite crystal structure. As grown NWs were detached from the growth substrate by sonication in isopropyl alcohol (IPA) and randomly deposited on a SiO_2/Si p++ substrate by drop-casting and contacted by e-beam lithography followed by an evaporation of a metallic Ti/Au (10/100 nm) bilayer. The resulting device layout includes a metallic serpentine heater (red), which can be fed by a current I_H to induce, thanks to Joule heating, a thermal gradient along the NW (green). Our architecture also includes a set of multiple contact electrodes (yellow) that allows to: (i) apply a voltage bias V and measure the current I flowing through the NW; (ii) perform a local measurement of the temperature by tracking the resistance of the central metallic part of the contact electrodes (see Apps. B.1, B.2 and B.3 for measurement details). The QD population and spectrum can be controlled by a set of field-effect gates including the SiO_2/Si p++ substrate, or back-gate (gray), and two side gates that can also be used to modify the radial confinement profile of the QD (purple) [176].

The control on the temperature of the system is obtained by setting the temperature of the bath T_{bath} in which the device is immersed and then by setting a temperature gradient across the NW so that its hot end is at a temperature T_H and its cold end is at a temperature T_C. The average temperature $T_{avg} = (T_H + T_C)/2$ is set high enough ($T_{avg} \sim 30$ K) so that we can benefit of the following advantages. (i) Since $\hbar\Gamma \ll k_B T_{avg}$ (where Γ is the characteristic tunnelling rate through the QD barriers) and ΔE is not much larger than $k_B T_{avg}$, sequential tunnelling processes dominate the thermoelectric transport and data analysis is relatively straightforward (see below for details); (ii) Since $\Delta T \ll T_{avg}$, non-linear response effects in thermal bias ΔT are negligible thus simplifying the theoretical analysis; (iii) charge transport can be explored for relatively large applied bias voltages (up to $V \approx k_B T_{avg}/e$) while remaining in the linear response regime. In this situation, the current I flowing through the QD is given by

$$I = G(V + S\Delta T), \tag{5.1}$$

where G is the electrical conductance and S is the Seebeck coefficient. The thermovoltage at open circuit conditions is thus given by $V_{th} = -S\Delta T$. It should be noted that both G and S are temperature dependent even if not explicitly indicated. Typical transport data from our QDs can be seen in Fig. 5.2(a), reporting a colorplot of I as a function of the gate voltage V_{gate} and the DS bias V at $T = 4.2$ K. Any of the three available gates (SG1, SG2 and BG) can be used to operate the device, but in the experiment reported here the QD was controlled using the lateral gate SG1 because it yielded the most stable control of the electronic configuration. Coulomb diamonds are clearly visible for various QD filling numbers N, and indicate a charging energy on the first spin-degenerate level $E_C = 7 \pm 1$ meV and an inter-level spacing $\Delta E = 5 \pm 1$ meV. In Fig. 5.2(a) $N = 0$ corresponds to a completely depleted QD, as further discussed in App. B.4 and as indicated by high-temperature transport data. However, the behavior of the device is not expected to critically depend on the presence of filled levels as long as they are far away in energy with respect to the relevant energy scales, in particular $k_B T_{avg}$. In Fig. 5.2(b) we report a set of $I(V)$ curves corresponding to vertical cross-sections at fixed V_{gate} taken from the region highlighted by the black rectangle in panel (a). The thermoelectric response of the device has been obtained from transport data in the linear regime. From the curve $I(V)$ curve restricted to the linear response range (see e.g. Fig 2 (b)), we determine G (slope) and $I_{th} = GS\Delta T$ (intercept) for each V_{gate} value and for a fixed ΔT using Eq. (5.1). From the knowledge of the slope and intercept of the lines it is possible

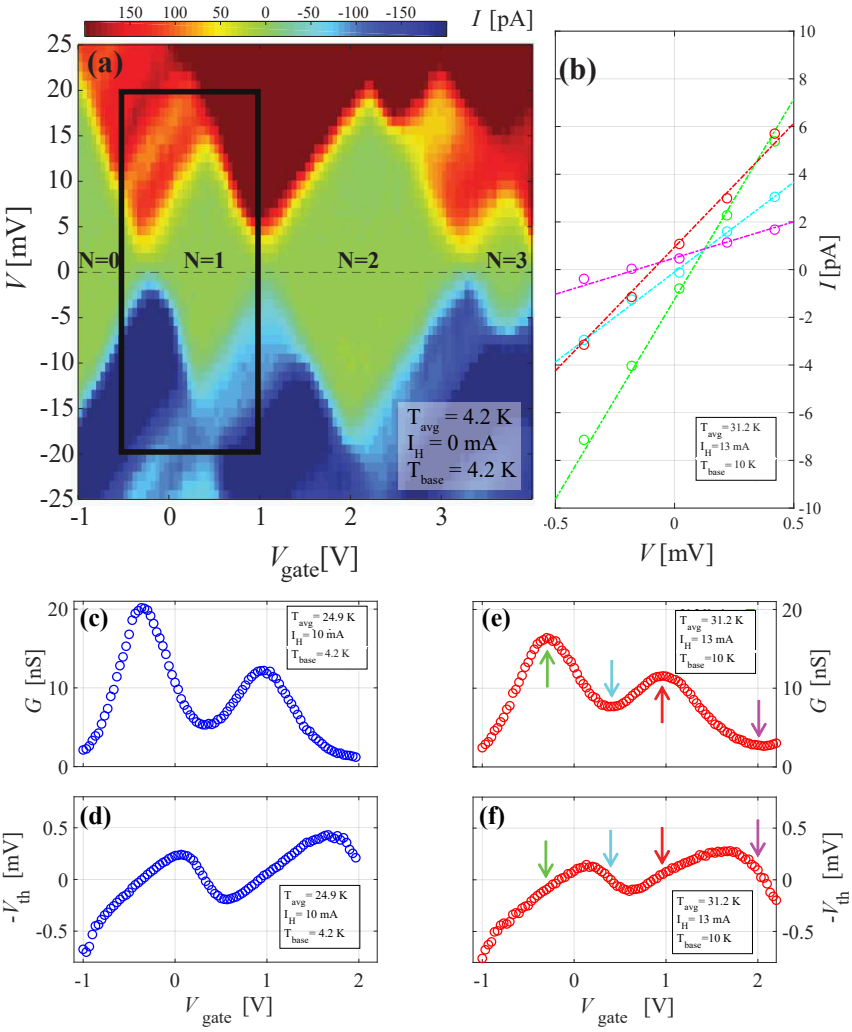

FIGURE 5.2: (a) Typical map of the QD current versus V and V_{gate} showing the QD filling N in each Coulomb blockade diamond. The analysis of the diamonds yields a charging energy $E_C = 7 \pm 1\,\mathrm{meV}$ and an energy spacing between the first and second QD level $\Delta E = 5 \pm 1\,\mathrm{meV}$. (b) $I(V)$ curves for several values of the gate voltage V_{gate}. Thermoelectric measurements are obtained in the linear response regime, i.e. for low applied voltage bias ($eV < K_B T$) for which the response of the system is linear and thus eq. 5.1 holds.(b) Current I, as a function of V, in the linear response range for four values of V_{gate} highlighted by arrows of the corresponding color in panels (e) and (f). (c) Extrapolated conductance G and (d) thermovoltage $-V_{\mathrm{th}}$ as function of the applied gate voltage V_{gate} for the first degenerate energy level for an average temperature $T_{\mathrm{avg}} = 24.9\,\mathrm{K}$ and for $I_{\mathrm{H}} = 10\,\mathrm{mA}$ current feeding the heating serpentine, when the system is in a $T_{\mathrm{bath}} = 4.2\,\mathrm{K}$ thermal bath. Panels (e) and (f) report equivalent data for $T_{\mathrm{avg}} = 31.2\,\mathrm{K}$ and $I_{\mathrm{H}} = 13\,\mathrm{mA}$ and $T_{\mathrm{bath}} = 10\,\mathrm{K}$. Temperatures are obtained by using the local metallic thermometers at the two NW ends.

to compute $V_{\mathrm{th}} = -S\Delta T$. Fig. 5.2(c)-(f) show the plots of $G(V_{\mathrm{gate}})$ and $-V_{\mathrm{th}}(V_{\mathrm{gate}})$ for two different bath temperatures and heating currents I_{H}, such that the average temperatures of the QD are $T_{\mathrm{avg}} = 24.9\,\mathrm{K}$ in panels (c) and (e) and $T_{\mathrm{avg}} = 31.2\,\mathrm{K}$ in panels (d) and (f), respectively.

5.2 Theoretical model and heat engine analysis

Experimental data are analyzed with a theoretical model based on a master equation accounting for sequential tunnelling of electrons between the leads and the QD [34, 70, 169]. As already mentioned in the introduction, we can reasonably assume that co-tunnelling processes are negligible when two conditions are met, namely $\hbar\Gamma \ll k_B T_{\rm avg}$ and $\Delta E \lesssim k_B T_{\rm avg}$. The first condition is required since small values of $\hbar\Gamma/k_B T_{\rm avg}$ suppress the coefficient of co-tunneling rates. The second condition comes from the fact that co-tunneling contributions decay as a power law with the energy difference δE between the chemical potential of the leads and the nearest resonance (measured in units of $k_B T_{\rm avg}$) [34]. This means that they may prevail over sequential contributions for large enough δE, since sequential tunneling contributions decay exponentially with $\delta E/k_B T_{\rm avg}$ [34, 69, 177]. Remarkably, the presence of two spin-degenerate levels, with spacing equal to ΔE, sets a bound to the energy difference δE. The second condition (for which $\Delta E \lesssim k_B T_{\rm avg}$), therefore, ensures that the exponential suppression of sequential tunnelling is limited and we can safely disregard co-tunneling effects. This is particularly relevant for values of $V_{\rm gate}$ such that the chemical potential of the leads is between the two spin-degenerate levels, where the thermopower is maximal even though the conductance is negligible.

Two spin-degenerate QD orbitals E_1 and E_2 are taken into account in the QD model and tunnelling rates are assumed to depend on the number of electrons N in the QD (see App. B.5 for details about the model). Further important outputs of the fitting procedure (detailed in App. B.6) are the electronic temperatures $T_{\rm H,fit}$ and $T_{\rm C,fit}$ that can be used to obtain a better estimate of the net temperature bias across the QD structure $\Delta T_{\rm fit}$. The average fit temperature $T_{\rm avg,fit} = (T_{\rm H,fit} + T_{\rm C,fit})/2$ matches nicely with the one obtained experimentally sing the metallic thermometers $T_{\rm avg}$, and confirms the good calibration of the resistive thermometers. On the contrary, $\Delta T_{\rm fit}$ is sizably smaller than ΔT. This is not very surprising since the NW has a finite heat conductance leading to a partitioning of the thermal bias as observed in experiments at lower temperatures [178]. Since $\Delta T_{\rm fit}$ is the relevant temperature bias for the analysis of the TE response of the QD, it has been used for all the subsequent estimates on the TE parameters of the nanostructure.

Fig. 5.3(a) and (b) show the experimental data (red dots) for the case $T_{\rm avg} = 31.2\,\mathrm{K}$, together with the fitted curves (solid lines) obtained using the model ($\Delta T_{\rm fit} = 2.05$ K). Different fitting models are compared: the solid black curve accounts for two spin-degenerate energy levels in the QD (here referred to as the *"four-level"* model); the green dashed curve accounts for a single (spin-degenerate) energy level (referred as the *"two-level"* model), as often done in the literature to model single [101, 104, 107, 112, 115] and double quantum dot system [32, 109, 116, 118, 179]. We notice that the four-level model nicely fits the experimental data for G and S in the whole range of values of $V_{\rm gate}$ under consideration, while the two-level model is accurate only for values $V_{\rm gate} < 1.6\,\mathrm{V}$ in the conductance plot (the first two peaks in Fig. 5.3(a)) and up to $V_{\rm gate} \simeq 1\,\mathrm{V}$ in the thermopower plot (Fig. 5.3(b)). The theory can now be employed to calculate the electronic thermal conductance K by using the fitting parameters obtained from the experimental data $G(V_{\rm gate})$ and $S(V_{\rm gate})$ (see App. B.6 for details about values obtained for the parameters). The resulting $K(V_{\rm gate})$ curves for the two models are plotted in Fig. 5.3(c). Remarkably, the curve relative to the two-level model departs even in the first peak from the curve of the four-level model. This is due to the fact that K, by definition, is the ratio between the heat current and the temperature difference in open circuit conditions, i.e. when I is zero. In a sequential single-level model, all electrons tunnel through

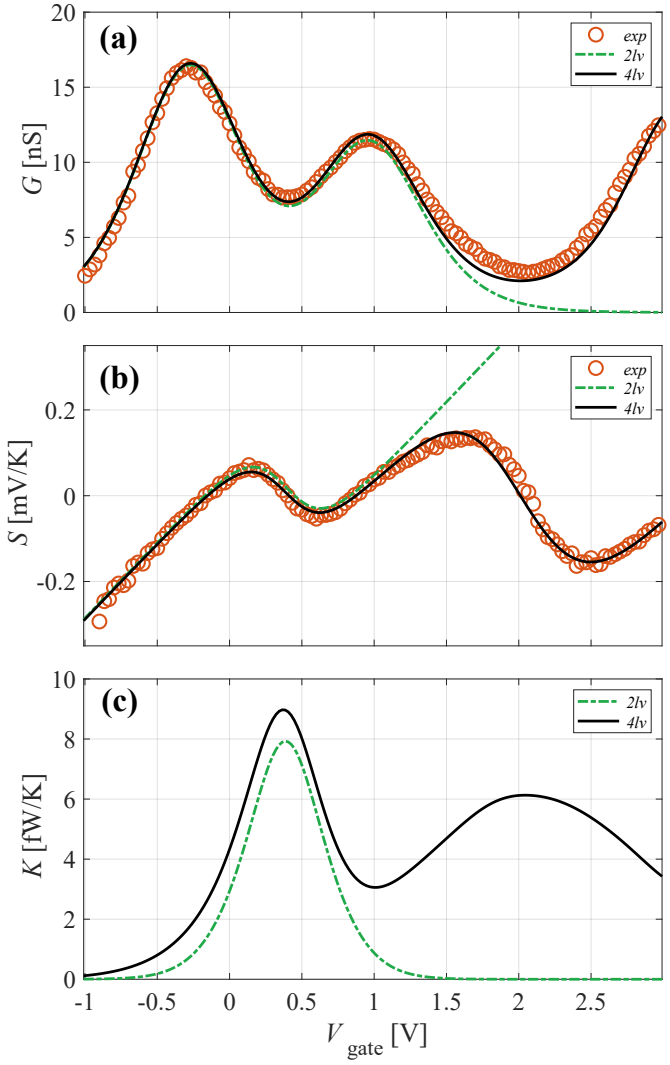

FIGURE 5.3: Theoretical fit of the experimental data and modeling of electronic thermal conductivity. Conductance (a) and thermopower (b) data shown in Fig.5.2(e)-(f) are compared with the result of the two-level and four-level models. Little discrepancy between the two emerges in the area of interest involving the first spin-degenerate state of the QD. Differently, sizable deviations start to appear in configurations corresponding to a QD filling $N \geq 2$. The absence of deviations below the first spin-degenerate level is consistent with the $N = 0$ filling. In the model, the experimental gate voltage values are converted into energy using a gate lever arm $\alpha_{\text{gate}} = 0.011 \pm 0.001\,\text{meV/V}$ (see App. B.4 for further details). (c) Electronic thermal conductance K obtained using the two-level (green dashed line) and four-level (black line) model. The large discrepancy between the two models on the high end of the plotted energy range indicates only a four-level model can yield a reliable estimate of K in the studied experimental configuration.

the QD at the same energy, thus the same amount of heat is transferred to/from a given reservoirs in each tunneling event. If $I = 0$, there is not net transfer of charge, thus there is no net transfer of heat. This implies K=0, regardless of the gate voltage. Conversely, if there are two or more energy levels, electrons can tunnel at different energies, and this possibility

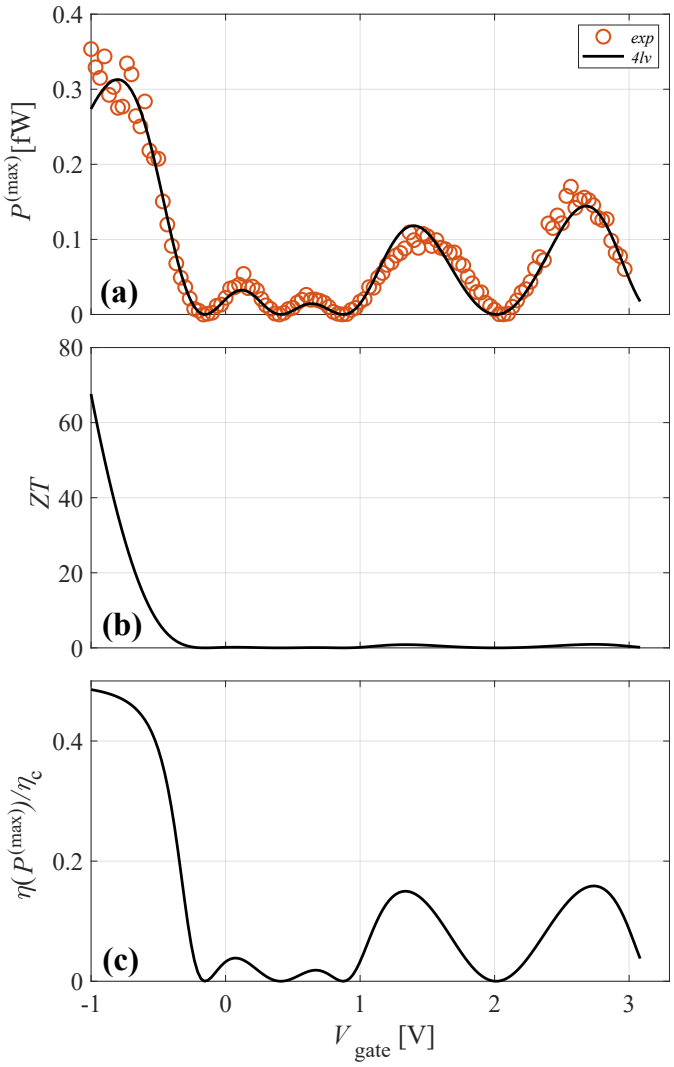

Figure 5.4: (a) Maximum Power extracted from the system as a function of the gate voltage. The experimental data (red dots) and the theoretical prediction (black curve) are computed as $GS^2\Delta T^2/4$ using respectively the experimental and theoretical values of G and S. (b) Electronic thermoelectric figure of merit dependence on the applied gate voltage, computed using the extrapolated curves for G, S and K (Fig. 5.3). (c) Electronic efficiency at maximum power in units of Carnot efficiency η_c.

allows for a net heat transfer at zero charge current [68, 169]. Therefore, as opposed to G and S, the value of K in the sequential regime is fully determined by the multilevel structure of the QD. It is thus crucial to employ the four-level model to estimate it properly.

Using the three transport coefficients G, S and K one can evaluate the performance of our QD system when operated as a heat engine. Indeed, the electric response to a temperature difference can be used to drive a current against a voltage bias, effectively extracting work from the system. The efficiency of a heat engine is then defined as the ratio between the extracted work and the heat provided by the hot reservoir. At fixed V_{gate} and temperature

difference, we define $P^{(\max)}$ as the maximum power that can be extracted by optimizing over the applied V. The corresponding efficiency will then be the efficiency at maximum power $\eta(P^{(\max)})$. It can be shown [11] that $P^{(\max)}$ also corresponds to the maximum power that can be performed on a variable load resistance in series with the QD. However, as shown in Sec. 3.1, within the linear response regime both $P^{(\max)}$ and $\eta(P^{(\max)})$ can be computed simply from the knowledge of the transport coefficients G, S and K through Eqs. (3.28) and (3.29). The maximum power is plotted in Fig. 5.4(a) as a function of the gate voltage V_{gate} using the theoretical (solid curve) and experimental (red circles) values of G and S together with the fitted value of ΔT_{fit}. The experimental data (available down to $V_{\text{gate}} \simeq -1\,\text{V}$) is well reproduced by the four-level model which presents several peaks, the largest one corresponding to $P^{(\max)}_{\text{peak}} = 0.37\,\text{fW}$ occurring at $V_{\text{gate}} \simeq -0.78\,\text{V}$. Remarkably, the corresponding value of the electronic figure of merit [plotted in Fig. 5.4(b)] is $ZT \approx 35$. ZT displays a fast increase as V_{gate} decreases below the first conductance peak, as expected for a single-level QD. This is due to the fact that there are no levels below the first conductance peak, so that our QD system approximately satisfies the requirement for achieving Carnot efficiency [5]. Indeed, the electronic efficiency at maximum power, plotted in Fig. 5.4(c), takes the value $\eta(P^{(\max)}) = 0.47\eta_{\text{c}}$ (where η_{c} is Carnot's efficency) for $V_{\text{gate}} \simeq -0.78\,\text{V}$, implying that our QD system can be operated at an electronic efficiency at maximum power very close to the Curzon-Ahlborn's linear response upper bound $\eta_{\text{CA}} = \eta_{\text{c}}/2$. It is worth observing that the electronic efficiency at maximum power is computed from the knowledge of ZT [11]. Interestingly, Fig. 5.4(c) shows that the electronic efficiency at maximum power roughly behaves as the maximum power [Fig. 5.4(a)], implying that both the maximum power and corresponding efficiency can be simultaneously maximized.

5.3 Summary

In this chapter we explored TE phenomena in InAs/InP NW QD-based devices at high temperature in the linear regime. Experimental data were analyzed using a multi-level model based on the resolution of a master equation which allowed us to compute the electronic thermal conductance of the system. This, in combination with the experimental data of conductance and thermopower, allowed us to estimate the electronic thermoelectric figure of merit ZT and the electronic efficiency at maximum power of our thermoelectric engine. We found that the ideal Curzon-Ahlborn's upper bound is nearly attained, and that a figure of merit $ZT \approx 35$ is reached while extracting the maximum power from the system. This study demonstrates the full electrostatic control of the heat engine features of a thermally biased NW QD operating in high temperature regimes. Our results shed light on the operation of few level thermoelectric engines, a key issue for the physics and technology addressing heat and charge transport mediated by single carrier. The electronic ZT, which neglects the contribution of the phonons to the thermal conductance, is a sound characterization of the electronic properties of the device which allows to compare the electronic performance of different thermoelectric materials. Furthermore, it is directly related to the efficiency of non-equilibrum devices, such as solars cells which aim at recovering the energy of out-of-equilibrium "hot carriers" excited by light [180, 181]. Possible applications include on-chip cooling, energy harvesting on cryogenic platforms and nanoscale thermometry.

6

Non-linear thermovoltage in a single-electron transistor

So far, most of the experimental investigations of thermal properties in nanostructures have focused on the thermal conductance [137, 167, 178, 182–188]. Conversely the thermovoltage, which describes the electrical response to a temperature difference and is directly related to both the power and efficiency of thermal machines, see Sec. 3.1, is much less studied. This is due to the difficulty in coupling local sensitive electron thermometers and heaters/coolers to the sample under study in order to have a well-defined, known temperature difference across the device. The thermovoltage has been measured in devices based on nanowires [189, 190] and on quantum dots [125, 127, 128, 132, 134, 135, 138, 139, 141, 164, 165, 168, 191]. In these experiments, however, the temperature of the electrodes were typically not measured directly, but rather determined as fitting parameters, and there are no experiments where the temperature of the electrodes and the thermovoltage are measured simultaneously. Furthermore, there are no experiments probing the thermovoltage in devices based on metallic islands, while theoretical works for these systems have focused only on the linear response regime [70, 78–80, 83, 85, 192]. The non-linear thermovoltage though has been theoretically studied in discrete-level systems in Refs. [75, 81, 84, 87–90, 96, 113, 169, 193].

In this chapter, we report on the first measurement of the thermovoltage in a metallic single-electron transistor (SET) using on-chip, local tunnel-junction-based thermometers and electron temperature control. The experiment was performed at the Aalto University, Finland. This system allows us to perform thermoelectric measurements with an unprecedented control, both within the linear and non-linear response regimes, imposing temperature differences exceeding the average temperature. Using a theoretical model which accounts for non-linear effects and co-tunneling processes, we find an excellent agreement with the experimental data with no free parameters. On one hand, this allows us to nail down quantitatively the role of co-tunneling processes on the thermovoltage. On the other hand, we find that in the non-linear regime the temperature of the island emerges as a crucial parameter. Surprisingly, although the thermovoltage is measured at zero net charge current, within the non-linear response the island tends to overheat to a temperature greater than the average lead temperature, which results in a suppression of the thermovoltage. We show, however,

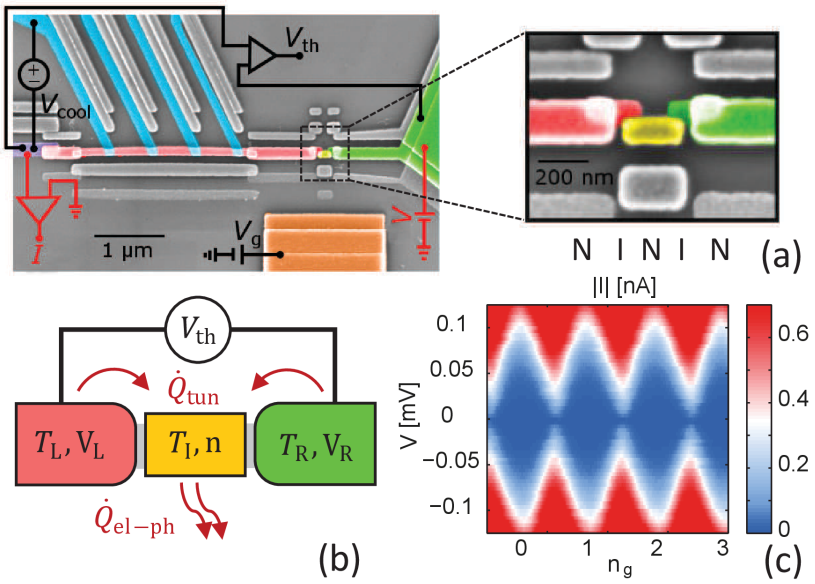

FIGURE 6.1: Representation and characterization of the single-electron transistor. a) False-colored SEM image of the full device and a zoomed in view around the metallic island (yellow) tunnel coupled to two normal leads (red and green). b) Schematic representation of the system with the same coloring as in the SEM image. The heat balance in the metallic island is represented by red arrows. c) Absolute value of the current through the SET as a function of the applied source drain voltage V and of the gate-induced charge n_g.

that the non-linear thermovoltage can be optimized up to a factor two with respect to the experimentally observed value by lowering the temperature of the island to the temperature of the cold lead. This could be achieved by exploiting the phonons in the island which act as a third thermal bath coupled to our system.

6.1 Experimental setup

Fig. 6.1a) is a colored scanning electron micrograph of the device and Fig. 6.1b) is a schematic representation of the experiment with the same colors highlighting the main elements of the fully normal-conducting SET. The left lead L (red) and right lead R (green) are tunnel and capacitively coupled to a central metallic island I (yellow), which is under the influence of a tunable gate electric field (orange). A voltage bias $V = V_L - V_R$ can be applied to the SET electrodes and the corresponding current I can be measured for an initial characterization of the device. The temperature T_R of the electrons in R is fixed to the bath temperature, given the strong electron-phonon coupling in the large and "bulky" lead. On the other hand, the electronic temperature T_L in the left lead (red) can both be varied and measured using the superconducting tunnel probes (blue). The tunability of the temperature is possible thanks to the superconducting wire (purple) in clean contact with the left lead through which there is no heat conduction, and thanks to the limited size of the normal (red) part of the lead that reduces the electron-phonon heat flux. Electrons within the island are in local equilibrium at temperature T_I since the electron-electron interaction is much faster than the tunneling rates [7]. The experiment is performed in a dilution refrigerator at bath temperatures typically between 50 and 400 mK. For the thermovoltage measurements, the

SET voltage bias source and current preamplifier (sketched in red in Fig. 1a) are disconnected. Crucially, the thermovoltage $V_{\rm th}$ is probed directly across the SET using a room-temperature voltage preamplifier with ultralow input bias current below 20 fA. Fabrication details can be found in Ref. [167] where "sample B" is the device used for this experiment.

Figure 6.1c) shows the absolute value of the current I across the device at 65 mK as a function of the potential bias V and of the gate-induced charge $n_{\rm g} = (C_{\rm L}V_{\rm L}+C_{\rm R}V_{\rm R}+C_{\rm g}V_{\rm g})/e$, where $C_{\rm L}$, $C_{\rm R}$ and $C_{\rm g}$ are, respectively, the capacitances of the island to L, R and to the gate electrode, and $V_{\rm g}$ is the gate voltage. In the dark blue regions, Coulomb diamonds, single electron tunneling between the leads and the island is not allowed, and the current is very small. At half integer values of $n_{\rm g}$, "degeneracy points", there are conductance peaks at zero bias since single electron tunneling is allowed for any finite voltage bias.

6.2 Model

The state of the SET is characterized by the probability $p(n)$ to have n excess charges on the island. The electrostatic energy necessary for this is

$$U(n) = E_C\,(n - n_{\rm g})^2\,, \tag{6.1}$$

where $E_C = e^2/(2C)$ is the charging energy with $C = C_{\rm L} + C_{\rm R} + C_{\rm g}$. Electron tunneling between the leads and the island induces transitions between charge states. The leading order process in a perturbative expansion in the tunnel coupling between the island and the leads corresponds to a single electron transfer between the leads and the island (sequential tunnelling) [34, 194]. The sequential-tunneling rates for transferring electrons from α = L,R (I) to β = I (L,R), with the island initially having n charges, is denoted by $\Gamma_{\alpha\beta}(n)$ (see App. C.1 for details).

Higher order processes can become dominant if all sequential-tunneling processes are energetically unfavorable [in the Coulomb diamond region in Fig. 6.1c)]. In particular, co-tunneling (second order process) refers to the transfer of an electron from one lead to another, without changing the charge state of the island but going through a virtual state. The dominant contribution of this kind is inelastic co-tunneling, i.e. the electron which tunnels from lead L, say, to I via a virtual state has a different energy with respect to the electron tunneling from I to R [1]. We denote the rate of inelastic co-tunneling that transfers a charge from α = L (R) to β = R (L), when n electrons are on the island before the process occurs, by $\gamma_{\alpha\beta}(n)$.

The probabilities $p(n)$ can be computed by solving tha Pauli master equation (see Chap. 2 and App. C.1 for details). The charge current can then be written as $I(V) = I^{\rm seq} + I^{\rm cot}$, where

$$I^{\rm seq} = e\sum_n p(n)\,[\Gamma_{\rm LI}(n) - \Gamma_{\rm IL}(n)] \tag{6.2}$$

is the sequential-tunneling contribution, given by electrons tunneling between lead L and I, and $I^{\rm cot} = e\sum_n p(n)[\gamma_{\rm LR}(n) - \gamma_{\rm RL}(n)]$ is the inelastic co-tunneling contribution [31, 32, 34, 79, 83]. We compute the sequential and co-tunneling rates exactly, without linearizing in the voltage bias and temperature difference (see App. C.1 for details).

[1] The process where the same electron tunnels from α = L, R to I and then to β = L, R is known as "elastic co-tunneling", since also the microscopic state on the island remains unchanged. As discussed in Refs. [34, 192], this process is relevant only when the thermal energy k_BT and the voltage bias are much smaller than $\sqrt{E_C\delta}$, where δ is the energy level spacing in the island. In our case the energy levels almost form a continuum, making $\sqrt{E_C\delta}$ the smallest energy scale at play.

In the presence of a fixed temperature bias ($T_R \neq T_L$), the thermovoltage V_{th} is the solution to

$$I(V_{th}) = 0. \tag{6.3}$$

Notice that the charge current also depends on the temperature of the island T_I. By imposing that the charge current and the net energy entering the island through electron tunneling are zero, we find that

$$T_I = \frac{T_L R_R + T_R R_L}{R_L + R_R}, \tag{6.4}$$

where R_L and R_R are respectively the resistance of the left and right tunnel junctions. Eq. (6.4), which is found performing a simple sequential tunneling calculation within linear response and in the two charge state approximation (valid for $E_C \gg k_B T$), reduces to $T_I = \bar{T} \equiv (T_L + T_R)/2$ in the present symmetric case where $R_L = R_R$. We will thus initially assume that T_I is given by the average lead temperature $\bar{T}$. However, as we will soon discuss in detail, we find that this assumption gives quantitatively wrong results beyond the linear response regime, leading us to the exploration of the impact of T_I on the thermovoltage.

6.3 Results

We focus on two data sets which represent two different regimes: linear response (Fig. 6.2), i.e. when the modulus of the temperature difference $\Delta T = T_L - T_R$ is smaller than the average lead temperature $\bar{T} = (T_L + T_R)/2$, and non-linear response (Fig. 6.3). In both cases, using the model detailed above, we could accurately reproduce the experimental data without any free parameter. The system parameters $E_C = 100\ \mu\text{eV} \approx k_B \times 1.16$ K and $R_L = R_R = 26\ \text{k}\Omega$ are independently extracted from charge current measurements. Figures 6.2 and 6.3a) present the same qualitative behavior, namely a periodic oscillation of the thermovoltage with the gate-induced charge n_g and a linear dependence around degeneracy points, but they exhibit different amplitudes (note that the sign of V_{th} is opposite in the two cases since the temperature biases are opposite).

We first analyze the linear response regime by choosing the set of data obtained when the temperature of the leads is $T_L = 134$ mK and $T_R = 190$ mK, such that $|\Delta T| < \bar{T}$. In Fig. 6.2 we compare the measured V_{th} (blue dots) as a function of n_g with different theoretical models. The red thin curve represents the typical sawtooth behavior which is predicted within linear response accounting only for sequential tunneling and two charge states. This is characterized by a linear function of n_g, crossing zero at the degeneracy points with slope $E_C \Delta T/\bar{T}$ [70]. The other two curves (red dashed and green solid) are instead determined by computing V_{th} using Eq. (6.3) and assuming that $T_I = \bar{T}$ [see Eq. (6.4)]. The red dashed curve, which only accounts for sequential tunneling, shows a smoothened sawtooth behavior as a consequence of including multiple charge states in the master equation and of a finite temperature. However, both models based on sequential tunneling (thin and dashed red curves) approximately fit the experimental data only near the degeneracy points (near half integer values of n_g). In this case, indeed, sequential tunneling is allowed and thus dominates over co-tunneling [83]. On the other hand the green solid curve, computed including co-tunneling contributions, shows a strong suppression of the thermovoltage as we move away from degeneracy points. The excellent agreement between this model and the experimental measurements pinpoints the critical dependence of the thermovoltage on inelastic co-tunneling processes.

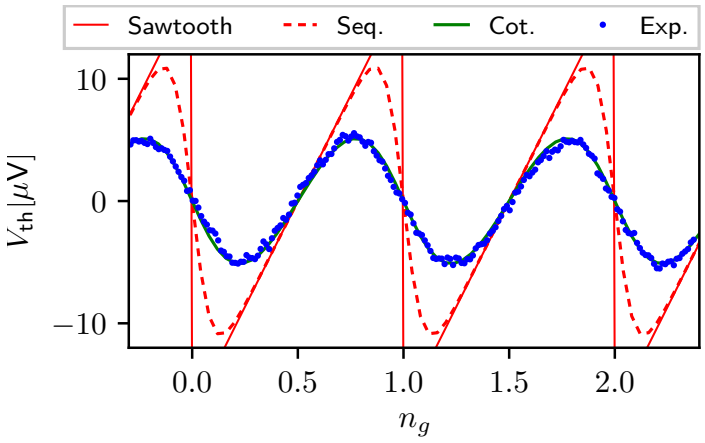

Figure 6.2: Experimental and theoretical thermovoltage as a function of n_{g}. The red thin curve represents the sawtooth behavior predicted with a sequential-tunneling calculation in linear response and accounting for two charge states. The dashed red curve is found by solving Eq. (6.3) including only sequential contributions, while the green curve includes also co-tunneling contributions. The temperatures of the leads are $T_{\mathrm{L}} = 134$ mK and $T_{\mathrm{R}} = 190$ mK and, according to Eq. (6.4), we assume that $T_{\mathrm{I}} = \bar{T}$.

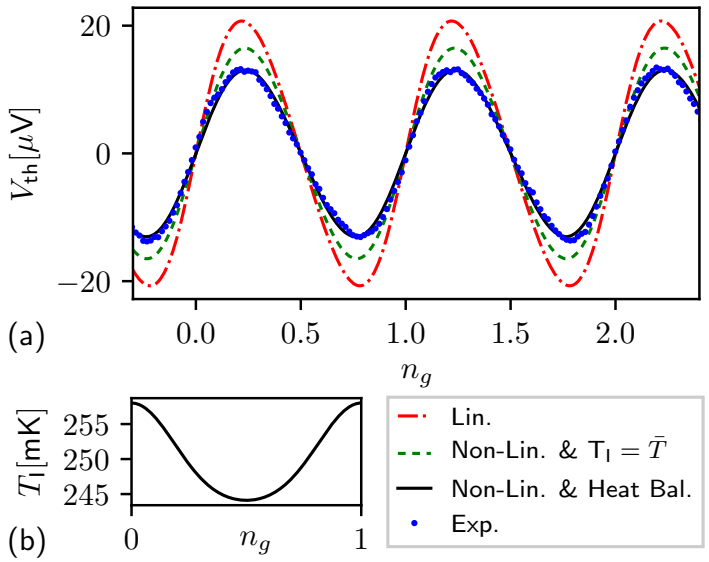

Figure 6.3: a) Experimental and theoretical thermovoltage as a function of n_{g}. All theoretical curves include co-tunneling. The red dashed-dotted curve corresponds to a linear response calculation around $\bar{T}$. The green dashed curve corresponds to a non-linear calculation where we fix $T_{\mathrm{I}} = \bar{T}$, while the black curve corresponds to a non-linear calculation where T_{I}, shown in b) as a function of n_{g}, is calculated solving the heat balance condition in Eq. (6.5) together with Eq. (6.3). The temperatures of the leads are $T_{\mathrm{L}} = 342$ mK and $T_{\mathrm{R}} = 63$ mK.

We now move to the non-linear regime. In Fig. 6.3a) we show the measured thermovoltage as a function of n_{g} (blue dots) compared to theoretical calculations, all of which include co-tunneling contributions. The lead temperatures are $T_{\mathrm{L}} = 342$ mK and $T_{\mathrm{R}} = 63$ mK, such that $|\Delta T| > \bar{T}$. The red dashed-dotted curve is computed within the linear response regime choosing the average lead temperature $\bar{T}$ as the characteristic temperature. More precisely, we solve Eq. (6.3) setting $T_{\mathrm{I}} = \bar{T}$ and choosing a small temperature difference of the leads

δT around $\bar{T}$ to find the thermopower $S \equiv V_{\rm th}/\delta T$ for $\delta T \to 0$. We then calculate the thermovoltage as $V_{\rm th} = S(T_{\rm L} - T_{\rm R})$, where now $T_{\rm L} = 342$ mK and $T_{\rm R} = 63$ mK are the actual lead temperatures. As we can see from Fig. 6.3a), this linear response model overestimates the thermovoltage almost by a factor two. A non-linear calculation (green dashed curve) improves the agreement with the experimental data. This calculation is performed by solving Eq. (6.3) using the actual lead temperatures and, as before, we fix the island temperature at $T_{\rm I} = \bar{T}$. The difference between the red dashed-dotted and green dashed curves proves that we are indeed in the non-linear response regime, and it shows that the main effect of the nonlinear response is to decrease the amplitude of the thermovoltage. However, we still do not obtain a good agreement with the experimental data.

We find that we can get a perfect agreement with the experimental data if we further improve the model by determining also the island temperature $T_{\rm I}$ through a heat balance equation, rather than fixing it at $\bar{T}$. More precisely [see Fig. 6.1b)], we denote by $\dot{Q}_{\rm tun}$ the heat current entering the island from sequential and co-tunneling events (see App. C.1 for details) and by $Q_{\text{el-ph}} = \Sigma\mathcal{V}(T_{\rm I}^5 - T_{\rm R}^5)$ the heat current flowing from electrons in the island to the phonons (we assume that the electronic temperature $T_{\rm R}$ in the bulky right electrode is equal to the temperature of the phonons). $\mathcal{V}$ is the island volume and Σ is the electron-phonon coupling constant which only depends on the material. The temperature of the island can thus be determined by the following heat balance equation

$$\dot{Q}_{\rm tun} = \dot{Q}_{\text{el-ph}}. \tag{6.5}$$

The values of the parameters entering $Q_{\text{el-ph}}$ that we use are determined independently: $\mathcal{V} = 225 \times 100 \times 29$ nm^3 is estimated from SEM images and Σ is obtained from Ref. [167] for this device (sample B). The value, $\Sigma = 2.8\,\mathrm{WK^{-5}m^{-3}}$, is close to the standard literature value for copper [7] and in agreement with measurements of other samples fabricated using the same Cu target.

The black curve in Fig. 6.3a) is thus determined by computing both $V_{\rm th}$ and $T_{\rm I}$ simultaneously by solving Eqs. (6.3) and (6.5) without any free parameters for each value of $n_{\rm g}$. As we can see, the non-linear model, complemented with the heat balance equation, is in excellent agreement with the experimental measurements, demonstrating that $T_{\rm I}$ is indeed an important parameter in the non-linear regime. Conversely we have verified that, using the parameters of Fig. 6.2 which are within the linear response regime, $V_{\rm th}$ only weakly depends on the particular choice of $T_{\rm I}$ between $T_{\rm L}$ and $T_{\rm R}$. In Fig. 6.3b) we plot the island temperature $T_{\rm I}$, as a function of $n_{\rm g}$ over a single period, determined in the same calculation that leads to the black curve in Fig. 6.3a). Remarkably, despite the very low phonon temperature (63 mK), the calculated $T_{\rm I} \approx 250$ mK is much larger than the average lead temperature $\bar{T} = 202.5$ mK. This means that while the net charge current across the SET is zero, the heat current due to electrons tunneling back and forth is overheating the island to a temperature that is significantly larger than the average temperature, resulting in a further decrease of the thermovoltage. This is another signature of the non-linear response of the system, as it violates Eq. (6.4). We further find that the island temperature displays a weak $n_{\rm g}$ modulation of approximately 10 mK, but this prediction cannot be confirmed in the present experiment.

Finally we discuss how the thermovoltage depends on $T_{\rm I}$. In Fig. 6.4 we plot $V_{\rm th}^{\rm max}$, the maximum amplitude of $V_{\rm th}$, computed by solving Eq. (6.3) at fixed lead temperatures $T_{\rm L} = 342$ mK and $T_{\rm R} = 63$ mK and varying $T_{\rm I}$ between the lead temperatures. The black solid lines and the gray area point to the actual experimental value of $V_{\rm th}^{\rm max}$ and to the corresponding computed $T_{\rm I}$ which differs from $\bar{T}$ [see black curves in Figs. 6.3a) and 6.3b)], while the

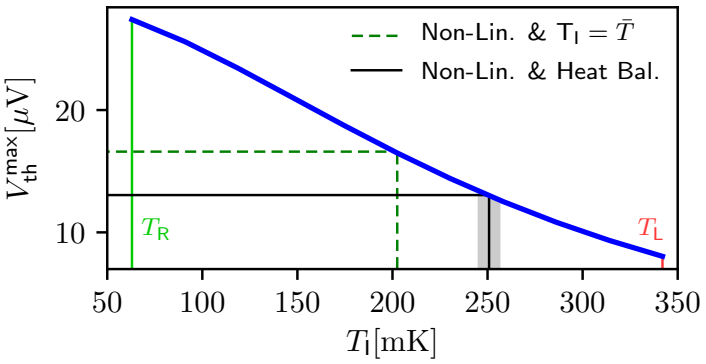

Figure 6.4: The maximum amplitude of the thermovoltage V_{th}^{max} is plotted as a function of the island temperature, for $T_R \leq T_I \leq T_L$. The green dashed lines point to the values of V_{th}^{max} and T_I found in the non-linear calculation at fixed $T_I = \bar{T}$ (see the green dashed curve of Fig. 6.3a) while the black solid lines and the gray area refer to the non-linear calculation including the heat balance equation (see the black solid curve of Fig. 6.3).

dashed green lines point to V_{th}^{max} calculated setting $T_I = \bar{T}$ [see the green dashed curve in Fig. 6.3a)]. We find that V_{th}^{max} strongly depends on the choice of T_I and that it increases as T_I is lowered. Indeed, at $T_I = T_R = 63$ mK, the amplitude of the thermovoltage reaches $27\,\mu$eV, twice the experimental value [see blue dots in Fig. 6.3a)]. Thus, by increasing the energy exchange between the electrons and phonons in the island, for example by increasing the island's volume, we can lower the temperature of the island which in turn results in an increase of V_{th}.

6.4 Summary

We performed measurements of thermovoltage in a metallic island tunnel coupled to normal leads. Within the linear regime we nailed down the role of co-tunneling in determining the thermovoltage. Within the non-linear response regime we explored temperature biases, determined with on-chip thermometers, even larger than the average lead temperature. Using a theoretical model which accounts for co-tunneling and non-linear effects, we found an accurate agreement with the experimental data without any free parameters. In particular, we found that the temperature of the metallic island becomes an important parameter which must be determined by solving a heat balance equation for the island. Surprisingly, even if the net charge current through the system is vanishing and the coupling to the leads is symmetric, the metallic island overheats to a temperature larger than the average lead temperature. As a consequence, the amplitude of the thermovoltage oscillations decreases.

7

Absorption refrigerators based on Coulomb-coupled single-electron systems

Absorption refrigerators, also known in literature as self-contained or autonomous refrigerators, are systems that extract heat from a cold thermal bath only by exploiting the incoherent interaction with other two thermal baths held at higher temperatures. No work is provided to the system, i. e. *cooling is achieved by heating*. The exploration for solid state implementations of absorption refrigerators has been recently attracting a considerable attention [195–212]. The question of identifying the smallest absorption quantum refrigerators was addressed by Linden et al. in Ref. [196], where systems such as two qubits, a qubit and a qutrit, or a single qutrit were considered. It has been later shown that these "minimal" systems can operate at Carnot efficiency[197, 198], and the role of quantum coherence and entanglement has been addressed [201, 202, 205–207, 209]. Besides being of fundamental interest in quantum thermodynamics, absorption refrigeration is also appealing for practical reasons: waste heat can be used to achieve cooling at the nanoscale without providing work nor requiring any external control of the system. There are already few experimental proposals[11, 199, 213–219], but the only experimental realization so far has been performed with trapped ions [220]. In Ref. [11], in particular, it was pointed out that the very simple setup consisting of two capacitively-coupled quantum dots could act as an absorption refrigerator, and the conditions under which its coefficient of performance (COP) can reach Carnot's limit were discussed (no entanglement or quantum coherence is required).

In this chapter, on one hand, we analyze in detail a setup consisting of two capacitively-coupled quantum dots. More precisely, we derive the general conditions under which the system operates as an absorption refrigerator, and determine the optimal system parameters which simultaneously maximize the cooling power and the COP. We find that, under these conditions, the system exhibits a particularly simple refrigeration COP, which can indeed reach Carnot's upper limit, and that the cooling power is directly proportional to a measurable charge current [11], allowing for an indirect measurement of a heat flow (notice that heat currents can be also measured directly in metallic islands (MIs), e. g. in Ref. [22]). Furthermore, we analyze the system as an autonomous Maxwell demon [221–228], finding that it can operate attaining the highest efficiencies for information creation and consumption, and

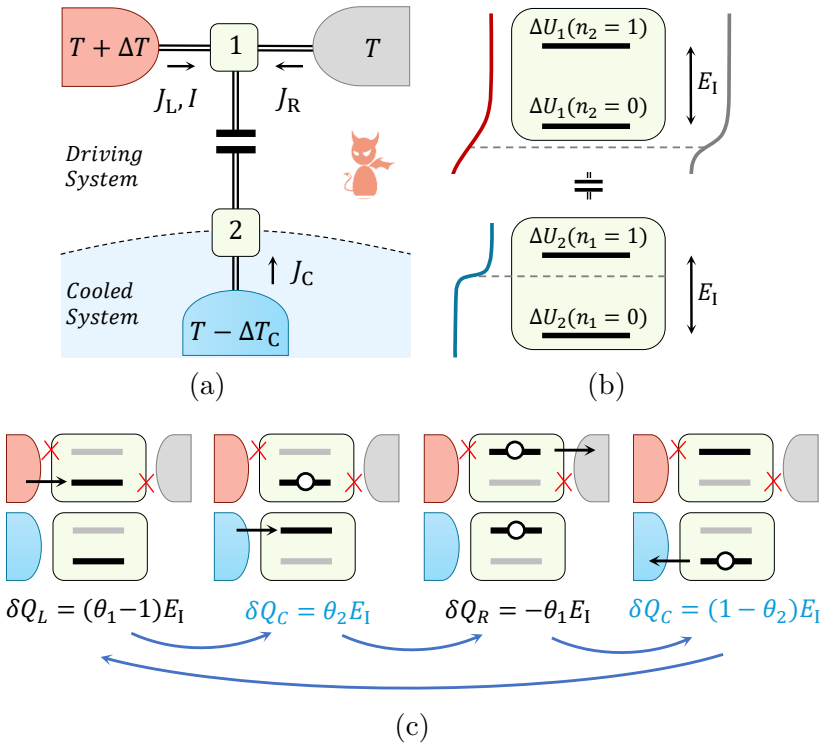

FIGURE 7.1: Panel (a): schematic representation of the system. Panel (b): the Fermi distribution of the leads (red upper left, gray upper right and blue lower left) is shown vertically. The black thick lines represent the transition energies $\Delta U_1(n_2)$ and $\Delta U_2(n_1)$ [Eq. (7.2)] that are measured with respect to common chemical potential of the leads (black dashed line). Panel (c): sequence of system states and electron transitions that provide cooling when conditions (7.7) and (7.8), represented by the red crosses, are satisfied. The black horizontal lines represent the actual transition energies as determined by the occupation of the other QD, while the grey horizontal lines represent the transition energies when the other QD has opposite occupation. δQ_α, for α=L,R,C, represents the heat extracted from reservoir α during the corresponding electron transition.

determining the expression that relate its COP to these efficiencies. Finally, we propose two experimental realizations, based either on quantum dots (QDs) or metallic islands, which can implement the non-trivial requirements for the system to behave as an absorption refrigerator. We demonstrate that these systems, which closely resemble existing experimental setups [22, 144, 145, 229–235], can attain an observable cooling power using realistic parameters.

7.1 Ideal setup

The system under investigation, depicted in Fig. 7.1(a), consists of two electronic reservoirs [upper left (L) and upper right (R)] tunnel coupled to a QD, denoted by 1. A second QD, 2, capacitively coupled to 1, is tunnel coupled to a third electronic reservoir (C). The number of electrons occupying each Coulomb-blockaded QD can be controlled through a gate of capacitance C_{gi} and applied voltage V_{gi}, with $i = 1, 2$. Reservoir L is kept at a higher temperature, $T_L = T + \Delta T$, with respect to the other reservoirs which are kept at temperature $T_R = T$ and $T_C = T - \Delta T_C$. The heat current leaving reservoir $\alpha = $ L,R,C is denoted by J_α, and the charge current flowing between reservoirs L and R is denoted by I. We describe the

transport in the entire system using the Pauli master equation (see Chap. 2) in the sequential tunneling limit. Although we expect higher order tunneling processes, such as co-tunneling, to decrease the cooling power, these corrections are suppressed if the conductances of the junctions are much smaller than the conductance quantum and temperature is not too small. The electrostatic energy of the system is given by

$$U(n_1,n_2) = E_{C1}(n_1-n_{x1})^2 + E_{C2}(n_2-n_{x2})^2 + E_{\rm I}(n_1-n_{x1})(n_2-n_{x2}), \tag{7.1}$$

where n_i (for $i=1,2$) is the number of electrons in QD i, $n_{xi} = V_{{\rm g}i}C_{{\rm g}i}/e$, and $E_{Ci} = e^2/(2C_i)$ is its charging energy. C_i is the capacitance of QD i to its surroundings, and $E_{\rm I}$ is the inter-system charging energy which is controlled by the capacitive coupling between the QDs. By assuming that $E_{Ci} \gg k_BT$ and constraining the values of n_{xi} to an appropriate range, we can restrict our analysis to 4 charge states, described by $n_1, n_2 = 0, 1$. The "transition energy", i.e. the energy necessary to add an electron to QD 1 (2), which also depends on the occupation of QD 2 (1), is given by $\Delta U_1(n_2) = U(1,n_2) - U(0,n_2)$ [$\Delta U_2(n_1) = U(n_1,1) - U(n_1,0)$]. Since $\Delta U_i(1) - \Delta U_i(0) = E_{\rm I}$, we can write

$$\Delta U_i(n) = \theta_i E_{\rm I} + (n-1)E_{\rm I}, \tag{7.2}$$

where

$$\theta_1 = 1 - n_{x2} + \frac{E_{C1}}{E_{\rm I}}(1-2n_{x1}), \tag{7.3}$$

$$\theta_2 = 1 - n_{x1} + \frac{E_{C2}}{E_{\rm I}}(1-2n_{x2}), \tag{7.4}$$

can be varied using the gate voltages. The transition energies are schematically represented in Fig. 7.1(b) and 7.1(c) as black thick lines. Let $\Gamma^{\rm in}_{\rm L/R}(n_2)$ [$\Gamma^{\rm out}_{\rm L/R}(n_2)$] be the rate of electrons tunneling from (to) reservoir L/R to (from) QD 1, and let $\Gamma^{\rm in}_{\rm C}(n_1)$ [$\Gamma^{\rm out}_{\rm C}(n_1)$] be the rate of electrons tunneling from (to) reservoir C to (from) QD 2. Note that the tunneling rates satisfy the detailed balance conditions [see Eq. (2.38)]

$$\Gamma^{\rm out}_\alpha(n) = \exp\left\{\left[\frac{\delta_\alpha(n)}{k_BT_\alpha}\right]\right\}\Gamma^{\rm in}_\alpha(n), \tag{7.5}$$

where $\delta_{\rm L}(n) = \delta_{\rm R}(n) = \Delta U_1(n)$ and $\delta_{\rm C}(n) = \Delta U_2(n)$. The currents can be calculated by specifying the tunneling rates for each process and by determining the probability p_{n_1,n_2} for the two QDs to have occupation numbers n_1 and n_2 (see App. D.1). We also use Eq. (7.5) to express $\Gamma^{\rm in}_\alpha(0)$ in terms of $\Gamma^{\rm out}_\alpha(0)$ and $\Gamma^{\rm out}_\alpha(1)$ in terms of $\Gamma^{\rm in}_\alpha(1)$. We emphasize, however, that the results we present in the next section do not depend on the specific form of the rates, as long as Eq. (7.5) is satisfied. Only a quantitative description of the cooling power will explicitly depend on the rates.

7.2 Optimal rates for cooling power and COP

The COP of an absorption refrigerator is defined as

$$C = \frac{J_{\rm C}}{J_{\rm L}}, \tag{7.6}$$

where $J_{\rm L} > 0$ is the input heat and $J_{\rm C} > 0$, the cooling power, is the heat extracted from reservoir C (their expressions are reported in App. D.1). Considering generic rates that are

only constrained by satisfying the detailed balance condition [Eq. (7.5)], we find that the cooling power is maximized, at fixed values of E_I, θ_1 and θ_2, when

$$\Gamma_\mathrm{L}^\mathrm{in}(1) = 0, \tag{7.7}$$
$$\Gamma_\mathrm{R}^\mathrm{out}(0) = 0, \tag{7.8}$$

and $\Gamma_\mathrm{L}^\mathrm{out}(0)$, $\Gamma_\mathrm{R}^\mathrm{in}(1)$, $\Gamma_\mathrm{C}^\mathrm{out}(0)$, $\Gamma_\mathrm{C}^\mathrm{in}(1)$, are as large as possible (see App. D.2 for details). In this situation [i. e. when Eqs. (7.7) and (7.8) hold and when $\theta_i > 1/2$, see App. D.1 for details] the condition for the positivity of J_C reduces to the simple inequality

$$\theta_1 > \theta_1^* \equiv 1 + \frac{1}{\eta_\mathrm{c} C_\mathrm{c}}, \tag{7.9}$$

where $\eta_\mathrm{c} = 1 - T/T_\mathrm{L}$ and $C_\mathrm{c} = T_\mathrm{C}/(T - T_\mathrm{C})$. Remarkably, in this situation the COP is also maximized (at least for $\Delta T_\mathrm{C} = 0$), and takes a particularly simple (i. e. independent of temperatures) form

$$C = \frac{1}{\theta_1 - 1}, \tag{7.10}$$

that only depends on θ_1 (which is determined by both gate voltages V_g1 and V_g2). Note that Eq. (7.9) implies that $\Delta U_1(1) > 0$ and $\Delta U_1(0) > 0$, i. e. both transition energies are above the common chemical potential of the reservoirs[1], as shown in Fig. 7.1(b). This observation holds also for generic rates that do not satisfy Eqs. (7.7) and (7.8), see App. D.2 for details.

Eq. (7.10) implies that the input heat is always smaller than the cooling power for $\theta_1 < 2$, and C is a decreasing function of θ_1. The COP C takes its maximum value when $\theta_1 = \theta_1^*$ [see Eq. (7.9)], the smallest value of θ_1 for which the system behaves as a refrigerator, giving

$$C^{(\max)} \equiv \eta_\mathrm{c} C_\mathrm{c}, \tag{7.11}$$

as expected for absorption refrigerators. Indeed, Eq. (7.11) states that $C^{(\max)}$ can be interpreted as the combination of two two-terminal reversible machines each operating at Carnot's efficiency. The first one is a reversible Carnot heat engine that produces work by using the temperature difference between reservoirs L and R, with $\eta_\mathrm{c} = 1 - T/T_\mathrm{L}$, while the second one is a reversible Carnot refrigerator operating between reservoirs C and R that is powered by the work of the heat engine, with $C_\mathrm{c} = T_\mathrm{C}/(T - T_\mathrm{C})$. $C^{(\max)}$ is the highest COP allowed by the second principle of thermodynamics, as can be proven by imposing energy conservation and zero entropy production, which read

$$J_\mathrm{L} + J_\mathrm{R} + J_\mathrm{C} = 0, \tag{7.12}$$
$$\frac{J_\mathrm{L}}{T_\mathrm{L}} + \frac{J_\mathrm{R}}{T_\mathrm{R}} + \frac{J_\mathrm{C}}{T_\mathrm{C}} = 0. \tag{7.13}$$

Finally, when the COP is given by Eq. (7.11), we find that the cooling power vanishes.

Another remarkable consequence of conditions (7.7) and (7.8), also noted in Refs. [11, 116], is that

$$J_\mathrm{C} = \frac{E_\mathrm{I}}{e} I. \tag{7.14}$$

Since the coupling between the upper and lower systems E_I is a measurable system parameter, Eq. (7.14) allows an indirect measurement of the cooling power simply by measuring the charge current in the upper system.

[1]

A simple picture of these results can be given using the energy scheme of Fig. 7.1(b) and the conditions (7.7) and (7.8) [represented by red crosses in Fig. 7.1(c)]. The sequence of electron transitions that leads to the removal of heat from reservoir C is shown in Fig. 7.1(c) and represented by blue arrows. For each step the heat exchanged in the corresponding transition is indicated as δQ_α (for example, in the first step $\delta Q_{\rm L} = \Delta U_1(0) = (\theta_1 - 1)E_{\rm I}$ is the input heat provided by L and associated to an electron tunneling from L to QD 1, event which can only occur when QD 2 is unoccupied). In one cycle, an electron is transferred from L to R, and an amount $\delta Q_C^{\rm tot} = E_{\rm I}$ of heat is extracted from C: this statement is equivalent to Eq. (7.14). Moreover, we notice that an amount $\delta Q_L^{\rm tot} = (\theta_1 - 1)E_{\rm I}$ of input heat is provided by L. Computing the COP over one cycle as $\delta Q_{\rm C}^{\rm tot}/\delta Q_{\rm L}^{\rm tot}$ yields precisely Eq. (7.10). Eqs. (7.7) and (7.8) guarantee that the system can only evolve along the cycle represented

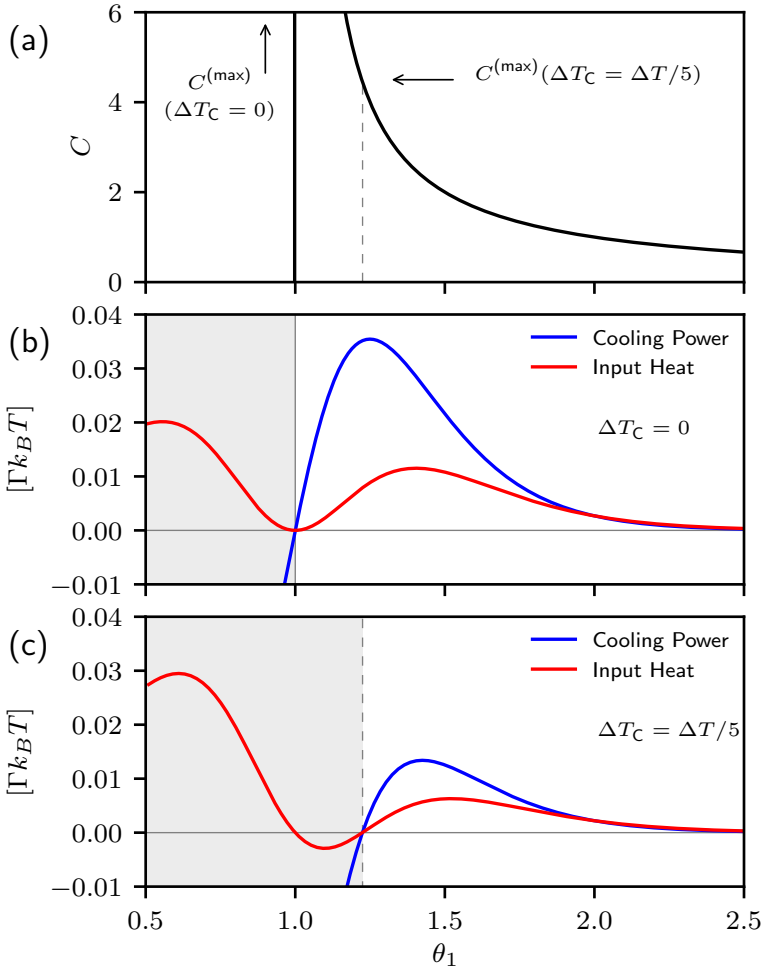

Figure 7.2: The coefficient of performance, COP, [panel (a)] and the heat currents in units of $\Gamma k_B T$ [panels (b) and (c)] are plotted as a function of θ_1, when Eqs. (7.7) and (7.8) are satisfied. Panel (b) refers to $\Delta T_{\rm C} = 0$, while panel (c) refers to $\Delta T_{\rm C} = \Delta T/5$. The parameters are $\Gamma_{\rm C}^{\rm out}(0) = \Gamma_{\rm C}^{\rm in}(1) = \Gamma_{\rm L}^{\rm out}(0) = \Gamma_{\rm R}^{\rm in}(1) \equiv \Gamma$, $\theta_2 = 1$, $E_{\rm I} = 6k_BT$ and $\Delta T/T = 1/10$. Since all rates are proportional to Γ, the heat currents depend linearly on the rate, so the plots in panel (b) and (c) do not depend on the value of Γ.

in blue arrows in Fig. 7.1(c), or in the opposite direction, which leads to heating of reservoir C. Cooling is obtained when the system evolution along the blue arrows prevails over the opposite direction, and this happens when Eq. (7.9) is satisfied.

In Fig. 7.2 we plot the cooling power J_C and input heat J_L, as functions of θ_1, for the case $\Delta T_C = 0$ [panel (b)] and $\Delta T_C = \Delta T/5$ [panel (c)] by imposing that Eqs. (7.7) and (7.8) are satisfied. The COP, given by a particularly simple law [Eq. (7.10)], is plotted in Fig. 7.2(a). The gray region in Fig. 7.2(b) and 7.2(c) denotes the values of θ_1 where the system does not act as a refrigerator for reservoir C [according to Eq. (7.9), $\theta_1^* = 1$ for $\Delta T_C = 0$ and $\theta_1^* \simeq 1.2$ for $\Delta T_C = \Delta T/5$ and $\Delta T/T = 1/10$]. Fig. 7.2(b) shows that the cooling power is zero when $\theta_1 = \theta_1^* = 1$ [where the COP diverges, see panel (a)] and it is maximum when $\theta_1 \simeq 1.2$, where $C \approx 5$ [see panel (a)]. Fig. 7.2(c), relative to $\Delta T_C = \Delta T/5$, shows that both the maximum cooling power and the corresponding COP decrease, with respect to the $\Delta T_C = 0$ case, since we are refrigerating a colder system. The value of the cooling power weakly depends on θ_2 in the range between 0 and 1.

7.3 Experimental proposals

The experimental realization of the proposed absorption refrigerator relies on the ability of implementing the crucial conditions (7.7) and (7.8). Such conditions could be, in principle, implemented by properly engineering the tunneling barrier which couple QD 1 to its reservoirs, in order to obtain tunneling rates for QD 1 that depend on the occupation of QD 2. In this section, we make use of an additional QD [116] to implement the crucial condition (7.7) that is found to be sufficient for obtaining heat extraction.

In the setup, schematically pictured in Fig. 7.3, we introduce an additional QD (3), tunnel-coupled to 1, and we require that its transition energy ΔU_3 is aligned with $\Delta U_1(0)$ [see Fig. 7.3(b)]. This way, the "energy filtering" effect of QD 3 is used to suppress $\Gamma_L^{\text{in}}(1)$ with respect to $\Gamma_L^{\text{out}}(0)$. To perform a quantitative analysis, we study the dynamics of the system

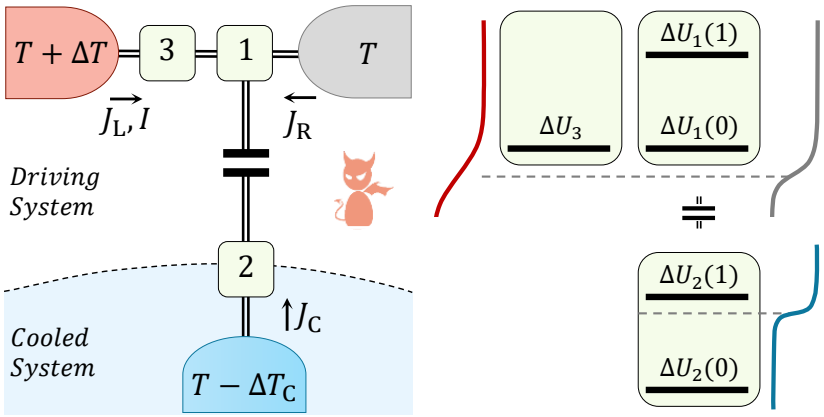

FIGURE 7.3: Left: schematic representation of the system, where 1, 2 and 3 represents either QDs or MIs. Right: representation of the transition energies in the case of the system with QDs. See Fig. 7.1 for details.

of the three QDs altogether under the assumption that the coupling between QDs 1 and 3 is much weaker than the coupling between such QDs are their reservoirs. The electrostatic

energy of the system [see Eq. (7.1) for two QDs] now takes the form

$$U(n_1,n_2,n_3) = E_{C1}(n_1-n_{x1})^2 + E_{C2}(n_2-n_{x2})^2 + E_{C3}(n_3-n_{x3})^2 + E_{\rm I}(n_1-n_{x1})(n_2-n_{x2}), \tag{7.15}$$

where we have added the third term, relative to the additional QD (3). Analogously to the two-QD case, we define $\Delta U_1(n_2) = U(1,n_2,n_3) - U(0,n_2,n_3)$, $\Delta U_2(n_1) = U(n_1,1,n_3) - U(n_1,0,n_3)$ and $\Delta U_3 = U(n_1,n_2,1) - U(n_1,n_2,0)$, which can be written as

$$\begin{aligned} \Delta U_1(n_2) &= E_{\rm I}(\theta_1 + n_2 - 1), \\ \Delta U_2(n_1) &= E_{\rm I}(\theta_2 + n_1 - 1), \\ \Delta U_3 &= E_{\rm I}(\theta_3 - 1), \end{aligned} \tag{7.16}$$

where we have defined the following 3 independent dimensionless parameters

$$\begin{aligned} \theta_1 &= (1-2n_{x1})E_{\rm C1}/E_{\rm I} + (1-n_{x2}) \\ \theta_2 &= (1-2n_{x2})E_{\rm C2}/E_{\rm I} + (1-n_{x1}) \\ \theta_3 &= (1-2n_{x3})E_{\rm C3}/E_{\rm I} + 1. \end{aligned} \tag{7.17}$$

If we assume that each QD can be only singly-occupied, we can restrict our analysis to the following 8 states: $|0,0,0\rangle$, $|0,0,1\rangle$, $|0,1,0\rangle$, $|1,0,0\rangle$, $|1,0,1\rangle$, $|0,1,1\rangle$, $|1,1,0\rangle$ and $|1,1,1\rangle$, where $|n_1,n_2,n_3\rangle$ is the state associated to the set of occupation numbers (n_1,n_2,n_3). The probability p_α for the system to be in the state $|\alpha\rangle = |n_1,n_2,n_3\rangle$ is calculated by solving the Pauli equation in the stationary case (see App. D.3 for details)

$$\dot{p}_\alpha = \sum_\nu \left(-\Gamma_{\alpha\nu}\, p_\alpha + \Gamma_{\nu\alpha}\, p_\nu\right), \tag{7.18}$$

where $\Gamma_{\alpha\nu}$ is the rate for the transition from state $|\alpha\rangle$ to state $|\nu\rangle$. The rates $\Gamma_{\alpha\nu}$ which account for the transfer of electrons between a QD and a reservoir can be expressed as [31]

$$\Gamma_{\alpha\nu} = \hbar^{-1}\gamma_\lambda f_\lambda(\Delta\tilde{U}_{\alpha\nu}), \tag{7.19}$$

where γ_λ is the coupling energy between the reservoir $\lambda = \lambda(\alpha,\nu)$ and a QD, where $\lambda = {\rm L}, {\rm R}, {\rm C}$ depends on the initial state $|\alpha\rangle$ and final state $|\nu\rangle$. In Eq. (7.19), $f_\lambda(\epsilon) = [1+e^{\epsilon/(k_B T_\lambda)}]^{-1}$ is the reservoir Fermi distribution function, while $\Delta\tilde{U}_{\alpha\nu} = \tilde{U}(\nu) - \tilde{U}(\alpha)$ is the transition energy, where $\tilde{U}(\alpha) = U(n_1,n_2,n_3)$ [see Eq. (7.15)] with the set of occupation numbers corresponding to the state $|\alpha\rangle$. The inter-dot transition rates, which account for the transfer of electrons between QD 1 and 3 [namely, $\Gamma_{(0,0,1),(1,0,0)}$ and $\Gamma_{(0,1,1),(1,1,0)}$], are obtained using the procedure outlined in App. D.3 under the assumption that the hopping element t is much smaller than the coupling energy between QDs and reservoirs [236–240].

The relevant heat currents can now be written as

$$J_{\rm C,L} = \sum_{\alpha\nu} \Delta\tilde{U}_{\alpha\nu}\left(\Gamma_{\alpha\nu}\, p_\alpha - \Gamma_{\nu\alpha}\, p_\nu\right), \tag{7.20}$$

where the sum runs over the states specified in App. D.3. In Fig. 7.4 we plot the cooling power $J_{\rm C}$, as a function of θ_1, for realistic parameters and setting $\theta_3 = \theta_1$ in order to obtain the resonant condition [i. e. $\Delta U_3 = \Delta U_1(0)$] which approximately implements condition (7.7). The solid black curve is relative to the case $\Delta T_{\rm C} = 0$, while the dashed red curve refers to $\Delta T_{\rm C} = \Delta T/10$. Fig. 7.4 shows that in both cases heat extraction is obtained

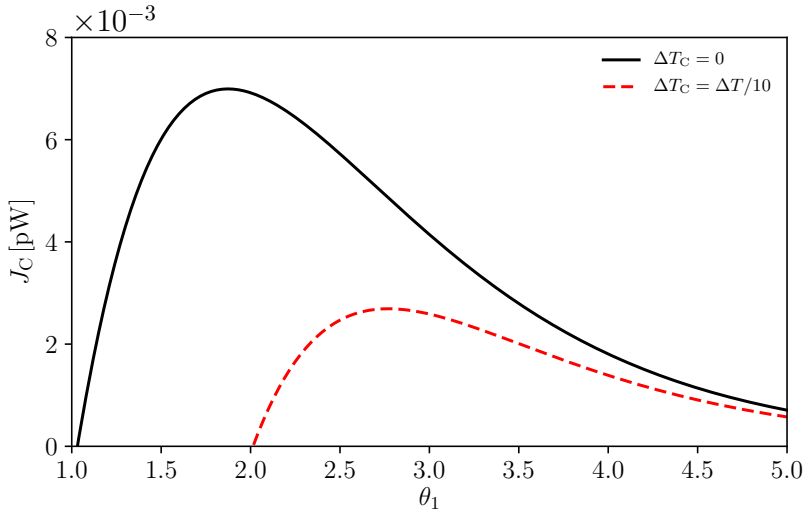

FIGURE 7.4: Cooling power J_C, relative to the system containing three QDs and represented in Fig. 7.3, under resonant condition [$\Delta U_3 = \Delta U_1(0)$]. J_C is plotted as a function of θ_1 for the case $\Delta T_C = 0$ (solid black curve) and the case $\Delta T_C = \Delta T/10$ (dashed red curve), setting $\theta_2 = 1/2$ and imposing $\theta_3 = \theta_1$. The parameters are of the order of the experimental ones reported in Ref. [234] and read: $E_I = 0.72$ meV, $\gamma_L = \gamma_R = \gamma_C = 0.036$ meV, $t = 0.016$ meV, and $T = \Delta T = 4.17$ K.

and that J_C takes a maximum value of the order of 10^{-2} pW. We notice that, as in the ideal case, the cooling power is weakly dependent on θ_2 in the range between 0 and 1, and that in this case J_C is maximized for $\theta_2 \simeq 1/2$. Moreover, we check that when the difference between ΔU_3 and $\Delta U_1(0)$ is not much larger than the coupling energies $\gamma_{L/R/C}$, the condition $\theta_3 = \theta_1$ is essentially fulfilled and the curves in Fig. 7.4 do not change appreciably. We have demonstrated that the implementation of the crucial condition (7.7) alone is sufficient to obtain heat extraction. Cooling power, as seen above, is expected to be maximal when the additional condition (7.8) is also satisfied. This could be implemented by adding another filtering QD in series with 1, between R and 1, and aligning its transition energy to $\Delta U_1(1)$. For experimental purposes, however, a simpler system is desirable, especially because the transition energies of the different QDs need to be tuned by individual gates (not shown in Fig. 7.3), operation that is further complicated by possible cross-couplings arising between them.

7.3.1 Metallic islands

We will now explore the possibility of replacing the QDs in the setup depicted in Fig. 7.3 with MIs. These are systems still characterized by a large charging energy but, as opposed to QDs, they present a continuous distribution of energy levels (the level spacing is much smaller than $k_B T$) so that electrons within the island are thermalized and distributed according to the Fermi distribution. Due to the absence of discrete levels, the sharp "filtering effect" discussed above in the QD system and exploited to satisfy the crucial conditions (7.7) and (7.8) is not possible. As we will show below, however, heat extraction can nonetheless be obtained in the setup depicted in Fig. 7.3, where 1, 2 and 3 are now usual metals and reservoir R (grey element) is superconducting. Our aim is to approximately satisfy Eq. (7.7) by properly tuning the chemical potential of MI 3. Conversely, by exploiting the superconducting gap of reservoir R, we aim at approximately satisfying Eq. (7.8) in order to suppress the electron transfer

with energy near $\Delta U_1(0)$. Unlike the case with QDs, here the detailed balance condition [Eq. (7.5)] is not satisfied by the rates between islands at different temperatures. As we shall see, however, this has only minor consequences.

The electrostatic energy of the system is equal to the one relative to the system of three QDs, Eq. (7.15). Also in this case we assume that each MI can only be singly-occupied so that our analysis can be restricted to the 8 states defined in the QD case. In the sequential tunneling regime, the stationary probability p_α that the system is in the state α is computed by solving the master equation (7.18), where, unlike in the QDs case, the rate for the transition from state α to state ν is given by

$$\Gamma_{\alpha\nu} = \frac{1}{e^2 R_{\alpha\nu}} \int d\epsilon \mathcal{N}_\lambda(\epsilon)\mathcal{N}_\mu(\epsilon - \Delta\tilde{U}_{\nu\alpha}) f_\lambda(\epsilon) \left[1 - f_\mu(\epsilon - \Delta\tilde{U}_{\nu\alpha})\right]. \tag{7.21}$$

Here, $R_{\alpha\nu}$ is the resistance of the tunneling barrier involved in the tunneling process, while $\lambda = \lambda(\alpha,\nu)$ and $\mu = \mu(\alpha,\nu)$ identify the indices of the MIs or reservoirs involved in the tunneling process. In Eq. (7.21), $\mathcal{N}_\lambda$ denote the normalized density of states, which takes the value $\mathcal{N}_\lambda = 1$ for $\lambda =$ 1,2,3,L,C, and

$$\mathcal{N}_{\mathrm{R}}(\epsilon) = \left| Re\left(\frac{\epsilon + i\gamma}{\sqrt{(\epsilon + i\gamma)^2 - \Delta^2}} \right) \right|, \tag{7.22}$$

for the superconducting reservoir [241, 242]. Here γ is a phenomenological inverse quasiparticle lifetime, and Δ is the superconducting gap. As before, the heat currents J_{L} and J_{C} are defined as the heat currents extracted from reservoirs L and C, and are computed in App. D.4.

In Fig. 7.5 the cooling power is plotted, using realistic parameters, as a function of θ_1, for $\Delta T_{\mathrm{C}} = 0$ (solid black curve) and for $\Delta T_C = 5$ mK (dashed red curve) and setting $\theta_2 = 1/2$. We assume that MIs 1 and 3 are at temperature T, while MI 2 is at temperature $T - \Delta T_{\mathrm{C}}$. Aiming at implementing the condition (7.7), we place the electrochemical potential ΔU_3 half way between $\Delta U_1(0)$ and $\Delta U_1(1)$, i. e. we set $\theta_3 = \theta_1 + 1/2$. In fact, this guarantees that (if $k_B T \lesssim E_{\mathrm{I}}$) the electron energy distribution in MI 3 is such that electron transfer to MI 1 is suppressed in the case where MI 2 is occupied. Note, however, that the opposite process (electron transfer from 1 to 3) is not suppressed. Indeed, to obtain heat extraction we need to further assume that electrode R is superconducting. Figure 7.5 shows that cooling is achieved in both cases, $\Delta T_{\mathrm{C}} = 0$ and $\Delta T_{\mathrm{C}} = 5$ mK. In the former case, the maximum cooling power is of the order 10^{-2} fW, while in the latter heat extraction is still possible, but the maximum cooling power decreases roughly by a factor 4. Interestingly, heat extraction occurs even for $\theta_1 < 1$, contrary to the prediction of Eq. (7.9). This can be attributed to the fact that the detailed balance condition (7.5) is not satisfied for the tunneling rates coupling MIs or reservoirs having different temperatures. An amount of heat equal to J_{C} is also extracted from MI 2 (see App. D.4 for details). Naturally no heat is extracted when reservoir R is in the normal state. We find that J_{C} is maximized when $\theta_2 \simeq 1/2$ and $\theta_3 \simeq \theta_1 + 1/2$, and that its increase with ΔT is at most linear. Nevertheless, we wish to point out that there is no simple condition to identify the optimal values of E_{I} and Δ. Yet by scaling all energies and temperatures of a given factor, the cooling power scales as the square of such factor.

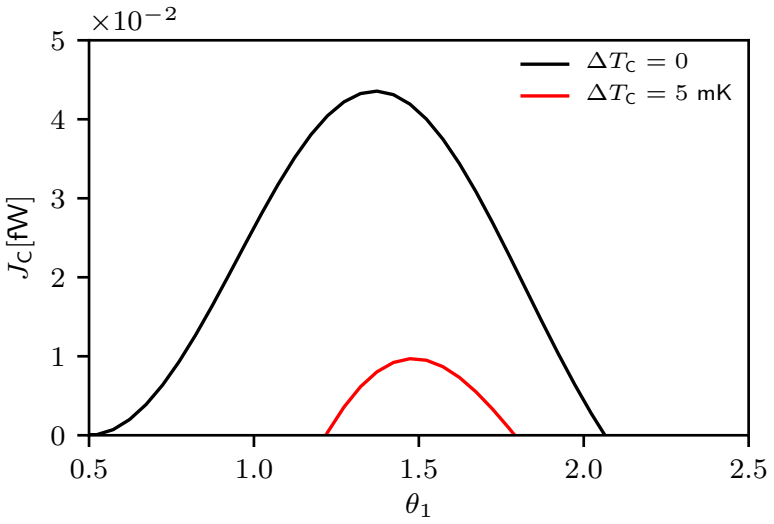

FIGURE 7.5: Cooling power, relative to the setup depicted in Fig. 7.3 for MIs, as a function of θ_1 for two different values of ΔT_C, and setting $\theta_2 = 1/2$ and $\theta_3 = \theta_1 + 1/2$. The parameters used are experimentally relevant, see for example Refs. [22, 167], and read: $E_I = 25$ μeV, $\Delta = 35$ μeV, $\gamma = 10^{-3}$ μeV, $T = 100$ mK, $\Delta T = 200$ mK and $R_{\alpha\nu} = 10$ kΩ for all barriers.

7.4 Maxwell demon: mutual information flow

Recent experimental advancements have turned the intriguing MD thought experiment [243, 244] into real experiments, spurring a vast experimental and theoretical research. A profound relation between information and thermodynamics was found [222, 245–250] and various manifestation of MDs have been theoretically[221, 224, 226–228, 251–259] and experimentally[22, 223, 225, 260–272] studied. In autonomous MDs, where the demon is part of the analyzed system, cooling has been studied from various standpoints, but, as far as we know, in all cases a voltage bias was used to "power" the demon. Conversely, our system does not require work, but it can be viewed as an autonomous MD since there is no direct heat transfer between the driving (D) and the cooled (C) system associated with electron tunneling; the cooling effect can thus be interpreted as due to information transfer.

According to the theoretical framework developed in Ref. [222], one can write the following inequalities

$$\dot{\mathcal{S}}_D^{(r)} - \dot{\mathcal{I}} \geq 0, \tag{7.23}$$

$$\dot{\mathcal{S}}_C^{(r)} + \dot{\mathcal{I}} \geq 0, \tag{7.24}$$

where $\dot{\mathcal{S}}_D^{(r)} = -J_L/T_L - J_R/T_R$ and $\dot{\mathcal{S}}_C^{(r)} = -J_C/T_C$ represent, respectively, the entropy variation in the driving and cooled reservoirs, while $\dot{\mathcal{I}}$ ($-\dot{\mathcal{I}}$) represents the variation of mutual information between system D and C due to tunneling events in D (C). The system behaves as a refrigerator, by extracting heat from reservoir C, when $\dot{\mathcal{S}}_C^{(r)} < 0$, which implies $\dot{\mathcal{I}} > 0$ in order to satisfy Eq. (7.24). We can thus interpret system D as a MD which acquires information by monitoring system C. In turn, system C uses this information as a resource to decrease its temperature. Eq. (7.24) shows that the cooling of reservoir C is bounded by $\dot{\mathcal{S}}_C^{(r)} \geq -\dot{\mathcal{I}}$, while Eq. (7.23) shows that reservoirs L and R are bound to dissipate at

least $\dot{\mathcal{S}}_{\rm D}^{(r)} \geq \dot{\mathcal{I}}$. This observation motivates the definition of the following thermodynamic efficiencies [222]

$$\eta_{\rm D} = \frac{\dot{\mathcal{I}}}{\dot{\mathcal{S}}_{\rm D}^{(r)}} \leq 1, \qquad \eta_{\rm C} = \frac{|\dot{\mathcal{S}}_{\rm C}^{(r)}|}{\dot{\mathcal{I}}} \leq 1, \tag{7.25}$$

where $\eta_{\rm D}$ represents the "information generation" efficiency, and $\eta_{\rm C}$ the "information consumption" efficiency. Notice that by definition $0 \leq \eta_{\rm D}, \eta_{\rm C} \leq 1$, and they are equal to 1 when, respectively, Eqs. (7.23) and (7.24) are strict equalities. While C is a quantity assigned to the entire system, $\eta_{\rm D}$ and $\eta_{\rm C}$ characterize the two subsystems, so that they can be viewed as a refinement to C [222]. By combining Eqs. (7.6), (7.12) and (7.25), the COP C can be written in terms of the product $\eta_{\rm D}\eta_{\rm C}$ and of $C_{\rm c}$ as

$$C = C^{(\max)} \frac{\eta_{\rm D}\eta_{\rm C}}{1 + C_{\rm c}(1 - \eta_{\rm D}\eta_{\rm C})}. \tag{7.26}$$

This is consistent with the fact that, in general, $\eta_{\rm D}$ and $\eta_{\rm C}$ individually provide more information than C, which is directly related only to their product $\eta_{\rm D}\eta_{\rm C}$. Using Eq. (7.26), we notice that $C = C^{(\max)}$ if and only if $\eta_{\rm D} = \eta_{\rm C} = 1$. This implies that for $\theta_1 = \theta_1^*$, where the COP reaches Carnot's limit [see Eq. (7.11)], we have that $\eta_{\rm D} = \eta_{\rm C} = 1$.

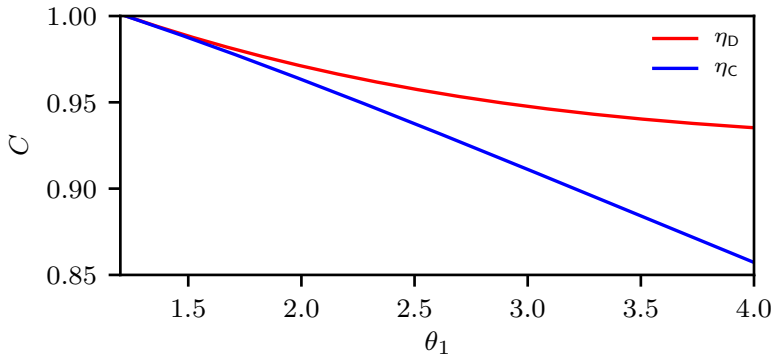

FIGURE 7.6: The efficiencies $\eta_{\rm D}$ and $\eta_{\rm C}$ are plotted as a function of θ_1 starting from $\theta_1 = \theta_1^*$ for the case $\Delta T_{\rm C} = \Delta T/5$. The parameters are the same as in Fig. 7.2(c).

In Fig. (7.6) we plot $\eta_{\rm D}$ and $\eta_{\rm C}$ as a function of θ_1. As expected, when $\theta_1 = \theta_1^*$, $\eta_{\rm D} = \eta_{\rm C} = 1$. For larger values of θ_1 the efficiencies decrease, but they remain close to 1. In general, finding high thermodynamic efficiencies in this model is not trivial [222, 226, 257, 272].

7.5 Summary

In this chapter, we studied several aspects of a minimal implementation of an absorption refrigerator based on two Coulomb coupled single-electron systems [11]. We derived the general condition to guarantee cooling by heating and we found the optimal rates that simultaneously maximize cooling power and coefficient of performance (COP). A simple relation between cooling power and charge current is also found. Analyzing the system as an autonomous Maxwell demon, we have shown that the efficiencies for information production

and consumption can reach their upper bounds, and we have related the COP to these efficiencies. Finally, we have put forward two experimental proposals, based on quantum dots (QDs) and metallic islands (MIs). In both proposals we have introduce an additional QD or MI that implements the non-trivial condition required to achieve cooling-by-heating. By plugging in realistic parameters we have shown that these proposals, which resemble existing experiments, yield observable heat currents [18, 42].

8

Heat rectification through a qubit

As discussed in the previous chapters, thermal transport in quantum devices has garnered vast attention in the last decade motivated by the miniaturization of current electronic and thermal devices. Improving thermal mangagement at the nanoscale became necessary to prevent overheating of the electronic circuitry. In addition, research in this field is growing thanks to recent advances in the experimental realization of nanoscale thermal devices [7, 17, 18, 273–275]. An intriguing phenomenon which may arise in nanoscale devices is thermal rectication, i. e. the asymmetric conduction of heat, whereby the heat flow in one direction is different with respect to the heat flow in the opposite direction, see Fig. 8.1. Thermal rectification, first observed experimentally by Starr in 1935 [276], has been studied in a variety of setups since then, both theoretically[96, 277–296] and experimentally[19, 140, 297–299].

Thermal rectification is interesting both from a practical and from a fundamental point of view. On the one hand, it can be used in a nanoscale device to evacuate heat from sensitive areas, while preventing it from flowing back in. On the other hand, from a conceptual point of view, it is interesting to understand what are the fundamental physical requirements for a system to exhibit thermal rectification, and what are the strategies to maximize this phenomenon. In this chapter we study thermal rectification through a qubit (S) coupled to two thermal baths at different temperatures as schematically sketched in Fig. 8.1. In panel (a) and panel (b), we depict the positive and negative bias cases. One bias condition is obtained from the other by inverting the temperature of the baths.

In order to observe thermal rectification, the presence of inelastic scattering is necessary, and the baths must be asymmetrically coupled to the system. In the absence of inelastic scattering, the heat current flowing from the left (L) to the right (R) heat bath can be described by the Landauer-Büttiker (LB) scattering approach [300, 301]

$$J_{\mathrm{LB}} = \int_{-\infty}^{+\infty} \frac{d\epsilon}{2\pi\hbar} \epsilon\, \mathfrak{T}(\epsilon)[n_{\mathrm{L}}(\epsilon) - n_{\mathrm{R}}(\epsilon)], \tag{8.1}$$

which is an energy integral of the transmission function $\mathfrak{T}(\epsilon)$, which does not depend on the bath temperatures, multiplied by the difference of energy distributions $n_\alpha(\epsilon)$, for $\alpha = \mathrm{L}, \mathrm{R}$. In this situation, no rectification is possible, since J_{LB} only changes sign (and not magnitude)

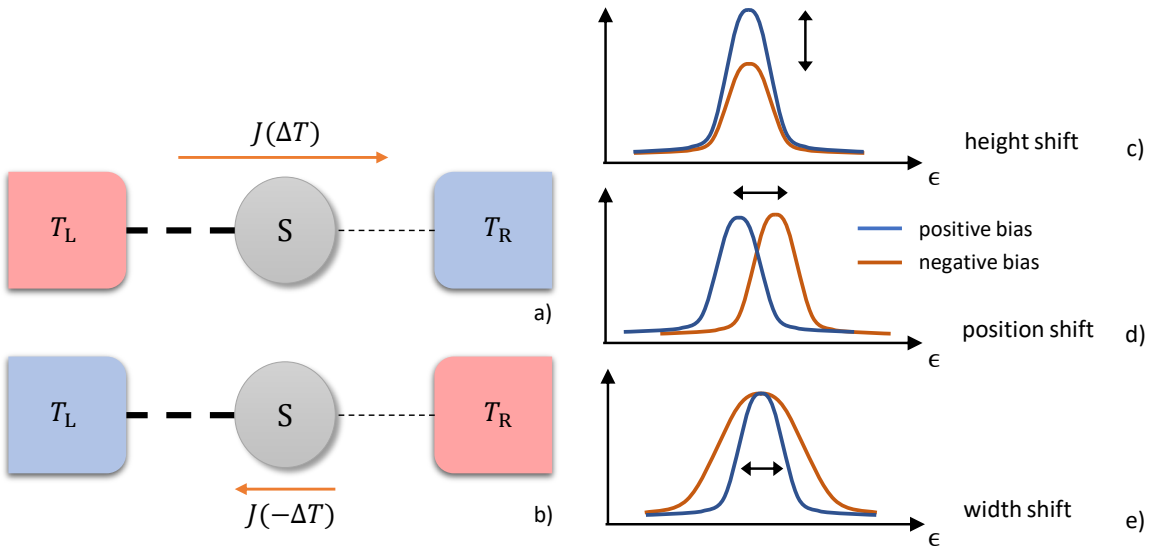

FIGURE 8.1: (a) and (b): Schematic representation of a central quantum system S (gray circle) coupled to the two heat baths. The left and right baths are characterized respectively by the temperatures T_L and T_R. Panel (a) represents the positive bias case, i.e. $T_L = T + \Delta T/2$ and $T_R = T - \Delta T/2$ with $\Delta T > 0$, while panel (b) represents the negative bias configuration where the sign of ΔT is reversed. In the presence of some asymmetry in the coupling to the baths (represented by the different thickness of the dashed lines), the magnitude of the heat currents flowing through the device may depend on the sign of ΔT, leading to thermal rectification. (c), (d) and (e): Schematic representation of the transmission function, as a function of the energy ϵ, for the positive and negative bias case. Each panel corresponds to a different kind of variation of the transmission function which can realize heat rectification.

upon exchange of the bath temperatures. Inelastic processes occur naturally in the presence of non-linearities, for example induced by interactions, or by time dependent driving in the Hamiltonian describing the system [302]. In the presence of interactions, at least when the spectral density of the baths have identical energy dependence, one can formally express the heat current analogous to the scattering theory with a "transmission function" which now depends also on the temperatures of the baths [295, 303] [see Eq. (8.15)]. If, in addition, the quantum system S is coupled asymmetrically to the two baths, thermal rectification can take place.

Within this framework we can identify three possible ways the transmission probability can change upon inverting the temperature bias (from positive to negative). As schematically shown in Fig. 8.1, the transmission functions can change in height (c), position (d) and width (e). The height shift is the main mechanism that allows rectification even in the weak coupling regime, and it is present whenever one accounts for inelastic processes. The position shift is caused by the real part of the self energy, known as Lamb shift, which accounts for the renormalization of the system energy scales due to the system-bath coupling. Finally, the width of the transmission probability may change when the system is strongly coupled to the baths. In most cases we consider, the width and height shift occur together.

In the literature, thermal rectification has been studied in different nanoscale systems, such as quantum dots [96, 287, 296], spin-boson models [279, 295], non-linear harmonic resonators [283], and hybrid quantum devices [284, 285, 289], to name a few. In most cases, the weak coupling wide band approximation is used to study thermal rectification. It has been

shown in Ref. [284] that asymmetric system-bath coupling and the presence of non-linearities are sufficient conditions to observe thermal rectification. Studying the spin-boson model [279, 295] and the non-linear harmonic resonator [283], it has been observed that thermal rectification increases as a function of the temperature difference and as a function of the asymmetry between the system-bath coupling strenghts. The spin-boson model has been studied also beyond the weak coupling regime in Ref. [295] using non equilibrium Green's function, and an enhancement in thermal rectification was observed.

Although thermal rectification has been studied in various specific systems, strategies to *maximize* rectification remain unclear. Moreover, it is not known if there are any fundamental bounds to the maximum rectification that can be obtained, and what is the impact of higher order coherent processes on rectification. In this chapter, we address these issues studying heat rectification across a qubit employing three different formalisms: (1) the master equation (ME) taking cotunneling into account, (2) non-equilibrium Green's functions (NEGF) and (3) exact calculations based on Feynman-Vernon path integral approach in the qubit case. Without assuming any specific model for the bath and system-bath Hamiltonian, we study how to maximize rectification and we derive general upper bounds valid within the weak coupling regime. Furthermore, we find that the rectification can be enhanced by exploiting the temperature dependence of the Lamb-shift, together with gapped density of states in the baths. We then perturbatively go beyond the weak coupling regime generalizing the calculation of Ref. [295] by addressing general spin couplings between the system and the baths, as well as the effect of the Lamb shift. Furthermore, employing the Feynman-Vernon path integral approach, we are able to exactly study the strong coupling regime. Thanks to these methods, we find that many bounds and limitations emerging in the weak coupling regime can be overcome, and that rectification can be enhanced by higher order quantum coherent processes. These violations provide clear and simple "strong coupling signatures" which are experimentally observable.

The chapter is organized as follows. In Sec. 8.1 we present the model and in Sec. 8.2 we define the rectification coefficient. In Sec. 8.3 we study the qubit case in the weak coupling regime, while in Sec. 8.4 we study the qubit beyond the weak coupling regime. At last, in Sec. 8.5 we provide a summary.

8.1 Model

We consider a qubit S arbitrarily coupled to two thermal baths denoted by L (left) and R (right) [see Fig. 8.1 for a sketch]. As in Chap. 2, the total Hamiltonian is given by

$$H_{\rm tot} = H_{\rm L} + H_{\rm R} + H_{\rm S} + H_{\rm S,L} + H_{\rm S,R}, \tag{8.2}$$

where H_α, for $\alpha = {\rm L}, {\rm R}$, is the Hamiltonian of bath α, $H_{\rm S}$ is the Hamiltonian of the system S and $H_{{\rm S},\alpha}$ describes the coupling between S and α. Each of these components - the baths, the system, and the couplings - contribute in different ways to the thermal properties of the device. We therefore describe each one in detail.

The baths are assumed to be "large" quantum systems which have a well defined temperature T_α and chemical potential μ_α in the fermionic case. We describe the baths as a collection of non-interacting bosons or fermions. Since the baths are assumed to be "macroscopic" compared to S, even if interactions are present in the baths it is reasonable to assume that a single particle description will hold by adopting a mean field approach. The parameters of the baths are therefore to be regarded as "effective" and emerging from a quasi-particle

description. The Hamiltonian of the bosonic (B) and fermionic (F) baths is given by

$$H_\alpha^{(\mathrm{B})} = \sum_k \epsilon_{\alpha k}\, b_{\alpha k}^\dagger b_{\alpha k}, \qquad H_\alpha^{(\mathrm{F})} = \sum_k \epsilon_{\alpha k}\, c_{\alpha k}^\dagger c_{\alpha k}, \tag{8.3}$$

where $b_{\alpha k}$ and $b_{\alpha k}^\dagger$ ($c_{\alpha k}$ and $c_{\alpha k}^\dagger$) are respectively the destruction and creation bosonic (fermionic) operators of an excitation with energy $\epsilon_{\alpha k}$ in bath α and quantum number k. The operators satisfy the usual commution and anticommutation relations: $[b_{\alpha k}, b_{\alpha' k'}^\dagger] = \delta_{\alpha,\alpha'}\delta_{k,k'}$, $[b_{\alpha k}, b_{\alpha' k'}] = 0$, $\{c_{\alpha k}, c_{\alpha' k'}^\dagger\} = \delta_{\alpha,\alpha'}\delta_{k,k'}$ and $\{c_{\alpha k}, c_{\alpha' k'}\} = 0$, where $[\dots,\dots]$ and $\{\dots,\dots\}$ denote, respectively, the commutator and anticommutator. Since the baths are at thermal equilibrium, we assume the bosonic baths to be prepared in a thermal Gibbs state $\rho_\alpha^{(\mathrm{B})} = e^{-H_\alpha^{(\mathrm{B})}/(k_\mathrm{B}T_\alpha)}/Z_\alpha^{(\mathrm{B})}$, where $Z_\alpha^{(\mathrm{B})} = \mathrm{Tr}\left[e^{-H_\alpha^{(\mathrm{B})}/(k_\mathrm{B}T_\alpha)}\right]$ is the partition function of bath α, while we assume the fermionic bath to be prepared in the state $\rho_\alpha^{(\mathrm{F})} = e^{-(H_\alpha^{(\mathrm{F})}-\mu_\alpha N_\alpha)/(k_\mathrm{B}T_\alpha)}/Z_\alpha^{(\mathrm{F})}$, where $Z_\alpha^{(\mathrm{F})} = \mathrm{Tr}\left[e^{-(H_\alpha^{(\mathrm{F})}-\mu_\alpha N_\alpha)/(k_\mathrm{B}T_\alpha)}\right]$ is the grand partition function of bath α and $N_\alpha = \sum_k c_{\alpha k}^\dagger c_{\alpha k}$ is the particle number operator of bath α.

The Hamiltonian of the qubit S is given by

$$H_\mathrm{S} = \frac{\Delta}{2}\sigma_z, \tag{8.4}$$

where Δ is the energy spacing between the ground and excited state, and σ_z denotes a Pauli matrix. Notice that any two-level Hamiltonian can be written as in Eq. (8.4) by choosing an appropriate basis. Physically, in a bosonic system, the qubit may represent a non-linear harmonic oscillator where the interaction is so strong that only the first two states are energetically accessible. In a fermionic system, instead, the two states of the qubit may represent the two states of a single levels QD: occupied, or unoccupied.

The coupling allows energy exchange between the baths and S. We can write the most general system-bath interaction as

$$H_{\mathrm{S},\alpha} = \sigma^+ \otimes B_\alpha + \sigma^- \otimes B_\alpha^\dagger + \sigma_z \otimes B_{\alpha z}, \tag{8.5}$$

where B_α is an arbitrary operator (not necessarily Hermitian) acting on the Hilbert space of bath α, while $B_{\alpha z}$ is an Hermitian operator acting on the space of bath α (see App. E.1 for details). This expression can be derived by expanding the operators acting on the tensor space of S and of the bath onto the product basis, and choosing the Pauli matrices and the identity as basis of Hermitian operators acting on the qubit space. After deriving some general properties, in this chapter we will explicitly consider the "linear coupling" and the "non-linear coupling" cases, i.e.

$$B_\alpha^{(\text{lin})} = \sum_k V_{\alpha k}\, d_{\alpha k}, \tag{8.6}$$

$$B_\alpha^{(\text{non-lin})} = \sum_k V_{\alpha k}\, d_{\alpha k}^2, \tag{8.7}$$

respectively, where the operator $d_{\alpha k}$ denotes $b_{\alpha k}$ when the baths are bosonic, while $d_{\alpha k}$ denotes $c_{\alpha k}$ when the baths are fermionic. The coupling strength is determined by the real coupling constants $V_{\alpha k}$. When assessing strong coupling effects, we will focus on the spin-boson (sb) model, i.e. we will consider a bosonic bath coupled to the qubit via the following interaction

$$H_{\mathrm{S},\alpha}^{(\mathrm{sb})} = \sum_{i=x,y,z} \hat{n}_{\alpha,i}\sigma_i \otimes \sum_k V_{\alpha k}\,(b_{\alpha k} + b_{\alpha k}^\dagger), \tag{8.8}$$

where $\hat{n}_\alpha = (\sin\theta_\alpha \cos\phi_\alpha, \sin\theta_\alpha \sin\phi_\alpha, \cos\theta_\alpha)$ is a unit vector parameterized by the angles θ_α and ϕ_α.

As we will see in the following, the system-bath interaction can be conveniently characterized by the spectral density

$$\gamma_\alpha(\epsilon) = 2\pi \sum_k |V_{\alpha k}|^2 \delta(\epsilon - \epsilon_{\alpha k}). \tag{8.9}$$

Taking the continuum limit for the energy spacing of the baths, and assuming that the coupling constants $V_{\alpha k}$ only depend on the energy $\epsilon_{\alpha k}$, we can rewrite Eq. (8.9) as

$$\gamma_\alpha(\epsilon) = 2\pi D_\alpha(\epsilon) |V_\alpha(\epsilon)|^2, \tag{8.10}$$

where $D_\alpha(\epsilon)$ is the density of states of bath α, and $V_\alpha(\epsilon_{\alpha k}) = V_{\alpha k}$. In the following, we will consider generic spectral densities for the two baths. In some cases, explicitly mentioned in the following, we will focus on bosonic baths with Ohmic spectral densities and an exponential cut-off energy ϵ_C, i.e.

$$\gamma_\alpha(\epsilon) = \pi K_\alpha \, \epsilon \, e^{-\epsilon/\epsilon_C} \equiv K_\alpha I(\epsilon), \tag{8.11}$$

where K_α is the dimensionless Ohmic coupling strength [304].

8.2 Heat current and rectification

We are interested in studying the steady-state heat current flowing across the device when a temperature bias is imposed between the baths. Specifically, as depicted in Fig. 8.1, we fix $T_L = T + \Delta T/2$ and $T_R = T - \Delta T/2$, where T is the average temperature. Since no work is performed on the system (in the fermionic case, we consider no chemical potential bias), the first principle of thermodynamics tell us that heat will flow from left to right if $\Delta T > 0$ (positive bias case, see Fig. 8.1a), otherwise it will flow from right to left (negative bias case, see Fig. 8.1b). Furthermore, since we consider steady state currents, the heat flowing out of one bath is equal to the one flowing into the other bath. Therefore, for simplicity we define the heat flowing out of the left lead as

$$J(\Delta T) \equiv - \lim_{t \to +\infty} \frac{d}{dt} \langle H_L \rangle (t), \tag{8.12}$$

where $\langle \ldots \rangle (t) = \mathrm{Tr}[\rho(t) \ldots]$, $\rho(t)$ being the density matrix representing the state of the total system at time t. Notice that the time variation of the energy associated with the coupling Hamiltonian vanishes in steady state [58].

As discussed in the introduction, it is possible to construct devices where the magnitude of the heat current depends on the sign of the temperature bias. Specifically, if the left-right symmetry is broken, the magnitude of the heat current $|J(\Delta T)|$ induced by a positive bias may be different respect to $|J(-\Delta T)|$, which is the heat current induced by a negative bias. We therefore define the rectification coefficient R as

$$R = \frac{|J(\Delta T)| - |J(-\Delta T)|}{|J(\Delta T)| + |J(-\Delta T)|}, \tag{8.13}$$

for $\Delta T > 0$. The definition is such that $|R| \leq 1$. Furthermore, $R = 0$ means that no rectification takes place, while $|R| = 1$ means that we have perfect rectification (i.e. the heat current is finite in one direction, and null in the other). Positive (negative) values of R indicate that the heat flow is greater for positive (negative) temperature biases.

Starting from the formal definition of the heat current given in Eq. (8.12), we can simplify the calculation of the heat current using a standard procedure known as "bath embedding"[41], which is valid whenever the operators of the bath appear linearly in $H_{\mathrm{S},\alpha}$. This approach does not apply to the non-linear coupling case, Eq. (8.7), which will be treated only in the weak coupling regime. Under such hypothesis, the formally exact Meir-Wingreen-type formula [305] for the heat current can be written as [303, 306–309]

$$J(\Delta T) = \pm \int \frac{d\epsilon}{2\pi\hbar}\, \epsilon\, \mathrm{Tr}\left[G^{<}(\epsilon)\Sigma_{\mathrm{L}}^{>}(\epsilon) - G^{>}(\epsilon)\Sigma_{\mathrm{L}}^{<}(\epsilon)\right], \tag{8.14}$$

where the integration is performed over $[0, +\infty]$ ($[-\infty, +\infty]$) for bosonic (fermionic) baths, while the minus sign in front of the integral applies only in the QD case where both the system and the baths are fermionic. $G^{\lessgtr}(\epsilon)$ is the Fourier transform of the lesser/greater Green's function of S in the presence of the baths, while $\Sigma_{\mathrm{L}}^{\lessgtr}(\epsilon)$ is the Fourier transform of the lesser/greater *embedded* self energy induced by the left bath. The lesser and greater embedded self energies can be determined from the Keldysh contour components $\Sigma_\alpha(z, z') = \int d\epsilon_k/(2\pi)\, \gamma_\alpha(\epsilon_k) g_{\alpha,\epsilon_k}(z, z')$, where $g_{\alpha,\epsilon_k}(z, z') = -i/\hbar\, \langle \mathcal{T}_c\{d_{\alpha k}(z) d^\dagger_{\alpha k}(z')\}\rangle_0$ is the *free* contour Green function of bath α, $\mathcal{T}_c$ denoting the contour ordering. The only quantities which must be determined in Eq. (8.14) are $G^{\lessgtr}(\epsilon)$.

There is a typical situation in which Eq. (8.14) can be written as a simpler and more transparent expression. Namely, if the spectral densities $\gamma_\alpha(\epsilon)$ of the baths are proportional, i.e. $\gamma_{\mathrm{L}}(\epsilon) \propto \gamma_{\mathrm{R}}(\epsilon)$, we can write Eq. (8.14) as [40]

$$J(\Delta T) = \int \frac{d\epsilon}{2\pi\hbar}\, \epsilon\, \mathcal{T}(\epsilon, T, \Delta T)\left[n_{\mathrm{L}}(\epsilon) - n_{\mathrm{R}}(\epsilon)\right], \tag{8.15}$$

where

$$\mathcal{T}(\epsilon, T, \Delta T) = i\, \mathrm{Tr}\left\{\frac{\gamma_{\mathrm{L}}(\epsilon)\gamma_{\mathrm{R}}(\epsilon)}{\gamma_{\mathrm{L}}(\epsilon) + \gamma_{\mathrm{R}}(\epsilon)}[G^{>}(\epsilon) - G^{<}(\epsilon)]\right\} \tag{8.16}$$

and $n_\alpha(\epsilon)$ denotes the energy distribution of bath α. Therefore, $n_\alpha(\epsilon) = (e^{\epsilon/(k_{\mathrm{B}}T_\alpha)} - 1)^{-1}$ for bosonic baths, while $n_\alpha(\epsilon) = (e^{(\epsilon-\mu_\alpha)/(k_{\mathrm{B}}T_\alpha)} + 1)^{-1}$ for fermionic baths. This formula was used in Ref. [295] to study the spin-boson problem. The dependence of $\mathcal{T}(\epsilon, T, \Delta T)$ on the temperatures may arise from $G^{\lessgtr}(\epsilon)$, which are indeed correlation functions of S computed in the presence of the baths. We notice that, in the absence of this temperature dependence, the magnitude of the heat current would remain the same in the positive and negative bias cases, and there would be no thermal rectification. Indeed, this is the case for non-interacting systems, where Eq. (8.16) reduces to the well known scattering formula with a transmission function that does not depend on the temperature of the baths [see Eq. (8.1)]. It is therefore crucial to introduce a non-linearity in the local system or in the coupling Hamiltonian to observe thermal rectification.

8.3 Weak coupling regime

In this section, we derive general properties and upper bounds to the rectification coefficient R only assuming that the baths are weakly coupled to the qubit, see Chap. 2. The approximation performed in this section allows us to consider height and position shift in the transmission function (see Fig. 8.1), but it neglects any width shift. Indeed, in this regime the width of the transmission function is the smallest energy scale, so it is infinitesimal. In the following sections, we will be able to observe also the impact of width shifts performing calculations beyond the weak-coupling regime.

Neglecting for the moment the Lamb-shift (which we discuss in Sec. 8.3.4) we find that (see App. E.2 for details)

$$R = \frac{1-C}{1+C}, \tag{8.17}$$

where

$$C = \frac{\Gamma_{\mathrm{L}}(\Delta, T_{\mathrm{H}})\Gamma_{\mathrm{R}}(\Delta, T_{\mathrm{C}})}{\Gamma_{\mathrm{L}}(\Delta, T_{\mathrm{C}})\Gamma_{\mathrm{R}}(\Delta, T_{\mathrm{H}})} \cdot \frac{\Gamma_{\mathrm{L}}(\Delta, T_{\mathrm{C}}) + \Gamma_{\mathrm{R}}(\Delta, T_{\mathrm{H}})}{\Gamma_{\mathrm{L}}(\Delta, T_{\mathrm{H}}) + \Gamma_{\mathrm{R}}(\Delta, T_{\mathrm{C}})}, \tag{8.18}$$

$\Gamma_\alpha(\Delta, T_\alpha) = \Gamma^+_\alpha(\Delta, T_\alpha) + \Gamma^-_\alpha(\Delta, T_\alpha)$ is the total dissipation rate induced by bath α and $T_{\mathrm{H/C}} = T \pm \Delta T/2$ for $\Delta T > 0$. $\Gamma^+_\alpha(\Delta, T_\alpha)$ $[\Gamma^-_\alpha(\Delta, T_\alpha)]$ represents the rate with which the qubit, being in the ground (excited) state, transits to the excited (ground) state by exchanging energy with bath α (these are equivalent to the sequential rates introduced in Chap. 2). Since bath α is prepared in a thermal state, these two rates are in general related by the detailed balance condition $\Gamma^+_\alpha(\Delta, T_\alpha) = e^{-\Delta/(k_{\mathrm{B}}T_\alpha)}\Gamma^-_\alpha(\Delta, T_\alpha)$ [see App. E.3 for details]. The dissipation rate can then be calculated by evaluating

$$\Gamma^-_\alpha(\Delta, T_\alpha) = \frac{1}{\hbar^2}\int_{-\infty}^{+\infty} dt\, e^{i\Delta t/\hbar}\left\langle B_\alpha(t)B^\dagger_\alpha(0)\right\rangle_\alpha, \tag{8.19}$$

where the expectation value is taken with respect to the *equilibrium* thermal state ρ_α of the bath, Δ is the energy spacing of the qubit [see Eq. (8.4)], and the operators $B_\alpha(t)$ and $B^\dagger_\alpha(t)$ are interaction picture operators (they evolve through H_α), thus the coupling to the qubit is neglected [see App. E.3 for a derivation of Eq. (8.19)].

We can now study R for any weakly coupled system using Eqs. (8.17) and (8.19), which are generally easy to compute (we will consider various models explicitly in the following sections). Interestingly, as a consequence of the weak coupling assumption, the coupling term $\sigma_z \otimes B_{\alpha z}$ [see Eq. (8.5)] does not contribute to $J(\Delta T)$, therefore neither to R. Intuitively, this is due to the fact that the heat current in the weak coupling regime is mediated by transitions in S induced by the baths. Therefore, the heat current only depends on the population of the qubit, which in turn is solely determined by the coupling terms proportional to σ^+ and σ^- (see App. E.2 for more details).

The rest of the section is organized as follows: in Sec. 8.3.1, we derive general bounds assuming that the baths are "similar" (this is a weak hypothesis; a proper definition will be given). We then study the impact of linear and non-linear coupling to the baths. In Sec. 8.3.2 we show that rectification can be enhanced when the baths are not "similar". In Sec. 8.3.3, we study a generic spin coupling to the bath. At last, in Sec. 8.3.4 we show how the Lamb-shift can be exploited to further enhance rectification.

8.3.1 Rectifying with "similar" system-bath coupling

In this section we assume that the left and right baths are "similar", i.e. we assume that the dissipation rate can be decomposed as

$$\Gamma(\Delta, T_\alpha) = \gamma_\alpha(\Delta) g(\Delta, T_\alpha), \tag{8.20}$$

where $\gamma_\alpha(\Delta)$ is the spectral density of bath α, given by Eq. (8.10), and $g(\Delta, T_\alpha) \geq 0$ is an arbitrary non-negative function. Equation (8.20) implies that the dissipation rates of the two baths, as a function of temperature, are equal up to a prefactor. However, the rates may have *any dependence* on the gap of the qubit through the spectral densities. Two baths are similar whenever the coupling Hamiltonians relative to the two baths are distinct linear

combinations of the *same operators*. For example, two bosonic baths, with distinct density of states, both coupled to the system through a linear or non-linear coupling, are similar baths.

Let us define the "asymmetry coefficient" λ as

$$\lambda = \frac{\gamma_{\mathrm{L}}(\Delta) - \gamma_{\mathrm{R}}(\Delta)}{\gamma_{\mathrm{L}}(\Delta) + \gamma_{\mathrm{R}}(\Delta)}, \tag{8.21}$$

such that $|\lambda| \leq 1$. Using Eq. (8.20), we can cast Eq. (8.17) into the simple form

$$R = \lambda \frac{g(\Delta, T_{\mathrm{C}}) - g(\Delta, T_{\mathrm{H}})}{g(\Delta, T_{\mathrm{C}}) + g(\Delta, T_{\mathrm{H}})}. \tag{8.22}$$

Without specifying the precise model, we can derive the following general properties of R:

- If $\lambda > 0$, R is a decreasing function of $g(\Delta, T_{\mathrm{H}})$, and an increasing function of $g(\Delta, T_{\mathrm{C}})$ (the monotonicity is inverted if $\lambda < 0$). Therefore, if $g(\Delta, T)$ is monotonous with respect to T, then R is monotonous with respect to ΔT.
- R is linear, therefore monotonous, with respect to λ.
- Given the first property, we can maximize the possible rectification by taking the limits where $g(\Delta, T_{\mathrm{H}})$ and $g(\Delta, T_{\mathrm{C}})$ respectively tend to zero and infinity. This yields the following bound

  $$|R| \leq |\lambda|. \tag{8.23}$$

  As a consequence, the maximum rectification is severely limited by the asymmetry ratio λ. As expected, for $\lambda = 0$ we find that there is no rectification, and the only way to obtain perfect rectification is to have a vanishingly small coupling to one bath.
- Given the second property, $|R|$ is bounded by $|(g(\Delta, T_{\mathrm{C}}) - g(\Delta, T_{\mathrm{H}}))/(g(\Delta, T_{\mathrm{C}}) + g(\Delta, T_{\mathrm{H}}))|$. We therefore have stronger rectification when $g(\Delta, T)$ has a strong temperature dependence.

Linear system-bath tunnel couplings

In this section we study heat rectification through a qubit where the coupling to the baths is linear, i.e. defined by Eq. (8.6). For fermionic baths weakly coupled to the qubit, we have that (see App. E.4.1, for details)

$$g(\Delta, T) = 1. \tag{8.24}$$

Plugging this value into Eq. (8.22) shows us that no rectification is possible. This is indeed expected, since a qubit coupled to fermionic reservoirs can be described by a non-interacting fermionic Hamiltonian, where the Landauer-Büttiker formula can be used to compute the heat current. Next, we consider bosonic baths. In this case, as shown in App. E.4.2, we have that

$$g(\Delta, T) = \coth\left[\Delta/(2k_{\mathrm{B}}T)\right], \tag{8.25}$$

so rectification is possible. In particular, we find the following properties:

- $g(\Delta, T)$ is a monotonous increasing function of T, thus λ and R have opposite signs. This means that more heat flows out of the weakly coupled lead.
- Since $g(\Delta, T)$ is a monotonous function of T, the rectification increases with ΔT.

- Since $g(\Delta, T)$ is never zero, but it diverges for $T \to \infty$, the bound in Eq. (8.23) is saturated only in the limit of infinitely hot reservoir ($T_{\mathrm{H}} \to \infty$).
- It can be explicitly seen that $|R|$ is a decreasing function of the gap Δ, so it is maximum in the limit $\Delta \to 0$. In this limit, we can expand the cotangent, finding the following bound

$$|R| \leq \lambda \frac{T_{\mathrm{H}} - T_{\mathrm{C}}}{T_{\mathrm{H}} + T_{\mathrm{C}}}. \tag{8.26}$$

Bosonic baths with non-linear coupling

In this section we consider bosonic baths coupled non-linearly to the system as defined in Eq. (8.7). As shown in App. E.4.3, this leads to [1]

$$g(\Delta, T) = 1 + \coth^2[\Delta/(4k_{\mathrm{B}}T)], \tag{8.27}$$

and we find the following properties:

- $g(\Delta, T)$, as a function of T, has the same monotonicity as the bosonic case with linear coupling, it only diverges for $T \to \infty$, and it is never zero. Therefore, it has the same first 3 properties of section 8.3.1.
- Also in this case, $g(\Delta, T)$ is monotonous with respect to Δ, such that R is maximized in the limit $\Delta \to 0$. Performing an expansion for small Δ, we find the following bound

$$|R| \leq \lambda \frac{T_{\mathrm{H}}^2 - T_{\mathrm{C}}^2}{T_{\mathrm{H}}^2 + T_{\mathrm{C}}^2}. \tag{8.28}$$

  Comparing with Eq. (8.26), we see that the non-linear coupling yields a *higher rectification*. This can be explicitly verified by comparing the exact expressions of R using Eq. (8.22).

8.3.2 Rectifying with "different" system-bath coupling

In this section, we check if relaxing the condition of Eq. (8.20) allows stronger rectification. Equation (8.20) does not hold whenever the correlation function in Eq. (8.19) is "different enough" for the two baths, and this may happen considering different bath Hamiltonians, and/or different coupling Hamiltonians.

As an example, we take the two bosonic baths, but we consider two different coupling Hamiltonians. We assume the left bath to be linearily coupled to the qubit (as in Subsec. 8.3.1) and the right bath to be non-linearly coupled to the qubit (as in Subsec. 8.3.1) and, as in the previous section, we define the quantity $\lambda = (\gamma_{\mathrm{L}}(\Delta) - \gamma_{\mathrm{R}}(\Delta))/(\gamma_{\mathrm{L}}(\Delta) + \gamma_{\mathrm{R}}(\Delta))$. Plugging the respective rates for the left and the right lead into Eq. (8.17) yields an exact expression for R which in the limit $\Delta \to 0$ is simply given by

$$R = \frac{T_{\mathrm{H}} - T_{\mathrm{C}}}{T_{\mathrm{H}} + T_{\mathrm{C}}} \tag{8.29}$$

regardless of λ [we assume that $\gamma_\alpha(\Delta \to 0)$ does not diverge]. Notably, a general property of "similar baths" is that $|R| \leq |\lambda|$, while here we have rectification even for $\lambda = 0$, and it can be made arbitrarily large simply by choosing larger and larger temperature differences. This proves that, in general, different system-bath couplings can produce a higher rectification coefficient.

[1] In this case, we define the function $g(\Delta, T)$ through $\Gamma_\alpha(\Delta, T) = \gamma_\alpha(\Delta/2) g(\Delta, T)/2$. This choice does not influence the results presented.

8.3.3 Arbitrary baths with different spin couplings to the system

In this section, we investigate what happens when the qubit is coupled to the baths through the same arbitrary bath operators, but through different Pauli spin matrices. As an example, we consider the coupling Hamiltonian given in Eq. (8.8) with $V_{\mathrm{L}k} = V_{\mathrm{R}k}$, although also non-linear couplings can be treated on the same footing. As shown in App. E.4.4, this system can be mapped into the "similar baths" case with an effective $\gamma_\alpha(\Delta) \propto \sin^2\theta_\alpha$. Therefore, all the properties derived in Sec. 8.3.1 hold in this case, where the asymmetry coefficient is given by

$$\lambda = \frac{\sin^2\theta_{\mathrm{L}} - \sin^2\theta_{\mathrm{R}}}{\sin^2\theta_{\mathrm{L}} + \sin^2\theta_{\mathrm{R}}}, \tag{8.30}$$

while the function $g(\Delta, T)$ depends on the bath and system-bath Hamiltonian [in the specific case of Eq. (8.8), we have $g(\Delta, T) = \coth\left[\Delta/(2k_{\mathrm{B}}T)\right]$, see Eq. (8.25)]. Interestingly, the rectification does not depend on the angle ϕ_α; as we will show, this property does not hold beyond the weak coupling regime thanks to coherent transport effects. The only relevant angle is θ_α, which is the angle between the coupling term and the qubit Hamiltonian (which is proportional to σ_z). Since the rectification is linear in λ, we find that the rectification is maximum when θ_{L} is 0 and θ_R is $\pi/2$, or viceversa.

8.3.4 Rectification enhanced by the Lamb-Shift

Until now we have ignored the Lamb shift, i.e. the renormalization of the energy gap of the qubit induced by the presence of the baths. The renormalization of the qubit gap depends on both bath temperatures, thus it may influence the rectification properties of the device. As we now show, this allows us to achieve rectification beyond the bounds derived in the previous sections.

As shown in App. E.6, if the system-bath Hamiltonian does not contain terms proportional to σ_z (i.e. $B_{\alpha z} = 0$), the Lamb shift Hamiltonian (which has to be summed to the "bare" Hamiltonian H_{S}) takes the following form [27]:

$$H_{\mathrm{LS}} = \left[\delta\Delta_{\mathrm{L}}(\Delta, T_{\mathrm{L}}) + \delta\Delta_{\mathrm{R}}(\Delta, T_{\mathrm{R}})\right]\sigma_z, \tag{8.31}$$

where

$$\delta\Delta_\alpha(\epsilon, T_\alpha) = \frac{1}{2\pi}\mathcal{P}\int_{-\infty}^{+\infty}\frac{\Gamma_\alpha(\epsilon', T_\alpha)}{\epsilon - \epsilon'}d\epsilon'. \tag{8.32}$$

In Eq. (8.32), $\mathcal{P}$ indicates a Cauchy principal value integration. We recall that the Δ appearing in Eq. (8.31) is the *bare gap*, neglecting the Lamb shift.

The renormalized gap is therefore given by

$$\tilde{\Delta}(\Delta T) = \Delta + \delta\Delta_{\mathrm{L}}(\Delta, T + \Delta T/2) + \delta\Delta_{\mathrm{R}}(\Delta, T - \Delta T/2), \tag{8.33}$$

and it may change upon inverting the temperature bias ($\Delta T \to -\Delta T$). In the presence of a Lamb shift, R is still given by Eq. (8.17) provided that we replace $\Delta \to \tilde{\Delta}(\Delta T)$.

In general, we notice that the renormalization terms $\delta\Delta_\alpha(\Delta, T_\alpha)$ is of the same order in the coupling strength as the rates $\Gamma_\alpha(\epsilon, T_\alpha)$ (which are evaluated at leading order in the coupling). Therefore, if the rates $\Gamma_\alpha(\epsilon, T_\alpha)$ are smooth functions of ϵ, their variation due to the Lamb shift will be beyond leading order in the coupling strength. Therefore, the effect of the Lamb shift on rectification is negligible in the weak coupling regime when the spectral density of the baths is a smooth function of the energy (on the $\hbar\Gamma_\alpha$ scale).

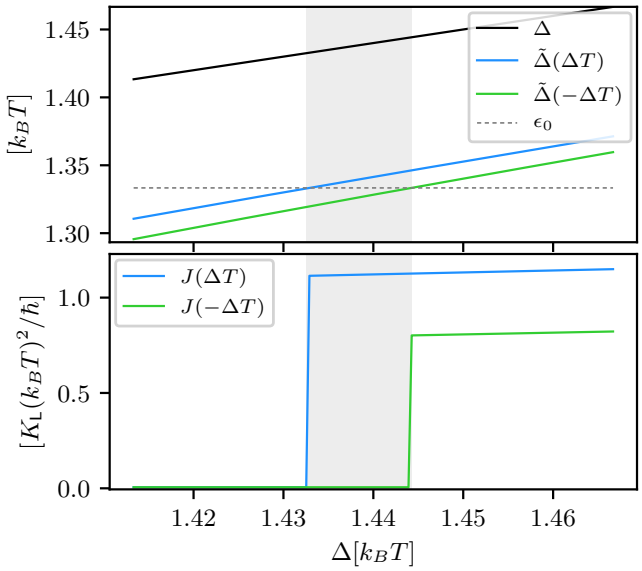

Figure 8.2: Upper panel: the bare gap Δ, the renormalized gap $\tilde{\Delta}(\Delta T)$ in the positive bias case and the renormalized gap $\tilde{\Delta}(-\Delta T)$ in the negative bias case, as a function of the bare gap Δ. The dashed gray line corresponds to the gap ϵ_0 in the density of states of the baths, while the region highlighted in gray shows where the renormalized gaps are respectively larger and smaller than ϵ_0. Lower panel: the heat currents $J(\Delta T)$ and $J(-\Delta T)$. In the highlighted region we have perfect rectification (up to higher order corrections in the coupling strength). The parameters are: $K_R = 5K_L$, $\epsilon_C = (20/3)\, k_B T$, $\epsilon_0 = (4/3)\, k_B T$ and $\Delta T/T = 2/3$.

However, the Lamb shift may become relevant for rectification whenever there is a strong energy dependence in $\Gamma_\alpha(\epsilon, T_\alpha)$, for example, if the density of states of the baths has a gap. As we will show in detail in the following, even a small renormalization of the gap can have a large impact on the current.

We consider two bosonic Ohmic baths with a cutoff frequency ϵ_C, but we add a gap in the density of states between zero and a certain value ϵ_0. We thus have that

$$\Gamma_\alpha(\epsilon, T_\alpha) = \frac{\pi}{\hbar} K_\alpha\, \theta(\epsilon - \epsilon_0)\, \epsilon\, e^{-\epsilon/\epsilon_C} \coth\left[\epsilon/(2k_B T_\alpha)\right], \tag{8.34}$$

where $\theta(\epsilon)$ is the Heaviside function which describes the gap in the density of states. In the upper panel of Fig. 8.2 we show the bare gap Δ (black curve), the renormalized gap $\tilde{\Delta}(\Delta T)$ for the positive bias case (blue curve), and the renormalized gap $\tilde{\Delta}(-\Delta T)$ for the negative bias case (green curve), as a function of the bare gap Δ. As we can see, the renormalized gaps are different in the positive and negative bias cases. In particular, in the highlighted region $\tilde{\Delta}(-\Delta T)$ is inside the gap, i.e. it is smaller than ϵ_0 (dashed gray line), while $\tilde{\Delta}(\Delta T)$ is outside the gap; we therefore expect a finite heat current in the latter case, and a zero heat current in the former. This is confirmed in the lower panel of Fig. 8.2 where $J(\Delta T)$ and $J(-\Delta T)$ are plotted as a function of the bare gap. The heat currents are computed using Eq. (E.7) with $\Delta \to \tilde{\Delta}(\Delta T)$ to account for the Lamb shift. As we can see, within the highlighted region we have perfect rectification. However, we expect that the inclusion of higher order effects in the coupling strength (for example co-tunneling effects) will reduce the rectification. Indeed, the perfect rectification visible in the gray region in the lower panel of Fig. 8.2 is a consequence of the current $J(-\Delta T)$ being directly proportional to the density

of states, therefore exactly zero for $\tilde{\Delta}(-\Delta T) < \epsilon_0$; on the other hand, higher order effects create small yet finite currents even in this parameter range. Nonetheless, we have identified a mechanism to enhance rectification exploiting the Lamb shift.

8.4 Beyond weak coupling regime

As we have seen, the weak coupling regime puts strong constraints on the rectification coefficient R. In this section, we show that some of these bounds can be overcome by going beyond the weak coupling regime. This implies that coherent quantum effects - beyond "sequential tunneling" - can be beneficial for rectification. From the point of view of the transmission function, see Fig. 8.1, going beyond the weak coupling regime allows us to consider also width shifts, which were neglected in the previous section.

We perform calculations beyond the weak coupling regime using three different techniques. First, we include co-tunneling effects in the master equation (ME), which allows us to intuitively interpret our results; next, we employ a perturbative approach based on non equilibrium Green's function (NEGF) theory which yields results beyond sequential and co-tunneling effects. Finally, we perform an exact calculation employing the Feynman-Vernon path integral approach.

For concreteness, we consider bosonic baths, and a general spin coupling to the baths as defined in Eq. (8.8). We will then mainly consider two different couplings: the "XX coupling", where both left and right baths are coupled to the system through σ_x, i.e. $\theta_{\rm L} = \theta_{\rm R} = \pi/2,\ \phi_{\rm L} = 0,\ \phi_{\rm R} = 0$, and the "YX coupling", i.e. $\theta_{\rm L} = \theta_{\rm R} = \pi/2,\ \phi_{\rm L} = \pi/2,\ \phi_{\rm R} = 0$. Since the XX and YX couplings only differ by the angle ϕ_α [see Eq. (8.8)], both cases display identical rectification within the weak coupling regime (see Sec. 8.3.3). As we will see, this property is violated beyond the weak coupling regime, signaling the effect of higher order coherent quantum effects. We will also consider arbitrary spin coupling in the $\Delta \to 0$ limit. This particular choice exhibits no current in the sequential tunneling limit. Hence, thermal current and thermal rectification becomes solely due to higher order processes.

In the following, we describe the ME technique including co-tunneling in Sec. 8.4.1, the NEGF method in Sec. 8.4.2, exact calculations based on Feynman-Vernon path integral approach in Sec. 8.4.3 and we discuss the impact on rectification in Sec. 8.4.4. The results for arbitrary spin coupling in the $\Delta \to 0$ limit will be presented in Sec. 8.4.5.

8.4.1 Master equation with co-tunneling

In this section we describe how to perform calculations beyond the weak coupling regime by adding rates to the ME that arise from second order processes in the coupling Hamiltonian. It can be shown that, both for the XX and YX couplings, only elastic cotunneling processes contribute, i.e. only those processes that coherently transfer an excitation from one bath to the other - via a virtual state - without changing the state of the qubit.

We find that the heat current, including co-tunneling effects, can be expressed as (see App. E.7 for details)

$$J(\Delta T) = J^{\rm seq}(\Delta T) + J^{\rm cot}(\Delta T), \tag{8.35}$$

where $J^{\rm seq}(\Delta T)$ is the heat current expected in the weak coupling regime, given by Eq. (E.7), and

$$J^{\rm cot}(\Delta T) = \int_0^\infty \frac{d\epsilon}{2\pi\hbar}\epsilon\gamma_{\rm L}(\epsilon)\gamma_{\rm R}(\epsilon)\left|\frac{1}{\Delta+\epsilon+i\eta} \pm \frac{1}{\Delta-\epsilon+i\eta}\right|^2 [n_{\rm R}(\epsilon) - n_{\rm L}(\epsilon)] \tag{8.36}$$

is the contribution due to co-tunneling, where η is an infinitesimal positive quantity, and $n_\alpha(\epsilon)$ is the Bose-Einstein distribution relative to bath α. The plus sign in Eq. (8.36) refers to the XX coupling, while the minus sign to the YX coupling.

Crucially, since the temperatures only enter through the Bose-Einstein distributions, $J^{\rm cot}(\Delta T)$ is an *anti-symmetric* function, i.e. $J^{\rm cot}(-\Delta T) = -J^{\rm cot}(\Delta T)$. Therefore the contribution of cotunneling to the heat current is the same both for the positive and negative bias case. Mathematically, Eq. (8.36) diverges logarithmically in the limit $\eta \to 0^+$. The co-tunneling rates can be "regularized" in a proper manner[32, 33, 83]. Assuming that the qubit is in the ground state, the first term inside the square modulus of Eq. (8.36) arises by virtually transferring an excitation from one bath to the qubit, and then from the qubit to the other bath. The second term instead arises by virtually creating an excitation both in one bath and in the qubit, and then by destroying an excitation in the qubit and in the other bath. The different XX and YX couplings produce opposite interference effects between these two processes. If we had neglected the "counter rotating" terms in $H^{\rm (sb)}_{{\rm S},\alpha}$ [Eq. (8.8)], the second term inside the square modulus would have vanished and the co-tunneling rates would have become the same in the XX and YX cases.

Exploiting the anti-symmetry of $J^{\rm cot}(\Delta T)$, the impact of co-tunneling on rectification can be easily appreciated by plugging Eq. (8.35) into Eq. (8.13):

$$R = \frac{|J^{\rm seq}(\Delta T)| - |J^{\rm seq}(-\Delta T)|}{|J^{\rm seq}(\Delta T)| + |J^{\rm seq}(-\Delta T)| + 2J^{\rm cot}(\Delta T)}, \tag{8.37}$$

where we fix $\Delta T > 0$. Notably, co-tunneling only appears at the denominator of Eq. (8.37). In addition, the cotunneling contribution of Eq. (8.36) represents an elastic process which would induce no rectification on its own. However, defining $R^{\rm seq} = (|J^{\rm seq}(\Delta T)| - |J^{\rm seq}(-\Delta T)|)/(|J^{\rm seq}(\Delta T)| + |J^{\rm seq}(-\Delta T)|)$, we see that if $J^{\rm cot}(\Delta T) < 0$, then

$$|R| > |R^{\rm seq}|, \tag{8.38}$$

whereas $|R| < |R^{\rm seq}|$ if $J^{\rm cot}(\Delta T) > 0$. Therefore, co-tunneling can enhance rectification. Interestingly, the co-tunneling contribution $J^{\rm cot}(\Delta T)$ is usually *negative* when sequential tunneling dominates. Indeed, the transmission function due to sequential tunneling is a delta function peaked around resonant condition. The cotunneling contribution increases the width of the transmission function giving it an effective bell shape (as shown in Fig. 8.1). As we increase the width of the transmission function, we move the weight from the peak of the transmission function to its tails. Therefore, where sequential dominates, co-tunneling contribution *decreases* the heat flow. On the other hand, if sequential tunneling is suppressed, i.e. in the tails of the transmission function, co-tunneling increases the heat flow. Therefore, we expect the following behavior: when sequential tunneling is dominant, we expect co-tunneling to *enhance* rectification. Instead, when the currents are dominated by co-tunneling, we expect the rectification to decrease in comparison to the weak-coupling predictions. This qualitative argument is confirmed by the calculations performed in Sec. 8.4.4.

8.4.2 Non-equilibrium Green's function method

In this section we describe how to employ the NEGF method to compute heat currents beyond the weak coupling limit. Since Green functions for spin operators cannot be expanded in a perturbative series using Wick's theorem, we first perform the following transformation [310, 311]

$$\sigma_a = -\frac{i}{2} \sum_{bc=x,y,z} \epsilon_{abc}\, \eta_b \eta_c, \tag{8.39}$$

where ϵ_{abc} is the Levi-Civita symbol, and η_a denotes three Majorana fermion operators (they satisfy the anticommutation relation $\{\eta_a, \eta_b\} = 0$ for $a \neq b$, $\eta_a^2 = 1$ and $\eta_a = \eta_a^\dagger$). The qubit and coupling Hamiltonians [see Eqs. (8.4) and (8.8)] therefore become (up to an irrelevant additive constant)

$$\begin{aligned} H_{\mathrm{S}} &= -i\frac{\Delta}{2}\eta_x\eta_y, \\ H_{\mathrm{S},\alpha}^{(\mathrm{sb})} &= -\frac{i}{2}\sum_{abc}\hat{n}_{\alpha,a}\epsilon_{abc}\,\eta_b\eta_c \otimes \sum_k V_{\alpha k}(b_{\alpha k} + b_{\alpha k}^\dagger), \end{aligned} \tag{8.40}$$

where the indices a, b and c run over x, y and z in the sum. Notice that in this representation the qubit Hamiltonian is still quadratic (therefore "free"), while $H_{\mathrm{S},\alpha}^{(\mathrm{sb})}$ is the product of three operators. Therefore, in the Majorana representation the system-bath coupling gives us the non-linear term which, as we discussed, is necessary to observe rectification.

Assuming that the spectral densities of the two baths are proportional, the heat current is given by Eq. (8.15) where $\mathcal{T}(\epsilon, T, \Delta T)$, in general, must be computed numerically. However, we are able to find an analytic expression for the transmission function by solving the Dyson equation for the Green's functions with an expression for the self energy expanded to leading order in the coupling Hamiltonian $H_{\mathrm{S},\alpha}^{(\mathrm{sb})}$ (see App. E.8 for details). In the XX coupling case, this method leads to

$$\mathcal{T}_{\mathrm{XX}}(\epsilon, T, \Delta T) = \frac{4\,\Delta^2\gamma_{\mathrm{L}}(\epsilon)\gamma_{\mathrm{R}}(\epsilon)}{\left(\epsilon^2 - 2\epsilon\left(\delta\Delta_{\mathrm{L}}(\epsilon, T_{\mathrm{L}}) + \delta\Delta_{\mathrm{R}}(\epsilon, T_{\mathrm{R}})\right) - \Delta^2\right)^2 + \xi^2(\epsilon)} \tag{8.41}$$

where $\xi(\epsilon) = \epsilon\sum_\alpha \gamma_\alpha(\epsilon)(1 + 2n_\alpha(\epsilon))$, and $\delta\Delta_\alpha(\epsilon, T_\alpha)$, which describes the Lamb shift induced by bath α, is defined in Eq. (8.32) with $\Gamma_\alpha(\epsilon', T_\alpha) = \gamma_\alpha(\epsilon')\coth\left[\epsilon'/(2k_{\mathrm{B}}T_\alpha)\right]$ [2]. Instead, in the YX coupling case we find

$$\mathcal{T}_{\mathrm{YX}}(\epsilon, T, \Delta T) = \frac{4\,\epsilon^2\,\gamma_{\mathrm{L}}(\epsilon)\gamma_{\mathrm{R}}(\epsilon)}{\left(\epsilon^2 - \mathcal{X}(\epsilon) - \Delta^2\right)^2 + \mathcal{Y}^2(\epsilon)}, \tag{8.42}$$

where

$$\mathcal{X}(\epsilon) = 2\epsilon\left(\delta\Delta_{\mathrm{L}}(\epsilon) + \delta\Delta_{\mathrm{R}}(\epsilon)\right) + \left(1 + 2n_{\mathrm{L}}(\epsilon)\right)\left(1 + 2n_{\mathrm{R}}(\epsilon)\right)\gamma_{\mathrm{L}}(\epsilon)\gamma_{\mathrm{R}}(\epsilon) - 4\delta\Delta_{\mathrm{L}}(\epsilon)\delta\Delta_{\mathrm{R}}(\epsilon), \tag{8.43}$$

and

$$\mathcal{Y}(\epsilon) = \sum_{\substack{\alpha,\beta=\mathrm{L},\mathrm{R} \\ \alpha\neq\beta}} \left(2\delta\Delta_\alpha(\epsilon) - \epsilon\right)\left(1 + 2n_\beta(\epsilon)\right)\gamma_\beta(\epsilon). \tag{8.44}$$

This approach provides results which are more accurate with respect to the ME approach (including co-tunneling contributions), since it contains higher order processes beyond sequential and cotunneling thanks to the implicit re-summation performed by solving the Dyson equation.

8.4.3 Spin-boson model: Exact calculation

In this section we consider the XX coupling case. Under these conditions an exact formal expression for the heat current Eq. (8.14) for general spectral densities of the two baths can

[2] In order to account for the counter-rotating terms in the coupling Hamiltonian, in the calculation of the Lamb-shift the spectral density $\gamma_\alpha(\epsilon')$ must be extended to negative values according to $\gamma_\alpha(-\epsilon') = -\gamma_\alpha(\epsilon')$. See App. E.8 for details.

be derived within the Feynmann-Vernon path-integral approach to the spin-boson problem [304]. Calculations are reported in App. E.9. When the spectral densities have the same energy dependence, i.e. $\gamma_{\rm L}(\epsilon) \propto \gamma_{\rm R}(\epsilon)$, the heat current takes the form of Eq. (8.15) with

$$\mathcal{T}^{(\rm ex)}_{\rm XX}(\epsilon, T, \Delta T) = 2\frac{\gamma_{\rm L}(\epsilon)\gamma_{\rm R}(\epsilon)}{\gamma_{\rm L}(\epsilon)+\gamma_{\rm R}(\epsilon)}{\rm Im}\left[\chi(\epsilon)\right], \tag{8.45}$$

where $\chi(\epsilon)$ is the Fourier transform of the qubit dynamical susceptibility in the presence of the two baths, $\chi(t) = (i/\hbar)\Theta(t)\langle[\sigma_x(t), \sigma_x(0)]\rangle$, given in Eq. (E.107).

We now focus on Ohmic spectral densities, defined as in Eq. (8.11). The dimensionless Ohmic coupling strength K_α enters the exact expression of the dynamical susceptibility in a form which allows the path summation in analytic form when $K_{\rm R}+K_{\rm L} = 1/2$, analogously to the Toulouse point of the Ohmic spin boson problem [304, 312], see Eq. (E.111). We obtain

$$\chi(t) = \frac{2\Delta^2}{\hbar^3\nu}\Theta(t)e^{-\nu t/2}\int_0^\infty d\tau P(\tau)\left[e^{-\nu|t-\tau|/2} - e^{-\nu|t+\tau|/2}\right], \tag{8.46}$$

where $\nu = \pi\Delta^2/(2\hbar\,\epsilon_{\rm C})$ and

$$P(\tau) = \prod_\alpha \left(\frac{\epsilon_{\rm C}}{\pi k_{\rm B}T_\alpha}\sinh\left(\frac{\pi|\tau|k_{\rm B}T_\alpha}{\hbar}\right)\right)^{-2K_\alpha}. \tag{8.47}$$

We note that $\chi(t)$ takes the same form of the spin-boson model at the Toulouse point with the only differnce that the bath-induced (dipole or intra-blip, see App. E.9) interactions involving the two baths enter $P(\tau)$ in factorized form. Indeed, in the limit $K_{\rm L} = K_{\rm R} = 1/4$ and $\Delta T = 0$ we recover the susceptibility of the Kondo problem at the Toulouse point. Under these conditions the heat current trivially vanishes. In the following we will evaluate heat rectification considering asymmetric couplings with the two baths under the"overal" strong coupling condition $K_{\rm L}+K_{\rm R} = 1/2$. All possible heat transfer processes are exactly included. To this end the heat current Eq. (8.15) with (8.46) is more conveniently written as

$$J = \frac{1}{\hbar}\frac{K_{\rm L}K_{\rm R}}{K_{\rm L}+K_{\rm R}}\,{\rm Im}\int_{-\infty}^{+\infty} dt\,\chi(t)F(-t), \tag{8.48}$$

where

$$F(-t) = (k_{\rm B}T_{\rm R})^3\psi^{(2)}\left(1+\frac{k_{\rm B}T_{\rm R}}{\epsilon_{\rm C}}\left(1-i\frac{\epsilon_{\rm C}\,t}{\hbar}\right)\right) - (k_{\rm B}T_{\rm L})^3\psi^{(2)}\left(1+\frac{k_{\rm B}T_{\rm L}}{\epsilon_{\rm C}}\left(1-i\frac{\epsilon_{\rm C}\,t}{\hbar}\right)\right) \tag{8.49}$$

and $\psi^{(2)}(z)$ denotes the second derivative of the digamma function.

8.4.4 Rectification beyond the weak-coupling regime

In this section we show that various general properties and bounds derived in Sec. 8.3 can be overcome, allowing the system to exibit stronger rectification than in the weak-coupling regime. We will also be able to identify the effect of higher order coherent transport on rectification. We will consider Ohmic spectral density, as in Eq. (8.11), for both baths.

In Fig. 8.3a we plot R as a function of $K_{\rm L}$ in the XX and YX case comparing the NEGF calculation, the ME calculation including cotunneling effects [ME(cot)] and the ME calculation in the weak coupling regime [ME(seq)]. The coupling constant $K_{\rm R} = 0.005$ and

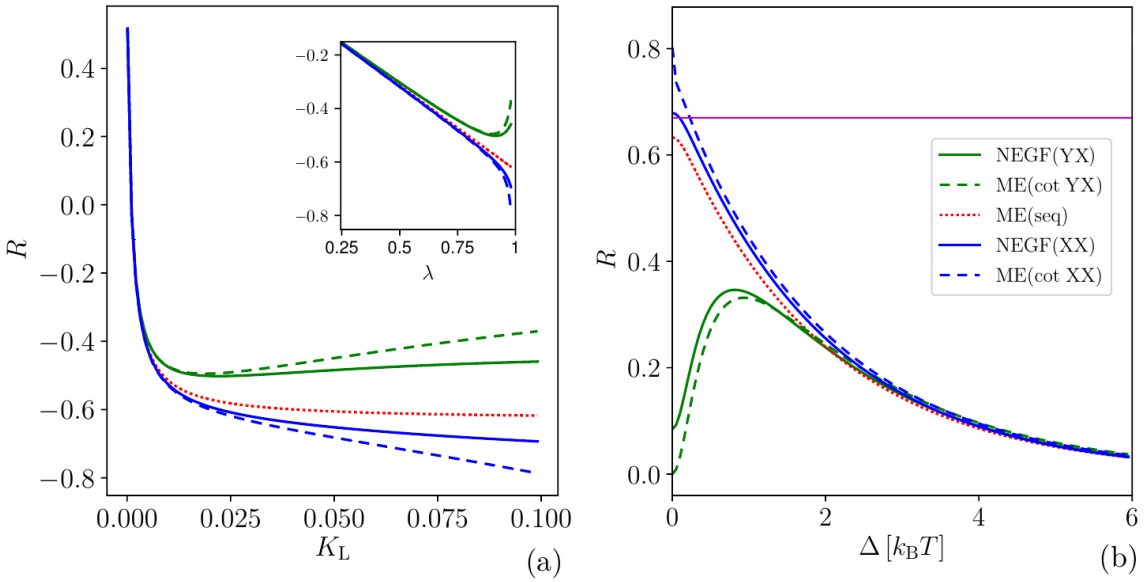

FIGURE 8.3: R, computed with the three methods described in the legend, as a function of K_L (a) and as a function of the gap Δ (b) both for the XX and YX couplings; the ME(seq) case is the same for both couplings. We denote with "NEGF" the calculations performed with the non-equilibrium Green's function method described in Sec. 8.4.2, with "ME(cot)" those performed with the master equation which includes co-tunneling described in Sec. 8.4.1, and with "ME(seq)" the calculations performed in the weak coupling limit as described in Sec. 8.3. We neglect the Lamb shift in this plot. The inset in (a) shows the same points plotted as a function of λ for $\lambda \in [0.25, 1]$. In panel (a), the parameters are $K_R = 0.001$, $\Delta = 0.8 k_B T$, $\epsilon_C = 10 k_B T$ and $\Delta T/T = 8/5$. In panel (b), the parameters are $K_L = 0.006$, $K_R = 0.03$, $\epsilon_C = 10 k_B T$ and $\Delta T/T = 1.9$.

the temperatures are fixed. First we notice that, for small values of K_L, i.e. in the weak coupling limit, all three curves coincide, as expected. As K_L increases, we notice that the NEGF and ME(cot) curves nicely agree up to $K_L \approx 0.025$, and then we see some deviations. Next, we notice that the rectification using NEGF and ME(cot) method is *different* in the XX and YX cases, whereas it is the same using the ME(seq) method. Indeed, in Sec. 8.3.3 we showed that, in the weak coupling regime, rectification only depends on the angle between the qubit (σ_z) and the coupling term. Higher order coherent processes, instead, are able to distinguish these different couplings, as they produce different interference effects [see the $\pm$ in Eq. (8.36)]. Next, we notice that rectification is *enhanced* in the XX coupling case thanks to higher order processes, while it is suppressed in the YX case (we will explain this behavior describing Fig. 8.3b). In the inset of Fig. 8.3a we plot the same points as a function of the asymmetry coefficient $\lambda = (K_L - K_R)/(K_L + K_R)$ [see Eq. (8.21)]. We recall that, in the weak coupling regime, we proved that R is linear in λ (see Sec. 8.3.1). Indeed, for small values of λ, the behavior is linear. Interestingly, the behaviour becomes non-linear for larger values of λ, which correspond to larger values of the coupling constant K_L. This non-linearity is yet another signature of higher order coherent processes.

In Fig. 8.3b we plot R, computed with the three methods described above, as a function of Δ for fixed values of the temperatures and of the coupling constants. There are many interesting facts to notice. First, the coupling constants are not very small, so the NEGF and ME(cot) methods, which qualitatively agree with each other, provide visible corrections to the ME(seq) calculations. As we noticed also in Fig. 8.3a, rectification is stronger in the

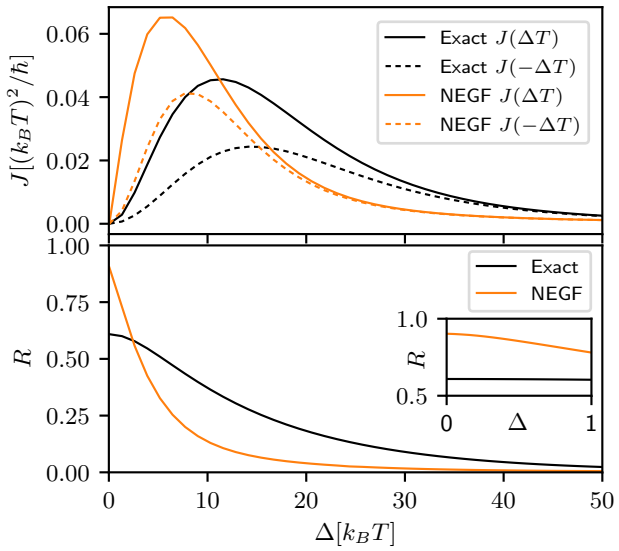

FIGURE 8.4: Comparison of thermal current and thermal rectification in the strong coupling regime computed using the two methods described in the legend, as a function of qubit gap Δ. The NEGF calculation includes the Lamb shift. The parameters are $K_{\mathrm{L}} = 0.01$, $K_{\mathrm{R}} = 0.49$, $\epsilon_{\mathrm{C}} = 100 k_{\mathrm{B}}T$ and $\Delta T/T = 1.9$.

XX case (blue curves), while it is weaker in the YX case (green curves) as compared to the ME(seq) calculations for $\Delta \leq 2k_{\mathrm{B}}T$. For $\Delta > 2k_{\mathrm{B}}T$, all the methods predict similar values of R. Interestingly, the value of R computed using the NEGF and ME(cot) methods in the XX case shows a violation of the general weak-coupling bound of Eq. (8.23), i.e. we find that $|R| > |\lambda| = 0.67$ (denoted with a horizontal magneta line in Fig. 8.3b) for small values of Δ. On the other hand, in the YX coupling case we notice that coherent processes decrease rectification. This different behavior is due to the following fact: the heat currents computed in the ME(seq) case tend to zero as $\Delta/(k_{\mathrm{B}}T) \to 0$ (see App. E.2 for details). In the XX case, the two terms inside the square modulus of Eq. (8.36) cancel each other, hence also the co-tunneling contribution vanishes; however, in the YX case, it remains finite. Therefore, in the $\Delta \to 0$ limit, sequential tunneling dominates over co-tunneling in the XX case, thus enhancing rectification (as discussed in Sec. 8.4.1). On the contrary, in the YX case co-tunneling dominates over sequential tunneling, thus suppressing rectification. This observation justifies also the large deviation between the ME(seq) curve and the other ones observed in the YX case for small Δ. At last, we notice that in the YX case, thanks to higher order processes, the NEGF and ME(cot) are non-monotonous with respect to Δ (as discussed in Sec. 8.3.1, R is monotonous in Δ in the weak coupling regime).

In Fig. 8.4 we plot the heat current (upper panel) and the rectification coefficient (lower panel) as a function of the qubit gap Δ fixing all other parameters as described in the caption. We compare the analytic results obtained in the XX case using the NEGF method including the Lamb-shift (see Sec. 8.4.2) with the exact calculation obtained using the Feynman-Vernon path integral approach (see Sec. 8.4.3). In doing so, we are constrained to fixing the coupling strength as $K_{\mathrm{L}} + K_{\mathrm{R}} = 1/2$. We observe that the exact and NEGF calculations for the heat current give quantitatively different results, i.e. the NEGF method tends to overestimate the magnitude of the heat current for values of $\Delta/(k_{\mathrm{B}}T) \lesssim 10$, while it underestimates the heat

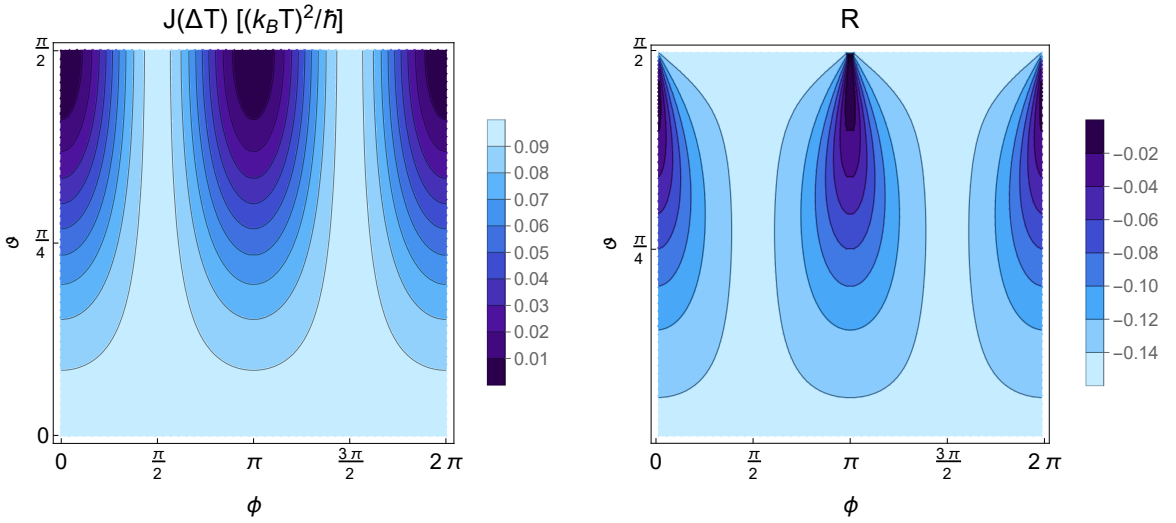

(a) (b)

FIGURE 8.5: Contour plot of $J(\Delta T)$, (a), and of R, (b), as a function of θ and ϕ. The parameters are: $\epsilon_C = 80 k_B T$, $K_L = K_R = 0.06$ and $\Delta T/T = 1.9$.

current for larger values of $\Delta/(k_B T)$. However, qualitatively there is a reasonable agreement between the two calculations. This is in fact surprising: the NEGF approach is perturbative in the coupling strength. Therefore, strictly speaking, it is valid only for $K_L + K_R \ll 1$, while $K_L + K_R = 1/2$ (strong coupling regime). On the other hand, the rectification coefficient is very different for small values of $\Delta/(k_B T)$: the NEGF approach strongly overestimates the rectification. However, this behavior is inverted upon increasing the qubit gap. Then, for large enough values of Δ, the two methods predict a more similar rectification coefficient, with the exact calculation predicting higher thermal rectification compared to the NEGF calculations. At last, for even larger values of Δ, the rectification coefficient predicted by both methods tends to 1, i.e. no rectification.

8.4.5 Rectification with arbitrary σ coupling

In this section we study the impact on rectification of more general couplings respect to the XX and YX cases using the NEGF formalism previously described (see App. E.8 for details about the calculation). We focus on the $\Delta/(k_B T) \to 0$ limit where heat transport is entirely due to higher order coherent processes. This is due to the fact that the heat current, computed in the weak coupling regime, tends to zero as $\Delta/(k_B T) \to 0$ (see App. E.2). We therefore consider the coupling Hamiltonian, given in Eq. (8.8), with an arbitrary coupling to the left bath, i.e. arbitrary $\theta_L = \theta$ and $\phi_L = \phi$, but with fixed σ_x coupling to the right lead, i.e. $\theta_R = \pi/2$ and $\phi_R = 0$. The XX and YX cases, considered in the previous sections, can be recovered respectively by setting $\theta = \pi/2$ and $\phi = 0$, or $\theta = \pi/2$ and $\phi = \pi/2$. Notice that, by considering a coupling with $\theta \neq \pi/2$, we are including also a σ_z coupling to the left lead. We recall that, in the weak coupling regime, the σ_z coupling does not contribute to the heat current. In order to isolate the impact on rectification of different spin couplings, we consider the case of identical spectral densities for the two baths, i.e. $\gamma_L(\epsilon) = \gamma_R(\epsilon)$. Therefore, the only asymmetry in the coupling, which can give rise to rectification, is given by the different directions described by $\hat{n}_L$ and $\hat{n}_R$.

In Fig. 8.5a we show a contour plot of the heat current $J(\Delta T)$, at fixed temperatures and for equal Ohmic spectral densities [i.e. $K_{\rm L} = K_{\rm R}$, see Eq. (8.11)], as a function of the two angles θ and ϕ in the small gap limit, i.e. for $\Delta/(k_{\rm B}T) \to 0$. For simplicity, we neglected the Lamb shift. Strikingly, the heat current is *maximum* when the left lead is coupled through σ_z, i.e. for $\theta = 0$ (lower part of Fig. 8.5a). This is surprising for two reasons: first, in the weak coupling limit the heat current at $\theta = 0$ would be null even for finite values of Δ, since σ_z does not contribute to the heat currents; second, regardless of the coupling strength, a single bath coupled to S through σ_z cannot transfer heat to the system, since the Hamiltonian of S would commute with the total Hamiltonian (and thus it would be a conserved quantity). In this case, the σ_z coupling would only produce dephasing in the qubit state. We can therefore qualitatively describe transport in this regime as a direct transfer of heat from one bath to the other. As θ increases, and therefore as the σ_z component decreases, the heat current decreases monotonously, to the point that it is null in the XX case ($\phi = n\pi$), while it remain constant in the YX case (along $\phi = \pi/2 + n\pi$).

Interestingly, also the rectification coefficients roughly follows a similar trend, i.e. it is maximum where also the heat currents are maximum. This can be seen in Fig. 8.5b, where R is contour-plotted as a function of θ and ϕ for the same parameters as in Fig. 8.5a. Indeed, R is maximum for $\theta = 0$, i.e. when the left lead is coupled only through σ_z. As θ increases, R decreases monotonically along $\phi = n\pi$, just as the heat current itself. However, it remain constant along $\phi = \pi/2 + n\pi$, while for intermediate values of ϕ it displays a non-monotonic behavior.

We can therefore conclude that the optimal operational points in the $\Delta/(k_{\rm B}T) \to 0$ limit are the YX and the ZX coupling cases. These couplings simultaneously maximize the magnitude of the heat current and of the rectification coefficient. We emphasize that the heat current, which is solely due to coherent quantum processes, behaves in the opposite way respect to what would be expected from weak coupling calculations (the heat currents should be zero both because $\Delta = 0$ and because σ_z does not contribute to the heat current).

8.5 Summary

In this chapter, we studied thermal rectification across a qubit. First, we derived general properties and bounds that emerge in the weak coupling regime. Then, employing various techniques such as the non-equilibrium Green functions, the master equation including co-tunneling rates, and an exact calculation based on Feynman-Vernon path integral approach, we analyzed rectification beyond the weak coupling regime. We found that various weak-coupling bounds can be violated, allowing the system to exhibit stronger rectification. Some of these violations provide simple and clear signatures of coherent tunneling effects beyond the weak coupling regime.

9

Maximum power and corresponding efficiency for two-level heat engines and refrigerators: optimality of fast cycles

Two thermal baths in contact through a working fluid that can be externally driven represent the prototypical setup that has been studied from the origin of thermodynamics up to our days. The energy balance can be described in terms of three quantities: the work extracted from the fluid and the heat exchanged with the hot/cold baths. The fundamental limitations to the inter-conversion of heat into work stem from the concept of irreversibility and are at the core of the second law of thermodynamics. A working medium in contact with two baths at different temperatures is also significant from a practical point of view, since it is the paradigm behind the following specific machines: the heat engine, the refrigerator [11, 200, 313, 314], the thermal accelerator [315], and the heater [315].

Quantum thermodynamics [17, 20, 316] has emerged both as a field of fundamental interest, and as a potential candidate to improve the performance of thermal machines [18, 42, 124, 171, 201, 317–327]. The optimal performance of these systems has been discussed within several frameworks and operational assumptions, ranging from low-dissipation and slow driving regimes[38, 57–60], to shortcuts to adiabaticity approaches [47–50], to endoreversible engines [328, 329]. Several techniques have been developed for the optimal control of two-level systems for achieving a variety of goals: from optimizing the speed [330–332], to generating efficient quantum gates [333, 334], to controlling dissipation [335, 336], and to optimizing thermodynamic performances [51–56].

The aim of the present chapter is to find the optimal strategy to deliver maximum power in all four previously mentioned machines. We perform this optimization in the simplest, yet non trivial, model of a machine which, in the spirit of quantum thermodynamics, is based on a two-level quantum system as working fluid. As opposed to current literature, we explicitly carry out the power maximization without making any assumptions on the operational regime, nor on the speed of the control parameters, nor on the specific coupling between the working fluid and the bath. We find that, if the evolution of the working

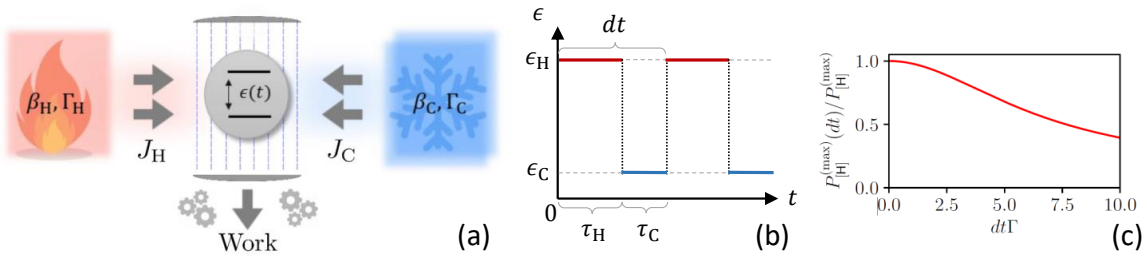

FIGURE 9.1: (a) Schematic representation of the setup. S (grey circle) is externally driven by modulating the level spacing $\epsilon(t)$ and coupled with the hot bath H (red box) and the cold bath C (blue box) at inverse temperatures β_H and β_C. J_H and J_C are the heat currents leaving the baths, while Γ_H and Γ_C are the associated dissipation rates. Depending on the controls the system can operates either as an heat engine (mode [E]), as a refrigerator (mode [R]), as a thermal accelerator (mode [A]), or as a heater (mode [H]). (b) Representation of the optimal protocol that maximizes the power in the limit $dt \to 0$; and (c) power in mode [H] for finite values of $dt\Gamma$ normalized to the maximum power. We assume a single bath coupled to S characterized by a dissipation rate $\Gamma(\epsilon)$ such that $\Gamma(\epsilon) = \Gamma(-\epsilon)$. In this case, the maximization in Eq. (9.8) yields $\epsilon^*_H = -\epsilon^*_C$, and Γ in (c) denotes $\Gamma(\epsilon^*_H)$.

medium is governed by a Markovian master equation [24, 25], the optimal driving takes a universal form: an infinitesimal Otto-cycle-like structure in which the control parameters must be varied between two extremal values as fast as possible. This is our first main results, described in Eq. (9.8). Surprisingly, the optimal solution is achieved in the "fast-driving" regime, i.e. when the driving frequency is faster than the typical dissipation rate induced by the baths, which has received little attention in literature [337–339]. Notice that the qubit-based heat engine studied in Sec. 3.2.2 is operated in the oppositive regime, i.e. in the infinetly slow regime.

By applying our optimal protocol to heat engines and refrigerators, we find new theoretical bounds on the efficiency at maximum power (EMP). Many upper limits to the EMP, strictly smaller than Carnot's efficiency, have been derived in literature, such as the Curzon-Ahlborn and Schmiedl-Seifert efficiencies. These are discussed in Sec. 3.2. In particular, the Schmiedl-Seifert efficiency has been proven to be universal in cyclic Brownian heat engines [39] and for any driven system operating in the slow-driving regime [38]. By studying the efficiency of our system at the ultimate power, i.e. in the fast-driving regime, we prove that there is no fundamental upper bound to the EMP. Indeed, we show that the Carnot efficiency is reachable *at maximum power* through a suitable engineering of the bath couplings. This is our second main results, illustrated in Figs. 9.2b, 9.2c and 9.3. In view of experimental implementations, we assess the impact of finite-time effects on our optimal protocol, finding that the maximum power does not decrease much if the external driving is not much slower than the typical dissipation rate induced by the baths [266, 274]. Furthermore, we apply our optimal protocol to two experimentally accessible models, namely photonic baths coupled to a qubit [18, 19, 27, 46, 340] and electronic leads coupled to a quantum dot [42, 112, 124, 266, 274, 341].

9.1 Maximum power

The setup we consider consists of a two-level quantum system S with energy gap $\epsilon(t)$ that can be externally modulated [1]. As schematically shown in Fig. 9.1a, the system is placed in thermal contact with two reservoirs, the hot bath H at inverse temperature $\beta_{\rm H}$ and the cold bath C at inverse temperature $\beta_{\rm C}$, respectively characterized by coupling constants $\lambda_{\rm H}(t)$ and $\lambda_{\rm C}(t)$ that can be modulated in time. The system can operate in four different modes: i) the heat engine mode [E], where S is used to produce work by extracting heat from H while donating it to C; ii) the refrigerator mode [R], where S is used to extract heat from C; iii) the thermal accelerator mode [A], where S operates to move as much heat as possible to C; iv) the heater mode [H], where we simply use S to deliver as much heat as possible to both H and C. Assuming cyclic modulation of the controls (i.e. of $\epsilon(t)$, $\lambda_{\rm H}(t)$ and $\lambda_{\rm C}(t)$) we are interested in maximizing the corresponding averaged output powers of each operating mode, i.e. the quantities

$$\begin{aligned} P_{[\rm E]} &= \langle J_{\rm H}\rangle + \langle J_{\rm C}\rangle\,, & P_{[\rm R]} &= \langle J_{\rm C}\rangle\,, \\ P_{[\rm A]} &= -\langle J_{\rm C}\rangle\,, & P_{[\rm H]} &= -\langle J_{\rm H}\rangle - \langle J_{\rm C}\rangle\,, \end{aligned} \tag{9.1}$$

where $J_{\rm H}$ and $J_{\rm C}$ are the instantaneous heat fluxes entering the hot and cold reservoirs respectively, and where the symbol $\langle\cdots\rangle$ stands for temporal average over a modulation cycle of the controls. To tackle the problem we adopt a Markovian Master Equation (MME) approach [27], discussed in Chap. 2, namely we write

$$\frac{d}{dt}\rho(t) = -\frac{i}{\hbar}[H_{\rm S}(\epsilon(t)),\rho(t)] + \sum_{\alpha={\rm H,C}} D_\alpha\left[\rho\right], \tag{9.2}$$

where ρ is the density matrix of the two-level system at time t, $H_{\rm S}(\epsilon(t)) := \epsilon(t)\sigma_+\sigma_-$ its local Hamiltonian, and

$$D_\alpha\left[\cdots\right] := \sum_{i=\pm}\lambda_\alpha(t)\Gamma_\alpha^{(i)}(\epsilon(t))(\sigma_i\cdots\sigma_i^\dagger - \frac{1}{2}\{\sigma_i^\dagger\sigma_i,\cdots\}) \tag{9.3}$$

is the Gorini-Kossakowski-Sudarshan-Lindblad dissipator [24, 25] associated with the bath $\alpha = {\rm H,C}$. We have denoted with σ_+ and σ_- the raising and lowering operators of S. D_α is characterized by dissipation rates $\Gamma_\alpha^{(i=\pm)}(\epsilon)$ and by the dimensionless coupling constant $\lambda_\alpha(t) \in [0,1]$ that plays the role of a "switch" control parameter. It is worth noticing that, since $[H_{\rm S}(\epsilon(t)), H_{\rm S}(\epsilon(t'))] = 0$, the MME we employ is valid also in the fast-driving regime, provided that the correlation time of the bath is the smallest timescale in our problem [45]. Therefore, the fast-driving regime is characterized by a control frequency which is faster than the typical dissipation rate, but slower than the inverse correlation time of the bath. Furthermore, we assume that the Hamiltonain $H_{\rm S,B}$, describing the system-bath interaction, is such that its expectation value on the Gibbs state of the baths is zero (this is true, for example, for tunnel-like Hamiltonians, where the number of creation/annihilation operators of the bath entering $H_{\rm S,B}$ is odd). Such assumption guarantees that no work is necessary to switch on and off the coupling between the system and the baths.

Without assigning any specific value to the dissipation rates, we only require them to obey the detailed balance equation $\Gamma_\alpha^{(+)}(\epsilon)/\Gamma_\alpha^{(-)}(\epsilon) = e^{-\beta_\alpha\epsilon}$. This ensures that, at constant level

[1] In principle, one can consider a broader family of controls including the possibility of rotating the Hamiltonian eigenvectors; however there is evidence that such an additional freedom does not help in two-level systems [54, 55]

spacing ϵ, the system S will evolve into a thermal Gibbs state characterized by an excitation probability

$$p_{\rm eq}^{(\alpha)}(\epsilon) := \frac{\Gamma_\alpha^{(+)}(\epsilon)}{\Gamma_\alpha^{(+)}(\epsilon)+\Gamma_\alpha^{(-)}(\epsilon)} = \frac{1}{1+e^{\beta_\alpha \epsilon}} \tag{9.4}$$

when in contact only with heat bath α. For simplicity, we consider the system to be coupled to one heat bath at the time, i.e. we assume that $\lambda_{\rm H}(t)+\lambda_{\rm C}(t)=1$, and that $\lambda_\alpha(t)$ can take the values 0 or 1. As we shall see in the following, this constraint, as well as the possibility of controlling the coupling constants $\lambda_\alpha(t)$, is not fundamental to derive our results, at least for those cases where the effective dissipation rate

$$\Gamma_\alpha(\epsilon) := \Gamma_\alpha^{(+)}(\epsilon)+\Gamma_\alpha^{(-)}(\epsilon) \tag{9.5}$$

of each bath is sufficiently peaked around distinct values. The instantaneous heat flux leaving the thermal bath α can now be expressed as [46]

$$J_\alpha(t) = {\rm Tr}[H_{\rm S}(\epsilon(t))D_\alpha[\rho(t)]] = -\epsilon(t)\lambda_\alpha(t)\Gamma_\alpha[\epsilon(t)](p(t)-p_{\rm eq}^{(\alpha)}[\epsilon(t)]), \tag{9.6}$$

where $p(t) := {\rm tr}[\sigma_+\sigma_-\rho(t)]$ is the probability of finding S in the excited state of $H_{\rm S}(\epsilon(t))$ at time t which obeys the following differential equation

$$\frac{d}{dt}p(t) = -\sum_{\alpha={\rm H,C}} \lambda_\alpha(t)\Gamma_\alpha[\epsilon(t)](p(t)-p_{\rm eq}^{(\alpha)}[\epsilon(t)]), \tag{9.7}$$

according to the MME specified above. By explicit integration of (9.7) we can hence transform all the terms in Eq. (9.1) into functionals of the controls which can then be optimized with respect to all possible choices of the latter.

As shown in App. F.1, we find that the protocols which maximize the average power of a fixed physical setup, i.e. at fixed dissipation rates, are cycles performed in the fast-driving regime, i.e. when the driving frequency is faster than the typical dissipation rate. More precisely, the optimal cycle is such that $\epsilon(t)$ instantaneously jumps between two values $\epsilon_{\rm H}$ and $\epsilon_{\rm C}$, see Fig. 9.1b, while being in contact, respectively, only with the hot and cold bath for infinitesimal times $\tau_{\rm H}$ and $\tau_{\rm C}$ fulfilling the condition $\tau_{\rm H}/\tau_{\rm C} = \sqrt{\Gamma_{\rm C}(\epsilon_{\rm C})/\Gamma_{\rm H}(\epsilon_{\rm H})}$ [2]. As in Otto cycles considered in literature (see the extensive literature on this topic, e.g. [318, 320, 327, 342–344]), no heat is transferred during the jumps and no work is done while the system is in contact with the baths. The resulting maximum power averaged over one period can then be cast into the following compact expression (see App.F.2 for details)

$$P_{[\nu]}^{(\max)} = \max_{(\epsilon_{\rm H},\epsilon_{\rm C})\in\mathcal{C}} \frac{\Gamma_{\rm H}(\epsilon_{\rm H})\Gamma_{\rm C}(\epsilon_{\rm C})\left(p_{\rm eq}^{({\rm H})}(\epsilon_{\rm H})-p_{\rm eq}^{({\rm C})}(\epsilon_{\rm C})\right)}{\left(\sqrt{\Gamma_{\rm H}(\epsilon_{\rm H})}+\sqrt{\Gamma_{\rm C}(\epsilon_{\rm C})}\right)^2}\,\widetilde{\epsilon}_{[\nu]}, \tag{9.8}$$

where ν = E,R,A,H and the quantity $\widetilde{\epsilon}_{[\nu]}$ is given by $\widetilde{\epsilon}_{[E]} = \epsilon_{\rm H}-\epsilon_{\rm C}$, $\widetilde{\epsilon}_{[\rm R]} = -\epsilon_{\rm C}$, $\widetilde{\epsilon}_{[\rm A]} = \epsilon_{\rm C}$, and $\widetilde{\epsilon}_{[H]} = \epsilon_{\rm C}-\epsilon_{\rm H}$. In Eq. (9.8) $\mathcal{C}$ is the range over which the energy gap $\epsilon(t)$ of S is allowed to be varied according to the possible technical limitations associated with the specific implementation of the setup.

Equation (9.8), which stems from the optimality of the fast-driving regime, is the first main result of the present work. We emphasize that, as opposed to current literature, our

[2] This particular scaling has been found also in the optimization of endoreversible Carnot Heat engines [317].

closed expression for the maximum power holds for *any* dissipation rate function $\Gamma_{\mathrm{H/C}}(\epsilon)$. In the following we will apply our result to specific implementations which are relevant experimentally and compute their associated efficiencies at maximum power. In particular we shall consider the case of fermionic (F_n) and bosonic (B_n) baths with associated effective rates of the form

$$\Gamma_{\alpha}^{(\mathrm{F}_n)}(\epsilon) = k_\alpha \epsilon^n, \qquad \Gamma_{\alpha}^{(\mathrm{B}_n)}(\epsilon) = k_\alpha \epsilon^n \coth\left(\beta_\alpha \epsilon/2\right), \tag{9.9}$$

with $n \geq 0$ integer and with k_α being a coupling strength constant. The fermionic rate [the first of Eq. (9.9)] for instance can describe two electronic leads, with density of states depending on n, tunnel coupled to a single-level quantum-dot [69, 169, 341]; the bosonic one instead is applied in the study of two-level atoms in a dispersive quantum electromagnetic cavity [345].

9.2 Heat engine mode $[E]$

It is common belief that the efficiency of a heat engine (work extracted over heat absorbed from the hot bath H), driven at maximum power (EMP), should exhibit a finite gap with respect to the Carnot efficiency $\eta_{\mathrm{c}} := 1-\beta_{\mathrm{H}}/\beta_{\mathrm{C}}$. Indeed, this is corroborated by various results on EMP bounds, discussed in Sec. 3.2: the Curzon-Ahlborn EMP $\eta_{\mathrm{CA}} := 1-\sqrt{1-\eta_{\mathrm{c}}}$ emerges in various specific models[37, 39, 59], and it has been derived by general arguments from linear irreversible thermodynamics [36], while the Schmiedl-Seifert EMP $\eta_{\mathrm{SS}} := \eta_{\mathrm{c}}/(2-\eta_{\mathrm{c}})$ has been proven to be universal for any driven system operating in the slow-driving regime [38]. However, the completely out-of-equilibrium and optimal cycles associated with the values of $P_{[E]}^{(\max)}$ reported in Eq. (9.8), do not fulfill such assumptions. As a matter of fact, by choosing particular "energy filtering" dissipation rates $\Gamma_\alpha(\epsilon)$ (instead of the regular ones given e.g. in Eq. (9.9)), we can produce configurations which approach Carnot's efficiency with arbitrary precision while delivering maximum power, proving the lack of any fundamental bound to the EMP. Before discussing this highly not trivial effect, it is worth analyzing the performances associated with the baths models of Eq. (9.9).

We remind that the efficiency of an Otto cycle heat engine working between the internal energies ϵ_{C} and ϵ_{H} is given by $\eta = 1-\epsilon_{\mathrm{C}}/\epsilon_{\mathrm{H}}$. Accordingly, indicating with ϵ_{H}^* and ϵ_{C}^* the values of the gaps that lead to the maximum of the r.h.s term of Eq. (9.8), we write the EMP of our scheme as

$$\eta(P_{[\mathrm{E}]}^{(\max)}) = 1-\epsilon_{\mathrm{C}}^*/\epsilon_{\mathrm{H}}^* = 1-(1-\eta_{\mathrm{c}})\,\epsilon_{\mathrm{C}}^*\beta_{\mathrm{C}}/\epsilon_{\mathrm{H}}^*\beta_{\mathrm{H}}\,. \tag{9.10}$$

In Fig. 9.2a we report the value of $\eta(P_{[\mathrm{E}]}^{(\max)})$ obtained from (9.10) for the rates of Eq. (9.9) for $n=0,1$. By a direct comparison with η_{CA} and η_{SS}, one notices that while the second is always respected by our optimal protocol, the first is outperformed at least for the baths F_0 and B_0, confirming the findings of Refs. [54, 112, 169]. For small temperature differences between the baths, the EMP can be expanded as a power series in η_{c} of the form $a_1\eta_{\mathrm{c}}+a_2\eta_{\mathrm{c}}^2+\cdots$. It has been shown that $a_1=1/2$ is a universal property of low dissipation heat engines [38] and, in this context, $a_2=1/8$ is associated with symmetric dissipation coefficients. As explicitly discussed in App. F.3, we find that also our protocol delivers an efficiency at maximum power with a first order expansion term $a_1=1/2$ and with a second order correction $a_2=1/8$ achieved if we assume that the two leads are symmetric, i.e. $\Gamma_{\mathrm{H}}(\epsilon,\beta)=\Gamma_{\mathrm{C}}(\epsilon,\beta)$, or if the rates are constants.

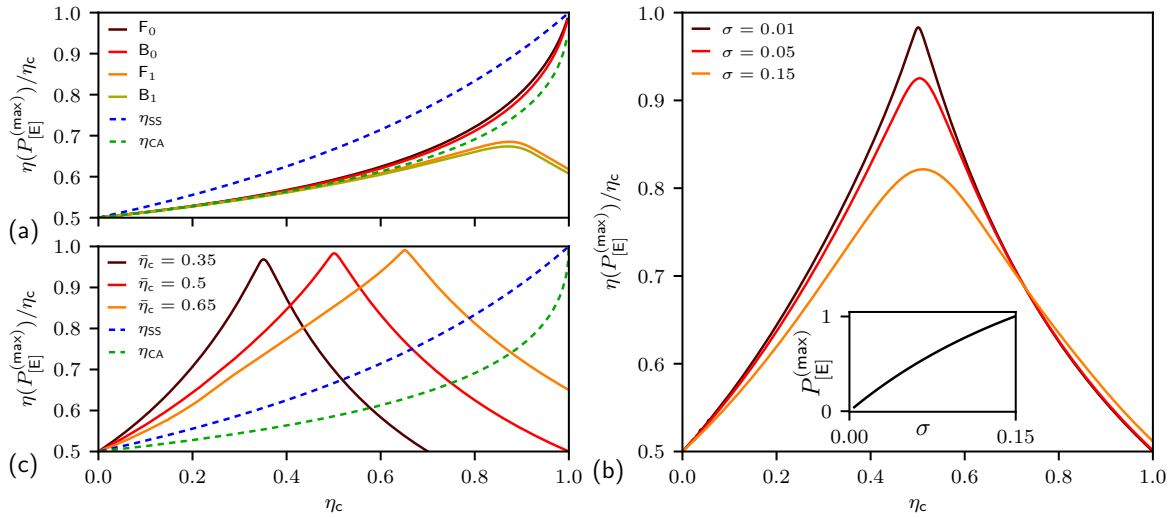

FIGURE 9.2: EMP for the heat engine mode [$\eta(P^{(\max)}_{[\mathrm{E}]})$ of Eq. (9.10)], normalized to η_c, as a function of η_c (varied by fixing β_H and sweeping over β_C). (a) shows $\eta(P^{(\max)}_{[\mathrm{E}]})$ for the fermionic models (F_0 and F_1) and the bosonic models (B_0 and B_1) of Eq. (9.9) together with the upper bounds η_{SS} [39] and η_{CA} [37]. Notice that as $\eta_c \to 0$ (small baths temperature difference), we have $\eta(P^{(\max)}_{[\mathrm{E}]}) \simeq \eta_c/2+\eta_c^2/8$ as expected. For $\eta_c \to 1$, instead, the value of $\eta(P^{\max}_{[\mathrm{E}]})$ for the models F_1 and B_1 saturates to a finite fraction of η_c, while the F_0 and B_0 models reach Carnot efficiency. The Fermionic model displays a slightly larger $\eta(P^{(\max)}_{[\mathrm{E}]})$ than the corresponding bosonic model. In all models we consider symmetric leads, i.e. $k_H = k_C$. Note that $\eta(P^{(\max)}_{[\mathrm{E}]})$ does not depend on the value of k_α. (b) and (c) show $\eta(P^{(\max)}_{[\mathrm{E}]})$ computed using Lorentzian filtering rates $\Gamma_\alpha(\epsilon_\alpha) = \gamma\sigma^2/(\sigma^2+(\epsilon_\alpha-\bar{\epsilon}_\alpha)^2)$ with γ, σ and $\bar{\epsilon}_\alpha$ positive constants (systems with multiple quantum-dots in series [346] e.g. exhibit such dependence). In both panels we fix $\bar{\epsilon}_C = 1$. (b): we set $\bar{\epsilon}_H = 2\bar{\epsilon}_C$ such that we expect to approach η_c at $\bar{\eta}_c = 1/2$. Indeed, as σ decreases, $\eta(P^{(\max)}_{[\mathrm{E}]})/\eta_c$ approaches one at $\bar{\eta}_c = 1/2$. Conversely, the corresponding maximum power decreases: in the inset, where $P^{(\max)}_{[\mathrm{E}]}$ is plotted as a function of σ for $\bar{\eta}_c = 1/2$, we see that the maximum power becomes vanishingly small for $\sigma \to 0$. The power is normalized to the its value for $\sigma = 0.15$, where $P^{(\max)}_{[\mathrm{E}]} = 0.0044\,\gamma\beta_H^{-1}$. (c): at fixed $\sigma = 0.01$, we show that the EMP can approach η_c at any bath temperature. We choose $\bar{\epsilon}_H/\bar{\epsilon}_C = 1/0.65$, $1/0.5$ and $1/0.35$, corresponding to $\bar{\eta}_c = 0.35$, 0.5 and 0.65. Energies are expressed in units of $1/\beta_H$, and the EMP does not depend on γ.

We now turn to the possibility of having $\eta(P^{(\max)}_{[\mathrm{E}]})$ arbitrarily close to η_c. By a close inspection of the second identity of Eq. (9.10) we notice that one can have $\eta(P^{(\max)}_{[\mathrm{E}]}) \simeq \eta_c$ for all those models where the maximum power (see Eq. (9.8)) is obtained for values of the gaps fulfilling the condition $\epsilon^*_C\beta_C \approx \epsilon^*_H\beta_H$. Consider hence a scenario where the rates $\Gamma_\alpha(\epsilon_\alpha)$ are such that the power is vanishingly small for all values of ϵ_α except for a windows of width σ around a given value $\bar{\epsilon}_\alpha$, a configuration that can be used to eliminate the presence of the activation controls $\lambda_\alpha(t)$ from the problem. Under the assumption of small enough σ, we expect the maximization in Eq. (9.8) to yield $\beta_C\epsilon^*_C \approx \beta_H\epsilon^*_H$ when the inverse temperature ratio is $\beta_C/\beta_H \approx \bar{\epsilon}_H/\bar{\epsilon}_C$, so that $\eta(P^{(\max)}_{[\mathrm{E}]}) \approx \eta_c$. This is indeed evident from Fig. 9.2b and 9.2c, where we report the value $\eta(P^{(\max)}_{[\mathrm{E}]})$ as a function of η_c (which represents the temperature of the baths) for rates having a Lorentzian shape dependence: by decreasing σ, the EMP approaches Carnot's efficiency at $\bar{\eta}_c := 1-\bar{\epsilon}_C/\bar{\epsilon}_H = 1/2$ (Fig. 9.2b), while by tuning the position of the peak of the Lorentzian rates, the EMP can approach Carnot's efficiency

at any given bath temperature configuration $\bar{\eta}_c$ (Fig. 9.2c). We emphasize that even our system with Lorentzian shaped rates would exhibit an EMP bounded by η_{SS} if operated in the slow-driving regime. The possibility of reaching Carnot's efficiency at maximum power is thus a characteristic which emerges thanks to the fast-driving regime. Conversely, as σ decreases and $\eta(P^{(\max)}_{[E]}) \to \eta_c$, the corresponding maximum power tends to zero (see the inset of Fig. 9.2b where the maximum power, at $\bar{\eta}_c = 1/2$, is plotted as a function of σ).

9.3 Refrigerator mode [R]

The efficiency of a refrigerator is quantified by the coefficient of performance (COP), i.e. the ratio between the heat extracted from the cold bath and the work done on the system. For an Otto-cylce the COP is given by $\mathrm{C} = \epsilon_C/(\epsilon_H - \epsilon_C)$ which, by replacing the values ϵ^*_C, ϵ^*_H that lead to the maximum $P^{(\max)}_{[R]}$ of Eq. (9.8), yields an associated COP at maximum power (CMP) equal to

$$\mathrm{C}(P^{\max}_{[R]}) = \frac{\epsilon^*_C}{(\epsilon^*_H - \epsilon^*_C)} = \left[\frac{\beta_H \epsilon^*_H}{\beta_C \epsilon^*_C}(1/\mathrm{C}_c + 1) - 1\right]^{-1} \tag{9.11}$$

where $\mathrm{C}_c := \beta_C^{-1}/(\beta_H^{-1} - \beta_C^{-1})$ is the maximum COP dictated by the second law. Remarkably, as in the heat engine case, we can produce configurations which approach C_c with arbitrary precision while delivering maximum power exploiting the same "energy filtering" dissipation rates. Before discussing this effect we present some universal properties of the CMP and we analyze the performance of the baths models of Eq. (9.9).

Assuming that the rates depend on the energy and on the temperature through the product $\beta\epsilon$, i.e. $\Gamma_\alpha(\epsilon_\alpha) = \Gamma_\alpha(\beta_\alpha \epsilon_\alpha)$ (e.g. the models (9.9) satisfy this hypothesis for $n = 0$, while they do not for $n > 0$), we find that the COP at maximum power reduces to the universal family of curves

$$\mathrm{C}(P^{\max}_{[R]}) = \mathrm{C}_0 \mathrm{C}_c/(1 + \mathrm{C}_0 + \mathrm{C}_c)\,, \tag{9.12}$$

where C_0 represents the COP when $\beta_H = \beta_C$. It thus follows that for these models the knowledge of $\mathrm{C}(P^{\max}_{[R]})$ at a single bath temperature configuration identifies unambiguously the COP for all other temperature differences. This feature is in contrast with the heat engine mode since, under the same hypothesis, the EMP at arbitrary temperatures depends on the details of the system.

Consider next the maximum power for the models described Eq. (9.9). We find that the maximization in Eq. (9.8) yields $\epsilon^*_H \to +\infty$ (and a finite value of ϵ^*_C), which implies

$$P^{(\max)}_{[R]} = c_n k_C/\beta_C^{n+1}\,, \qquad \mathrm{C}(P^{\max}_{[R]}) = 0\,, \tag{9.13}$$

where c_n is a dimensionless number which only depends on n for $n > 0$, while it is a function of k_H/k_C if $n = 0$ (see App. F.4 for details). The fact that the corresponding COP is equal to zero is a direct consequence of the divergent value of ϵ^*_H: physically it means that the maximum cooling power [which is finite, see Eq. (9.13)] is obtained by performing an infinite work, thus by releasing an infinite amount of heat into the hot bath. In the more realistic scenario where there are limitations on our control of the gaps, say $|\epsilon_\alpha| \leq \Delta$, the resulting value of $P^{(\max)}_{[R]}$ will be smaller than in Eq. (9.13) but the associated COP will be non-zero with a scaling that for large enough Δ goes as $\mathrm{C}(P^{\max}_{[R]}) \propto 1/(\beta_C \Delta)$ (see App. F.4 for details).

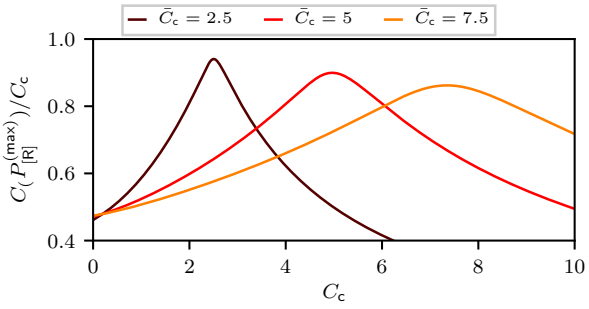

FIGURE 9.3: $C(P^{(\max)}_{[\mathrm{R}]})$ as a function of C_c (varied by fixing β_H and sweeping over β_C), computed using the same Lorentzian filtering rates discussed in Fig. 9.2. Fixing $\sigma = 0.01$ and $\bar{\epsilon}_\mathrm{C} = 1$ as in Fig. 9.2c, we choose $\bar{\epsilon}_\mathrm{H}/\bar{\epsilon}_\mathrm{C} = 7/5$, $6/5$ and $17/15$, corresponding to bath temperature configurations $\bar{C}_\mathrm{c} = 2.5$, 5 and 7.5. Energies are expressed in units of $1/\beta_\mathrm{H}$ and the CMP does not depend on γ.

Equation (9.13) shows that in all models the maximum cooling power only depends on the temperature $1/\beta_\mathrm{C}$ of the cold lead as a simple power law, and it vanishes as $1/\beta_\mathrm{C} \to 0$. Intuitively this makes sense since it is harder to refrigerate a colder bath and at $1/\beta_\mathrm{C} = 0$ there is no energy to extract from the bath. Furthermore, for $n > 0$ the properties of the hot bath (i.e. temperature and coupling constant) do not enter the $P^{(\max)}_{[\mathrm{R}]}$ formula.

We now return to the possibility of having the CMP arbitrarily close to $\mathrm{C_c}$. As in the heat engine case, from the second equality of Eq. (9.11) we see that, if the maximization in Eq. (9.8) yields values of ϵ^*_H and ϵ^*_C such that $\epsilon^*_\mathrm{H}\beta_\mathrm{H} \approx \epsilon^*_\mathrm{C}\beta_\mathrm{C}$, then $\mathrm{C}(P^{\max}_{[\mathrm{R}]}) \approx \mathrm{C_c}$. Indeed, as we can see in Fig. 9.3, we are able to have a CMP close to $\mathrm{C_c}$ at any desired temperature configuration $\bar{C}_\mathrm{c}$ by considering appropriately tuned Lorentzian rates (described in Fig. 9.2).

9.4 Thermal accelerator [A] and heater [H] modes

For the physical models described in Eq. (9.9) it turns out that in order to maximize the heat entering the cold bath, it is more convenient to release heat into both baths ($J_\mathrm{H}, J_\mathrm{C} < 0$), rather than extracting heat from the hot bath H and releasing it into the cold bath ($J_\mathrm{H} > 0, J_\mathrm{C} < 0$). The thermal accelerator mode [A] thus appears to be useless if we are just interested in maximizing the heat delivered to the cold bath. Accordingly, in the following we shall focus on the heater [H] mode only with a single bath (or equivalently with two baths at the same temperature). Assuming to have some physical limit $|\epsilon| \leq \Delta$ on the way we can control the gap, from Eq. (9.8) we find

$$P^{(\max)}_{[\mathrm{H}]} = \frac{k\Delta^{n+1}}{2} \times \begin{cases} \tanh\frac{\beta\Delta}{2}, & (\mathrm{F}_n \text{ model}), \\ 1, & (\mathrm{B}_n \text{ model}), \end{cases} \tag{9.14}$$

where k is the coupling constant appearing in Eq. (9.9). Equation (9.14) shows that the maximum power diverges as $\Delta \to +\infty$, the exponent of Δ depending on the density of states associated with the rates. Interestingly, the maximum power that can be delivered to the bath vanishes for high temperatures ($\beta\Delta \ll 1$) in the fermionic models, while it is finite and insensitive to temperature in the bosonic models. This is due to the peculiar rates of the bosonic models which diverge for $\beta\epsilon \ll 1$. On the contrary, for low temperatures ($\beta\Delta \gg 1$) both models yield the same value of $P^{(\max)}_{[\mathrm{H}]}$.

9.5 Finite-time corrections

The derivation of our main equation (9.8) was obtained under the implicit assumption that one could implement infinitesimal control cycles. Yet this hypothesis is not as crucial as it may appear. Indeed the feasibility of an infinitesimal Otto cycle relies on the ability of performing a very fast driving with respect to the typical time scales of the dynamics, a regime that can be achieved in several experimental setups [266, 274]. Furthermore by taking the square-wave protocol shown in Fig. 9.1b characterized by finite time intervals $\tau_{\rm H}$ and $\tau_{\rm C}$ still fulfilling the ratio $\tau_{\rm H}/\tau_{\rm C} = \sqrt{\Gamma_{\rm C}(\epsilon_{\rm C})/\Gamma_{\rm H}(\epsilon_{\rm H})}$, we find that, at leading order in dt, the maximum power $P^{(\max)}_{[\nu]}(dt)$ only different from the ideal value $P^{(\max)}_{[\nu]}$ of Eq. (9.8) by a quadratic correction, i.e. $P^{(\max)}_{[\nu]}(dt) \approx (1 - \widetilde{\Gamma}_{\rm H}\widetilde{\Gamma}_{\rm C}dt^2/12)P^{(\max)}_{[\nu]}$, where $\widetilde{\Gamma}_\alpha = (\widetilde{\Gamma}\Gamma_\alpha)^{1/2}$, $\widetilde{\Gamma} = \Gamma_{\rm H}\Gamma_{\rm C}/(\sqrt{\Gamma_{\rm H}}+\sqrt{\Gamma_{\rm C}})^2$, and all rates are computed for $\epsilon_{\rm H}$ and $\epsilon_{\rm C}$ that maximize Eq. (9.8). Besides, even in the regime where $\widetilde{\Gamma}_{\rm H}dt, \widetilde{\Gamma}_{\rm C}dt \gg 1$, $P^{(\max)}_{[\nu]}(dt)$ can be shown (see App. F.2 for details) to only decrease as $(\widetilde{\Gamma}_{\rm H}dt/2)^{-1} + (\widetilde{\Gamma}_{\rm C}dt/2)^{-1}$, implying that a considerable fraction of $P^{(\max)}_{[\nu]}$ can still be achieved also in this case (e.g. see Fig. 9.1c where we report the dt dependence of $P^{(\max)}_{[\rm H]}(dt)$ in the heater mode). On the contrary deviations from Eq. (9.8) due to finite time corrections in the quenches turns out to be more relevant. These last are first order in the ration between the duration of the quench (now different from 0) and the period of the protocol dt (see App. F.2 for details).

9.6 Summary

In this chapter we proved that a cycle switching between two extremal values in the fast-driving regime achieves universally the maximum power and the maximum cooling rate (respectively for a working medium operating as a heat engine or as a refrigerator), regardless of the specific dissipation rates, and we found a general expression for the external control during the cycle. The power advantage of modulating the control fields with rapid adiabatic transformations has been observed in the literature [338, 343, 347] for some specific model and this intuition is in agreement with our general results. We also found that the first coefficient of the expansion in power of $\eta_{\rm c}$ of the EMP is universal while the second one is linked to the symmetry of the dissipation coefficients. This chapter enlights that the features mentioned above are valid also strongly out of equilibrium, while already proven in low dissipation [341] and steady state [11] heat engines. If the bath spectral densities can be suitably tailored through energy filters (as for instance in [346]) our protocol allows to reach the Carnot bound at maximum power both operating as a heat engine or refrigerator, although at the cost of a vanishing power. This observation proves the lack of universal upper bounds to the efficiency at maximum power. Finally, we showed a new scaling for the COP of a bath with flat spectral density and we established a clear dependence of the EMP and the COP at maximum power on the spectral densities of the two thermal baths. The results were discussed in detail for some specific models, from flat bosonic and fermionic baths to environments with more complicated spectral densities, and finite driving speed effects were analyzed.

10

Maximum power heat engines and refrigerators in the fast-driving regime

The most important thermal machines that can be constructed utilizing two or more thermal baths are the heat engine and the refrigerator. As discussed in Chap. 3, these machines are mainly characterized by two figures of merit: the efficiency (or coefficient of performance COP for the refrigerator) and the extracted power (or cooling power). The optimal strategy to maximize the efficiency (and the COP) was identified already in the 19$^{\text{th}}$ century, and it is closely related to the second law of thermodynamics. As such it is characterized by a universal strategy: *infinitely slow* transformations, known as reversible transformations, must be performed [348]. On the other hand, the maximization of the extracted power or cooling power requires finite-time thermodynamics, which relies on a microscopic model to describe the evolution of the system. Therefore, the maximization of the power is usually regarded as a model-specific task, thus lacking a universal characterization [46, 320, 324, 341].

Conversely, the last decade has witnessed tremendous advances in experimental techniques which allow us to control quantum system and to operate them as thermodynamic machines [11, 18, 42, 51–53, 55, 56, 124, 169, 171, 200, 201, 274, 317–327, 337–339, 349, 350]. We are now at the point that it is possible to fabricate devices which behave as qubits or qutrits, and couple them to thermal baths [17–19, 347, 351, 352]. Typical experimental platforms, which range from trapped ions [12, 13], to electron spins associated with nitrogen-vacancy centers [14], to circuit quantum electrodynamics [15], to single-electron transistors [16], are all characterized by a set of "control parameters", e.g. electric or magnetic fields, that can be controlled in time by the experimentalist. The available control parameters may be subject to constraints, and may only grant us a partial control over the system dynamics. Given this framework, a fundamental question, which has not been tackled in general, is how to optimally drive the control parameters as to maximize the power of periodically driven classical or quantum thermal machines. This is the aim of the current chapter.

In general, this is a formidable task, as it requires us to solve the time-dependent dynamics of an open quantum system, coupled to thermal baths, and to perform a functional optimization over all available control parameters. Within the slow-driving regime [38, 57–60, 353], a universal strategy to maximize the power has been recently derived [354]. Beyond

this regime, common strategies to improve the power extracted from a quantum engine rely on performing fast and effectively adiabatic quantum operations through the Shortcut to Adiabaticity technique [47–50] or using Floquet engineering [355, 356]. The variety of frameworks considered in such analysis spans from the optimization of finite time Carnot cycles [59, 354, 357, 358] to Otto engines [318, 320, 327, 342–344, 359, 360] to endoreversible models [328, 329].

However within this *mare magnum* of frameworks and methods, in the context of systems described by Markovian dynamics, recent evidence suggests that the optimal strategy to extract maximum power may consist of varying the control parameters *infinitely fast* [39, 52, 55, 340, 361] (see also Chap. 9). This observation would imply a profound "duality" between efficiency and power: both would be maximized according to two opposite universal strategies (infinitely slow, or infinitely fast control speed).

In this chapter we discuss the optimization of thermal machines in the fast driving regime. This last, characterized by driving time scales which are much faster than the thermal relaxation, is introduced and discussed in the context of Markovian dynamics, see Sec. 3.2. Among all the possible control strategies and protocols, we provide a universal proof that the power is optimized by "generalized Otto cycles", i.e. by performing sudden variations of the control parameters among a finite number of fixed values. We denote these sudden variations as "quenches". The generality of the proof is guaranteed by the fact that it holds for *any* Hamiltonian describing the working fluid, the baths, and the coupling. Furthermore, it holds regardless of the number of baths, and regardless of the specific form of the time dependent dissipators in the Lindblad master equation, that can depend on an arbitrary number of external controls subject to arbitrary constraints. In addition, it holds for the maximization of any linear combination of the heat currents, which includes the extracted power of a heat engine, the cooling power of a refrigerator, the dissipated heat by a heater, and so on.

The optimal protocol, i.e. the generalized Otto cycle, is characterized by L time intervals, connected by quenches, in which the control parameters are held constant. We prove that, in general, $L \leq d^2$, where d is the dimension of the Hilbert space of the working fluid, while $L \leq d$ in the semi-classical case, when the Hamiltonian commutes with itself at different times. Our general bound on the number of quenches also poses a strict constraint on the number of thermal baths that are necessary to maximize the power.

In a large class of systems characterized by a "simple relaxation" model, we further prove that two time intervals are sufficient, recovering the standard Otto cycle. In such cases, assuming to have total control over the Hamiltonian of the working fluid, we are able to explicitly identify the optimal shape of the control, which corresponds to producing highly-degenerate many-body spectrum characterized by a single energy gap. On the one hand, this allows us to prove that the generation of coherence is detrimental for the maximization of the power. On the other, it allows us to compare the power of a heat engine and of a refrigerator, driven in the optimal way, using n non-interacting (NI) qubits, or n interacting (I) qubits. While the power of the NI qubits scales linearly in n, we find that the power in the I case displays a super-linear transient regime, yet it asymptotically scales linearly for any finite temperature difference ΔT. Interestingly, a heat engine in the I case operated at small temperature differences can deliver a power which is linear in ΔT in the thermodynamic limit of many qubits. On the other hand thermoelectric engines, slowly-driving arbitrary systems, and the NI case are all universally characterized by a maximum power which, to leading order, scales as ΔT^2. Therefore, the ratio between the power in the I case and all these other engines scales as $1/\Delta T$, signaling that there is a many-body advantage in the limit of small temperature differences enabled by the fast driving regime. Instead, for a refrigerator, we

find that the I case can at most deliver a power which is approximately 2.49 times larger than the NI case in the thermodynamic limit. This implies that, as opposed to the heat engine case, many-body working fluids do not provide a significant advantage in the construction of refrigerators at maximum power. It may thus be more convenient to construct a refrigerator based on many simple independent systems working in parallel.

We then apply our general results to a system characterized by a qutrit as working fluid. We numerically show that while the standard Otto cycle is optimal for typical thermalization models used to describe Bosonic and Fermionic baths, the generalized Otto cycle (characterized in this case by three quenches) outperforms the standard Otto cycle for a specific choice of the dissipation. This implies that our bound is, in general, tight. Furthermore, as opposed to the maximum efficiency, we show that the power can be enhanced by the presence of more than two thermal baths at different temperatures. At last, we provide numerical evidence supporting the hypothesis that the fast driving regime may indeed be optimal in this setup.

From an operational point of view, our results hugely simplify the numerical procedure of finding optimal protocols. Indeed, instead of having to optimize over all possible protocols, which are piece-wise continuous functions, using e.g. complex variational techniques [54], we only have to optimize a function of a fixed number of variables which scales at most quadratically with the dimensionality of the Hilbert space of the working fluid, linearly in the semi-classical case, and remains constant in a large class of models characterized by "simple relaxation".

In Sec. 10.1 we describe and characterize a thermal machine composed of a quantum system, denoted as the "working fluid", coupled to an arbitrary number of Markovian thermal baths. In Sec. 10.2 we introduce and characterize the fast driving regime for periodically driven systems. In Sec. 10.2.1 we prove the optimality of the generalized Otto cycle and we derive bounds on the number of time intervals. In Sec. 10.3 we restrict our analysis to a class of systems characterized by a "simple relaxation" model. Under this hypothesis, tighter bounds on the number of quenches can be obtained and, assuming total control over the working fluid, the full optimization of the power can be carried out. Using these results, we compare the performance of many non-interacting and interacting qubits optimally driven. In Sec. 10.4 we apply our general results to a thermal machine composed of a qutrit as working fluid. We numerically compute the optimal protocol for various dissipation models and we find that, for particular values of the dissipators, the maximum power is achieved by coupling the qutrit alternatively to three baths at different temperature. This protocol is shown to outperform the standard Otto cycle. In sec. 10.5 we provide a summary.

10.1 The model

As schematically depicted in Fig. 10.1, we consider a d-dimensional quantum system S (the working medium or working fluid of the model) that is weakly coupled to N thermal baths characterized by inverse temperatures β_α, for $\alpha = 1, \dots, N$. We assume S to be externally controlled through a set of time-dependent control parameters collectively represented by a real vector function

$$\vec{u}(t) : [0, \tau] \to \mathbb{D} \subseteq \mathbb{R}^M, \tag{10.1}$$

where τ is the total duration of the driving, and $\mathbb{D}$ represents the set of the allowed values the controls can assume, accounting for possible experimental constraints. In the following,

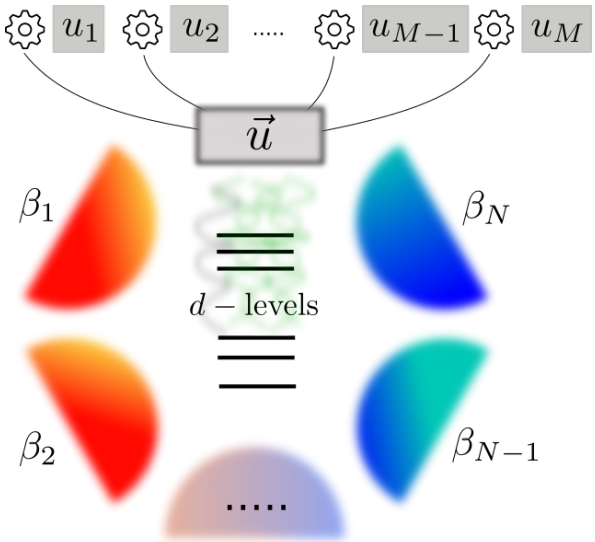

FIGURE 10.1: An arbitrary d-level system, controlled by M parameters $\vec{u}(t)$, is coupled to N thermals baths.

we denote the function $\vec{u}(t)$ as the protocol or the driving. In our analysis $\vec{u}(t)$ acts as a modulator both for the local Hamiltonian of the system $H_{\vec{u}(t)}$ (denoted with $H_{\rm S}$ in the rest of this thesis) as well as for the interactions with the thermal baths which, adopting the Gorini-Kossakowski-Sudarshan-Lindblad (GKSL) formalism [24, 25] (see Chap. 2), we describe in terms of the super-operator dissipators $D_{\alpha,\vec{u}(t)}$. We hence assign the temporal evolution of the system in terms of the following Master Equation (ME) for the reduced density matrix $\rho(t)$ of S,

$$\partial_t \rho(t) = \mathcal{L}_{\vec{u}(t)}\left[\rho(t)\right] \equiv -\frac{i}{\hbar}\left[H_{\vec{u}(t)}, \rho(t)\right] + \sum_{\alpha=1}^{N} D_{\alpha,\vec{u}(t)}\left[\rho(t)\right], \tag{10.2}$$

where $\mathcal{L}_{\vec{u}(t)}$ is the (time-dependent) quantum Liouvillian generator of the dynamics. In this chapter, we consider dissipators $D_{\alpha,\vec{u}(t)}$ which may have an arbitrary functional dependence upon $\vec{u}(t)$ [1]. We note that, through this dependence, we can include the possibility of deciding which bath is coupled to S at any given time. If only bath α is coupled to S, and if we fix the control parameters $\vec{u}(t) = \vec{u}$, we expect S to thermalize by evolving towards the Gibbs density operator

$$\rho^{(\rm eq)}_{\alpha;\vec{u}} \equiv \exp[-\beta_\alpha H_{\vec{u}}]/Z_{\alpha;\vec{u}}\ , \tag{10.3}$$

$Z_{\alpha;\vec{u}} \equiv \mathrm{Tr}[\exp[-\beta_\alpha H_{\vec{u}}]]$ being the partition function. We frame this physical statement in mathematical terms by requiring all the dissipators $D_{\alpha,\vec{u}}$ to be irreducible and adjoint-stable [29, 362], two conditions which, as we discuss in Appendix G.1, are typically satisfied

[1] This is a quite weak assumption: indeed, in general, the dissipators only depend on the instantaneous values of $\vec{u}(t)$ whenever the Hamiltonian commutes with itself at different times, or whenever the driving is sufficiently slow as to guarantee the validity of the quantum adiabatic theorem is the absence of the baths [43–45], i.e. $\hbar\dot{\vec{u}} \ll \Delta E$, where ΔE is the smallest gap in S, and the "dot" denotes the time derivative. This hypothesis is not in contrast with what we denote as the fast driving regime. Indeed, the fast driving regime requires the driving to be faster than the typical thermalization scale. While the thermalization scale is inversely proportional to the system-bath coupling, and thus can be made arbitrarily big in the weak coupling regime, the validity of the adiabatic theorem does not depend on the system-bath coupling strength. Incidentally, we notice that the generalized Otto cycle always respects this last hypothesis, since there is no driving while the system is coupled to the bath.

by non-pathological dissipators.

The instantaneous heat flux flowing out of bath α can then be computed as [46]

$$J_\alpha(t) \equiv \mathrm{Tr}\left[H_{\vec{u}(t)} D_{\alpha,\vec{u}(t)}\left[\rho(t)\right]\right]. \tag{10.4}$$

Exploiting a projection technique, we can replace the dynamical generator $\mathcal{L}_{\vec{u}(t)}$ with the superoperator $\mathcal{G}_{\vec{u}(t)}$ which has the important property of being invertible on the (d^2-1)-dimensional linear subspace of traceless linear operators $\mathfrak{L}_{\mathrm{S}}^0$ acting on S. Specifically, Eq. (10.2) can be rewritten in the more convenient form

$$\partial_t \tilde{\rho}(t) = \mathcal{G}_{\vec{u}(t)}\left[\tilde{\rho}^{(\mathrm{eq})}_{\vec{u}(t)} - \tilde{\rho}(t)\right], \tag{10.5}$$

where $\rho^{(\mathrm{eq})}_{\vec{u}(t)}$ is the (unique) fixed points of $\mathcal{L}_{\vec{u}(t)}$ and where, for all density matrices ρ of S, we define

$$\tilde{\rho} \equiv \rho - \mathbb{1}/d\,, \tag{10.6}$$

its traceless component.

We are interested in performing thermodynamic cycles, i.e. in performing a periodic driving $\vec{u}(t)$, with period T, such that the variation of internal energy

$$U(t) \equiv \mathrm{Tr}[H_{\vec{u}(t)}\rho(t)] \tag{10.7}$$

of the working fluid is zero after each cycle. In this regime, the first law of thermodynamics guarantees us that all the work extracted from the system is only provided by the heat baths, and not by some particular state preparation of S. As we see from Eq. (10.7), the periodicity of $U(t)$ requires both $\vec{u}(t)$ and $\rho(t)$ to be periodic functions. In general, $\rho(t)$ is not a periodic function. However, using the fact that the dissipators $\mathcal{D}_{\alpha,\vec{u}(t)}$ are irreducible and adjoint-stable, the Lindblad master equation enjoys the following property (a proof is provided by Theorem 2 of Ref. [29]): if $\vec{u}(t)$ is a T-periodic function, then the solution of Eq. (10.2) asymptotically converges toward a "limiting cycle" solution $\rho^{(\mathrm{lc})}_{[\vec{u}]}(t)$, which is independent of the initial condition of the system, and which is periodic with the same period T of the controls, i.e. $\rho^{(\mathrm{lc})}_{[\vec{u}]}(t+T) = \rho^{(\mathrm{lc})}_{[\vec{u}]}(t)$ for all t (the name "limiting cycle" follows from the fact that S naturally approaches it when we repeat the periodic protocol "many times" [363]). The subscript in $\rho^{(\mathrm{lc})}_{[\vec{u}]}(t)$ emphasizes that the limiting cycle is a functional of the whole protocol, i.e. it depends on the control parameters along the whole cycle. In this asymptotic regime, the internal energy $U(t)$ becomes a periodic function, providing us with a thermodynamic cycle. From now on, we therefore focus solely on this regime.

We now wish to identify the optimal choice of $\vec{u}(t)$ that allows us to maximize the extracted power from a heat engine, or the cooling power of a refrigerator, averaged over a cycle. Both these quantities can be expressed as linear combinations of time integrals of the currents, defined in Eq. (10.4). Therefore, given an arbitrary collection c_α of real coefficients, we define the Generalized Average Power (GAP), which is a functional of the whole protocol, as

$$P_{\mathbf{c}}[\vec{u}] \equiv \frac{1}{T}\sum_{\alpha=1}^{N}\int_0^T c_\alpha J_\alpha(t)\,dt = \frac{1}{T}\int_0^\tau \mathrm{Tr}\left[H_{\vec{u}(t)}\sum_\alpha c_\alpha D_{\alpha,\vec{u}(t)}\left[\rho^{(\mathrm{lc})}_{[\vec{u}]}(t)\right]\right]dt. \tag{10.8}$$

For instance, if we choose $c_\alpha = 1$ for all α, Eq. (10.8) represents the average of the total extracted heat flux, which coincides with the *average extracted power* for periodically driven heat engines; if instead $c_\alpha = \delta_{\alpha,N}$, with $\alpha = N$ labelling the coldest bath and δ representing the Kronecker delta, Eq. (10.8) represents the average *cooling power*, which measures the performance of a refrigerator; if $c_\alpha = -1$ for all α, Eq. (10.8) represents the average *dissipated heat flux*, which measures the performance of a *heater*, and so on.

10.2 Fast driving regime

Finding the optimal value of $\vec{u}(t)$ that maximize the functional (10.8) is, in general, a formidable task. Nonetheless, as we shall see, an explicit solution to the problem can be obtained when studying the performance in the *fast driving regime*. This is characterized by driving the system with a protocol $\vec{u}(t)$ whose period T is much shorter than the typical relaxation times induced by the baths. Therefore, we may expect that the limiting cycle state of S "does not have time" to thermalize with the bath, so it might actually converge to a fixed, time-independent out-of-equilibrium state. This is precisely what happens.

More specifically, let us denote with $\eta_{[\vec{u}]}$ the typical rate which characterizes the ME (10.5) (see App. G.2.2 for a formal definition of $\eta_{[\vec{u}]}$). Formally, we can expand $\rho^{(\mathrm{lc})}_{[\vec{u}]}(t)$ in a power series in $\eta_{[\vec{u}]}T \ll 1$. As we prove in App. G.2.2, it turns out that the leading order term $\rho^{(0)}_{[\vec{u}]}$ is indeed time-independent. Furthermore, its traceless component (10.6) is determined by

$$\tilde{\rho}^{(0)}_{[\vec{u}]} \equiv \left(\int_{I_{[\vec{u}]}} \mathcal{G}_{\vec{u}(t)}dt\right)^{-1}\left[\int_{I_{[\vec{u}]}} \mathcal{G}_{\vec{u}(t)}[\tilde{\rho}^{(\mathrm{eq})}_{\vec{u}(t)}]\,dt\right], \tag{10.9}$$

where $I[\vec{u}]$ denotes the time interval of one cycle of duration T. The invertibility of $\int_{I_{[\vec{u}]}} \mathcal{G}_{\vec{u}(t)}dt$ is guaranteed by the assumption that the dissipators are irreducible and adjoint-stable (see App. G.1 for details). Using the approximation $\rho^{(\mathrm{cl})}_{[\vec{u}]}(t) \approx \rho^{(0)}_{[\vec{u}]}$, we can write the GAP in Eq. (10.8) in the fast driving regime as

$$P_{\mathbf{c}}[\vec{u}] = \frac{1}{T}\int_{I_{[\vec{u}]}} \mathrm{Tr}\left[H_{\vec{u}(t)}\sum_{\alpha} c_\alpha D_{\alpha,\vec{u}(t)}\left[\rho^{(0)}_{[\vec{u}]}\right]\right]dt, \tag{10.10}$$

which is guaranteed to be valid up to linear corrections in the expansion parameter $\eta_{[\vec{u}]}T$ (however, it should be stressed that, by direct evaluation, the GAP of the optimal protocol turns out to be valid up to second order corrections in $\eta_{[\vec{u}]}T$ in two level systems [52, 361] and in the qutrit case studied in Sec. 10.4).

Equations (10.9) and (10.10) are the main starting point of our analysis: they allow us to express the GAP as an explicit functional of the protocol $\vec{u}(t)$ without requiring us to solve the ME. This procedure is somewhat analogous to what happens in the opposite regime, the *slow driving*, in which the time scales of the driving are much slower than the dissipative dynamics induced by the baths. Optimal protocols for maximizing GAPs in this regime have been extensively discussed [59, 354, 364, 365]. The reasoning above shows that, by exploiting the concept of time scale separation, we can simplify the characterization of the GAP in thermal machines. Dealing with the dynamics of $\rho(t)$ in intermediate regimes is in general more difficult, and this can be tackled, for instance, using the Pontryagin minimum principle technique [52, 56, 366].

10.2.1 Optimality of sudden quenches

Instead of performing a direct constrained functional optimization of the GAP [see Eq. (10.10)] with respect to $\vec{u}(t)$, we will employ an iterative procedure that eventually leads to the identification of the "generalized Otto cycle" as the optimal one. The main idea of the proof is the following: given any assigned periodic protocol which respects the constraint $\vec{u}(t) : [0, T] \to \mathbb{D}$, we prove that it is possible to "cut away" parts of it to build a new, shorter, cycle which delivers a higher or equal GAP than the starting one. By reiterating this process

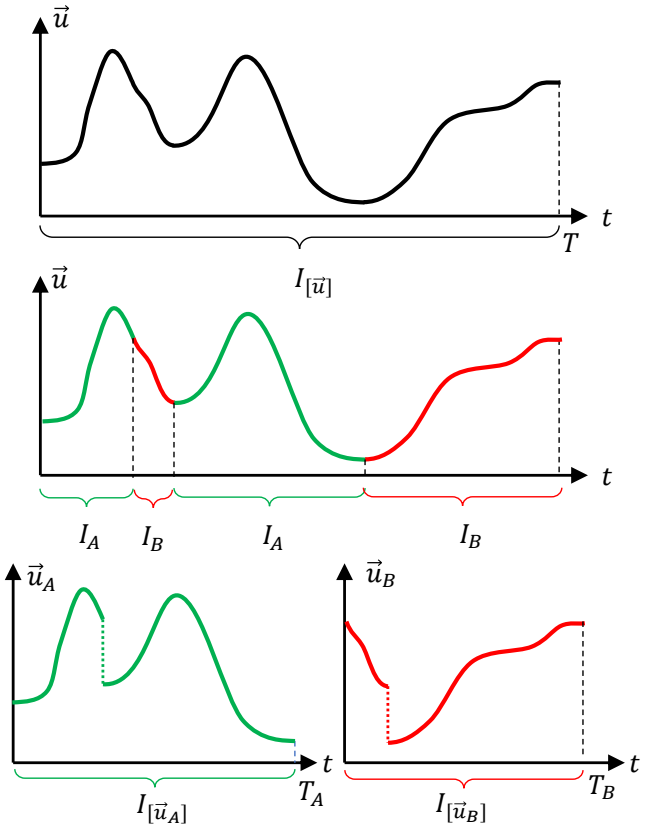

Figure 10.2: Schematic representation of the *cut-and-choose* procedure for $M = 1$. Upper panel: representation of an arbitrary protocol $\vec{u}(t)$ defined on the time interval $I_{[\vec{u}]}$ of duration T. Central panel: we partition $I_{[\vec{u}]}$ into two disjoing subsets I_A and I_B. Lowe panel: we define two new sub-protocols $\vec{u}_A(t)$ and $\vec{u}_B(t)$ by restricting $\vec{u}(t)$ respectively to I_A and I_B. This process may introduce discontinuities in the controls, denoted as quenches.

over and over, we end up with the generalized Otto cycle. We therefore denote this procedure as *cut-and-choose*.

In order to detail the *cut-and-choose* procedure, let us first formally introduce the notion of cyclic sub-protocols. Given an arbitrary cyclic protocol $\vec{u}(t)$ of period T and fundamental period $I_{[\vec{u}]} = [0, T]$, consider a subset I_A of $I_{[\vec{u}]}$ of non-zero measure T_A. A cyclic sub-protocol $\vec{u}_A(t)$ of $\vec{u}(t)$ with period T_A and fundamental period $I_{[\vec{u}_A]} \equiv [0, T_A]$ is hence obtained by rigidly joining the various parts which compose the restriction of $\vec{u}(t)$ on I_A. This procedure may introduce localized discontinuities, i.e. quenches, within the protocol – see Fig. 10.2 for an example for $M = 1$. Assume now to drive S by repeating many times the selected sub-protocol: since the image points of the curve $\vec{u}_A(t) : I_{[\vec{u}_A]} \to \mathbb{D}$ form a proper subset of those of $\vec{u}(t) : I_{[\vec{u}]} \to \mathbb{D}$, it follows that if the fast driving limit holds for the latter, i.e. if $\eta_{[\vec{u}]} T \ll 1$, then the same condition applies also to $\vec{u}_A(t)$, i.e. $\eta_{[\vec{u}_A]} T_A \ll 1$ – see Appendix G.2.3. Furthermore, by construction, the new cyclic sub-protocol satisfies the constraint on the values of the control.

Since Eq. (10.9) holds for any periodic protocol in the fast driving regime, by repeating $\vec{u}_A(t)$ many times, the state of S will tend to a new asymptotic constant state $\rho^{(0)}_{[\vec{u}_A]}$ whose

traceless component reads

$$\tilde{\rho}^{(0)}_{[\vec{u}_A]} = \left(\int_{I_{[\vec{u}_A]}} \mathcal{G}_{\vec{u}_A(t)} dt \right)^{-1} \left[\int_{I_{[\vec{u}_A]}} \mathcal{G}_{\vec{u}_A(t)} [\tilde{\rho}^{(\mathrm{eq})}_{\vec{u}_A(t)}] \, dt \right]. \tag{10.11}$$

It goes without mentioning that analogous conclusions can be drawn also for the sub-protocol $\vec{u}_B(t)$ that is obtained by considering the restriction of $\vec{u}(t)$ to the complement I_B of I_A, i.e. the set $I_B = I_{[\vec{u}]}/I_A$ of measure $T_B = T - T_A$: once more, under iterated application of such driving, the state of S will tend to a constant asymptotic state $\rho^{(0)}_{[\vec{u}_B]}$ given by Eq. (10.11) by simply replacing everywhere the index A with B; see Fig. 10.2 for an example.

Assume next that the states $\rho^{(0)}_{[\vec{u}_A]}$ and $\rho^{(0)}_{[\vec{u}_B]}$ introduced above coincide and are equal to $\rho^{(0)}_{[\vec{u}]}$, i.e.

$$\rho^{(0)}_{[\vec{u}_A]} = \rho^{(0)}_{[\vec{u}_B]} = \rho^{(0)}_{[\vec{u}]} \, . \tag{10.12}$$

Equation (10.12) is a rather strong requirement which in general is not met by generic choices of I_A and I_B: still, as we shall discuss in the next section, the possibility of identifying sub-protocols fulfilling this property is always granted. For the moment we hence assume that Eq. (10.12) is satisfied. The GAPs $P_{\mathbf{c}}[\vec{u}_A]$ and $P_{\mathbf{c}}[\vec{u}_B]$ delivered respectively by the sub-protocols $\vec{u}_A$ and $\vec{u}_B$ can be computed using Eq. (10.10). Assuming Eq. (10.12) is fulfilled, we notice that the integrands entering $P_{\mathbf{c}}[\vec{u}]$, $P_{\mathbf{c}}[\vec{u}_A]$ and $P_{\mathbf{c}}[\vec{u}_B]$ are all the same. Therefore, exploiting the linearity of the integral respect to the its integration domain (i.e. time), and recalling that $T = T_A + T_B$, we have that

$$P_{\mathbf{c}}[\vec{u}] = \frac{T_A P_{\mathbf{c}}[\vec{u}_A] + T_B P_{\mathbf{c}}[\vec{u}_B]}{T_A + T_B}. \tag{10.13}$$

The above equation establishes that the GAP of the original protocol $\vec{u}(t)$ can be expressed as a non-trivial convex combination of the GAPs of the sub-protocols $\vec{u}_A(t)$ and $\vec{u}_B(t)$: therefore it must be smaller or equal to the maximum of those two quantities, i.e.

$$P_{\mathbf{c}}[\vec{u}] \leq P_{\mathbf{c}}[\vec{u}_A], \tag{10.14}$$

where, without loss of generality we assumed $P_{\mathbf{c}}[\vec{u}_B] \leq P_{\mathbf{c}}[\vec{u}_A]$. Inequality (10.14) implies that given a generic periodic protocol $\vec{u}(t)$, it is possible to construct a *shorter* one $\vec{u}_A$ that delivers a larger or equal GAP. This is the reason for the name *cut-and-choose* procedure. We can now re-iterate the *cut-and-choose* procedure starting from $\vec{u}_A(t)$, thus obtaining another (even shorter) protocol $\vec{u}_{AA}(t)$ that produces a greater or equal GAP, and so on and so forth. After many iterations of the *cut-and-choose* procedure, we end up with a protocol that cannot be further optimized via this technique. This is a generalized Otto cycle.

This protocol is characterized by an infinitesimal domain I of duration $d\tau$, divided into L segments of length $d\tau_i$, such that the controls $\vec{u}(t)$ take on a constant value $\vec{u}_i \equiv \vec{u}(t_i) \in \mathbb{D}$ during each time interval $d\tau_i$; see Fig. 10.3 for a schematic representation. Using Eq. (10.10), the associated GAP of such protocol can hence be expressed as

$$P_{\mathbf{c}}[\{\vec{u}_i, \mu_i\}] = \sum_{j=1}^{L} \mu_j \mathrm{Tr} \left[H_{\vec{u}_j} \sum_{\alpha} c_\alpha D_{\alpha,\vec{u}_j} \left[\rho^{(0)}_{[\{\vec{u}_i,\mu_i\}]} \right] \right], \tag{10.15}$$

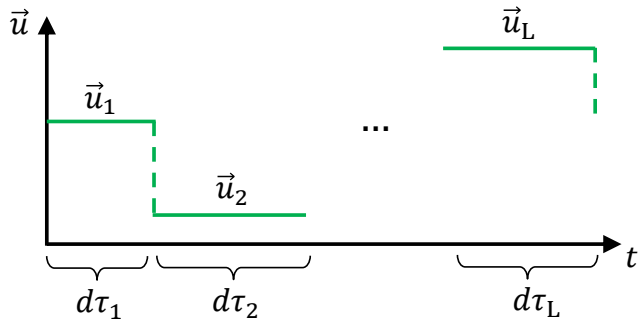

Figure 10.3: Representation of a generalized Otto cycle, which results from a large number of re-iterations of the *cut-and-choose* procedure depicted in Fig. 10.2. L (infinitesimally short) constant controls are alternated with quenches. Finite upper bounds can be obtained for the maximum value of L that is needed for the optimization (see Table 10.1).

	Quantum	Semi-classical	Simple relax.
max L	d^2	d	2^*
Scalar Params	$d^2(M+1)-1$	$d(M+1)-1$	$2^*(M+1)-1$

Table 10.1: Maximum value of L and maximum number of scalar parameters which determine the generalized Otto cycle in the general quantum case, in the semi-classical case, and for a simple choice of the Lindbladian form (cfr. Sec.10.3).
*: 2 holds for the refrigerator, while this value is $\min(N,d)$ in the heat engine case. See Sec. 10.3 for details.

where $\mu_i = d\tau_i/d\tau$ represents the percentage of the total protocol time spent at each point $\vec{u}_i$, and $\rho^{(0)}_{[\{\vec{u}_i,\mu_i\}]}$ is the time-independent limiting cyclic state whose traceless component is [see Eq. (10.9)]

$$\tilde{\rho}^{(0)}_{[\{\vec{u}_i,\mu_i\}]} \equiv \left(\sum_{j=1}^{L}\mu_j\mathcal{G}_{\vec{u}_j}\right)^{-1}\left[\sum_{j=1}^{L}\mu_j\mathcal{G}_{\vec{u}_j}[\tilde{\rho}^{(\mathrm{eq})}_{\vec{u}_j}]\right] . \tag{10.16}$$

Crucially, we are able to place a finite upper bound to the number L of time intervals of the optimal generalized Otto cycle. In App. G.3.2 we prove that, in general, L is at most equal to the degrees of freedom of the density matrix plus one. Therefore, in general we have $L \leq d^2$; we denote this the "quantum case", since all elements in the density matrix are assumed to contribute to the evaluation of the GAP. Instead, if the system is "semi-classical", i.e. if $[H_{\vec{u}(t)}, H_{\vec{u}(t')}] = 0$ for all t and t', this upper bound is reduced to $L \leq d$ since, under this condition, only the populations of the instantaneous eigenstantes, which are d, play a role in the evaluation of the GAP. Furthermore, as discussed in Sec. 10.3, if the dissipator of each bath is characterized by a single (control-dependent) timescale and $N = 2$, then $L = 2$ regardless of the dimensionality of the system; in this case, the optimal protocol reduces to a conventional infinitesimal quantum Otto cycle.

We therefore proved that the generalized Otto cycle universally maximizes the GAP. The particular values of the controls $\vec{u}_i$ and of the time fractions μ_i that maximize Eq. (10.15) are instead model specific, and must be determined case by case. The total number of scalar parameters over which Eq. (10.15) must be optimized is given by $(L-1)+ML$, where $L-1$ comes from the time fractions (note that $\sum_i \mu_i = 1$), and ML is the number of scalar control parameters. We report a summary of these results in Table 10.1.

In order to gain further physical insight into our result, let us consider the paradigmatic case in which our system S can only be coupled to one bath at the time. Mathematically, this assumption can be described by a specific control parameter, say $\alpha(t)$, whose value is the index of the bath we are coupled to, $\alpha = 1, \dots, N$. Therefore, S must be coupled only to a single bath in each time interval $d\tau_i$. In this scenario, it is interesting to notice that our bound on the number of time intervals poses a limit to the maximum number of thermal baths necessary to maximize the GAP: indeed, at most L baths will be used. Therefore, for low dimensional working fluids, the maximum number of thermal baths necessary to maximize the GAP is strongly limited. However, we also explicitly show in Sec. 10.4 that three thermal baths at different temperatures can outperform two thermal baths when the working fluid is a qutrit. This result is in contrast with the maximization of the efficiency, which is always obtained by coupling S only to the hottest and coldest bath available.

As a final technical remark, we discuss how to simplify the optimization over the choice of the bath coupled to S. In principle, any bath can be coupled to S during each time interval $d\tau_i$. However, by direct inspection of Eqs. (10.15) and (10.16), it can be seen that the GAP is invariant under permutations of $\vec{u}_i$ and μ_i. Therefore, the number of independent choices of the bath is given by the binomial coefficient $\binom{L+N-1}{N-1}$ which e.g. scales linearly in L when only two thermal baths are available. The maximization of the GAP is thus carried out by repeating the optimization of Eq. (10.15) over the other control parameters for each independent choice of the baths, and then choosing the configuration delivering the largest GAP.

10.2.2 A geometric interpretation of Eq. (10.12)

The argument presented in the previous section relies on the assumption (10.12) that one can identify two new sub-protocols $\vec{u}_A(t)$ and $\vec{u}_B(t)$ that preserve the asymptotic state $\rho^{(0)}_{[\vec{u}]}$ of the original protocol $\vec{u}(t)$. We provide an explicit proof that such condition can always be fulfilled by translating it into a geometric problem.

For this purpose, let us define the curves $\gamma_{[\vec{u}]} \equiv \{v_{\vec{u}(t)} | t \in I_{[\vec{u}]}\}$, $\gamma_{[\vec{u}_A]} \equiv \{v_{\vec{u}_A(t)} | t \in I_{[\vec{u}_A]}\}$, and $\gamma_{[\vec{u}_B]} \equiv \{v_{\vec{u}_B(t)} | t \in I_{[\vec{u}_B]}\}$ generated by the functions

$$v_{\vec{u}(t)} \equiv \mathcal{G}_{\vec{u}(t)} \left[\tilde{\rho}^{(\mathrm{eq})}_{\vec{u}(t)} - \tilde{\rho}^{(0)}_{[\vec{u}]} \right] , \tag{10.17}$$

$$v_{\vec{u}_{A,B}(t)} \equiv \mathcal{G}_{\vec{u}_{A,B}(t)} \left[\tilde{\rho}^{(\mathrm{eq})}_{\vec{u}_{A,B}(t)} - \tilde{\rho}^{(0)}_{[\vec{u}]} \right] . \tag{10.18}$$

Since the domains $I_{[\vec{u}_A]}$ and $I_{[\vec{u}_B]}$ are complementary and provide a decomposition of $I_{[\vec{u}]}$, $\gamma_{[\vec{u}_A]}$ and $\gamma_{[\vec{u}_B]}$ are disjoint, and their union coincides with $\gamma_{[\vec{u}]}$ (see upper panels of Fig. 10.4 for a schematic representation). It is important to notice that the functions in Eq. (10.18), thus also the curves $\gamma_{[\vec{u}]}$, $\gamma_{[\vec{u}_A]}$, and $\gamma_{[\vec{u}_B]}$, belong to the special subspace of $\mathfrak{L}^0_{\mathrm{S}}$ formed by the traceless Hermitian operators of S which, being isomorphic to $\mathbb{R}^D$ with $D \equiv d^2 - 1$, can be parameterized in terms of D real parameters.

Since $\tilde{\rho}^{(0)}_{[\vec{u}]}$ satisfies Eq. (10.9), the curve $\gamma_{[\vec{u}]}$ has a null "center of mass" $O_{[\vec{u}]}$ (represented by the black dot in Fig. 10.4), i.e.

$$O_{[\vec{u}]} \equiv \int_{I_{[\vec{u}]}} v_{\vec{u}(t)} \, dt = 0 . \tag{10.19}$$

Using the linearity of the integral respect to its integration domain, it is easy to verify that the sum of the "centers of mass" $O_{[\vec{u}_A]} \equiv \int_{I_{[\vec{u}_A]}} v_{\vec{u}_A(t)} \, dt$ with $O_{[\vec{u}_B]} \equiv \int_{I_{[\vec{u}_B]}} v_{\vec{u}_B(t)} \, dt$ is null,

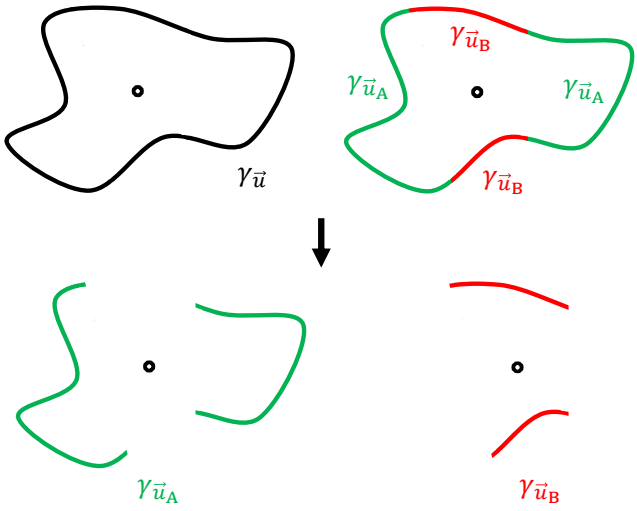

Figure 10.4: Upper left: schematic representation of $\gamma_{[\vec{u}]}$ and of its center of mass. Upper right: schematic representation of a partition of $\gamma_{[\vec{u}]}$ into $\gamma_{[\vec{u}]_A}$ and $\gamma_{[\vec{u}]_B}$. Lower panels: schematic representation of the sub-curves $\gamma_{[\vec{u}]_A}$ and $\gamma_{[\vec{u}]_B}$ which preserve the center of mass of the original curve $\gamma_{[\vec{u}]}$.

i.e.

$$O_{[\vec{u}_A]} + O_{[\vec{u}_B]} = O_{[\vec{u}]} = 0 \,. \tag{10.20}$$

We claim that a necessary and sufficient condition for Eq. (10.12) to hold is that the curve $\gamma_{[\vec{u}_A]}$ (and hence due to Eq. (10.20), also $\gamma_{[\vec{u}_B]}$) must have a null center of mass too. Indeed, exploiting the invertibility of $\int_{I_{[\vec{u}_A]}} \mathcal{G}_{\vec{u}_A(t)} dt$ on $\mathfrak{L}^0_{\mathrm{S}}$, one can observe that setting $O_{[\vec{u}_A]} = 0$ is fully equivalent to having

$$\tilde{\rho}^{(0)}_{[\vec{u}]} = \left(\int_{I_{[\vec{u}_A]}} \mathcal{G}_{\vec{u}_A(t)} dt \right)^{-1} \left[\int_{I_{[\vec{u}_A]}} \mathcal{G}_{\vec{u}_A(t)} [\tilde{\rho}^{(\mathrm{eq})}_{\vec{u}_A(t)}] \, dt \right] = \tilde{\rho}^{(0)}_{[\vec{u}_A]}, \tag{10.21}$$

where, in the last step, we used Eq. (10.11) to recognize $\tilde{\rho}^{(0)}_{[\vec{u}_A]}$. An analogous conclusion holds also for the sub-protocol $\vec{u}_B(t)$ thanks to Eq. (10.20).

This is the geometric reformulation of Eq. (10.12) we were looking for: our partitioning technique works if, starting from a generic curve $\gamma_{[\vec{u}]}$ in $\mathbb{R}^D$ having a null center of mass, we are able to split it into two sub-curves $\gamma_{[\vec{u}_A]}$ and $\gamma_{[\vec{u}_B]}$ such that these still have a null center of mass (this concept is schematically represented in Fig. 10.4). In Appendix G.3 we prove that it is indeed possible assuming that the original protocol $\vec{u}(t)$ possesses some weak notion of regularity. The main idea is that, given an arbitrary curve in $\mathbb{R}^D$ with zero center of mass, it is always possible to identify a null convex combination of at most $D+1$ points lying on the curve. For sufficiently regular curves, the implicit function theorem allows us to extend these points to a piecewise continuous curve of finite size.

Reiterating this *cut-and-choose* procedure many times may lead to a piecewise continuous curves with a large number of discontinuities. Crucially, in App. G.3.2 we show that it is always possible to end up with a curve characterized by at most $D+1$ discontinuities. This result gives rise to the bounds on L summarized in Table 10.1.

10.3 Simple relaxation case

In this section we discuss a simplified model of thermalization where the super-operator $\mathcal{G}_{\vec{u}(t)}$ of Eq. (10.5) is purely multiplicative, leading to a ME of the form

$$\partial_t \tilde{\rho}(t) = \Gamma_{\vec{u}(t)}(\tilde{\rho}^{(\mathrm{eq})}_{\vec{u}(t)} - \tilde{\rho}(t)), \tag{10.22}$$

with $\Gamma_{\vec{u}(t)} > 0$ a scalar number which defines the rate of thermalization of all the observables of the system. Furthermore, we assume that the model allows S to be coupled to a single bath at the time. As discussed in the final part of Sec. 10.2.1, we formally introduce a single control parameter, denoted with $\alpha(t)$, indexing the bath we are coupled to at time t. Notice that, for all values of $\vec{u}(t)$, the equilibrium states $\rho^{(\mathrm{eq})}_{\vec{u}(t)}$ always correspond to the Gibbs distribution of bath $\alpha(t)$, i.e. $\rho^{(\mathrm{eq})}_{\alpha(t);\vec{u}(t)}$ as in Eq. (10.3). As discussed in the first part of this chapter, the maximum GAP is given by Eqs. (10.15) and (10.16) which, using Eq. (10.22), can be rewritten as

$$P_{\mathbf{c}}[\{\vec{u}_i, \mu_i\}] = \frac{\sum_{i,j=1}^{L} c_{\alpha_i} \mu_i \mu_j \Gamma_{\vec{u}_i} \Gamma_{\vec{u}_j} P_{i\leftarrow j}}{\sum_{i=1}^{L} \mu_i \Gamma_{\vec{u}_i}}, \tag{10.23}$$

$$\tilde{\rho}^{(0)}_{[\{\vec{u}_i,\mu_i\}]} = \frac{\sum_{i=1}^{L} \mu_i \Gamma_{\vec{u}_i} \tilde{\rho}^{(\mathrm{eq})}_{\vec{u}_i}}{\sum_{i=1}^{L} \mu_i \Gamma_{\vec{u}_i}}, \tag{10.24}$$

where α_i is the constant value of $\alpha(t)$ during the interval $d\tau_i$, and

$$P_{i\leftarrow j} \equiv \mathrm{Tr}\left[H_{\vec{u}_i}\left(\tilde{\rho}^{(\mathrm{eq})}_{\vec{u}_i} - \tilde{\rho}^{(\mathrm{eq})}_{\vec{u}_j}\right)\right]. \tag{10.25}$$

We used the assumption that S can be coupled to a single bath at the time to remove the sum over α in Eq. (10.23). Notice that $P_{i\leftarrow i} = 0$, while

$$P_{j\leftarrow k} + P_{k\leftarrow j} \leq 0 \tag{10.26}$$

when S is coupled to the same temperature during the time intervals $d\tau_j$ and $d\tau_k$. This is given by the fact that $P_{j\leftarrow k} + P_{k\leftarrow j}$ is equal to $P_{\mathbf{c}}[\{\vec{u}_i, \mu_i\}]$ with $c_\alpha = 1\ \forall i$, and $\mu_i = 0\ \forall i \neq j, k$, which physically represents the average power extracted from a heat engine operating between equal temperatures (and therefore cannot be positive) [2].

Using these properties, we show that with the only assumption of the dynamics being described by Eq. (10.22), it is possible to greatly simplify the optimization of the GAP of thermal machines. Specifically, we find that starting from a generalized Otto cycle made of L intervals, it is always possible to increase the performance by using only a subset $l \leq L$ of the initial time intervals. We now characterize l.

As shown in Appendix G.4, we consider *positive* GAPs, i.e. generalized average powers consisting of a positive linear combination of the heat currents extracted from the different thermal baths (formally we assume that $c_\alpha \geq 0\ \forall \alpha$). This hypothesis includes both the average power extracted from a heat engine ($c_\alpha = 1\ \forall \alpha$), and the cooling power of a refrigerator ($c_\alpha = \delta_{\alpha,N}$, with $\alpha = N$ labelling the coldest bath). We prove that, in order to maximize a positive GAP, it is sufficient to consider a protocol with at most one time interval per temperature; therefore $l \leq N$. Moreover, if more than one heat current is neglected in the

[2] Property (10.26) can also be inferred by the fact that if the temperature of the baths at the time intervals $d\tau_j$ and $d\tau_k$ are the same and equal to $1/\beta$, then $P_{j\leftarrow k} + P_{k\leftarrow j} = -\beta^{-1}\left(S(\tilde{\rho}^{(\mathrm{eq})}_{\vec{u}_k} \parallel \tilde{\rho}^{(\mathrm{eq})}_{\vec{u}_j}) + S(\tilde{\rho}^{(\mathrm{eq})}_{\vec{u}_j} \parallel \tilde{\rho}^{(\mathrm{eq})}_{\vec{u}_k})\right)$.

definition of the GAP, it is possible to further reduce the number of intervals. Specifically, given $\kappa \leq N$ the number of distinct temperatures of the baths for which $c_\alpha \neq 0$, we prove that

$$l \leq \min(N, \kappa + 1) \ . \tag{10.27}$$

This implies that a refrigerator ($\kappa = 1$) is always characterized by $l = 2$, regardless of the number of baths, while a heat engine ($\kappa = N$) by $l \leq N$. In the following, for simplicity, we focus on the refrigerator and heat engine case with two thermal baths at our disposal. As a consequence, $l = 2$. Under this hypothesis, we find that:

(i) The optimal durations of the time intervals and the resulting maximum GAPs can be determined (Sec.s 10.3.1-10.3.2).

(ii) If the thermalization rates are a function of the bath $\alpha(t)$, but only weakly depend on the specific value of the other control parameters, i.e. $\Gamma_{\vec{u}_i} = \Gamma_{\alpha_i}$, and if we assume to have total control over the system Hamiltonian, we can fully carry out the maximization of the GAP, finding that the optimal control strategies involve degenerate spectra of the Hamiltonian of the working fluid (Sec. 10.3.3).

(iii) Under the hypothesis of (ii), we find that generating coherence in the eigenstate basis does not improve the GAP of thermal machines (Sec. 10.3.3).

(iv) Under the hypothesis of (ii), we compare the GAP of a heat engine and of a refrigerator delivered by n non-interacting qubits [$\mathrm{GAP}_{\mathrm{NI}}(n)$], with the GAP of n interacting qubits [$\mathrm{GAP}_{\mathrm{I}}(n)$] in the most favorable case (i.e. of full control over the many-body n qubit Hamiltonian, see Sec. 10.3.4). By definition, $\mathrm{GAP}_{\mathrm{NI}}(n)$ scales linearly in n. We find that $\mathrm{GAP}_{\mathrm{I}}(n)$ displays a super-linear transient regime, yet it asymptotically scales linearly for any finite temperature difference ΔT. Interestingly, in the heat engine case, for small temperature differences ΔT, we find the asymptotic behavior $\mathrm{GAP}_{\mathrm{I}}(n)/\mathrm{GAP}_{\mathrm{NI}}(n) \propto 1/\Delta T$, signaling that there is a significant many-body advantage when operating heat engines at small temperature differences. On the other hand, for a refrigerator, we find that the asymptotic value of $\mathrm{GAP}_{\mathrm{I}}(n)/\mathrm{GAP}_{\mathrm{NI}}(n)$ is given by the universal value $\ln 2/W(1/e) \approx 2.49$, where $W(z)$ is the Lambert function. Therefore, for a refrigerator, many-body interactions do not provide a relevant advantage over non-interacting and independent constituents.

10.3.1 Refrigerator

Let us consider two inverse temperatures β_1 and β_2 such that $\beta_1 < \beta_2$. The average cooling power of a refrigerator, $P_{[\mathrm{R}]}$, is described by the GAP with $c_2 = 1$ on the cold bath while $c_1 = 0$. Since $l = 2$, Eq. (10.23) reduces to

$$P_{[\mathrm{R}]} = \frac{\mu_1 \mu_2 \Gamma_{\vec{u}_1} \Gamma_{\vec{u}_2} P_{2\leftarrow 1}}{\mu_1 \Gamma_{\vec{u}_1} + \mu_2 \Gamma_{\vec{u}_2}} \tag{10.28}$$

where $\mu_2 = 1 - \mu_1$. We can thus explicitly maximize the above expression over the choice of the time fraction μ_1, leading to

$$P^{(\max)}_{[\mathrm{R}]} = \frac{\mathrm{Tr}\left[H_{\vec{u}_2}\left(\tilde{\rho}^{(\mathrm{eq})}_{\vec{u}_2} - \tilde{\rho}^{(\mathrm{eq})}_{\vec{u}_1}\right)\right]}{\left(\sqrt{\Gamma^{-1}_{\vec{u}_1}} + \sqrt{\Gamma^{-1}_{\vec{u}_2}}\right)^2}, \tag{10.29}$$

which is obtained for $\mu_1 = \sqrt{\Gamma_{\vec{u}_2}}/(\sqrt{\Gamma_{\vec{u}_2}} + \sqrt{\Gamma_{\vec{u}_1}})$. Notably, the expression of the maximum cooling power in Eq. (10.29) only requires a maximization over $\vec{u}_1$ and $\vec{u}_2$, which in general is model dependent.

10.3.2 Engine

Let us consider the same setting $\beta_1 < \beta_2$. The average extracted power of a heat engine, $P_{[\mathrm{E}]}$, is described by the GAP with $c_1 = c_2 = 1$. Since $l = 2$, Eq. (10.23) reduces to

$$P_{[\mathrm{E}]} = \frac{\mu_1\mu_2\Gamma_{\vec{u}_1}\Gamma_{\vec{u}_2}\left(P_{1\leftarrow 2} + P_{2\leftarrow 1}\right)}{\mu_1\Gamma_{\vec{u}_1} + \mu_2\Gamma_{\vec{u}_2}} \tag{10.30}$$

It follows that the optimization over the time fraction μ_1 is identical to that of the refrigerator, see Eq. (10.28), leading to

$$P_{[\mathrm{E}]}^{(\max)} = \frac{\mathrm{Tr}\left[\left(H_{\vec{u}_1} - H_{\vec{u}_2}\right)\left(\tilde{\rho}_{\vec{u}_1}^{(\mathrm{eq})} - \tilde{\rho}_{\vec{u}_2}^{(\mathrm{eq})}\right)\right]}{\left(\sqrt{\Gamma_{\vec{u}_1}^{-1}} + \sqrt{\Gamma_{\vec{u}_2}^{-1}}\right)^2}, \tag{10.31}$$

which is obtained for $\mu_1 = \sqrt{\Gamma_{\vec{u}_2}}/(\sqrt{\Gamma_{\vec{u}_2}} + \sqrt{\Gamma_{\vec{u}_1}})$. Also in this case, Eq. (10.31) only requires a model-dependent maximization over $\vec{u}_1$ and $\vec{u}_2$.

10.3.3 Full maximization

The maximum average power for the refrigerator and the heat engine that we found in Eqs. (10.29) and (10.31) has been maximized over the time fractions spent in contact with each bath. However $P_{[\mathrm{R}]}^{(\max)}$ and $P_{[\mathrm{E}]}^{(\max)}$ still need to be maximized over $\vec{u}_1$ and $\vec{u}_2$ among the experimentally available controls. Until now, we did not make any assumption on the functional form of $\Gamma_{\vec{u}}$, nor of $H_{\vec{u}}$.

We now assume that the rates $\Gamma_{\vec{u}_i} = \Gamma_{\alpha_i}$ are fixed for each bath (i.e. they do not depend on the value of the control $\vec{u}$, but only on the bath index α), and that the control on the Hamiltonians is total (i.e. that we can generate any Hamiltonian). In such case, the maximization of $P_{[\mathrm{E}]}^{(\max)}$ is carried out by maximizing

$$\mathrm{Tr}\left[\left(H_1 - H_2\right)\left(e^{-\beta_1 H_1}/Z_1 - e^{-\beta_2 H_2}/Z_2\right)\right] \tag{10.32}$$

with respect to the choice of the two Hamiltonians H_1 and H_2. This maximization has been carried out in Ref. [357], finding that H_1 and H_2 must be diagonal in the same basis $|\nu\rangle$, and that the spectrum must be given by a non-degenerate ground state, and a $d-1$ degenerate excited state. We therefore have

$$H_i = \sum_{\nu=2}^{d} \varepsilon_i \left|\nu\right\rangle\left\langle\nu\right|, \tag{10.33}$$

where ε_1 and ε_2 can be found by maximizing the form taken by (10.32) in this case

$$\frac{(\varepsilon_1 - \varepsilon_2)(e^{-\beta_1\varepsilon_1} - e^{-\beta_2\varepsilon_2})(d-1)}{(1 + (d-1)e^{-\beta_1\varepsilon_1})(1 + (d-1)e^{-\beta_2\varepsilon_2})}\,. \tag{10.34}$$

Analogously, it can be shown that the maximization of $P_{[\mathrm{R}]}^{(\max)}$ is carried out by maximizing

$$\mathrm{Tr}\left[H_2\left(e^{-\beta_2 H_2}/Z_2 - e^{-\beta_1 H_1}/Z_1\right)\right] \tag{10.35}$$

with respect to H_1 and H_2. The optimal Hamiltonians are again of the form of Eq. (10.33), with $\varepsilon_1 \to \infty$ (physically, the hot bath attempts to drive S towards its ground state, to obtain a better cooling), while ε_2 can be obtained as the maximum of the following expression

$$\frac{\varepsilon_2 e^{-\beta_2 \varepsilon_2}(d-1)}{1+(d-1)e^{-\beta_2\varepsilon_2}} \,. \tag{10.36}$$

Incidentally, we notice here that the optimality of Hamiltonians with $d-1$ degenerate spectra was found also in the regime opposite to the fast driving, that is in the slow driving, high efficiency regime [354].

10.3.4 Non-interacting vs many-body qubits

In this section we compare the maximum GAP of a heat engine and of a refrigerator delivered by n non-interacting qubits [$\mathrm{GAP}_{\mathrm{NI}}(n)$] driven independently, with the GAP of n interacting qubits [$\mathrm{GAP}_{\mathrm{I}}(n)$]. In the NI case, we assume that we have full control over the Hamiltonian of the single qubits, while in the I case we assume to have full control over the total many-body Hamiltonian of n qubits. Furthermore, we work under the assumptions of Secs. 10.3.3, i.e. we consider rates Γ_α, for $\alpha = 1, 2$, that only depend on the bath index, and not on the precise value of the control. The comparison between the two model is made fair by enforcing that both systems thermalize within the same time scale, i.e. we consider a master equation with the same thermalization rates Γ_α.

Under these assumptions, the GAP delivered by a single qubit can be computed as described in Sec. 10.3.3 setting $d = 2$. $\mathrm{GAP}_{\mathrm{NI}}(n)$ will then be equal to n times the power of a single qubit. Instead, $\mathrm{GAP}_{\mathrm{I}}(n)$ can be computed as described in Sec. 10.3.3 setting $d = 2^n$.

Fixing as usual $\beta_1 < \beta_2$, in Fig. 10.5 we show the maximum GAP of a heat engine, $P^{(\max)}_{[\mathrm{E}]}$ (left panel), and the maximum GAP of a refrigerator, $P^{(\max)}_{[\mathrm{R}]}$ (right panel), as a function of the number of qubits n in a log-log plot. The black curve, corresponding to $\mathrm{GAP}_{\mathrm{NI}}(n)$, is a linear function of n. Notably, there is a transient regime, roughly between 10^0 and 10^2, where $\mathrm{GAP}_{\mathrm{I}}(n)$ is superlinear: in particular, $P^{(\max)}_{[\mathrm{E}]}$ scales as n^2 (the dashed orange line is a reference quadratic function), whereas $P^{(\max)}_{[\mathrm{R}]}$ scales as a n^δ, with $1 < \delta < 2$. However, for large enough n (thermodynamic limit), we see that $\mathrm{GAP}_{\mathrm{I}}(n)$ is again a linear function of n, displaying a finite gap with respect to $\mathrm{GAP}_{\mathrm{NI}}(n)$. In App. G.5 we prove that the asymptotic behavior is given by

$$\begin{aligned} P^{(\max)}_{[\mathrm{E}]} &\overset{n\to\infty}{=} \ln 2 \, \frac{\beta_1^{-1} - \beta_2^{-1}}{\left(\sqrt{\Gamma_1^{-1}} + \sqrt{\Gamma_2^{-1}}\right)^2} \, n, \\ P^{(\max)}_{[\mathrm{R}]} &\overset{n\to\infty}{=} \ln 2 \, \frac{\beta_2^{-1}}{\left(\sqrt{\Gamma_1^{-1}} + \sqrt{\Gamma_2^{-1}}\right)^2} \, n, \end{aligned} \tag{10.37}$$

which is indeed linear in n. We plot these functions respectively in the left and right panel of Fig. 10.5 as dashed green lines.

Remarkably, in the heat engine case, the asymptotic behavior of $P^{(\max)}_{[\mathrm{E}]}$ is linear in the temperature difference $\Delta T = (\beta_1^{-1} - \beta_2^{-1})/k_B$. This is quite surprising: indeed, any slowly-driven quantum system [354] or any steady-state thermoelectric heat engine [11] delivers a power which, for small ΔT, scales as ΔT^2. Furthermore, also the maximum average power

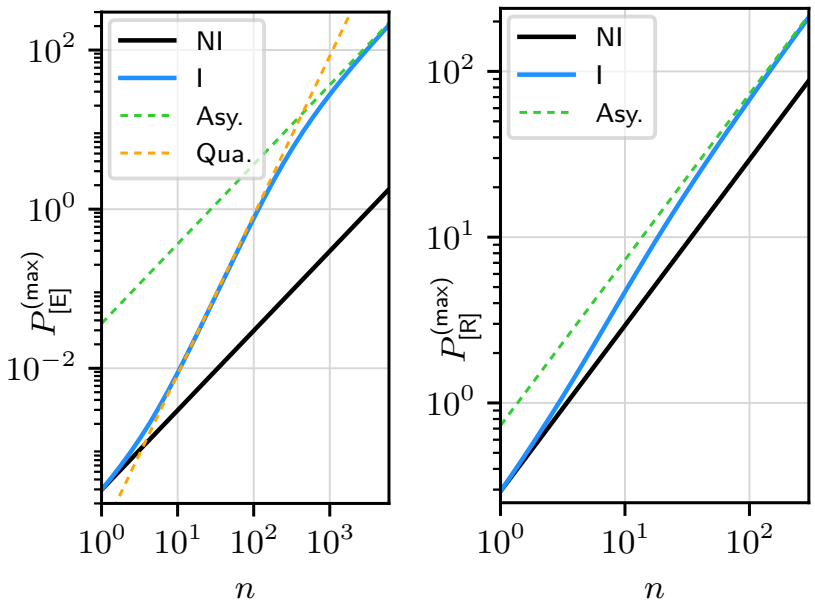

Figure 10.5: $P^{(\max)}_{[E]}$ (left panel) and $P^{(\max)}_{[R]}$ (right panel), measured in units of $\beta_2^{-1}/(\sqrt{\Gamma_1^{-1}} + \sqrt{\Gamma_2^{-1}})^2$, as a function of the number of qubits n displayed in a log-log plot. The black curve corresponds to the non-interacting case, while the blue curve to the interacting case. The dashed green curve is the analytic asymptotic value we find for $n \to \infty$, see Eq. (10.37), while the dashed orange line is a reference quadratic function. The temperatures are chosen such that $\beta_1 = 0.95\,\beta_2$.

of a qubit-based heat engine is proportional to ΔT^2 (see Ref. [361]), yielding $\mathrm{GAP}_{\mathrm{NI}}(n) = c_0\, n\, (\sqrt{\Gamma_1^{-1}} + \sqrt{\Gamma_2^{-1}})^{-2}\, k_B \Delta T^2/T$, where $c_0 \approx 0.11$ is solution to a transcendental equation. This implies that, for small temperature differences

$$\mathrm{GAP}_{\mathrm{I}}(n)/\mathrm{GAP}_{\mathrm{NI}}(n) \propto 1/(\Delta T/T), \tag{10.38}$$

which *diverges* in the limit $\Delta T/T \to 0$. This is clear evidence of the advantage of many-body systems over non-interacting systems for the construction of a heat engine. This also implies that a many-body heat engine in the thermodynamic limit and in the regime of small ΔT can outperform any slowly driven or thermoelectric heat engine thanks to the fast-driving regime.

In the refrigerator case, the maximum average cooling power can be computed analytically (see App. G.5 for details). Surprisingly, it turns out that, in the thermodynamic limit,

$$\mathrm{GAP}_{\mathrm{I}}(n)/\mathrm{GAP}_{\mathrm{NI}}(n) = \ln 2/W(1/e) \approx 2.49, \tag{10.39}$$

where $W(x)$ is the Lambert function. As opposed to the heat engine case, the universality of this ratio implies that there is no relevant advantage in using a many-body interacting working fluid over a non-interacting system to construct refrigerators at maximum power. It is therefore reasonable to consider operating many simple and independent systems in parallel to implement a refrigerator at maximum cooling power.

10.4 Case study: a qutrit heat engine

In this section we discuss and apply our optimal strategy to a setup consisting of a qutrit (a three-level system) which can be coupled to two or three thermal baths operated as a heat engine. We assume that the control is such that we operate in the semi-classical regime, i.e. $[H_{\vec{u}(t)}, H_{\vec{u}(t')}] = 0 \ \forall t, t' \in I_{[\vec{u}]}$. We therefore know, from our general result, that at most $L = d = 3$ intervals will be sufficient to maximize the power in the fast driving regime.

By studying this example, we show that standard models used to describe Fermionic and Bosonic baths are optimized simply by 2 quenches, i.e. the standard Otto cycle, with a spectrum as the one derived in Sec. 10.3.3 for a simpler model. Then, we explicitly construct an example of physical system where the generalized Otto cycle with 3 quenches outperforms the standard Otto cycle both in the presence of 2 or 3 thermal baths. Incidentally, this implies that the power can be enhanced by the presence of more than 2 heat baths, even if we can only couple the system to one bath at the time. At last we show that - in all cases mentioned above - the power decreases monotonically as we increase the period of the protocol T. This is evidence that, in this model, the fast driving regime is indeed the optimal regime to maximize the GAP.

The Hamiltonian of the system is given by

$$H_{\vec{u}(t)} = \epsilon_2(t) \left|2\right\rangle \left\langle 2\right| + \epsilon_3(t) \left|3\right\rangle \left\langle 3\right|, \tag{10.40}$$

where $|n\rangle$, for $n = 1, 2, 3$, are the three eigenstates with energies $\epsilon_n(t)$. Without loss of generality, we set $\epsilon_1(t) = 0$. Our control vector is given by $\vec{u}(t) = (\epsilon_2(t), \epsilon_3(t))$, and we assume that we can couple the system to one bath at the time. This hypothesis is mathematically described by an additional control $\alpha(t)$ that labels the bath we are coupled to. Following the standard microscopic derivation of the Lindblad master equation, we find that the populations $p_n(t) \equiv \langle n|\rho(t)\left|n\right\rangle$ satisfy the following rate equation (see App. G.6 for details)

$$\partial_t p_n(t) = \sum_{m \neq n} \left[-p_n(t)\Gamma_{nm}(\vec{u}(t), \alpha(t)) + p_m(t)\Gamma_{mn}(\vec{u}(t), \alpha(t))\right], \tag{10.41}$$

where the scalar quantity $\Gamma_{nm}(\vec{u}, \alpha)$ represents the transition rate, induced by the bath α, from state $|n\rangle$ to state $|m\rangle$, and $\partial_t p_n(t)$ denotes the time derivative of $p_n(t)$. Since the thermal baths are assumed to be in a Gibbs state, the rates satisfy the detailed balance equation

$$\Gamma_{nm}(\vec{u}, \alpha) = e^{\beta_\alpha(\epsilon_n - \epsilon_m)}\Gamma_{mn}(\vec{u}, \alpha), \tag{10.42}$$

which fix half of the rates. With this notation, the GAP of a heat engine, i.e. Eq. (10.8) with $c_\alpha = 1$, is given by (see App. G.6 for details)

$$P_{[E]}[\vec{u}] = \sum_n \epsilon_n(t)\partial_t p_n(t). \tag{10.43}$$

When the baths are given by a continuum of free Fermionic (F) or Bosonic (B) particles, and the Hamiltonian describing the system-bath coupling is quadratic, the rates are given by

$$\begin{aligned} \Gamma^{(\mathrm{F})}_{nm}(\vec{u}, \alpha) &= \gamma(\alpha) f[\beta_\alpha(\epsilon_m - \epsilon_n)], \\ \Gamma^{(\mathrm{B})}_{nm}(\vec{u}, \alpha) &= \gamma(\alpha)(\epsilon_m - \epsilon_n) n[\beta_\alpha(\epsilon_m - \epsilon_n)], \end{aligned} \tag{10.44}$$

where $f(x) = (e^x + 1)^{-1}$ and $n(x) = (e^x - 1)^{-1}$ are respectively the Fermi and Bose distributions. Notice that, in Eq. (10.44), we are assuming that the spectral density is flat in the

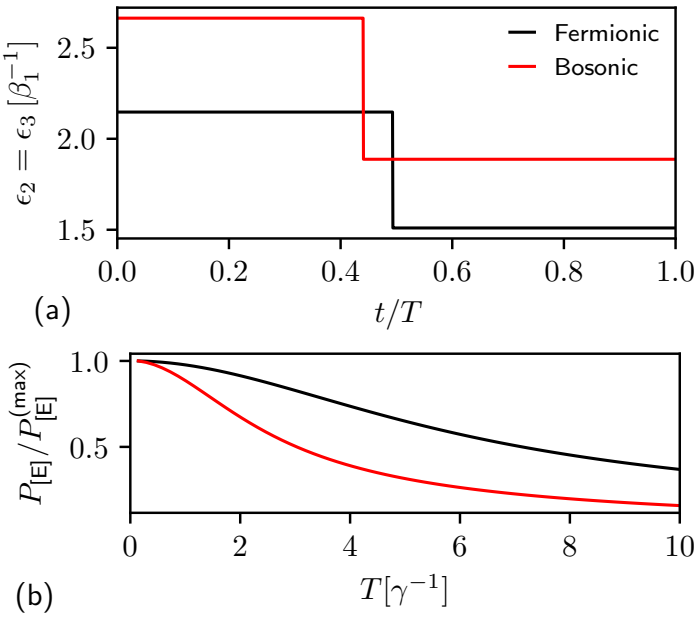

FIGURE 10.6: (a) The optimal protocol, described by $\epsilon_1(t) = 0$ and $\epsilon_2(t) = \epsilon_3(t)$, as a function of time t normalized to the protocol period T for the Fermionic and Bosonic models. The system is first coupled to bath $\alpha = 1$, then to $\alpha = 2$ after the quench. (b) Average power, normalized to the peak value, as a function of the period T. In both panel the parameters are $\beta_2 = 2\beta_1$ and $\gamma(\alpha) = \gamma$, where γ is a fixed timescale.

Femionic case, and Ohmic in the Bosonic case. Physically, these models may describe respectively electronic leads coupled to a quantum dot [42, 112, 124, 169, 266, 341] or photonic baths coupled to an (artifical) atom [18, 19, 27, 46, 340].

We now apply our results to this model. As detailed in App. G.6, we determine the optimal protocol by maximizing Eq. (10.43) driven by a generalized Otto cycle with $L = 3$ in the fast-driving regime. We therefore perform a maximization over 8 parameters: two time fractions μ_i (since $\sum_i \mu_i = 1$) and 6 control values $\epsilon_n^{(i)}$, where we defined $\epsilon_n^{(i)}$ as the value of $\epsilon_n(t)$ during the time interval $i = 1, 2, 3$. Notice that we only optimize over $\epsilon_n^{(i)}$ for $n = 2, 3$ since $\epsilon_1(t) = 0$. Assuming that we have two thermal baths at inverse temperatures $\beta_2 = 2\beta_1$, we try all possible temperature configurations as discussed in Sec. 10.2.1.

Notably, we find that both the Bosonic and the Fermionic models are optimized by a standard Otto cycle with only 2 quenches. Furthermore, the maximum power is achieved when $\epsilon_2^{(i)} = \epsilon_3^{(i)}$, which is exactly the energy spectrum which we proved to be optimal in a simpler relaxation model, see Sec. 10.3.3. In Fig. 10.6(a), we plot the optimal protocol, described by $\epsilon_1(t) = 0$ and $\epsilon_2(t) = \epsilon_3(t)$, as a function of time, while in Fig. 10.6(b) we plot a finite-time numerical calculation of the average extracted power $P_{[\mathrm{E}]}$ as a function of the protocol duration T, while maintaining the time fractions μ_i constant. Interestingly, we notice that in both models the power decreases monotonically with T, providing us with evidence that - in this case - the fast driving regime may be optimal to maximize power extraction. We also notice that the derivative of $P_{[\mathrm{E}]}$ respect to T, at $T = 0$, is null, hinting that our fast driving results may hold up to second order in γT. Furthermore, a large fraction of the maximum power can still be extracted even when the driving is slower than the characteristic rate γ, showing that our upper bound is "robust" to finite-time corrections.

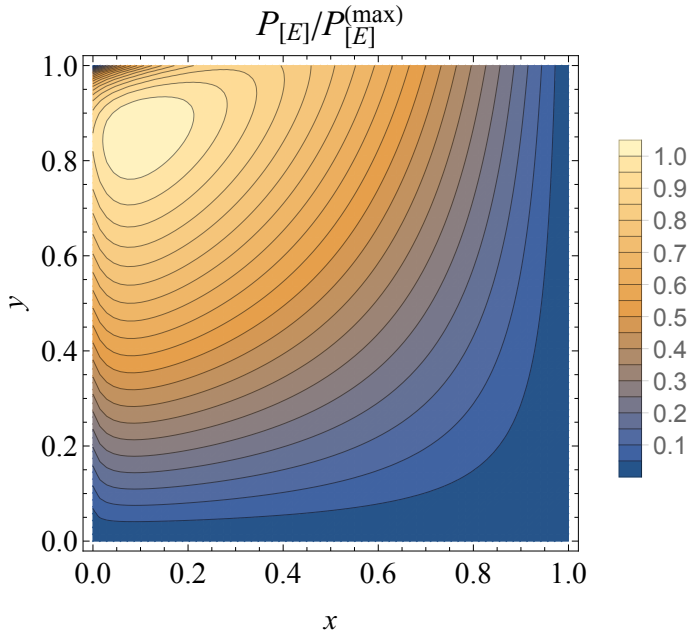

Figure 10.7: Contour plot of the average power, normalized to the peak value $P_{[\mathrm{E}]}^{(\max)}$, as a function of x and y. The parameters are: $\beta_1 = 8.12\beta_2$, $\beta_3 = 7.81\beta_2$, $\epsilon_2^{(1)} = 1.85\beta_2^{-1}$, $\epsilon_3^{(1)} = 1.56\beta_2^{-1}$, $\epsilon_2^{(2)} = 10.07\beta_2^{-1}$, $\epsilon_3^{(2)} = 9.58\beta_2^{-1}$, $\epsilon_2^{(3)} = 1.75\beta_2^{-1}$, $\epsilon_3^{(3)} = 8.12\beta_2^{-1}$, $\gamma_{12}(1) = \gamma$, $\gamma_{13}(1) = 1.21\gamma$, $\gamma_{23}(1) = 2.28\gamma$, $\gamma_{12}(2) = 9.45\gamma$, $\gamma_{13}(2) = 2.53\gamma$, $\gamma_{23}(2) = 5.26\gamma$, $\gamma_{12}(3) = 5.9\gamma$, $\gamma_{13}(3) = 1.4\gamma$, $\gamma_{23}(3) = 6.22\gamma$.

We now show that there are cases in which a generalized Otto cycle with 3 quenches can outperform a standard Otto cycle. As a "counter-example", let us consider the case where the rates $\Gamma_{nm}(\vec{u}, \alpha)$ are vanishingly small for all controls $\vec{u}$, except for a set of discrete points. Physically, this could be implemented through peaked density of states in the baths. We therefore consider 3 thermal baths at inverse temperatures β_α (for $\alpha = 1, 2, 3$), such that each one induces a non-null rate only when the controls $\epsilon_2(t)$ and $\epsilon_3(t)$ take the values $\tilde{\epsilon}_2^{(\alpha)}$ and $\tilde{\epsilon}_3^{(\alpha)}$, respectively. Mathematically, we can describe this scenario defining

$$\Gamma_{nm}(\vec{u}, \alpha) = \gamma_{nm}(\alpha)\, \chi(\vec{u}, \alpha), \tag{10.45}$$

where $\gamma_{nm}(\alpha)$ are constants, and $\chi(\vec{u}, \alpha)$ is an indicator function which is one if $\epsilon_2(t) = \tilde{\epsilon}_2^{(\alpha)}$ and $\epsilon_3(t) = \tilde{\epsilon}_3^{(\alpha)}$, otherwise it is zero. In this scenario, the optimal values of $\epsilon_n^{(i)}$ are simply given by $\tilde{\epsilon}_n^{(i)}$. The only parameters over which we must optimize are the time fractions μ_i, which we express as

$$\theta_1 = x, \qquad \theta_2 = (1 - x)y, \qquad \theta_3 = (1 - x)(1 - y), \tag{10.46}$$

where $x \in [0, 1]$ and $y \in [0, 1]$ cover all possibilities. This parameterization is such that one of the three time fractions μ_i is null if and only if x and/or y takes the values 0 or 1. In Fig. 10.7 we show a contour-plot of the average power $P_{[\mathrm{E}]}$ as a functions of x and y (see caption for the parameters used). As we can see, the maximum power does not occur on the sides of the box: this implies that all optimal μ_i are finite, so the generalized Otto cycle with three finite intervals outperforms the standard Otto cycle. Numerically, we find that the optimal power

occurs at $x \approx 0.092$ and $y \approx 0.86$. This result also proves that the power can be enhanced by using three thermal baths; this is in contrast with the optimization of the efficiency, which only requires coupling to the hottest and the coldest bath. Physically, this is due to the fact that, even if the third bath has a temperature between the coldest and the hottest, it may have a thermalization rate which is higher than the other baths, thus speeding up the heat exchange.

At last, we verified numerically that there are cases where 3 quenches outperform 2 quenches even when we only have two thermal baths. Furthermore, we computed the exact finite-time average power $P_{[\mathrm{E}]}$ as a function of T, performing the optimal protocol found through the maximization in Fig. 10.7. Notably, as in the Fermionic and Bosonic models, we find that the power decreases monotonically as T increases, with the same qualitative behavior as in Fig. 10.6(b). Again, this hints at the optimality of the fast driving regime.

10.5 Summary

In this chapter we exhaustively discussed the optimization of thermal machines in the fast driving regime. We proved in full generality that in this regime the optimal protocols are universally given by generalized Otto cycles, which are composed by a certain number L of time intervals where the control is fixed. We then bound L from above in terms of the dimension of the Hilbert space of the working fluid. The proof holds regardless of the specific choice of the control-dependent dissipators, of possible constraints on the control parameters, and regardless of the specific form of the Hamiltonian of the working fluid.

Studying a simpler class of master equations, we found tighter bounds on L, and we showed that the standard Otto cycle (characterized by $L = 2$) is optimal in a vast class of systems. We then considered baths characterized by a single thermalization timescale. Assuming full control over the system, we explicitly found the optimal driving strategy, which involves producing highly degenerate states, revealing an interesting connection with the results of [357] and [354]. In this scenario, we found that the generation of coherence in the instantaneous eigenstate basis is detrimental for power maximization. We then compared the performance of a heat engine and of a refrigerator based on n interacting (I) qubits or on n non-interacting (NI) qubits. We found that while there is a transient regime where the power of the I model is superlinear in n, in the thermodynamic limit ($n \to \infty$), both models deliver a power linear in n. In the heat engine case, the power in the thermodynamic limit scales linearly with the temperature difference ΔT. Conversely, the maximum power of thermoelectric heat engines, slowly driven heat engines, and of the NI case universally scales as ΔT^2. Therefore, for small temperature differences and in the thermodynamic limit, there is a clear many-body advantage enabled by the fast-driving regime. On the contrary, we proved that the power of a refrigerator in the I case is universally ≈ 2.49 greater than in the NI case, proving that many-body effects provide a very marginal advantage over operating independent systems. It is therefore reasonable to consider constructing a refrigerator operating in parallel many simple independent units.

Besides their theoretical relevance, these results lead to a great simplification in the optimization of thermodynamic problems from a practical point of view, due to the intrinsic simplicity of the generalized Otto cycle. This simplification can be exploited both for analytical and numerical treatments, as we explicitly showed studying a qutrit-based heat engine. In this setup, we analyzed typical configurations, such as fermionic and bosonic baths, and we found a specific form of the dissipators such that the optimal protocol consists of coupling

the system to three baths at different temperatures. This result marks a difference with the maximization of the efficiency, that always require only two thermal sources, and shows that the bound on the number of intervals derived in the first part of the chapter is actually tight in this case.

This work unlocks the possibility of analytically and/or numerically optimizing the performance of many quantum thermal machines. As future directions, it is interesting to assess the role of coherence under general master equations, and to understand for which classes of systems the fast driving regime is optimal for power extraction. Furthermore, by providing strict bounds on optimal protocols, our results can be used as benchmarks to assess if effects beyond the Markovian regime and weak coupling approximation can indeed enhance, or decrease, the performance of thermal machines. By highlighting the importance of many-body interactions for the performance of a heat engine regime, a future venue would be to identify and study realistic systems which display the ΔT scaling of the maximum power in the thermodynamic limit. At last, it seems natural to investigate the properties of the fast-driving regime respect to other thermodynamic figures of merit, such as the efficiency at maximum power, or work fluctuations.

11 Conclusions

In this thesis we studied the thermodynamic properties of quantum systems, focusing in particular on the performance of quantum thermal machines. In Chap. 2 we presented a general formalism to study open quantum system which we employed throughout the entire thesis to study the dynamics of mesoscopic systems coupled to thermal baths. We then presented an extension of this formalism to account for coherent tunneling processes beyond leading order in the system-bath coupling. In Chap. 3 we applied this formalism to describe various thermal machines, such as heat engines and refrigerators operating in different regimes. The following chapters presented original work.

In Chaps. 4, 5, 6, 7 and 8 we dealt with thermoelectric machines, i.e. with system operating in the steady state. In particular, in Chap. 4 we studied the thermoelectric properties of an interacting, multilevel quantum dot operated as a heat engine. We assessed the impact of the multilevel structure and of interactions on the performance of the heat engine, studying the power, the efficiency, and the efficiency at maximum power. Furthermore, we found that the correlation between tunneling electrons imposed by Coulomb repulsion improves the efficiency of the heat engine by enhancing the energy filtering mechanism. In Chap. 5 we applied the formalism developed in Chaps. 2, 3 and 4 to analyze experimental measurements of an InAs/InP nanowire quantum dot. We studied the system as a thermoelectric heat engine, finding that it can reach efficiencies close to the thermodynamic bound. In Chap. 6 we assessed the impact of coherent tunneling effects - beyond the weak coupling regime - on the thermovoltage across a metallic island, and we were able to accurately describe experimental measurements without any free fitting parameter. In Chap. 7 we studied an absorption refrigerator - a system that exploits a temperature difference to refrigerate an even colder thermal bath without requiring any external work - based on Coulomb coupled single electron systems. We found the conditions under which it can operate at maximum coefficient of performance, and we analyzed the system as an autonomous Maxwell daemon. In Chap. 8 we studied thermal rectification across qubits, deriving exact upper bounds and general properties which hold in the weak coupling regime. We then performed calculations beyond the weak coupling regime, finding that higher order coherent processes can violate the aforementioned bounds, allowing for stronger rectification and providing us with simple signatures of higher order coherent processes.

In Chaps. 9 and 10 we dealt with driven thermal machines. In particular, in Chap. 9 we searched for the optimal cycle that maximizes the extracted power from a heat engine, and the cooling power from a refrigerator, using a qubit as working fluid. Without any assumptions on the particular system-bath coupling, we found that the power is always maximized by an Otto cycle performed in the fast-driving regime, i.e. when the driving is faster than the typical relaxation rate induced by the baths. Inspired by this result, in Chap. 10 we studied an arbitrary quantum system operated in the fast-driving regime. Among all possible cycles in the fast-driving regime, we found that the "generalized Otto cycle" universally maximizes the power of heat engines and the cooling power of refrigerators. We related the complexity of the cycle to the size of the Hilbert space of the working fluid. In certain classes of systems, we found that the optimal cycle reduces to the standard Otto cycle. At last, we compared the performance of a heat engine composed of n interacting and non interacting qubits, finding that interactions can boost the performance, also in the thermodynamic limit, when the temperature difference between the leads is small. Conversely, we proved that interaction effects provide a very limited advantage when operating as a refrigerator.

As future direction, it is interesting to further assess the impact of quantum effects, such as coherence, entanglement, and strong system-bath coupling, on the performance of thermal machines. While these effects lead to the idea of "quantum supremacy" in the field of quantum computation, it is still not clear whether such advantage extends also to quantum thermodynamics. Another direction which should be further investigated is the relation between thermoelectric and steady state heat engines, and understanding under which hypothesis a driven quantum thermal machine delivers maximum power in the fast-driving regime.

A

Appendix: thermoelectric properties of an interacting quantum dot-based heat engine

In this appendix we present the details of some calculations relative to Chap. 4, and we report the analytic non linear study of a single energy level QD system.

A.1 The Pauli master equation always allows a non-trivial solution.

To prove this statements, let us consider the Pauli equation as written in Eq. (4.11). This equation is made up of a sum over p of the following expression:

$$(\delta_{n_p,1} - \delta_{n_p,0}) \left[p\left(\{n_i\}, n_p = 0\right) A_{\widetilde{N},p} \; - p\left(\{n_i\}, n_p = 1\right) B_{\widetilde{N},p} \right], \tag{A.1}$$

which is a function of a generic configuration $\{n_i\}$. Let us sum this expression for the two particular configurations: $(\{n_i\}, n_p = 1)$ and $(\{n_i\}, n_p = 0)$. When $n_p = 1$, the first term in round parenthesis gives a plus sign, while when $n_p = 0$, it gives a minus sign. The rest of the expression does not depend on n_p, since $\widetilde{N} = \sum_{i \neq p} n_i$, thus the sum over the above configurations exactly vanishes. Now let us go back to Eq. (4.11), and let us sum over the two configurations $(\{n_i\}, n_k = 1)$ and $(\{n_i\}, n_k = 0)$, k being a given index. According to the argument given above, the term in the sum where $p = k$ vanishes, and we obtain

$$\sum_{n_k=0,1} \sum_{p \neq k} (\delta_{n_p,1} - \delta_{n_p,0}) \left[p\left(\{n_i\}, n_p = 0\right) A_{\widetilde{N},p} - p\left(\{n_i\}, n_p = 1\right) B_{\widetilde{N},p} \right] = 0. \tag{A.2}$$

Thus by summing over a given occupation number $n_k = 0, 1$ we have removed the case $p = k$ in the sum over p. If we now sum over all occupation numbers, we will remove all terms from the sum, yielding zero [1]. The sum over all occupation numbers $\{n_i\}$ is the sum of all 2^L equations in the Pauli master equation: this demonstrates that any equation in the Pauli

[1] By summing over all occupation numbers except for a fixed n_p, we could demonstrate that the LBEs derive from the Pauli equation.

master equation is linearly dependent from the other ones. Thus the matrix M defined by the master equation has a null space of dimension at least 1, since we demonstrated that the rows of M are not linearly independent. Furthermore, if we perform the same sum over all occupation numbers to the time dependent Pauli master equation, given in Eq. (4.4), we find that:

$$\frac{\partial}{\partial t}\left(\sum_{\{n_i\}} p(\{n_i\})\right) = 0. \tag{A.3}$$

This is an obvious but important property that says that the probability normalization does not depend on time.

A.2 The PDBEs are not consistent in general

In general, if $E_C \neq 0$, the PDBEs are not consistent. This means that no set of $p(\{n_i\})$ exists that can simultaneously satisfy all the PDBEs. In App. (A.3) we will discuss which conditions guarantee their consistency within the linear response regime.

Here let us demonstrate their inconsistency in the special case $L = 2$. Let us start from Eq. (4.15) and consider non null temperature and electrochemical potential differences. We will show that these equations form an over-complete set for $p(\{n_i\})$ that in general does not allow any non null solution. Since $L = 2$, we have $2^L = 4$ unknown probabilities, and the number of PDBEs is $2^{L-1}2 = 4$. In this case, the PDBEs can be represented in matrix form as follows

$$M_D\vec{p} \equiv \begin{pmatrix} A_{0,1} & -B_{0,1} & 0 & 0 \\ 0 & 0 & A_{1,1} & -B_{1,1} \\ A_{0,2} & 0 & -B_{0,2} & 0 \\ 0 & A_{1,2} & 0 & -B_{1,2} \end{pmatrix} \begin{pmatrix} p_{00} \\ p_{01} \\ p_{10} \\ p_{11} \end{pmatrix} = \begin{pmatrix} 0 \\ 0 \\ 0 \\ 0 \end{pmatrix}, \tag{A.4}$$

where $p_{n_2 n_1} \equiv p(n_2, n_1)$ and the coefficients are defined in Eqs. (4.12) and (4.13). In order to show that this linear algebra problem does not allow a non null solution, we will show that the determinant $\det(M_D)$ is in general not zero. We have

$$\begin{aligned}\det(M_D) = \Gamma_{\rm tot}(1)\Gamma_{\rm tot}(2)\left(A_{0,2}A_{1,1} - A_{0,1}A_{1,2}\right) + \Gamma_{\rm tot}(1)A_{0,2}A_{1,2}\left(A_{0,1} - A_{1,1}\right) \\ + \Gamma_{\rm tot}(2)A_{0,1}A_{1,1}\left(A_{1,2} - A_{0,2}\right),\end{aligned} \tag{A.5}$$

where $\Gamma_{\rm tot}(p) = \sum_\alpha \Gamma_\alpha(p)$. It is pretty clear that since $\Gamma_\alpha(p)$, E_p and E_C are arbitrary, this determinant cannot be in general zero. For instance, choosing a two terminal system with $\Gamma_1(p) = \Gamma_2(p) = \Gamma$, $\Delta\mu_2 = 4k_BT$, $E_1 = 1/2k_BT$, $E_2 = 3/2k_BT$, $\mu = \Delta T_2 = 0$ we obtain $\det(M_D)/\Gamma^4 \simeq 0.20$. It is interesting to notice that at equilibrium ($\Delta\mu_2 = \Delta T_2 = 0$), the PDBEs are all exactly satisfied by the gran canonical distribution. Furthermore, in the non-interacting limit $E_C = 0$, the coefficients $A_{\widetilde{N},p}$ and $B_{\widetilde{N},p}$ depend only on p, so that we can drop the $\widetilde{N}$ argument. Thus $\det(M_D) = A_2A_1B_1B_2 - A_1A_2B_2B_1 \equiv 0$.

The proof can be extended to any number L of levels as follows. We rewrite the PDBEs, Eq. (4.15), as

$$\ln p\left(\{n_i\}, n_p = 0\right) - \ln p\left(\{n_i\}, n_p = 1\right) = \ln \frac{B_{\widetilde{N},p}}{A_{\widetilde{N},p}}. \tag{A.6}$$

This equation has the same form as the LDBEs (A.8) which we will consider in App. A.3, where the unknown probabilities are replaced by the logarithm of the probabilities, and where

$$\delta_p(\widetilde{N}) = \ln \frac{B_{\widetilde{N},p}}{A_{\widetilde{N},p}}. \tag{A.7}$$

As we shall show in App. A.3, these equations are consistent if $\delta_p(\widetilde{N})$ satisfies property (A.10). This is the case if $E_C = 0$, since $A_{\widetilde{N},p}$ and $B_{\widetilde{N},p}$ are then independent of $\widetilde{N}$. Then condition (A.10) is trivially fulfilled with $c = 0$ and the PDBEs are consistent.

To summarize, as we will see in Appendix A.3, the PDBEs are not consistent in general, but they are if we set $E_C = 0$ or $\Delta\mu_\alpha = \Delta T_\alpha = 0$ for all α. Furthermore, within the linear response regime, they are valid in many more cases, for example if the tunneling rates are proportional, i.e. $\Gamma_\alpha(p) = k_\alpha \Gamma_1(p)$ for $\alpha = 2, 3, \ldots, \mathcal{N}$.

A.3 Conditions of validity of the linearized PDBEs

In this Appendix we will assess under which conditions the linearized PDBEs are consistent. We start by rewriting Eq. (4.30) in the following way:

$$\psi(\{n_i\}, n_p = 0) - \psi(\{n_i\}, n_p = 1) = \delta_p(\widetilde{N}), \tag{A.8}$$

where

$$\delta_p(\widetilde{N}) \equiv -\frac{1}{k_B T} \sum_\alpha \frac{\Gamma_\alpha(p)}{\Gamma_{\text{tot}}(p)} \left[\left(E_p + (2\widetilde{N} + 1) E_C - \mu \right) \frac{\Delta T_\alpha}{T} + \Delta\mu_\alpha \right]. \tag{A.9}$$

We will prove that the linearized PDBEs, written in Eq. (A.8), are consistent if $\delta_p(\widetilde{N})$ satisfies the property

$$\delta_p(N) - \delta_p(M) = c(N - M), \tag{A.10}$$

where c is a constant that does not depend on p, N or M. This statement will be explicitly proven for a two energy level system, then it will be extended to L energy levels by induction.

Property (A.10) is in general satisfied if the tunneling rates are proportional, i.e. $\Gamma_\alpha(p) = k_\alpha \Gamma_1(p)$, or if $E_C = 0$, or if $\Delta T_\alpha = 0$ for all α. Furthermore, in a three terminal system, property (A.10) is satisfied also if $\Delta T_2 = 0$ and $\Gamma_3(p) = k\Gamma_{\text{tot}}(p)$, or if $\Delta T_3 = 0$ and $\Gamma_2(p) = k\Gamma_{\text{tot}}(p)$. These conditions can be generalized to a generic $\mathcal{N}$-terminal system by requiring that

$$E_C \sum_\alpha \frac{\Gamma_\alpha(p)}{\Gamma_{\text{tot}}(p)} \Delta T_\alpha \tag{A.11}$$

is independent of p.

A.3.1 Two energy level system ($L = 2$)

We will prove that if property (A.10) is satisfied, then the linearized PDBEs allow a solution. Eq. (A.8) represents a linear algebra problem for $\psi(\{n_i\})$. For $L = 2$, $\psi(\{n_i\}) = \psi(n_2, n_1) \equiv \psi_{n_2,n_1}$. Let $\vec{\psi}$ be the vector $(\psi_{00}, \psi_{01}, \psi_{10}, \psi_{11})$ and let B be the corresponding matrix such that Eq. (A.8) can be written as

$$B\vec{\psi} = \begin{pmatrix} 1 & -1 & 0 & 0 \\ 0 & 0 & 1 & -1 \\ 1 & 0 & -1 & 0 \\ 0 & 1 & 0 & -1 \end{pmatrix} \begin{pmatrix} \psi_{00} \\ \psi_{01} \\ \psi_{10} \\ \psi_{11} \end{pmatrix} = \begin{pmatrix} \delta_1(0) \\ \delta_1(1) \\ \delta_2(0) \\ \delta_2(1) \end{pmatrix} \equiv \vec{\delta}. \tag{A.12}$$

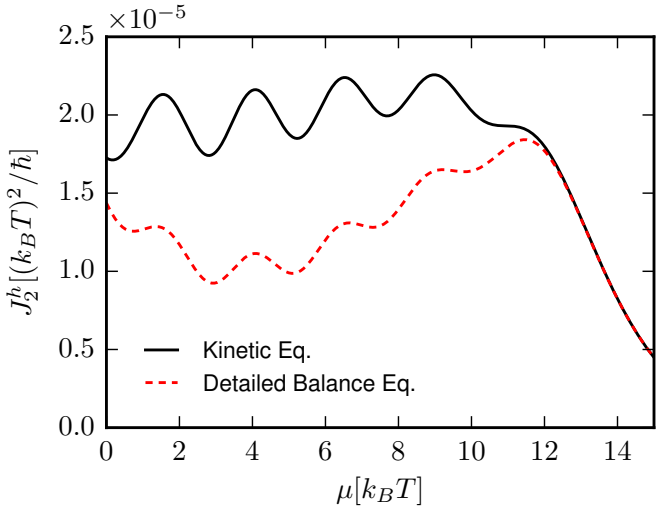

Figure A.1: (Color online) Heat current computed using Eq. (4.10) and using non equilibrium probabilities found solving exactly the Pauli master equation (black solid line) and a subset of independent PDBEs (red dashed line), as a function of the electrochemical potential μ. The parameters used are: $\Delta T/T = 10^{-4}$, $\Delta\mu = 0$, $E_C = k_BT$, 5 equidistant energy levels with $\Delta E = 0.2k_BT$, $\hbar\Gamma_1(p) = (5)^{p-1}k_BT$, and $\hbar\Gamma_2(p) = (0.01)^{p-1}k_BT$.

Matrix B has a null space of dimension 1, generated by $\vec{\psi} = (1,1,1,1)$, thus it is not invertible. This vector actually represents the equilibrium distribution: when $\Delta T_\alpha = \Delta\mu_\alpha = 0$, $\delta_p(\tilde{N}) = 0$, so $\vec{\psi} = (1,1,1,1)$ satisfies Eq. (A.12). Since $p = p_{eq}(1+\psi)$, $p = 2p_{eq}$. Normalizing the probabilities yields $p \equiv p_{eq}$, so we have demonstrated that the equilibrium distribution is in fact given by the grand canonical distribution. Eq. (A.12) will allow a solution if and only if vector $\vec{\delta}$ belongs to the image of matrix B. The dimension of the image of matrix B is 3, so there is a one dimensional space orthogonal to the image of B that cannot be obtained by linear combinations of B's columns. Vector

$$\vec{v_0} = \begin{pmatrix} 1 \\ -1 \\ -1 \\ 1 \end{pmatrix} \tag{A.13}$$

is orthogonal to the columns of B, so it is a generator of this one dimensional space. Thus a solution $\vec{\psi}$ will exist if and only if vector $\vec{\delta}$ only belongs to the image of B, thus it cannot have a projection on $\vec{v_0}$. The projection is zero when

$$0 = \vec{v_0} \cdot \vec{\delta} = \delta_1(0) - \delta_1(1) - \delta_2(0) + \delta_2(1) \tag{A.14}$$

which is satisfied using property (A.10).

As we have shown in Sec. 4.2, Eq. (4.26) for the linearized charge current is correct in general, instead the linearized heat current given in Eq. (4.31) is correct only if the linearized PDBE are consistent. We verified numerically all these statements computing exactly, for small temperature and electrochemical potential differences, the charge and heat currents using both the PDBEs and the Pauli master equation. As demonstrated by Fig. A.1, which

shows the heat current as a function of μ for a choice of tunneling rates that are not proportional to each other, a particular subset of PDBEs leads to an incorrect result (red dashed curve) which differs from the one obtained using the Pauli master equation (black solid curve). On the other hard, there is no difference when plotting the charge current using the same parameters as in Fig. A.1.

A.3.2 L energy level system

We extend the previous demonstration to a generic system with L energy levels. We will use the following notation and conventions:

- $\{n_i\}$ indicates a generic set of occupation numbers, conventionally ordered the following way: $\{n_L, n_{L-1}, \ldots, n_2, n_1\}$.
- $(n_p = 1, \{n_i\})$ is a shorthand notation for: $\{n_L, \ldots, n_{p+1}, 1, n_{p-1}, \ldots, n_1\}$.
- $(n_p = 0, \{n_i\})$ is a shorthand notation for: $\{n_L, \ldots, n_{p+1}, 0, n_{p-1}, \ldots, n_1\}$.
- $(n_p = 1, \{0\})$ is a shorthand notation for: $\{0, \ldots, 0, 1, 0, \ldots, 0\}$, where the 1 is relative to $n_p = 1$.
- $(n_p = 0, \{0\})$ is equivalent to: $\{0, \ldots, 0\}$.
- $\vec{\psi}_i$ is the component of vector $\vec{\psi}$ with index i.
- Each linearized PDBE in Eq. (A.8) can be uniquely defined by specifying p and $\{n_i\}$, so $[p|\{n_i\}]$ is a shorthand notation to indicate that given equation.
- Let A be a matrix written in block form, for example:

$$A = \left(\begin{array}{c|c} B & 0 \\ 0 & C \\ D & E \end{array}\right), \tag{A.15}$$

  where B, C, D and E are matrices. By "block row" we intend the set of rows in the block. For example, the first block row of A is $(B, 0)$, the second block row of A is $(0, C)$, and so on.

In order to represent the linearized PDBE, given in Eq. (A.8), in matrix form, we will put the 2^L unknowns $\psi(\{n_i\})$ into a vector as follows: $\vec{\psi}_{I(\{n_i\})} \equiv \psi(\{n_i\})$, where $I(\{n_i\}) = \sum_{i=1}^{L} n_i 2^{i-1}$.

Let us define $B(L)$ as the $L2^{L-1} \times 2^L$ matrix such that Eq. (A.8) can be represented as follows:

$$B(L)\vec{\psi} = \vec{\delta}(L), \tag{A.16}$$

where $\vec{\delta}(L)$ is a vector containing the various values of $\delta_p(\widetilde{N})$. Each row of $B(L)$ contains zeros except for a $+1$ and a -1 in the position corresponding to $\psi(n_p = 0, \{n_i\})$ and $\psi(n_p = 1, \{n_i\})$. Let's notice that $B(L)$ has the following property:

$$B(L)\begin{pmatrix} 1 \\ \vdots \\ 1 \end{pmatrix} = \begin{pmatrix} 0 \\ \vdots \\ 0 \end{pmatrix}. \tag{A.17}$$

This property is trivial since, as we just discussed, each row of $B(L)$ only has a $+1$ and a -1.

Recursive decomposition

We want to write $B(L)$ in terms of $B(L-1)$. We will thus order the rows in $B(L)$, and accordingly the elements of $\vec{\delta}(L)$, starting from those LDBE $[p|\{n_i\}]$ where $p < L$, then we will add the ones involving level L. In particular, we will first put equations $[p|(n_L = 0, \{n_i\})]$ with $p < L$, then we will add equations $[p|(n_L = 1, \{n_i\})]$ with $p < L$, and at last we will add equations $[L|\{n_i\}]$, which are the ones involving level L. For example, $B(2)$ will be written as in Eq. (A.12).

This ordering allows us to relate $B(L)$ to $B(L-1)$. The first set of equations $[p|(n_L = 0, \{n_i\})]$, with $p < L$, represents all possible LDBE between elements of $\vec{\psi}$ with $n_L = 0$, so they are equivalent to the LDBE for $L-1$ levels. Since $n_L = 0$, according to our indexing convention, these rows involve all indexes of $\vec{\psi}_i$ with $0 \leq i < 2^{L-1}$, which corresponds to the first half of vector $\vec{\psi}$. Instead, the equations $[p|(n_L = 1, \{n_i\})]$, with $p < L$, represents all possible LDBE between elements of $\vec{\psi}$ with $n_L = 1$, so also these equations are equivalent to the LDBE for $L-1$ levels. Since $n_L = 1$, according to our indexing convention, these rows involve all indexes of $\vec{\psi}_i$ with $i \geq 2^{L-1}$, which corresponds to the second half of vector $\vec{\psi}$. At last, equations $[L, \{n_i\}]$ relate components of ψ where only the occupation number n_L is changed. Since $I(n_L = 1, \{n_i\}) = I(n_L = 0, \{n_i\}) + 2^{L-1}$, these equations relate indexes of $\vec{\psi}$ that are distant 2^{L-1}, thus they mix elements between the first and second half of $\vec{\psi}$. We will thus have the following block representation:

$$B(L) = \left(\begin{array}{c|c} B(L-1) & 0 \\ 0 & B(L-1) \\ I_d(L-1) & -I_d(L-1) \end{array}\right), \tag{A.18}$$

where $I_d(L)$ is the $2^L \times 2^L$ identity matrix. Since we trivially have that $B(1) = (1, -1)$, Eq. (A.18) can be used to define $B(L)$ recursively, yielding a precise row ordering. For example, as we can see in Eq. (A.12), $B(2)$ can be obtained by applying Eq. (A.18) to $B(1)$.

Also $\vec{\delta}(L)$ allows a decomposition in terms of $\vec{\delta}(L-1)$. The first block row in Eq. (A.18), $(B(L-1), 0)$, corresponds to equations $[p|(n_L = 0, \{n_i\})]$ with $p < L$. Recalling Eq. (A.9), we will notice that $\delta_p(\widetilde{N})$ depends on level L only through:

$$\widetilde{N}(L) = \sum_{i \neq p}^{L} n_i = \sum_{i \neq p}^{L-1} n_i = \widetilde{N}(L-1), \tag{A.19}$$

since $n_L = 0$. So in the first block row we have that $\vec{\delta}(L) = \vec{\delta}(L-1)$. The second block row, $(0, B(L-1))$, corresponds to equations $[p|(n_L = 1, \{n_i\})]$ with $p < L$. So this time the presence of level L will change the values of $\widetilde{N}$ the following way:

$$\widetilde{N}(L) = \sum_{i \neq p}^{L} n_i = 1 + \sum_{i \neq p}^{L-1} n_i = 1 + \widetilde{N}(L-1), \tag{A.20}$$

since $n_L = 1$. So in the second block row $\vec{\delta}(L)$ is given by $\vec{\delta}(L-1)$ replacing $\widetilde{N}$ with $\widetilde{N} + 1$. Using property (A.10), we have that:

$$\delta_p(\widetilde{N} + 1) = \delta_p(\widetilde{N}) + c, \tag{A.21}$$

where c is a constant that does not depend on p or $\widetilde{N}$. So in the second block row we will have that $\vec{\delta}(L) = \vec{\delta}(L-1) + c$. The last row $(I_d(L-1), -I_d(L-1))$ in Eq. (A.18) corresponds to

equations $[L|\{n_i\}]$, which involve level L. So let us define $\vec{\partial}(L)$ as the vector that corresponds to $\vec{\delta}(L)$ in the third block row.

Using these observations and Eq. (A.18), we can rewrite Eq. (A.16) using the following decomposition:

$$\left(\begin{array}{c|c} B(L-1) & 0 \\ 0 & B(L-1) \\ I_d(L-1) & -I_d(L-1) \end{array}\right) \begin{pmatrix} \vec{\psi}(n_L=0,\{n_i\}) \\ \vec{\psi}(n_L=1,\{n_i\}) \end{pmatrix} = \begin{pmatrix} \vec{\delta}(L-1) \\ \vec{\delta}(L-1)+c \\ \vec{\partial}(L) \end{pmatrix}. \tag{A.22}$$

This decomposition will be the main tool to perform a demonstration by induction.

The independent part of $B(L)$

Among the $L2^{L-1}$ rows of $B(L)$, we will explicitly show how to extract 2^L-1 linearly independent rows; we will later show that all other rows can be obtained by linear combinations. Let's define $\widetilde{B}(L)$ as the matrix containing only the rows of $B(L)$ corresponding to equations $[p|\{n_i\}]$ with $n_i=0$ for $i<p$; these are 2^L-1 rows. We will now prove by induction that all the rows of $\widetilde{B}(L)$ are linearly independent.

Since $\widetilde{B}(L)$ is made by selecting rows from $B(L)$, we can decompose it in terms of $\widetilde{B}(L-1)$ just like we did for $B(L)$ in Eq. (A.18). An interesting characteristic of $\widetilde{B}(L)$ is that it only has one equation in the block $[L|\{n_i\}]$ involving $\psi(0,0,\ldots,0)$ and $\psi(1,0,\ldots,0)$. So the decomposition becomes:

$$\widetilde{B}(L) = \left(\begin{array}{c|c} \widetilde{B}(L-1) & 0 \\ 0 & \widetilde{B}(L-1) \\ 1,0,\ldots,0 & -1,0,\ldots,0 \end{array}\right). \tag{A.23}$$

We can use Eq. (A.23) to define $\widetilde{B}(L)$ recursively noticing that $\widetilde{B}(1)=B(1)=(1,-1)$.

Now we can prove by induction over L the following statement: all the rows of $\widetilde{B}(L)$ are linearly independent. This statement is obvious for $L=1$ and $L=2$. We will now assume that our statement is valid for $L-1$, and we will show that this implies that it is valid for L. The first block row in Eq. (A.23) contains rows that are linearly independent by hypothesis. The same is true for the second block row. Also putting together the first and second block row yields 2^L-2 independent rows, since the space generated by the respective linear combinations are clearly orthogonal thanks to the block decomposition. So we have to show that the last row cannot be written as a linear combination of previous rows. We will make a proof by contradiction. Let's assume that the last row $\vec{v}=(1,0,\ldots,0|-1,0,\ldots,0)$ can be written as a linear combination of a vector belonging to the space generated the first block row, $\vec{w_0}$, and of one belonging to the second block row, $\vec{w_1}$:

$$\vec{v}=\vec{w_0}+\vec{w_1}. \tag{A.24}$$

If we define $\vec{n}=(1,\ldots,1|0,\ldots,0)$, we will have that:

$$\begin{aligned} \vec{n}\cdot\vec{w_0}&=0, \\ \vec{n}\cdot\vec{w_1}&=0. \end{aligned} \tag{A.25}$$

The first equation is zero because, as we have shown in Eq. (A.17), $B(L)$ has the property that $B(L)(1,\ldots,1)^T=0$, so it is true also for $\widetilde{B}(L)$. The second equation is zero because $\vec{n}$ has zeroes on all non null components of $\vec{w_1}$. So multiplying each sides of Eq. (A.24) by $\vec{n}$ yields $\vec{n}\cdot\vec{v}=\vec{n}\cdot(\vec{w_0}+\vec{w_1})=0$, which is absurd because $\vec{n}\cdot\vec{v}=1$. Thus we have completed the proof by induction.

Consistency of the linearized PDBEs

We will now show that if property (A.10) is valid, the linearized PDBEs are consistent and allow a solution for ψ given by a one dimensional space; the unique solution can then be found by imposing the normalization condition on the probabilities. We will thus prove by induction over L the following statement: if $\delta_p(N)$ satisfies property (A.10), all equation in the linear algebra system in Eq. (A.22) can be written as linear combinations of the equations involving the rows of $\widetilde{B}(L)$. Since there are $2^L - 1$ independent rows in $\widetilde{B}(L)$, by virtue of Rouché-Capelli's theorem we will have a solution given by a $2^L - (2^L - 1) = 1$ dimensional space. This statement is trivially true for $L = 1$, since $B(1) = \widetilde{B}(1)$, and we have proved it explicitly for $L = 2$, so we will show that if it's valid for $L - 1$, then it's valid for L.

Let's consider the subset of rows of Eq. (A.22) where $B(L) = \widetilde{B}(L)$. Among these equations, we will denote by "set 0" those belonging to the first block row, and "set 1" those belonging to the second block row. As we can see from Eq. (A.23), this leaves out one equation in the last block row, which is:

$$\psi(0, 0, \ldots, 0) - \psi(1, 0, \ldots, 0) = \delta_L(0). \tag{A.26}$$

By induction hypothesis, all equations in the first block row of Eq. (A.22) can be written as linear combinations of set 0. Furthermore, if $\delta_p(N)$ satisfies property (A.10), also $\delta_p(N) + c$ satisfies the same property, so by induction hypothesis, also all equations in the second block row of Eq. (A.22) can be written as linear combinations of set 1. So any row in the first and second block row in Eq. (A.22) can be written as linear combinations of those equations involving $\widetilde{B}(L)$.

We are left to show that equations in the last block row of Eq. (A.22) can be written as linear combinations of equations involving $\widetilde{B}(L)$. Thanks to what we have just demonstrated, this is is equivalent to showing that the equations in the last block row are linear combinations of the first two block rows of Eq. (A.22), and of Eq. (A.26). The equations of the last block row of Eq. (A.22) are of the form

$$\psi(n_L = 0, \{n_i\}) - \psi(n_L = 1, \{n_i\}) = \delta_L(\widetilde{N}). \tag{A.27}$$

Given any fixed set of $\{n_i\}$, which fixes $\widetilde{N} = \sum_{i \neq L} n_i$, we will now show how to obtain Eq. (A.27) by relating $\psi(n_L = 0, \{n_i\})$ to $\psi(n_L = 1, \{n_i\})$ only using the equations of the first two block rows of Eq. (A.22) and Eq. (A.26). We can first relate $\psi(n_L = 0, \{n_i\})$ to $\psi(n_L = 0, \{0\})$ using the equations in the first block row $\widetilde{N}$ times, each time changing a non null n_i to zero. We will obtain the following result:

$$\psi(n_L = 0, \{n_i\}) - \psi(n_L = 0, \{0\}) = -\sum_{i=1}^{\widetilde{N}} \delta_{p_i}(\widetilde{N} - i), \tag{A.28}$$

where p_i is the energy level whose occupation number has been changed to zero at step i; the argument $\widetilde{N} - i$ is given by the fact that at each step we use a linearized PDBE where $\sum_{i \neq p_i} n_i$ decreases by one. Using Eq. (A.26) we obtain

$$\psi(n_L = 0, \{n_i\}) - \psi(n_L = 1, \{0\}) = \delta_L(0) - \sum_{i=1}^{\widetilde{N}} \delta_{p_i}(\widetilde{N} - i). \tag{A.29}$$

Now we can relate $\psi(n_L = 1, \{0\})$ to $\psi(n_L = 1, \{n_i\})$ using the equations of the second block row to set each non null n_i back to 1. If we do this in the exact same order as we did in the

previous step, we will obtain

$$\psi(n_L=0,\{n_i\})-\psi(n_L=1,\{n_i\})=\sum_{i=1}^{\widetilde{N}}\delta_{p_i}(i)+\delta_L(0)-\sum_{i=1}^{\widetilde{N}}\delta_{p_i}(\widetilde{N}-i). \tag{A.30}$$

The "new" term has the same set of $\{p_i\}$, and the argument i is given by the fact that $\sum_{i\neq p_i} n_i$ increases by one at each step, and it starts from 1 since now $n_L=1$. Eq. (A.27) is of the same form, therefore the equations on the last block row can be expressed as linear combinations of $\widetilde{B}(L)$ if and only if they represent the same equation, which requires:

$$\delta_L(\widetilde{N})-\delta_L(0)=\sum_{i=1}^{\widetilde{N}}\left[\delta_{p_i}(i)-\delta_{p_i}(\widetilde{N}-i)\right]. \tag{A.31}$$

Using property (A.10), this last equation reduces to $\widetilde{N}=\widetilde{N}$, concluding the proof by induction.

A.4 Non-interacting QD: Non-linear effects

In this Appendix we will study the transport coefficients, maximum and peak efficiency and efficiency at peak power of a two-terminal non-interacting QD. We will first consider a single-level QD and then a two-levels QD (with energy-independent tunneling rates).

Let us first consider a QD with a single energy level E_1. In this case, the Pauli master equation with $E_C=0$ reduces to a single simple equation, so it is possible to compute the currents. Using the two-terminal notation introduced in Secs. 4.2.2 and 4.3 we obtain

$$\begin{aligned} I &= -e\gamma(f_2-f_1),\\ J_2^h &= (\bar{\Delta}_{\min}+\theta_0 eV)\gamma(f_2-f_1), \end{aligned} \tag{A.32}$$

where

$$\begin{aligned} f_1 &= f\left(\frac{\bar{\Delta}_{\min}-(1-\theta_0)eV}{k_BT_1}\right),\\ f_2 &= f\left(\frac{\bar{\Delta}_{\min}+\theta_0 eV}{k_BT_2}\right),\\ \bar{\Delta}_{\min} &= E_1-\mu, \end{aligned} \tag{A.33}$$

with the Fermi function $f(x)=[1+\exp(x)]^{-1}$. Note that the same result could be obtained using the Landauer-Büttiker scattering formalism with a narrow in energy single-level QD transmission probability. Using Eq. (A.32), we can compute

$$G\equiv\left.\frac{\partial I}{\partial V}\right|_{\Delta T=0}=\frac{e^2\gamma}{4k_BT}\left[\frac{\theta_0}{\cosh^2\left(\frac{\bar{\Delta}_{\min}+\theta_0 eV}{2k_BT}\right)}+\frac{1-\theta_0}{\cosh^2\left(\frac{\bar{\Delta}_{\min}-(1-\theta_0)eV}{2k_BT}\right)}\right]. \tag{A.34}$$

Note that the value of θ_0 can be determined by measuring G.

We can also compute S using Eq. (A.32). The condition $I=0$ is satisfied when the arguments of the two Fermi distributions f_1 and f_2 are equal, so we obtain

$$S\equiv-\left.\frac{V}{\Delta T}\right|_{I=0}=-\frac{1}{eT^*}\bar{\Delta}_{\min}, \tag{A.35}$$

where

$$T^* = \theta_0 T_1 + (1-\theta_0) T_2 \tag{A.36}$$

is the average reservoir temperature, weighed with θ_0. As we can see, the slope of $S(\mu)$ beyond the linear response regime is strongly determined by θ_0. In the linear response regime $T^* \simeq T$, where T is the average reservoirs' temperature, so once again we obtain the result we obtained in the quantum limit linear response regime of an interacting QD neglecting the fine structure oscillations, due to other energy levels.

It is now interesting to study the influence of a second energy level on S. In Fig. A.2 we show the comparison between the thermopower of a non-interacting two energy level QD (dashed lines) and the multilevel interacting QD considered in Fig. 4.6 (solid lines), for different values of ΔT. For the sake of comparison, we choose the value for the two energy levels E_1 and E_2 to match the two dominant transition energies of the multilevel interacting QD, in particular $E_1 = \mu_{N=3} = 290\ k_B\bar{T}$ and $E_2 = \mu_{N=4} = 410\ k_B\bar{T}$. On one hand, the

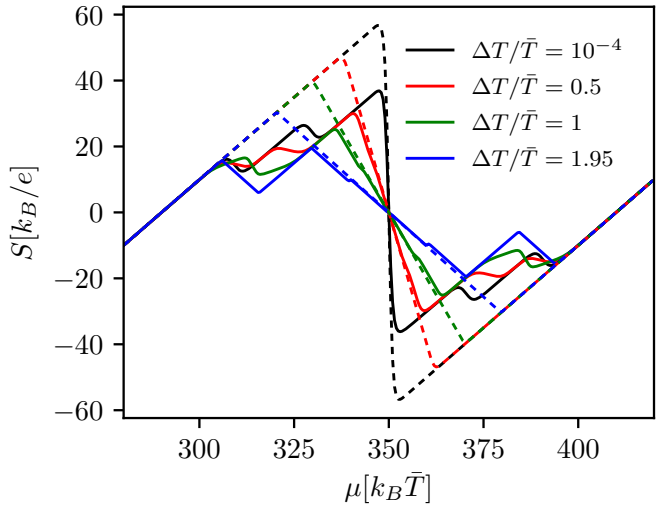

Figure A.2: (Color online) Thermopower S as a function of μ for a two-level non-interacting QD with energies $E_1 = 290 k_B\bar{T}$ and $E_2 = 410 k_B\bar{T}$ (dashed lines) and of a multi-level interacting QD (solid lines), considered in Sec. 4.3, with the same parameters used in Fig. 4.6.

non-interacting thermopower shows a linear dependence on μ when μ is close to E_1 or E_2, whose slope is independent of ΔT (only because $\theta_0 = 1/2$) and is the same as the interacting QD when $|\Delta_{\min}| < \Delta E$. On the other, when μ is close to the middle point $\mu^* = (E_1 + E_2)/2$ between E_1 and E_2, the thermopower depends linearly on μ with a negative slope ($S \simeq \alpha\delta\mu$, with $\delta\mu$ being a small displacement with respect to μ^*) which depends on the temperatures as

$$\alpha = -\frac{1}{e\Delta T}\frac{T_1 \cosh^2(\frac{\Delta\varepsilon}{4k_BT_1}) - T_2\cosh^2(\frac{\Delta\varepsilon}{4k_BT_2})}{\theta_0 T_1\cosh^2(\frac{\Delta\varepsilon}{4k_BT_1}) + (1-\theta_0)T_2\cosh^2(\frac{\Delta\varepsilon}{4k_BT_2})}, \tag{A.37}$$

where $\Delta\varepsilon = E_2 - E_1$. Eq. (A.37) has been found by expanding the charge current around $\mu = \mu^*$. Once again, the slope of the interacting and non-interacting QDs are the same in this region. In between instead the fine structure oscillations of the interacting QD create a substantial difference that causes the maximum value of S to decrease.

At last we can compute the Peltier coefficient for a single energy level QD using Eq. (A.32):

$$\Pi \equiv \left.\frac{J_2^h}{I}\right|_{\Delta T=0} = -\frac{\bar{\Delta}_{\min}}{e} - \theta_0 V. \tag{A.38}$$

Surprisingly, we would have obtained the same result also without setting $\Delta T = 0$. On the other hand, it strongly depends on V: increasing the voltage shifts Π by $\theta_0 V$, so measuring this shift would allow to measure θ_0. Furthermore, if we compute Π in the linear response regime, setting $V = 0$ in Eq. (A.38), we can explicitly verify that $\Pi = TS$ is respected. If we set $\theta_0 = 0$, we see that $\Pi = T^*S$, even beyond the linear response regime, for arbitrary temperature and voltage differences. Interestingly, in the presence of two levels the Peltier coefficient beyond linear response Π still satisfies the relation $(\Pi + \theta_0 V) = TS_{\rm lin}$, where $S_{\rm lin}$ is the linear-response thermopower (black dashed curve in Fig. A.2), so that $(\Pi + \theta_0 V)$ does not depend on V.

The linearization of G and S for a single-level non-interacting QD yields the same results obtained for a multilevel interacting QD, in the quantum limit linear response regime, if we restrict $|\Delta_{\min}| < \Delta E$. We could expect this result since considering a single energy level is intuitively equivalent to sending ΔE and E_C to infinity in the interacting QD. On the contrary, a single level QD model cannot be used to estimate K since it predicts $K = 0$ [in fact, from Eq. (A.32) we have that $J_2^h \propto I$, so K, caluclated at $I = 0$, vanishes].

We now want to study the power and efficiency of a single-level QD. Considering $\Delta T = T_2 - T_1 > 0$ and inserting Eq. (A.32) into the definitions in Eqs. (4.19) and (7.6), we can write the power and efficiency as

$$P = -VI = \gamma e V (f_2 - f_1), \tag{A.39}$$

$$\eta = \frac{P}{J_2^h} = \frac{eV}{\theta_0 eV + \bar{\Delta}_{\min}}. \tag{A.40}$$

We will consider a fixed temperature difference $\Delta T = T_2 - T_1 > 0$, and a variable V such that the system behaves as a heat engine ($P > 0$). The power is positive when $V \in [0, V_{\rm stop}]$, where $V_{\rm stop}$ is the non zero voltage that creates a null charge current. Imposing this condition we find

$$V_{\rm stop} = \frac{\bar{\Delta}_{\min}}{e}\frac{\eta_{\rm c}}{1 - \theta_0 \eta_{\rm c}}. \tag{A.41}$$

Without loss of generality, we can specify our analysis to the region where $\mu < E_1$, E_1 being the energy of the single energy level; thus $\bar{\Delta}_{\min} > 0$, so $V_{\rm stop}$ is positive, and our system will behave as a heat engine when

$$0 \le V \le V_{\rm stop} = \frac{\bar{\Delta}_{\min}}{e}\frac{\eta_{\rm c}}{1 - \theta_0 \eta_{\rm c}}. \tag{A.42}$$

Let us now discuss the peak efficiency of the system. We have to maximize Eq. (A.40) with respect to $\bar{\Delta}_{\min}$ and V, at fixed $\Delta T > 0$, respecting $\bar{\Delta}_{\min} > 0$ and Eq. (A.42). Since η is a growing function of V for $\bar{\Delta}_{\min} > 0$, η will be maximum when computed at the highest allowed voltage, $V_{\rm stop}$. Inserting $V_{\rm stop}$ in Eq. (A.40) yields:

$$\eta^{(\max)} = \eta_{\rm c}. \tag{A.43}$$

Thus a single level QD in the sequential tunneling regime always achieves $\eta^{(\max)} = \eta_{\rm c}$, regardless of the the temperature difference, θ_0 and the distance between μ and E_1 [151, 152].

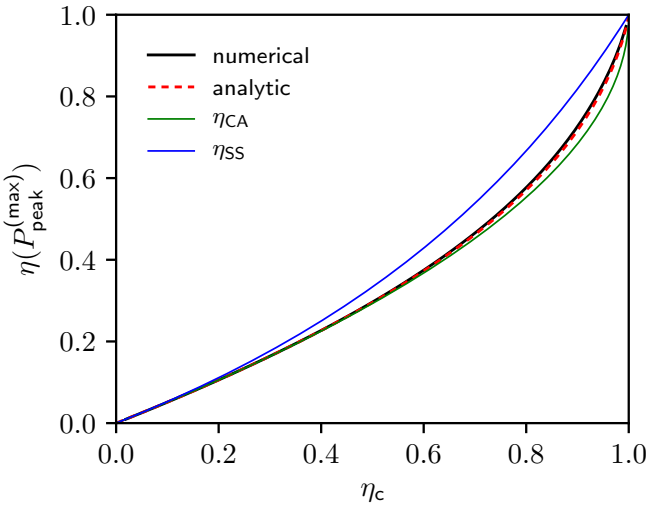

Figure A.3: (Color online) Comparison between $\eta(P^{(\max)}_{\text{peak}})$ computed numerically and using Eq. (A.44). Also η_{CA} and η_{SS} are displayed.

Using Eq. (A.39) we can compute the power when η is maximum, i.e. when $V = V_{\text{stop}}$: this yields $P = 0$. These results agrees with the expectation that Carnot's efficiency is reached when the heat exchange is "reversible", thus when the power is vanishingly small.

Let us now study the efficiency at peak power, $\eta(P^{(\max)}_{\text{peak}})$. $P^{(\max)}_{\text{peak}}$ is obtained by maximizing the power with respect to $\bar{\Delta}_{\min}$ and V, at fixed $\Delta T > 0$, imposing $\bar{\Delta}_{\min} > 0$ and Eq. (A.42). By imposing this request we obtain two coupled equations that cannot be solved analytically [112]. However, the Fermi function is always evaluated when the argument is positive, and we approximate it with its exponential tail. By doing so, we obtain

$$\begin{aligned} \eta(P^{(\max)}_{\text{peak}}) &= \eta_c \frac{\eta_c}{\eta_c - (1-\eta_c)\ln(1-\eta_c)}, \\ P^{(\max)}_{\text{peak}} &= \gamma \bar{e} k_B \Delta T \frac{\eta_c}{\left[1 + \bar{e}(1-\eta_c)^{1-1/\eta_c}\right]\left[\bar{e} + (1-\eta_c)^{1/\eta_c}\right]}, \end{aligned} \tag{A.44}$$

where $\bar{e}$ is Napier's constant. These equations provide an approximate expression of $P^{(\max)}_{\text{peak}}$ and $\eta(P^{(\max)}_{\text{peak}})$ for a single level QD, valid for any reservoir temperatures. Note how $\eta(P^{(\max)}_{\text{peak}})$ only depends on η_c, while $P^{(\max)}_{\text{peak}}$ depends on both T_1 and T_2 through η_c and ΔT. Note $\eta(P^{(\max)}_{\text{peak}}) \to \eta_c/2$ as $\eta_c \to 0$, as expected from the fact that $ZT \to \infty$ for a narrow transmission probability [5]. As we can see in Fig. A.3, there is a good agreement between $\eta(P^{(\max)}_{\text{peak}})$ given in Eq. (A.44) and a numerical calculation: the analytic expression slightly underestimates $\eta(P^{(\max)}_{\text{peak}})$. Furthermore, we can see that the efficiency at peak power goes beyond η_{CA}, while it remains under η_{SS}. We have also verified that $P^{(\max)}_{\text{peak}}$ given in Eq. (A.44) is in good agreement with the numerical calculation.

To further assess the validity of the approximate analytical formulas (A.44), we expand them around $\eta_c = 0$ and $\eta_c = 1$, and compare the obtained results with the exact expansions

known in these limiting cases [112]. An expansion of Eq. (A.44) around $\eta_c = 0$ yields

$$\begin{aligned} \eta(P_{\text{peak}}^{(\max)}) &= \frac{\eta_c}{2} + \frac{\eta_c^2}{8} + \frac{7}{96}\eta_c^3 + O(\eta_c^4), \\ P_{\text{peak}}^{(\max)} &= \gamma k_B T \frac{\bar{e}^2}{(1+\bar{e}^2)^2} \left(\frac{\Delta T}{T}\right)^2 + O\left((\Delta T/T)^3\right), \end{aligned} \tag{A.45}$$

where T is the average temperature in the linear response regime. Our result for $\eta(P_{\text{peak}}^{(\max)})$ has to be compared with exact expansion of Ref. [112],

$$\eta(P_{\text{peak}}^{(\max)}) = \frac{\eta_c}{2} + \frac{\eta_c^2}{8} + \frac{7}{96}(1+0.0627)\eta_c^3 + O(\eta_c^4). \tag{A.46}$$

As we can see the first two orders are exactly the same, while the third order only has $\approx 6\%$

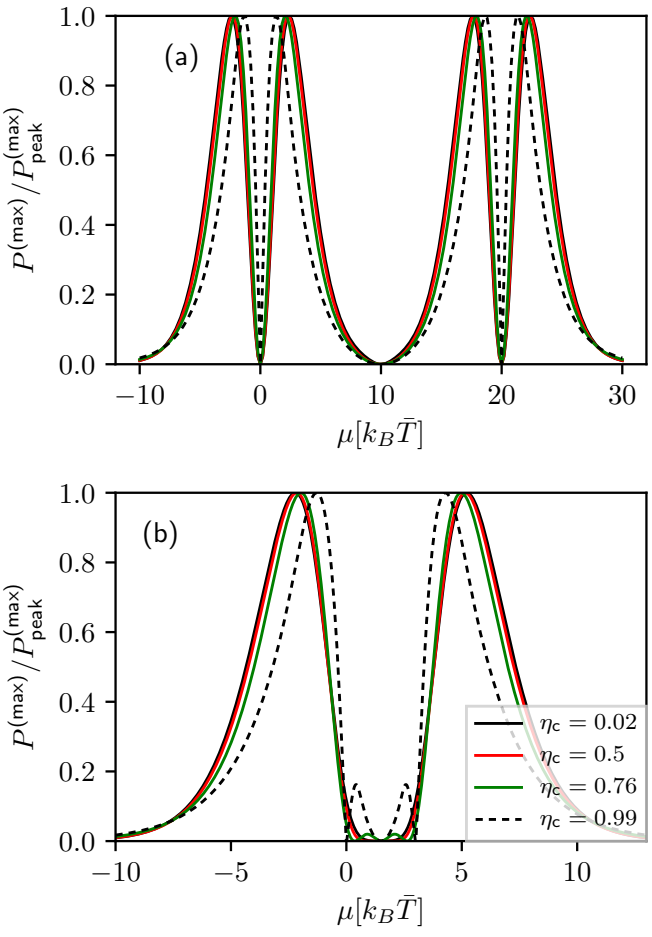

Figure A.4: (Color online) Maximum power, normalized to the peak value, plotted as a function of μ for different values of η_c with $\Delta E = 20\, k_B\bar{T}$ and $E_C = 0$ (top panel) and with $\Delta E = 3\, k_B\bar{T}$ and $E_C = 0$ (bottom panel). Tunneling rates are $\hbar\Gamma_1(p) = \hbar\Gamma_2(p) = 0.01 k_B\bar{T}$.

correction, confirming that Eq. (A.44) slightly underestimates the exact result. The expansion of $P_{\text{peak}}^{(\max)}$ instead confirms that in the linear response regime the peak power depends on ΔT^2.

Furthermore, evaluating the coefficient numerically yields $P_{\text{peak}}^{(\max)} \approx 0.105\gamma k_B T(\Delta T/T)^2$, which is in very good agreement with the result obtained in Eq. (4.50) for a multilevel QD in the quantum limit linear response regime (note that $P_{\text{peak}}^{(\max)} = Q^*\Delta T^2/4$).

An expansion of Eq. (A.44) around $\eta_c = 1$ yields

$$\eta(P_{\text{peak}}^{(\max)}) \approx 1 + (1-\eta_c)\ln(1-\eta_c), \tag{A.47}$$

$$P_{\text{peak}}^{(\max)} \approx \frac{\gamma k_B \Delta T}{1+\bar{e}}\left(1 + \frac{\bar{e}}{1+\bar{e}}(1-\eta_c)\ln(1-\eta_c)\right), \tag{A.48}$$

to be compared with the exact expansion [112]

$$\eta(P_{\text{peak}}^{(\max)}) \approx 1 + \frac{(1-\eta_c)\ln(1-\eta_c)}{1.278}. \tag{A.49}$$

There is a good agreement between the two formulas, and we can see that Eq. (A.44) slightly underestimates $\eta(P_{\text{peak}}^{(\max)})$. We stress that the expression of $P_{\text{peak}}^{(\max)}$ for $\eta_c \approx 1$, Eq. (A.48), shows that the peak power is proportional to ΔT, as opposed to ΔT^2 as in the linear response regime. Furthermore the peak power approaches its maximum value given by $P_{\text{peak}}^{(\max)} = \gamma k_B \Delta T/(1+\bar{e})$ when $\eta_c = 1$.

At last, we have computed numerically the maximum power $P_{\text{max}}^{(\max)}$ in the case of a two-level non-interacting QD. $P_{\text{max}}^{(\max)}$ is computed by maximizing the power only over V; the peak of $P_{\text{max}}^{(\max)}$ as a function of μ will thus yield $P_{\text{peak}}^{(\max)}$. In Fig. A.4 $P^{(\max)}/P_{\text{peak}}^{(\max)}$ is plotted as a function of μ for $\Delta E = 20\,k_B T$ and $\Delta E = 2\,k_B T$ respectively in panel (a) and (b). Each curve corresponds to a different value of η_c, starting from the linear-response case (black solid curve) to the extremely non-linear behavior (black dashed curve) at $\eta_c = 0.99$. In panel (a), representing the quantum limit, all curves nearly coincide with the linear-response one (apart for very large values of η_c). For each value of η_c the height of the four peaks is equal, contrary to the case where interaction is present (see Fig 4.11). This is to be expected, since the two energy levels do not influence each other in the quantum limit in the absence of interaction, so the behavior is essentially dictated by a single level. In the bottom panel instead, representing a case away from the quantum limit, the external peaks are much higher with respect to the internal peaks, especially for small values of η_c. This is due to the fact that ΔE is of the order of $k_B\bar{T}$ and therefore we cannot consider a single energy level at a time, and this produces the peak asymmetry.

B

Appendix: Thermoelectric conversion at 30 K in InAs/InP nanowire quantum dots

In this appendix we report experimental and theoretical details concerning Chap. 5.

B.1 Materials and methods

InAs/InP heterostructured NWs were fabricated using a chemical beam epitaxy process seeded by metallic nanoparticles obtained from thermal dewetting of a Au thin film [367]. Growth was performed at 420 ± 10 °C using trimethylindium (TMIn), tert-butylarsine (TBA), and tributylphosphine (TBP). The TBAs and TBP are thermally cracked at around 1000 °C upon entering the growth chamber, while the TMIn decomposes on the substrate surface. The metallorganic pressures were 0.3, 1.0, and 4.0 Torr for TMIn, TBAs, and TBP, respectively. These growth conditions ensure to achieve InAs/InP NW heterostructures with straight morphology, constant diameter, wurtzite crystal structure and atomically sharp interfaces [175, 368]. InAs/InP and InP/InAs interfaces where realized without any interruption by switching the group V precursors. The position of the dot inside the NW is determined based on its average distance from the Au nanoparticle, as measured from an ensemble of wires with STEM. This leads to a typical alignment error of ±50 nm, based on NW imaging statistics and on alignment errors during the lithographic process. Ohmic contacts are obtained by thermal evaporation of a Ti/Au (10/100 nm) bilayer, after a chemical passivation step based on a standard $(NH_4)S_x$ solution.

The NW voltage bias was obtained using the auxiliary output of a Stanford Research lock-in amplifier SR830 and a resistor divider. Charge current was measured using a DL1211 current preamplifier and an Agilent 34401A multimeter. Each of the thermometers was excited by an AC current of 1 μA, obtained using the sinusoidal output of a SR830 amplifier connected to a 1 MΩ bias resistor. The local heater was supplied using a Keithley 2400 SourceMeter. The gate voltage was controlled using a Yokogawa 7651 DC source.

B.2 Measurement setup circuit

The developed experimental platform allows to acquire simultaneously the temperatures and to perform transport measurements. To do so, we use two 1:1 audio transformers to isolate the circuit used to feed and acquire data from the thermometers to the circuit used to apply bias voltage and measure the flowing current. The electrical scheme is shown in Fig. B.1. The

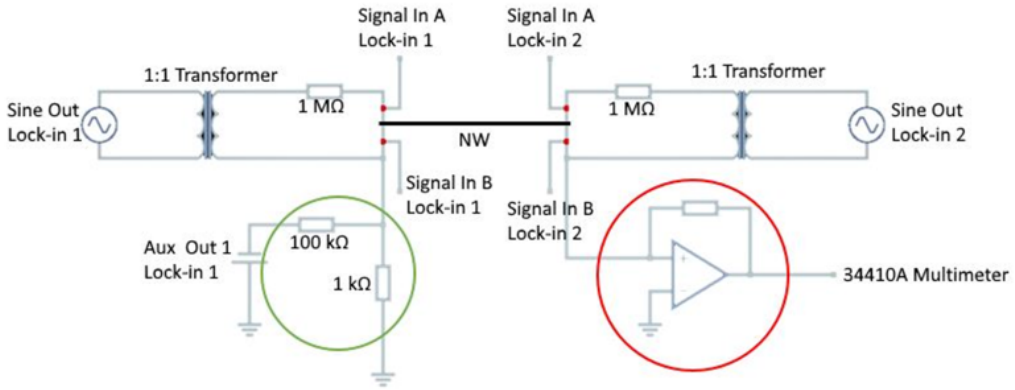

Figure B.1: Experimental circuit electrical scheme. Two 1:1 audio transformers are used to disentangle the circuit applying voltage bias and thermometers. Two SR830 Lock-in amplifiers (Lock-in 1 and 2) are used in order to perform high precision 4-wire measurements. The voltage is applied using a SR830 DC output passing through a 1/100 voltage divider (green circle) inserted in order to avoid overcharging the nanowire. Current flowing through the nanostructure is measured by a multimeter digitalizing the output of a current pre-amplifier (red circle).

thermometers are fed with a constant 5 μA amplitude AC current, provided by the oscillating input of two SR830 lock-in amplifiers (5 V amplitude) connected in series with 1 MΩ resistors. The working frequencies are 781 Hz and 1151 Hz, respectively. Phase-locked measurements are used to measure the voltage drop between the central leads of the thermometers (Signal in A lock-in 1(2) and Signal in B lock-in 1(2) in Fig. B.1), which is directly related to the local temperature via the dependence of the gold layer resistance on temperature. In order to perform temperature measurements, a calibration procedure is needed to link the voltage reading to a temperature measurement. Details about the thermometers calibration is provided in Sec. B.3.

On the other side, the biasing voltage is provided by a SR830 DC voltage output (Aux out 1 in Fig. B.1). The source is connected to a 1/100 protective voltage divider, used to avoid providing excessive bias voltage to the nanostructure and thus damaging it. Furthermore, current flowing through the NW is measured by means of a pre-amplifying stage (DL1211), whose output is digitalized by an Agilent 34410A multimeter.

B.3 Thermometer and heater calibration

As previously anticipated, calibration procedures are needed in order to properly use the micro-thermometers embedded in the developed architecture.

These calibration procedures are performed for every device during the cool-down procedure. This means that the thermometers are fed as described in Sec. B.2 and the voltage drop between the central leads is measured during the insertion of the sample in the cryostat, i.e. going from 300K to 4K, every 1 s.

The resulting curve is shown in Fig. B.2, in which calibration curves are displayed for the thermometer near (red curve) and far (blue curve) from the heating serpentine in the temperature interval from 80 K to 4 K. Higher temperatures are not reported in the figure, being the calibration curve trivially linear and temperature higher than 80 K out of interest in this study.

Figure B.2 shows the calibration curves without any offset, and the differences between them can be related to the fabrication procedure not being ideal (e.g. slight differences in the thickness of the gold layer defining the thermometers). It is worth to notice that

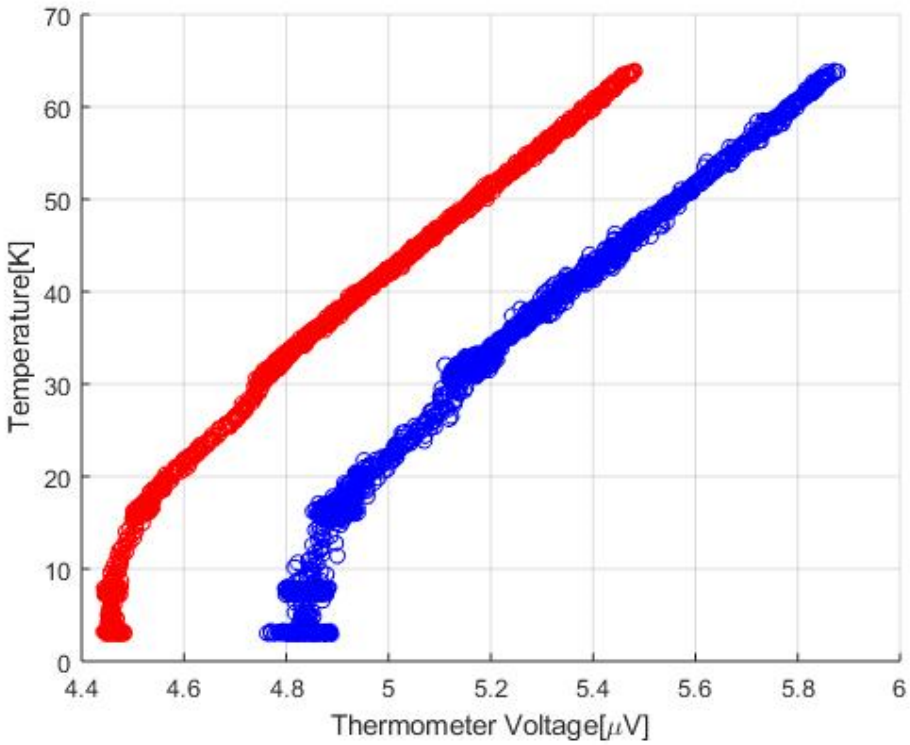

Figure B.2: Thermometer calibration curves from 65K to 4K. Red color is referring to the thermometer near the heater, while blue color is used for the far from heater thermometer. Differences between curves can be attributable to the non-ideality of fabrication procedures.

thermometers tend to "saturate" for temperatures less than 10 K and are not responsive to further changes in temperature. This behavior can be attributed to the metallic nature of the thermometers and does not represent a limitation for this study, in which temperatures higher than 10 K are considered.

After having measured the response of the thermometers, it is possible to have a local temperature measurement by acquiring the voltage drop value and comparing it with the measured curve.

Moreover, after having retrieved the calibration curves for the thermometers, we verify their response to the local heating serpentine. To do so, we feed the heater by a constant current by using a Keithley 2400 SourceMeter and measure the variation on the voltage drop between the central leads of the thermometers for different values of the heating current. The obtained curves are shown in Fig. B.3, in which response to current flowing through the heater is reported for both thermometers. It is possible to notice that the red curve is more responsive for lower values of the heating current, coherently with the relative thermometer being near the heater. By comparing the measured value for the voltage drop of the thermometer at a

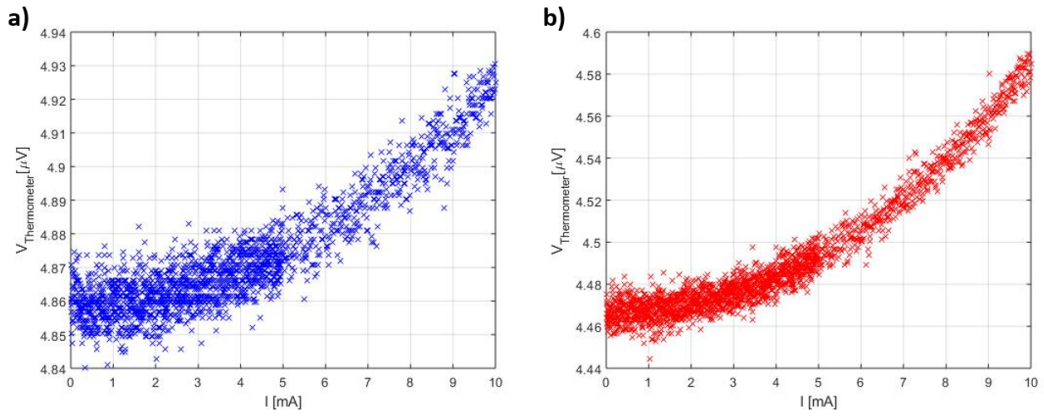

Figure B.3: Thermometer response to current flowing through the heating serpentine. Blue color refers to the thermometer far from the heater, while the red curve represents the response of the thermometer near the heater. The red curve is responsive to the heater for lower current values compared to the red curve. This behavior is coherent with the thermometer position relatively to the serpentine.

fixed value for the current flowing through the serpentine with the thermometer calibration curve shown in Fig. B.2, we can directly evaluate the effect of the heater on the system mean temperature and temperature gradient.

B.4 Quantum dot characterization

In this experiment, more than 5 devices have been fabricated and measured. Results presented in Chap. 5 are from device D1, while data from device D2 and D3 are presented here. All devices are fabricated in the same configuration. Preceding the data acquisition with applied thermal bias, quantum dot characterization has been performed for every device under analysis. This allows to have a better comprehension of the observed phenomenology, which severely depends of the position of the resonant energy levels involved in transport. Figure B.4 shows the preliminary quantum dot characterization, consisting in visualizing the "Coulomb diamonds" and exploring the "pinch-off" voltage zone, in which the dot is completely depleted – which is of particular interest in our experiment, being thermoelectric effects intimately linked to the occupation number of the nanostructure. It is worth to mention here that in general in QD measurements the suppression of electrical transport below the pinch-off

voltage may not be sufficient to assert the absence of any other electronic levels below what is considered the first one. This is due the fact that the electronic transport could be quenched elsewhere in the electronic path. In this particular case, ancillary measurements show that we truly are able to fully deplete the QD, as:

1. Excited state spectroscopy of the "$N = 0$" state does not show excited states, which are present for any state above $N = 1$.

2. High T measurements do not show any indication of additional levels involved in transport due to thermal energy.

3. Electrical transport is modulated by using both the back-gate and the side gates, which are local structures and act only in the vicinity of the heterostructured QD.

Furthermore, even if some other level was present below the $N = 0$ state that would have made no difference in terms of the model used for data analysis and thoroughly explained in Sec. B.5 of the present document. Moreover, in order to relate the applied gate voltages to

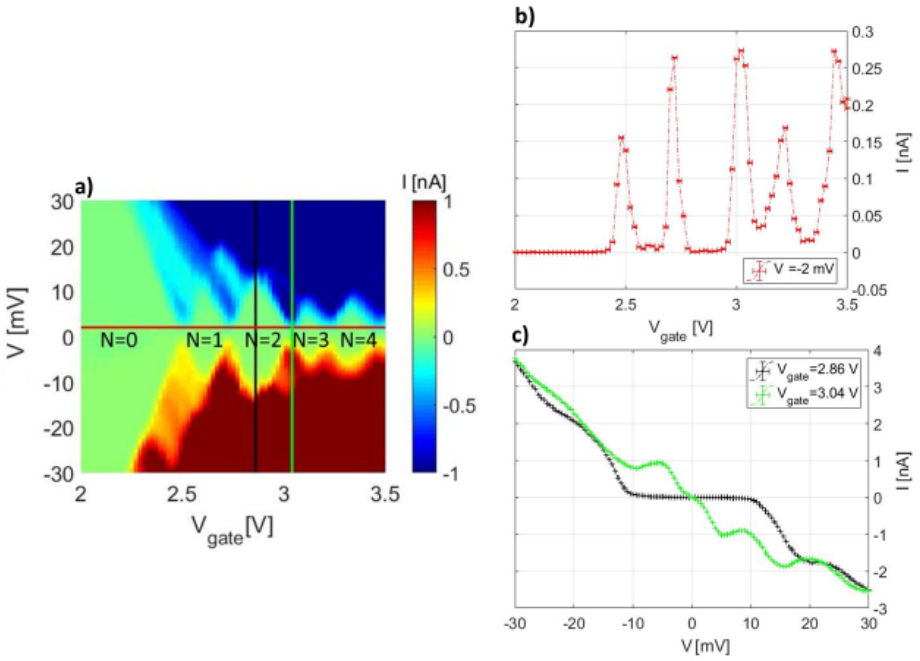

Figure B.4: (a) Current measurements in the parameters space defined by applied bias and gate voltages. The typical Coulomb blockade diamonds are visible, as well as the completely depleted region marked with the $N = 0$ occupation number ("pinch-of"). (b)(c) Horizontal and vertical cuts corresponding the colorplot shown in (a).

actual energies in the energy spectrum of the quantum dot and thus compare the experimental data with theoretical predictions, it is necessary to extract important parameters such as the gate lever arm, α_{BG}. Figure B.5 shows the relation between Coulomb diamonds and the system energetics used to extrapolate this parameter (data belongs to a different dot with respect to what is shown in Fig. B.4).

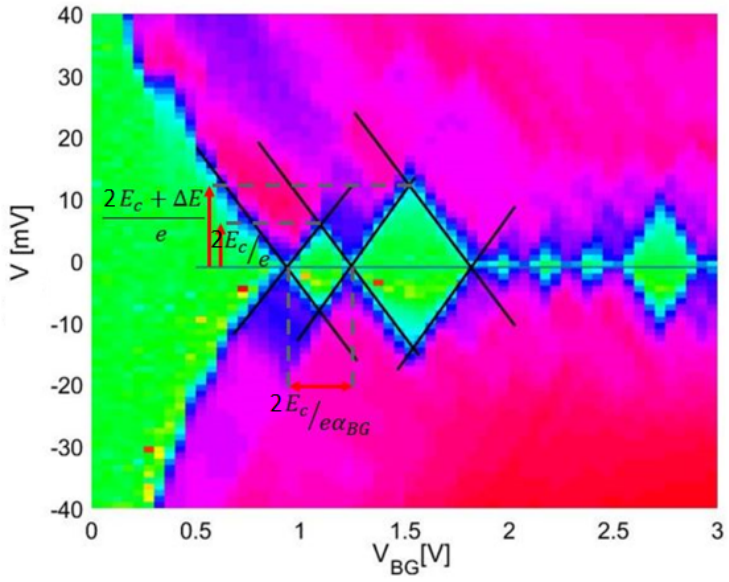

Figure B.5: Coulomb diamonds. The arrows represent the relation between the diamond dimensions and the system energetics. By acquiring the dimensions of the diamonds, it is possible to evaluate the system charging energy E_C, the spacing between two resonant energy levels of the quantum dot ΔE, and the gate lever arm α_{BG}.

B.5 Theoretical model

We now describe the theoretical model used to fit the data and to compute the electronic thermal conductance. According to the theory developed in Ref. [70] and further studied in Ref. [169], we employ a master equation approach that accounts for sequential tunneling. As discussed in Chap. 5, co-tunneling can be neglected when $\hbar\Gamma$ is much smaller than k_BT and when the level spacing and charging energy are not "too large" respect to k_BT. Indeed, in our experiment typical values of $\hbar\Gamma/(k_BT)$ are around 3×10^{-3}. We further verified that co-tunneling can be disregarded by computing G, S, K and the electronic ZT theoretically (only in the two-level model) both including and neglecting co-tunneling. Using the parameters relative to the measurement at $T_{\mathrm{avg}} = 24.9$K, we could see no deviations between the two cases in the range of the experimental data. However, deviations are observed in the range of V_{gate} much smaller than -1V where both G and K are exponentially small respect to their peak value. At last, we wish to emphasize that if co-tunneling can be neglected at $T_{\mathrm{avg}} = 24.9$K, it is even more justified at higher temperatures ($T_{\mathrm{avg}} = 31.2$K).

We account for two single-electron degenerate levels in the QD, labelled by $p = 1, 2$. The occupation of each level, n_p, can thus take values $0, 1, 2$. The single electron energy of level p is given by $E_p = \delta_{2,p}\Delta E$, where the first level is chosen at zero energy, and ΔE is the energy level spacing. The electrostatic energy necessary to have N electrons in the QD is given by $U(N) = E_C N^2$. Thus, the energy necessary to add 1 electron to level p of the QD, which initially has N electrons, is given by

$$\Delta U(N,p) = E_p + U(N+1) - U(N) - \mu, \tag{B.1}$$

where $\mu = \alpha_{\mathrm{BG}} e V_{\mathrm{gate}}$ is an energy shift induced by the applied gate voltage. The state of the QD is described by the 2 occupation numbers $\{n_0, n_1\}$. In the weak coupling regime, sequential tunneling of electrons between the leads and the QD induces transition between

the states. The rate of sequential tunneling of electrons from(to) lead $\alpha = \mathrm{L}, \mathrm{R}$ to (from) level p of the QD with a fixed spin when there are N electrons before the transition occurs is given respectively by

$$\begin{aligned}\Gamma_\alpha^+(N,p) =& \gamma_\alpha(N,p) f_\alpha[\Delta U(N,p)],\\ \Gamma_\alpha^-(N,p) =& \gamma_\alpha(N-1,p)\left[1 - f_\alpha[\Delta U(N-1,p)]\right],\end{aligned} \tag{B.2}$$

where $\gamma_\alpha(N,p)$ is a characteristic of the system which depends on the density of states of lead α at energy $\Delta U(N,p)$ and on the coupling between lead α and the QD, and $f_\alpha(\epsilon) = (1 + e^{(\epsilon-\mu_\alpha)/(k_B T_\alpha)})^{-1}$ is the Fermi distribution of electrons in lead α at temperature T_α and chemical potential μ_α. In the presence of a voltage bias V, the chemical potential of the leads is $\mu_{\mathrm{L/R}} = \pm eV/2$.

We can describe transport through the system by calculating the out-of-equilibrium occupation probabilities $p_{n_0 n_1}$ of finding the system in state $\{n_0, n_1\}$. This is done by solving the master equation

$$\begin{aligned}
\partial p_{00}/\partial t &= -p_{00}(2\Gamma_{01}^+ + 2\Gamma_{02}^+) + p_{10}\Gamma_{11}^- + p_{01}\Gamma_{12}^-,\\
\partial p_{01}/\partial t &= -p_{01}(2\Gamma_{11}^+ + \Gamma_{12}^- + \Gamma_{12}^+) + p_{11}\Gamma_{21}^- + p_{00}2\Gamma_{02}^+ + p_{02}2\Gamma_{22}^-,\\
\partial p_{02}/\partial t &= -p_{02}(2\Gamma_{21}^+ + 2\Gamma_{22}^-) + p_{12}\Gamma_{31}^- + p_{01}\Gamma_{12}^+,\\
\partial p_{10}/\partial t &= -p_{10}(\Gamma_{11}^- + \Gamma_{11}^+ + 2\Gamma_{12}^+) + p_{00}2\Gamma_{01}^+ + p_{20}2\Gamma_{21}^- + p_{11}\Gamma_{12}^+,\\
\partial p_{11}/\partial t &= -p_{11}(\Gamma_{21}^- + \Gamma_{21}^+ + \Gamma_{22}^- + \Gamma_{22}^+) + p_{01}2\Gamma_{11}^+ + p_{21}2\Gamma_{31}^- + p_{10}2\Gamma_{12}^+ + p_{12}2\Gamma_{32}^-,\\
\partial p_{12}/\partial t &= -p_{12}(\Gamma_{31}^- + \Gamma_{31}^+ + 2\Gamma_{32}^-) + p_{02}2\Gamma_{21}^+ + p_{22}2\Gamma_{42}^- + p_{11}\Gamma_{22}^+,\\
\partial p_{20}/\partial t &= -p_{20}(2\Gamma_{21}^- + 2\Gamma_{22}^+) + p_{10}\Gamma_{11}^+ + p_{21}\Gamma_{32}^-,\\
\partial p_{21}/\partial t &= -p_{21}(2\Gamma_{31}^- + \Gamma_{32}^- + \Gamma_{32}^+) + p_{11}\Gamma_{21}^+ + p_{20}2\Gamma_{22}^+ + p_{22}2\Gamma_{42}^-,\\
\partial p_{22}/\partial t &= -p_{22}(2\Gamma_{41}^- + 2\Gamma_{42}^-) + p_{12}\Gamma_{31}^+ + p_{21}\Gamma_{32}^+,\\
\sum p_{n_1 n_2} &= 1,
\end{aligned} \tag{B.3}$$

in the stationary case (i.e. imposing $(\partial p_{n_1 n_2})/\partial t = 0$). We defined $\Gamma_{Np}^\pm \equiv \Gamma_{\mathrm{L}}^\pm(N,p) + \Gamma_{\mathrm{R}}^\pm(N,p)$. Once the probabilities are known, we can compute the charge and heat currents leaving the left reservoir as

$$\begin{aligned}
I &= -e \sum_{n_1,n_2,p} p_{n_1 n_2}\left[\delta_{n_p,0} 2\Gamma_{\mathrm{L}}^+(N,p) + \delta_{n_p,1}\left(\Gamma_{\mathrm{L}}^+(N,p) - \Gamma_{\mathrm{L}}^-(N,p)\right) - \delta_{n_p,2} 2\Gamma_{\mathrm{L}}^-(N,p)\right],\\
J_{\mathrm{L}} &= \sum_{n_1,n_2,p} p_{n_1 n_2}\left[\delta_{n_p,0} 2\epsilon^+\Gamma_{\mathrm{L}}^+(N,p) + \delta_{n_p,1}\left(\epsilon^+\Gamma_{\mathrm{L}}^+(N,p) - \epsilon^-\Gamma_{\mathrm{L}}^-(N,p)\right) - \delta_{n_p,2} 2\epsilon^-\Gamma_{\mathrm{L}}^-(N,p)\right],
\end{aligned} \tag{B.4}$$

where $N = n_1 + n_2$ and $\epsilon^+ = \Delta U(N,p) - \mu_{\mathrm{L}}$ is the heat removed from the left reservoir (L) when an electron tunnels from L to the QD, $\epsilon^- = \Delta U(N-1,p) - \mu_{\mathrm{L}}$ is the heat injected in the left reservoir when an electron tunnels from the QD to L. At last, the transport coefficients are computed using their definition provided in Eqs. (3.24), (3.25) and (3.26).

B.6 Parameter estimation

Experimental values of G and V_{th} are determined the following way: for each fixed V_{gate} value, we consider the curve $I(V)$ for which the linear response holds ($|eV| \ll k_B T$). We then fit the curve $I(V) = GV + GS\Delta T$ which allows us to determine G from the angular coefficient and $S\Delta T$ from the intercept.

The model described in Sec. B.5 allows us to compute G and V_{th}. Thus, by fitting the computed curves for the conductance and thermovoltage we are able to retrieve the values of the parameters involved in defining these quantities describing the system, i.e. the system average temperature and applied temperature bias, the charging energy and the tunneling rates of the barriers defining the QD.

Within the linear response regime, the currents do not depend separately on the tunneling rates relative to the two leads, instead they depend on a combination of the two [70]. Therefore, we can assume that $\gamma_\alpha(N,p)$ does not depend on α. Furthermore, we find that we can obtain a good fit assuming that the rates only depend on the number of electrons N. We thus define $\gamma^{(N)} = \gamma_\alpha(N,p)$ for $N = 0,1,2,3$. At last, given the lack of experimental points around the third and fourth peak of the conductance, we take $\gamma^{(2)} = \gamma^{(3)}$.

We determine the rates $\gamma^{(N)}$ and the average temperature T_{avg} by fitting G with the theoretical model described in Sec. B.5. By using these extracted parameters, we can compute the Seebeck coefficient S and estimate ΔT by fitting the measured $S\Delta T$. However, we find that we can further improve the parameter estimation by fitting simultaneously G and $S\Delta T$ varying $\gamma^{(N)}$, T_{avg} and ΔT around the values previously estimated.

The following tables shows the extracted parameters for two different explored temperatures:

T(K)	ΔT(K)	E_C(meV)	$\gamma^{(0)}$(GHz)	$\gamma^{(1)}$(GHz)	$\gamma^{(2)}$(GHz)	$\gamma^{(3)}$(GHz)
24.9	1.85	6.5	1.56	0.97	2.0	2.0
31.2	2.05	5.9	1.6	1.1	1.31	1.31

C

Appendix: Non-linear thermovoltage in a single-electron transistor

In this appendix we report details about the calculations performed in Chap. 6.

C.1 Computing charge and heat currents

As in Chap. 2, the system is described by the following Hamiltonian

$$H = H_{\rm I} + \sum_{\alpha=L,R} H_\alpha + H_{\rm I,B}, \tag{C.1}$$

where $H_\alpha = \sum_{k\sigma}(\epsilon_k + eV_\alpha)a^\dagger_{k\sigma\alpha}a_{k\sigma\alpha}$ is the Hamiltonian of the free electrons in lead α = L,R, $H_{\rm I} = \sum_{k\sigma}\epsilon_k c^\dagger_{k\sigma}c_{k\sigma} + E_C(\hat{n}-n_g)^2$ is the Hamiltonian of the electrons in the metallic island and $H_{\rm I,B} = \sum_{kp\sigma\alpha} t^{(\alpha)}_{kp} c^\dagger_{p\sigma}a_{k\sigma\alpha}$ + h.c. is the usual tunneling Hamiltonian between the leads and the island. $a_{k\sigma\alpha}$ ($a^\dagger_{k\sigma\alpha}$) is the destruction (creation) operator of electrons in lead α with energy $\epsilon_k + eV_\alpha$ and spin σ, $c_{k\sigma}$ ($c^\dagger_{k\sigma}$) is the destruction (creation) operator of electrons in the metallic island with energy ϵ_k and spin σ, and $\hat{n}$ is the operator for the number of excess electrons on the island.

In order to describe charge and heat transport in the system, we employ the Pauli master equation approach to compute the probabilities $p(n)$ in terms of all processes that can induce transitions between charges states (the tunneling rates) - see Chap. 2. Sequential tunneling of electrons between the island and the leads changes the charge state by one, so it enters the master equation. Co-tunneling processes instead transfer an electron from one lead to another one via a virtual state in the island, but the overall process does not change the number of electrons in the island; consequently, the master equation does not depend on co-tunneling. Second order processes that transfer two electrons from/to the leads to/from the island can be safely neglected as the charging energy E_C is much larger than the thermal energy k_BT and than the voltage bias range considered in this work. The master equation

reads

$$\frac{\partial p(n)}{\partial t} = \sum_{\alpha=L,R} \{-p(n)\left[\Gamma_{\alpha I}(n) + \Gamma_{I\alpha}(n)\right] + p(n-1)\Gamma_{\alpha I}(n-1) + p(n+1)\Gamma_{I\alpha}(n+1)\}\,, \tag{C.2}$$

and we solve it by setting $\partial p(n)/\partial t = 0$ for every n. Eq. (E.4) states that the probability of being in charge state n can decrease (first r.h.s. term) if the island has n excess charge states and an electron tunnels into or out of the island, while it can increase (second and third r.h.s. terms) if, after a sequential tunneling process, the number of excess charges on the island is n.

Given the probabilities, the charge current can be computed by summing $I^{\rm seq}$ and $I^{\rm cot}$ given in Eq. (6.2) and below. The energy entering the metallic island $\dot{Q}_{\rm tun}$ can be computed as

$$\dot{Q}_{\rm tun} \equiv J^{\rm e}_{\rm L} + J^{\rm e}_{\rm R} = J^{\rm h}_{\rm L} + J^{\rm h}_{\rm R} + e(V_{\rm L} - V_{\rm R})I, \tag{C.3}$$

where $J^{\rm e}_\alpha$ and $J^{\rm h}_\alpha$ are respectively the energy (measured respect to the common voltage ground) and heat currents leaving reservoir α, and we used the fact that $J^{\rm e}_{\rm L} = J^{\rm h}_{\rm L} + eV_{\rm L}I$ and $J^{\rm e}_{\rm L} = J^{\rm h}_{\rm R} - eV_{\rm R}I$. We can simply interpret the r.h.s. of Eq. (C.3) by noticing that the heat entering the metallic island is given by the sum of the heat leaving the leads and the heat generated by Joule effect. We notice that a shift of the energy reference shifts $V_{\rm L}$ and $V_{\rm R}$, but it does not change $J^{\rm h}_{\rm L}$ and $J^{\rm h}_{\rm R}$, so $\dot{Q}_{\rm tun}$, as defined in Eq. (C.3), does not depend on the un-physical energy reference.

The heat currents can be calculated in terms of "heat rates". We thus define $\Gamma^h_{\alpha{\rm I}}(n)$ as the rate of heat leaving reservoir α when electrons tunnel sequentially from lead α to the island with n initial electrons, and $\Gamma^h_{{\rm I}\alpha}(n)$ as the rate of heat entering lead α when electrons tunnel sequentially from the island to lead α with n initial electrons. Analogously, we define $\gamma^{h/{\rm out}}_{\alpha\beta}(n)$ as the rate of heat leaving lead α when a co-tunneling process transfers one electron from lead α to lead β with n electrons in the island, and $\gamma^{h/{\rm in}}_{\alpha\beta}(n)$ as the rate of heat entering lead β when a co-tunneling process transfers one electron from lead α to lead β with n electrons in the island. Notice that also co-tunneling processes where $\alpha = \beta$ must be considered in the heat currents, since the electron leaving and the one entering the same lead can have different energies. Also the heat currents can be written as $J^{\rm h}_\alpha = J^{\rm h/seq}_\alpha + J^{\rm h/cot}_\alpha$, where

$$J^{\rm h/seq} = \sum_n p(n)\left[\Gamma^h_{\alpha{\rm I}}(n) - \Gamma^h_{{\rm I}\alpha}(n)\right] \tag{C.4}$$

is the sequential-tunneling contribution, given by electrons tunneling between lead α and I, and

$$J^{\rm h/cot}_\alpha = \sum_{n,\beta={\rm L,R}} p(n)\left[\gamma^{h/{\rm out}}_{\alpha\beta}(n) - \gamma^{h/{\rm in}}_{\beta\alpha}(n)\right] \tag{C.5}$$

is the inelastic co-tunneling contribution.

Using the $\mathcal{T}$-matrix theory (or generalized Fermi golden rule) [30–32], we can compute sequential and co-tunneling rates as described in Sec. 2.2. The transition rate from a given initial state $|\psi_i\rangle$ to a final state $|\psi_f\rangle$ is given by

$$\Gamma_{i\to f} = \frac{2\pi}{\hbar} W_i(1 - W_f)\,|\,\langle\psi_f|\mathcal{T}|\psi_i\rangle|^2\,\delta(\varepsilon_f - \varepsilon_i), \tag{C.6}$$

where W_i and W_f are the probabilities of finding the system in state $|\psi_i\rangle$ and $|\psi_f\rangle$, ε_i and ε_f are the energies of states $|\psi_i\rangle$ and $|\psi_f\rangle$ and $\mathcal{T} = H_{\rm I,B} + H_{\rm I,B}G_0H_{\rm I,B} + \ldots$ is the $\mathcal{T}$ matrix

with $G_0 = 1/(\varepsilon_i - H_0 + i\eta)$ denoting the Green function in the absence of the $H_{\mathrm{I,B}}$, i.e. $H_0 = H_{\mathrm{B}} + H_{\mathrm{I}}$. We compute sequential rates by taking $\mathcal{T}$ at first order in $H_{\mathrm{I,B}}$. We thus take $T = H_{\mathrm{I,B}}$ in Eq. (C.6) and sum over all states in the lead and in the island, yielding

$$\Gamma_{\alpha I}(n) = \frac{2\pi}{\hbar} \sum_{k_1\sigma_1, k_2\sigma_2} f_\alpha(\epsilon_{k_1}) f_I^-(\epsilon_{k_2}) \left| \langle 0 | c_{k_2\sigma_2} H_{\mathrm{I,B}} a^\dagger_{k_1\sigma_1\alpha} | 0 \rangle \right|^2 \delta\left[\epsilon_{k_2} - \epsilon_{k_1} + \Delta E_\alpha(n)\right], \quad \text{(C.7)}$$

where $\Delta E_\alpha(n) = U(n+1) - U(n) - eV_\alpha$ is the electrostatic energy difference to move an electron from lead α to the island, $f_{\alpha/\mathrm{I}}(\epsilon) = [1+\exp\left\{(\epsilon/(k_B T_{\alpha/I}))\right\}]^{-1}$ is the Fermi distribution of lead α at temperature T_α or of the island at temperature T_{I}, $f^-_{\alpha/\mathrm{I}}(\epsilon) = f_{\alpha/\mathrm{I}}(-\epsilon) = 1 - f_{\alpha/\mathrm{I}}(\epsilon)$, and k_B is the Boltzmann constant. An analogous expression holds for $\Gamma_{I\alpha}(n)$. The heat rates are computed in the same way, taking into account that an amount of heat ϵ_k is removed(injected) from(into) a lead if an electron with momentum k tunnels from(into) the lead. We thus have that

$$\begin{aligned}
\Gamma^h_{\alpha I}(n) &= \frac{2\pi}{\hbar} \sum_{k_1\sigma_1, k_2\sigma_2} \epsilon_{k_1} f_\alpha(\epsilon_{k_1}) f_I^-(\epsilon_{k_2}) \left| \langle 0 | c_{k_2\sigma_2} H_{\mathrm{I,B}} a^\dagger_{k_1\sigma_1\alpha} | 0 \rangle \right|^2 \delta\left[\epsilon_{k_2} - \epsilon_{k_1} + \Delta E_\alpha(n)\right], \\
\Gamma^h_{I\alpha}(n) &= \frac{2\pi}{\hbar} \sum_{k_1\sigma_1, k_2\sigma_2} \epsilon_{k_2} f_{\mathrm{I}}(\epsilon_{k_1}) f_\alpha^-(\epsilon_{k_2}) \left| \langle 0 | a_{k_2\sigma_2\alpha} H_{\mathrm{I,B}} c^\dagger_{k_1\sigma_1} | 0 \rangle \right|^2 \delta\left[\epsilon_{k_2} - \epsilon_{k_1} - \Delta E_\alpha(n-1)\right].
\end{aligned} \quad \text{(C.8)}$$

By assuming that the energy levels in the leads and in the island form a continuum, by taking a constant density of states around the Fermi energy and by replacing the hopping parameters $t^{(\alpha)}_{kp}$ with their averaged value over k and p, we can write the sequential rates and heat rates in terms of the functions

$$\begin{aligned}
\Upsilon_\alpha(\Delta E) &\equiv \frac{1}{e^2 R_\alpha} \int_{-\infty}^{+\infty} d\epsilon f_\alpha(\epsilon) f_{\mathrm{I}}^-(\epsilon - \Delta E), \\
\Upsilon^h_\alpha(\Delta E) &\equiv \frac{1}{e^2 R_\alpha} \int_{-\infty}^{+\infty} d\epsilon\, \epsilon f_\alpha(\epsilon) f_{\mathrm{I}}^-(\epsilon - \Delta E),
\end{aligned} \quad \text{(C.9)}$$

where R_α is the tunnel resistance between lead α and the island, as follows:

$$\begin{aligned}
\Gamma_{\alpha\mathrm{I}}(n) &= \Upsilon_\alpha[\Delta E_\alpha(n)], \quad & \Gamma_{\mathrm{I}\alpha}(n+1) &= \Upsilon_\alpha[-\Delta E_\alpha(n)], \\
\Gamma^h_{\alpha\mathrm{I}}(n) &= \Upsilon^h_\alpha[\Delta E_\alpha(n)], \quad & \Gamma^h_{\mathrm{I}\alpha}(n+1) &= -\Upsilon^h_\alpha[-\Delta E_\alpha(n)].
\end{aligned} \quad \text{(C.10)}$$

Co-tunneling rates are second order processes that involve initial and final states with two electrons, so we now consider $\mathcal{T} = H_{\mathrm{I,B}} G_0 H_{\mathrm{I,B}}$. We thus take $|\psi_i\rangle = a^\dagger_{k_1\sigma_1\alpha} c^\dagger_{q_1\tau_1} |0\rangle$ and $|\psi_f\rangle = a^\dagger_{q_2\tau_2\beta} c^\dagger_{k_2\sigma_2} |0\rangle$, which corresponds to considering the process where an electron in state $k_1\sigma_1$ tunnels from lead α to the island into state $k_2\sigma_2$, and another one coherently tunnels from the island in state $q_1\tau_1$ to lead β into state $q_2\tau_2$. From Eq. (C.6) we have that

$$\begin{aligned}
\gamma_{\alpha\beta}(n) = \frac{2\pi}{\hbar} \sum_{\substack{k_1\sigma_1, k_2\sigma_2 \\ q_1\tau_1, q_2\tau_2}} f_\alpha(\epsilon_{k_1}) f_{\mathrm{I}}(\epsilon_{q_1}) f_\beta^-(\epsilon_{q_2}) f_{\mathrm{I}}^-(\epsilon_{k_2}) \left| \sum_\nu \frac{\langle \psi_f | H_{\mathrm{I,B}} | \psi_\nu \rangle \, \langle \psi_\nu | H_{\mathrm{I,B}} | \psi_i \rangle}{\varepsilon_i - \varepsilon_\nu + i\eta} \right|^2 \\
\times \delta\left[\epsilon_{q_2} + \epsilon_{k_2} - \epsilon_{q_1} - \epsilon_{k_1} + e(V_\beta - V_\alpha)\right],
\end{aligned} \quad \text{(C.11)}$$

where $\varepsilon_i = \epsilon_{q_1} + \epsilon_{k_1} + eV_\alpha + U(n)$ is the energy of state $|\psi_i\rangle$, the sum over $|\psi_\nu\rangle$ runs over a complete set of eigenstates $\{|\psi_\nu\rangle\}$ of H_0, and ε_ν is the energy, evaluated with H_0, of state $|\psi_\nu\rangle$. As we did for the sequential rates, we notice that in the processes described in Eq. (C.11), the heat leaving reservoir α is ϵ_{k_1}, while the heat entering reservoir β is ϵ_{q_2}. The co-tunneling heat rate leaving reservoir α, $\gamma_{\alpha\beta}^{h/\mathrm{out}}(n)$, is thus given by Eq. (C.11) adding an ϵ_{k_1} inside the sum over the initial and final states, while the co-tunneling heat rate entering reservoir β, $\gamma_{\alpha\beta}^{h/\mathrm{in}}(n)$, is also given by Eq. (C.11) adding an ϵ_{q_2} inside the sum over the initial and final states. Manipulating Eq. (C.11) using the same approximations mentioned for the sequential rates, we find that by defining

$$\upsilon_{\alpha\beta}(\Delta E, \Delta E_1, \Delta E_2) = \frac{\hbar}{2\pi}\int_{-\infty}^{+\infty} d\epsilon \Upsilon_\alpha(-\epsilon)\Upsilon_\beta(\epsilon+\Delta E)\left|\frac{1}{\epsilon+\Delta E_1 - i\eta} - \frac{1}{\epsilon-\Delta E_2+\Delta E+i\eta}\right|^2, \tag{C.12}$$

$$\upsilon_{\alpha\beta}^{h/\mathrm{out}}(\Delta E, \Delta E_1, \Delta E_2) = \frac{\hbar}{2\pi}\int_{-\infty}^{+\infty} d\epsilon \Upsilon_\alpha^h(-\epsilon)\Upsilon_\beta(\epsilon+\Delta E)\left|\frac{1}{\epsilon+\Delta E_1 - i\eta} - \frac{1}{\epsilon-\Delta E_2+\Delta E+i\eta}\right|^2, \tag{C.13}$$

$$\upsilon_{\alpha\beta}^{h/\mathrm{in}}(\Delta E, \Delta E_1, \Delta E_2) = -\frac{\hbar}{2\pi}\int_{-\infty}^{+\infty} d\epsilon \Upsilon_\alpha(-\epsilon)\Upsilon_\beta^h(\epsilon+\Delta E) \times \left|\frac{1}{\epsilon+\Delta E_1 - i\eta} - \frac{1}{\epsilon-\Delta E_2+\Delta E+i\eta}\right|^2, \tag{C.14}$$

we can write the co-tunneling rates and heat rates as

$$\gamma_{\alpha\beta}(n) = \upsilon_{\alpha\beta}\left[e(V_\beta - V_\alpha), \Delta U_\alpha(n), -\Delta U_\beta(n-1)\right], \tag{C.15}$$

$$\gamma_{\alpha\beta}^{h/\mathrm{out}}(n) = \upsilon_{\alpha\beta}^{h/\mathrm{out}}\left[e(V_\beta - V_\alpha), \Delta U_\alpha(n), -\Delta U_\beta(n-1)\right], \tag{C.16}$$

$$\gamma_{\alpha\beta}^{h/\mathrm{in}}(n) = \upsilon_{\alpha\beta}^{h/\mathrm{in}}\left[e(V_\beta - V_\alpha), \Delta U_\alpha(n), -\Delta U_\beta(n-1)\right]. \tag{C.17}$$

At last, we notice that the integrals in Eqs. (C.12), (C.13) and (C.14) are divergent in the limit $\eta \to 0^+$. In order to overcome this problem, we adopt a commonly used "regularization scheme" [31, 32, 34, 79, 83]. All three integrals can be written in the form

$$\mathcal{I} = \int_{-\infty}^{+\infty} d\epsilon\, g(\epsilon)\left|\frac{1}{\epsilon-\alpha_1-i\eta} - \frac{1}{\epsilon-\alpha_2+i\eta}\right|^2 = \sum_{i=1,2}\left\{\int_{-\infty}^{+\infty} d\epsilon\, g(\epsilon)\left|\frac{1}{\epsilon-\alpha_i-i\eta}\right|^2\right\} - 2\int_{-\infty}^{+\infty} d\epsilon\, g(\epsilon)\,\mathrm{Re}\left\{\frac{1}{(\epsilon-\alpha_1+i\eta)(\epsilon-\alpha_2+i\eta)}\right\} = \sum_{i=1,2}\left\{\mathcal{I}_i^{(1)}\right\} - 2\mathcal{I}^{(2)} \tag{C.18}$$

where $g(\epsilon)$ is a suitable function and α_1 and α_2 are suitable constants. We now analyze each

integral:

$$\mathcal{I}_i^{(1)} = \int_{-\infty}^{+\infty} d\epsilon\, g(\epsilon) \left| \frac{1}{\epsilon - \alpha_i - i\eta} \right|^2 = \int_{-\infty}^{+\infty} d\epsilon \frac{g(\epsilon) - g(\alpha_i) + g(\alpha_i)}{(\epsilon - \alpha_i)^2 + \eta^2}$$
$$= g(\alpha_i) \int_{-\infty}^{+\infty} d\epsilon \frac{1}{(\epsilon - \alpha_i)^2 + \eta^2} + \int_{-\infty}^{+\infty} d\epsilon \frac{g(\epsilon) - g(\alpha_i)}{(\epsilon - \alpha_i)^2 + \eta^2} = \frac{\pi g(\alpha_i)}{\eta} + \mathcal{P} \int_{-\infty}^{+\infty} d\epsilon \frac{g(\epsilon) - g(\alpha_i)}{(\epsilon - \alpha_i)^2} + O(\eta), \tag{C.19}$$

where $\mathcal{P}$ denotes a principal value integration. We notice that the last step of Eq. (C.19) is an expansion for small η. In particular, the first term diverges as $1/\eta$, the second one is finite and independent of η, while the third one goes to zero if $\eta \to 0$. The regularization scheme consists of dropping the divergent term and retaining only the second term, which is finite and independent of η:

$$\mathcal{I}_i^{(1)} \to \mathcal{P} \int_{-\infty}^{+\infty} d\epsilon \frac{g(\epsilon) - g(\alpha_i)}{(\epsilon - \alpha_i)^2}. \tag{C.20}$$

Let's now turn to

$$\mathcal{I}^{(2)} = \int_{-\infty}^{+\infty} d\epsilon\, g(\epsilon)\, \mathrm{Re} \left\{ \frac{1}{(\epsilon - \alpha_1 + i\eta)(\epsilon - \alpha_2 + i\eta)} \right\} =$$
$$\int_{-\infty}^{+\infty} d\epsilon g(\epsilon) \frac{(\epsilon - \alpha_1)(\epsilon - \alpha_2) - \eta^2}{\left[(\epsilon - \alpha_1)(\epsilon - \alpha_2) - \eta^2\right]^2 + \eta^2 \left[(\epsilon - \alpha_1) + (\epsilon - \alpha_2)\right]^2} =$$
$$\int_{-\infty}^{+\infty} d\epsilon g(\epsilon) \frac{(\epsilon - \alpha_1)(\epsilon - \alpha_2) - \eta^2}{(\epsilon - \alpha_1)^2(\epsilon - \alpha_2)^2 + \eta^2 \left[(\epsilon - \alpha_1)^2 + (\epsilon - \alpha_2)^2 + \eta^2\right]}. \tag{C.21}$$

We notice that the denominator in Eq. (C.21) is always positive and non-zero. In the limit $\eta \to 0$, the term proportional to $(\epsilon - \alpha_1)(\epsilon - \alpha_2)$ turns into a principal value integration, while the term proportional to $-\eta^2$ vanishes. The regularization scheme thus consists of

$$\mathcal{I}^{(2)} \to \mathcal{P} \int_{-\infty}^{+\infty} d\epsilon \frac{g(\epsilon)}{(\epsilon - \alpha_1)(\epsilon - \alpha_2)}, \tag{C.22}$$

which is now finite and independent of η.

D

Appendix: Absorption refrigerators based on Coulomb-coupled single-electron systems

In this appendix, we provide details on the calculations performed in Chap. 7.

D.1 Pauli equation

The probability p_{n_1,n_2} that the system is in a state with n_1 and n_2 electrons in QDs 1 and 2 is calculated by solving the following linear system of equations

$$\begin{aligned} -\left[\Gamma_{\rm L}^{\rm in}(0)+\Gamma_{\rm R}^{\rm in}(0)+\Gamma_{\rm C}^{\rm in}(0)\right]p_{0,0}+\Gamma_{\rm C}^{\rm out}(0)p_{0,1}+\left[\Gamma_{\rm L}^{\rm out}(0)+\Gamma_{\rm R}^{\rm out}(0)\right]p_{1,0}&=0\\ \left[\Gamma_{\rm L}^{\rm in}(1)+\Gamma_{\rm R}^{\rm in}(1)\right]p_{0,1}+\Gamma_{\rm C}^{\rm in}(1)p_{1,0}-\left[\Gamma_{\rm L}^{\rm out}(1)+\Gamma_{\rm R}^{\rm out}(1)+\Gamma_{\rm C}^{\rm out}(1)\right]p_{1,1}&=0\\ \Gamma_{\rm C}^{\rm in}(0)p_{0,0}-\left[\Gamma_{\rm L}^{\rm in}(1)+\Gamma_{\rm R}^{\rm in}(1)+\Gamma_{\rm C}^{\rm out}(0)\right]p_{0,1}+\left[\Gamma_{\rm L}^{\rm out}(1)+\Gamma_{\rm R}^{\rm out}(1)\right]p_{1,1}&=0\\ p_{0,0}+p_{0,1}+p_{1,0}+p_{1,1}&=1 \end{aligned} \tag{D.1}$$

The first three equations correspond to the master equations where the time-derivatives $\dot{p}_{0,0}$, $\dot{p}_{1,1}$, and $\dot{p}_{0,1}$ are set to zero, while the last equation corresponds to the normalization requirement. The charge current is given by

$$I=e\left[p_{0,0}\Gamma_{\rm L}^{\rm in}(0)+p_{0,1}\Gamma_{\rm L}^{\rm in}(1)-p_{1,0}\Gamma_{\rm L}^{\rm out}(0)-p_{1,1}\Gamma_{\rm L}^{\rm out}(1)\right], \tag{D.2}$$

where e is the electron charge, and the heat current leaving reservoir α is given by

$$J_\alpha=p_{0,0}\Gamma_\alpha^{\rm in}(0)\Delta U_1(0)-p_{1,1}\Gamma_\alpha^{\rm out}(1)\Delta U_1(1)+p_{0,1}\Gamma_\alpha^{\rm in}(1)\Delta U_1(1)-p_{1,0}\Gamma_\alpha^{\rm out}(0)\Delta U_1(0), \tag{D.3}$$

for $\alpha=$ L,R, and

$$J_{\rm C}=p_{0,0}\Gamma_{\rm C}^{\rm in}(0)\Delta U_2(0)-p_{1,1}\Gamma_{\rm C}^{\rm out}(1)\Delta U_2(1)+p_{1,0}\Gamma_{\rm C}^{\rm in}(1)\Delta U_2(1)-p_{0,1}\Gamma_{\rm C}^{\rm out}(0)\Delta U_2(0). \tag{D.4}$$

Note that one can exploit the symmetry of the transitions energies with respect to the common chemical potential when $\theta_1=\theta_2=1/2$ [see Eqs. (7.2) and Fig. 7.1(b)] to restrict the analysis

to the range $\theta_1 \geq 1/2$, without loss of generality. In fact, the heat currents relative to the case $\theta_i = \bar{\theta}_i < 1/2$ are equal to the ones obtained with $\theta_i = 1 - \bar{\theta}_i (> 1/2)$, while the charge currents relative to the case $\theta_i = \bar{\theta}_i < 1/2$ are equal in amplitude but with opposite sign with respect to the ones obtained with $\theta_i = 1 - \bar{\theta}_i (> 1/2)$. This can be explicitly verified by substituting $\theta_i \to 1 - \theta_i$ and $\Gamma_\alpha^{\text{in/out}}(n) \to \Gamma_\alpha^{\text{out/in}}(1-n)$ in Eqs. (7.2), (D.1), (D.2), (D.3) and (D.4).

D.2 Optimal rates for cooling power and COP

By substituting the probability p_{n_1,n_2}, solution of Eq. (D.1), into the expression (D.4) for J_{C} and imposing the detailed balance condition (10.42), we find that $J_{\text{C}} > 0$ if and only if

$$\Gamma_{\text{L}}^{\text{out}}(0)\Gamma_{\text{R}}^{\text{in}}(1)\left(e^{j\eta_{\text{c}}(\theta_1-1)}-1\right) - \Gamma_{\text{L}}^{\text{in}}(1)\left[\Gamma_{\text{L}}^{\text{out}}(0)\left(1-e^{-j\eta_{\text{c}}}\right)+\Gamma_{\text{R}}^{\text{out}}(0)\left(1-e^{-j\eta_{\text{c}}\theta_1}\right)\right] - \left[\Gamma_{\text{L}}^{\text{out}}(0)+\Gamma_{\text{R}}^{\text{out}}(0)\right]\left[\Gamma_{\text{L}}^{\text{in}}(1)+\Gamma_{\text{R}}^{\text{in}}(1)\right](e^{j/C_{\text{c}}}-1) > 0. \quad \text{(D.5)}$$

Interestingly, the condition (D.5) does not depend on the rates $\Gamma_{\text{C}}^{(\text{in/out})}$ relative to the cooled system, nor on θ_2. In Eq. (D.5), $\eta_{\text{c}} = 1 - T/T_{\text{L}}$ is the Carnot efficiency of a heat engine operating between L and R, $C_{\text{c}} = T_{\text{C}}/(T - T_{\text{C}})$ is the Carnot COP of a refrigerator operating between R and C, and $j = E_{\text{I}}/k_B T$. Restricting to the range $\theta_1 \geq 1/2$ (see App. D.1 for details), the first line of Eq. (D.5) is the only term that can be positive, so that a necessary non-trivial condition to satisfy Eq. (D.5) is that $\theta_1 > 1$.

When Eq. (D.5) is satisfied, at fixed E_{I}, θ_1 and θ_2, we find that J_{C} is a decreasing function of $\Gamma_{\text{L}}^{\text{in}}(1)$ and $\Gamma_{\text{R}}^{\text{out}}(0)$, so that the optimal choice for such parameters is

$$\Gamma_{\text{L}}^{\text{in}}(1) = \Gamma_{\text{R}}^{\text{out}}(0) = 0. \quad \text{(D.6)}$$

Now, assuming (D.6), J_{C} is an increasing function of the remaining rates $\Gamma_{\text{L}}^{\text{out}}(0)$, $\Gamma_{\text{R}}^{\text{in}}(1)$, $\Gamma_{\text{C}}^{\text{out}}(0)$, $\Gamma_{\text{C}}^{\text{in}}(1)$, so that the optimal choice is to take them as large as possible, compatibly with the validity of the sequential tunneling picture.

D.3 Derivation of the master equation for the system with three QDs

The Hamiltonian of the system with three QDs can be represented as

$$H_{\text{S}} = \sum_\alpha \epsilon_\alpha |\alpha\rangle\langle\alpha| + E_{\text{I}}(|1,1,0\rangle\langle 1,1,0| + |1,1,1\rangle\langle 1,1,1|) + t(|1,0,0\rangle\langle 0,0,1| + |1,1,0\rangle\langle 0,1,1| + \text{h.c.}), \quad \text{(D.7)}$$

where ϵ_α is the energy of state $|\alpha\rangle$ in the absence of coupling, t is the hopping element between the two tunnel coupled QDs (3 and 1), and E_{I} represents the inter-dot charging energy between the capacitively-coupled QDs, 1 and 2. Under the assumption that the hopping element t is much smaller than the coupling energy between QDs and reservoirs, in Refs. [236–240] it was shown that the density matrix ρ (whose components are defined as $\rho_{\alpha\beta} = \langle\alpha|\rho|\beta\rangle$) satisfies a modified Liouville equation. In particular, the diagonal components $\rho_{\alpha\alpha}$ satisfy[346]

$$\dot{\rho}_{\alpha\alpha} = -i[H_{\text{S}}, \rho]_{\alpha\alpha} - \sum_\nu \Gamma_{\alpha\nu}\rho_{\alpha\alpha} + \sum_\delta \Gamma_{\delta\alpha}\rho_{\delta\delta}, \quad \text{(D.8)}$$

while the off-diagonal components, resulting from coherent tunneling of electrons between QDS 3 and 1, satisfy

$$\dot{\rho}_{\alpha\beta} = -i[H_{\rm S}, \rho]_{\alpha\beta} - \frac{1}{2}\sum_{\nu}\left(\Gamma_{\alpha\nu} + \Gamma_{\beta\nu}\right)\rho_{\alpha\beta}. \tag{D.9}$$

In Eqs. (D.8) and (D.9), the first (Liouville) term contains the system Hamiltonian (D.7), while the other terms describe the coupling of the QDs with the reservoirs. In Eq. (D.9), $|\alpha\rangle = |0,0,1\rangle$ and $|\beta\rangle = |1,0,0\rangle$ (and viceversa), or $|\alpha\rangle = |0,1,1\rangle$ and $|\beta\rangle = |1,1,0\rangle$ (and viceversa), since the only non-zero off-diagonal terms are the ones related to electron tunneling between QDs 1 and 3 (with 2 either occupied or unoccupied). Note that Eqs. (D.8) and (D.9) depend explicitly only on the transition rate $\Gamma_{\alpha\nu}$, from state $|\alpha\rangle$ to state $|\nu\rangle$, which accounts for the transfer of electrons between a QD and the corresponding reservoir $\lambda = \lambda(\alpha,\nu)$. In particular, the transition rates for tunnelling events between 1 and 3, such as $\Gamma_{(0,0,1),(1,0,0)}$ and $\Gamma_{(0,1,1),(1,1,0)}$, do not appear in Eqs. (D.8) and (D.9). The rates appearing in Eqs. (D.8) and (D.9) can be expressed as [31]

$$\Gamma_{\alpha\nu} = \hbar^{-1}\gamma_\lambda f_\lambda(\Delta\tilde{U}_{\alpha\nu}), \tag{D.10}$$

where γ_λ is the coupling energy between reservoir λ and QD, $f_\lambda(\epsilon) = [1 + e^{\epsilon/(k_B T_\lambda)}]^{-1}$ is the reservoir Fermi distribution function, while $\Delta\tilde{U}_{\alpha\nu} = \tilde{U}(\nu) - \tilde{U}(\alpha)$ is the transition energy, where $\tilde{U}(\alpha) = U(n_1, n_2, n_3)$ [see Eq. (7.15)] with the set of occupation numbers corresponding to the state $|\alpha\rangle$.

In order to keep the notation compact, we assign an index to each set of occupation numbers as follows: $(0,0,0) \to 0$, $(1,0,0) \to 1$, $(0,1,0) \to 2$, $(0,0,1) \to 3$, $(1,1,0) \to 4$, $(0,1,1) \to 5$, $(1,0,1) \to 6$ and $(1,1,1) \to 7$. We will show now that the inter-dot tunneling rates, i. e. $\Gamma_{3,1} \equiv \Gamma_{(0,0,1),(1,0,0)}$ and $\Gamma_{5,4} \equiv \Gamma_{(0,1,1),(1,1,0)}$, can be obtained by using Eqs. (D.8) and (D.9). [369] Let us consider the component $(3,3)$ of Eq. (D.8), i.e.

$$\dot{\rho}_{3,3} = -it(\rho_{1,3} - \rho_{3,1}) - \left(\Gamma_{3,0} + \Gamma_{3,5} + \Gamma_{3,6}\right)\rho_{3,3} + \Gamma_{0,3}\,\rho_{0,0} + \Gamma_{5,3}\,\rho_{5,5} + \Gamma_{6,3}\,\rho_{6,6}. \tag{D.11}$$

In the steady state ($\dot{\rho} = 0$), the components $(3,1)$ and $(5,4)$ of Eq. (D.9) can be written, respectively, as

$$\rho_{3,1} = \frac{t\,(\rho_{3,3} - \rho_{1,1})}{\epsilon_3 - \epsilon_1 - i\frac{\tilde{\Gamma}^{(0)}}{2}} \tag{D.12}$$

and

$$\rho_{5,4} = \frac{t\,(\rho_{5,5} - \rho_{4,4})}{\epsilon_5 - \epsilon_4 - E_{\rm I} - i\frac{\tilde{\Gamma}^{(1)}}{2}}, \tag{D.13}$$

where $\tilde{\Gamma}^{(0)} = \Gamma_{3,6} + \Gamma_{3,5} + \Gamma_{3,0} + \Gamma_{1,6} + \Gamma_{1,4} + \Gamma_{1,0}$ accounts for all the processes which lead to the decay of the states $|3\rangle$ and $|1\rangle$, and $\tilde{\Gamma}^{(1)} = \Gamma_{5,3} + \Gamma_{5,2} + \Gamma_{5,7} + \Gamma_{4,1} + \Gamma_{4,2} + \Gamma_{4,7}$ accounts for all the processes which lead to the decay of the states $|0,1,1\rangle$ and $|1,1,0\rangle$. By substituting Eq. (D.12) into Eq. (D.11), with $\rho_{1,3} = \rho^*_{3,1}$, the latter equation will contain only diagonal elements of the density matrix, thus representing an ordinary master equation of the form

$$\dot{p}_3 = \sum_{\nu=0,5,6}\left(-\Gamma_{3\nu}\,p_3 + \Gamma_{\nu 3}\,p_\nu\right) - \Gamma_{3,1}p_3 + \Gamma_{1,3}p_1, \tag{D.14}$$

where $p_\alpha = \rho_{\alpha\alpha}$ represents the probability for the state $|\alpha\rangle$. In Eq. (D.14), the two terms (in $\Gamma_{3,1}$ and $\Gamma_{1,3}$) accounting for the transitions between states $|0,0,1\rangle$ and $|1,0,0\rangle$, when QD 2

is unoccupied, now appear. The associated inter-dot tunneling rate takes the form

$$\Gamma_{3,1} = \frac{t^2 \tilde{\Gamma}^{(0)}}{(\epsilon_3 - \epsilon_1)^2 + \left(\frac{\tilde{\Gamma}^{(0)}}{2}\right)^2}. \tag{D.15}$$

Similarly, using Eq. (D.13) in the expression for $\dot{\rho}_{5,5}$ or $\dot{\rho}_{4,4}$, one obtains the inter-dot tunneling rate

$$\Gamma_{5,4} = \frac{t^2 \tilde{\Gamma}^{(1)}}{(\epsilon_3 - \epsilon_1 - E_{\rm I})^2 + \left(\frac{\tilde{\Gamma}^{(1)}}{2}\right)^2} \tag{D.16}$$

in the case where QD 2 is occupied. Note that both inter-dot tunneling rates have a Lorentzian profile.

The relevant heat currents can be written as

$$J_{\rm C,L} = \sum_{\alpha,\nu} \Delta\tilde{U}_{\alpha\nu} \left(\Gamma_{\alpha\nu}\, p_\alpha - \Gamma_{\nu\alpha}\, p_\nu\right), \tag{D.17}$$

where the sum runs over the indices $(\alpha,\nu) = (0,2)$, $(1,4)$, $(3,5)$, $(6,7)$ for the cooling power $J_{\rm C}$, and over the values $(\alpha,\nu) = (0,3)$, $(1,6)$, $(2,5)$, $(4,7)$ for the input heat $J_{\rm L}$.

D.4 Heat currents in the system with metallic islands

Since MIs presents a continuum of states, the heat exchanged in a single electron transition is not fixed by the electrostatic energy difference as in Eq. (7.20), but it depends on the energy of the electron that is tunneling. We thus need to define the following heat rates [32]

$$\Gamma^{h,\rm out}_{\alpha\nu} = \frac{1}{e^2 R_{\alpha\nu}} \int d\epsilon\, \epsilon\, \mathcal{N}_\lambda(\epsilon)\mathcal{N}_\mu(\epsilon - \Delta\tilde{U}_{\nu\alpha}) f_\lambda(\epsilon) \left[1 - f_\mu(\epsilon - \Delta\tilde{U}_{\nu\alpha})\right] \tag{D.18}$$

and

$$\Gamma^{h,\rm in}_{\alpha\nu} = \frac{1}{e^2 R_{\alpha\nu}} \int d\epsilon\, (\epsilon - \Delta\tilde{U}_{\nu\alpha})\mathcal{N}_\lambda(\epsilon)\mathcal{N}_\mu(\epsilon - \Delta\tilde{U}_{\nu\alpha}) f_\lambda(\epsilon) \left[1 - f_\mu(\epsilon - \Delta\tilde{U}_{\nu\alpha})\right]. \tag{D.19}$$

$\Gamma^{h,\rm out}_{\alpha\nu}$ is to the heat rate extracted from $\lambda(\alpha,\nu)$ (the reservoir or island from which the electron is tunneling) and $\Gamma^{h,\rm in}_{\alpha\nu}$ corresponds to the heat injected into $\mu(\alpha,\nu)$ (the reservoir or island to which the electron is tunneling to) when the system undergoes a transition from α to ν. We thus have that

$$J_{\rm C,L} = \sum_{\alpha,\nu} \left(\Gamma^{h,\rm out}_{\alpha\nu}\, p_\alpha - \Gamma^{h,\rm in}_{\nu\alpha}\, p_\nu\right), \tag{D.20}$$

where, as in Eq. (D.17), the sum runs over the values $(\alpha,\nu) = (0,2)$, $(1,4)$, $(3,5)$, $(6,7)$, for $J_{\rm C}$, and over $(\alpha,\nu) = (0,3)$, $(1,6)$, $(2,5)$, $(4,7)$, for $J_{\rm L}$. The heat extracted from MI 2 can also be computed as in Eq. (D.20) by summing over the values $(\alpha,\nu) = (2,0)$, $(4,1)$, $(5,3)$, $(7,6)$.

E

Appendix: Heat rectification in low-dimensional quantum systems

In this appendix, we provide details on the calculations performed in Chap. 8.

E.1 Most Generic System-Bath Coupling

In this appendix we prove that the system bath interaction described by Eq. (8.5) is indeed the most generic system-bath interaction.

The most generic Hermitian operator acting on the tensor product space between of S (a two-dimensional Hilbert space) and the baths (an arbitrary dimensional Hilbert space) can be expanded on the product basis of the two Hilbert spaces. We therefore consider a basis $\{\mathcal{B}_i\}_i$ of Hermitian operators acting on the space of the bath, and the specific basis $\vec{\sigma}_j \equiv \{\mathbb{1}, \sigma_x, \sigma_y, \sigma_z\}$ of Hermitian operators acting on the qubit space. This yields

$$H_{\mathrm{S},\alpha} = \sum_{i,j} a_{ij}\, \mathcal{B}_i \otimes \sigma_j = \sum_j B_j \otimes \sigma_j, \tag{E.1}$$

where $B_j = \sum_i a_{ij} \mathcal{B}_i$ is an Hermitian operator acting on the bath space. Using the relations

$$\begin{aligned} \sigma_x &= \sigma^+ + \sigma^- \\ \sigma_y &= i\sigma^+ - i\sigma^-, \end{aligned} \tag{E.2}$$

we obtain Eq. (8.5), where $B_\alpha = B_x + iB_y$.

E.2 Rectification in the weak coupling regime

We now compute the heat current flowing out of the leads in the weak coupling regime, valid when $H_{\mathrm{S},\alpha}$ is "small enough". As shown in Ref. [27], the evolution of the reduced density matrix ρ of the qubit obeys a Lindblad master equation. Furthermore, when the qubit is not degenerate (i.e. when $\Delta \neq 0$), the Lindblad master equation can be cast in the form of a rate equation for the occupation probabilities of the qubit, defined by $p_1 = \mathrm{Tr}\{\rho\sigma^+\sigma^-\}$ and

$p_0 = 1 - p_1$. Interestingly, only the terms in $H_{\mathrm{S},\alpha}$ proportional to σ^+ and σ^- contribute to the rate equation. Indeed, rewriting $H_{\mathrm{S},\alpha}$ as in Eq. (E.1), the rate equation only depends on the following matrix elements of the σ_j operators [27]:

$$\langle 0|\sigma_j|1\rangle\,, \tag{E.3}$$

where $\{|0\rangle\,,|1\rangle\}$ are the eigenstates of the qubit. In other words, only terms which can induce transitions in the qubit spectrum contribute to the master equation. Since $\langle 0|\sigma_j|1\rangle = 0$ for $\sigma_j = \mathbb{1}, \sigma_z$, the only terms that determine the populations are the ones proportional to σ_x and σ_y, and therefore to σ^+ and σ^-.

Neglecting for the moment the Lamb shift, as seen in Chap. 2, the probabilities satisfy [27]

$$\frac{\partial}{\partial t}\begin{pmatrix} p_0 \\ p_1 \end{pmatrix} = \begin{pmatrix} -\Gamma^+(\Delta) & \Gamma^-(\Delta) \\ \Gamma^+(\Delta) & -\Gamma^-(\Delta) \end{pmatrix}\begin{pmatrix} p_0 \\ p_1 \end{pmatrix}, \tag{E.4}$$

where $\Gamma^\pm(\Delta) = \Gamma^\pm_{\mathrm{L}}(\Delta, T_{\mathrm{L}}) + \Gamma^\pm_{\mathrm{R}}(\Delta, T_{\mathrm{R}})$, and $\Gamma^\pm_\alpha(\Delta, T_\alpha)$, for $\alpha = \mathrm{L}, \mathrm{R}$, is defined as in Sec. 2.1 (see App. E.3 for a derivation of the expression for the rates). Using Eq. (E.4) and $p_0 + p_1 = 1$, we can find the steady state populations

$$p_0 = \frac{\Gamma^-(\Delta)}{\Gamma^-(\Delta) + \Gamma^+(\Delta)}, \qquad p_1 = \frac{\Gamma^+(\Delta)}{\Gamma^-(\Delta) + \Gamma^+(\Delta)}. \tag{E.5}$$

The heat current flowing out of bath α at inverse temperature β_α can then be computed as

$$J_\alpha(\beta_\alpha) = \Delta\left(p_0\Gamma^+_\alpha(\Delta, T_\alpha) - p_1\Gamma^-_\alpha(\Delta, T_\alpha)\right). \tag{E.6}$$

Notice that also the steady-state heat current only depends on the rates, which in turn only depend on the terms in $H_{\mathrm{S},\alpha}$ proportional to σ^+ and σ^-. Therefore, also the rectification coefficient, withing the weak-coupling regime, only depends on the terms proportional to σ^+ and σ^-. Since $\Gamma^+_\alpha(\Delta, T_\alpha)$ and $\Gamma^-_\alpha(\Delta, T_\alpha)$ are related by the detailed balance equation (see Sec. 2.1), we can express them as $\Gamma^\pm_\alpha(\Delta, T_\alpha) = \Gamma_\alpha(\Delta, T_\alpha) f(\pm\Delta/(k_{\mathrm{B}}T_\alpha))$, where $f(x) = (1 + e^x)^{-1}$ and where $\Gamma_\alpha(\Delta, T_\alpha)$ is defined as in Sec. 2.1. Using Eqs. (E.5) and (E.6), and choosing as bath temperatures $T_{\mathrm{L}} = T + \Delta T/2$ and $T_{\mathrm{R}} = T - \Delta T/2$, we find that

$$J(\Delta T) = \Delta\frac{\Gamma_{\mathrm{L}}(\Delta, T_{\mathrm{L}})\Gamma_{\mathrm{R}}(\Delta, T_{\mathrm{R}})}{\Gamma_{\mathrm{L}}(\Delta, T_{\mathrm{L}}) + \Gamma_{\mathrm{R}}(\Delta, T_{\mathrm{R}})}\left[f(\Delta/(k_{\mathrm{B}}T_{\mathrm{L}})) - f(\Delta(k_{\mathrm{B}}T_{\mathrm{R}}))\right]. \tag{E.7}$$

We now have a general expression for the heat current which only depends on the tunneling rates $\Gamma_\alpha(\Delta, T_\alpha)$. In turn, given any bath and qubit-bath Hamiltonian, we are able to compute the rates as discussed in Sec. 2.1.

At last, we can find a general expression for R by plugging Eq. (E.7) into Eq. (8.13). This yields Eq. (8.17).

E.3 Tunneling Rates

In this section we prove Eq. (8.19). In order to use the results of Ref. [27], we consider the system-bath Hamiltonian as written in Eq. (E.1), such that all operators are Hermitian. Furthermore, as argued in App. E.2, the term proportional to σ_z does not contribute to the heat current. Therefore we have that

$$H_{\mathrm{S},\alpha} = B_x \otimes \sigma_x + B_y \otimes \sigma_y, \tag{E.8}$$

where

$$B_x = \frac{B^\dagger + B}{2}, \qquad B_y = \frac{i(B^\dagger - B)}{2}. \tag{E.9}$$

Using results of Ref. [27] with $H_{\mathrm{S},\alpha}$ given by to Eq. (E.8), we find

$$\Gamma^-_\alpha(\Delta, T_\alpha) = \sum_{i,j=\{x,y\}} \gamma_{ij} \langle 1|\sigma_i|0\rangle \langle 0|\sigma_j|1\rangle = \gamma_{xx} + \gamma_{yy} + i\gamma_{yx} - i\gamma_{xy} = \int_{-\infty}^{+\infty} dt\, e^{i\Delta t} \langle B(s)B^\dagger(0)\rangle\,, \tag{E.10}$$

where

$$\gamma_{ij} = \int_{-\infty}^{+\infty} dt\, e^{i\Delta t} \langle B_i^\dagger(t) B_j(0)\rangle\,, \tag{E.11}$$

and $B_i(t)$ is the time evolution of B_i in the interaction picture, i.e. $B_i(t)$ is the Heisenberg picture operator evolved solely according to Hamiltonian of the bath H_α. In the last step of Eq. (E.10) we used Eq. (E.9) to express B_x and B_y in terms of B and $B^\dagger$. This concludes the proof.

E.4 Tunneling Rates in Specific Models

In this section we derive the expression for $\Gamma_\alpha(\Delta, T)$ in various models.

E.4.1 Fermionic baths with linear (tunnel) couplings

In this subsection we consider a fermionic bath $H_\alpha^{(\mathrm{F})}$, as defined in Eq. (8.3). Furthermore, we consider the case of equal chemical potentials, which can be treated by considering the energies $\epsilon_{\alpha k}$ in Eq. (8.3) as measured respect to the common chemical potential μ. Therefore, the energies $\epsilon_{\alpha k}$ are defined in the interval $[-\infty, +\infty]$. Plugging the linear coupling Hamiltonian, given in Eq. (8.6), into Eq. (8.19) yields

$$\Gamma^-_\alpha(\Delta, T_\alpha) = \sum_{k,k'} V_{\alpha k} V^*_{\alpha k'} \int_{-\infty}^{+\infty} dt\, e^{i\Delta t} \left\langle c_{\alpha k}(t) c^\dagger_{\alpha k'} \right\rangle. \tag{E.12}$$

In the interaction picture, time-evolved bath operators $\hat{O}$ satisfy (with $\hbar = 1$)

$$\frac{d\hat{O}(t)}{dt} = i\left[H_\alpha, \hat{O}(t)\right]. \tag{E.13}$$

Using the fact that $[H_\alpha, c_{\alpha k}] = -\epsilon_{\alpha k} c_{\alpha k}$, we find

$$c_{\alpha k}(t) = e^{-i\epsilon_{\alpha k} t} c_{\alpha k}. \tag{E.14}$$

Plugging Eq. (E.14) into Eq. (E.12) yields

$$\Gamma^-_\alpha(\Delta, T_\alpha) = 2\pi \sum_k |V_{\alpha k}|^2 \langle c_{\alpha k} c^\dagger_{\alpha k}\rangle\, \delta(\Delta - \epsilon_{\alpha k}) = 2\pi \sum_k |V_{\alpha k}|^2 [1 - f(\beta_\alpha \epsilon_{\alpha k})] \delta(\Delta - \epsilon_{\alpha k}), \tag{E.15}$$

where $f(x) = (\exp(x) + 1)^{-1}$. Recognizing the spectral function, defined in Eq. (8.9), we have that

$$\Gamma^-_\alpha(\Delta, T_\alpha) = \gamma_\alpha(\Delta)[1 - f(\Delta/(k_{\mathrm{B}} T_\alpha))], \tag{E.16}$$

where $V = V_k$ such that $\epsilon_k = \Delta$. Using the detailed balance condition, we find that

$$\Gamma_\alpha(\Delta, T) = \gamma_\alpha(\Delta), \tag{E.17}$$

which implies $g(\Delta, T) = 1$. This proves Eq. (8.24).

E.4.2 Bosonic baths with linear (tunnel-like) coupling

In this section we consider a bosonic bath $H_\alpha^{(\mathrm{B})}$, as defined in Eq. (8.3), and a linear coupling as in Eq. (8.6). As in the fermionic case, we have that $[H_\alpha^{(\mathrm{B})}, b_{\alpha k}] = -\epsilon_{\alpha k} b_{\alpha k}$, so also in this case we have that the interaction picture destruction operator is given by

$$b_{\alpha k}(t) = e^{-i\epsilon_{\alpha k} t} b_{\alpha k}. \tag{E.18}$$

Performing the same steps as in the fermionic case, we end up with Eq. (E.15) with $\langle b_{\alpha k} b_{\alpha k}^\dagger \rangle$ instead of $\langle c_{\alpha k} c_{\alpha k}^\dagger \rangle$, which leads to having $1 + n(\epsilon_{\alpha k}/(k_\mathrm{B} T_\alpha))$ instead of $1 - f(\epsilon_{\alpha k}/(k_\mathrm{B} T_\alpha))$, where $n(x) \equiv (\exp(x) - 1)^{-1}$. We therefore find

$$\Gamma_\alpha^-(\Delta, T_\alpha) = \gamma_\alpha(\Delta)[1 + n(\Delta/(k_\mathrm{B} T_\alpha))], \tag{E.19}$$

which, using the detailed balance condition, leads to

$$\Gamma_\alpha(\Delta, T_\alpha) = \gamma_\alpha(\Delta) \coth\left(\Delta/(2k_\mathrm{B} T_\alpha)\right). \tag{E.20}$$

This proves Eq. (8.25).

E.4.3 Bosonic baths with non-linear coupling

In this section we consider a bosonic bath $H_\alpha^{(\mathrm{B})}$, as defined in Eq. (8.3), and a non-linear coupling as in Eq. (8.7). Using Eq. (8.19), we have that

$$\Gamma_\alpha^-(\Delta, T_\alpha) = \sum_{k,k'} V_k V_{k'}^* \int_{-\infty}^{+\infty} dt\, e^{i\Delta t} \left\langle b_k^2(t) (b_{k'}^\dagger)^2 \right\rangle. \tag{E.21}$$

Using Eq. (E.18), we can compute the time integral, finding

$$\Gamma_\alpha^-(\Delta, T_\alpha) = 2\pi \sum_k |V_{\alpha k}|^2 \left\langle b_{\alpha k}^2 (b_{\alpha k}^\dagger)^2 \right\rangle \delta(\Delta - 2\epsilon_{\alpha k}). \tag{E.22}$$

We therefore need to compute the expectation value $\langle b_{\alpha k}^2 (b_{\alpha k}^\dagger)^2 \rangle$. Using the commutation relations, we have that

$$\langle b_{\alpha k}^2 (b_{\alpha k}^\dagger)^2 \rangle = \langle n_{\alpha k}^2 \rangle + 3n(\epsilon_{\alpha k}/(k_\mathrm{B} T_\alpha)) + 2, \tag{E.23}$$

where $\langle n_{\alpha k}^2 \rangle = \langle (b_{\alpha k}^\dagger b_{\alpha k})^2 \rangle$ is the thermal expectation value of the square number. The calculation of $\langle n_{\alpha k}^2 \rangle$ is performed in App. E.5. Using Eq. (E.38), we have that

$$\langle b_{\alpha k}^2 (b_{\alpha k}^\dagger)^2 \rangle = 2\left[n(\epsilon_{\alpha k}/(k_\mathrm{B} T_\alpha)) + 1\right]^2. \tag{E.24}$$

Plugging this into Eq. (E.22), recalling that $\delta(\Delta - 2\epsilon_k) = \delta(\Delta/2 - \epsilon_k)/2$ (which can be proven changing variables), and recognizing the spectral function, we find

$$\Gamma_\alpha^-(\Delta, T_\alpha) = \gamma_\alpha(\Delta/2)[1 + n(\Delta/(2k_\mathrm{B} T_\alpha))]^2. \tag{E.25}$$

Finally, using the detailed balance condition we find

$$\Gamma_\alpha(\Delta, T_\alpha) = \frac{1}{2}\gamma_\alpha\left(\frac{\Delta}{2}\right)\left[1 + \coth^2(\Delta/(4k_\mathrm{B} T_\alpha))\right], \tag{E.26}$$

which proves Eq. (8.27).

E.4.4 Arbitrary baths with different σ couplings

In this subsection we consider arbitrary baths coupled to the qubit via Eq. (8.8). In fact, in this appendix we consider a more general case given by

$$H_{\mathrm{S},\alpha} = \sum_{i=x,y,z} (\hat{n}_{\alpha,i}\sigma_i) \otimes (B_\alpha + B_\alpha^\dagger), \tag{E.27}$$

where $\hat{n}_\alpha = (\sin\theta_\alpha \cos\phi_\alpha, \sin\theta_\alpha \sin\phi_\alpha, \cos\theta_\alpha)$ is a unit vector, and B_α is an arbitrary bath operator. As discussed in Sec. 2.1, the term proportional to σ_z does not contribute to the heat current, so we can neglect it. The term that matters is

$$\hat{n}_{\alpha,x}\sigma_x + \hat{n}_{\alpha,y}\sigma_y = \sin\theta_\alpha \left(e^{i\phi_\alpha}\sigma^+ + e^{-i\phi_\alpha}\sigma^-\right). \tag{E.28}$$

Assuming that $B^\dagger$ produces excitations in the bath with positive energy, also the terms proportional to $B^\dagger\sigma^+$ and $B\sigma^-$ vanish. The relevant terms of the interacting Hamiltonian thus become

$$H_{\mathrm{S},\alpha} = \sigma^+ \otimes \tilde{B}_\alpha + \sigma^- \otimes \tilde{B}_\alpha^\dagger, \tag{E.29}$$

where we define

$$\tilde{B}_\alpha = \sin\theta_\alpha e^{i\phi_\alpha} B_\alpha. \tag{E.30}$$

This interacting Hamiltonian is now of the form of Eq. (8.5). Therefore, the tunneling rates can be computed from Eq. (8.19), yielding

$$\Gamma_\alpha^-(\Delta, T_\alpha) = \sin^2\theta_\alpha h(\Delta, T_\alpha), \tag{E.31}$$

where $h(\Delta, T_\alpha) = \int dt\, e^{i\Delta t} \langle B_\alpha(t) B_\alpha^\dagger(0)\rangle_\alpha$ only depends on the bath through the temperature, and it does not depend on θ_α nor ϕ_α. Using the detailed balance condition we find

$$\Gamma_\alpha(\Delta, T_\alpha) = \sin^2\theta_\alpha h(\beta_\alpha)(1 + e^{-\beta_\alpha\Delta}). \tag{E.32}$$

This case is therefore described by the "similar bath" assumption [see Eq. (8.20)], where $\gamma_\alpha(\Delta) = \sin^2\theta_\alpha$, and $g(\beta) = h(\beta)(1 + e^{-\beta\Delta})$.

E.5 Thermal Averages

In this section we show how to compute the expectation value $\langle n_{\alpha k}^2\rangle$ for the bosonic bath. Let us define the inverse temperature $\beta_\alpha = 1/(k_{\mathrm{B}}T_\alpha)$ The partition function Z_α is given by

$$Z = \sum_{\{n_i\}=0}^{+\infty} p(\{n_i\}), \tag{E.33}$$

where the sum is over each n_i from 0 to $+\infty$, and where

$$p(\{n_i\}) = e^{-\beta_\alpha \sum_j n_j \epsilon_{\alpha j}} \tag{E.34}$$

is the canonical probability of finding the bath in a Fock state with occupation numbers $\{n_i\}$. Using these two definitions, and recalling that $\langle n_{\alpha k}^m\rangle \equiv \sum p(\{n_i\})\, n_k^m$, it is easy to prove that

$$-\frac{1}{\beta}\frac{\partial \ln Z}{\partial \epsilon_{\alpha k}} = \langle n_{\alpha k}\rangle, \tag{E.35}$$

$$\frac{1}{\beta^2}\frac{\partial^2 \ln Z}{\partial \epsilon_{\alpha k}^2} = \langle n_{\alpha k}^2\rangle - \langle n_{\alpha k}\rangle^2. \tag{E.36}$$

Plugging Eq. (E.34) into (E.33), and recognizing that we can perform all the sums as geometric series, we can express the logarithm of the bosonic partition function as

$$\ln Z = -\sum_j \ln\left(1 - e^{-\beta\epsilon_{\alpha j}}\right). \tag{E.37}$$

Plugging Eq. (E.37) into (E.35), we find the well know result that $\langle n_{\alpha k}\rangle = n(\beta_\alpha \epsilon_{\alpha k})$. Plugging Eq. (E.37) into (E.36), we find

$$\langle n_{\alpha k}^2\rangle = 2n^2(\beta_\alpha\epsilon_{\alpha k}) + n(\beta\epsilon_{\alpha k}). \tag{E.38}$$

E.6 Lamb shift

In this section we compute the Lamb shift of the qubit gap induced by the bath. In order to use the results of Ref. [27], we consider a coupling Hamiltonian as written in Eq. (E.8). As shown in Ref. [27], we have that

$$H_{\mathrm{LS}} = \sum_{\substack{\epsilon=\{0,\pm\Delta\}\\ i,j=\{x,y\}}} S_{xy}(\epsilon)\sigma_i^\dagger(\epsilon)\sigma_j(\epsilon), \tag{E.39}$$

where

$$S_{ij}(\epsilon) = \frac{1}{2\pi}\mathcal{P}\int_{-\infty}^{+\infty}\frac{\gamma_{ij}(\omega)}{\epsilon-\omega}d\omega \equiv \mathcal{S}_\epsilon[\gamma_{ij}(\omega)], \tag{E.40}$$

with

$$\gamma_{ij}(\omega) = \int_{-\infty}^{+\infty} dt\, e^{i\omega t}\,\langle B_i^\dagger(t)B_j(0)\rangle \tag{E.41}$$

defined exactly as in Eq. (E.11), where Δ is replaced with ω, and where

$$\sigma_i(\epsilon) = \sum_{\epsilon'-\epsilon''=\epsilon} |\epsilon''\rangle\,\langle\epsilon''|\,\sigma_i\,|\epsilon'\rangle\,\langle\epsilon'|\,. \tag{E.42}$$

Notice that the functional $\mathcal{S}_\epsilon[\dots]$, defined in Eq. (E.40), is linear, and that ϵ'' and ϵ' run over the two eigenvalues of the qubit, $-\Delta/2, \Delta/2$. For ease of notation, we identify the excited state of the qubit with $|1\rangle = |\Delta/2\rangle$, and the ground state with $|0\rangle = |-\Delta/2\rangle$. Expanding the sum in Eq. (E.42), we have

$$\begin{aligned}
\sigma_i(\Delta) &= \langle 0|\sigma_i|1\rangle\ |0\rangle\langle 1|\,,\\
\sigma_i(-\Delta) &= \langle 1|\sigma_i|0\rangle\ |1\rangle\langle 0|\,,\\
\sigma_i(0) &= \sum_{k=0,1}\langle k|\sigma_i|k\rangle\ |k\rangle\langle k| = 0,
\end{aligned} \tag{E.43}$$

where we used the fact that both σ_x and σ_y have only zeros on the diagonal in the last equality. Therefore, the non-null elements are given by

$$\begin{aligned}
\sigma_x(\Delta) &= \sigma^-, \qquad \sigma_x(-\Delta) = \sigma^+,\\
\sigma_y(\Delta) &= -i\sigma^-, \quad \sigma_y(-\Delta) = i\sigma^+.
\end{aligned} \tag{E.44}$$

Plugging these results into Eq. (E.39), using the anti-commutation relation $\{\sigma^-,\sigma^+\} = \mathbb{1}$, and neglecting the terms proportional to the identity, we find

$$\begin{aligned}
H_{\mathrm{LS}} = \sigma_z\left[S_{xx}(\Delta) + S_{yy}(\Delta) - iS_{xy}(\Delta) + iS_{yx}(\Delta)\right]\\
- \sigma_z\left[S_{xx}(-\Delta) + S_{yy}(-\Delta) + iS_{xy}(-\Delta) - iS_{yx}(-\Delta)\right].
\end{aligned} \tag{E.45}$$

Expressing $S_{ij}(\pm\Delta)$ in terms of the functional $\mathcal{S}_\epsilon$ yields

$$H_{\rm LS} = \sigma_z \mathcal{S}_\Delta \left[\gamma_{xx}(\omega) + \gamma_{yy}(\omega) - i\gamma_{xy}(\omega) + i\gamma_{yx}(\omega)\right] - \sigma_z \mathcal{S}_{-\Delta} \left[\gamma_{xx}(\omega) + \gamma_{yy}(\omega) + i\gamma_{xy}(\omega) - i\gamma_{yx}(\omega)\right]. \quad \text{(E.46)}$$

Using the definition of $\gamma_{ij}(\omega)$ in Eq. (E.41), and expressing B_x and B_y in terms of B and $B^\dagger$ through Eq. (E.9), it can be shown that

$$\begin{aligned} \gamma_{xx}(\omega) + \gamma_{yy}(\omega) - i\gamma_{xy}(\omega) + i\gamma_{yx}(\omega) &= \Gamma^-(\omega), \\ \gamma_{xx}(\omega) + \gamma_{yy}(\omega) + i\gamma_{xy}(\omega) - i\gamma_{yx}(\omega) &= \Gamma^+(-\omega), \end{aligned} \quad \text{(E.47)}$$

where $\Gamma^-(\omega)$ and $\Gamma^+(\omega)$ are the rates introduced in Eq. (E.4). Plugging Eq. (E.47) into Eq. (E.46) yields

$$H_{\rm LS} = \sigma_z \left(\mathcal{S}_\Delta \left[\Gamma^-(\omega)\right] - \mathcal{S}_{-\Delta} \left[\Gamma^+(-\omega)\right]\right) \quad \text{(E.48)}$$

Using Eq. (E.40), it can be shown that the operator $\mathcal{S}_\Delta[\dots]$ satisfies the general property $\mathcal{S}_{-\Delta}[f(-\omega)] = -\mathcal{S}_\Delta[f(\omega)]$. Therefore, we find

$$H_{\rm LS} = \sigma_z \mathcal{S}_\Delta \left[\Gamma^-(\omega) + \Gamma^+(\omega)\right]. \quad \text{(E.49)}$$

Finally, recalling that $\Gamma^\pm(\omega) = \Gamma^\pm_{\rm L}(\omega, T_{\rm L}) + \Gamma^\pm_{\rm R}(\omega, T_{\rm R})$, we have that

$$\Gamma^-(\omega) + \Gamma^+(\omega) = \Gamma_{\rm L}(\omega, T_{\rm L}) + \Gamma_{\rm R}(\omega, T_{\rm R}). \quad \text{(E.50)}$$

Therefore, we find

$$H_{\rm LS} = \sigma_z \left(\mathcal{S}_\Delta \left[\Gamma_{\rm L}(\omega, T_{\rm L})\right] + \mathcal{S}_\Delta \left[\Gamma_{\rm R}(\omega, T_{\rm R})\right]\right), \quad \text{(E.51)}$$

which proves Eq. (8.31).

E.7 Co-tunneling calculation

In this appendix we derive Eq. (8.36), i.e. the expression for the heat current adding co-tunneling rates to the ME calculation performed in the weak coupling regime (see Sec. 8.3). We will focus on the XX and YX coupling cases, defined in Sec. 8.4. For simplicity, in this appendix we express the system bath Hamiltonian $H^{\rm (sb)}_{{\rm S},\alpha}$ as

$$\begin{aligned} H^{\rm (sb)}_{\rm S,L} &= (q\sigma^+ + q^*\sigma^-) \otimes \sum_k V_{\alpha k}(b_{\alpha k} + b^\dagger_{\alpha k}), \\ H^{\rm (sb)}_{\rm S,R} &= (\sigma^+ + \sigma^-) \otimes \sum_k V_{\alpha k}(b_{\alpha k} + b^\dagger_{\alpha k}), \end{aligned} \quad \text{(E.52)}$$

where q is a complex coefficient given by $q = 1$ in the XX case (since $\sigma_x = \sigma^+ + \sigma^-$) and by $q = i$ in the YX case (since $\sigma_y = i\sigma^+ - i\sigma^-$).

Co-tunneling (see Sec. 2.2 for more details) is a second order process where a state of the uncoupled system evolves into another state of the uncoupled system passing through a "virtual state" by interacting twice with $H^{\rm (sb)}_{{\rm S},\alpha}$. Since $H^{\rm (sb)}_{{\rm S},\alpha}$ contains the operators σ^+ and σ^-, and since co-tunneling rates are obtained by acting twice with $H^{\rm (sb)}_{{\rm S},\alpha}$, the state of the qubit remain unaltered during a co-tunneling process. This property, which is denoted as "elastic co-tunneling", implies that co-tunneling rates do not enter the master equation for the probabilities.

We now consider all processes which transfer an excitation from the left to the right bath while the qubit is in the ground state. For simplicity, let us denote with $|0\rangle$ and $|1\rangle$ the ground and excited state of the qubit, and with $|n_\alpha\rangle_k$ a Fock state with n_α excitations in mode k of bath α. The initial $|i\rangle$, final $|f\rangle$, and intermediate states $|\nu_i\rangle$ involved in the co-tunneling process are respectively given by

$$\begin{aligned} |i\rangle &= |0\rangle \otimes |n_{\mathrm{L}}\rangle_k \otimes |n_{\mathrm{R}}\rangle_{k'}\,, \\ |f\rangle &= |0\rangle \otimes |n_{\mathrm{L}}-1\rangle_k \otimes |n_{\mathrm{R}}+1\rangle_{k'}\,, \\ |\nu_1\rangle &= |1\rangle \otimes |n_{\mathrm{L}}-1\rangle_k \otimes |n_{\mathrm{R}}\rangle_{k'}\,, \\ |\nu_2\rangle &= |1\rangle \otimes |n_{\mathrm{L}}\rangle_k \otimes |n_{\mathrm{R}}+1\rangle_{k'}\,, \end{aligned} \tag{E.53}$$

for all choices of k and k'. Using the Fermi golden rule, the rate of transition from the initial state $|i\rangle$ to the final state $|f\rangle$ is given by

$$\Gamma_{i\to f} = \frac{2\pi}{\hbar}\,|A_{if}|^2\,\delta(\epsilon_i-\epsilon_f), \tag{E.54}$$

where $\epsilon_{i/f}$ is the energy of the initial/final state in the absence of the system-bath interaction, and

$$A_{if} = \sum_j \frac{\langle f|\sum_\alpha H^{(\mathrm{sb})}_{\mathrm{S},\alpha}|\nu_j\rangle\langle\nu_j|\sum_\alpha H^{(\mathrm{sb})}_{\mathrm{S},\alpha}|i\rangle}{\epsilon_i-\epsilon_{\nu_j}+i\eta}, \tag{E.55}$$

η being an infinitesimal positive quantity and ϵ_{ν_j} the energy of $|\nu_j\rangle$. Using Eqs. (E.52) and (E.53), we have that the non-null matrix elements are

$$\begin{aligned} \langle f|H^{(\mathrm{sb})}_{\mathrm{S,R}}|\nu_1\rangle &= \langle\nu_2|H^{(\mathrm{sb})}_{\mathrm{S,R}}|i\rangle = V_{\mathrm{R}k_{\mathrm{R}}}\sqrt{n_{\mathrm{R}}+1}, \\ \langle\nu_1|H^{(\mathrm{sb})}_{\mathrm{S,L}}|i\rangle &= \langle f|H^{(\mathrm{sb})}_{\mathrm{S,L}}|\nu_2\rangle = q\,V_{\mathrm{L}k_{\mathrm{L}}}\sqrt{n_{\mathrm{L}}}. \end{aligned} \tag{E.56}$$

The total co-tunneling rate of energy $\Gamma^{\mathrm{cot}(0)}_{\mathrm{L}\to\mathrm{R}}$ that accounts for the transfer of an excitation from left to right, while the qubit is in state $|0\rangle$, is obtained by performing a weighed sum, according to the equilibrium probabilities, over all the initial and final states of the quantity $\Gamma_{i\to f}$ multiplied by the transferred energy. Combining Eqs. (E.56), (E.55) and (E.54), and using for simplicity $\epsilon_k = \epsilon_{\mathrm{L}k}$ and $\epsilon_{k'} = \epsilon_{\mathrm{R}k'}$, we have that

$$\Gamma^{\mathrm{cot}(0)}_{\mathrm{L}\to\mathrm{R}} = \frac{2\pi}{\hbar}\sum_{kk'}\epsilon_k\,|V_{\mathrm{L}k}|^2|V_{\mathrm{R}k'}|^2 n_{\mathrm{L}}(\epsilon_{\mathrm{k}})[1+n_{\mathrm{R}}(\epsilon_{\mathrm{k}'})]\left|\frac{q^*}{\Delta+\epsilon_{\mathrm{k}}+i\eta}+\frac{q}{\Delta-\epsilon_{\mathrm{k}}+i\eta}\right|\delta(\epsilon_{\mathrm{k}}-\epsilon_{\mathrm{k}'}). \tag{E.57}$$

As usual, we assume that the energies in the leads form a continuum, so we can replace the sum with an integral. Performing some calculations, and recalling that $|q|^2=1$ both in the XX and XY case, we have that

$$\Gamma^{\mathrm{cot}(0)}_{\mathrm{L}\to\mathrm{R}} = \int_0^{+\infty}\frac{d\epsilon}{2\pi\hbar}\,\epsilon\,\gamma_{\mathrm{L}}(\epsilon)\gamma_{\mathrm{R}}(\epsilon)n_{\mathrm{L}}(\epsilon)[1+n_{\mathrm{R}}(\epsilon)]\left|\frac{1}{\Delta+\epsilon+i\eta}+\frac{q}{q^*}\frac{1}{\Delta-\epsilon+i\eta}\right|. \tag{E.58}$$

Note that the term q/q^* is respectively 1 and -1 in the XX and YX cases.

The total cotunneling rate of energy $\Gamma^{\mathrm{cot}(0)}_{\mathrm{R}\to\mathrm{L}}$ transferring an excitation from right to left when the qubit is in the ground state is given by Eq. (E.58) exchanging $\mathrm{L}\leftrightarrow\mathrm{R}$. We thus find that the net energy rate $\Gamma^{\mathrm{cot}(0)} \equiv \Gamma^{\mathrm{cot}(0)}_{\mathrm{L}\to\mathrm{R}} - \Gamma^{\mathrm{cot}(0)}_{\mathrm{R}\to\mathrm{L}}$ is given by

$$\Gamma^{\mathrm{cot}(0)} = \int_0^{+\infty}\frac{d\epsilon}{2\pi\hbar}\,\epsilon\,\gamma_{\mathrm{L}}(\epsilon)\gamma_{\mathrm{R}}(\epsilon)[n_{\mathrm{L}}(\epsilon)-n_{\mathrm{R}}(\epsilon)]\left|\frac{1}{\Delta+\epsilon+i\eta}+\frac{q}{q^*}\frac{1}{\Delta-\epsilon+i\eta}\right|. \tag{E.59}$$

Repeating the same derivation assuming that the qubit is in the excited state, it can be shown that the net rate $\Gamma^{\mathrm{cot}(1)}$ is the same, i.e. $\Gamma^{\mathrm{cot}(0)} = \Gamma^{\mathrm{cot}(1)}$. Therefore, the heat current will be given by adding Eq. (E.59) to the ME expression, proving Eq. (8.36).

E.8 Non equilibrium Green's function calculation

In this appendix, we will consider a qubit in contact with bosonic baths. As described in Sec. 8.4.2, we express the spin operators in terms of Majorana fermions. In this representation, the total Hamiltonian is given by $H_{\mathrm{tot}} = \sum_\alpha (H_\alpha^{(\mathrm{B})} + H_{\mathrm{S},\alpha}^{(\mathrm{sb})}) + H_{\mathrm{S}}$, where we recall that

$$\begin{aligned} H_\alpha^{(\mathrm{B})} &= \sum_k \epsilon_{\alpha k}\, b_{\alpha k}^\dagger b_{\alpha k} \\ H_{\mathrm{S}} &= -i\frac{\Delta}{2}\eta_x\eta_y, \\ H_{\mathrm{S},\alpha}^{(\mathrm{sb})} &= -\frac{i}{2}\sum_{abc}\hat{n}_{\alpha,a}\epsilon_{abc}\,\eta_b\eta_c \otimes \sum_k V_{\alpha k}(b_{\alpha k} + b_{\alpha k}^\dagger). \end{aligned} \tag{E.60}$$

In all our calculations, we fix the coupling on the right hand side to have only the σ_x component, i. e. $\hat{n}_{\mathrm{R},y} = \hat{n}_{\mathrm{R},z} = 0$ and $\hat{n}_{\mathrm{R},x} = 1$. The one particle Green's function for the spin operator is defined as

$$\begin{aligned} G_{l,l'}^{<}(t,t') &= -i\langle\sigma_{l'}(t')\sigma_l(t)\rangle, \\ G_{l,l'}^{r}(t,t') &= -i\theta(t-t')\langle[\hat{\sigma}_l(t),\sigma_{l'}(t')]\rangle. \end{aligned} \tag{E.61}$$

The relations between the Green's function in the Majorana representation and the Green's function in spin representation are given by[370, 371],

$$\begin{aligned} G_{l,l'}^{</>}(t,t') &= \mp\Pi_{l,l'}^{</>}(t,t') \\ G^r(t,t') &= \theta(t-t')\left[\Pi^{>}(t,t') + \Pi^{<}(t,t')\right], \end{aligned} \tag{E.62}$$

where $\Pi_{l,l'}^{</>}(t,t') = \pm i\langle\eta_{l'}(t')\eta_l(t)\rangle$ are the lesser/greater Green's functions for Majorana operators. The heat current flowing from the lead R to the system is given by (setting $\hbar = 1$)

$$J_{\mathrm{R}}(t) = i\,\langle[H_{\mathrm{R}}(t), H_{\mathrm{S}}(t)]\rangle = -2\sum_k \epsilon_{\mathrm{R}k}V_{\mathrm{R}k}\mathrm{Re}\left[G_{x,\mathrm{R}k}^{<}(t,t)\right], \tag{E.63}$$

where $G_{x,\mathrm{R}k}^{<}(t,t') = -i\,\langle b_{\mathrm{R}k}^\dagger(t')\sigma_x(t)\rangle$. Following standard Keldysh NEGF treatment using Langreth theorem, the steady state heat current can be written as:

$$J(\Delta T) = 2\int d\epsilon\;\epsilon\;\mathrm{Re}\left[G_{xx}^r(\epsilon)D_{\mathrm{R}}^{<}(\epsilon) + G_{xx}^{<}(\epsilon)D_{\mathrm{R}}^a(\epsilon)\right], \tag{E.64}$$

where $D_{\mathrm{R}}(\epsilon) = \sum_k |V_{\mathrm{R}k}|^2 g_{\mathrm{R}k}(\epsilon)$ is the embedded self energy of the bath R and $g_{\mathrm{R}k}(\epsilon)$ is the Green's function for the uncoupled bath R. Applying the relations of Eq. (E.62), the heat current can be computed as

$$J(\Delta T) = \int_0^\infty \frac{d\epsilon}{2\pi}\epsilon\left[\Pi_{xx}^{>}(\epsilon)D_{\mathrm{R}}^{<}(\epsilon) + \Pi_{xx}^{<}(\epsilon)D_{\mathrm{R}}^{>}(\epsilon)\right]. \tag{E.65}$$

The embedded self energies can be written more explicitly as $D_{\mathrm{R}}^{<}(\epsilon) = -in_{\mathrm{R}}(\epsilon)\gamma_{\mathrm{R}}(\epsilon)$ and $D_{\mathrm{R}}^{>}(\epsilon) = -i(1+n_{\mathrm{R}}(\epsilon))\gamma_{\mathrm{R}}(\epsilon)$. In order to evaluate the heat currents, one needs to calculate the lesser and greater components of Majorana Green's function.

E.8.1 Derivation of Green's function

In this section, we will derive the Green's functions in Majorana representation. It is useful to write the Majorana operators in terms of Dirac operators[370]

$$\eta_x = f + f^\dagger; \quad \eta_y = i(f^\dagger - f); \quad \eta_z = g + g^\dagger. \tag{E.66}$$

The fermionic nature of f is consistent with,

$$f = \frac{\eta_x + i\eta_y}{2}; \quad f^2 = 0; \quad f^{\dagger 2} = 0; \quad \left\{f, f^\dagger\right\} = 1; \tag{E.67}$$

the same holds for g. The Majorana representation does not suffer from vertex problem [370] and the constraints on spins are naturally imposed on Majorana operators[311]. The Hamiltonian for the qubit becomes

$$H_{\rm S} = \frac{\Delta}{2}(1 - 2f^\dagger f), \tag{E.68}$$

whereas the contact Hamiltonian

$$H_{\rm S,L} = \sum_k V_{{\rm L}k}\Big[n_{{\rm L},x}\,(f^\dagger - f)\eta_z - i n_{{\rm L},y}\,\eta_z(f + f^\dagger) + n_{{\rm L},z}(1 - 2f^\dagger f)\Big](b_{{\rm L}k} + b^\dagger_{{\rm L}k}), \tag{E.69}$$

and

$$H_{\rm S,R} = \sum_k V_{{\rm R}k}(f^\dagger - f)\eta_z(b_{{\rm R}k} + b^\dagger_{{\rm R}k}). \tag{E.70}$$

Note that we consider general spin coupling in the left lead whereas a fixed σ_x coupling in the right. The contour ordered Green's function for the Majorana operators can be written as:

$$\Pi_{xx}(\tau, \tau') = \begin{bmatrix} \Pi^t_{xx}(t,t') & \Pi^<_{xx}(t,t') \\ \Pi^>_{xx}(t,t') & \Pi^{\bar{t}}_{xx}(t,t') \end{bmatrix} \tag{E.71}$$

We also define the Green's function for Dirac f - fermions in the Bogolyubov-Nambu representation, $\psi \equiv (f, f^\dagger)^T$ and $\psi^\dagger \equiv (f^\dagger, f)$, such that $G_\psi(\tau,\tau') = -i\,\langle \mathcal{T}\psi(\tau)\psi(\tau')\rangle$. On expansion in the Keldysh contour,

$$G_\psi(\tau,\tau') = \begin{bmatrix} G^t_{ff^\dagger}(t,t') & G^t_{ff}(t,t') & G^<_{ff^\dagger}(t,t') & G^<_{ff}(t,t') \\ G^t_{f^\dagger f^\dagger}(t,t') & G^t_{f^\dagger f}(t,t') & G^<_{f^\dagger f^\dagger}(t,t') & G^<_{f^\dagger f}(t,t') \\ G^>_{ff^\dagger}(t,t') & G^>_{ff}(t,t') & G^{\bar{t}}_{ff^\dagger}(t,t') & G^{\bar{t}}_{ff}(t,t') \\ G^>_{f^\dagger f^\dagger}(t,t') & G^>_{f^\dagger f}(t,t') & G^{\bar{t}}_{f^\dagger f^\dagger}(t,t') & G^{\bar{t}}_{f^\dagger f}(t,t') \end{bmatrix}, \tag{E.72}$$

where for instance, $G_{ff^\dagger}(\tau,\tau') = -i\left\langle \mathcal{T} f(\tau) f^\dagger(\tau')\right\rangle$. For more clarification, see Eqs. (A2) and (A3) in Ref.[295]. The lesser and greater Green's function in Majorana representation can then be computed using

$$\begin{aligned} \Pi^{<,>}_{xx}(t,t') &= \begin{bmatrix} 1 & 1 \end{bmatrix} G^{<,>}_\psi(t,t') \begin{bmatrix} 1 \\ 1 \end{bmatrix}, \\ \Pi^{<,>}_{yy}(t,t') &= \begin{bmatrix} 1 & -1 \end{bmatrix} G^{<,>}_\psi(t,t') \begin{bmatrix} 1 \\ -1 \end{bmatrix}. \end{aligned} \tag{E.73}$$

E.8.2 Calculation of Dyson equation

We now show how to compute G_ψ using the Dyson equation together with a leading order expansion of the self energy in the system-bath coupling. The Dyson equation for G_ψ is given by

$$G_\psi(\tau,\tau') = G^0_\psi(\tau,\tau') + \int d\tau_1 d\tau_2\, G_\psi(\tau,\tau_1)\Sigma_\psi(\tau_1,\tau_2)G^0_\psi(\tau_2,\tau'), \tag{E.74}$$

where Σ_ψ is the self-energy and G^0_ψ is the free Green's function. To leading order in the coupling Hamiltonian, we find that $\Sigma_\psi = \Sigma_{\psi,\mathrm{L}} + \Sigma_{\psi,\mathrm{R}}$, where

$$\begin{aligned}\Sigma_{\psi,\mathrm{L}}(\tau_1,\tau_2) = i\Sigma_{\mathrm{L}}(\tau_1,\tau_2)\Big(&\hat{n}^2_{\mathrm{L},x}\Pi^0_{z,z}(\tau_1,\tau_2)\hat{\lambda} \\ &+ \hat{n}^2_{\mathrm{L},y}\Pi^0_{z,z}(\tau_1,\tau_2)\hat{1} + 4\hat{n}^2_{\mathrm{L},z}\begin{bmatrix} G^0_{ff^\dagger}(\tau_1,\tau_2) & 0 \\ 0 & G^0_{f^\dagger f}(\tau_1,\tau_2)\end{bmatrix}\Big),\end{aligned} \tag{E.75}$$

and

$$\Sigma_{\psi,\mathrm{R}}(\tau_1,\tau_2) = i\Sigma_{\mathrm{R}}(\tau_1,\tau_2)\Pi^0_{z,z}(\tau_1,\tau_2)\hat{\lambda}. \tag{E.76}$$

$\hat{1}$ is the matrix of ones, and

$$\Sigma_\alpha(\tau_1,\tau_2) = -i\sum_k |V_{\alpha k}|^2 \left\langle \mathcal{T}\left[(b_{\alpha k}(\tau_1) + b^\dagger_{\alpha k}(\tau_1))(b_{\alpha k}(\tau_2) + b^\dagger_{\alpha k}(\tau_2))\right]\right\rangle_0, \tag{E.77}$$

with $\langle\ldots\rangle_0$ denoting an expectation value in the absence of the system-bath coupling, and

$$\hat{\lambda} = \begin{bmatrix} 1 & -1 \\ -1 & 1\end{bmatrix}.$$

Since we are interested in steady-state currents, we perform the Fourier transform exploiting time-translation invariance. The retarded and advanced components of Σ_α are thus given by

$$\Sigma^{r/a}_\alpha(\epsilon) = \sum_k |V_{\alpha k}|^2 \left(\frac{1}{\epsilon - \epsilon_{\alpha k} \pm i\eta} - \frac{1}{\epsilon + \epsilon_{\alpha k} \pm i\eta}\right) = \Lambda_\alpha(\epsilon) \mp \frac{i}{2}\left(\gamma_\alpha(\epsilon) - \gamma_\alpha(-\epsilon)\right), \tag{E.78}$$

where $\Lambda_\alpha(\epsilon)$ is defined as

$$\Lambda_\alpha(\epsilon) = \mathcal{P}\int_{-\infty}^{\infty}\frac{d\epsilon'}{2\pi}\left(\frac{\gamma_\alpha(\epsilon')}{\epsilon - \epsilon'} - \frac{\gamma_\alpha(\epsilon')}{\epsilon + \epsilon'}\right). \tag{E.79}$$

The lesser and greater components of $\Sigma_\alpha(\epsilon)$ take the form

$$\begin{aligned}\Sigma^<_\alpha(\epsilon) &= -in_\alpha(\epsilon)\left(\gamma_\alpha(\epsilon) - \gamma_\alpha(-\epsilon)\right), \\ \Sigma^>_\alpha(\epsilon) &= -i(1 + n_\alpha(\epsilon))\left(\gamma_\alpha(\epsilon) - \gamma_\alpha(-\epsilon)\right).\end{aligned} \tag{E.80}$$

In order to extract the various components of the self energy from Eqs. (E.75) and (E.76), we use the Langreth rules Ref. [40]. Given an expression of the form

$$\Sigma(\tau_1,\tau_2) = A(\tau_1,\tau_2)B(\tau_1,\tau_2), \tag{E.81}$$

the Langreth rules state that

$$\begin{aligned}\Sigma^<(\tau_1,\tau_2) &= A^<(\tau_1,\tau_2)B^<(\tau_1,\tau_2), \\ \Sigma^r(\tau_1,\tau_2) &= A^<(\tau_1,\tau_2)B^r(\tau_1,\tau_2) + A^r(\tau_1,\tau_2)B^<(\tau_1,\tau_2) + A^r(\tau_1,\tau_2)B^r(\tau_1,\tau_2).\end{aligned} \tag{E.82}$$

Since both Eqs. (E.75) and (E.76) have the form of Eq. (E.81), one can obtain the lesser ($\Sigma^{<}_{\psi,\alpha}$), greater ($\Sigma^{>}_{\psi,\alpha}$), retarded ($\Sigma^{r}_{\psi,\alpha}$) and advanced ($\Sigma^{a}_{\psi,\alpha}$) self energies in terms of different components of $\Sigma_\alpha(\epsilon)$ and of the free Green's function for the system using Eq. (E.82), and then performing the Fourier transform. For instance,

$$\Sigma^{<}_{\psi,\mathrm{L}}(\epsilon) = i\int \frac{d\epsilon'}{2\pi}\Sigma^{<}_{\mathrm{L}}(\epsilon-\epsilon')\Big(\hat{n}^2_{\mathrm{L},x}\Pi^{0,<}_{z,z}(\epsilon')\hat{\lambda} + \hat{n}^2_{\mathrm{L},y}\Pi^{0,<}_{z,z}(\epsilon')\hat{1} + 4\hat{n}^2_{\mathrm{L},z}\begin{bmatrix} G^{0,<}_{ff^\dagger}(\epsilon') & 0 \\ 0 & G^{0,<}_{f^\dagger f}(\epsilon')\end{bmatrix}\Big), \tag{E.83}$$

$$\Sigma^{<}_{\psi,\mathrm{R}}(\epsilon) = i\int \frac{d\epsilon'}{2\pi}\Sigma^{<}_{\mathrm{R}}(\epsilon-\epsilon')\Pi^{0,<}_{z,z}(\epsilon')\hat{\lambda}. \tag{E.84}$$

Eqs. (E.78) and (E.80) give all the components of the $\Sigma_\alpha(\epsilon)$. The only quantities which we haven't specified yet are the free Green's functions of the system. The free dynamics of the system Hamiltonian can be easily computed to obtain

$$\begin{aligned} G^{0,r}_{ff^\dagger}(\epsilon) &= \mathcal{P}\left\{\frac{1}{\epsilon+\Delta}\right\} - i\pi\delta(\epsilon+\Delta), \\ G^{0,r}_{f^\dagger f}(\epsilon) &= \mathcal{P}\left\{\frac{1}{\epsilon-\Delta}\right\} - i\pi\delta(\epsilon-\Delta). \end{aligned} \tag{E.85}$$

We can use the relation, $G^r - G^a = G^> - G^<$ to write

$$\begin{aligned} G^{0,>}_{f^\dagger f}(\epsilon) - G^{0,<}_{f^\dagger f}(\epsilon) &= -2i\pi\delta(\epsilon-\Delta), \\ G^{0,>}_{ff^\dagger}(\epsilon) - G^{0,<}_{ff^\dagger}(\epsilon) &= -2i\pi\delta(\epsilon+\Delta). \end{aligned} \tag{E.86}$$

Using the fluctuation dissipation relation[40], $G^{0,<}(\epsilon) = -f(\epsilon)\left(G^{0,>}(\epsilon) - G^{0,<}(\epsilon)\right)$ and $G^{0,>}(\epsilon) = (1-f(\epsilon))\left(G^{0,>}(\epsilon) - G^{0,<}(\epsilon)\right)$ where $f(\epsilon)$ is the Fermi distribution of the system defined at average temperature of the two baths, we can write

$$\begin{aligned} G^{0,</>}_{f^\dagger f}(\epsilon) &= \pm 2i\pi f(\pm\epsilon)\delta(\epsilon-\Delta), \\ G^{0,</>}_{ff^\dagger}(\epsilon) &= \pm 2i\pi f(\pm\epsilon)\delta(\epsilon+\Delta). \end{aligned} \tag{E.87}$$

The retarded and advanced Green's function for the system in the Majorana notation is

$$\Pi^{0,r/a}_{z,z}(\omega) = \frac{2}{\omega \pm i\eta}, \tag{E.88}$$

such that

$$\Pi^{0,r}_{z,z}(\omega) - \Pi^{0,a}(\omega) = \Pi^{0,>}_{z,z}(\omega) - \Pi^{0,<}_{z,z}(\omega) = -4i\pi\delta(\omega). \tag{E.89}$$

If we take the effective temperature of the Majorana fermions to be given by $\beta_{\mathrm{eff}}(\beta_\mathrm{L},\beta_\mathrm{R})$, we have from the fluctuation-dissipation theorem for the ordinary fermionic system in equilibrium[40]:

$$\Pi^{0,>}_{z,z}(\omega) + \Pi^{0,<}_{z,z}(\omega) = \left(\Pi^{0,r}_{z,z}(\omega) - \Pi^{0,a}_{z,z}(\omega)\right)\tanh\left(\frac{\beta_{\mathrm{eff}}\omega}{2}\right). \tag{E.90}$$

Using Eqs. (E.89) and (E.90), one can find the lesser and greater Green's function for the Majorana operators.

Similarly, the time ordered and anti-time ordered self energies are obtained from

$$\begin{aligned}\Sigma^{t}_{\psi}(\epsilon)+\Sigma^{\bar{t}}_{\psi}(\epsilon) &= \Sigma^{>}_{\psi}(\epsilon)+\Sigma^{<}_{\psi}(\epsilon),\\ \Sigma^{t}_{\psi}(\epsilon)-\Sigma^{\bar{t}}_{\psi}(\epsilon) &= \Sigma^{a}_{\psi}(\epsilon)+\Sigma^{r}_{\psi}(\epsilon).\end{aligned} \tag{E.91}$$

Performing the Fourier transform of Eq. (E.74), and assuming time translation invariance, we obtain:

$$\hat{G}^{-1}_{\psi}(\epsilon)=\hat{G}^{0^{-1}}_{\psi}(\epsilon)-\hat{\Sigma}_{\psi}(\epsilon), \tag{E.92}$$

where the bare system Green's function is

$$\hat{G}^{0,t^{-1}}_{\psi}(\epsilon)=-\hat{G}^{0,\bar{t}^{-1}}_{\psi}(\epsilon)=\epsilon\hat{\mathbb{1}}+\Delta\sigma_z. \tag{E.93}$$

This finally yields

$$\hat{m}\hat{G}_{\psi}(\epsilon)=\begin{bmatrix} \epsilon+\Delta-[\Sigma^{t}_{\psi}(\epsilon)]_{11} & -[\Sigma^{t}_{\psi}(\epsilon)]_{12} & -[\Sigma^{<}_{\psi}(\epsilon)]_{11} & -[\Sigma^{<}_{\psi}(\epsilon)]_{12}\\ -[\Sigma^{t}_{\psi}(\epsilon)]_{21} & \epsilon-\Delta-[\Sigma^{t}_{\psi}(\epsilon)]_{22} & -[\Sigma^{<}_{\psi}(\epsilon)]_{21} & -[\Sigma^{<}_{\psi}(\epsilon)]_{22}\\ [\Sigma^{>}_{\psi}(\epsilon)]_{11} & [\Sigma^{>}_{\psi}(\epsilon)]_{12} & \epsilon+\Delta+[\Sigma^{\bar{t}}_{\psi}(\epsilon)]_{11} & [\Sigma^{\bar{t}}_{\psi}(\epsilon)]_{12}\\ [\Sigma^{>}_{\psi}(\epsilon)]_{21} & [\Sigma^{>}_{\psi}(\epsilon)]_{22} & [\Sigma^{\bar{t}}_{\psi}(\epsilon)]_{21} & \epsilon-\Delta+[\Sigma^{\bar{t}}_{\psi}(\epsilon)]_{22}\end{bmatrix}^{-1}, \tag{E.94}$$

where $\hat{m}=\mathrm{diag}(1,1,-1,-1)$ is introduced to keep the appropriate sign for two different branches of the Keldysh contour [295]. Using Eq. (E.73) along with Eq. (E.94), one can obtain the lesser and greater Green's function in the Majorana representation. Substituting the Majorana Green's functions in Eq. (E.65), we obtain the final expression for current with general spin coupling in the left lead and a fixed spin coupling σ_x in the right lead.

This procedure allows us to compute the current for any coupling to the left lead, so the various expressions derived in Chap. 8 can be computed choosing the appropriate unit vector $\hat{n}_{\mathrm{L,i}}$.

E.9 Exact calculation

In this section we derive the formal exact expressions for the dynamical susceptibility

$$\chi(t)=\frac{i}{\hbar}\Theta(t)\langle[\sigma_x(t),\sigma_x(0)]\rangle \tag{E.95}$$

within the path-integral approach to the spin-boson model [304]. To deal with a correlated initial state at time $t=0$ we assume that the system starts at a preparation time $t_p<0$ in a factorized state (Feynman Vernon)

$$W_{tot}=\rho_{\mathrm{L}}(T_{\mathrm{L}})\otimes\rho_{\mathrm{R}}(T_{\mathrm{R}})\otimes\rho(t_p) \tag{E.96}$$

where each bath is in the thermal equilibrium state described by the density matrix $\rho_{\alpha}(T_{\alpha})$ and $\rho(t_p)$ is a general state of the qubit at the preparation time. Assuming that the system is ergodic, the response function will not depend on the chosen initial state when $t_p\to-\infty$.

For the sake of simplicity, we assume that the qubit starts in a diagonal state of σ_x, $|\eta_p\rangle$, with $\eta_p = 1$. We introduce the conditional propagating function

$$J(\zeta, t; \zeta_0, 0; \zeta_p, t_p) \tag{E.97}$$

to find the qubit in the state ζ at time t, conditioned to having measured the system in state ζ_0 at time $t = 0$ and having prepared it in state ζ_p at time t_p. Here ζ labels the four states of the density matrix, denoted in the following with the greek letter $\eta = \pm 1$ for diagonal states and $\xi = \pm 1$ for off-diagonal states.

The conditional propagating function can be written as real time path integral

$$\int \mathcal{D}\sigma(\ \cdot\ )\mathcal{D}\sigma'(\ \cdot\ )\mathcal{A}[\sigma(\ \cdot\ )]\mathcal{A}^*[\sigma'(\ \cdot\ )]\,\mathcal{F}[\sigma(\ \cdot\ ), \sigma'(\ \cdot\ )] \tag{E.98}$$

where the functional $\mathcal{A}[\sigma(\ \cdot\ )]$ is the probability amplitude for the free qubit to follow the path $\sigma(t)$ (each path can only take values ∓ 1 of the "coordinate" corresponding to the operator σ_x), and $\mathcal{F}[\sigma(\ \cdot\ ), \sigma'(\ \cdot\ )]$ is the real-time influence functional including the effects of the two baths. It is usual to express the paths in terms of the symmetric and anti-symmetric paths $\zeta(t)$ and $\xi(t)$:

$$\eta(t) = \frac{1}{2}[\sigma(t) + \sigma'(t)]\ ,\ \xi(t) = \frac{1}{2}[\sigma(t) - \sigma'(t)]\,. \tag{E.99}$$

When $\eta = \pm 1$ the qubit is in one of the two diagonal states of the density matrix expressed in the σ_x basis. It is usually said that the system is in a *sojourn*. Instead when $\xi(t) = \pm 1$ the system is in an off-diagonal state of the density matrix, or in a *blip* state. The double path integral in Eq. (E.98) can be visualized as a single path over the four states of the density matrix. During a sojourn of duration τ it is $\xi(\tau) = 0$ and vice-versa during a blip lasting τ it is $\eta(\tau) = 0$.

The influence functional in the presence of two baths coupled to the qubit via σ_x takes the simple form

$$\mathcal{F}[\sigma, \sigma'; t_0] = \exp\Big\{ \int_{t_0}^{t} dt' \int_{t_0}^{t'} dt'' \sum_{\nu} \Big[\dot{\xi}(t') \\ \mathrm{Re}\left[Q_\alpha(t' - t'')\right] \dot{\xi}(t'') + i\dot{\xi}(t')\mathrm{Im}\left[Q_\alpha(t' - t'')\right] \dot{\eta}(t'')\Big]\Big\} \tag{E.100}$$

where $Q_\alpha(t) = \mathrm{Re}[Q_\alpha(t)] + i\mathrm{Im}[Q_\alpha(t)]$ is the complex bath-α correlation function

$$Q_\alpha(t) = \int_0^\infty \frac{d\omega}{\pi\hbar} \frac{2\gamma_\alpha(\hbar\omega)}{\omega^2} \Big[\coth\left(\frac{\hbar\omega}{2k_{\mathrm{B}}T_\alpha}\right)(1 - \cos(\omega t)) + i\sin(\omega t)\Big]\,. \tag{E.101}$$

In terms of conditional propagating functions the dynamical susceptibility, Eq. (E.95) is given by

$$\chi(t) = \frac{i}{\hbar}\Theta(t) \lim_{t_p \to -\infty} \sum_{\eta=\pm 1} \sum_{\xi_0=\pm 1} \eta\xi_0 J(\eta, t; \xi_0, 0; \eta_p, t_p)\,. \tag{E.102}$$

Here Eq. (E.97) is evaluated for a path staring in a sojourn η_p at t_p, in a blip ξ_0 at time zero and again in a sojourn at time t. We find

$$J(\eta, t; \xi_0, 0; \eta_p, t_p) = \\ \eta\eta_p \sum_{m,n=1}^{\infty} (-\frac{\Delta^2}{4\hbar^2})^{m+n-1} \int_{t_p}^{t} \mathcal{D}_{2m-1,2n-1}\{t_j\} \sum_{\{\xi_j=\pm 1\}'} G^L_{n+m-1} G^R_{n+m-1} \sum_{\{\eta=\pm 1\}'} H^L_{n+m-1} H^R_{n+m-1} \tag{E.103}$$

where the the symbol $\{\}'$ reminds that the sum is over all sequences of blips and sojourns in accordance with the constraints indicated in the argument. Paths consist of $2n-1$ transitions for $t_p < t' < 0$ and $2m-1$ transitions for $0 < t' < t$. The blip-sojourn interactions enter the H_is, whereas the G_js include the blip-blip interactions and are given by

$$H^{\alpha}_{n+m-1} = \exp\left\{ i \sum_{k=0}^{m+n-2} \sum_{j=0}^{m+n-1} \xi_j X^{\alpha}_{j,k} \eta_k \right\} \tag{E.104}$$

$$G^{\alpha}_{n+m-1} = \exp\left\{ -\sum_{j=1}^{n+m} \mathrm{Re}\left[Q^{\alpha}_{2j,2j-1} \right] \right\} \exp\left\{ -i \sum_{j=2}^{m+n} \sum_{k=1}^{j-1} \xi_j \xi_k \Lambda^{\alpha}_{j,k} \right\} \tag{E.105}$$

$$\begin{aligned} X^{\alpha}_{j,k} &= \mathrm{Im}\left[Q^{\alpha}_{2j,2k+1} + Q^{\alpha}_{2j-1,2k} - Q^{\alpha}_{2j,2k} - Q^{\alpha}_{2j-1,2k+1} \right], \\ \Lambda^{\alpha}_{j,k} &= \mathrm{Re}\left[Q^{\alpha}_{2j,2k-1} + Q^{\alpha}_{2j-1,2k} - Q^{\alpha}_{2j,2k} - Q^{\alpha}_{2j-1,2k-1} \right]. \end{aligned} \tag{E.106}$$

Inserting the conditional propagating function Eq. (E.97) in the susceptibility Eq. (E.102) it is possible to perform the sum over the sojourns leading to

$$\begin{aligned} \chi(t) = \frac{2}{\hbar} \lim_{t_p \to -\infty} \sum_{m=1}^{\infty} \sum_{n=1}^{\infty} \left(-\frac{\Delta^2}{2\hbar^2} \right)^{m+n-1} \int_{t_p}^{t} \mathcal{D}_{2m-1,2n-1}\{t_j\} \sum_{\{\xi_j = \pm 1\}} \xi_n G^{L}_{n+m-1} G^{R}_{n+m-1} \\ \sin\left(\phi^{L}_{0,n+m-1} + \phi^{R}_{0,n+m-1} \right) \Pi_{k=1}^{m+n-2} \cos\left(\phi^{L}_{k,n+m-1} + \phi^{R}_{k,n+m-1} \right) \end{aligned} \tag{E.107}$$

where

$$\phi^{\alpha}_{k,m} = \sum_{j=k+1}^{m} \xi_j X^{\alpha}_{j,k} \,. \tag{E.108}$$

Eq. (E.107) is the formal exact expression for the susceptibility for a qubit simultaneously coupled to two harmonic baths at different temperatures for general spectral densities and temperatures.

Ohmic baths and the case $K_{\mathbf{L}} + K_{\mathbf{R}} = 1/2$

We now specialize to the case of two baths with Ohmic damping defined in Eq. (8.11) where we assume identical dependence on the energies included in $I(\epsilon)$. The bath correlation functions take the form

$$\begin{aligned} Q_{\alpha}(t) &= 2K_{\alpha} \ln\left\{ \left(\frac{\epsilon_{\mathrm{C}}}{\pi k_{\mathrm{B}} T_{\alpha}} \right) \sinh\left(\frac{\pi k_{\mathrm{B}} T_{\alpha} |t|}{\hbar \beta_{\alpha}} \right) \right\} \\ &+ i\pi K_{\alpha} \mathrm{sgn}(t) \,. \end{aligned} \tag{E.109}$$

The blip-sojourn interactions and the phases $\phi^{\nu}_{k,m}$, Eq (E.108) simplify, taking the form

$$\begin{aligned} X^{\alpha}_{j,k} &= \pi K_{\alpha} \,, \text{ for } j = k+1 \qquad X^{\alpha}_{j,k} = 0 \,, \text{ for } j \neq k+1 \\ \phi^{\alpha}_{k,n+m} &= \xi_{k+1} \pi K_{\alpha} \,. \end{aligned} \tag{E.110}$$

The susceptibility E.107 becomes

$$\chi(t) = \frac{2}{\hbar}\lim_{t_p\to-\infty}\sum_{m=1}^{\infty}\sum_{n=1}^{\infty}\left(-\frac{\Delta^2}{2\hbar^2}\right)^{m+n-1}\int_{t_p}^{t}\mathcal{D}_{2m-1,2n-1}\{t_j\}\sum_{\{\xi_j=\pm1\}}\xi_1\xi_n G^L_{n+m-1}G^R_{n+m-1}$$
$$\sin(\pi(K_\mathrm{L}+K_\mathrm{R}))\cos(\pi(K_\mathrm{L}+K_\mathrm{R}))^{n+m-2} \quad \text{(E.111)}$$

We observe that dependence from the damping strenghts K_α coming from the blip-sojourn interactions $X_{i,j}$, is in the simple form $K_\mathrm{L}+K_\mathrm{R}$. Thus we expect that in the case of two Ohmic baths coupled to the qubit with strengths $K_\mathrm{L}+K_\mathrm{R}=1/2$ these interactions can be treated analogously to the standard spin-boson model for a qubit coupled to a single bath at $K=1/2$. We remark that in Eq. (E.111) the coupling strengths enter non linearly the blip-blip interactions, $G^L_{n+m-1}G^R_{n+m-1}$, which include the temperatures of the two baths. Therefore, the two baths at $K_\mathrm{L}+K_\mathrm{R}=1/2$ are not simply equivalent to a single bath at $K=1/2$ with an "effective" temperature.

We proceed with the evaluation of Eq. (E.111) for $K_\mathrm{L}+K_\mathrm{R}=1/2$. We observe that all the terms in the sum, except for the first one $m=n=1$, have $n+m-2$ zeros from $\cos(\pi(K_\mathrm{L}+K_\mathrm{R}))^{n+m-2}$. They give a non-vanishing contribution if a proper divergency comes from the interaction terms between the system's transitions included in the $G^L_{n+m-1}G^R_{n+m-1}$. This is the typical case of a bath at $K=1/2$. Finite contributions arise whenever a "pair"-interaction can be cast in the following form, written in Laplace space

$$\lim_{K\to1/2}\Delta^2\cos(\pi K)\int_0^\infty d\tau e^{-\lambda\tau}e^{-\mathrm{Re}[Q(\tau)]} = \frac{\pi}{2}\frac{\Delta^2}{\epsilon_\mathrm{C}} \equiv \hbar\gamma\,. \quad \text{(E.112)}$$

The divergency of the integral comes from the $\tau\to0$ behavior of the pair interaction for $K=1/2$

$$e^{-\mathrm{Re}[Q(\tau)]} = \left(\frac{\epsilon_\mathrm{C}}{\pi k_\mathrm{B}T}\sinh\left(\frac{\pi k_\mathrm{B}T|t|}{\hbar}\right)\right)^{-2K} \to \left(\frac{\hbar}{\epsilon_\mathrm{C}\tau}\right)^{2K}. \quad \text{(E.113)}$$

The zero is compensated by the short distance singularity of the attractive interaction between nearest neighbor transitions, which can be thought of as opposite charges of a dipole. In the case of two baths with $K_\mathrm{L}+K_\mathrm{R}=1/2$ we have

$$e^{-\sum_\alpha \mathrm{Re}[Q_\alpha(\tau)]} = \prod_\alpha\left(\frac{\epsilon_\mathrm{C}}{\pi k_\mathrm{B}T_\alpha}\sinh\left(\frac{\pi k_\mathrm{B}T_\alpha|t|}{\hbar}\right)\right)^{-2K_\alpha} \to \left(\frac{\hbar}{\epsilon_\mathrm{C}\tau}\right)^{2K_\mathrm{L}}\left(\frac{\hbar}{\epsilon_\mathrm{C}\tau}\right)^{2K_\mathrm{R}} = \frac{\hbar}{\epsilon_\mathrm{C}\tau}\,. \quad \text{(E.114)}$$

The $\tau\to0$ behavior does not depend on the temperatures and we get diverging factors which exactly cancel the zero of the $\cos(\pi(K_\mathrm{L}+K_\mathrm{R}))$, as for a single bath at $K=1/2$

$$\lim_{K_\mathrm{L}+K_\mathrm{R}\to1/2}\Delta^2\cos(\pi(K_\mathrm{L}+K_\mathrm{R}))\int_0^\infty d\tau e^{-\lambda\tau}e^{-\sum_\alpha \mathrm{Re}[Q_\alpha(\tau)]} = \frac{\pi}{2}\frac{\Delta^2}{\epsilon_\mathrm{C}} \equiv \hbar\gamma\,. \quad \text{(E.115)}$$

Such an integral describes a *collapsed* dipole which does not interact with any other dipole, having effectively a zero dipole moment. This mechanism allows to sum the different terms of the sum in Eq. (E.111), leading to

$$\chi(t) = \frac{4}{\hbar^3}\frac{\Delta^2}{2\gamma}\Theta(t)\,e^{-\gamma t/2}\int_0^\infty d\tau e^{-\sum_\alpha \mathrm{Re}[Q_\alpha(\tau)]}[e^{-\gamma|t-\tau|/2} - e^{-\gamma(t+\tau)/2}]\,. \quad \text{(E.116)}$$

Performing its Fourier transform and inserting it in the Meir Wingreen formula we can get the heat current between two harmonic baths under the "strong" coupling condition $K_L+K_R=1/2$.

F

Appendix: Maximum power and corresponding efficiency for two-level heat engines and refrigerators: optimality of fast cycles

In this appendix, we provide details on the calculations performed in Chap. 9.

F.1 Optimality of infinitesimal Otto cycles

In this appendix we present explicit proof that infinitesimal Otto cycles are optimal for reaching maximum power performances for our two-level setting.

As a preliminary result we clarify that under periodic modulations of the control parameters, the Pauli equation (9.7) produces solutions which asymptotically are also periodic. For this purpose let us write Eq. (9.7) as $\dot{p}(t) = A(t)p(t) + B(t)$ where, for ease of notation, we introduced the functions

$$A(t) = -\sum_{\alpha=\mathrm{H,C}} \lambda_\alpha(t)\Gamma_\alpha[\epsilon(t)]\,, \qquad B(t) = \sum_{\alpha=\mathrm{H,C}} \lambda_\alpha(t)\Gamma_\alpha[\epsilon(t)]p_{\mathrm{eq}}^{(\alpha)}[\epsilon(t)]\,, \tag{F.1}$$

and consider periodical driving forces such that $A(t+\tau) = A(t)$, $B(t+\tau) = B(t)$ for all t. By explicitly integration we get

$$p(t) = \int_0^t e^{\int_{t'}^t A(t'')dt''} B(t')dt' + e^{\int_0^t A(t')dt'} p(0). \tag{F.2}$$

Decompose then the integral on the right hand side as

$$\int_0^t e^{\int_{t'}^t A(t'')dt''} B(t')dt' = \int_{t-\tau}^t e^{\int_{t'}^t A(t'')dt''} B(t')dt' + \int_0^{t-\tau} e^{\int_{t'}^{t-\tau} A(t'')dt''} e^{\int_{t-\tau}^t A(t'')dt''} B(t')dt'. \tag{F.3}$$

Notice now that, since $A(t)$ and $B(t)$ are periodic, the quantity $c(t) = \int_{t-\tau}^t e^{\int_{t'}^t A(t'')dt''} B(t')dt'$ is also periodic with period τ, while $d = e^{\int_{t-\tau}^t A(t'')dt''}$ is constant in time. Substituting the

previous definitions in Eq. (F.3) and then in Eq. (F.2) we find

$$p(t) = c(t) + d \int_0^{t-\tau} e^{\int_{t'}^{t-\tau} A(t'')dt''} B(t')dt' + e^{\int_0^t A(t')dt'} p(0). \tag{F.4}$$

In the asymptotic limit where the initial condition $p(0)$ has been completely forgotten (since $A(t) \leq 0$ at all times, the contribution of the initial condition decays exponentially), Eq. (F.2) gives

$$p(t-\tau) \approx \int_0^{t-\tau} e^{\int_{t'}^{t-\tau} A(t'')dt''} B(t')dt', \tag{F.5}$$

which substituted in Eq. (F.4) allows us to write

$$p(t) \approx c(t) + dp(t-\tau), \tag{F.6}$$

where we neglected again the contribution coming from the initial condition. Equation (F.6) defines a recursive succession, with limit point equal to $c(t)/(1-d)$, the periodicity of $c(t)$ concludes the proof. This result can also be framed in the general context of Floquet theory [372]. The Floquet theorem states that a fundamental matrix solution of a first order differential equation with periodically driven coefficients is quasi-periodical, namely can be written as $y(t) = P(t)e^{Mt}$ where $P(t)$ is a periodic matrix function (with the same period of the coefficients) and e^{Mt} is the so called *monodromy matrix*. The real parts of the eigenvalues of M are responsible of the asymptotic behavior of the solutions and are known as Lyapunov exponents, a stable cyclic solution is characterized by their negativity. In the case of Eq. (9.7), our calculations reveal that the monodromy matrix is given by the constant d, the sign of the Lyapunov exponent is given by $\log d < 0$, confirming our predictions about the stability.

In the above paragraph we showed that the asymptotic solution of Eq. (9.7) is periodic with the same period of the external driving $\epsilon(t)$. Notice that in the equilibrium scenario the previous result is trivial, since the population instantly relaxes to the Gibbs state that is a monotonic function of the control parameter ϵ. In our case we can establish only that $p(t)$ and $\epsilon(t)$ share the same period, although finding the proper functional relation between the two is absolutely non trivial (cfr. for example [52]). However we don't need any additional information to prove that any cycle that is not infinitesimal, namely a square wave protocol in which the controls jump at a time much faster that the typical dynamical scale Γ, cannot achieve the maximum power. The proof is outlined in the following: since $\epsilon(t)$ and $p(t)$ share the same periodicity, a cycle can be represented in the (p, ϵ) plane as a closed curve. Let us suppose that the optimal cycle $\mathcal{T}$ is not infinitesimal, for example as in Fig. F.1. Thus, it is possible to perform an instantaneous quench, for example, in the middle (where the probability is halfway between the minimum and maximum value), and divide the transformation in two smaller sub-cycles $\mathcal{T}_1$ and $\mathcal{T}_2$ (cfr. Fig F.1). Since the quenches are instantaneous, they don't contribute to the heat exchanged and to the time duration of the process. Furthermore, performing the two sub-cycles in series effectively builds a transformation with the same average power of the original cycle, a property that in symbols we can exemplify as $P(\mathcal{T}) = P(\mathcal{T}_1 \circ \mathcal{T}_2)$. Simple calculations reveal that the power of the single sub-cycles cannot be both greater or smaller than the power of the original one, thus we are left with two possibilities, $P(\mathcal{T}_1) \leq P(\mathcal{T}_1 \circ \mathcal{T}_2) \leq P(\mathcal{T}_2)$ or $P(\mathcal{T}_2) \leq P(\mathcal{T}_1 \circ \mathcal{T}_2) \leq P(\mathcal{T}_1)$. In both cases the original cycle is sub-optimal, that is absurd, unless $P(\mathcal{T}_1) = P(\mathcal{T}_1 \circ \mathcal{T}_2) = P(\mathcal{T}_2)$ but even in this case we can choose one of the two sub-cycles still preserving optimality.

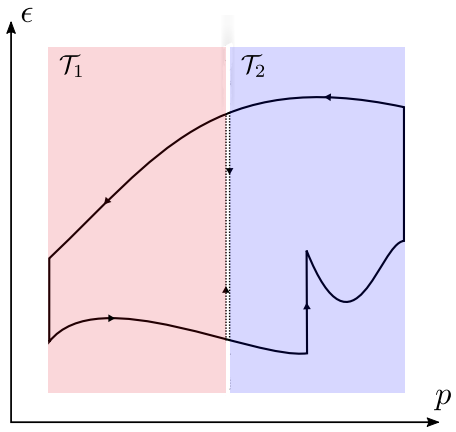

Figure F.1: The original cycle is represented by a black line following a closed path in the (p, ϵ) plane. The two sub-cycles are the portions of the original one enclosed in the light red and in the light blue squares, respectively denoted with $\mathcal{T}_1$ and $\mathcal{T}_2$.

The previous argument shows that the only candidates for power maximization are those cycles that cannot be divided with a quench as done in the above proof, thus being infinitesimal. Notice that the previous proof strongly relies on the possibility of performing effectively instantaneous quenches, a characteristic that is better analyzed in the next appendix. At last, by using Pontryagin's minimum principle, it can be shown that if coupling constants $\lambda_{\rm H}(t)$ and $\lambda_{\rm C}(t)$ fulfill a "trade-off relation" (i.e. if one increases, the other one decreases), then the optimal cycle will have $\lambda_{\rm C}(t) = 0$ and $\lambda_{\rm H}(t) = 1$, or $\lambda_{\rm C}(t) = 0$ and $\lambda_{\rm H}(t) = 1$ at all times [52]. This implies that the coupling to the baths must be switched during the quenches of the infinitesimal Otto-cycle.

F.2 Maximum power formula and finite-time corrections

In this appendix we prove Eq. (9.8) and discuss the finite-time corrections.

As as shown in the previous appendix, the optimal cycle *must* be an infinitesimal Otto cycle, so we consider a protocol (depicted in Fig. 9.1b) where $\epsilon(t) = \epsilon_{\rm H}$, $\lambda_{\rm H} = 1$ and $\lambda_{\rm C} = 0$ for $t \in [0, \tau_{\rm H}]$, and $\epsilon(t) = \epsilon_{\rm C}$, $\lambda_{\rm H} = 0$ and $\lambda_{\rm C} = 1$ for $t \in [\tau_{\rm H}, \tau_{\rm H} + \tau_{\rm C}]$. The optimal cycle and corresponding power will then be found by taking the limit $dt = \tau_{\rm H} + \tau_{\rm C} \to 0$ and maximizing over the free parameters $\epsilon_{\rm H}$, $\epsilon_{\rm C}$ and $\tau_{\rm H}/\tau_{\rm C}$.

We proceed the following way: first we perform an exact calculation, for arbitrary $\tau_{\rm H}$ and $\tau_{\rm C}$, of the heat rates $\langle J_{\rm H}\rangle$, $\langle J_{\rm C}\rangle$, averaged over one period, flowing out of the hot and cold bath respectively. Then, in the limit $dt \to 0$, we find the ratio $\tau_{\rm H}/\tau_{\rm C}$ that maximizes the power and we find the corresponding expression of the maximum power, proving Eq. (9.8) and the optimal ratio condition

$$\tau_{\rm H}/\tau_{\rm C} = \sqrt{\Gamma_{\rm C}(\epsilon_{\rm C})/\Gamma_{\rm H}(\epsilon_{\rm H})}\,. \tag{F.7}$$

The instantaneous heat currents can be computed by plugging the probability $p(t)$, solution of Eq. (9.7), into Eq. (9.6). We denoted with $p_{\rm H}(t)$ and $p_{\rm C}(t)$ the solution of Eq. (9.7) respectively in the time intervals $\mathcal{I}_{\rm H} = [0, \tau_{\rm H}]$ and $\mathcal{I}_{\rm C} = [\tau_{\rm H}, \tau_{\rm H} + \tau_{\rm C}]$. Since the control parameters (i.e. $\epsilon(t)$, $\lambda_{\rm H}(t)$ and $\lambda_{\rm C}(t)$) are constant in each interval, we have that

$$p_{\rm H}(t) = He^{-\Gamma_{\rm H} t} + p_{\rm eq}^{\rm (H)}, \quad p_{\rm C}(t) = Ce^{-\Gamma_{\rm C} t} + p_{\rm eq}^{\rm (C)}, \tag{F.8}$$

where H and C are two constants and where, for ease of notation, we introduced the symbols $\Gamma_\alpha := \Gamma_\alpha(\epsilon_\alpha)$ and $p_{\rm eq}^{(\alpha)} := p_{\rm eq}^{(\alpha)}(\epsilon_\alpha)$ (for $\alpha = {\rm H}, {\rm C}$). We determine the two constants H and C by imposing that the probability $p(t)$ is continuous in $t = \tau_{\rm H}$, i.e.

$$p_{\rm H}(\tau_{\rm H}) = p_{\rm C}(\tau_{\rm H}) \tag{F.9}$$

and that $p(t)$ is periodic with period $\tau_{\rm H} + \tau_{\rm C}$, i.e.

$$p_{\rm H}(0) = p_{\rm C}(\tau_{\rm H} + \tau_{\rm C}). \tag{F.10}$$

We impose periodic boundary conditions because, as discussed in the previous appendix, a periodic protocol produces a periodic $p(t)$ after an initial transient time, and we are indeed interested in the "asymptotic" regime. Equations (F.9) and (F.10) reduce to the following linear-algebra problem for the constants H and C:

$$\frac{1}{p_{\rm eq}^{(\rm C)} - p_{\rm eq}^{(\rm H)}} \begin{pmatrix} e^{-\Gamma_{\rm H}\tau_{\rm H}} & -e^{-\Gamma_{\rm C}\tau_{\rm H}} \\ 1 & -e^{-\Gamma_{\rm C}(\tau_{\rm H}+\tau_{\rm C})} \end{pmatrix} \begin{pmatrix} H \\ C \end{pmatrix} = \begin{pmatrix} 1 \\ 1 \end{pmatrix}, \tag{F.11}$$

with solution

$$\begin{pmatrix} H \\ C \end{pmatrix} = \frac{\left(p_{\rm eq}^{(\rm C)} - p_{\rm eq}^{(\rm H)}\right)}{\sinh\left[(\Gamma_{\rm H}\tau_{\rm H} + \Gamma_{\rm C}\tau_{\rm C})/2\right]} \begin{pmatrix} e^{\Gamma_{\rm H}\tau_{\rm H}/2}\sinh\left(\Gamma_{\rm C}\tau_{\rm C}/2\right) \\ -e^{\Gamma_{\rm C}\tau_{\rm H}}e^{\Gamma_{\rm C}\tau_{\rm C}/2}\sinh\left(\Gamma_{\rm H}\tau_{\rm H}/2\right) \end{pmatrix}, \tag{F.12}$$

which, via Eq. (F.8), completely determine $p(t)$. By substituting Eq. (F.8) into Eq. (9.6), we can write the averaged heat rates $\langle J_{\rm H}\rangle$ and $\langle J_{\rm C}\rangle$ as

$$\begin{aligned} \langle J_{\rm H}\rangle &= \tfrac{1}{\tau_{\rm H}+\tau_{\rm C}} \int_{\mathcal{I}_{\rm H}} J_{\rm H} dt = \tfrac{\epsilon_{\rm H}}{\tau_{\rm H}+\tau_{\rm C}} \int_{\mathcal{I}_{\rm H}} \dot{p}_{\rm H} dt = \tfrac{\epsilon_{\rm H} H}{\tau_{\rm H}+\tau_{\rm C}} \left[e^{-\Gamma_{\rm H}\tau_{\rm H}} - 1\right], \\ \langle J_{\rm C}\rangle &= \tfrac{1}{\tau_{\rm H}+\tau_{\rm C}} \int_{\mathcal{I}_{\rm C}} J_{\rm C} dt = \tfrac{\epsilon_{\rm C}}{\tau_{\rm H}+\tau_{\rm C}} \int_{\mathcal{I}_{\rm C}} \dot{p}_{\rm C} dt = \tfrac{\epsilon_{\rm C} C}{\tau_{\rm H}+\tau_{\rm C}} e^{-\Gamma_{\rm C}\tau_{\rm H}} \left[e^{-\Gamma_{\rm C}\tau_{\rm C}} - 1\right], \end{aligned} \tag{F.13}$$

where we use the fact that $\epsilon(t)$ is constant in each $\mathcal{I}_\alpha$ and the fact that, since the two-level system is coupled to one bath at a time, $\dot{p}_\alpha = \dot{p}$ with $p(t) = p_{\rm H}(t)$ during $\mathcal{I}_{\rm H}$ and $p(t) = p_{\rm C}(t)$ during $\mathcal{I}_{\rm C}$. Using the expressions for H and C given in Eq. (F.12), we can rewrite Eq. (F.13) as

$$\langle J_{\rm H/C}\rangle = \pm \frac{\epsilon_{\rm H/C}}{\tau_{\rm H}+\tau_{\rm C}} \frac{\Gamma_{\rm H}\tau_{\rm H}\Gamma_{\rm C}\tau_{\rm C}}{\Gamma_{\rm H}\tau_{\rm H}+\Gamma_{\rm C}\tau_{\rm C}} \left(p_{\rm eq}^{(\rm H)} - p_{\rm eq}^{(\rm C)}\right) \frac{(\Gamma_{\rm H}\tau_{\rm H}/2)^{-1} + (\Gamma_{\rm C}\tau_{\rm C}/2)^{-1}}{\coth\left(\Gamma_{\rm H}\tau_{\rm H}/2\right) + \coth\left(\Gamma_{\rm C}\tau_{\rm C}/2\right)}. \tag{F.14}$$

We now impose that $dt = \tau_{\rm H} + \tau_{\rm C}$ by setting $\tau_{\rm H} = \theta dt$ and $\tau_{\rm C} = (1-\theta)dt$, for $\theta \in [0,1]$, in Eq. (F.14). Taking hence the infinitesimal cycle limit $dt \to 0$ we get

$$\langle J_{\rm H/C}\rangle = \pm \epsilon_{\rm H/C} \frac{\Gamma_{\rm H}\theta\, \Gamma_{\rm C}(1-\theta)}{\Gamma_{\rm H}\theta + \Gamma_{\rm C}(1-\theta)} \left(p_{\rm eq}^{(\rm H)} - p_{\rm eq}^{(\rm C)}\right). \tag{F.15}$$

The maximization over θ of the above expression yields the condition

$$\frac{\theta}{1-\theta} = \sqrt{\frac{\Gamma_{\rm C}}{\Gamma_{\rm H}}}, \tag{F.16}$$

which, multiplying by dt the numerator and the denominator of the left hand side of Eq. (F.16), proves Eq. (F.7). Solving hence Eq. (F.16) for θ and plugging the result into Eq. (F.15) yields

$$\langle J_{\rm H/C}\rangle = \pm \epsilon_{\rm H/C} \frac{\Gamma_{\rm H}\Gamma_{\rm C}}{\left(\sqrt{\Gamma_{\rm H}} + \sqrt{\Gamma_{\rm C}}\right)^2} \left(p_{\rm eq}^{(H)} - p_{\rm eq}^{(C)}\right), \tag{F.17}$$

which replaced into Eq. (9.1), and maximizing with respect to the only two free parameters left, i.e. $\epsilon_{\rm H}$ and $\epsilon_{\rm C}$, allows us to derive Eq. (9.8) for all four thermal machine modes. An additional comment has to be made for the accelerator mode [A], that aims at maximizing the heat released into the cold bath while extracting heat from the hot bath. By definition, we must restrict the maximization in Eq. (9.8) to guarantee $\langle J_{\rm H}\rangle \geq 0$, e.g. by forcing $\mathcal{C}$ to be $(\epsilon_{\rm H}\geq 0 \cap \beta_{\rm C}\epsilon_{\rm C}\geq\beta_{\rm H}\epsilon_{\rm H})\cup(\epsilon_{\rm H}\leq 0\cap\beta_{\rm C}\epsilon_{\rm C}\leq\beta_{\rm H}\epsilon_{\rm H})$. On the other hand, the heater mode consists of heating a single reservoir whose interaction with the two-level system is described by a rate $\Gamma(\epsilon)$ and equilibrium probability $p_{\rm eq}(\epsilon)$. So in this case the maximization must be performed taking $\Gamma_\alpha(\epsilon)=\Gamma(\epsilon)$ and $p_{\rm eq}^{(\alpha)}(\epsilon)=p_{\rm eq}(\epsilon)$ (for $\alpha={\rm H},\,{\rm C}$). If we also require that $\Gamma(\epsilon)=\Gamma(-\epsilon)$, which physically means that the rates do not distinguish which one of the two energy levels is the ground and excited state, we find that Eq. (9.8) can be simplified to

$$P_{[{\rm H}]}^{(\max)} = \max_{\epsilon\geq 0,\,\epsilon\in\mathcal{C}} \frac{1}{2}\,\epsilon\,\Gamma(\epsilon)\,[1-2p_{\rm eq}(\epsilon)]\,, \tag{F.18}$$

and the corresponding optimal cycle is given by an Otto cycle where $\tau_{\rm H}=\tau_{\rm C}$ and the value ϵ that maximizes Eq. (F.18) determines $\epsilon_{\rm H}=-\epsilon_{\rm C}=\epsilon$. Thus the optimal cycle in the heater case corresponds to attempting continuous population inversions.

F.2.1 Finite-Time Corrections part one

Setting $\tau_{\rm H}=\theta dt$ and $\tau_{\rm C}=(1-\theta)dt$ in Eq. (F.14), and plugging in the expression of θ that satisfies Eq. (F.16), we find that the average heat rate for an arbitrary period dt is given by

$$\langle J_{\rm H/C}(dt)\rangle = \pm\epsilon_{\rm H/C}\frac{\Gamma_{\rm H}\Gamma_{\rm C}}{\left(\sqrt{\Gamma_{\rm H}}+\sqrt{\Gamma_{\rm C}}\right)^2}\left(p_{\rm eq}^{(H)}-p_{\rm eq}^{(C)}\right)\frac{(\widetilde{\Gamma}_{\rm H}dt/2)^{-1}+(\widetilde{\Gamma}_{\rm C}dt/2)^{-1}}{\coth\left(\widetilde{\Gamma}_{\rm H}dt/2\right)+\coth\left(\widetilde{\Gamma}_{\rm C}dt/2\right)}, \tag{F.19}$$

where $\widetilde{\Gamma}_\alpha=(\widetilde{\Gamma}\Gamma_\alpha)^{1/2}$ and $\widetilde{\Gamma}=\Gamma_{\rm H}\Gamma_{\rm C}/(\sqrt{\Gamma_{\rm H}}+\sqrt{\Gamma_{\rm C}})^2$. Plugging this results into Eq. (9.1) and maximizing over $\epsilon_{\rm H}$ and $\epsilon_{\rm C}$ yields the expression

$$P_{[\nu]}^{(\max)}(dt) = \frac{(\widetilde{\Gamma}_{\rm H}dt/2)^{-1}+(\widetilde{\Gamma}_{\rm C}dt/2)^{-1}}{\coth\left(\widetilde{\Gamma}_{\rm H}dt/2\right)+\coth\left(\widetilde{\Gamma}_{\rm C}dt/2\right)}\,P_{[\nu]}^{(\max)}, \tag{F.20}$$

which provides the finite time version of Eq. (9.8). On one hand, as anticipated in Chap. 9, by expanding Eq. (F.20) for small dt, we find the following quadratic correction

$$P_{[\nu]}^{(\max)}(dt)\approx(1-\widetilde{\Gamma}_{\rm H}\widetilde{\Gamma}_{\rm C}dt^2/12)P_{[\nu]}^{(\max)}\,. \tag{F.21}$$

On the other hand for $\widetilde{\Gamma}_{\rm H}dt,\widetilde{\Gamma}_{\rm C}dt\gg 1$, we get

$$P_{[\nu]}^{(\max)}(dt)\approx\frac{(\widetilde{\Gamma}_{\rm H}dt/2)^{-1}+(\widetilde{\Gamma}_{\rm C}dt/2)^{-1}}{2}\,P_{[\nu]}^{(\max)}\,, \tag{F.22}$$

implying that a considerable fraction of $P_{[\nu]}^{(\max)}$ can be achieved even if the driving frequency is slower than the typical rate. Notice that Eq. (F.20) is a strictly decreasing function of dt; this is consistent with the fact that an infinitesimal cycle is indeed the optimal solution.

We conclude by observing that we can simplify Eq. (F.20) for the heater mode where a single reservoir is coupled to the two-level system. Under the hypothesis leading to Eq. (F.18), we find that

$$P_{[{\rm H}]}^{(\max)}(dt)=\frac{\tanh\left(dt\Gamma/4\right)}{dt\Gamma/4}P_{[{\rm H}]}^{(\max)}, \tag{F.23}$$

where Γ is computed in the value of ϵ that maximizes Eq. (F.18). Figure 9.1c, which is a plot of Eq. (F.23), shows that $P_{[\mathrm{H}]}^{(\max)}(dt) \approx P_{[\mathrm{H}]}^{(\max)}$ up to $dt\Gamma \approx 2$, while for $dt\Gamma = 10 \gg 1$, $P_{[\mathrm{H}]}^{(\max)}(dt)$ is only decreased of a factor two.

F.2.2 Finite-Time Corrections part two: the Quenches

Finite-time corrections to the power may not only arise from the finite duration of the isothermal transformations (i.e. from a finite value of τ_{C} and τ_{H}), but also from a finite duration τ of the quenches, i.e. of the transformations during which ϵ changes between the two extremal values ϵ_{C} and ϵ_{H}. We will thus assume that each quench is carried out in a time τ. The aim of this appendix is to show how these effects could be accounted for, and to estimate the leading order corrections to the maximum power delivered by the heat engine due to this effect; analogous considerations hold also for the other machines. We will thus restrict ourself to the regime $\tau \ll dt \ll \gamma^{-1}$, where $dt = \tau_{\mathrm{C}} + \tau_{\mathrm{H}}$ and γ is the characteristic rate of the system during the protocol. The first inequality states that the duration of the quenches is much smaller than the duration of the isothermal transformations. The second inequality implies that the finite-time corrections discussed in the previous subsection are neglected, since they have been previously discussed.

Using the results of App. F.1, we know that $p(t)$ has a limit cycle with the same period of $\epsilon(t)$. If we further assume that the protocol is much faster than γ, the probability tends to a fixed value $\bar{p}$ given by

$$\bar{p} = \frac{\int_0^T ds \Gamma(s) p_{\mathrm{eq}}(s)}{\int_0^T ds \Gamma(s)}, \tag{F.24}$$

where $T = dt + 2\tau$ is the total duration of the protocol, $\Gamma(s) = \lambda_{\mathrm{H}}(s)\Gamma_{\mathrm{H}}[\epsilon(s)] + \lambda_{\mathrm{C}}(s)\Gamma_{\mathrm{C}}[\epsilon(s)]$ and

$$p_{\mathrm{eq}}(s) = \frac{\lambda_{\mathrm{H}}(s)\Gamma_{\mathrm{H}}[\epsilon(s)] p_{\mathrm{eq}}^{(\mathrm{H})}[\epsilon(s)] + \lambda_{\mathrm{C}}(s)\Gamma_{\mathrm{C}}[\epsilon(s)] p_{\mathrm{eq}}^{(\mathrm{C})}[\epsilon(s)]}{\lambda_{\mathrm{H}}(s)\Gamma_{\mathrm{H}}[\epsilon(s)] + \lambda_{\mathrm{C}}(s)\Gamma_{\mathrm{C}}[\epsilon(s)]}. \tag{F.25}$$

By using again the hypothesis that the protocol is much faster than γ, we can write the power of the heat engine, averaged over one period, as

$$P_{[\mathrm{E}]}(\lambda) = \frac{1}{T} \int_0^T ds\, \epsilon(s)\Gamma(s) \left[p_{\mathrm{eq}}(s) - \bar{p} \right]. \tag{F.26}$$

As in the ideal protocol (see Fig. 9.1b), we will assume that during the two isothermal transformations we respectively have $\epsilon(s) = \epsilon_{\mathrm{H}}$, $\lambda_{\mathrm{H}}(s) = 1$, $\lambda_{\mathrm{C}}(s) = 0$ and $\epsilon(s) = \epsilon_{\mathrm{C}}$, $\lambda_{\mathrm{H}}(s) = 0$, $\lambda_{\mathrm{C}}(s) = 1$. This means that we are coupled to one bath at a time. Instead, during the quenches we assume that all three control parameters ($\epsilon(s)$, $\lambda_{\mathrm{H}}(s)$ and $\lambda_{\mathrm{C}}(s)$) vary linearly in time between the corresponding extremal values. We thus divide the integral in Eq. (F.26) in the four different transformations:

$$P_{[\mathrm{E}]}(\tau) = \frac{\int_0^{\tau_{\mathrm{H}}}(\dots) + \int_{\tau_{\mathrm{H}}}^{\tau_{\mathrm{H}}+\tau}(\dots) + \int_{\tau_{\mathrm{H}}+\tau}^{\tau_{\mathrm{H}}+\tau_{\mathrm{C}}+\tau}(\dots) + \int_{\tau_{\mathrm{H}}+\tau_{\mathrm{C}}+\tau}^{\tau_{\mathrm{H}}+\tau_{\mathrm{C}}+2\tau}(\dots)}{dt + 2\tau} \equiv \frac{\mathcal{W}_{\mathrm{H}} + \mathcal{W}_{\mathrm{H}\to\mathrm{C}} + \mathcal{W}_{\mathrm{C}} + \mathcal{W}_{\mathrm{C}\to\mathrm{H}}}{dt + 2\tau}, \tag{F.27}$$

where $(\dots)$ stands for $ds\, \epsilon(s)\Gamma(s) \left[p_{\mathrm{eq}}(s) - \bar{p} \right]$. In the regime we consider the power, up to leading order corrections in τ/dt, can be written as

$$P_{[\mathrm{E}]}(\tau) = \frac{\mathcal{W}_{\mathrm{H}} + \mathcal{W}_{\mathrm{C}}}{dt} \left(1 - \frac{2\tau}{dt} \right) + \frac{\mathcal{W}_{\mathrm{H}\to\mathrm{C}} + \mathcal{W}_{\mathrm{C}\to\mathrm{H}}}{dt}, \tag{F.28}$$

where the first addend is obtained by means of a first order expansion in τ/dt of the denominator in the r.h.s. of Eq. (F.27).

We wish to compare Eq. (F.28) to the power $P_{[\mathrm{E}]}^{(\max)}$ achieved in the ideal protocol, so we will estimate the four terms $\mathcal{W}_{\mathrm{H}}$, $\mathcal{W}_{\mathrm{C}}$, $\mathcal{W}_{\mathrm{H}\to\mathrm{C}}$ and $\mathcal{W}_{\mathrm{C}\to\mathrm{H}}$. First, we notice that $\bar{p}$ depends on the whole protocol, see Eq. (F.24). We can thus write

$$\bar{p} = \bar{p}^{(0)} + \delta\bar{p}^{(1)}, \tag{F.29}$$

where $\bar{p}^{(0)}$ is the value of $\bar{p}$ in the ideal protocol, and $\delta\bar{p}^{(1)}$ the corrections due to the finite-time quenches. These two terms can be calculated simply by dividing the integrals in the definition of $\bar{p}$ as we did for $P_{[\mathrm{E}]}(\tau)$. It is easy to see that $\delta\bar{p}^{(1)}$ is of the order τ/dt. Since $\mathcal{W}_{\mathrm{H}}$ and $\mathcal{W}_{\mathrm{C}}$ are linear functions of $\bar{p}$, and $\bar{p} = \bar{p}^{(0)} + \delta\bar{p}^{(1)}$, we have that, for $\alpha = \mathrm{H}, \mathrm{C}$,

$$\mathcal{W}_\alpha = \tau_\alpha \epsilon_\alpha \Gamma_\alpha(\epsilon_\alpha) \left[p_{\mathrm{eq}}^{(\alpha)}(\epsilon_\alpha) - \bar{p} \right] = \mathcal{W}_\alpha^{(0)} + \mathcal{W}_\alpha^{(1)}, \tag{F.30}$$

where $\mathcal{W}_\alpha^{(0)}$ is the work extracted in the ideal protocol during the isothermal transformation, while $\mathcal{W}_\alpha^{(1)}$ represents the corrections due to the variation in population $\bar{p}$ induced by the finite-time quenches. We have that

$$\mathcal{W}_\alpha^{(1)} = -\tau_\alpha \epsilon_\alpha \Gamma_\alpha(\epsilon_\alpha) \delta\bar{p}^{(1)} \propto \epsilon_\alpha O(\gamma\tau), \tag{F.31}$$

where the last term means that $\mathcal{W}_\alpha^{(1)}$ is of the order $\gamma\tau$.

Next, we need to estimate $\mathcal{W}_{\mathrm{H}\to\mathrm{C}}$ and $\mathcal{W}_{\mathrm{C}\to\mathrm{H}}$. By inspecting the definition, we see that

$$\mathcal{W}_{\mathrm{H}\to\mathrm{C}} = \mathcal{W}_{\mathrm{C}\to\mathrm{H}} \propto \langle\epsilon\rangle\, O(\gamma\tau), \tag{F.32}$$

where $\langle\epsilon\rangle$ is a characteristic value of the energy gap during the quench.

Now we can return to Eq. (F.28). Using Eqs. (F.30), (F.31) and (F.32), and noticing that the order of magnitude of $\gamma\,\langle\epsilon\rangle$ is the same as $P_{[\mathrm{E}]}^{(\max)}$, we find that all the corrections previously discussed are of the order γ/dt. We thus conclude that

$$P_{[\mathrm{E}]}(\tau) = P_{[\mathrm{E}]}^{(\max)} \left[1 - O(\tau/dt)\right], \tag{F.33}$$

where the corrections must be negative by virtue of the theorem proved in App. F.1. The impact of finite time quenches is thus first order τ/dt.

F.3 Efficiency at maximum power

For small temperature differences, i.e. for small values of η_{c}, we can consider an expansion of the efficiency at maximum power of the kind

$$\eta(P_{[\mathrm{E}]}) = a_1\eta_{\mathrm{c}} + a_2\eta_{\mathrm{c}}^2 + \dots. \tag{F.34}$$

In this appendix we prove that $a_1 = 1/2$, while for symmetric or constant rates we further have $a_2 = 1/8$. The maximum power of a heat engine (without constraints on the control parameters) can be written as [see Eq. (9.8)]

$$P_{[\mathrm{E}]}^{(\max)} = \max_{(x_{\mathrm{H}}, x_{\mathrm{C}})} P_{[\mathrm{E}]}(x_{\mathrm{H}}, x_{\mathrm{C}}), \tag{F.35}$$

where

$$P_{[\mathrm{E}]}(x_{\mathrm{H}}, x_{\mathrm{C}}) := \frac{g(x_{\mathrm{H}}, x_{\mathrm{C}};\, \eta_{\mathrm{c}})}{\beta_{\mathrm{H}}} \left[x_{\mathrm{H}} - x_{\mathrm{C}}(1-\eta_{\mathrm{c}})\right] \left[f(x_{\mathrm{H}}) - f(x_{\mathrm{C}})\right], \tag{F.36}$$

$x_\alpha = \epsilon_\alpha \beta_\alpha$ (for $\alpha = \mathrm{H}, \mathrm{C}$), $f(x) := [1 + \exp\{(x)\}]^{-1}$ and, expressing the Γ_α as a function of the gap ϵ and of the inverse temperature β_α of lead α,

$$g(x_{\mathrm{H}}, x_{\mathrm{C}};\, \eta_{\mathrm{c}}) := \frac{\Gamma_{\mathrm{H}}(x_{\mathrm{H}}, \beta_{\mathrm{H}})\, \Gamma_{\mathrm{C}}(x_{\mathrm{C}}, \beta_{\mathrm{H}}/(1-\eta_{\mathrm{c}}))}{\left(\sqrt{\Gamma_{\mathrm{H}}(x_{\mathrm{H}}, \beta_{\mathrm{H}})} + \sqrt{\Gamma_{\mathrm{C}}(x_{\mathrm{C}}, \beta_{\mathrm{H}}/(1-\eta_{\mathrm{c}}))}\right)^2}. \tag{F.37}$$

In Eq. (F.37) we decide to express β_{C} as $\beta_{\mathrm{H}}/(1-\eta_{\mathrm{c}})$ because we are interested in performing an expansion in η_{c} around a single inverse temperature β_{H}. Let x^*_{H} and x^*_{C} be respectively the values of x_{H} and x_{C} that maximize $P_{[\mathrm{E}]}(x_{\mathrm{H}}, x_{\mathrm{C}})$. By inspecting Eqs. (F.36) and (F.37), we see that x^*_α is a function of η_{c} (and of β_{H} through g), so we can express x^*_α as a power series in η_{c}:

$$\begin{aligned} x^*_{\mathrm{H}} &= m_0 + m_1\eta_{\mathrm{c}} + m_2\eta_{\mathrm{c}}^2 + \dots, \\ x^*_{\mathrm{C}} &= m_0 + n_1\eta_{\mathrm{c}} + n_2\eta_{\mathrm{c}}^2 + \dots. \end{aligned} \tag{F.38}$$

Both x^*_{H} and x^*_{C} have the same leading order term. This can be seen considering Eq. (F.36) at $\eta_{\mathrm{c}} = 0$: $g(x_{\mathrm{H}}, x_{\mathrm{C}};\, 0)/\beta_{\mathrm{H}} \geq 0$, while $[x_{\mathrm{H}} - x_{\mathrm{C}}]\,[f(x_{\mathrm{H}}) - f(x_{\mathrm{C}})] \leq 0$, so the maximum power is zero (at equal temperatures, the second law forbids the possibility of extracting work). Inspecting Eq. (F.36), it is easy to see that zero power at $\eta_{\mathrm{c}} = 0$ implies $x_{\mathrm{H}} = x_{\mathrm{C}}$. Using Eq. (9.10), we have that

$$\eta(P^{(\max)}_{[\mathrm{E}]}) = 1 - \frac{x^*_{\mathrm{C}}}{x^*_{\mathrm{H}}}\,(1-\eta_{\mathrm{c}}), \tag{F.39}$$

so plugging Eq. (F.38) into Eq. (F.39) and expressing $\eta(P^{(\max)}_{[\mathrm{E}]})$ as a power series in η_{c}, we find that

$$\eta(P^{(\max)}_{[\mathrm{E}]}) = (1+b_1)\eta_{\mathrm{c}} + \frac{1}{2}(1+b_2)\eta_{\mathrm{c}}^2, \tag{F.40}$$

where

$$b_1 = \frac{m_1 - n_1}{m_0}, \qquad b_2 = \frac{m_1}{m_0} + 2\frac{m_2 - n_2}{m_0}.$$

Thus, the knowledge of b_1 and b_2 implies also the knowledge of a_1 and a_2. Also the maximum power $P_{[\mathrm{E}]}(x^*_{\mathrm{H}}, x^*_{\mathrm{C}})$ can be written as a power series in η_{c} by plugging the expansion Eq. (F.38) into Eq. (F.36). This yields

$$P_{[\mathrm{E}]}(x^*_{\mathrm{H}}, x^*_{\mathrm{C}}) = \frac{1}{\beta_{\mathrm{H}}} \sum_{n=0}^{+\infty} P^{(n)}_{[\mathrm{E}]}\, \eta_{\mathrm{c}}^n, \tag{F.41}$$

where the coefficients $P^{(n)}_{[\mathrm{E}]}$ are functions of m_i, n_i (for $i = 0, 1, 2, \dots$) and of β_{H}. We now wish to determine b_1 and b_2 by maximizing $P^{(n)}_{[\mathrm{E}]}$, starting from the lowest orders. We find that $P^{(0)}_{[\mathrm{E}]} = P^{(1)}_{[\mathrm{E}]} = 0$ and

$$P^{(2)}_{[\mathrm{E}]} = \left[-\frac{b_1(1+b_1)}{2}\right] \frac{m_0^2\, g(m_0, m_0;\, 0)}{1 + \cosh m_0}, \tag{F.42}$$

where we expressed n_1 in terms of b_1. The last fraction in Eq. (F.42) is positive, so $P^{(2)}_{[\mathrm{E}]}$ is maximized by choosing b_1 that maximizes the term in square brackets, and m_0 that maximizes the last fraction. The maximization of the first term yields $b_1 = -1/2$, which readily implies [see Eq. (F.40)] $a_1 = 1/2$, as we wanted to prove. The maximization of the second term allows us to find the following implicit expression for m_0

$$g(m_0, m_0; 0)\left[2 - m_0 \tanh\left(\frac{m_0}{2}\right)\right] + m_0\left[\partial_{x_\mathrm{H}} g(m_0, m_0; 0) + \partial_{x_\mathrm{C}} g(m_0, m_0; 0)\right] = 0, \quad \text{(F.43)}$$

where $\partial_{x_\alpha} g(m_0, m_0; 0)$ denotes the partial derivative of $g(x_\mathrm{H}, x_\mathrm{C}; \eta_\mathrm{c})$, respect to x_α, calculated in $x_\mathrm{H} = x_\mathrm{C} = m_0$ and $\eta_\mathrm{c} = 0$. In order to compute b_2, we must maximize also higher order terms of the power. It turns out that $P^{(3)}_{[\mathrm{E}]}$ only depends on m_0 if we impose that $b_1 = -1/2$ and that m_0 satisfies Eq. (F.43). Thus, there is nothing to optimize, so we must analyze the next order. $P^{(4)}_{[\mathrm{E}]}$ is a function of m_0, m_1, n_1, m_2, n_2 and β_C. We write m_1 in terms of b_2, which is the only coefficient that determines a_2. We further express n_1 in terms of b_1, and impose $b_1 = -1/2$. At last, we write $g(m_0, m_0; 0)$ in terms of its partial derivatives using Eq. (F.43). This leads to an expression of $P^{(4)}_{[\mathrm{E}]}$ as a function of m_0 (which is implicitly known), b_2, m_2, n_2 and β_H. We maximize $P^{(4)}_{[\mathrm{E}]}$ by setting to zero both partial derivatives of $P^{(4)}_{[\mathrm{E}]}$ respect to b_2 and m_2. We thus find the following expression for b_2:

$$b_2 = \frac{m_0 \tanh\left(\frac{m_0}{2}\right)}{8} \cdot \frac{\partial_{x_\mathrm{H}} g - \partial_{x_\mathrm{C}} g}{\partial_{x_\mathrm{H}} g + \partial_{x_\mathrm{C}} g} - \frac{2\partial_{x_\mathrm{H}} g + \partial_{x_\mathrm{C}} g}{2\left(\partial_{x_\mathrm{H}} g + \partial_{x_\mathrm{C}} g\right)}, \quad \text{(F.44)}$$

where all partial derivatives of g are computed in $x_\mathrm{H} = x_\mathrm{C} = m_0$ and $\eta_\mathrm{c} = 0$. This is, in principle, a closed expression for b_2, thus for a_2, since m_0 is defined in Eq. (F.43), and Eq. (F.44) only depends on m_0. Eq. (F.44) shows that in general b_2, thus a_2, will depend on the specific rates. However, if $\partial_{x_\mathrm{H}} g = \partial_{x_\mathrm{C}} g$, the first term in Eq. (F.44) vanishes, while the second one reduces to a number, yielding $b_2 = -3/4$. Indeed, plugging this value of b_2 into Eq. (F.40) yields precisely $a_2 = 1/8$. We conclude the proof by noticing that if the rates are symmetric, i.e. $\Gamma_\mathrm{H}(\epsilon, \beta) = \Gamma_\mathrm{C}(\epsilon, \beta)$, $g(x_\mathrm{H}, x_\mathrm{C}; 0)$ is a symmetric function upon exchange of x_H and x_C. This implies that $\partial_{x_\mathrm{H}} g(m_0, m_0; 0) = \partial_{x_\mathrm{C}} g(m_0, m_0; 0)$, so $a_2 = 1/8$. At last, if the rates are constants, also $g(x_\mathrm{H}, x_\mathrm{C}; \eta_\mathrm{c})$ is constant, trivially satisfying $\partial_{x_\mathrm{H}} g = \partial_{x_\mathrm{C}} g = 0$.

F.4 COP at maximum power

In this appendix we prove Eqs. (9.12) and (9.13) and we derive the scaling of the COP at maximum power for large values of the maximum gap Δ given by $\mathrm{C}(P^{\max}_{[\mathrm{R}]}) \propto 1/(\beta_\mathrm{C}\Delta)$. The COP at maximum power can be written as [see Eq. (9.11)]

$$\mathrm{C}(P^{\max}_{[\mathrm{R}]}) = \frac{\epsilon^*_\mathrm{C}}{\epsilon^*_\mathrm{H} - \epsilon^*_\mathrm{C}}, \quad \text{(F.45)}$$

where ϵ^*_H and ϵ^*_C are respectively the values of ϵ_H and ϵ_C that maximize [see Eq. (9.8)]

$$P_{[\mathrm{R}]}(\epsilon_\mathrm{H}, \epsilon_\mathrm{C}) := -g(\epsilon_\mathrm{H}, \epsilon_\mathrm{C})\epsilon_\mathrm{C}\left[f(\beta_\mathrm{H}\epsilon_\mathrm{H}) - f(\beta_\mathrm{C}\epsilon_\mathrm{C})\right], \quad \text{(F.46)}$$

where $f(x) := [1 + \exp\{(x)\}]^{-1}$ and

$$g(\epsilon_\mathrm{H}, \epsilon_\mathrm{C}) := \frac{\Gamma_\mathrm{H}(\epsilon_\mathrm{H})\Gamma_\mathrm{C}(\epsilon_\mathrm{C})}{\left(\sqrt{\Gamma_\mathrm{H}(\epsilon_\mathrm{H})} + \sqrt{\Gamma_\mathrm{C}(\epsilon_\mathrm{C})}\right)^2}. \quad \text{(F.47)}$$

We first prove that the COP at maximum power takes the universal form of Eq. (9.12) if the rates depend on the energy and on the temperature only through $\beta\epsilon$, i.e. $\Gamma_\alpha(\epsilon) = \Gamma_\alpha(\beta_\alpha\epsilon_\alpha)$. We rewrite Eq. (F.45) as a function of $x^*_\alpha = \beta_\alpha\epsilon^*_\alpha$ (for $\alpha = \mathrm{H}, \mathrm{C}$):

$$\mathrm{C}(P^{\max}_{[\mathrm{R}]}) = \left[\frac{x^*_\mathrm{H}}{x^*_\mathrm{C}}\left(\frac{1}{\mathrm{C_c}}+1\right)-1\right]^{-1}, \tag{F.48}$$

where $\mathrm{C_c}$ is the Carnot COP for a refrigerator. We can determine x^*_α by maximizing

$$P_{[\mathrm{R}]}(x_\mathrm{H}, x_\mathrm{C}) := -\frac{1}{\beta_\mathrm{C}}\frac{\Gamma_\mathrm{H}(x_\mathrm{H})\Gamma_\mathrm{C}(x_\mathrm{C})}{\left(\sqrt{\Gamma_\mathrm{H}(x_\mathrm{H})}+\sqrt{\Gamma_\mathrm{C}(x_\mathrm{C})}\right)^2} x_\mathrm{C}\left[f(x_\mathrm{H})-f(x_\mathrm{C})\right]. \tag{F.49}$$

Crucially, given our hypothesis on the rates, there is no explicit dependence on the temperatures in Eq. (F.49) (except for the prefactor $1/\beta_\mathrm{C}$), so the maximization of $P_{[\mathrm{R}]}(x_\mathrm{H}, x_\mathrm{C})$ will simply yield two values of x^*_H and x^*_C that do not depend on the temperatures. Thus, for all bath temperatures the COP at maximum power will be given by Eq. (F.48), where x^*_H and x^*_C are two fixed values. The ratio $x^*_\mathrm{H}/x^*_\mathrm{C}$ will depend on the specific rates we consider. By imposing in Eq. (F.48) that the COP at maximum power of the system for $\beta_\mathrm{H} = \beta_\mathrm{C}$ (i.e. for $\mathrm{C_c} \to \infty$) is C_0, we can eliminate the ratio $x^*_\mathrm{H}/x^*_\mathrm{C}$ in favor of C_0, concluding the proof of Eq. (9.12).

We now prove Eq. (9.13). Since Eq. (F.46) remains unchanged by sending both $\epsilon_\mathrm{H} \to -\epsilon_\mathrm{H}$ and $\epsilon_\mathrm{C} \to -\epsilon_\mathrm{C}$, we can assume without loss of generality that $\epsilon_\mathrm{C} \geq 0$ (this is a general property which applies independently of the specific choice of bath models). Furthermore, we must ensure that the system is acting as a refrigerator by imposing $P_{[\mathrm{R}]}(\epsilon_\mathrm{H}, \epsilon_\mathrm{C}) \geq 0$. This implies that $f(\beta_\mathrm{H}\epsilon_\mathrm{H}) \leq f(\beta_\mathrm{C}\epsilon_\mathrm{C})$, thus

$$0 \leq \beta_\mathrm{C}\epsilon_\mathrm{C} \leq \beta_\mathrm{H}\epsilon_\mathrm{H}. \tag{F.50}$$

We now show that in the models described by Eq. (9.9), the partial derivative of $P_{[\mathrm{R}]}(\epsilon_\mathrm{H}, \epsilon_\mathrm{C})$ respect to ϵ_H is non negative for all values of ϵ_H and ϵ_C satisfying Eq. (F.50), which implies that $\epsilon^*_\mathrm{H} \to +\infty$. Using Eq. (F.50), the condition $\partial P_{[\mathrm{R}]}(\epsilon_\mathrm{H}, \epsilon_\mathrm{C})/\partial\epsilon_\mathrm{H} \geq 0$ can be written as

$$\frac{\partial}{\partial\epsilon_\mathrm{H}} \ln g(\epsilon_\mathrm{H}, \epsilon_\mathrm{C}) \geq -\frac{\beta_\mathrm{H}}{2\left[1+\cosh\left(\beta_\mathrm{H}\epsilon_\mathrm{H}\right)\right]}. \tag{F.51}$$

Since $\partial \ln g(\epsilon_\mathrm{H}, \epsilon_\mathrm{C})/\partial\epsilon_\mathrm{H}$ has the same sign as $d\Gamma_\mathrm{H}(\epsilon_\mathrm{H})/d\epsilon_\mathrm{H}$, and since the r.h.s. of Eq. (F.51) is strictly negative, Eq. (F.51) is certainly satisfied whenever $\Gamma_\mathrm{H}(\epsilon_\mathrm{H})$ is a growing function. This proves that $\epsilon^*_\mathrm{H} \to +\infty$ when the baths are described by the F_n model [see Eq. (9.9)] even when the two baths have different powers n. The B_n model is more tricky to analyze since the rates are decreasing functions around the origin. Nonetheless, using Eq. (F.50) it is possible to show that Eq. (F.51) is satisfied also in the B_n model by plugging $\Gamma^{(\mathrm{B}_n)}_\alpha(\epsilon)$ [see Eq. (9.9)] into Eq. (F.51). This result holds also when the two baths have different powers n.

We now know that $\epsilon^*_\mathrm{H} \to +\infty$ in the F_n and B_n models. Since both $\Gamma^{(\mathrm{F}_n)}_\mathrm{H}(\epsilon)$ and $\Gamma^{(\mathrm{B}_n)}_\mathrm{H}(\epsilon)$ diverge for $n > 0$ when $\epsilon^*_\mathrm{H} \to +\infty$, we have that

$$g(+\infty, \epsilon_\mathrm{C}) = \Gamma_\mathrm{C}(\epsilon_\mathrm{C}) = k_\mathrm{C}\,\epsilon^n_\mathrm{C}\,h(\beta_\mathrm{C}\epsilon_\mathrm{C}) = k_\mathrm{C}\,\frac{x^n_\mathrm{C}}{\beta^n_\mathrm{C}}\,h(x_\mathrm{C}), \tag{F.52}$$

where, as before, $x_\mathrm{C} = \beta_\mathrm{C}\epsilon_\mathrm{C}$ and $h(x) := 1$ for the F_n model and $h(x) := \coth x/2$ for the B_n model [see Eq. (9.9)]. Thus, using x_C instead of ϵ_C, and noting that $f(\epsilon_\mathrm{H}\beta_\mathrm{H})$ vanishes for $\epsilon_\mathrm{H} \to +\infty$, we can write $P_{[\mathrm{R}]}(+\infty, \epsilon_\mathrm{C})$ [see Eq. (F.46)] as

$$P^{(n>0)}_{[\mathrm{R}]} = \frac{k_\mathrm{C}}{\beta^{n+1}_\mathrm{C}}\,x^{n+1}_\mathrm{C} h(x_\mathrm{C}) f(x_\mathrm{C}). \tag{F.53}$$

Equation (F.53) is non-negarive for all values of x_C and it vanishes in $x_C = 0$ and $x_C \to +\infty$ thanks to the exponential decrease of $f(x_C)$ for large values of x_C. Therefore, Eq. (F.53) will be maximum for the finite value x_C^* that maximizes $x_C^{n+1} h(x_C) f(x_C)$, and plugging x_C^* into Eq. (F.53) yields the first relation in Eq. (9.13), where $c_n = (x_C^*)^{n+1} h(x_C^*) f(x_C^*)$. For $n = 0$, we separately analyze the F_0 and B_0 models. In the F_0 model, $g(\epsilon_H, \epsilon_C) = k_H k_C/(\sqrt{k_H} + \sqrt{k_C})^2$, so $P_{[R]}(+\infty, \epsilon_C)$ can be written as

$$P_{[R]}^{(F_0)} = \frac{k_C}{\beta_C} \frac{r}{(\sqrt{r}+1)^2} x_C f(x_C), \tag{F.54}$$

where $r := k_H/k_C$. Using the same argument as before, Eq. (F.54) implies a finite value of x_C^* which arises from the maximization of $x_C f(x_C)$. We thus proved the first relation in Eq. (9.13) for the F_0 model, where $c_0 = r/(\sqrt{r}+1)^2 x_C^* f(x_C^*)$. At last, in the B_0 model $g(\epsilon_H \to +\infty, \epsilon_C) = k_H k_C \coth(x_C/2)/[\sqrt{k_H} + \sqrt{k_C \coth(x_C/2)}]^2$. Thus, $P_{[R]}(+\infty, \epsilon_C)$ can be written as

$$P_{[R]}^{(B_0)} = \frac{k_C}{\beta_C} \frac{r \coth(x_C/2)}{(\sqrt{r} + \sqrt{\coth(x_C/2)})^2} x_C f(x_C). \tag{F.55}$$

Again, x_C^* is a finite value which can be found by maximizing $r \coth(x_C/2)/(\sqrt{r} + \sqrt{\coth(x_C/2)})^2 x_C f(x_C)$. Only in this case, x_C^* depends on the ratio r. We thus proved the first relation in Eq. (9.13) for the B_0 model, where $c_0 = r \coth(x_C^*/2)/(\sqrt{r} + \sqrt{\coth(x_C^*/2)})^2 x_C^* f(x_C^*)$.

The second relation in Eq. (9.13) stems from the fact that in all models $\epsilon_H^* \to +\infty$ while ϵ_C^* is finite. Thus, Eq. (F.45) implies that the $C(P_{[R]}^{max})$ vanishes. At last we want to roughly estimate the behavior of $C(P_{[R]}^{max})$ in the presence of a large yet finite constraint on the maximum gap: $|\epsilon(t)| \leq \Delta$. Since ϵ_H would diverge if there was no constraint, we can assume that, in the presence of Δ, $\epsilon_H^* = \Delta$. On the other hand, ϵ_C^* is a finite quantity (which is given by $\epsilon_C^* = x_C^*/\beta_C$ in the unconstrained case), so if we assume that $\Delta \gg \epsilon_C^*$, from Eq. (F.45) we have that

$$C(P_{[R]}^{max}) \approx \frac{\epsilon_C^*}{\epsilon_H^*} \approx \frac{x_C^*}{\beta_C \Delta} \propto \frac{1}{\beta_C \Delta}. \tag{F.56}$$

G

Appendix: Maximum power heat engines and refrigerators in the fast-driving regime

In this appendix, we provide details on the calculations performed in Chap. 10.

G.1 Projected form of the ME

Using projection techniques in this section we show how one can cast the master equation (10.2) in the more convenient form (10.5). For this purpose we find it useful to first recall some structural properties of GKSL generators which hold true in the finite dimensional case we are analyzing in the present work. In particular in Secs. G.1.1 and G.1.2 we shall introduce the notions of ergodicity, mixing, irreducibility, and adjoint-stability. After that we proceed with the derivation of Eq. (10.5) in Sec. G.1.3.

G.1.1 Ergodic, Mixing, Irreducible and adjoint-stable GKSL generators

Let S be a quantum system of finite dimension d. To fix the notation we indicate with $\mathfrak{L}_{\rm S}$ the d^2-dimensional vector space of linear operators on S and define $\mathfrak{S}_{\rm S}$ and $\mathfrak{L}^0_{\rm S}$ its subsets formed respectively by the density and zero-trace operators of the model, i.e.

$$\mathfrak{S}_{\rm S} \equiv \{\rho \in \mathfrak{L}_{\rm S} | {\rm Tr}[\rho] = 1 \, , \rho \geq 0\} \ , \qquad \mathfrak{L}^0_{\rm S} \equiv \{\Theta \in \mathfrak{L}_{\rm S} | {\rm Tr}[\Theta] = 0\} \ . \tag{G.1}$$

The the latter forms a (d^2-1)-dimensional vector subspace of $\mathfrak{L}_{\rm S}$ for which we can identify a projector introducing the super-operator

$$\mathcal{Q}[\cdots] \ \equiv \ {\rm Id}[\cdots] - {\rm Tr}[\cdots]\frac{\mathbb{I}}{d} \, , \tag{G.2}$$

and its orthogonal complement $\mathcal{P} \equiv {\rm Id} - \mathcal{Q}$, Id being the identity channel (notice in fact that using "$\circ$" to represent the composition of super-operators we have $\mathcal{Q} \circ \mathcal{Q} = \mathcal{Q}$, $\mathcal{P} \circ \mathcal{P} = \mathcal{P}$, $\mathcal{P} \circ \mathcal{Q} = \mathcal{Q} \circ \mathcal{P} = 0$, and that ${\rm Tr}[\mathcal{Q}[\Theta]] = 0$ with $\mathcal{Q}[\Theta] = \Theta$ iff $\Theta \in \mathfrak{L}^0_{\rm S}$).

Consider next a GKSL generator $\mathcal{L}$ for a generic time-independent master equation

$$\partial_t \rho(t) = \mathcal{L}[\rho(t)] \, , \tag{G.3}$$

for the density matrices of S. By general properties of the theory we know that $\mathcal{L}$ is a super-operator on $\mathfrak{L}_{\rm S}$ which can always be casted in the standard form

$$\mathcal{L}[\cdots] = -i[H,\cdots] + \mathcal{D}[\cdots]\,, \tag{G.4}$$

$$\mathcal{D}[\cdots] = \sum_j \left(A_j[\cdots]A_j^\dagger - \frac{A_j^\dagger A_j[\cdots] + [\cdots]A_j^\dagger A_j}{2} \right), \tag{G.5}$$

where H is a hermitian operator identifying the Hamiltonian of the system, and $\mathcal{D}$ is a purely dissipator component written in terms of the (Lindblad) operators $A_j \neq 0$. It is also a well know fact that $\mathcal{L}$ transforms any $\Theta \in \mathfrak{L}_{\rm S}$ into an element of traceless subset $\mathfrak{L}_{\rm S}^0$ (i.e. $\mathrm{Tr}[\mathcal{L}[\Theta]] = 0$), which formally translates into the following identity

$$\mathcal{Q} \circ \mathcal{L} = \mathcal{L}\,, \tag{G.6}$$

and that it admits always at least a fix-point state $\rho^{(\rm eq)} \in \mathfrak{S}_{\rm S}$, i.e. a density matrix of S which is an eigen-operator of $\mathcal{L}$ associated with the eigenvalue zero,

$$\mathcal{L}[\rho^{(\rm eq)}] = 0\,. \tag{G.7}$$

Thanks to the above properties we can hence observe that for all density matrices ρ, we have

$$\mathcal{L}[\rho] = (\mathcal{Q}\circ\mathcal{L})[\rho] = (\mathcal{Q}\circ\mathcal{L})[\rho-\rho^{(\rm eq)}] = (\mathcal{Q}\circ\mathcal{L}\circ\mathcal{Q})[\rho-\rho^{(\rm eq)}] = (\mathcal{Q}\circ\mathcal{L}\circ\mathcal{Q})[\tilde{\rho}-\tilde{\rho}^{(\rm eq)}]\,, \tag{G.8}$$

where in the third passage we use the fact that $\rho-\rho^{(\rm eq)}$ has trace zero, while in the final one we adopt the short hand notation $\tilde{\Theta}$ to indicate the projected component of Θ on $\mathfrak{L}_{\rm S}^0$, i.e.

$$\tilde{\Theta} \equiv \mathcal{Q}[\Theta]\,. \tag{G.9}$$

Notice finally that from $\rho(t) = (\mathcal{Q}+\mathcal{P})[\rho(t)] = \tilde{\rho}(t) + \frac{\mathbb{I}}{d}$ follows that $\partial_t\rho(t) = \partial_t\tilde{\rho}(t)$. Thus using this and (G.8) evaluated for $\rho = \rho(t)$, we can hence conclude that an equivalent way to express Eq. (G.3) is

$$\partial_t\tilde{\rho}(t) = \mathcal{G}[\tilde{\rho}^{(\rm eq)} - \tilde{\rho}(t)]\,, \tag{G.10}$$

where

$$\mathcal{G} \equiv -\mathcal{Q}\circ\mathcal{L}\circ\mathcal{Q} = -\mathcal{L}\circ\mathcal{Q}\,, \tag{G.11}$$

is (minus) the restriction of $\mathcal{L}$ on $\mathfrak{L}_{\rm S}^0$.

Equation (G.10) is valid for all the finite-dimensional GKSL processes, but it becomes particularly handy when specified under ergodicity assumptions [373], i.e. for those $\mathcal{L}$ for which the fix-point state $\rho^{(\rm eq)}$ introduced in Eq. (G.7) constitute the unique eigenvectors with zero eigenvalue.

Definition: *The generator $\mathcal{L}$ is said to be* **ergodic** *if $\rho^{(\rm eq)} \in \mathfrak{S}_{\rm S}$ exists such that*

$$\mathcal{L}[\Theta] = 0 \quad\Longleftrightarrow\quad \Theta = \lambda\rho^{(\rm eq)}\,, \tag{G.12}$$

where λ is an arbitrary complex constant.

For our purposes, the main consequence of the above definition is that for an ergodic GKSL generator $\mathcal{L}$ the corresponding restriction $\mathcal{G}$ defined in Eq. (G.11) is invertible when acting on the elements of the (d^2-1)-dimensional linear subspace $\mathfrak{L}_{\rm S}^0$. Indeed using the fact that $\rho^{(\rm eq)}$ has trace 1, we can conclude that under ergodic assumption (G.12) it holds

$$\mathcal{G}[\Theta] = 0 \quad \Longleftrightarrow \quad \mathcal{Q}[\Theta] = 0 \,, \tag{G.13}$$

or equivalently that $\mathcal{G}$ has no zero eigenvalue on $\mathfrak{L}_{\rm S}^0$.

The ergodicity property (G.12) has been extensively studied in several works. In particular a necessary and sufficient condition for $\mathcal{L}$ to be ergodic can be found e.g. in Ref. [373] where it has been also shown that this property is very common on the set of the GKSL generators (the non-ergodic examples being indeed a set of zero measure). Interestingly enough it turns out that at least for the finite dimensional case we are studying here, Eq. (G.12) is equivalent to asking that the associated ME should induce a purely mixing evolution which asymptotically sends all input states $\rho \in \mathfrak{S}_{\rm S}$ of the system into $\rho^{(\rm eq)}$, i.e.

$$\lim_{t\to\infty} \|\rho(t) - \rho^{(\rm eq)}\|_1 = 0 \,, \tag{G.14}$$

where $\rho(t) = e^{t\mathcal{L}}[\rho]$ is the completely positive evolution obtained by integrating (G.3) and $\|\cdots\|_1$ is the trace norm (the fact that (G.14) implies (G.12) is relatively easy to verify, while an explicit proof of the opposite implication can be found in Refs. [374–377]). Given all that the main drawback of the ergodic property is that (G.12) does not well behave under summation of the GKSL generators, i.e. the sum of ergodic generators is not necessarily ergodic (see [373] for an explicit counterexample). Nonetheless, a slightly stronger version of the ergodicity notion does not suffer from this limitation. This is the set of GKSL generators $\mathcal{L}$ which are **irreducible** and **adjoint-stable** [29, 362]:

Definition: *Given a GKSL generator $\mathcal{L}$ and $\mathcal{A} \equiv \mathrm{Span}\{A_i\}$ the set spanned by its Lindblad operators, we say that $\mathcal{L}$* is **irreducible** if $[A, B] = 0$ for all $A \in \mathcal{A}$ implies that $B = \lambda\mathbb{1}$ for some complex number λ, and that $\mathcal{L}$ is **adjoint-stable** if $A \in \mathcal{A}$ implies $A^\dagger \in \mathcal{A}$.

First of all it is worth noticing that both these two properties only involve the dissipative component $\mathcal{D}$ of $\mathcal{L}$ (indeed they are independent of the system Hamiltonian H). Secondly, as discussed in Refs. [29, 362] it follows that all $\mathcal{L}$ which are **irreducible** and **adjoint-stable** induce dynamical evolutions which are mixing (i.e. obey to Eq. (G.14) with $\rho^{(\rm eq)}$ being identified with the steady state solution of the model) and hence, via the above mentioned equivalence, ergodic, i.e.

$$\mathcal{L} \textbf{ irreducible} \text{ and } \textbf{adjoint-stable} \Longrightarrow \mathcal{L} \textbf{ ergodic}. \tag{G.15}$$

Most importantly it also follows that, at variance with the ergodic set, the set of irreducible and adjoint-stable GKSL generators is closed under summation (in particular they form a convex set): more specifically given $\mathcal{L}$ irreducible and adjoint-stable, and $\mathcal{L}'$ adjoint-stable but not necessarily irreducible, their sum is irreducible and adjoint-stable, i.e.

$$\mathcal{L} \textbf{ irreducible} \text{ and } \textbf{adjoint-stable}, \mathcal{L}' \textbf{ adjoint-stable} \Longrightarrow \mathcal{L} + \mathcal{L}' \textbf{ irreducible} \text{ and } \textbf{adjoint-stable}. \tag{G.16}$$

We now focus on a special subset of ergodic GKSL generators $\mathcal{L}$ which provide a rather general description of thermalization events, see e.g. [27].

Definition: *Given $\beta \geq 0$, a generator GKSL $\mathcal{L}$ is said to be* **thermalizing** *if it is adjoint-stable and ergodic with fixed point provided by the Gibbs density matrix*

$$\rho_\beta^{(\mathrm{eq})} \equiv \exp[-\beta H]/Z_\beta \ , \qquad Z_\beta \equiv \mathrm{Tr}[\exp[-\beta H]] \ . \tag{G.17}$$

Notice that requiring adjoint-stability for a thermalizing map is in agreement with the underlying open system derivation of the master equation. Indeed, if this last is derived from a microscopic model in which the system is weakly coupled to a thermal bath of inverse temperature β, the adjoint stability of the GKSL generator can be proven using the Kubo-Martin-Schwinger relations for the bath correlation functions [27].

We now claim that a thermalizing generator satisfies also a weak notion of irreducibility. To begin we notice that in Eq. (G.17) the parameter β plays the role of an inverse temperature and that, for all finite values of such quantity, the density matrix $\rho_\beta^{(\mathrm{eq})}$ is a full rank state (for $\beta \to \infty$, i.e. as the temperature drops to zero, this property is not longer guaranteed as $\rho_\beta^{(\mathrm{eq})}$ converges to the ground state of H). Accordingly we can invoke Theorem 5.2 of [362] to claim that for thermalizing processes the linear set $\mathcal{A}_H \equiv \mathrm{Span}\{A_i, H\}$ spanned by the Lindblad operators A_i and by the Hamiltonian H is irreducible, i.e. that the following implication holds

$$[B, A] = 0 \qquad \forall A \in \mathcal{A}_H \ , \qquad \Longrightarrow B = \lambda \mathbb{1} \ , \tag{G.18}$$

with λ generic complex constant. We will refer to the condition (G.18) as to **weak irreducibility**, since it is less demanding than the standard irreducibility, that can be recovered with some assumptions on the nature of the Lindblad operators.

G.1.2 Irreducibility for physical GKSL generators

Within the assumption of a Thermalizing GKSL generator, let us suppose the Lindblad operators to be represented by jump operators, *i.e.* of the form $\sqrt{\gamma_{E_j \to E_i}} |E_i\rangle\langle E_j|$ where $|E_i\rangle$ denotes an eigenvector of the system Hamiltonian, whose levels are assumed to be non-degenerate.

In this case we have, for every operator $B = \sum_{i',j'} m_{i',j'} |E_{i'}\rangle\langle E_{j'}|$ with $0 \leq i', j' \leq D$:

$$[B, \sqrt{\gamma_{E_j \to E_i}} |E_i\rangle\langle E_j|] = \sqrt{\gamma_{E_j \to E_i}} \Big(\sum_{i',j'} m_{i',i} |E_{i'}\rangle\langle E_j| + m_{j,j'} |E_i\rangle\langle E_{j'}| \Big). \tag{G.19}$$

Using the equation above, we have

$$[B, \sqrt{\gamma_{E_j \to E_i}} |E_i\rangle\langle E_j|] = 0 \quad \leftrightarrow \quad m_{i,i} = m_{j,j}, \ \ m_{i',i} = m_{j,j'} = 0 \ \ \forall i' \neq i, \ j' \neq j. \tag{G.20}$$

Since the condition $[B, H] = 0$ does not constrain the diagonal of B, the only way to obtain $B = \lambda \mathbb{1}$ as required by Eq. (G.18) and fulfil weak irreducibility is that the set $\mathcal{A}_{\mathcal{H}}$ contains jumps connecting all the energy levels, *i.e.* for every i there is at least one Lindblad operator $\sqrt{\gamma_{E_i \to E_k}} |E_k\rangle\langle E_i|$ connecting $|E_i\rangle$ with some other level $|E_k\rangle$. In this way, the first of the two conditions in the r.h.s. of (G.20) imposes that all the diagonal elements of B are equal. In addition, using the second condition in the r.h.s. of (G.20) we can set all the off diagonal elements to 0 eventually obtaining $B = \lambda I$. Since the latter has been proven without imposing $[H, B] = 0$, we just proved that by choosing the jump operators as Lindblad operators we have that weak irriducibility implies **irreducibility**.

More in general, a Lindblad operator is the sum of jump operators connecting couples of levels with the same energy difference [27], $A(\omega) = \sum_{l,l'} f_{l,l'} |E_l\rangle\langle E_{l'}|$ where $E_l - E_{l'} = \omega \; \forall l, l'$.

We analyze the condition (G.20) in the case of a Lindblad operator composed by two jumps, that is

$$[B, f_{i_1,j_1}|E_{i_1}\rangle\langle E_{j_1}| + f_{i_2,j_2}|E_{i_2}\rangle\langle E_{j_2}|] = 0, \tag{G.21}$$

we obtain that this last is equivalent to require the r.h.s. of the (G.20) for both i_1, j_1 and i_2, j_2, with the exception that the four off diagonal elements m_{i_1,i_2}, m_{j_1,j_2}, m_{i_2,i_1}, m_{j_2,j_1} are not necessarily 0, but satisfy the following linear system

$$\begin{aligned} f_{i_2,j_2} m_{i_1,i_2} - f_{i_1,j_1} m_{j_1,j_2} &= 0, \\ f_{i_1,j_1} m_{i_2,i_1} - f_{i_2,j_2} m_{j_2,j_1} &= 0. \end{aligned} \tag{G.22}$$

Using the adjoint stability property, the (G.22) preserves its validity when replacing the elements of B with the ones of $B^\dagger$, thus

$$\begin{aligned} f^*_{i_2,j_2} m_{i_2,i_1} - f^*_{i_1,j_1} m_{j_2,j_1} &= 0, \\ f^*_{i_1,j_1} m_{i_1,i_2} - f^*_{i_2,j_2} m_{j_1,j_2} &= 0. \end{aligned} \tag{G.23}$$

The solution of Eqs. (G.22) and (G.23) is the null vector provided that $|f_{i_2,j_2}|^2 \neq |f_{i_1,j_1}|^2$. In this last case, the conditions imposed on B by requiring Eq. (G.21) to be valid are equivalent to the ones obtained for two distinct jump operators. So we can reproduce the reasoning done at the beginning of this section and state that **weak irreducibility** implies **irreducibility** also in the case of Lindblad operators composed by two jumps between energy eigenstates, apart from cases in which particular criteria for the values of the couplings $f_{l,l'}$ are met. The calculations for the case in which some of the Lindblad operators are the linear combination of more than two jumps allows to derive conditions on the $f_{l,l'}$ linking the matrix elements of B associated to transitions between the levels connected by the jumps, similarly to what observed in the two jumps case. To summarize, when the master equation is an effective description of the dynamics induced by the weak coupling of the system with a thermal bath, the generator belongs to the adjoint-stable subset of the ergodic maps and tipically satisfies irreducibility. Hence not only the associated restrictions $\mathcal{G}$ (G.11) of a thermalizing generator is invertible on $\mathfrak{L}^0_S$, but thanks to Eq. (G.16) this property is also shared by all the sums of an arbitrary collection of thermalizing generators.

G.1.3 Derivation of Eqs. (10.5)

Equipped with the results derived in the previous subsection it is now easy to explicitly show how to reformulate the master equation (10.2) in the form (10.5) with the super-operator $\mathcal{G}_{\vec{u}(t)}$ being invertible on their domain of definition.

As anticipated in the main text, we can obtain this by imposing that for all choices of the control vectors $\vec{u} \in \mathbb{D}$ for which $\mathcal{D}_{\alpha,\vec{u}}$ is not explicitly null, we ask those super-operators to be thermalizing with fixed point provided by

$$\rho^{(\mathrm{eq})}_{\alpha;\vec{u}} \equiv \exp\Big[-\beta_\alpha H_{\vec{u}(t)}\Big]/Z_{\alpha;\vec{u}} \; , \qquad Z_{\alpha;\vec{u}} \equiv \mathrm{Tr}[\exp[-\beta_\alpha H_{\vec{u}}]] \; . \tag{G.24}$$

From the physical point of view this is a rather natural requirement to ask: it simply tell us that, by putting S in contact with bath α, the model will reach the steady state configuration defined by the corresponding thermal state $\rho^{(\mathrm{eq})}_{\alpha;\vec{u}}$. As discussed in the previous section, in

this setting it is natural to consider the dissipator $\mathcal{D}_{\alpha,\vec{u}}$ to be adjoint stable and irreducible. From (G.16) it follows that for all assigned $\vec{u}(t)$, also the super-operator $\mathcal{L}_{\vec{u}(t)}$ is irreducible and adjoint-stable, due to the fact that according to Eq. (10.2) it is given by the sum of the $\mathcal{D}_{\alpha,\vec{u}(t)}$'s plus an irrelevant Hamiltonian contribution which plays no role in deciding these properties, i.e.

$$\mathcal{L}_{\vec{u}(t)} = \mathcal{H}_{\vec{u}(t)} + \sum_{\alpha=1}^{N} \mathcal{D}_{\alpha,\vec{u}(t)} \,, \tag{G.25}$$

where we used $\mathcal{H}_{\vec{u}(t)}$ to identify the commutator with $H_{\vec{u}(t)}$, i.e. $\mathcal{H}_{\vec{u}(t)}[\cdots] \equiv -i[H_{\vec{u}(t)}, \cdots]$. Therefore, introducing $\rho^{(\mathrm{eq})}_{\vec{u}(t)}$ as the unique fixed point of $\mathcal{L}_{\vec{u}(t)}$ and invoking (G.8), we can again write

$$\mathcal{L}_{\vec{u}(t)}[\rho] = \mathcal{G}_{\vec{u}(t)}[\tilde{\rho} - \tilde{\rho}^{(eq)}_{\vec{u}(t)}] \,, \tag{G.26}$$

for all ρ, with

$$\mathcal{G}_{\vec{u}(t)} \equiv -\mathcal{Q} \circ \mathcal{L}_{\vec{u}(t)} \circ \mathcal{Q} = -\mathcal{L}_{\vec{u}(t)} \circ \mathcal{Q} \,, \tag{G.27}$$

which is also invertible on the traceless operator set $\mathfrak{L}^0_{\mathrm{S}}$. Specified in the case where ρ is the evolved density matrix of S at time t during its interaction with the baths of the model, and using the property $\partial_t \rho(t) = \partial_t \tilde{\rho}(t)$, we finally end up to rewrite (10.2) in the form (10.5).

G.2 Asymptotic solutions of the fast periodically driven ME

Here we discuss the asymptotic solutions of the system ME. We start in Sec. G.2.1 formally introducing the notion of limit cycle solutions, valid for arbitrary driving speed. Then in Sec. G.2.2 we give a formal derivation of Eq. (10.9) of the main text, valid in the fast-driving regime. Finally in Sec. G.2.3 we show that any sub-protocol extract from a fast cyclic control also fulfil the fast limit condition.

G.2.1 Periodic driving

Consider the case where the control vector $\vec{u}(t)$ of our model, and hence the generator $\mathcal{L}_{\vec{u}(t)}$ of Eq. (10.2), is periodic with period T, i.e. $\vec{u}(t+T) = \vec{u}(t)$, for all t. We have already commented in Appendix G.1, that requiring the $\mathcal{D}_{\alpha,\vec{u}(t)}$s to be irreducible and adjoint stable, ensures that $\mathcal{L}_{\vec{u}(t)}$ is irreducible and adjoint-stable. Invoking Theorem 2 of Ref. [29] we can thus claim that our ME admits a limit cycle solution $\rho^{(\mathrm{lc})}_{\vec{u}(t)} = \rho^{(\mathrm{lc})}_{\vec{u}(t+T)} \in \mathfrak{S}_S$ that is independent from the initial conditions of S, and such that

$$\lim_{t\to\infty} (\rho(t) - \rho^{(\mathrm{lc})}_{\vec{u}(t)}) = 0 \,, \tag{G.28}$$

the convergency being evaluated e.g. in the trace norm.

G.2.2 Fast driving limit

In the fast cyclic driving limit we assume that the period T of the cyclic driving $\vec{u}(t)$ is the shortest timescale appearing in the master equation. In this scenario we want to show that, up linear correction in T, we can approximate the limit cycle solution $\rho^{(\mathrm{lc})}_{\vec{u}(t)}$ with a term which is constant in time.

To begin with, let us observe that according to Eq. (10.5), we can identify the times scale of the system dynamics associated with the driving of the model by using the quantity

$$\eta_{[\vec{u}]} \equiv \max_{t\in I_{[\vec{u}]}} \|\mathcal{G}_{\vec{u}(t)}\| \,, \tag{G.29}$$

where the maximum is taken on period and where $\|\cdots\|$ is the induced trace-norm for super-operators [378], i.e.

$$\|\mathcal{G}_{\vec{u}(t)}\| \equiv \max_{\Theta\in\mathfrak{L}_S} \frac{\|\mathcal{G}_{\vec{u}(t)}[\Theta]\|_1}{\|\Theta\|_1} \,, \tag{G.30}$$

with $\|\Theta\|_1 \equiv \sqrt{\mathrm{Tr}[\Theta^\dagger\Theta]}$. Since the system is finite dimensional, any other choice will be fine as well, the above choice however allows for some simplification. In particular, by direct integration of Eq. (10.5) on a generic interval $[t_1, t_2]$ we can write

$$\begin{aligned}\|\rho(t_2)-\rho(t_1)\|_1 = \|\int_{t_1}^{t_2} dt' \mathcal{G}_{\vec{u}(t')}\left[\tilde{\rho}^{(\mathrm{eq})}_{\vec{u}(t')} - \tilde{\rho}(t')\right]\|_1 \leq \int_{t_1}^{t_2} dt' \|\mathcal{G}_{\vec{u}(t')}\| \|\tilde{\rho}^{(\mathrm{eq})}_{\vec{u}(t')} - \tilde{\rho}(t')\|_1 \\ \leq (t_2-t_1)\,\eta_{[\vec{u}]} \,,\end{aligned} \tag{G.31}$$

which explicitly shows that the speed of variation of the density matrix of S along the trajectory induced by control $\vec{u}(t)$ is explicitly upper bounded by $\eta_{[\vec{u}]}$. Accordingly we now formally identifies the fast-driving regime by restricting the analysis to those protocols which fulfil the constraint

$$\eta_{[\vec{u}]} T \ll 1 \,. \tag{G.32}$$

Next we prove that, in the cyclic and fast driving regime, $\rho^{(\mathrm{lc})}_{[\vec{u}]}(t)$ is approximately given by $\rho^{(0)}_{[\vec{u}]}$. Accordingly, we can use Eq. (G.31) to claim that the distance between $\rho^{(\mathrm{lc})}_{[\vec{u}]}(t)$ and $\rho^{(\mathrm{lc})}_{[\vec{u}]}(t^*)$ is upper bounded by $|t-t^*|\,\eta_{[\vec{u}]}$. Taking a fixed value of t^* and an arbitrary time $t \in [t^*, t^*+T]$ we have that

$$\|\rho^{(\mathrm{lc})}_{[\vec{u}]}(t) - \rho^{(\mathrm{lc})}_{[\vec{u}]}(t^*)\|_1 \leq \eta_{[\vec{u}]} T \,. \tag{G.33}$$

Therefore, invoking the fast driving condition in Eq. (G.32), we find that at zeroth order in $\eta_{[\vec{u}]}T$, all values of $\rho^{(\mathrm{lc})}_{[\vec{u}]}(t)$ are given by the same fixed state, which we denote with $\rho^{(0)}_{[\vec{u}]}$. We now want to show that, up to first order corrections in $\eta_{[\vec{u}]}T$, the constant term $\rho^{(0)}_{[\vec{u}]}$ is given by Eq. (10.9) of the main text. For this purpose let notice that since $\mathcal{L}_{[\vec{u}]} \equiv \int_{I_{[\vec{u}]}} \mathcal{L}_{\vec{u}(t)} dt$ is a positive sum of $\mathcal{L}_{\vec{u}(t)}$ which in our construction are irreducible and adjoint-stable, from (G.16) we can also claim that such superar-operator fulfils the same property. Accordingly

$$\mathcal{G}_{[\vec{u}]} \equiv -\mathcal{Q}\circ\mathcal{L}_{[\vec{u}]}\circ\mathcal{Q} = -\mathcal{Q}\circ\int_{I_{[\vec{u}]}} \mathcal{L}_{\vec{u}(t)}dt \circ \mathcal{Q} = \int_{I_{[\vec{u}]}} \mathcal{G}_{\vec{u}(t)}dt \,, \tag{G.34}$$

must be invertible on $\mathfrak{L}^0_S$. Integrating hence (10.5) over the interval $I_{[\vec{u}]}$ and considering the limiting cycle solution $\rho^{(\mathrm{lc})}(t)$, we get

$$\int_{I_{[\vec{u}]}} \mathcal{G}_{\vec{u}(t)}\left[\tilde{\rho}^{(\mathrm{eq})}_{\vec{u}(t)} - \tilde{\rho}^{(\mathrm{lc})}_{[\vec{u}]}(t)\right] dt = \int_{I_{[\vec{u}]}} \partial_t \tilde{\rho}^{(\mathrm{lc})}_{[\vec{u}]}(t) dt = \tilde{\rho}^{(\mathrm{lc})}_{\vec{u}(T)} - \tilde{\rho}^{(\mathrm{lc})}_{\vec{u}(0)} = 0 \,, \tag{G.35}$$

where the last identity follows from the periodicity of $\rho^{(\mathrm{lc})}_{\vec{u}(t)}$. We therefore have that

$$\int_{I_{[\vec{u}]}} \mathcal{G}_{\vec{u}(t)} \left[\tilde{\rho}^{(\mathrm{lc})}_{[\vec{u}]}(t)\right] dt = \int_{I_{[\vec{u}]}} \mathcal{G}_{\vec{u}(t)} \left[\tilde{\rho}^{(\mathrm{eq})}_{\vec{u}(t)}\right] dt \,. \tag{G.36}$$

In the fast driving limit (G.32), the left-hand-side of the above expression can be approximated as $\mathcal{G}_{[\vec{u}]}[\tilde{\rho}^{(0)}_{[\vec{u}]}]$ up to linear correction in $\eta_{[\vec{u}]}T$. Accordingly in this regime (G.36) allows us to finally write

$$\mathcal{G}_{[\vec{u}]}\left[\tilde{\rho}^{(0)}_{[\vec{u}]}\right] \simeq \int_{I_{[\vec{u}]}} \mathcal{G}_{\vec{u}(t)} \left[\tilde{\rho}^{(\mathrm{eq})}_{\vec{u}(t)}\right] dt \qquad \Longrightarrow \qquad \tilde{\rho}^{(0)}_{[\vec{u}]} \simeq \mathcal{G}^{-1}_{[\vec{u}]} \left[\int_{I_{[\vec{u}]}} \mathcal{G}_{\vec{u}(t)} \left[\tilde{\rho}^{(\mathrm{eq})}_{\vec{u}(t)}\right] dt\right] , \tag{G.37}$$

where we used the above-mentioned invertibility of $\mathcal{G}_{[\vec{u}]}$. This expression, valid at leading order in the expansion in $\eta_{[\vec{u}]}T$, corresponds to Eq. (10.9).

G.2.3 Sub-protocols of fast driving controls

Here we show that a generic sub-protocol $\vec{u}_A(t)$ extracted from a cyclic trajectory $\vec{u}(t)$ fulfilling the fast driving limit condition (G.32), also fulfils the same condition.

As detailed in Sec. 10.2.1 of the main text, a generic sub-protocol $\vec{u}_A(t)$ is constructed from reduction of $\vec{u}(t)$ on a proper subset I_A of the fundamental period $I_{[\vec{u}]}$. Accordingly, from Eq. (G.29) it follows that

$$\eta_{[\vec{u}]} = \max_{t\in I_{[\vec{u}]}} \|\mathcal{G}_{\vec{u}(t)}\| \geq \max_{t\in I_A} \|\mathcal{G}_{\vec{u}(t)}\| = \max_{t\in I_{[\vec{u}_A]}} \|\mathcal{G}_{\vec{u}_A(t)}\| = \eta_{[\vec{u}_A]} \,. \tag{G.38}$$

Also, indicating with T_A the measure of the interval I_A, we have by construction $T_A \leq T$: putting this together the thesis finally follows via the inequality

$$\eta_{[\vec{u}_A]} T_A \leq \eta_{[\vec{u}]} T \ll 1 \,. \tag{G.39}$$

G.3 Selection of the infinitesimal protocol

As discussed in Sec. 10.2.2, proving the possibility of fulfilling the condition (10.12) of the main text, is equivalent to showing that starting from a generic curve in $\mathbb{R}^D$ ($D = d^2 - 1$) that has a null center of mass, we can always split it into two (non-trivial) sub-curves such that these still have a null center of mass. This result is proven explicitly in Sec. G.3.1. Then in Sec. G.3.2 we give a characterization of the maximum number L of time intervals entering in Eq. (10.15).

G.3.1 Main result

Let $\gamma \equiv \{\vec{v}(t) | t \in [0,T]\}$ be a piecewise C^1 curve generated by the function $\vec{v}(t) : [0,T] \to \mathbb{R}^D$, that satisfies

$$\int_0^T \vec{v}(t) dt = 0. \tag{G.40}$$

We want to show that there exist $k \leq (D+1)^2$ points on the curve $\vec{v}(t_1), \cdots, \vec{v}(t_k)$ and parameters $\tau_1, \cdots, \tau_k > 0$ such that

$$\int_{t_1}^{t_1+\tau_1} \vec{v}(t) dt + \cdots + \int_{t_k}^{t_k+\tau_k} \vec{v}(t) dt = 0. \tag{G.41}$$

Indeed, in such case the sub-curve identified by the restriction of $\vec{v}(t)$ to $[t_1, t_1+\tau_1]\cup\cdots\cup[t_k, t_k+\tau_k]$ would have a null center of mass.

We can suppose that this curve does not lay on any hyperplane V strictly contained in $\mathbb{R}^D$, otherwise we can simply repeat the proof in the smaller space $V \cong \mathbb{R}^{D-1}$.

We first notice that, calling C the convex hull of the range of the curve $\{\vec{v}(t) : t \in [0,T]\}$ and $\mathring{C}$ its interior, then $0 \in \mathring{C}$. Indeed, if by contradiction this is not the case, by the Hahn-Banach theorem [379] there exists a unitary vector $\vec{w} \in \mathbb{R}^D$ such that $\vec{w}\cdot\vec{x} \geq 0$ for every $\vec{x} \in C$. Since $\vec{v}(t) \in C$ for every t, $\vec{v}(t)\cdot\vec{w}$ is a non negative function, but using Eq. (G.40) we have

$$\int \vec{v}(t)\cdot\vec{w}dt = \left(\int \vec{v}(t)dt\right)\cdot\vec{w} = 0,$$

hence $\vec{v}(t)\cdot\vec{w} = 0$ for every t. This is equivalent to saying that $\vec{v}$ lies on the hyperplane $\{\vec{w}\cdot\vec{x} = 0\}$, that is a contradiction.

Since $0 \in \mathring{C}$, we can find $D+1$ points $\vec{p}_1, \cdots, \vec{p}_{D+1} \in \mathring{C}$,

$$\begin{aligned}
\vec{p}_1 &= \varepsilon\left(1-\tfrac{1}{D+1}, -\tfrac{1}{D+1}, \cdots, -\tfrac{1}{D+1}\right) ,\\
\vec{p}_2 &= \varepsilon\left(-\tfrac{1}{D+1}, 1-\tfrac{1}{D+1}, \cdots, -\tfrac{1}{D+1}\right) ,\\
\vec{p}_D &= \varepsilon\left(-\tfrac{1}{D+1}, -\tfrac{1}{D+1}, \cdots, 1-\tfrac{1}{D+1}\right) ,\\
\vec{p}_{D+1} &= \varepsilon\left(-\tfrac{1}{D+1}, -\tfrac{1}{D+1}, \cdots, -\tfrac{1}{D+1}\right) ,
\end{aligned}$$

with ε a positive constant, so that $\vec{p}_1, \cdots, \vec{p}_{D+1}$ do not lie in any hyperplane and

$$\frac{\vec{p}_1 + \cdots + \vec{p}_{D+1}}{D+1} = 0. \tag{G.42}$$

Moreover, since $\vec{p}_j \in C$, there exist $t_1^j, \cdots, t_{m_j}^j \in [0,T]$ and a set of coefficients $\alpha_1^j, \cdots, \alpha_{m_j}^j \in (0,1)$ with $m_j \leq D+1, \alpha_1^j + \cdots + \alpha_{m_j}^j = 1$, such that

$$\alpha_1^j \vec{v}(t_1^j) + \cdots + \alpha_{m_j}^j \vec{v}(t_{m_j}^j) = \vec{p}_j. \tag{G.43}$$

Since the $\vec{p}_j$ by construction do not lie on any hyperplane, the same holds true for the family $\vec{v}(t_k^j)$. To simplify the notation, we reindex $t_k^j = t_l$, $1 \leq l \leq m \leq (D+1)^2$, where $m = \sum_{j=1}^{D+1} m_j$, and from (G.42) and (G.43), we notice that there exist positive numbers $a_1, \cdots, a_m$ with $a_1 + \cdots + a_m = 1$ such that

$$a_1\vec{v}(t_1) + \cdots + a_m\vec{v}(t_m) = 0. \tag{G.44}$$

Moreover, the vectors $\vec{v}(t_1), \cdots, \vec{v}(t_m)$ do not lie on any hyperplane. Up to reordering, we can assume that $\vec{v}(t_{m-D+1}), \cdots, \vec{v}(t_m)$ are linearly independent. We define the maps

$$f_l(\tau) = \begin{cases} \int_{t_l}^{t_l+\tau} \vec{v}(t)dt & \text{if } t_l < T, \\ \int_{T-\tau}^{T} \vec{v}(t)dt & \text{if } t_l = T, \end{cases} \tag{G.45}$$

and

$$F(\tau_1, \cdots, \tau_m) = f_1(\tau_1) + \cdots + f_m(\tau_m). \tag{G.46}$$

Then (G.41) is proven if we have that for some choice of $\tau_1, \cdots, \tau_m > 0$ arbitrarily small, $F(\tau_1, \cdots, \tau_m) = 0$. For this purpose, we notice that $\partial_\tau f_l(0) = \vec{v}(t_l)$, and

$$\nabla_{\tau_{m-D+1}, \cdots, \tau_D} F|_{\tau_{m-D+1}=0, \cdots, \tau_m=0} = \begin{pmatrix} \vec{v}(t_{m-D+1}), & \cdots & \vec{v}(t_m) \end{pmatrix} \tag{G.47}$$

which is an invertible matrix, since the vectors $\vec{v}(s_{m-D+1}), \cdots, \vec{v}(s_m)$ are linearly independent. Moreover, $F(0, \cdots, 0) = 0$. Therefore, by the implicit function theorem [379], in a neighborhood of 0, there exist C^1 functions $\sigma_{m-D+1}(\tau_1, \cdots, \tau_{m-D}), \cdots, \sigma_D((\tau_1, \cdots, \tau_{m-D}))$ such that

$$F(\tau_1, \cdots, \tau_{m-D}, \sigma_{m-D+1}(\tau_1, \cdots, \tau_{m-D}), \cdots, \sigma_D((\tau_1, \cdots, \tau_{m-D}))) = 0 \tag{G.48}$$

and $\sigma_j(0, \cdots, 0) = 0$. If we have that for an appropriate choice of $\tau_1, \cdots, \tau_{m-D} > 0$, then $\sigma_j(\tau_1, \cdots, \tau_{m-D}) > 0$ for every j, we obtain (G.41). Differentiating

$$0 = F(a_1 t, \cdots, a_{m-D} t, \sigma_{m-D+1}(a_1 t, \cdots, a_{m-D} t), \cdots, \sigma_m(a_1 t, \cdots, a_{m-D} t))$$

in $t = 0$, we obtain

$$a_1 \vec{v}(t_1) + \cdots + a_{m-D} \vec{v}(t_{m-D}) + \frac{d}{dt}\sigma_{m-D+1}(0)\vec{v}(t_{m-D+1}) + \cdots + \frac{d}{dt}\sigma_m(0)\vec{v}(t_m) = 0. \tag{G.49}$$

Combining this with (G.44) and recalling that $\vec{v}(t_{m-D+1}), \cdots, \vec{v}(t_m)$ are linearly independent, we obtain that

$$\frac{d}{dt}\sigma_j(0) = a_j > 0. \tag{G.50}$$

Therefore, for δ small enough, $\sigma_j(\delta a_1, \cdots, \delta a_{m-D}) > 0$, and we obtain (G.41) by choosing $\tau_j = a_j \delta$ for $j \leq m - D$, and $\tau_{m-D+j} = \sigma_{m-D+j}(\delta a_1, \cdots, \delta a_{m-D})$, and the analogous choice if $t_j = T$ for some j.

G.3.2 Maximum number of sudden quenches

As discussed in Sec. 10.2.2 and in App. G.3, the most powerful protocol is a generalized Otto cycle composed by a finite number k of infinitesimal segments where the control is constant. Here we will prove that $k \leq L = D - 1$, where D is the dimension of the vector space in which the function $\vec{v}(t)$ introduced in Sec. 10.2.2 lives.

We start by considering an infinitesimal protocol, associated to a curve composed by k infinitesimal segments each one starting from a vector $\vec{w}_i \in \mathbb{R}^D$ with $0 \leq i \leq k$. We assume this curve to have null center of mass, i.e. that Eq. (G.41) is valid. For an infinitesimal protocol, Eq. (G.41) reduces to

$$\sum_{i=1}^{k} \alpha_i \vec{w}_i = 0, \tag{G.51}$$

where $\alpha_i = \tau_i / T > 0$ is such that $\sum \alpha_i = 1$.

Let C be the convex hull generated by the vectors $\{\vec{w}_i : i = 1, ..k\}$. As argued in the previous appendix, Eq. (G.51) implies that 0 belongs to $\mathring{C}$. Assuming that the original vectors do not lie on any hyperplane, by linear independence we can identify a subset S of indices of $\{1, 2, ..., k\}$ and some coefficients ξ_i such that $\sum_{i \in S} \xi_i \vec{w}_i = 0$ and $\sum_{i \in S} \xi_i = 1$. Moreover, S has at most $D + 1$ elements.

We now take a linear combination of $\sum_{i \in S} \xi_i \vec{w}_i = 0$ and Eq. (G.51) obtaining, up to reordering the vectors

$$(\alpha_1 - c\xi_1)\vec{w}_1 + \cdots + (\alpha_{D+1} - c\xi_{D+1})\vec{w}_{D+1} + a_{D+2}\vec{w}_{D+2} + \cdots + a_k \vec{w}_k = 0, \tag{G.52}$$

where c is a positive constant. If $c = 0$, all coefficients are positive, whereas for large values of c, the first $D + 1$ coefficients become negative. We therefore choose the smallest value of c such that one coefficient is null, and the other ones are positive, that is

$$c = \min_{i=1,\cdots D+1} \frac{\alpha_i}{\xi_i}. \tag{G.53}$$

The following argument can be simply generalized to the case where more than one coefficient is null. We can assume that the index that minimizes the right hand side of Eq. (G.53) is $i = 1$. With this choice, we have that

$$\begin{cases} c\xi_1\vec{w}_1 + \cdots c\xi_{D+1}\vec{w}_{D+1} = 0, \\ (\alpha_2 - c\xi_2)\vec{w}_2 + \cdots (\alpha_{D+1} - c\xi_{D+1})\vec{w}_{D+1} + \alpha_{D+2}\vec{w}_{D+2} + \cdots + \alpha_k\vec{w}_k = 0. \end{cases} \tag{G.54}$$

We now define two new sub-curves, A and B, of the original infinitesimal curve through Eq. (G.54). The first is given by $D+1$ infinitesimal segments, centered around $\vec{w}_1, \ldots, \vec{w}_{D+1}$, with time duration $\tau_i^{(\mathrm{A})}/T$ given by the coefficients of the first row of Eq. (G.54). The second is centered around $\vec{w}_2, \ldots, \vec{w}_k$ with time duration $\tau_i^{(\mathrm{B})}/T$ given by the coefficients of the second row of Eq. (G.54). Thanks to Eq. (G.54), these two sub curve have null center of mass [they satisfy Eq. (G.41)], and thanks to the fact that $\sum_i \tau_i^{(\mathrm{A})} + \sum_i \tau_i^{(\mathrm{B})} = 1$, they are a disjoint partition of the initial curve into two sub-curves. Each one of the two sub-curves is associated to a sub-protocol, and following the partition argument introduced in Sec. 10.2.1, we know that the sub-protocol relative to one or the other sub-curve is not less powerful than the original one. If this procedure selects the curve supported on $D+1$ vectors, the proof is over. If the most powerful one is the one composed of $k-1 > D+1$ vectors, we can reiterate this argument until we end up with a protocol made up of $D+1$ vectors.

G.4 One control per temperature is sufficient for positive GAPs

Consider the expression of the generalized power (10.23), which can be rewritten as

$$P_{\mathbf{c}}[\{\vec{u}_i, \mu_i\}] = \frac{\sum_{i,j=1}^{L} c_{\alpha_i}\pi_i\pi_j P_{i\leftarrow j}}{\sum_{i=1}^{L}\pi_i}, \tag{G.55}$$

(G.56)

where α_i is the constant value of $\alpha(t)$ during the interval $d\tau_i$, and $\pi_i \equiv \mu_i\Gamma_{\vec{u}_i}$.

We assume now that the GAP to maximize is *positive*, that is it consists of a positive average of the currents extracted from some of the thermal sources i.e. $c_{\alpha_i} \geq 0\ \forall i$ (note that this is the case both for the engine and the refrigerator). In such a case it is easy to see that

$$P_{\mathbf{c}}[\{\vec{u}_i, \mu_i\}] \leq \frac{\sum_{i,j=1}^{L} c_{\alpha_i}\pi_i\pi_j \tilde{P}_{i\leftarrow j}}{\sum_{i=1}^{L}\pi_i}, \tag{G.57}$$

Where $\tilde{P}_{i\leftarrow j} = P_{i\leftarrow j}$ if $T_i \neq T_j$ while $\tilde{P}_{i\leftarrow j} = 0$ if the two temperatures are the same. The inequality holds thanks to the fact that $c_{\alpha_i} \equiv c_{T_i} \geq 0$ is positive and only depends on the temperature, plus property (10.26) (that is, $P_{i\leftarrow j} + P_{j\leftarrow i} \leq 0$ when $T_i = T_j$). We will now maximize the right hand side of (G.57), which in the end will result in a maximization of $P_{\mathbf{c}}$ as for the optimal control the inequality is saturated. Consider the list of controls to be ordered in such a way to collect in the first k entries all the points at temperature T_1, i.e.

$$T_i = T_1 \Leftrightarrow 1 \leq i \leq k \tag{G.58}$$

Then the right hand side of (G.57) can be cast as

$$\frac{\sum_{i\leq k, j>k}\pi_i\pi_j(c_1\tilde{P}_{i\leftarrow j} + c_j\tilde{P}_{j\leftarrow i}) + \sum_{i>k,j>k} c_i\pi_i\pi_j\tilde{P}_{i\leftarrow j}}{\sum_{i\leq k}\pi_i + \sum_{i>k}\pi_i}. \tag{G.59}$$

It is possible to re-express the above equation in terms of the time ratios spent on each control point μ_i. Focusing on the controls at temperature T_1 we consider the renormalized fraction of time spent on the first k points, i.e. we introduce

$$\theta_i^{(1)} = \frac{\mu_i}{\sum_{j=1}^{k} \mu_j} \ , \tag{G.60}$$

meaning that the vector $\vec{\theta}^{(1)}$ represents a normalized probability distribution on those points. With this definition we see easily that expression (G.59) is in the form

$$\frac{\vec{\theta}^{(1)} \cdot \vec{a} + A}{\vec{\theta}^{(1)} \cdot \vec{b} + B} \tag{G.61}$$

for appropriate definitions of $\vec{a}$, A, $\vec{b}$, B. When tuning the time fractions spent on each point at temperature T_1 the best option will be thus to concentrate on one point only, i.e. $\theta_i^{(1)} = \delta_{i\bar{i}}$ where $\bar{i}$ reaches the maximum in the following affine inequality (see **Lemma** below)

$$\frac{\vec{\theta}^{(1)} \cdot \vec{a} + A}{\vec{\theta}^{(1)} \cdot \vec{b} + B} \leq \max_i \frac{a_i + A}{b_i + B} \ . \tag{G.62}$$

It is then sufficient to repeat the same argument for each temperature to prove that for any positive GAP at most one control point per temperature is needed in the maximization.

The power can be thus optimized on the form

$$P_{\mathbf{c}}[\{\vec{u}_\alpha, \mu_\alpha\}] = \frac{\sum_{\alpha,\beta=1}^{N} c_\alpha \pi_\alpha \pi_\beta P_{\alpha \leftarrow \beta}}{\sum_{\alpha=1}^{N} \pi_\alpha} \ , \tag{G.63}$$

which is the same as (10.23), except for the indices running only on different temperatures. We notice also that if more than one coefficient c_α is zero the optimization can be reduced again. That is, suppose $c_\alpha \neq 0$ for $\alpha = 1, \ldots, \kappa$ with $\kappa \leq N - 2$. Then the above expression takes the form

$$\frac{\sum_{\alpha,\beta \leq \kappa} c_\alpha \pi_\alpha \pi_\beta P_{\alpha \leftarrow \beta} + \sum_{\alpha \leq \kappa, \beta > \kappa} c_\alpha \pi_\alpha \pi_\beta P_{\alpha \leftarrow \beta}}{\sum_{\alpha=1}^{\kappa} \pi_\alpha + \sum_{\alpha=\kappa+1}^{N} \pi_\alpha} \ , \tag{G.64}$$

and the Lemma can be used again to collapse all the last $N - \kappa$ controls in one, remaining with $\kappa + 1$ points. This has the immediate consequence, that e.g. for a refrigerator two controls are always sufficient to optimize a refrigerator, where $\kappa = 1$.

Lemma Given a probability distribution $\vec{p}$, a vector $\vec{a}$, a positive vector $\vec{b} \geq 0$, a constant A and a positive constant $B \geq 0$, it holds that

$$\frac{\vec{p} \cdot \vec{a} + A}{\vec{p} \cdot \vec{b} + B} \leq \max_i \frac{a_i + A}{b_i + B} \ . \tag{G.65}$$

Proof. First notice that the values of A and B can be reabsorbed in the definitions of $\vec{a}$ and $\vec{b}$, due to $\vec{p}$ being a probability distribution $p_i \geq 0$, $\sum_i^n p_i = 1$. Formally

$$a'_i = a_i + \frac{A}{n} \ , \quad b'_i = b_i + \frac{B}{n} \quad \Rightarrow \frac{\vec{p} \cdot \vec{a} + A}{\vec{p} \cdot \vec{b} + B} = \frac{\vec{p} \cdot \vec{a'}}{\vec{p} \cdot \vec{b'}} \tag{G.66}$$

Now consider a convex combination $\vec{p} = \lambda\vec{p}^{(1)} + (1-\lambda)\vec{p}^{(2)}$ and without loss of generality

$$r^{(1)} \equiv \frac{\vec{p}^{(1)} \cdot \vec{a}'}{\vec{p}^{(1)} \cdot \vec{b}'} \leq \frac{\vec{p}^{(2)} \cdot \vec{a}'}{\vec{p}^{(2)} \cdot \vec{b}'} \equiv r^{(2)} \ . \tag{G.67}$$

It follows that

$$\begin{aligned} \frac{\lambda\vec{p}^{(1)} \cdot \vec{a}' + (1-\lambda)\vec{p}^{(2)} \cdot \vec{a}'}{\lambda\vec{p}^{(1)} \cdot \vec{b}' + (1-\lambda)\vec{p}^{(2)} \cdot \vec{b}'} &= \frac{\lambda r^{(1)}\vec{p}^{(1)} \cdot \vec{b}' + (1-\lambda) r^{(2)}\vec{p}^{(2)} \cdot \vec{b}'}{\lambda\vec{p}^{(1)} \cdot \vec{b}' + (1-\lambda)\vec{p}^{(2)} \cdot \vec{b}'} \\ &\geq \frac{\lambda r^{(2)}\vec{p}^{(1)} \cdot \vec{b}' + (1-\lambda) r^{(2)}\vec{p}^{(2)} \cdot \vec{b}'}{\lambda\vec{p}^{(1)} \cdot \vec{b}' + (1-\lambda)\vec{p}^{(2)} \cdot \vec{b}'} = r^{(2)} \ . \end{aligned} \tag{G.68}$$

where in the last inequality we used that $\vec{b}' \geq 0$. The same inequality be carried out in the other sense and both inequalities can be condensed as

$$\frac{\vec{p}^{(1)} \cdot \vec{a}'}{\vec{p}^{(1)} \cdot \vec{b}'} \leq \frac{\lambda\vec{p}^{(1)} \cdot \vec{a}' + (1-\lambda)\vec{p}^{(2)} \cdot \vec{a}'}{\lambda\vec{p}^{(1)} \cdot \vec{b}' + (1-\lambda)\vec{p}^{(2)} \cdot \vec{b}'} \leq \frac{\vec{p}^{(2)} \cdot \vec{a}'}{\vec{p}^{(2)} \cdot \vec{b}'} \ . \tag{G.69}$$

If follows in particular that expression is convex and is obtained on the extremal points of the polytope in which $\vec{p}$ lives. The extremal points are deterministic points ($p_i = \delta_{i\bar{i}}$ for some $\bar{i}$), and thus inequality (G.65) is proven.

G.5 Power of many interacting qubits

In this appendix we prove Eqs. (10.37) and (10.39). We start from the refrigerator case. As discussed in Sec. 10.3.3, the maximum average cooling power is given by

$$P_{[\mathrm{R}]}^{(\max)} = \frac{1}{\left(\sqrt{\Gamma_{\alpha_1}^{-1}} + \sqrt{\Gamma_{\alpha_2}^{-1}}\right)^2} \frac{1}{\beta_2} \max_{\varepsilon_2} \beta_2\varepsilon_2 \frac{e^{-\beta_2\varepsilon_2}(d-1)}{1+(d-1)e^{-\beta_2\varepsilon_2}}. \tag{G.70}$$

Defining $x = \beta_2\varepsilon_2$, we need to find the maximum of the function

$$f(x) = \frac{xe^{-x}(d-1)}{1+(d-1)e^{-x}}. \tag{G.71}$$

Setting to zero the derivative of $f(x)$, the optimal value x^* is determined by solving

$$e^{x^*}(x^*-1) = d-1. \tag{G.72}$$

The solution to this equation can be given in terms of the Lambert function $W(z)$, which is defined implicitly by the relation $z = W\,e^W$. We therefore find

$$x^* = 1 + W\left(\frac{d-1}{e}\right). \tag{G.73}$$

Plugging this into $f(x_1)$, and using the relation $e^{-W(x)} = W(x)/x$, we have that

$$f(x^*) = W\left(\frac{d-1}{e}\right). \tag{G.74}$$

This is an exact solution. The behavior of the Lambert function, for large arguments, is given by

$$W(z) = \ln(z) - \ln(\ln(z)) + O(1). \tag{G.75}$$

Retaining only the largest contribution in the limit $d \to \infty$, we find

$$f(x^*) \approx \ln(d). \tag{G.76}$$

Plugging this result into Eq. (G.70) with $d = 2^n$ yields the second relation of Eq. (10.37). In the NI case, the cooling power of n qubits is given by n times the power of a single qubit. Setting $d = 2$ in Eq. (G.74) and plugging the result into Eq. (G.70) gives an an exact expression of the maximum cooling power of a single qubit. Equation (10.39) is therefore proven by combining this relation with Eq. (10.37).

We now turn to the heat engine case. As discussed in Sec. 10.3.3, the maximum average extracted power is given by

$$P_{[\mathrm{E}]}^{(\max)} = \frac{1}{\left(\sqrt{\Gamma_{\alpha_1}^{-1}} + \sqrt{\Gamma_{\alpha_2}^{-1}}\right)^2} \frac{1}{\beta_1\beta_2} \max_{\varepsilon_1\,\varepsilon_2} \frac{(\beta_1\varepsilon_1\,\beta_2 - \beta_2\varepsilon_2\,\beta_1)(e^{-\beta_1\varepsilon_1} - e^{-\beta_2\varepsilon_2})(d-1)}{(1+(d-1)e^{-\beta_1\varepsilon_1})(1+(d-1)e^{-\beta_2\varepsilon_2})}\,. \tag{G.77}$$

Defining $x_1 = \beta_1\varepsilon_1$ and $x_2 = \beta_2\varepsilon_2$, we need to find the maximum of the function

$$f(x_1, x_2) = \frac{(x_1\beta_2 - x_2\beta_1)(e^{-x_1} - e^{-x_2})(d-1)}{(1+(d-1)e^{-x_1})(1+(d-1)e^{-x_2})} \tag{G.78}$$

in the limit of $d \to +\infty$. Approximating $d - 1 \approx d$ and setting the partial derivatives of $f(x_1, x_2)$ to zero, the optimal values x_1^* and x_2^* are determined by solving

$$\begin{aligned}
\beta_1 e^{x_1^*}(d + e^{x_2^*})x_2^* - \beta_2\left(e^{2x_1^*} - de^{x_2^*} + e^{x_1^*+x_2^*}(x_1^* - 1) + de^{x_1^*}(1 + x_1^*)\right) = 0,\\
\beta_2 e^{x_2^*}(d + e^{x_1^*})x_1^* - \beta_1\left(e^{2x_2^*} - de^{x_1^*} + e^{x_1^*+x_2^*}(x_2^* - 1) + de^{x_2^*}(1 + x_2^*)\right) = 0.
\end{aligned} \tag{G.79}$$

We were not able to explicitly find a solution to this set of equation. We therefore search for a perturbative solution, which is valid in the limit of large d. We do this by choosing an "ansatz" of the form

$$\begin{aligned}
x_1^* &= \sum_i a_1^{(i)} g_i(d),\\
x_2^* &= \sum_i a_2^{(i)} g_i(d),
\end{aligned} \tag{G.80}$$

where $g_i(d)$ are a set of functions that capture the asymptotic behavior of x_1^* and x_2^*, and $a_1^{(i)}$ and $a_2^{(i)}$ are a set of coefficients that do not depend on d, which we determine by imposing Eq. (G.79), i.e. by setting to zero the coefficients of the terms which diverge fastest in d. We choose the same set of functions $g_i(d)$ for both x_1^* and x_2^* since this simplifies the calculation, and since it is a reasonable assumption given that $f(x_1, x_2) = f(x_2, x_1)$, provided that we also exchange the temperatures.

Unfortunately, a straightforward expansion in powers of d does not work. This is due to the fact that we have both polynomial and exponential terms in Eq. (G.79). To find a good "ansatz", we thus take inspiration from the exact solution x_1^* found in the refrigerator case: indeed, the functions $f(x)$ in the refrigerator case and $f(x_1, x_2)$ in the heat engine case

are formally very similar. Using the asymptotic expansion of the Lambert function, from Eq. (G.73) we have that, in the refrigerator case,

$$x^* \approx \ln d - \ln\ln d + O(1). \tag{G.81}$$

Using this intuition, and performing some attempts, we choose the following ansatz:

$$\begin{aligned} x_1^* &= \ln d - \ln\ln d - \ln a_1, \\ x_2^* &= \ln d + \ln\ln d + \ln a_2. \end{aligned} \tag{G.82}$$

Plugging this ansatz into Eq. (G.79), and retaining only the fastest diverging term with respect to d, we find (up to an irrelevant prefactor)

$$\begin{aligned} (a_1\beta_2 + \beta_1 - \beta_2)\ d^2 \ln d = 0, \\ (a_2\beta_1 + \beta_1 - \beta_2)\ d^2 \ln^2 d = 0. \end{aligned} \tag{G.83}$$

In order to suppress these fast diverging term, we set the coefficient to zero, finding

$$a_1 = \frac{\beta_2 - \beta_1}{\beta_2}, \qquad a_2 = \frac{\beta_2 - \beta_1}{\beta_1}. \tag{G.84}$$

We now have an approximate expression for x_1^* and x_2^* which is asymptotically correct. Retaining only the fastest diverging term with respect to d, we find

$$f(x_1^*, x_2^*) \approx (\beta_2 - \beta_1)\ln d. \tag{G.85}$$

Using Eq. (G.85) to evaluate Eq. (G.77), and setting $d = 2^n$ proves the first relations in Eq. (10.37).

G.6 Qutrit model

In this appendix we present the model we employ to describe a qutrit in the Markovian regime. The Hamiltonian of the system is given by Eq. (10.40), and the dynamics of the local density matrix is described by Eq. (10.2). Following the standard derivation of the Lindbald master equation [27], and accounting for the fact that we only couple one bath at the time to the qutrit, we write the total dissipator $\mathcal{D}_{\vec{u}(t)}[\rho] = \sum_\alpha \mathcal{D}_{\alpha,\vec{u}(t)}[\rho]$ as

$$\mathcal{D}_{\vec{u}(t)}[\rho] := \sum_{i\neq j} \Gamma_{ij}(\vec{u}(t), \alpha(t)) \left(A_{ij}\rho A_{ij}^\dagger - \frac{1}{2}\left[A_{ij}^\dagger A_{ij}, \rho(t)\right]_+ \right), \tag{G.86}$$

where $\alpha(t)$ is an additional control labelling the bath we are coupled to, and $[\cdots,\cdots]_+$ denotes the anti-commutator operations. $\Gamma_{ij}(\vec{u}(t), \alpha(t))$ is the dissipation rate induced by reservoir α which describes a transition from eigenstate $|i\rangle$ to eigenstate $|j\rangle$ of $\mathcal{H}$ and $A_{ij} = |i\rangle\langle j|$.

We now define the occupation probabilities $p_n(t) = \langle n|\,\rho(t)\,|n\rangle$. By projecting Eq. (10.2), provided with Eq. (G.86), onto the eigenstates of $\mathcal{H}$, we can derive a closed set of equations for $p_n(t)$, given by Eq. (10.41). Explicitly, we have that

$$\begin{pmatrix} \partial_t p_1 \\ \partial_t p_2 \\ \partial_t p_3 \end{pmatrix} = \begin{pmatrix} -\Gamma_{12} - \Gamma_{13} & \Gamma_{21} & \Gamma_{31} \\ \Gamma_{12} & -\Gamma_{21} - \Gamma_{23} & \Gamma_{32} \\ \Gamma_{13} & \Gamma_{23} & -\Gamma_{32} - \Gamma_{31} \end{pmatrix} \cdot \begin{pmatrix} p_1 \\ p_2 \\ p_3 \end{pmatrix}, \tag{G.87}$$

where we omitted for simplity the arguments of the probabilities and of the rates.

In general, the probabilities associated with the limiting cycle can be computed solving Eq. (10.41) imposing periodic boundary conditions, i.e. $p_n(0) = p_n(T)$, and imposing that $\sum_n p_n = 1$. The instantaneous heat flux flowing out of all baths $J(t) = \sum_\alpha J_\alpha(t)$ can then be computed as

$$\begin{aligned} J(t) = \mathrm{Tr}\left[H_{\vec{u}(t)}\mathcal{D}_{\vec{u}(t)}\left[\rho(t)\right]\right] &= \sum_n \epsilon_n(t)\partial_t p_n(t) \\ &= \sum_{m\neq n} \epsilon_n(t)\left[-p_n(t)\Gamma_{nm}(\vec{u}(t),\alpha(t)) + p_m(t)\Gamma_{mn}(\vec{u}(t),\alpha(t))\right] \end{aligned} \tag{G.88}$$

where, in the last equality, we used Eq. (10.41). The average power delivered by the heat engine is then given

$$P_{[\mathrm{E}]} = \frac{1}{T}\int_0^T J(t)dt. \tag{G.89}$$

This is the procedure used for the numerical calculations at finite period T.

In order to simplify this calculation in the fast-driving regime, we first need to cast Eq. (G.87) into a form equivalent to Eq. (10.5). We do this using a slightly different approach respect to the one detailed in the main text, that yields equivalent results. Inserting the relation $p_1 = 1 - p_2 - p_3$ into Eq. (G.87), and using the detailed balance condition (10.42), we find

$$\partial_t \hat{p}(t) = G(\vec{u}(t),\alpha(t)) \cdot (\hat{p}(t) - \hat{p}^{(\mathrm{eq})}_{\alpha(t);\vec{u}(t)}), \tag{G.90}$$

where we defined $\hat{p}(t) = (p_2(t), p_3(t))$, and where $\hat{p}^{(\mathrm{eq})}_{\alpha(t);\vec{u}(t)} = ([p^{(\mathrm{eq})}_{\alpha(t);\vec{u}(t)}]_2, [p^{(\mathrm{eq})}_{\alpha(t);\vec{u}(t)}]_3)$ are the Gibbs probabilities of being in state $|2\rangle$ and $|3\rangle$ when in contact with bath $\alpha(t)$. Omitting the explicit argument, the matrix $G(\vec{u}(t),\alpha(t))$ is given by

$$G = \begin{pmatrix} \Gamma_{12}+\Gamma_{21}+\Gamma_{23} & +\Gamma_{12}-\Gamma_{32} \\ +\Gamma_{13}-\Gamma_{23} & +\Gamma_{13}+\Gamma_{31}+\Gamma_{32} \end{pmatrix}, \tag{G.91}$$

which can be shown to be strictly positive definite using the detailed balance condition (10.42) and assuming that the bath temperatures are finite. Therefore, any sum of $G(\vec{u}(t),\alpha(t))$ at different times will be positive definite, thus invertible. All relations in the main text thus hold by replacing $\rho(t)$ with $p(t)$, $\tilde{\rho}(t)$ with $\hat{p}(t)$ and $\mathcal{G}_{\vec{u}(t)}$ with $G(\vec{u}(t),\alpha(t))$. Specifically, defining $\hat{\epsilon}(t) = (\epsilon_2(t), \epsilon_3(t))$, Eqs. (10.15) and (10.16), become in this notation

$$P_{[\mathrm{E}]}[\{\vec{u}_i,\mu_i\}] = \sum_{j=1}^{L} \mu_j \ \hat{\epsilon}_j^T \cdot G(\vec{u}_j,\alpha_j) \cdot (\hat{p}^{(0)}_{[\{\vec{u}_i,\mu_i\}]} - \hat{p}^{(\mathrm{eq})}_{\alpha(t);\vec{u}(t)}), \tag{G.92}$$

and

$$\hat{p}^{(0)}_{[\{\vec{u}_i,\mu_i\}]} = \left(\sum_{j=1}^{L}\mu_j G(\vec{u}_j,\alpha_j)\right)^{-1}\left[\sum_{j=1}^{L}\mu_j G(\vec{u}_j,\alpha_j)\cdot \hat{p}^{(\mathrm{eq})}_{\alpha_j;\vec{u}_j}\right], \tag{G.93}$$

where $\hat{\epsilon}_j$ denotes the value of the energies during the j^{th} time interval, as determined by the control $\vec{u}_j$. We can therefore compute the power of a Generalized Otto cycle in the fast driving regime using Eqs. (G.92) and (G.93), which is much easier than solving the dynamics explicitly. The optimization of $P_{[\mathrm{E}]}[\{\vec{u}_i,\mu_i\}]$ is then performed as described in Sec. 10.4.

References

[1] R. R. N. Alves, *Chapter 18 - The Ethnozoological Role of Working Animals in Traction and Transport* (Academic Press, 2018). 1

[2] B. C. O'Neill, M. Oppenheimer, R. Warren, S. Hallegatte, R. E. Kopp, H. O. Pörtner, R. Scholes, J. Birkmann, W. Foden, R. Licker, *et al.*, *Ipcc reasons for concern regarding climate change risks*, Nat. Clim. Change **7**, 28 (2017), URL https://doi.org/10.1038/nclimate3179. 1

[3] L. D. Hicks, T. C. Harman, and M. S. Dresselhaus, *Use of quantum-well superlattices to obtain a high figure of merit from nonconventional thermoelectric materials*, Appl. Phys. Lett. **63**, 3230 (1993), URL https://doi.org/10.1063/1.110207. 1, 33

[4] L. D. Hicks and M. S. Dresselhaus, *Thermoelectric figure of merit of a one-dimensional conductor*, Phys. Rev. B **47**, 16631(R) (1993), URL https://doi.org/10.1103/PhysRevB.47.16631. 1

[5] G. D. Mahan and J. O. Sofo, *The best thermoelectric*, Proc. Natl. Acad. Sci. U.S.A. **93**, 7436 (1996), URL https://doi.org/10.1073/pnas.93.15.7436. 1, 2, 20, 33, 44, 48, 65, 72, 158

[6] G. Fagas, L. Gammaitoni, D. Paul, and G. A. Berini, *ICT - Energy - Concepts Towards Zero Power Information and Communication Technology* (InTech, 2014). 1

[7] F. Giazotto, T. T. Heikkilä, A. Luukanen, A. M. Savin, and J. P. Pekola, *Opportunities for mesoscopics in thermometry and refrigeration: Physics and applications*, Rev. Mod. Phys. **78**, 217 (2006), URL https://doi.org/10.1103/RevModPhys.78.217. 1, 74, 78, 93

[8] A. Volta, *Nuova memoria sull'elettricità animale*, Lettere al signor Abate Anton Maria Vassalli (1794). 1, 13

[9] T. J. Seebeck, *Ueber den magnetismus der galvanische kette*, Abhandlungen der Deutschen Akademie der Wissenschaften zur Berlin (1822). 1

[10] A. F. Ioffe, *Semiconductor Thermoelements and Thermoelectric Cooling* (Pion Ltd, 1958). 1

[11] G. Benenti, G. Casati, K. Saito, and R. S.Whitney, *Fundamental aspects of steady-state conversion of heat to work at the nanoscale*, Phys. Rep. **694**, 1 (2017), URL https://doi.org/10.1016/j.physrep.2017.05.008. 1, 17, 18, 19, 20, 33, 65, 72, 81, 84, 91, 113, 121, 123, 137

[12] H. Friedenauer, H. Schmitz, J. Glueckert, D. Porras, and T. Schaetz, *Simulating a quantum magnet with trapped ions*, Nat. Phys. **4**, 757 (2008), URL https://doi.org/10.1038/nphys1032. 2, 123

[13] R. Blatt and C. Roos, *Quantum simulations with trapped ions*, Nat. Phys. **8**, 277 (2012), URL https://doi.org/10.1038/nphys2252. 2, 123

[14] L. Childress, M. V. Gurudev Dutt, J. M. Taylor, A. S. Zibrov, F. Jelezko, J. Wrachtrup, P. R. Hemmer, and M. D. Lukin, *Coherent dynamics of coupled electron and nuclear spin qubits in diamond*, Science **314**, 281 (2006), URL https://doi.org/10.1126/science.1131871. 2, 123

[15] A. Wallraff, D. I. Schuster, A. Blais, L. Frunzio, R.-S. Huang, J. Majer, S. Kumar, S. M. Girvin, and R. J. Schoelkopf, *Strong coupling of a single photon to a superconducting qubit using circuit quantum electrodynamics*, Nature **431**, 162 (2004), URL https://doi.org/10.1038/nature02851. 2, 123

[16] M. A. Kastner, *The single-electron transistor*, Rev. Mod. Phys. **64**, 849 (1992), URL https://doi.org/10.1103/RevModPhys.64.849. 2, 123

[17] J. P. Pekola, *Towards quantum thermodynamics in electronic circuits*, Nat. Phys. **11**, 118 (2015), URL https://doi.org/10.1038/nphys3169. 2, 65, 93, 113, 123

[18] A. Ronzani, B. Karimi, J. Senior, Y.-C. Chang, J. T. Peltonen, C.-D. Chen, and J. P. Pekola, *Tunable photonic heat transport in a quantum heat valve*, Nat. Phys. **14**, 991 (2018), URL https://doi.org/10.1038/s41567-018-0199-4. 92, 93, 113, 114, 123, 140

[19] J. Senior, A. Gubaydullin, B. Karimi, J. T. Peltonen, J. Ankerhold, and J. P. Pekola, *Heat rectification via a superconducting artificial atom*, Commun. Phys. **3**, 40 (2020), URL https://doi.org/10.1038/s42005-020-0307-5. 2, 93, 114, 123, 140

[20] S. Vinjanampathy and J. Anders, *Quantum thermodynamics*, Contemp. Phys. **57**, 545 (2016), URL https://doi.org/10.1080/00107514.2016.1201896. 2, 113

[21] F. Binder, L. Correa, C. Gogolin, J. Anders, and G. Adesso, *Thermodynamics in the Quantum Regime: Fundamental Aspects and New Directions*, Fundamental Theories of Physics (Springer International Publishing, 2019). 2

[22] J. V. Koski, A. Kutvonen, I. M. Khaymovich, T. Ala-Nissila, and J. P. Pekola, *On-chip maxwell's demon as an information-powered refrigerator*, Phys. Rev. Lett. **115**, 260602 (2015), URL https://doi.org/10.1103/PhysRevLett.115.260602. 3, 81, 82, 90

[23] I. Chuang and M. Nielsen, *Quantum Computation and Quantum Information* (Cambridge University Press, 2000). 5

[24] V. Gorini, A. Kossakowski, and E. C. G. Sudarshan, *Completely positive dynamical semigroups of N-level systems*, J. Math. Phys. **17**, 821 (1976), URL https://doi.org/10.1063/1.522979. 6, 114, 115, 126

[25] G. Lindblad, *On the generators of quantum dynamical semigroups*, Commun. Math. Phys **48**, 119 (1976), URL https://doi.org/10.1007/BF01608499. 6, 114, 115, 126

[26] E. B. Davies, *Markovian master equations*, Commun. Math. Phys **39**, 91 (1974), URL https://doi.org/10.1007/BF01608389. 6

[27] H. Breuer and F. Petruccione, *The theory of open quantum systems* (Oxford University Press, 2002). 6, 27, 102, 114, 115, 140, 179, 180, 181, 184, 209, 210, 211, 221

[28] H. Spohn, *An algebraic condition for the approach to equilibrium of an open n-level system*, Math. Phys. **2**, 33 (1977), URL https://doi.org/10.1007/BF00420668. 10

[29] P. Menczel and K. Brandner, *Limit cycles in periodically driven open quantum systems*, J. Phys. A Math. Theor. **52**, 43LT01 (2019), URL https://doi.org/10.1088/1751-8121/ab435a. 10, 27, 126, 127, 209, 212

[30] H. Bruus and K. Flensberg, *Many-body quantum theory in condensed matter physics* (Oxford University Press, New York, 2004). 11, 170

[31] K. Kaasbjerg and A.-P. Jauho, *Correlated coulomb drag in capacitively coupled quantum-dot structures*, Phys. Rev. Lett. **116**, 196801 (2016), URL https://doi.org/10.1103/PhysRevLett.116.196801. 75, 87, 172, 177

[32] B. Bhandari, G. Chiriacò, P. A. Erdman, R. Fazio, and F. Taddei, *Thermal drag in electronic conductors*, Phys. Rev. B **98**, 035415 (2018), URL https://doi.org/10.1103/PhysRevB.98.035415. 69, 75, 105, 170, 172, 178

[33] P. A. Erdman, J. T. Peltonen, B. Bhandari, B. Dutta, H. Courtois, R. Fazio, F. Taddei, and J. P. Pekola, *Nonlinear thermovoltage in a single-electron transistor*, Phys. Rev. B **99**, 165405 (2019), URL https://doi.org/10.1103/PhysRevB.99.165405. 11, 105

[34] Y. V. Nazarov and Y. M. Banter, *Quantum Transport* (Cambridge, New York, 2009). 12, 36, 69, 75, 172

[35] R. Franz and G. Wiedemann, *Ueber die wärme-leitungsfähigkeit der metalle*, Ann. Phys. **165**, 497 (1853), URL https://doi.org/10.1002/andp.18531650802. 13

[36] C. V. den Broeck, *Thermodynamic efficiency at maximum power*, Phys. Rev. Lett. **95**, 190602 (2005), URL https://doi.org/10.1103/PhysRevLett.95.190602. 17, 28, 34, 40, 117

[37] F. Curzon and B. Ahlborn, *Efficiency of a carnot engine at maximum power output*, Am. J. Phys. **43**, 22 (1975), URL https://doi.org/10.1119/1.10023. 17, 28, 34, 40, 59, 117, 118

[38] M. Esposito, R. Kawai, K. Lindenberg, and C. V. den Broeck, *Efficiency at maximum power of low-dissipation carnot engines*, Phys. Rev. Lett. **105**, 150603 (2010), URL https://doi.org/10.1103/PhysRevLett.105.150603. 17, 28, 59, 113, 114, 117, 123

[39] T. Schmiedl and U. Seifert, *Efficiency at maximum power: An analytically solvable model for stochastic heat engines*, Europhys. Lett. **81**, 20003 (2008), URL https://doi.org/10.1209/0295-5075/81/20003. 17, 59, 114, 117, 118, 124

[40] H. Haug and A.-P. Jauho, *Quantum Kinetics in Transport and Optics of Semiconductors* (Springer-Verlag Berlin Heidelberg, 2008). 21, 98, 189, 190

[41] G. Stefanucci and R. van Leeuwen, *Nonequilibrium Many-Body Theory of Quantum Systems* (Cambridge University Press, 2013). 21, 98

[42] M. Josefsson, A. Svilans, A. M. Burke, E. A. Hoffmann, S. Fahlvik, C. Thelander, M. Leijnse, and H. Linke, *A quantum-dot heat engine operating close to the thermodynamic efficiency limits*, Nat. Nanotechnol. **13**, 920 (2018), URL https://doi.org/10.1038/s41565-018-0200-5. 24, 25, 33, 65, 66, 92, 113, 114, 123, 140

[43] E. B. Davies and H. Spohn, *Open quantum systems with time-dependent hamiltonians and their linear response*, J. Stat. Phys. **19**, 511 (1978), URL https://doi.org/10.1007/BF01011696. 26, 126

[44] M. Grifoni and P. Hänggi, *Driven quantum tunneling*, Phys. Rep. **304**, 229 (1998), URL https://doi.org/10.1016/S0370-1573(98)00022-2.

[45] R. Dann, A. Levy, and R. Kosloff, *Time-dependent markovian quantum master equation*, Phys. Rev. A **98**, 052129 (2018), URL https://doi.org/10.1103/PhysRevA.98.052129. 26, 115, 126

[46] R. Alicki, *The quantum open system as a model of the heat engine*, J. Phys. A: Math. Gen. **12**, L103 (1979), URL https://doi.org/10.1088/0305-4470/12/5/007. 27, 114, 116, 123, 127, 140

[47] Q.-h. Deng, J.and Wang, Z. Liu, P. Hänggi, and G. J., *Boosting work characteristics and overall heat-engine performance via shortcuts to adiabaticity: Quantum and classical systems*, Phys. Rev. E **88**, 062122 (2013), URL https://doi.org/10.1103/PhysRevE.88.062122. 28, 113, 124

[48] E. Torrontegui, S. Ibáñez, S. Martínez-Garaot, M. Modugno, A. del Campo, D. Guéry-Odelin, A. Ruschhaupt, X. Chen, and J. G. Muga, *Shortcuts to adiabaticity*, Adv. At., Mol., Opt. Phys. **62**, 117 (2013), URL https://doi.org/10.1016/B978-0-12-408090-4.00002-5.

[49] A. del Campo, J. Goold, and M. Paternostro, *More bang for your buck: Superadiabatic quantum engines*, Sci. Rep. **4**, 6208 (2014), URL https://doi.org/10.1038/srep06208.

[50] B. Çakmak and O. E. Müstecaplıoğlu, *Spin quantum heat engines with shortcuts to adiabaticity*, Phys. Rev. E **99**, 032108 (2019), URL https://doi.org/10.1103/PhysRevE.99.032108. 28, 113, 124

[51] M. Campisi, J. Pekola, and R. Fazio, *Nonequilibrium fluctuations in quantum heat engines: theory, example, and possible solid state experiments*, New J. Phys. **17**, 035012 (2015), URL https://doi.org/10.1088/1367-2630/17/3/035012. 28, 113, 123

[52] V. Cavina, A. Mari, A. Carlini, and V. Giovannetti, *Variational approach to the optimal control of coherently driven, open quantum system dynamics*, Phys. Rev. A **98**, 052125 (2018), URL https://doi.org/10.1103/PhysRevA.98.052125. 124, 128, 196, 197

[53] N. Suri, F. C. Binder, and S. Muralidharan, B. amd Vinjanampathy, *Speeding up thermalisation via open quantum system variational optimisation*, Eur. Phys. J. Spec. Top. **227**, 203 (2018), URL https://doi.org/10.1140/epjst/e2018-00125-6. 123

[54] V. Cavina, A. Mari, A. Carlini, and V. Giovannetti, *Optimal thermodynamic control in open quantum systems*, Phys. Rev. A **98**, 012139 (2018), URL https://doi.org/10.1103/PhysRevA.98.012139. 115, 117, 125

[55] J. P. Pekola, B. Karimi, G. Thomas, and D. V. Averin, *Supremacy of incoherent sudden cycles*, Phys. Rev. B **100**, 085405 (2019), URL https://doi.org/10.1103/PhysRevB.100.085405. 115, 123, 124

[56] P. Menczel, T. Pyhäranta, C. Flindt, and K. Brandner, *Two-stroke optimization scheme for mesoscopic refrigerators*, Phys. Rev. B **99**, 224306 (2019), URL https://doi.org/10.1103/PhysRevB.99.224306. 28, 113, 123, 128

[57] J. Wang, J. He, and X. He, *Performance analysis of a two-state quantum heat engine working with a single-mode radiation field in a cavity*, Phys. Rev. E **84**, 041127 (2011), URL https://doi.org/10.1103/PhysRevE.84.041127. 28, 113, 123

[58] M. F. Ludovico, F. Battista, F. von Oppen, and L. Arrachea, *Adiabatic response and quantum thermoelectrics for ac-driven quantum systems*, Phys. Rev. B **93**, 075136 (2016), URL https://doi.org/10.1103/PhysRevB.93.075136. 97

[59] V. Cavina, A. Mari, and V. Giovannetti, *Slow dynamics and thermodynamics of open quantum systems*, Phys. Rev. Lett. **119**, 050601 (2017), URL https://doi.org/10.1103/PhysRevLett.119.050601. 117, 124, 128

[60] P. Abiuso and V. Giovannetti, *Non-markov enhancement of maximum power for quantum thermal machines*, Phys. Rev. A **99**, 052106 (2019), URL https://doi.org/10.1103/PhysRevA.99.052106. 28, 113, 123

[61] P. Chambadal, *Les centrales nucleaires* (Armand Colin, Paris, 1957). 28, 34, 40

[62] I. I. Novikov, *The efficiency of atomic power stations (a review)*, Ann. Nucl. Energy **7**, 125 (1958), URL https://doi.org/10.1016/0891-3919(58)90244-4. 28, 34, 40

[63] M. S. Dresselhaus, G. Chen, M. Y. Tang, R. G. Yang, H. Lee, D. Z. Wang, Z. F. Ren, J. P. Fleurial, and P. Gogna, *New directions for low-dimensional thermoelectric materials*, Adv. Mater. **19**, 1043 (2007), URL https://doi.org/10.1002/adma.200600527. 33, 65

[64] C. J. Vineis, A. Shakouri, A. Majumdar, and M. G. Kanatzidis, *Nanostructured thermoelectrics: Big efficiency gains from small features*, Adv. Mater. **22**, 3970 (2010), URL https://doi.org/10.1002/adma.201000839. 65

[65] G. J. Snyder and E. S. Toberer, *Complex thermoelectric materials*, Nat. Mater. **7**, 105 (2008), URL https://doi.org/10.1038/nmat2090.

[66] J. Schulenborg, A. D. Marco, J. Vanherck, M. R. Wegewijs, and J. Splettstoesser, *Thermoelectrics of interacting nanosystems—exploiting superselection instead of time-reversal symmetry*, Entropy **19** (2017), URL https://doi.org/10.3390/e19120668. 33

[67] X. Zianni, *Coulomb oscillations in the electron thermal conductance of a dot in the linear regime*, Phys. Rev. B **75**, 045344 (2007), URL https://doi.org/10.1103/PhysRevB.75.045344. 33, 42, 45, 46, 65

[68] X. Zianni, *Theory of the energy-spectrum dependence of the electronic thermoelectric tunneling coefficients of a quantum dot*, Phys. Rev. B **78**, 165327 (2008), URL https://doi.org/10.1103/PhysRevB.78.165327. 33, 61, 65, 66, 71

[69] C. W. J. Beenakker, *Theory of coulomb-blockade oscillations in the conductance of a quantum dot*, Phys. Rev. B **44**, 1646 (1991), URL https://doi.org/10.1103/PhysRevB.44.1646. 34, 36, 39, 41, 42, 62, 66, 69, 117

[70] C. W. J. Beenakker and A. A. M. Staring, *Theory of the thermopower of a quantum dot*, Phys. Rev. B **46**, 9667 (1992), URL https://doi.org/10.1103/PhysRevB.46.9667. 33, 34, 36, 41, 42, 44, 45, 46, 55, 62, 65, 69, 73, 76, 166, 168

[71] T. Rejec, R. Žitko, J. Mravlje, and A. Ramšak, *Spin thermopower in interacting quantum dots*, Phys. Rev. B **85**, 085117 (2012), URL https://doi.org/10.1103/PhysRevB.85.085117.

[72] B. Muralidharan and M. Grifoni, *Thermoelectric spin accumulation and long-time spin precession in a noncollinear quantum dot spin valve*, Phys. Rev. B **88**, 045402 (2013), URL https://doi.org/10.1103/PhysRevB.88.045402.

[73] P. A. Jacquet, *Thermoelectric transport properties of a chain of quantum dots with self-consistent reservoirs*, J. Stat. Phys. **134**, 709 (2009), URL https://doi.org/10.1007/s10955-009-9697-1.

[74] O. Entin-Wohlman and A. Aharony, *Three-terminal thermoelectric transport under broken time-reversal symmetry*, Phys. Rev. B **85**, 085401 (2012), URL https://doi.org/10.1103/PhysRevB.85.085401. 65

[75] R. Sánchez, B. Sothmann, A. N. Jordan, and M. Büttiker, *Correlations of heat and charge currents in quantum-dot thermoelectric engines*, New J. Phys. **15**, 125001 (2013), URL https://doi.org/10.1088/1367-2630/15/12/125001. 73

[76] D. M. Kennes and V. Meden, *Interacting resonant-level model in nonequilibrium: Finite-temperature effects*, Phys. Rev. B **87**, 075130 (2013), URL https://doi.org/10.1103/PhysRevB.87.075130. 65

[77] G. Billings, A. D. Stone, and Y. Alhassid, *Signatures of exchange correlations in the thermopower of quantum dots*, Phys. Rev. B **81**, 205303 (2010), URL https://doi.org/10.1103/PhysRevB.81.205303.

[78] B. Kubala and J. König, *Quantum-fluctuation effects on the thermopower of a single-electron transistor*, Phys. Rev. B **73**, 195316 (2006), URL https://doi.org/10.1103/PhysRevB.73.195316. 73

[79] J. Koch, F. von Oppen, Y. Oreg, and E. Sela, *Thermopower of single-molecule devices*, Phys. Rev. B **70**, 195107 (2004), URL https://doi.org/10.1103/PhysRevB.70.195107. 75, 172

[80] A. V. Andreev and K. A. Matveev, *Coulomb blockade oscillations in the thermopower of open quantum dots*, Phys. Rev. Lett. **86**, 280 (2001), URL https://doi.org/10.1103/PhysRevLett.86.280. 73

[81] P. Dutt and K. L. Hur, *Strongly correlated thermoelectric transport beyond linear response*, Phys. Rev. B **88**, 235133 (2013), URL https://doi.org/10.1103/PhysRevB.88.235133. 73

[82] T. A. Costi and V. Zlatić, *Thermoelectric transport through strongly correlated quantum dots*, Phys. Rev. B **81**, 235127 (2010), URL https://doi.org/10.1103/PhysRevB.81.235127.

[83] M. Turek and K. A. Matveev, *Cotunneling thermopower of single electron transistors*, Phys. Rev. B **65**, 115332 (2002), URL https://doi.org/10.1103/PhysRevB.65.115332. 73, 75, 76, 105, 172

[84] D. Boese and R. Fazio, *Thermoelectric effects in kondo-correlated quantum dots*, Europhys. Lett. **56**, 576 (2001), URL https://doi.org/10.1209/epl/i2001-00559-8. 73

[85] B. Kubala, J. König, and J. Pekola, *Violation of the wiedemann-franz law in a single-electron transistor*, Phys. Rev. Lett **100**, 066801 (2008), URL https://doi.org/10.1103/PhysRevLett.100.066801. 73

[86] P. Mani, N. Nakpathomkun, E. A. Hoffmann, and H. Linke, *A nanoscale standard for the seebeck coefficient*, Nano Lett. **11**, 4679 (2011), URL https://doi.org/10.1021/nl202258f. 65

[87] R. López and D. Sánchez, *Nonlinear heat transport in mesoscopic conductors: Rectification, peltier effect, and wiedemann-franz law*, Phys. Rev. B **88**, 045129 (2013), URL https://doi.org/10.1103/PhysRevB.88.045129. 73

[88] M. A. Sierra and D. Sánchez, *Strongly nonlinear thermovoltage and heat dissipation in interacting quantum dots*, Phys. Rev. B **90**, 115313 (2014), URL https://doi.org/10.1103/PhysRevB.90.115313.

[89] N. A. Zimbovskaya, *The effect of coulomb interactions on nonlinear thermovoltage and thermocurrent in quantum dots*, J. Chem. Phys. **142**, 244310 (2016), URL https://doi.org/10.1063/1.4922907.

[90] J. Schulenborg, M. R. Wegewijs, and J. Splettstoesser, *Thermovoltage in quantum dots with attractive interaction*, Appl. Phys. Lett. **116**, 243103 (2020), URL https://doi.org/10.1063/5.0008866. 33, 65, 73

[91] I. Weymann and J. Barnaś, *Spin thermoelectric effects in kondo quantum dots coupled to ferromagnetic leads*, Phys. Rev. B **88**, 085313 (2013), URL https://doi.org/10.1103/PhysRevB.88.085313. 33

[92] S. Donsa, S. Andergassen, and K. Held, *Double quantum dot as a minimal thermoelectric generator*, Phys. Rev. B **89**, 125103 (2014), URL https://doi.org/10.1103/PhysRevB.89.125103. 33

[93] B. Sothmann and M. Büttiker, *Magnon-driven quantum-dot heat engine*, Europhys. Lett. **99**, 27001 (2012), URL https://doi.org/10.1209/0295-5075/99/27001. 34

[94] Y.-S. Liu, D.-B. Zhang, X.-F. Yang, and J.-F. Feng, *The role of coulomb interaction in thermoelectric effects of an aharonov–bohm interferometer*, Nanotechnology **22**, 225201 (2011), URL https://doi.org/10.1088/0957-4484/22/22/225201. 33

[95] D. M.-T. Kuo and Y.-C. Chang, *Thermoelectric properties of a quantum dot array connected to metallic electrodes*, Nanotechnology **24**, 175403 (2013), URL https://doi.org/10.1088/0957-4484/24/17/175403. 33

[96] D. M.-T. Kuo and Y.-C. Chang, *Thermoelectric and thermal rectification properties of quantum dot junctions*, Phys. Rev. B **81**, 205321 (2010), URL https://doi.org/10.1103/PhysRevB.81.205321. 33, 34, 73, 93, 94

[97] M. Wierzbicki and R. Świrkowicz, *Enhancement of thermoelectric efficiency in a two-level molecule*, J. Phys.: Condens. Matter **22**, 185302 (2010), URL https://doi.org/10.1088/0953-8984/22/18/185302. 33

[98] G. Rosselló, R. López, and R. Sánchez, *Dynamical coulomb blockade of thermal transport*, Phys. Rev. B **95**, 235404 (2017), URL https://doi.org/10.1103/PhysRevB.95.235404. 33

[99] C. A. Perroni, D. Ninno, and V. Cataudella, *Thermoelectric efficiency of molecular junctions*, J. Phys.: Condens. Matter **28**, 373001 (2016), URL https://doi.org/10.1088/0953-8984/28/37/373001. 34

[100] B. Szukiewicz, U. Eckern, and K. I. Wysokiński, *Optimisation of a three-terminal nonlinear heat nano-engine*, New J. Phys. **18**, 023050 (2016), URL https://doi.org/10.1088/1367-2630/18/2/023050. 34

[101] F. Mazza, R. Bosisio, G. Benenti, V. Giovannetti, R. Fazio, and F. Taddei, *Thermoelectric efficiency of three-terminal quantum thermal machines*, New J. Phys. **16**, 085001 (2014), URL https://doi.org/10.1088/1367-2630/16/8/085001. 33, 40, 42, 43, 51, 69

[102] D. M. T. Kuo, C.-C. Chen, and Y.-C. Chang, *Large enhancement in thermoelectric efficiency of quantum dot junctions due to increase of level degeneracy*, Phys. Rev. B **95**, 075432 (2017), URL https://doi.org/10.1103/PhysRevB.95.075432. 62

[103] M. Krawiec and K. I. Wysokiński, *Thermoelectric effects in strongly interacting quantum dot coupled to ferromagnetic leads*, Phys. Rev. B **73**, 075307 (2006), URL https://doi.org/10.1103/PhysRevB.73.075307.

[104] P. Murphy, S. Mukerjee, and J. Moore, *Optimal thermoelectric figure of merit of a molecular junction*, Phys. Rev. B **78**, 161406(R) (2008), URL https://doi.org/10.1103/PhysRevB.78.161406. 69

[105] D. M.-T. Kuo, *Thermoelectric properties of multiple quantum dots junction system*, Jap. J. App. Phys. **48**, 125005 (2009), URL https://doi.org/10.1143/JJAP.48.125005.

[106] Y. Dubi and M. D. Ventra, *Thermospin effects in a quantum dot connected to ferromagnetic leads*, Phys. Rev. B **79**, 081302(R) (2009), URL https://doi.org/10.1103/PhysRevB.79.081302.

[107] O. Entin-Wohlman, Y. Imry, and A. Aharony, *Three-terminal thermoelectric transport through a molecular junction*, Phys. Rev. B **82**, 115314 (2010), URL https://doi.org/10.1103/PhysRevB.82.115314. 69

[108] O. Karlström, H. Linke, G. Karlström, and A. Wacker, *Increasing thermoelectric performance using coherent transport*, Phys. Rev. B **84**, 113415 (2011), URL https://doi.org/10.1103/PhysRevB.84.113415. 65

[109] P. Trocha and J. Barnaś, *Large enhancement of thermoelectric effects in a double quantum dot system due to interference and coulomb correlation phenomena*, Phys. Rev. B **85**, 085408 (2012), URL https://doi.org/10.1103/PhysRevB.85.085408. 65, 69

[110] Y.-C. Tseng, D. M.-T. Kuo, Y.-C. Chang, and C.-W. Tsai, *Thermoelectric effects of quantum dot arrays embedded in nanowires*, https://arxiv.org/abs/1504.06082 (2015).

[111] E. Taylor and D. Segal, *Thermoelectric performance of strongly correlated quantum impurity models*, Phys. Rev. B **92**, 125401 (2015), URL https://doi.org/10.1103/PhysRevB.92.125401. 33

[112] M. Esposito, K. Lindenberg, and C. V. den Broeck, *Thermoelectric efficiency at maximum power in a quantum dot*, Eurphys. Lett. **85**, 60010 (2009), URL https://doi.org/10.1209/0295-5075/85/60010. 34, 69, 114, 117, 140, 158, 159, 160

[113] R. Świrkowicz, M. Wierzbicki, and J. Barnaś, *Thermoelectric effects in transport through quantum dots attached to ferromagnetic leads with noncollinear magnetic moments*, Phys. Rev. B **80**, 195409 (2009), URL https://doi.org/10.1103/PhysRevB.80.195409. 73

[114] M. Leijnse, M. R. Wegewijs, and K. Flensberg, *Nonlinear thermoelectric properties of molecular junctions with vibrational coupling*, Phys. Rev. B **82**, 045412 (2010), URL https://doi.org/10.1103/PhysRevB.82.045412.

[115] N. Nakpathomkun, H. Q. Xu, and H. Linke, *Thermoelectric efficiency at maximum power in low-dimensional systems*, Phys. Rev. B **82**, 235428 (2010), URL https://doi.org/10.1103/PhysRevB.82.235428. 69

[116] R. Sánchez and M. Büttiker, *Optimal energy quanta to current conversion*, Phys. Rev. B **83**, 085428 (2011), URL https://doi.org/10.1103/PhysRevB.83.085428. 65, 69, 84, 86

[117] B. Muralidharan and M. Grifoni, *Performance analysis of an interacting quantum dot thermoelectric setup*, Phys. Rev. B **85**, 155423 (2012), URL https://doi.org/10.1103/PhysRevB.85.155423.

[118] A. N. Jordan, B. Sothmann, R. Sánchez, and M. Büttiker, *Powerful and efficient energy harvester with resonant-tunneling quantum dots*, Phys. Rev. B **87**, 075312 (2013), URL https://doi.org/10.1103/PhysRevB.87.075312. 65, 69

[119] B. De and B. Muralidharan, *Thermoelectric study of dissipative quantum-dot heat engines*, Phys. Rev. B **94**, 165416 (2016), URL https://doi.org/10.1103/PhysRevB.94.165416. 33

[120] A. Agarwal and B. Muralidharan, *Power and efficiency analysis of a realistic resonant tunneling diode thermoelectric*, Appl. Phys. Lett. **105**, 013104 (2014), URL https://doi.org/10.1063/1.4888859. 33, 34

[121] X. Zianni, *Effect of electron-phonon coupling on the thermoelectric efficiency of single-quantum-dot devices*, Phys. Rev. B **82**, 165302 (2010), URL https://doi.org/10.1103/PhysRevB.82.165302. 33, 65

[122] J. Liu, Q. F. Sun, and X. C. Xie, *Enhancement of the thermoelectric figure of merit in a quantum dot due to the coulomb blockade effect*, Phys. Rev. B **81**, 245323 (2010), URL https://doi.org/10.1103/PhysRevB.81.245323. 33

[123] B. Sothmann, R. Sánchez, and A. N. Jordan, *Thermoelectric energy harvesting with quantum dots*, Nanotechnology **26**, 032001 (2015), URL https://doi.org/10.1088/0957-4484/26/3/032001. 33, 65

[124] D. Prete, P. A. Erdman, V. Demontis, V. Zannier, D. Ercolani, L. Sorba, F. Beltram, F. Rossella, F. Taddei, and S. Roddaro, *Thermoelectric conversion at 30 k in inas/inp nanowire quantum dots*, Nano Lett. **19**, 3033 (2019), URL https://doi.org/10.1021/acs.nanolett.9b00276. 33, 113, 114, 123, 140

[125] M. C. Llaguno, J. E. Fischer, A. T. Johnson, and J. Hone, *Observation of thermopower oscillations in the coulomb blockade regime in a semiconducting carbon nanotube*, Nano Lett. **4**, 45 (2003), URL https://doi.org/10.1021/nl0348488. 73

[126] H. Thierschmann, M. Henke, J. Knorr, L. Maier, C. Heyn, W. Hansen, H. Buhmann, and L. W. Molenkamp, *Diffusion thermopower of a serial double quantum dot*, New J. Phys. **15**, 123010 (2013), URL https://doi.org/10.1088/1367-2630/15/12/123010.

[127] R. Scheibner, E. G. Novik, T. Borzenko, M. König, D. Reuter, H. B. A. D. Wieck, and L. W. Molenkamp, *Sequential and cotunneling behavior in the temperature-dependent thermopower of few-electron quantum dots*, Phys. Rev. B **75**, 041301(R) (2007), URL https://doi.org/10.1103/PhysRevB.75.041301. 65, 73

[128] S. F. Godijn, S. Möller, H. Buhmann, L. W. Molenkamp, and S. A. van Langen, *Thermopower of a chaotic quantum dot*, Phys. Rev. Lett. **82**, 2927 (1999), URL https://doi.org/10.1103/PhysRevLett.82.2927. 73

[129] P. Reddy, S.-Y. Jang, R. A. Segalman, and A. Majumdar, *Thermoelectricity in molecular junctions*, Science **315**, 1568 (2007), URL https://doi.org/10.1126/science.1137149.

[130] A. S. Dzurak, C. G. Smith, C. H. W. Barnes, M. Pepper, L. Martín-Moreno, C. T. Liang, D. A. Ritchie, and G. A. C. Jones, *Thermopower measurements of semiconductor quantum dots*, Physica B Condens. Matter **249-251**, 281 (1998), URL https://doi.org/10.1016/S0921-4526(98)00115-X. 65

[131] A. Svilans, A. M. Burke, S. F. Svensson, M. Leijnse, and H. Linke, *Nonlinear thermoelectric response due to energy-dependent transport properties of a quantum dot*, Physica E Low Dimens. Syst. Nanostruct. **82**, 34 (2016), URL https://doi.org/10.1016/j.physe.2015.10.007. 65

[132] S. F. Svensson, A. I. Persson, E. A. Hoffmann, N. Nakpathomkun, H. A. Nilsson, H. Q. Xu, L. Samuelson, and H. Linke, *Lineshape of the thermopower of quantum dots*, New J. Phys. **14**, 033041 (2012), URL https://doi.org/10.1088/1367-2630/14/3/033041. 65, 66, 73

[133] A. Svilans, M. Leijnse, and H. Linke, *Experiments on the thermoelectric properties of quantum dots*, C. R. Phys. **17**, 1096 (2016), URL https://doi.org/10.1016/j.crhy.2016.08.002.

[134] R. Scheibner, H. Buhmann, D. Reuter, M. N. Kiselev, and L. W. Molenkamp, *Thermopower of a kondo spin-correlated quantum dot*, Phys. Rev. Lett. **95**, 176602 (2005), URL https://doi.org/10.1103/PhysRevLett.95.176602. 73

[135] A. S. Dzurak, C. G. Smith, M. Pepper, D. A. Ritchie, J. E. F. Frost, G. A. C. Jones, and D. G. Hasko, *Observation of coulomb blockade oscillations in the thermopower of a quantum dot*, Solid State Commun. **87**, 1145 (1993), URL https://doi.org/10.1016/0038-1098(93)90819-9. 65, 73

[136] T. C. Harman, P. J. Taylor, M. P. Walsh, and B. E. LaForge, *Quantum dot superlattice thermoelectric materials and devices*, Science **297**, 2229 (2002), URL https://doi.org/10.1126/science.1072886.

[137] L. W. Molenkamp, T. Gravier, H. van Houten, O. J. A. Buijk, M. A. A. Mabesoone, and C. T. Foxon, *Peltier coefficient and thermal conductance of a quantum point contact*, Phys. Rev. Lett. **68**, 3765 (1992), URL https://doi.org/10.1103/PhysRevLett.68.3765. 73

[138] A. A. M. Staring, L. W. Molenkamp, B. W. Alphenaar, H. van Houten, O. J. A. Buyk, M. A. A. Mabesoone, C. W. J. Beenakker, and C. T. Foxon, *Coulomb-blockade oscillations in the thermopower of a quantum dot*, Europhys. Lett. **22**, 57 (1993), URL https://doi.org/10.1209/0295-5075/22/1/011. 65, 73

[139] A. G. Pogosov, M. V. Budantsev, R. A. Lavrov, A. E. Plotnikov, A. K. Bakarov, A. I. Toropov, and J. C. Portal, *Coulomb blockade and the thermopower of a suspended quantum dot*, JETP Lett. **83**, 122 (2006), URL https://doi.org/10.1134/S002136400603009X. 73

[140] R. Scheibner, M. König, D. Reuter, A. D. Wieck, C. Gould, H. Buhmann, and L. W. Molenkamp, *Quantum dot as thermal rectifier*, New J. Phys. **10**, 083016 (2008), URL https://doi.org/10.1088/1367-2630/10/8/083016. 93

[141] S. F. Svensson, E. A. Hoffmann, N. Nakpathomkun, P. M. Wu, H. Q. Xu, H. A. Nilsson, D. Sánchez, V. Kashcheyevs, and H. Linke, *Nonlinear thermovoltage and thermocurrent in quantum dots*, New J. Phys. **15**, 105011 (2013), URL https://doi.org/10.1088/1367-2630/15/10/105011. 65, 66, 73

[142] J. Matthews, F. Battista, D. Sánchez, P. Samuelsson, and H. Linke, *Experimental verification of reciprocity relations in quantum thermoelectric transport*, Phys. Rev. B **90**, 165428 (2014), URL https://doi.org/10.1103/PhysRevB.90.165428.

[143] B. Roche, P. Roulleau, T. Jullien, Y. Jompol, I. Farrer, and D. A. Ritchie, *Harvesting dissipated energy with a mesoscopic ratchet*, Nat. Commun. **6**, 6738 (2015), URL https://doi.org/10.1038/ncomms7738.

[144] F. Hartmann, P. Pfeffer, S. Höfling, M. Kamp, and L. Worschech, *Voltage fluctuation to current converter with coulomb-coupled quantum dots*, Phys. Rev. Lett. **114**, 146805 (2015), URL https://doi.org/10.1103/PhysRevLett.114.146805. 82

[145] H. Thierschmann, R. Sánchez, B. Sothmann, F. Arnold, C. Heyn, W. Hansen, H. Buhmann, and L. W. Molenkamp, *Three-terminal energy harvester with coupled quantum dots*, Nat. Nanotechnol. **10**, 854 (2015), URL https://doi.org/10.1038/nnano.2015.176. 33, 82

[146] J. Yvon, *Proceedings of the International Conference on Peaceful Uses of Atomic Energy* (United Nations, New York, 1955). 34, 40

[147] J. Meair and P. Jacquod, *Scattering theory of nonlinear thermoelectricity in quantum coherent conductors*, J. Phys. Condens. Matter **25**, 082201 (2013), URL https://doi.org/10.1088/0953-8984/25/8/082201. 34

[148] R. S. Whitney, *Thermodynamic and quantum bounds on nonlinear dc thermoelectric transport*, Phys. Rev. B **87**, 115404 (2013), URL https://doi.org/10.1103/PhysRevB.87.115404.

[149] D. Sánchez and R. López, *Scattering theory of nonlinear thermoelectric transport*, Phys. Rev. Lett. **110**, 026804 (2013), URL https://doi.org/10.1103/PhysRevLett.110.026804. 34

[150] P. A. Erdman, *Thermoelectric efficiency of a multilevel interacting quantum dot*, https://etd.adm.unipi.it/theses/available/etd-06272016-190534/ (2016). 43, 44

[151] T. E. Humphrey, R. Newbury, R. P. Taylor, and H. Linke, *Reversible quantum brownian heat engines for electrons*, Phys. Rev. Lett. **89**, 116801 (2002), URL https://doi.org/10.1103/PhysRevLett.89.116801. 44, 157

[152] T. E. Humphrey and H. Linke, *Reversible thermoelectric nanomaterials*, Phys. Rev. Lett. **94**, 096601 (2005), URL https://doi.org/10.1103/PhysRevLett.94.096601. 44, 157

[153] M. Tsaousidou and G. P. Triberis, *Thermoelectric properties of a weakly coupled quantum dot: enhanced thermoelectric efficiency*, J. Phys.: Condens. Matter **22**, 355304 (2010), URL https://doi.org/10.1088/0953-8984/22/35/355304. 48, 50

[154] R. S. Whitney, *Nonlinear thermoelectricity in point contacts at pinch off: A catastrophe aids cooling*, Phys. Rev. B **88**, 064302 (2013), URL https://doi.org/10.1103/PhysRevB.88.064302. 54

[155] G. Benenti, K. Saito, and G. Casati, *Thermodynamic bounds on efficiency for systems with broken time-reversal symmetry*, Phys. Rev. Lett. **106**, 230602 (2011), URL https://doi.org/10.1103/PhysRevLett.106.230602. 54

[156] V. Balachandran, G. Benenti, and G. Casati, *Efficiency of three-terminal thermoelectric transport under broken time-reversal symmetry*, Phys. Rev. B **87**, 165419 (2013), URL https://doi.org/10.1103/PhysRevB.87.165419.

[157] K. Brandner, K. Saito, and U. Seifert, *Strong bounds on onsager coefficients and efficiency for three-terminal thermoelectric transport in a magnetic field*, Phys. Rev. Lett. **110**, 070603 (2013), URL https://doi.org/10.1103/PhysRevLett.110.070603.

[158] K. Brandner and U. Seifert, *Multi-terminal thermoelectric transport in a magnetic field: bounds on onsager coefficients and efficiency*, New J. Phys. **15**, 105003 (2013), URL https://doi.org/10.1088/1367-2630/15/10/105003.

[159] K. Yamamoto, O. Entin-Wohlman, A. Aharony, and N. Hatano, *Efficiency bounds on thermoelectric transport in magnetic fields: The role of inelastic processes*, Phys. Rev. B **94**, 121402 (2016), URL https://doi.org/10.1103/PhysRevB.94.121402. 54

[160] L. H. W. van Beveren, R. Hanson, I. T. Vink, F. H. L. Koppens, L. P. Kouwenhoven, and L. M. K. Vandersypen, *Spin filling of a quantum dot derived from excited-state spectroscopy*, New J. Phys. **7**, 182 (2005), URL https://doi.org/10.1088/1367-2630/7/1/182. 55

[161] L. D. Hicks and M. S. Dresselhaus, *Effect of quantum-well structures on the thermoelectric figure of merit*, Phys. Rev. B **47**, 12727 (1993), URL https://doi.org/10.1103/PhysRevB.47.12727. 65

[162] L. Shi, *Thermal and thermoelectric transport in nanostructures and low-dimensional systems*, Nanoscale Microscale Thermophys. Eng. **16**, 79 (2012), URL https://doi.org/10.1080/15567265.2012.667514. 65

[163] E. A. Hoffmann, N. Nakpathomkun, A. I. Persson, H. Linke, H. A. Nilsson, and L. Samuelson, *Quantum-dot thermometry*, Appl. Phys. Lett. **91**, 252114 (2007), URL https://doi.org/10.1063/1.2826268. 65

[164] L. Molenkamp, A. A. M. Staring, B. W. Alphenaar, H. van Houten, and C. W. J. Beenakker, *Sawtooth-like thermopower oscillations of a quantum dot in the coulomb blockade regime*, Semicond. Sci. Technol. **9**, 903 (1994), URL http://stacks.iop.org/0268-1242/9/i=5S/a=136. 65, 73

[165] A. S. Dzurak, C. G. Smith, C. H. W. Barnes, M. Pepper, L. Martín-Moreno, C. T. Liang, D. A. Ritchie, and G. A. C. Jones, *Thermoelectric signature of the excitation spectrum of a quantum dot*, Phys. Rev. B **55**, 10197(R) (1997), URL https://doi.org/10.1103/PhysRevB.55.R10197. 73

[166] A. V. Feshchenko, J. V. Koski, and J. P. Pekola, *Experimental realization of a coulomb blockade refrigerator*, Phys. Rev. B **90**, 201407 (2014), URL https://doi.org/10.1103/PhysRevB.90.201407.

[167] B. Dutta, J. T. Peltonen, D. S. Antonenko, M. Meschke, M. A. Skvortsov, B. Kubala, J. König, C. B. Winkelmann, H. Courtois, and J. P. Pekola, *Thermal conductance of a single-electron transistor*, Phys. Rev. Lett. **119**, 077701 (2017), URL https://doi.org/10.1103/PhysRevLett.119.077701. 73, 75, 78, 90

[168] B. Dutta, D. Majidi, A. G. Corral, P. A. Erdman, S. Florens, T. A. Costi, H. Courtois, and C. B. Winkelmann, *Direct probe of the seebeck coefficient in a kondo-correlated single-quantum-dot transistor*, Nano Lett. **19**, 506 (2019), URL https://doi.org/10.1021/acs.nanolett.8b04398. 65, 73

[169] P. A. Erdman, F. Mazza, R. Bosisio, G. Benenti, R. Fazio, and F. Taddei, *Thermoelectric properties of an interacting quantum dot based heat engine*, Phys. Rev. B **95**, 245432 (2017), URL https://doi.org/10.1103/PhysRevB.95.245432. 65, 66, 69, 71, 73, 117, 123, 140, 166

[170] V. Blickle and C. Bechinger, *Realization of a micrometre-sized stochastic heat engine*, Nat. Phys. **8**, 143 (2012), URL https://doi.org/10.1038/nphys2163. 65

[171] J. Roßnagel, S. T. Dawkins, K. N. Tolazzi, O. Abah, E. Lutz, F. Schmidt-Kaler, and K. Singer, *A single-atom heat engine*, Science **352**, 325 (2016), URL https://doi.org/10.1126/science.aad6320. 65, 113, 123

[172] M. T. Björk, C. Thelander, A. E. Hansen, L. E. Jensen, M. W. Larsson, L. R. Wallenberg, and L. Samuelson, *Few-electron quantum dots in nanowires*, Nano Lett. **4**, 1621 (2004), URL https://doi.org/10.1021/nl049230s. 65

[173] L. Romeo, S. Roddaro, A. Pitanti, D. Ercolani, L. Sorba, and F. Beltram, *Electrostatic spin control in InAs/InP nanowire quantum dots*, Nano Lett. **12**, 4490 (2012), URL https://doi.org/10.1021/nl301497j.

[174] F. Rossella, A. Bertoni, D. Ercolani, M. Rontani, L. Sorba, F. Beltram, and S. Roddaro, *Nanoscale spin rectifiers controlled by the stark effect*, Nat. Nanotechnol. **9**, 997 (2014), URL https://doi.org/10.1038/nnano.2014.251. 65

[175] V. Zannier, F. Rossi, D. Ercolani, and L. Sorba, *Growth dynamics of InAs/InP nanowire heterostructures by au-assisted chemical beam epitaxy*, Nanotechnology **30**, 094003 (2019), URL https://doi.org/10.1088/1361-6528/aaf7ab. 67, 161

[176] S. Roddaro, A. Pescaglini, D. Ercolani, L. Sorba, and F. Beltram, *Manipulation of electron orbitals in hard-wall inas/inp nanowire quantum dots*, Nano Lett. **11**, 1695 (2011), URL https://doi.org/10.1021/nl200209m. 67

[177] D. V. Averin and Y. V. Nazarov, *Single Charge Tunneling* (Springer US, 1992). 69

[178] E. A. Hoffmann, H. A. Nilsson, J. E. Matthews, N. Nakpathomkun, A. I. Persson, L. Samuelson, and H. Linke, *Measuring temperature gradients over nanometer length scales*, Nano Lett. **9**, 779 (2009), URL https://doi.org/10.1021/nl8034042. 69, 73

[179] P. A. Erdman, B. Bhandari, R. Fazio, J. P. Pekola, and F. Taddei, *Absorption refrigerators based on coulomb-coupled single-electron systems*, Phys. Rev. B **98**, 045433 (2018), URL https://doi.org/10.1103/PhysRevB.98.045433. 69

[180] S. Limpert, S. Bremner, and H. Linke, *Reversible electron–hole separation in a hot carrier solar cell*, New J. Phys. **17**, 095004 (2015), URL https://doi.org/10.1088/1367-2630/17/9/095004. 72

[181] S. Limpert, A. Burke, I.-J. Chen, N. Anttu, S. Lehmann, S. Fahlvik, S. Bremner, G. Conibeer, C. Thelander, M.-E. Pistol, and H. Linke, *Single-nanowire, low-bandgap hot carrier solar cells with tunable open-circuit voltage*, Nanotechnology **28**, 434001 (2017), URL https://doi.org/10.1088/1361-6528/aa8984. 72

[182] K. Schwab, E. Henriksen, J. Worlock, and M. L. Roukes, *Measurement of the quantum of thermal conductance*, Nature **404**, 974 (2000), URL https://doi.org/10.1038/35010065. 73

[183] O. Chiatti, J. T. Nicholls, Y. Y. Proskuryakov, N. Lumpkin, I. Farrer, and D. A. Ritchie, *Quantum thermal conductance of electrons in a one-dimensional wire*, Phys. Rev. Lett. **97**, 056601 (2006), URL https://doi.org/10.1103/PhysRevLett.97.056601.

[184] M. Meschke, W. Guichard, and J. P. Pekola, *Single-mode heat conduction by photons*, Nature **444**, 187 (2006), URL https://doi.org/10.1038/nature05276.

[185] S. Jezouin, F. D. Parmentier, A. Anthore, U. Gennser, A. Cavanna, Y. Jin, and F. Pierre, *Quantum limit of heat flow across a single electronic channel*, Science **342**, 601 (2013), URL https://doi.org/10.1126/science.1241912.

[186] M. Banerjee, M. Heiblum, A. Rosenblatt, Y. Oreg, D. E. Feldman, A. Stern, and V. Umansky, *Observed quantization of anyonic heat flow*, Nature **545**, 75 (2017), URL https://doi.org/10.1038/nature22052.

[187] L. Cui, W. Jeong, S. Hur, M. Matt, J. C. Klöckner, F. Pauly, P. Nielaba, J. C. Cuevas, E. Meyhofer, and P. Reddy, *Quantized thermal transport in single-atom junctions*, Science **355**, 1192 (2017), URL https://doi.org/10.1126/science.aam6622.

[188] N. Mosso, U. Drechsler, F. Menges, P. Nirmalraj, S. Karg, H. Riel, and B. Gotsmann, *Heat transport through atomic contacts*, Nat. Nanotechnol. **12**, 430 (2017), URL https://doi.org/10.1038/nnano.2016.302. 73

[189] S. Roddaro, D. Ercolani, M. A. Safeen, S. Suomalainen, F. Rossella, F. Giazotto, L. Sorba, and F. Beltram, *Giant thermovoltage in single inas nanowire field-effect transistors*, Nano Lett. **13**, 3638 (2013), URL https://doi.org/10.1021/nl401482p. 73

[190] P. M. Wu, J. Gooth, X. Zianni, S. F. Svensson, J. G. Gluschke, K. A. Dick, C. Thelander, K. Nielsch, and H. Linke, *Large thermoelectric power factor enhancement observed in inas nanowires*, Nano Lett. **13**, 4080 (2013), URL https://doi.org/10.1021/nl401501j. 73

[191] S. Möller, H. Buhmann, S. F. Godijn, and L. W. Molenkamp, *Charging energy of a chaotic quantum dot*, Phys. Rev. Lett. **81**, 5197 (1998), URL https://doi.org/10.1103/PhysRevLett.81.5197. 73

[192] A. S. Vasenko, D. M. Basko, and F. W. J. Hekking, *Giant mesoscopic fluctuations of the elastic cotunneling thermopower of a single-electron transistor*, Phys. Rev. B **91**, 085310 (2015), URL https://doi.org/10.1103/PhysRevB.91.085310. 73, 75

[193] D. Pérez Daroca, P. Roura-Bas, and A. A. Aligia, *Enhancing the nonlinear thermoelectric response of a correlated quantum dot in the kondo regime by asymmetrical coupling to the leads*, Phys. Rev. B **97**, 165433 (2018), URL https://doi.org/10.1103/PhysRevB.97.165433. 73

[194] D. V. Averin and K. K. Likharev, *Mesoscopic Phenomena in Solids* (North-Holland, Amsterdam, 1991). 75

[195] J. P. Pekola and F. W. J. Hekking, *Normal-metal-superconductor tunnel junction as a brownian refrigerator*, Phys. Rev. Lett. **98**, 210604 (2007), URL https://doi.org/10.1103/PhysRevLett.98.210604. 81

[196] N. Linden, S. Popescu, and P. Skrzypczyk, *How small can thermal machines be? the smallest possible refrigerator*, Phys. Rev. Lett. **105**, 130401 (2010), URL https://doi.org/10.1103/PhysRevLett.105.130401. 81

[197] P. Skrzypczyk, N. Brunner, N. Linden, and S. Popescu, *The smallest refrigerators can reach maximal efficiency*, J. Phys. A **44**, 492002 (2011), URL https://doi.org/10.1088/1751-8113/44/49/492002. 81

[198] N. Brunner, N. Linden, S. Popescu, and P. Skrzypczyk, *Virtual qubits, virtual temperatures, and the foundations of thermodynamics*, Phys. Rev. E **85**, 051117 (2012), URL https://doi.org/10.1103/PhysRevE.85.051117. 81

[199] B. Cleuren, B. Rutten, and C. Van den Broeck, *Cooling by heating: Refrigeration powered by photons*, Phys. Rev. Lett. **108**, 120603 (2012), URL https://doi.org/10.1103/PhysRevLett.108.120603. 81

[200] R. Kosloff and A. Levy, *Quantum heat engines and refrigerators: Continuous devices*, Annu. Rev. Phys. Chem. **65**, 365 (2014), URL https://doi.org/10.1146/annurev-physchem-040513-103724. 113, 123

[201] N. Brunner, M. Huber, N. Linden, S. Popescu, R. Silva, and P. Skrzypczyk, *Entanglement enhances cooling in microscopic quantum refrigerators*, Phys. Rev. E **89**, 032115 (2014), URL https://doi.org/10.1103/PhysRevE.89.032115. 81, 113, 123

[202] L. A. Correa, J. P. Palao, D. Alonso, and G. Adesso, *Quantum-enhanced absorption refrigerators*, Sci. Rep. **4**, 03949 (2014), URL https://doi.org/10.1038/srep03949. 81

[203] L. A. Correa, *Multistage quantum absorption heat pumps*, Phys. Rev. E **89**, 042128 (2014), URL https://doi.org/10.1103/PhysRevE.89.042128.

[204] L. A. Correa, J. P. Palao, G. Adesso, and D. Alonso, *Optimal performance of endoreversible quantum refrigerators*, Phys. Rev. E **90**, 062124 (2014), URL https://doi.org/10.1103/PhysRevE.90.062124.

[205] D. Gelbwaser-Klimovsky and G. Kurizki, *Heat-machine control by quantum-state preparation: From quantum engines to refrigerators*, Phys. Rev. E **90**, 022102 (2014), URL https://doi.org/10.1103/PhysRevE.90.022102. 81

[206] J. B. Brask and N. Brunner, *Small quantum absorption refrigerator in the transient regime: Time scales, enhanced cooling, and entanglement*, Phys. Rev. E **92**, 062101 (2015), URL https://doi.org/10.1103/PhysRevE.92.062101.

[207] M. T. Mitchison, M. P. Woods, J. Prior, and M. Huber, *Coherence-assisted single-shot cooling by quantum absorption refrigerators*, New J. Phys. **17**, 115013 (2015), URL https://doi.org/10.1088/1367-2630/17/11/115013. 81

[208] R. Silva, P. Skrzypczyk, and N. Brunner, *Small quantum absorption refrigerator with reversed couplings*, Phys. Rev. E **92**, 012136 (2015), URL https://doi.org/10.1103/PhysRevE.92.012136.

[209] P. Doyeux, B. Leggio, R. Messina, and M. Antezza, *Quantum thermal machine acting on a many-body quantum system: Role of correlations in thermodynamic tasks*, Phys. Rev. E **93**, 022134 (2016), URL https://doi.org/10.1103/PhysRevE.93.022134. 81

[210] R. Silva, G. Manzano, P. Skrzypczyk, and N. Brunner, *Performance of autonomous quantum thermal machines: Hilbert space dimension as a thermodynamical resource*, Phys. Rev. E **94**, 032120 (2016), URL https://doi.org/10.1103/PhysRevE.94.032120.

[211] Z.-c. He, X.-y. Huang, and C.-s. Yu, *Enabling the self-contained refrigerator to work beyond its limits by filtering the reservoirs*, Phys. Rev. E **96**, 052126 (2017), URL https://doi.org/10.1103/PhysRevE.96.052126.

[212] G. Marchegiani, P. Virtanen, and F. Giazotto, *On-chip cooling by heating with superconducting tunnel junctions*, Europhys. Lett. **124**, 48005 (2018), URL https://doi.org/10.1209/0295-5075/124/48005. 81

[213] Y.-X. Chen and S.-W. Li, *Quantum refrigerator driven by current noise*, Europhys. Lett. **97**, 40003 (2012), URL https://doi.org/10.1209/0295-5075/97/40003. 81

[214] A. Mari and J. Eisert, *Cooling by heating: Very hot thermal light can significantly cool quantum systems*, Phys. Rev. Lett. **108**, 120602 (2012), URL https://doi.org/10.1103/PhysRevLett.108.120602.

[215] D. Venturelli, R. Fazio, and V. Giovannetti, *Minimal self-contained quantum refrigeration machine based on four quantum dots*, Phys. Rev. Lett. **110**, 256801 (2013), URL https://doi.org/10.1103/PhysRevLett.110.256801.

[216] B. Leggio, B. Bellomo, and M. Antezza, *Quantum thermal machines with single nonequilibrium environments*, Phys. Rev. A **91**, 012117 (2015), URL https://doi.org/10.1103/PhysRevA.91.012117.

[217] P. P. Hofer, M. Perarnau-Llobet, J. B. Brask, R. Silva, M. Huber, and N. Brunner, *Autonomous quantum refrigerator in a circuit qed architecture based on a josephson junction*, Phys. Rev. B **94**, 235420 (2016), URL https://doi.org/10.1103/PhysRevB.94.235420.

[218] M. T. Mitchison, M. Huber, J. Prior, M. P. Woods, and M. B. Plenio, *Realising a quantum absorption refrigerator with an atom-cavity system*, Quantum Sci. Technol. **1**, 015001 (2016), URL https://doi.org/10.1088/2058-9565/1/1/015001.

[219] R. Sánchez, H. Thierschmann, and L. W. Molenkamp, *Single-electron thermal devices coupled to a mesoscopic gate*, New J. Phys. **19**, 113040 (2017), URL https://doi.org/10.1088/1367-2630/aa8b94. 81

[220] G. Maslennikov, S. Ding, R. Hablätzel, J. Gan, A. Roulet, S. Nimmrichter, J. Dai, V. Scarani, and D. Matsukevich, *Quantum absorption refrigerator with trapped ions*, Nat. Commun. **10**, 202 (2019), URL https://doi.org/10.1038/s41467-018-08090-0. 81

[221] P. Strasberg, G. Schaller, T. Brandes, and M. Esposito, *Thermodynamics of a physical model implementing a maxwell demon*, Phys. Rev. Lett. **110**, 040601 (2013), URL https://10.1103/PhysRevLett.110.040601. 81, 90

[222] J. M. Horowitz and M. Esposito, *Thermodynamics with continuous information flow*, Phys. Rev. X **4**, 031015 (2014), URL http://doi.org/10.1103/PhysRevX.4.031015. 90, 91

[223] J. V. Koski, V. F. Maisi, T. Sagawa, and J. P. Pekola, *Experimental observation of the role of mutual information in the nonequilibrium dynamics of a maxwell demon*, Phys. Rev. Lett. **113**, 030601 (2014), URL https://doi.org/10.1103/PhysRevLett.113.030601. 90

[224] Y. Zhang, G. Lin, and J. Chen, *Three-terminal quantum-dot refrigerators*, Phys. Rev. E **91**, 052118 (2015), URL https://doi.org/10.1103/PhysRevE.91.052118. 90

[225] J. V. Koski and J. P. Pekola, *Maxwell's demons realized in electronic circuits*, C. R. Phys. **17**, 1130 (2016), URL https://doi.org/10.1016/j.crhy.2016.08.011. 90

[226] A. Kutvonen, J. Koski, and T. Ala-Nissila, *Thermodynamics and efficiency of an autonomous on-chip maxwell's demon*, Sci. Rep. **6**, 21126 (2016), URL https://doi.org/10.1038/srep21126. 90, 91

[227] A. Kutvonen, T. Sagawa, and T. Ala-Nissila, *Thermodynamics of information exchange between two coupled quantum dots*, Phys. Rev. E **93**, 032147 (2016), URL https://doi.org/10.1103/PhysRevE.93.032147.

[228] D. V. Averin and J. P. Pekola, *Reversing the landauer's erasure: Single-electron maxwell's demon operating at the limit of thermodynamic efficiency*, Phys. Status Solidi B **254**, 1600677 (2017), URL https://doi.org/10.1002/pssb.201600677. 81, 90

[229] D. T. McClure, L. DiCarlo, Y. Zhang, H.-A. Engel, C. M. Marcus, M. P. Hanson, and A. C. Gossard, *Tunable noise cross correlations in a double quantum dot*, Phys. Rev. Lett. **98**, 056801 (2007), URL https://doi.org/10.1103/PhysRevLett.98.056801. 82

[230] G. Shinkai, T. Hayashi, T. Ota, K. Muraki, and T. Fujisawa, *Bidirectional current drag induced by two-electron cotunneling in coupled double quantum dots*, Appl. Phys. Express **2**, 081101 (2009), URL https://doi.org/10.1143/APEX.2.081101.

[231] G. Shinkai, T. Hayashi, T. Ota, and T. Fujisawa, *Correlated coherent oscillations in coupled semiconductor charge qubits*, Phys. Rev. Lett. **103**, 056802 (2009), URL https://doi.org/10.1103/PhysRevLett.103.056802.

[232] D. Bischoff, M. Eich, O. Zilberberg, C. Rössler, T. Ihn, and K. Ensslin, *Measurement back-action in stacked graphene quantum dots*, Nano Lett. **15**, 6003 (2015), URL https://doi.org/10.1021/acs.nanolett.5b02167.

[233] C. Volk, S. Engels, C. Neumann, and C. Stampfer, *Back action of graphene charge detectors on graphene and carbon nanotube quantum dots*, Phys. Status Solidi B **252**, 2461 (2015), URL https://doi.org/10.1002/pssb.201552445.

[234] A. J. Keller, J. S. Lim, D. Sánchez, R. López, S. Amasha, J. A. Katine, H. Shtrikman, and D. Goldhaber-Gordon, *Cotunneling drag effect in coulomb-coupled quantum dots*, Phys. Rev. Lett. **117**, 066602 (2016), URL https://doi.org/10.1103/PhysRevLett.117.066602. 88

[235] S. Singh, E. Roldán, I. Neri, I. M. Khaymovich, D. S. Golubev, V. F. Maisi, J. T. Peltonen, F. Jülicher, and J. P. Pekola, *Extreme reductions of entropy in an electronic double dot*, Phys. Rev. B **99**, 115422 (2019), URL https://doi.org/10.1103/PhysRevB.99.115422. 82

[236] S. A. Gurvitz, *Rate equations for quantum transport in multidot systems*, Phys. Rev. B **57**, 6602 (1998), URL https://doi.org/10.1103/PhysRevB.57.6602. 87, 176

[237] B. L. Hazelzet, M. R. Wegewijs, T. H. Stoof, and Y. V. Nazarov, *Coherent and incoherent pumping of electrons in double quantum dots*, Phys. Rev. B **63**, 165313 (2001), URL https://doi.org/10.1103/PhysRevB.63.165313.

[238] B. Dong, H. L. Cui, and X. L. Lei, *Quantum rate equations for electron transport through an interacting system in the sequential tunneling regime*, Phys. Rev. B **69**, 035324 (2004), URL https://doi.org/10.1103/PhysRevB.69.035324.

[239] D. Sztenkiel and R. Świrkowicz, *Electron transport through parallel double quantum dots with interdot correlations*, Phys. Status Solidi B **244**, 2543 (2007), URL https://doi.org/10.1002/pssb.200674623.

[240] B. Dong, X. L. Lei, and N. J. M. Horing, *First-order coherent resonant tunneling through an interacting coupled-quantum-dot interferometer: Generic quantum rate equations and current noise*, Phys. Rev. B **77**, 085309 (2008), URL https://doi.org/10.1103/PhysRevB.77.085309. 87, 176

[241] R. C. Dynes, V. Narayanamurti, and J. P. Garno, *Direct measurement of quasiparticle-lifetime broadening in a strong-coupled superconductor*, Phys. Rev. Lett. **41**, 1509 (1978), URL https://doi.org/10.1103/PhysRevLett.41.1509. 89

[242] J. P. Pekola, V. F. Maisi, S. Kafanov, N. Chekurov, A. Kemppinen, Y. A. Pashkin, O.-P. Saira, M. Möttönen, and J. S. Tsai, *Environment-assisted tunneling as an origin of the dynes density of states*, Phys. Rev. Lett. **105**, 026803 (2010), URL https://doi.org/10.1103/PhysRevLett.105.026803. 89

[243] H. S. Leff and A. F. Rex, *Maxwell's demon: entropy, information, computing* (Princeton University Press, 2014). 90

[244] C. H. Bennett, *The thermodynamics of computation—a review*, Int. J. Theor. Phys. **21**, 905 (1982), URL https://doi.org/10.1007/BF0208415. 90

[245] T. Sagawa and M. Ueda, *Second law of thermodynamics with discrete quantum feedback control*, Phys. Rev. Lett. **100**, 080403 (2008), URL https://doi.org/10.1103/PhysRevLett.100.080403. 90

[246] T. Sagawa and M. Ueda, *Generalized jarzynski equality under nonequilibrium feedback control*, Phys. Rev. Lett. **104**, 090602 (2010), URL https://doi.org/10.1103/PhysRevLett.104.090602.

[247] M. Esposito and G. Schaller, *Stochastic thermodynamics for "maxwell demon" feedbacks*, EPL **99**, 30003 (2012), URL https://doi.org/10.1209/0295-5075/99/30003.

[248] S. Deffner and C. Jarzynski, *Information processing and the second law of thermodynamics: An inclusive, hamiltonian approach*, Phys. Rev. X **3**, 041003 (2013), URL https://doi.org/10.1103/PhysRevX.3.041003.

[249] A. C. Barato and U. Seifert, *Unifying three perspectives on information processing in stochastic thermodynamics*, Phys. Rev. Lett. **112**, 090601 (2014), URL https://doi.org/10.1103/PhysRevLett.112.090601.

[250] J. M. Parrondo, J. M. Horowitz, and T. Sagawa, *Thermodynamics of information*, Nat. Phys. **11**, 131 (2015), URL https://doi.org/10.1038/NPHYS3230. 90

[251] D. V. Averin, M. Möttönen, and J. P. Pekola, *Maxwell's demon based on a single-electron pump*, Phys. Rev. B **84**, 245448 (2011), URL https://doi.org/10.1103/PhysRevB.84.245448. 90

[252] D. Mandal and C. Jarzynski, *Work and information processing in a solvable model of maxwell's demon*, Proc. Natl. Acad. Sci. U.S.A. **109**, 11641 (2012), URL https://doi.org/10.1073/pnas.1204263109.

[253] R. Sánchez and M. Büttiker, *Detection of single-electron heat transfer statistics*, EPL **100**, 47008 (2012), URL https://doi.org/10.1209/0295-5075/100/47008.

[254] A. C. Barato and U. Seifert, *An autonomous and reversible maxwell's demon*, EPL **101**, 60001 (2013), URL https://doi.org/10.1209/0295-5075/101/60001.

[255] J. Bergli, Y. M. Galperin, and N. B. Kopnin, *Information flow and optimal protocol for a maxwell-demon single-electron pump*, Phys. Rev. E **88**, 062139 (2013), URL https://doi.org/10.1103/PhysRevE.88.062139.

[256] P. Strasberg, G. Schaller, T. Brandes, and C. Jarzynski, *Second laws for an information driven current through a spin valve*, Phys. Rev. E **90**, 062107 (2014), URL https://doi.org/10.1103/PhysRevE.90.062107.

[257] K. Tanabe, *Coupled-double-quantum-dot environmental information engines: A numerical analysis*, J. Phys. Soc. Jpn. **85**, 064003 (2016), URL https://doi.org/10.7566/JPSJ.85.064003. 91

[258] R. S. Whitney, R. Sánchez, F. Haupt, and J. Splettstoesser, *Thermoelectricity without absorbing energy from the heat sources*, Physica E Low Dimens. Syst. Nanostruct. **82**, 176 (2016), URL https://doi.org/10.1016/j.physe.2015.09.025.

[259] R. Sánchez, *Correlation-induced refrigeration with superconducting single-electron transistors*, Appl. Phys. Lett. **111**, 223103 (2017), URL https://doi.org/10.1063/1.5008481. 90

[260] V. Serreli, C.-F. Lee, E. R. Kay, and D. A. Leigh, *A molecular information ratchet*, Nature **445**, 523 (2007), URL https://doi.org/10.1038/nature05452. 90

[261] G. N. Price, S. T. Bannerman, K. Viering, E. Narevicius, and M. G. Raizen, *Single-photon atomic cooling*, Phys. Rev. Lett. **100**, 093004 (2008), URL https://doi.org/10.1103/PhysRevLett.100.093004.

[262] J. J. Thorn, E. A. Schoene, T. Li, and D. A. Steck, *Experimental realization of an optical one-way barrier for neutral atoms*, Phys. Rev. Lett. **100**, 240407 (2008), URL https://doi.org/10.1103/PhysRevLett.100.240407.

[263] M. G. Raizen, *Comprehensive control of atomic motion*, Science **324**, 1403 (2009), URL https://doi.org/10.1126/science.1171506.

[264] S. Toyabe, T. Sagawa, M. Ueda, E. Muneyuki, and M. Sano, *Experimental demonstration of information-to-energy conversion and validation of the generalized jarzynski equality*, Nat. Phys. **6**, 988 (2010), URL https://doi.org/10.1038/nphys1821.

[265] A. Bérut, A. Arakelyan, A. Petrosyan, S. Ciliberto, R. Dillenschneider, and E. Lutz, *Experimental verification of landauer/'s principle linking information and thermodynamics*, Nature **483**, 187 (2012), URL https://doi.org/10.1038/nature10872.

[266] J. V. Koski, V. F. Maisi, J. P. Pekola, and D. V. Averin, *Experimental realization of a szilard engine with a single electron*, Proc. Natl. Acad. Sci. U.S.A. **111**, 13786 (2014), URL https://doi.org/10.1073/pnas.1406966111. 114, 121, 140

[267] É. Roldán, I. A. Martinez, J. M. Parrondo, and D. Petrov, *Universal features in the energetics of symmetry breaking*, Nat. Phys. **10**, 457 (2014), URL https://doi.org/10.1038/nphys2940.

[268] K. Chida, K. Nishiguchi, G. Yamahata, H. Tanaka, and A. Fujiwara, *Thermal-noise suppression in nano-scale si field-effect transistors by feedback control based on single-electron detection*, Appl. Phys. Lett. **107**, 073110 (2015), URL https://doi.org/10.1063/1.4928656.

[269] P. A. Camati, J. P. S. Peterson, T. B. Batalhão, K. Micadei, A. M. Souza, R. S. Sarthour, I. S. Oliveira, and R. M. Serra, *Experimental rectification of entropy production by maxwell's demon in a quantum system*, Phys. Rev. Lett. **117**, 240502 (2016), URL https://doi.org/10.1103/PhysRevLett.117.240502.

[270] H. Thierschmann, R. Sánchez, B. Sothmann, H. Buhmann, and L. W. Molenkamp, *Thermoelectrics with coulomb-coupled quantum dots*, C. R. Phys. **17**, 1109 (2016), URL https://doi.org/10.1016/j.crhy.2016.08.001.

[271] M. D. Vidrighin, O. Dahlsten, M. Barbieri, M. Kim, V. Vedral, and I. A. Walmsley, *Photonic maxwell's demon*, Phys. Rev. Lett. **116**, 050401 (2016), URL https://doi.org/10.1103/PhysRevLett.116.050401.

[272] K. Chida, S. Desai, K. Nishiguchi, and A. Fujiwara, *Power generator driven by maxwell's demon*, Nat. Commun. **8** (2017), URL https://doi.org/10.1038/ncomms15301. 90, 91

[273] F. Giazotto and M. J. Martínez-Pérez, *The josephson heat interferometer*, Nature **492**, 401 (2012), URL https://doi.org/10.1038/nature11702. 93

[274] O. Maillet, P. A. Erdman, V. Cavina, B. Bhandari, E. T. Mannila, J. T. Peltonen, A. Mari, F. Taddei, C. Jarzynski, V. Giovannetti, and J. P. Pekola, *Optimal probabilistic work extraction beyond the free energy difference with a single-electron device*, Phys. Rev. Lett. **122**, 150604 (2019), URL https://doi.org/10.1103/PhysRevLett.122.150604. 114, 121, 123

[275] O. Maillet, D. A. S. Rengel, J. T. Peltonen, D. S. Golubev, and J. P. Pekola, *Electric field control of radiative heat transfer in a superconducting circuit*, https://arxiv.org/abs/2002.11591 (2020). 93

[276] C. Starr, *The copper oxide rectifier*, Physics **7**, 15 (1936), URL https://doi.org/10.1063/1.1745338. 93

[277] M. Terraneo, M. Peyrarad, and G. Casati, *Controlling the energy flow in nonlinear lattices: A model for a thermal rectifier*, Phys. Rev. Lett. **88**, 094302 (2002), URL https://doi.org/10.1103/PhysRevLett.88.094302. 93

[278] B. Li, L. Wang, and G. Casati, *Thermal diode: Rectification of heat flux*, Phys. Rev. Lett. **93**, 184301 (2004), URL https://doi.org/10.1103/PhysRevLett.93.184301.

[279] D. Segal and A. Nitzan, *Spin-boson thermal rectifier*, Phys. Rev. Lett. **94**, 034301 (2005), URL https://doi.org/10.1103/PhysRevLett.94.034301. 94, 95

[280] J. P. Eckmann and C. M. Monasterio, *Thermal rectification in billiardlike systems*, Phys. Rev. B **97**, 094301 (2006), URL https://doi.org/10.1103/PhysRevLett.97.094301.

[281] N. Zeng and J. S. Wang, *Mechanisms causing thermal rectification: The influence of phonon frequency, asymmetry, and nonlinear interactions*, Phys. Rev. B **78**, 024305 (2008), URL https://doi.org/10.1103/PhysRevB.78.024305.

[282] T. Ojanen, *Selection-rule blockade and rectification in quantum heat transport*, Phys. Rev. B **80**, 180301(R) (2009), URL https://doi.org/10.1103/PhysRevB.80.180301.

[283] T. Ruokola, T. Ojanen, and A. P. Jauho, *Thermal rectification in nonlinear quantum circuits*, Phys. Rev. B **79**, 144306 (2009), URL https://doi.org/10.1103/PhysRevB.79.144306. 94, 95

[284] L. A. Wu and D. Segal, *Sufficient conditions for thermal rectification in hybrid quantum structures*, Phys. Rev. Lett. **102**, 095503 (2009), URL https://doi.org/10.1103/PhysRevLett.102.095503. 94, 95

[285] L. A. Wu, C. X. Yu, and D. Segal, *Nonlinear quantum heat transfer in hybrid structures: Sufficient conditions for thermal rectification*, Phys. Rev. E **80**, 041103 (2009), URL https://doi.org/10.1103/PhysRevE.80.041103. 94

[286] C. R. Otey, W. T. Lau, and S. Fan, *Thermal rectification through vacuum*, Phys. Rev. Lett. **104**, 154301 (2010), URL https://doi.org/10.1103/PhysRevLett.104.154301.

[287] T. Ruokola and T. Ojanen, *Single-electron heat diode: Asymmetric heat transport between electronic reservoirs through coulomb islands*, Phys. Rev. B **83**, 241404(R) (2011), URL https://doi.org/10.1103/PhysRevB.83.241404. 94

[288] K. G. S. H. Gunawardana, K. Mullen, J. Hu, Y. P. Chen, and X. Ruan, *Tunable thermal transport and thermal rectification in strained graphene nanoribbons*, Phys. Rev. B **85**, 245417 (2012), URL https://doi.org/10.1103/PhysRevB.85.245417.

[289] M. J. Martínez-Pérez and F. Giazotto, *Efficient phase-tunable josephson thermal rectifier*, Appl. Phys. Lett. **102**, 182602 (2013), URL https://doi.org/10.1063/1.4804550. 94

[290] G. T. Landi, E. Novais, M. J. de Oliveira, and D. Karevski, *Flux rectification in the quantum xxz chain*, Phys. Rev. E **90**, 042142 (2014), URL https://doi.org/10.1103/PhysRevE.90.042142.

[291] Y. Y. Liu, W. X. Zhou, L. M. Tang, and K. Q. Chen, *An important mechanism for thermal rectification in graded nanowires*, Appl. Phys. Lett. **105**, 203111 (2014), URL https://doi.org/10.1063/1.4902427.

[292] J. H. Jiang, M. Kulkarni, D. Segal, and Y. Imry, *Phonon thermoelectric transistors and rectifiers*, Phys. Rev. B **92**, 045309 (2015), URL https://doi.org/10.1103/PhysRevB.92.045309.

[293] R. Sánchez, B. Sothmann, and A. N. Jordan, *Heat diode and engine based on quantum hall edge states*, New J. Phys. **17**, 075006 (2015), URL https://doi.org/10.1088/1367-2630/17/7/075006.

[294] K. Joulain, J. Drevillon, Y. Ezzahari, and J. Ordonez-Miranda, *Quantum thermal transistor*, Phys. Rev. Lett. **116**, 200601 (2016), URL https://doi.org/10.1103/PhysRevLett.116.200601.

[295] B. K. Agarwalla and D. Segal, *Energy current and its statistics in the nonequilibrium spin-boson model: Majorana fermion representation*, New J. Phys. **19**, 043030 (2017), URL https://doi.org/10.1088/1367-2630/aa6657. 94, 95, 98, 188, 191

[296] A. Marcos-Vicioso, C. López-Jurado, M. Ruiz-Garcia, and R. Sánchez, *Thermal rectification with interacting electronic channels: Exploiting degeneracy, quantum superpositions, and interference*, Phys. Rev. B **98**, 035414 (2018), URL https://doi.org/10.1103/PhysRevB.98.035414. 93, 94

[297] C. W. Chang, D. Okawa, A. Majumdar, and A. Zettl, *Solid-state thermal rectifier*, Science **314**, 1121 (2006), URL https://doi.org/10.1126/science.1132898. 93

[298] M. Schmotz, J. Maier, E. Scheer, and P. Leiderer, *A thermal diode using phonon rectification*, New J. Phys. **13**, 113027 (2011), URL https://doi.org/10.1088/1367-2630/13/11/113027.

[299] M. J. Martínez-Pérez, A. Fornieri, and F. Giazotto, *Rectification of electronic heat current by a hybrid thermal diode*, Nat. Nanotechnol. **10**, 303 (2015), URL https://doi.org/10.1038/nnano.2015.11. 93

[300] R. Landauer, *Spatial variation of currents and fields due to localized scatterers in metallic conduction*, IBM J. Res. Dev. **1**, 223 (1957), URL https://doi.org/10.1147/rd.13.0223. 93

[301] M. Büttiker, Y. Imry, R. Landauer, and S. Pinhas, *Generalized many-channel conductance formula with application to small rings*, Phys. Rev. B **31**, 6207 (1985), URL https://doi.org/10.1103/PhysRevB.31.6207. 93

[302] A. Riera-Campeny, M. Mehboudi, M. Pons, and A. Sanpera, *Dynamically induced heat rectification in quantum systems*, Phys. Rev. E **99**, 032126 (2019), URL https://doi.org/10.1103/PhysRevE.99.032126. 94

[303] T. Ojanen and A. P. Jauho, *Mesoscopic photon heat transistor*, Phys. Rev. Lett. **100**, 155902 (2008), URL https://doi.org/10.1103/PhysRevLett.100.155902. 94, 98

[304] U. Weiss, *Quantum Dissipative Systems* (World Scientific, 2012). 97, 107, 191

[305] Y. Meir and N. S. Wingreen, *Landauer formula for the current through an interacting electron region*, Phys. Rev. Lett. **68**, 2512 (1992), URL https://doi.org/10.1103/PhysRevLett.68.2512. 98

[306] J. S. Wang, J. Wang, and N. Zeng, *Nonequilibrium green's function approach to mesoscopic thermal transport*, Phys. Rev. B **74**, 033408 (2006), URL https://doi.org/10.1103/PhysRevB.74.033408. 98

[307] K. Saito, *Energy dissipation and fluctuation response in driven quantum langevin dynamics*, Europhys. Lett. **83**, 50006 (2008), URL https://doi.org/10.1209/0295-5075/83/50006.

[308] K. A. Velizhanin, M. Thoss, and H. Wang, *Meir–wingreen formula for heat transport in a spin-boson nanojunction model*, J. Chem. Phys. **133**, 084503 (2010), URL https://doi.org/10.1063/1.3483127.

[309] D. Segal, *Heat transfer in the spin-boson model: A comparative study in the incoherent tunneling regime*, Phys. Rev. E **90**, 012148 (2014), URL https://doi.org/10.1103/PhysRevE.90.012148. 98

[310] J. Liu, H. Xu, B. Li, and C. Wu, *Energy transfer in the nonequilibrium spin-boson model: From weak to strong coupling*, Phys. Rev. E **96**, 012135 (2017), URL https://doi.org/10.1103/PhysRevE.96.012135. 105

[311] P. Schad, Y. Makhlin, B. Narozhny, G. Schön, and A. Shnirman, *Majorana representation for dissipative spin systems*, Ann. Phys. (N. Y.) **361**, 401 (2015), URL https://doi.org/10.1016/j.aop.2015.07.006. 105, 188

[312] M. Sassetti and U. Weiss, *Correlation functions for dissipative two-state systems: Effects of the initial preparation*, Phys. Rev. A **41**, 5383 (1990), URL https://doi.org/10.1103/PhysRevA.41.5383. 107

[313] R. Kosloff, *Quantum thermodynamics: a dynamical viewpoint.*, Entropy **15**, 2100 (2013), URL https://doi.org/10.3390/e15062100. 113

[314] R. Alicki and R. Kosloff, *Thermodynamics in the Quantum Regime: Fundamental Aspects and New Directions* (Springer, Berlin, 2019). 113

[315] L. Buffoni, A. Solfanelli, P. Verrucchi, A. Cuccoli, and M. Campisi, *Quantum measurement cooling*, Phys. Rev. Lett. **122**, 070603 (2019), URL https://doi.org/10.1103/PhysRevLett.122.070603. 113

[316] J. Goold, M. Huber, A. Riera, L. del Rio, and P. Skrzypczyk, *The role of quantum information in thermodynamics-a topical review*, J. Phys. A: Math. Theor. **49**, 143001 (2016), URL https://doi.org/10.1088/1751-8113/49/14/143001. 113

[317] J. Chen, *The maximum power output and maximum efficiency of an irreversible carnot heat engine*, J. Phys. D **27**, 1144 (1994), URL https://doi.org/10.1088/0022-3727/27/6/011. 113, 116, 123

[318] Y. Rezek and R. Kosloff, *Irreversible performance of a quantum harmonic heat engine*, New J. Phys. **8**, 83 (2006), URL https://doi.org/10.1088/1367-2630/8/5/083. 116, 124

[319] M. O. Scully, K. R. Chapin, K. E. Dorfman, M. B. Kim, and A. Svidzinsky, *Quantum heat engine power can be increased by noise-induced coherence*, Proc. Natl. Acad. Sci. U.S.A. **108**, 15097 (2011), URL https://doi.org/10.1073/pnas.1110234108.

[320] O. Abah, J. Roßnagel, G. Jacob, S. Deffner, F. Schmidt-Kaler, K. Singer, and E. Lutz, *Single-ion heat engine at maximum power*, Phys. Rev. Lett. **109**, 203006 (2012), URL https://doi.org/10.1103/PhysRevLett.109.203006. 116, 123, 124

[321] L. A. Correa, J. P. Palao, G. Adesso, and D. Alonso, *Performance bound for quantum absorption refrigerators*, Phys. Rev. E **87**, 042131 (2013), URL https://doi.org/10.1103/PhysRevE.87.042131.

[322] K. E. Dorfman, D. V. Voronine, S. Mukamel, and M. O. Scully, *Photosynthetic reaction center as a quantum heat engine*, Proc. Natl. Acad. Sci. U.S.A. **110**, 2746 (2013), URL https://doi.org/10.1073/pnas.1212666110.

[323] S. Juergens, F. Haupt, M. Moskalets, and J. Splettstoesser, *Thermoelectric performance of a driven double quantum dot*, Phys. Rev. B **87**, 245423 (2013), URL https://doi.org/10.1103/PhysRevB.87.245423.

[324] K. Zhang, F. Bariani, and P. Meystre, *Quantum optomechanical heat engine*, Phys. Rev. Lett. **112**, 150602 (2014), URL https://doi.org/10.1103/PhysRevLett.112.150602. 123

[325] M. Campisi and R. Fazio, *The power of a critical heat engine*, Nat. Commun. **7**, 11895 (2016), URL https://doi.org/10.1038/ncomms11895.

[326] K. Brandner, M. Bauer, and S. U., *Universal coherence-induced power losses of quantum heat engines in linear response*, Phys. Rev. Lett. **119**, 170602 (2017), URL https://doi.org/10.1103/PhysRevLett.119.170602.

[327] G. Watanabe, B. P. Venkatesh, P. Talkner, and A. del Campo, *Quantum performance of thermal machines over many cycles*, Phys. Rev. Lett. **118**, 050601 (2017), URL https://doi.org/10.1103/PhysRevLett.118.050601. 113, 116, 123, 124

[328] M. H. Rubin and B. Andresen, *Optimal staging of endoreversible heat engines*, J. Appl. Phys. **53**, 1 (1982), URL https://doi.org/10.1063/1.331592. 113, 124

[329] H. Song, L. Chen, and F. Sun, *Endoreversible heat-engines for maximum power-output with fixed duration and radiative heat-transfer law*, Appl. Energy **84**, 374 (2007), URL https://doi.org/10.1016/j.apenergy.2006.09.003. 113, 124

[330] A. C. V. Mukherjee, A. Mari, T. Caneva, S. Montangero, T. Calarco, R. Fazio, and V. Giovannetti, *Speeding up and slowing down the relaxation of a qubit by optimal control*, Phys. Rev. A **88**, 062326 (2013), URL https://doi.org/10.1103/PhysRevA.88.062326. 113

[331] B. Bonnard, M. Chyba, and D. Sugny, *Time-minimal control of dissipative two-level quantum systems: the generic case*, IEEE Trans. Aut. Control **54**, 2598 (2009), URL https://doi.org/10.1109/TAC.2009.2031212.

[332] T. M. Zhang, R. B. Wu, F. H. Zhang, T. J. Tarn, and G. L. Long, *Minimum-time selective control of homonuclear spins*, IEEE Trans. Control Syst. Technol. **23**, 2018 (2015), URL https://doi.org/10.1109/TCST.2015.2390191. 113

[333] R. Roloff, M. Wenin, and W. Pötz, *Optimal control for open quantum systems: qubits and quantum gates*, J. Comp. Theor. Nanoscience **6**, 1837 (2009), URL https://doi.org/10.1166/jctn.2009.1246. 113

[334] T. Schulte-Herbrüggen, A. Spörl, N. Khaneja, and S. J. Glaser, *Optimal control for generating quantum gates in open dissipative systems*, J. Phys. B: At. Mol. Opt. Phys. **44**, 154013 (2011), URL https://doi.org/10.1088/0953-4075/44/15/154013. 113

[335] S. Sauer, C. Gneiting, and A. Buchleitner, *Optimal coherent control to counteract dissipation*, Phys. Rev. Lett. **111**, 030405 (2013), URL https://doi.org/10.1103/PhysRevLett.111.030405. 113

[336] A. Carlini, A. Hosoya, T. Koike, and Y. Okudaira, *Time-optimal quantum evolution*, Phys. Rev. Lett. **96**, 060503 (2006), URL https://doi.org/10.1103/PhysRevLett.96.060503. 113

[337] T. Feldmann, E. Geva, R. Kosloff, and P. Salamon, *Heat engines in finite time governed by master equations*, Am. J. Phys. **64**, 485 (1996), URL https://doi.org/10.1119/1.18197. 114, 123

[338] T. Feldmann and R. Kosloff, *Performance of discrete heat engines and heat pumps in finite time*, Phys. Rev. E **61**, 4774 (2000), URL https://doi.org/10.1103/PhysRevE.61.4774. 121

[339] L. Cerino, A. Puglisi, and A. Vulpiani, *Linear and nonlinear thermodynamics of a kinetic heat engine with fast transformations*, Phys. Rev. E **93**, 042116 (2016), URL https://doi.org/10.1103/PhysRevE.93.042116. 114, 123

[340] E. Geva and R. Kosloff, *A quantum-mechanical heat engine operating in finite time. a model consisting of spin-1/2 systems as the working fluid*, J. Chem. Phys. **96**, 3054 (1992), URL https://doi.org/10.1063/1.461951. 114, 124, 140

[341] M. Esposito, R. Kawai, K. Lindenberg, and C. Van den Broeck, *Quantum-dot carnot engine at maximum power*, Phys. Rev. E **81**, 041106 (2010), URL https://doi.org/10.1103/PhysRevE.81.041106. 114, 117, 121, 123, 140

[342] H. Quan, Y. Liu, C. Sun, and F. Nori, *Quantum thermodynamic cycles and quantum heat engines*, Phys. Rev. E **76**, 031105 (2007), URL https://doi.org/10.1103/PhysRevE.76.031105. 116, 124

[343] B. Karimi and J. P. Pekola, *Otto refrigerator based on a superconducting qubit: Classical and quantum performance*, Phys. Rev. B **94**, 184503 (2016), URL https://doi.org/10.1103/PhysRevB.94.184503. 121

[344] R. Kosloff and Y. Rezek, *The quantum harmonic otto cycle*, Entropy **19**, 136 (2017), URL https://doi.org/10.3390/e19040136. 116, 124

[345] J. Wang, Z. Wu, and J. He, *Quantum otto engine of a two-level atom with single-mode fields*, Phys. Rev. E **85**, 041148 (2012), URL https://doi.org/10.1103/PhysRevE.85.041148. 117

[346] M. R. Wegewijs and Y. V. Nazarov, *Resonant tunneling through linear arrays of quantum dots*, Phys. Rev. B **60**, 14318 (1999), URL https://doi.org/10.1103/PhysRevB.60.14318. 118, 121, 176

[347] N. V. Horne, D. Yum, T. Dutta, P. Hänggi, J. Gong, D. Poletti, and M. Mukherjee, *Single-atom energy-conversion device with a quantum load*, NPJ Quantum Inf. **6**, 37 (2020), URL https://doi.org/10.1038/s41534-020-0264-6. 121, 123

[348] K. Huang, *Statistical Mechanics, 2nd ed.* (Wiley, 1987). 123

[349] L. Arrachea, M. Moskalets, and L. Martin-Moreno, *Heat production and energy balance in nanoscale engines driven by time-dependent fields*, Phys. Rev. B **75**, 245420 (2007), URL https://doi.org/10.1103/PhysRevB.75.245420. 123

[350] B. Bhandari, P. T. Alonso, F. Taddei, F. von Oppen, R. Fazio, and L. Arrachea, *Geometric properties of adiabatic quantum thermal machines*, https://arxiv.org/abs/2002.02225 (2020). 123

[351] J. Klatzow, J. N. Becker, P. M. Ledingham, C. Weinzetl, K. T. Kaczmarek, D. J. Saunders, J. Nunn, I. A. Walmsley, R. Uzdin, and E. Poem, *Experimental demonstration of quantum effects in the operation of microscopic heat engines*, Phys. Rev. Lett. **122**, 110601 (2019), URL https://doi.org/10.1103/PhysRevLett.122.110601. 123

[352] D. von Lindenfels, O. Gräb, C. T. Schmiegelow, V. Kaushal, J. Schulz, M. T. Mitchison, J. Goold, F. Schmidt-Kaler, and U. G. Poschinger, *Spin heat engine coupled to a harmonic-oscillator flywheel*, Phys. Rev. Lett. **123**, 080602 (2019), URL https://doi.org/10.1103/PhysRevLett.123.080602. 123

[353] J. E. Avron, M. Fraas, G. M. Graf, and P. Grech, *Adiabatic theorems for generators of contracting evolutions*, Commun. Math. Phys. **314**, 163 (2012), URL https://doi.org/10.1007/s00220-012-1504-1. 123

[354] P. Abiuso and M. Perarnau-Llobet, *Optimal cycles for low-dissipation heat engines*, Phys. Rev. Lett. **124**, 110606 (2020), URL https://doi.org/10.1103/PhysRevLett.124.110606. 123, 124, 128, 137, 142

[355] P. W. Claeys, M. Pandey, D. Sels, and A. Polkovnikov, *Floquet-engineering counterdiabatic protocols in quantum many-body systems*, Phys. Rev. Lett. **123**, 090602 (2019), URL https://doi.org/10.1103/PhysRevLett.123.090602. 124

[356] T. Villazon, A. Polkovnikov, and A. Chandran, *Swift heat transfer by fast-forward driving in open quantum systems*, Phys. Rev. A **100**, 012126 (2019), URL https://doi.org/10.1103/PhysRevA.100.012126. 124

[357] A. E. Allahverdyan, K. V. Hovhannisyan, A. V. Melkikh, and S. G. Gevorkian, *Carnot cycle at finite power: Attainability of maximal efficiency*, Phys. Rev. Lett. **111**, 050601 (2013), URL https://doi.org/10.1103/PhysRevLett.111.050601. 124, 136, 142

[358] R. Dann and R. Kosloff, *Qunatum signatures in the quantum carnot cycle*, New J. Phys. **22**, 013055 (2020), URL https://doi.org/10.1088/1367-2630/ab6876. 124

[359] J. Chen, C. Sun, and H. Dong, *Boosting the performance of quantum otto heat engines*, Phys. Rev. E **100**, 032144 (2019), URL https://doi.org/10.1103/PhysRevE.100.032144. 124

[360] A. Das and V. Mukherjee, *Quantum-enhanced finite-time otto cycle*, Phys. Rev. B **2**, 033083 (2020), URL https://doi.org/10.1103/PhysRevResearch.2.033083. 124

[361] P. A. Erdman, V. Cavina, R. Fazio, F. Taddei, and V. Giovannetti, *Maximum power and corresponding efficiency for two-level heat engines and refrigerators: optimality of fast cycles*, New J. Phys. **21**, 103049 (2019), URL https://doi.org/10.1088/1367-2630/ab4dca. 124, 128, 138

[362] H. Spohn, *Kinetic equations from hamiltonian dynamics: Markovian limits*, Rev. Mod. Phys. **52**, 569 (1980), URL https://doi.org/10.1103/RevModPhys.52.569. 126, 209, 210

[363] G. Teschl, *Ordinary differential equations and dynamical systems* (American Mathematical Soc., 2012). 127

[364] P. Salamon and R. S. Berry, *Thermodynamic length and dissipated availability*, Phys. Rev. Lett. **51**, 1127 (1983), URL https://doi.org/10.1103/PhysRevLett.51.1127. 128

[365] M. Scandi and M. Perarnau-Llobet, *Thermodynamic length in open quantum systems*, Quantum **3**, 197 (2019), URL https://doi.org/10.22331/q-2019-10-24-197. 128

[366] D. E. Kirk, *Optimal Control Theory: an Introduction* (Dover, 2004). 128

[367] U. P. Gomes, D. Ercolani, V. Zannier, F. Beltram, and L. Sorba, *Controlling the diameter distribution and density of InAs nanowires grown by au-assisted methods*, Semicond. Sci. Technol. **30**, 115012 (2015), URL https://doi.org/10.1088/0268-1242/30/11/115012. 161

[368] V. Zannier, F. Rossi, V. G. Dubrovskii, D. Ercolani, S. Battiato, and L. Sorba, *Nanoparticle stability in axial InAs–InP nanowire heterostructures with atomically sharp interfaces*, Nano Lett. **18**, 167 (2017), URL https://doi.org/10.1021/acs.nanolett.7b03742. 161

[369] H. Sprekeler, G. Kießlich, A. Wacker, and E. Schöll, *Coulomb effects in tunneling through a quantum dot stack*, Phys. Rev. B **69**, 125328 (2004), URL https://doi.org/10.1103/PhysRevB.69.125328. 177

[370] W. Mao, P. Coleman, C. Hooley, and D. Langreth, *Spin dynamics from majorana fermions*, Phys. Rev. Lett. **91**, 207203 (2003), URL https://doi.org/10.1103/PhysRevLett.91.207203. 187, 188

[371] A. Shnirman and Y. Makhlin, *Spin-spin correlators in the majorana representation*, Phys. Rev. Lett. **91**, 207204 (2003), URL https://doi.org/10.1103/PhysRevLett.91.207204. 187

[372] C. Chicone, *Ordinary Differential Equations with Applications* (Springer-Verlag, New York, 1999). 196

[373] D. Burgarth, G. Chiribella, V. Giovannetti, P. Perinotti, and K. Yuasa, *Ergodic and mixing quantum channels in finite dimensions*, New J. Phys. **15**, 073045 (2013), URL https://doi.org/10.1088/1367-2630/15/7/073045. 208, 209

[374] A. S. Holevo, *Statistical Structure of Quantum Theory* (Springer, 2001). 209

[375] R. Alicki and K. Lendi, *Statistical Structure of Quantum Theory* (Springer, 2007).

[376] S. G. Schirmer and X. Wang, *Stabilizing open quantum systems by markovian reservoir engineering*, Phys. Rev. A **81**, 062306 (2010), URL https://doi.org/10.1103/PhysRevA.81.062306.

[377] B. Baumgartner and H. Narnhofer, *The structures of state space concerning quantum dynamical semigroups*, Rev. Math. Phys. **24**, 1250001 (2012), URL https://doi.org/10.1142/S0129055X12500018. 209

[378] J. Watrous, *The theory of quantum information* (Cambridge University Press, 2018). 213

[379] W. Rudin, *Principles of mathematical analysis* (McGraw-hill, 1964). 215, 216